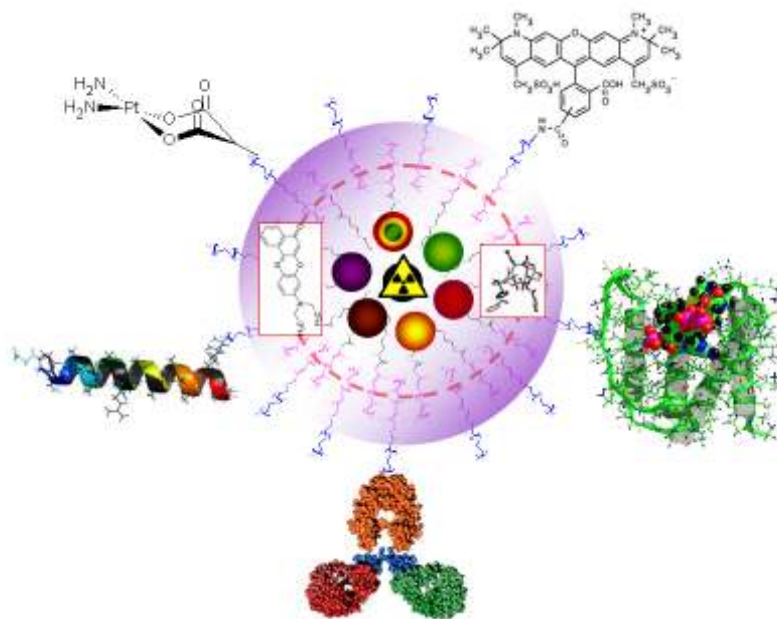




PEO-ligand design for biofunctionalisation of hydrophobic nanoparticles and their use in theragnostics



Dissertation

submitted to the
Department of Chemistry, University of Hamburg

for the degree
Doctor of Natural Sciences

by

Elmar Pöselt

Hamburg 2009



Meiner Familie & meiner Nina in Liebe gewidmet.

The work described in this thesis was carried out in the institute of physical chemistry at the university of Hamburg in the group of Prof. Dr. Horst Weller and Prof. Dr. Stephan Förster.

1. Referee: Prof. Dr. Horst Weller
2. Referee: Prof. Dr. Stephan Förster

Tag der Disputation: 13.11.2009

list of abbreviations

AIBN	azobisisobutyronitrile
AZT	azidothymidine
BSA	bovine serum albumine
CAN	center for applied nanotechnology (Hamburg)
CDI	1,1'-carbonyldiimidazol
CEACAM	carcinoembryonic antigen-related cell adhesion molecule
DCC	dicyclohexylcarbodiimide
DCM	dichlormethane
DDA	dodecylamine
DETA	2,2'-diaminodiethylamine
DLS	dynamic light scattering
DMAP	4-dimethylaminopyridine
DMSO	dimethyl sulfoxide
DVB	divinylbenzene
EDC	1-ethyl-3-(3-dimethylaminopropyl) carbodiimide hydrochloride
ELISA	enzyme-linked immunosorbent assay
eq.	equivalent
<i>et al.</i>	<i>et altera</i>
Fab	fragment, antigen-binding
F(ab) ₂	fragment, antigen-binding
FACS	fluorescence activated cell sorting
FMOc	fluorenylmethyloxycarbonyl
Fc	fragment, crystallizable
FRET	(Förster-) fluorescence resonance energy transfer
FTIR	fourier transformed infrared spectroscopy
HMBC	heteronuclear multiple bond correlation
HMQC	heteronuclear multiple quantum coherence
HR-TEM	high resolution transmission electron microscopy
PCL	poly(ϵ -caprolactone)
PEG	poly(ethylene glycol) (PEO)
PEI	poly(ethylene imine)
PEO	poly(ethylene oxide) (PEG)
PI	poly(isoprene)
MALDI-TOF	matrix assisted laser desorption/ionisation - time of flight
MeOH	methanol
MES	2-(<i>N</i> -morpholino)ethanesulfonic
MRI	magnetic resonance imaging
MWCO	molecular weight cut off

NMR	nuclear magnetic resonance
NP	nanoparticle
N3	2,2'-diaminodiethylamine (DETA)
N4	tris(2-aminoethyl)amine
PBS	phosphate buffered saline
PSD	particle size distribution
QD/P	quantum dot to ligand ratio
QDs	quantum dots
QY	quantum yield
rpm	revolutions per minute
scFv	single chain fragment variable
SDBS	sodium dodecyl benzene sulfonate
SDS	sodium dodecyl sulfate
SEC	size exclusion chromatography (GPC)
SPIONs	superparamagnetic iron oxide nanoparticles
sulfo-NHS	<i>N</i> -hydroxysulfosuccinimide
TEM	transmission electron microscopy
TG	thermogravimetric analysis
THF	tetrahydrofuran
TOP	tri- <i>n</i> -octylphosphine
TOPO	tri- <i>n</i> -octylphosphine oxide
Tween [®] 80	polyoxyethylene(20)-sorbitan-monooleat (polysorbat 80)
VA044	2,2'-azobis[2-(2-imidazolin-2-yl)propane]dihydrochloride (WAKO)
v/v	volume per volume
w/v	weight per volume
XRD	powder X-ray diffraction measurements

table of contents

1	Introduction & Background	9
1.1	Properties of nanoparticles	11
1.2	Ligand shell	11
1.2.1	TOP/TOPO-shell	11
1.2.2	Hydrophilic ligands	12
1.2.3	Benefits of poly(ethylene oxide) (PEO) as a ligand	14
1.2.4	Functionalisation of the ligand shell	15
1.2.5	Emulsionpolymerisation	15
1.2.5.1	Miniemulsion	17
1.2.5.2	Microemulsion	18
1.3	Biological applications	19
1.3.1	Protein (antibody) coupling	24
2	Results and Discussion	27
2.1	Synthesis and characterization of PEO- <i>b</i> -PCL- <i>b</i> -PEI	27
2.1.1	Terminal functionalisation of PEO- <i>b</i> -PCL- <i>b</i> -PEI	30
2.2	Ligand exchange with PEO- <i>b</i> -PCL- <i>b</i> -PEI	37
2.2.1	Fluorescence and stability in water	42
2.2.2	Fluorescence in biological buffers	44
2.2.3	Self assembly to multifunctional beads	47
2.2.4	Binding motif $R^1R^2N(-C(S)S^-)$	54
2.2.5	Binding motif PEI-(DDA) ₇₋₈	55
2.2.6	MMA polymerization in the presence of QDs	58
2.3	Synthesis and characterization of PI- <i>b</i> -PEO & PI-N3	59
2.3.1	Terminal functionalisation of PI- <i>b</i> -PEO	61
2.3.1.1	Coupling of carbohydrates, drugs, and dye molecules	68

2.3.1.1.1	Carbohydrate attachment	68
2.3.1.1.2	Dye attachment	70
2.3.1.1.3	Drug attachment	72
2.3.1.1.4	Biomolecule attachment	77
2.4	Ligand exchange with PI- <i>b</i> -PEO	79
2.4.1	Self Assembly to Multifunctional Beads	85
2.4.2	Dilution stability of PI- <i>b</i> -PEO nanocomposites	87
2.4.3	Stability in biological buffers	89
2.4.4	(Förster-) fluorescence resonance energy transfer (FRET) measurements	94
2.5	Phase-transfer based on emulsion polymerisation	101
2.5.1	Emulsifier approach	102
2.5.2	Surfmer approach	108
2.5.3	Surfmer approach using Tween [®] 80	111
2.5.4	Stability tests of Tween [®] 80 emulsion particles	116
2.5.5	Functionalization of Tween [®] 80	117
2.5.6	Fluorescence quenching by (Förster-) fluorescence resonance energy transfer (FRET) 121	
2.6	Relaxivity of clustered SPIONs	123
2.7	Relaxivity of GdPO ₄ nanoparticles	125
2.8	Vesicle formation	126
2.9	Bioapplication	130
2.9.1	Cytotoxicity	130
2.9.2	<i>in vitro</i> & <i>in vivo</i> experiments	136
2.9.3	<i>in vitro</i> cell experiments	137
2.9.3.1	Biacore technique	141
2.9.3.2	Cell culture experiments with anti-CEACAM specific SPIONs	145
2.9.4	<i>in vivo</i> applications	148
2.9.4.1	Anti-CEACAM specific SPIONs	148
2.9.4.2	Anti-YKL-40 specific SPIONs and QDs	151
2.9.4.3	GdPO ₄ nanoparticles in comparison with Magnevist [®]	155

2.9.5	Drug delivery systems	157
2.9.6	Multi-targeting	160
3	Conclusions.....	163
3.1	Ligand shell	163
3.2	Emulsionpolymerization.....	166
3.3	Functionalisation of the ligand shell.....	166
3.4	Integretion and coupling of (bio-)molecules	167
3.5	<i>in vivo</i> applications	168
3.6	Properties of nanoparticles	169
3.7	Self assembly to multifunctional beads	170
4	Zusammenfassung.....	172
5	Summary.....	176
6	Danksagung.....	180
7	Experimental Section.....	183
7.1	Preparation of nanoparticles	183
7.1.1	General preparation of CdSe/CdS/ZnS core/shell/shell nanoparticles	183
7.2	Preparation of ligands	184
7.2.1	PEO- <i>b</i> -PCL- <i>b</i> -PEI based ligands	185
7.2.1.1	Polymer synthesis	185
7.2.1.1.1	Synthesis of poly(ethylene oxide) (PEO)	185
7.2.1.1.2	Synthesis of PEO- <i>b</i> -PCL block copolymers	186
7.2.1.2	Ligand synthesis	186
7.2.1.2.1	Synthesis of PEO- <i>b</i> -PCL- <i>b</i> -PEI	186
7.2.1.2.2	Synthesis of PEO- <i>b</i> -PEI and PEO-N4.....	187
7.2.1.2.3	Binding motif R ¹ R ² N(-C(S)S ⁻)	188
7.2.1.2.4	Binding motif PEI-(DDA) ₇₋₈	188

7.2.1.2.5	Summary of ligands and abbreviations	188
7.2.1.3	Ligand-addition (“exchange”) with PEO- <i>b</i> -PCL- <i>b</i> -PEI.....	189
7.2.1.4	Ligand exchange with PEO-N4 and PEO- <i>b</i> -PEI.....	190
7.2.1.5	Functionalisation	190
7.2.1.6	Buffer tests.....	191
7.2.1.7	MMA polymerization in the presence of QDs	191
7.2.2	PI- <i>b</i> -PEO based ligands.....	192
7.2.2.1	Polymer synthesis	192
7.2.2.1.1	Synthesis of poly(isoprene) (PI)	192
7.2.2.1.2	Synthesis of PI- <i>b</i> -PEO block copolymers	193
7.2.2.2	Synthesis of PI-DETA (PI-N3)	194
7.2.2.3	Ligand exchange.....	194
7.2.2.4	Ligandaddition.....	195
7.2.2.5	Ligand functionalisation	196
7.2.2.5.1	Synthesis of an aldehyde	196
7.2.2.5.1.1	Dess-Martin oxidation	197
7.2.2.5.1.2	Oxidation via PDC	197
7.2.2.5.1.3	Pfitzner-Moffatt oxidation.....	197
7.2.2.5.2	Synthesis of a terminal epoxid	198
7.2.2.5.3	Synthesis of a terminal carboxylic acid function	199
7.2.2.5.4	Synthesis of a terminal azide.....	200
7.2.2.5.5	Synthesis of a terminal amine.....	201
7.2.2.5.6	Synthesis of a terminal alkine.....	203
7.2.2.5.7	Synthesis of a terminal alkene	204
7.2.2.5.8	Synthesis of a terminal boronic acid ester	205
7.2.2.5.9	Synthesis of a terminal halogen.....	206
7.2.2.5.10	Synthesis of a terminal thiol	208
7.2.2.5.11	Synthesis of a terminal pentafluorophenyl ester.....	209
7.2.2.5.12	Modification of carbohydrates	209
7.2.2.6	Coupling strategies	210
7.2.2.6.1	Biofunctionalisation with carbohydrates	210
7.2.2.6.1.1	Huisgen cycloaddition (“click-chemistry”).....	210

7.2.2.6.1.2	EDC & sulfo-NHS coupling.....	212
7.2.2.6.2	Dyes accoutrement	215
7.2.2.6.3	Coupling of chemotherapeutics	216
7.2.2.6.3.1	Coupling of cis-platin	216
7.2.2.6.3.2	Coupling of azidothymidine (AZT).....	217
7.2.2.6.3.3	Coupling of 5-fluorouracil (5-Fu).....	217
7.2.2.6.3.4	Coupling of doxorubicin (DXR, Adriamycin®)	218
7.2.2.6.4	Coupling of bio-molecules	218
7.2.2.6.4.1	Coupling of antibodies (-fragments) via a terminal active ester	218
7.2.2.6.4.2	Coupling of FMOC-glycine.....	219
7.2.2.6.4.3	Coupling of biotin.....	219
7.2.2.6.4.4	Coupling of (±)-α-lipoic acid.....	219
7.2.2.6.4.5	Coupling of arabinogalactan.....	220
7.2.3	Emulsion polymerization.....	220
7.2.3.1	Materials	220
7.2.3.2	Polymerization.....	221
7.2.3.2.1	Emulsifier approach.....	221
7.2.3.2.2	Surfmer approach	222
7.2.3.2.3	Purification of emulsion particles.....	223
7.2.3.3	Functionalisation of emulsifier	223
7.2.3.3.1	Synthesis of w-carboxyl-polyoxyethylenesorbitan monooleate	224
7.2.3.3.2	Implementation of aldehyde terminated Tween®80	225
7.2.3.3.3	Implementation of epoxid terminated Tween®80.....	226
7.2.3.3.4	Implementing of an alkine group into Tween®80	226
7.2.3.3.5	Implementing of an bromide into Tween®80	227
7.2.3.4	Calorimetric Measurements.....	227
7.2.3.5	(Förster-) fluorescence resonance energy transfer (FRET)	227
7.3	Vesicle formation	228
7.4	Biological applications	228
7.4.1	Cell culture	228
7.4.1.1	Determination of the cell count	229
7.4.1.2	Laboratory animals	229

7.4.1.3	Application	230
7.4.1.4	Cellincubation experiments	230
7.4.1.4.1	Incubation of cells	230
7.4.1.4.2	Incubation of cells with anti-CEACAM specific SPIONs	231
7.4.1.4.3	Magnetic resonance imaging (MRI).....	231
7.4.1.4.4	Cell experiments in cooperation with CAN	232
7.4.1.5	Fluorescence activated cell sorting (FACS)	232
7.4.1.6	Biacore technique	234
7.4.1.6.1	coating of nanoparticles.....	235
7.5	Analytic	236
7.5.1	Nuclear magnetic resonance spectroscopy (NMR)	236
7.5.2	Fourier transformed infrared spectroscopy (FTIR)	236
7.5.3	UV-Vis- and fluorescence spectroscopy	236
7.5.4	Transmission electron microscopy (TEM).....	237
7.5.5	Powder X-ray diffraction measurements (XRD).....	237
7.5.6	Dynamic light scattering (DLS)	237
7.5.7	Matrix assisted laser desorption/ionisation time of flight mass spectrometry (MALDI-TOF).....	238
7.5.8	(Förster-) fluorescence resonance energy transfer (FRET)	238
7.5.9	Biacore.....	238
7.5.10	Light microscopy	238
7.5.11	Biological applications	239
7.5.11.1	Magnetic resonance imaging (MRI).....	239
7.5.11.2	Cryo-transection-technique	239
7.5.11.3	Fluorescence microscopy	240
7.5.11.4	Fluorescence activated cell sorting (FACS).....	241
7.5.11.5	Confocal fluorescence microscopy.....	241
8	Literature.....	242

9	Appendix.....	260
9.1	Optical properties of semiconductor nanoparticles (quantum dots).....	260
9.1.1	Valence bond degeneracy and spin-orbit coupling.....	264
9.1.2	Excitonic fine structure.....	266
9.1.3	Blinking behaviour	267
9.1.4	Nonradiative processes in quantum dots	268
9.1.5	Type I/II structures	272
9.2	Core/shell- and multishell-nanocrystals with a CdSe-core.....	273
9.2.1	CdSe/CdS- and CdSe/CdS/ZnS-nanocrystals.....	273
9.3	Magnetic nanoparticles (SPIONs).....	275
9.3.1	Dia- and paramagnetism.....	275
9.3.2	Ferromagnetism	277
9.3.2.1	Domain-formation	279
9.3.2.2	Magnetisation of a ferromagnet.....	281
9.3.3	Antiferromagnetism and ferrimagnetism.....	282
9.4	Magnetism of nanoparticles.....	283
9.4.1	Magnetic resonance imaging	287
9.5	Cytotoxicity	291
9.5.1	LDH-assay	291
9.5.2	Wst-assay.....	292
9.5.3	ROS-assay	292
9.5.4	Cellomics pictures (CAN)	293
9.5.4.1	DEM controls	293
9.5.4.2	FeCl ₃ controls	294
9.5.4.3	PI- <i>b</i> -PEO-CHO.....	295
9.5.4.4	PI- <i>b</i> -PEO-NH ₂	296
9.5.4.5	PI- <i>b</i> -PEO-OH	297
9.5.4.6	PI- <i>b</i> -PEO-COOH.....	298
9.5.4.7	Controll with only cells	299

9.5.5	Cellomics pictures (CAN) using cytotoxicity kit 2	300
9.5.5.1	Valinomycin	300
9.5.5.2	CdCl ₂ & FeCl ₃ control	302
9.5.5.3	PI- <i>b</i> -PEO-CHO	305
9.5.5.4	PI- <i>b</i> -PEO-OH	306
9.5.5.5	PI- <i>b</i> -PEO-COOH	308
9.6	Used chemicals and their safety precaution information	310
9.6.1	Risk phrases (R-Phrases)	313
9.6.2	Combination of risks	315
9.6.3	Safety precaution phrases (S-Phrases)	316
9.6.4	Combined safety phrases	319
10	Erklärung	320

1 Introduction & Background

The multifaceted properties of particles in the size-range of a few nanometers have improved material properties like rigidity, electronics and optical behaviour. Due to the versatile physical properties of such so called nanoparticles, they are currently under focus by a lot of research groups. Their application range spans over sensing, labelling, optical imaging, magnetic resonance imaging (MRI), cell separation, and treatment of disease in the field of biological and medical application^[1-5] to technical tasks like chemical catalysis, stabilizer in colorants, detectors, chips, and solar cells.

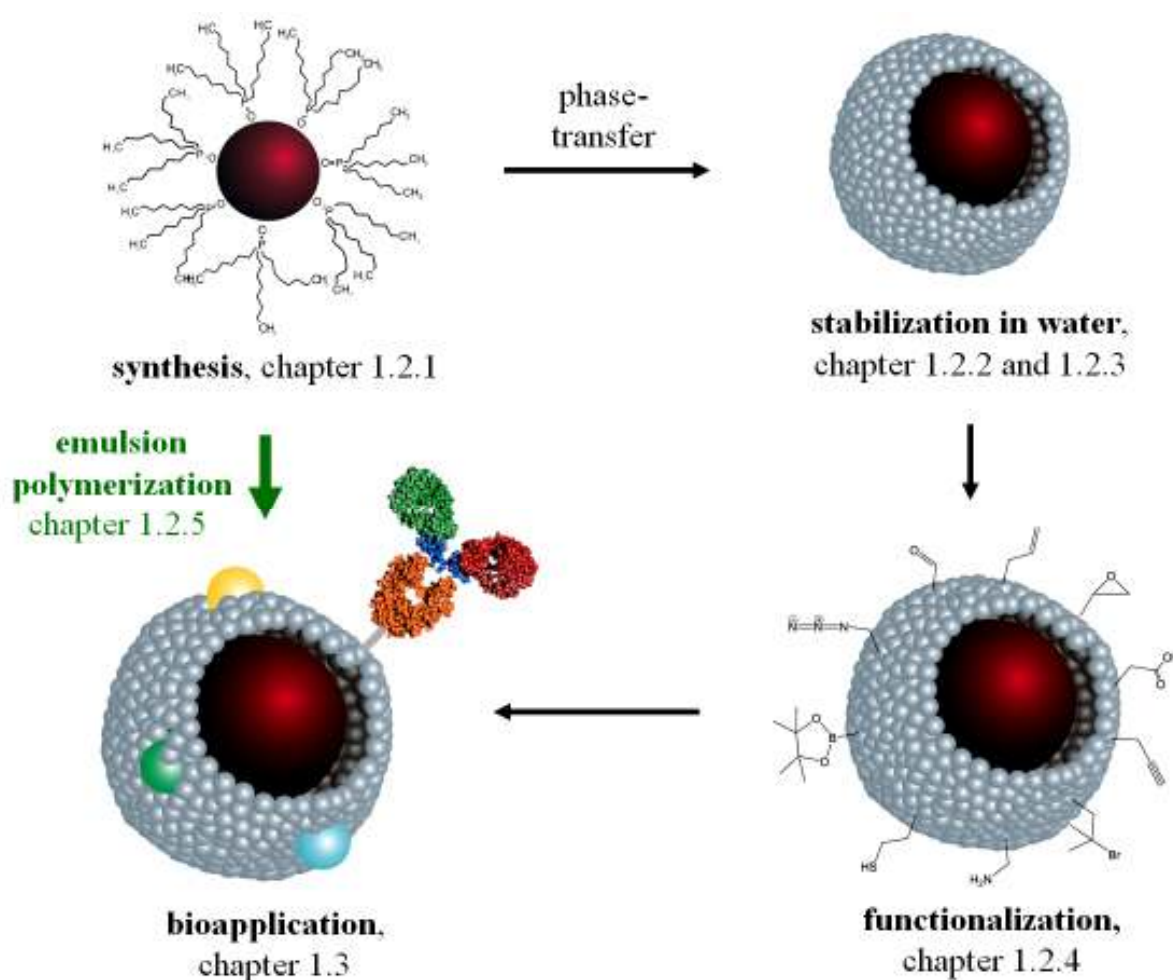
Within the scope of the present doctor thesis the main focus was set on the establishment of nanoparticles in the assignment of medical treatments. The susceptibility of the optical attributes of semiconducting nanoparticles, often referred to as quantum dots (QDs), has inspired attempts to modify them for biological use. Design strategies to gain *inter alia* water solubility should be transferable from the semiconductor nanoparticles to other nanoparticle systems.

Regarding the size-dependent chemical and physical properties^[6] of high-quality bulk II – VI semiconductor nanocrystals (figure 1) a range of applications in medical science has recently come into focus^[7]. In the field of fluorescence labelling CdSe nanocrystals have become the most extensively investigated nanocrystals due to their photoluminescence efficiency, their unique size-dependent tunable emission, their resistance to photobleaching, and their high brightness^[3, 8-11].



figure 1: CdSe/CdS core/shell nanoparticles (CAN dots) of different sizes under UV excitation.

Previously the high exigencies of *in vivo* administration have constrained the adoption of quantum dots and nanoparticles with superparamagnetic properties in for cancer diagnosis and therapy. Therefore, the objective of the present doctoral study was the design of nanoparticles as marker and as a multi-tool delivery system for *in vivo* and *in vitro* exertions. Therefore a polymer coating had to be developed, which stabilizes the quantum dots in aqueous media. A non-immunogenic, protein-resisting, and non-antigenic poly(ethylene oxide) based ligand system was desired, which can stabilize nanoparticles in water and preserve their physical properties, while providing functional groups to derivatize the nanoparticle with molecules like antibodies, oligopeptides, or drugs.



schema 1: overview of the doctor thesis.

An overview of the work done through the doctor thesis is presented in schema 1. It is divided in the nanoparticle synthesis, the stabilization of nanoparticles in water, (bio-)functionalization and bioapplication of nanoparticles.

1.1 Properties of nanoparticles

Nanoparticles consist of a few hundred atoms. Therefore nanoparticles have physical properties, which relate on their size and surface. Semiconducting nanoparticles, so called quantum dots, show a quantum confinement effect since their diameter is of the magnitude as the wavelength of an electron wave function^[12], while magnetic particles show a superparamagnetic behaviour. When the materials are so small, their electronic, magnetic and optical properties deviate substantially from those of bulk materials. See chapter 9.1 - 9.4 for a more detailed information.

1.2 Ligand shell

The surface ligands used in high-temperature synthesis of high-quality nanocrystals are usually quite bulky, with a small anchoring group for bonding onto the surface of nanoparticles and a long/large hydrocarbon chain^[13, 14]. Such ligands kinetically stabilize the thermodynamically unstable nanoparticles. But the coordination of the ligand must be sufficiently weak at high temperatures to maintain a dynamic bonding behaviour of the surface ligands of nanoparticles, which allows an adequate growth rate during nanoparticle synthesis^[15].

1.2.1 TOP/TOPO-shell

Tri-*n*-octylphosphine (TOP) and tri-*n*-octylphosphine oxide (TOPO) are commonly used solvents for nanoparticle synthesis. Different impurities in commercially obtained TOPO (like di-*n*-octylphosphine oxide (DOPO)) dramatically affect the growth of high-quality colloidal CdSe nanocrystals^[16].

The multiple crystallographic facets exposed and defect (vertex, edge) sites on the surfaces of small nanoparticles produce quite different bond strengths of the TOP/TOPO molecules.

1.2.2 Hydrophilic ligands

Biological applications demand water solubility and a high stability of the nanoparticles in the aqueous solution^[17]. Great efforts have therefore been made to exchange the weak hydrophobic ligand shell, which has stabilised the metastable nanocrystals kinetically during the synthesis, with hydrophilic, organic ligands achieving water solubility^[1, 3, 4, 17, 18] and to some extent an organic passivation trap states in case of inhomogeneous inorganic shells. A key problem of this process is the thermodynamic adsorption equilibrium of chemical ligands, needed for stabilisation, at the particles' surfaces.

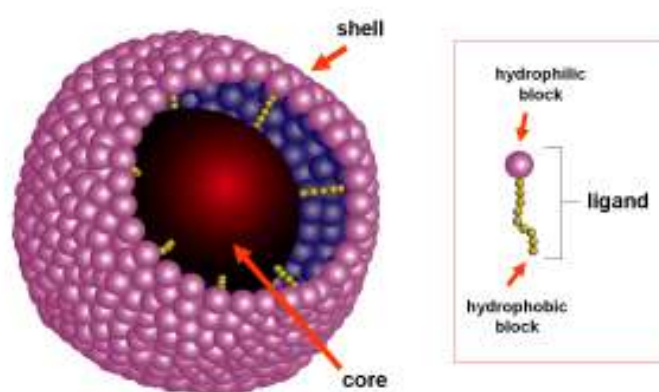
For the utilization of the physical highlights of nanoparticles in *inter alia* biochemical systems different ways exist: 1. adsorption of the protein on the nanoparticle surface due to electrostatic interactions^[19, 20]. This system shows poor stability and interference with the flexibility of the protein. It could only be implemented in the case of gold nanoparticles. 2. nanoparticles are getting stabilized by ligands via coordinative binding. 3. stabilization of nanoparticles by means of hydrophobic effects (van der Waals forces)^[17, 21-23].

In literature coordinating ligands are often discussed, which possess binding groups such as thiols^[24, 25], amines, phosphines, and carboxylates. To generate nanoparticles with such ligands, a ligand exchange has to be arranged^[3, 4, 26-29]. But the binding energy to the nanoparticle surface is often insufficient. In addition, the photogenerated holes inside of semiconducting nanoparticles catalyse reactions at the particle surface. Attaching a nucleophilic binding group (e.g. thiols, amines) on the surface of nanoparticles makes them thereby regrettably a target for such a reaction. Thiols are already converted to disulfides in basic environment as well as in acidic environment in the presence of oxygen. Semiconducting nanoparticles (quantum dots) can catalyse this reaction as well as the reaction of primary amines to secondary amines^[30]. Thus, improved ligand shells must guarantee a stable binding to the particles. This can be achieved by multidentate binding blocks or encapsulation into a crosslinked polymer shell.

Several quenching studies^[31-35] using a multiplicity of ligands have been reported in the literature in efforts to achieve efficient passivation of trap states on the surface of nanoparticles. However, Algar *et al.*^[36] credit changes in quantum yield largely to changes in the radiative decay rates, determined by the nature of the ligand, and to a smaller extent to nonradiative decay rates, which depend on passivation and subsequent exposure to the surrounding solvent matrix. They could show that the degree of bathochromic shift correlates with the extent of ligand ionization. The cause of this ligand-chromism is related to the observed solvatochromism^[37] in CdSe nanoparticles. Due to stronger dipolar interactions between the

excited state of the fluorophore and the surrounding solvent, organic fluorophores often exhibit increasing red shifts in their emission maxima with increasing solvent polarity^[38]. Considering an inhomogeneous shell, a dipolar or electrostatic interaction between ligand, solvent and nanoparticle is possible.

The new ligand shell often has an effect on the nanoparticles. In case of quantum dots, this can lead to a drop in quantum yield, resulting from a reduced passivation of the nanoparticle surface arising from steric requirements of the new ligands and changes on the nanoparticle surface. The micellar coating by hydrophobic interaction (schema 2), which conserves the primary hydrophobic shell of the nanoparticle is an alternative approach^[21, 22, 39, 40].



schema 2: illustration of the structure of a micelle.

Micellar encapsulation of hydrophobic drugs and nanoparticles coated with diblock polymers has been shown to be sufficiently stable for *in vivo* applications and therefore hold great potential for biomedical applications^[22, 41-46]. For the most part polymeric micelles are produced from self assembly of amphiphilic block copolymers in selective solvents^[47-56]. In solvents that are selective for one of the two copolymer blocks, the aggregation of the non-soluble block leads to the formation of the micelle with predictable sizes and morphologies.

But this packing also suffers low stability and/or high nonspecific binding with nontarget biomolecules^[57]. Dual interaction ligands combine the two feasibilities of coating nanoparticles^[58], through hydrophobic van der Waals interactions and coordinate bonding. But the coupling to antibodies requires that the ligand-antibody construct remains stable on the nanoparticle surface in the presence of antigens and higher flow rates like for example in the blood stream during *in vivo* applications. Therefore a covalent crosslinking of one of the blocks in the copolymer shell is inevitable, as has been described in literature for polymeric micelles^[59-66]. To assure flexibility of the polymer shell the inner part of the polymer coating should be extensively covalently crosslinked.

In particular on quantum dots water has a strong influence. Due to stronger dipolar interactions between the excited state of the fluorophore and the surrounding solvent, organic fluorophores often exhibit increasing red shifts in their emission maxima with increasing solvent polarity^[37, 38], accompanied with the stabilisation of electrons in trap states. Those trap states are located at the CdSe surface and their number depends on the quality of the inorganic passivation due to the CdS and ZnS shells. The trapped electrons can absorb emitted quanta of other excitons and elongate the dark state of the nanoparticle. Considering an inhomogeneous shell a dipolar or electrostatic interaction between ligand, solvent and nanoparticle is possible, and the importance of the ligand becomes evident.

Regarding the cytotoxicity of the nanoparticles, ligands also show effects. Hence, in particular poly(ethylene oxide) (PEO) is suitable for biological applications^[67, 68]. The inert polymer reduces nonspecific accumulation, which often contributes to cytotoxic effects^[69].

1.2.3 Benefits of poly(ethylene oxide) (PEO) as a ligand

Poly(ethylene oxide) (PEO) is a known biocompatible polymer^[70-72]. The polymer holds the capacity of preventing protein adsorption^[73], cell adhesion, and, consequently, phagocytosis, non-initiation of an immune response, thus, increasing the *in vivo* circulation lifetime (serum lifetime)^[74-77]. The reduction of nonspecific accumulation of the inert polymer, which is ascribed to cytotoxic effects^[69], makes PEO very suitable for biological applications^[67, 68]. The causation is composed of the reduced interface energy of the PEO/water system, the steric repulsion effect^[78-81] based on entropic effects regarding the excluded volume and mixing interactions^[82]. The loss of conformational changes of the protein and the decline in free space of the polymer strains, which is accompanied with the approach of the protein, leads to a repulsive energy. The closer the PEO packing the more preferred is the helical conformation instead of the all-trans conformation, which amplifies the protein repulse^[83, 84].

The attachment of PEO decreases immunogenicity and antigenicity of proteins.^[85], can extend significantly the blood lifetime of liposomes, nanoparticles, and proteins, and diminish their uptake by reticuloendothelial system (RES) organs, liver and spleen^[86]. Also thrombogenicity as well as cell and protein adherence, can be reduced in the case of PEO-grafted surfaces^[87].

PEO-coating of nanoparticles and the protein-nanoparticle complexation respectively is known not only to minimize non-specific adsorption but also for enhancing the stability of attached molecules^[88, 89]. The non-appearance of interactions with PEO allows the conjugation of

enzymes and other biomolecules with preservation of their biological activity^[90, 91]. The negative charges in case of the carboxyl-functionalised PEO are also conducive to these effects, since they increase the blood circulation time additional^[92]. The negative charged particles interact repulsive with the negatively charged amphipathic phospholipids of cell-membranes.

1.2.4 Functionalisation of the ligand shell

The advance of nanotechnology in biochemistry is mirrored in the assignment of the ligand shell, which stabilize nanoparticles in solvents. To augment the usage of the unique *inter alia* optical and magnetic properties binding sites are desired to expand nanocomposites with molecules like for example catalysts, drugs, dyes and targeting molecules onto the nanoparticles.

At this juncture certain challenges have to be taken in consideration. Most ligands possess a nucleophilic group, which is responsible for the attachment of the ligand on the nanoparticle surface. The nucleophilicity of such chemical groups complicates the further functionalisation of the ligand. In particular in the case of polymer based ligands that allow water-solubility like poly(ethylene oxide) based ligands, steric hindrance and complications in purification from side-products occur. Applying protective groups during functionalisation is often demanding since polymers possess high masses and their functional groups are in many cases inaccessible due to steric considerations. Furthermore, the interference of the produced functional group with other nanoparticles can lead to agglomeration, which hinders the application of nanoparticles.

1.2.5 Emulsionpolymerisation

The term 'emulsion polymerization' signifies a polymerization in a disperse system, containing a continuous and a discontinuous phase. Regarding the classical emulsion polymerization the continuous phase is an aqueous solution, while oil represents the discontinuous phase. These systems can also be described as oil in water emulsions (o/w). The corresponding inverse systems with oil as the continuous phase are called water in oil emulsions (w/o).

The dispersed phase must be stabilized by a surface active substance. Such typical emulsifiers are cationic, anionic and non-ionic surfactants like sodium dodecyl sulfate (SDS) or dodecyltrimethylammonium bromide (DTAB)^[93]. In solution, the emulsifier builds micelles for

concentrations above the critical micelle concentration (CMC). With the assistance of coemulsifiers, such as 1-pentanol, SDS can form transparent microemulsions.

The addition of monomer, which is mainly insoluble in the continuous phase, leads to the formation of big monomer droplets. Some of the monomer dissolves in the continuous phase and some diffuses into the emulsifier-micelles^[94, 95]. In the case of the addition of an initiator for the polymerization, which is soluble in the continuous phase, the first step of the reaction occurs in the continuous phase. The decay of the initiator generates free radicals, which react with monomer units, forming an oligomer-radical which becomes more and more insoluble in the aqueous phase as the length of the oligomer increases. Eventually the oligomer-radical enters the micelles or the droplets^[96]. Because the total surface of the monomer filled micelles is bigger than that of the few monomer droplets, the micelles are the main destination. For most systems the number of micelles formed is two (or more) orders-of-magnitude greater than the number of droplets present in the initial emulsion.

In the micelles additional polymerization takes place with the interplay of diffusion of monomer from the droplets into the micelles, and this leads to the formation of polymer dots^[97]. This mechanism is called micellar nucleation (figure 2).



figure 2: micellar nucleation.

The classical emulsion polymerization can be divided into three phases: the first phase represents the generation of particles, in which the monomer filled micelles receive the radicals and start to react. In this phase the reaction rate increases till it reaches a maximum, which institutes the second phase. In this, as particle growth period specified, phase no more particles are initiated, whereas monomer diffuses from the droplets via the continuous phase into the micelles, where the reaction takes place. The reaction rate is constant. When the monomer droplets disappear, the reaction enters the third phase, called monomer depletion phase. The remaining monomer in the micelles is consumed during the polymerization process. The abatement of the reaction rate to zero is accompanied by a decline of the particle-diameter, due to the increased density of the polymer compared to the monomer.

Next to the conventional emulsion polymerization special methods such as emulsifier-free emulsion polymerization, microemulsion polymerization and miniemulsion polymerization could be established^[98-103].

1.2.5.1 Miniemulsion

Miniemulsions are classically defined as aqueous dispersions of relatively stable oil droplets within a size range of ~30-100 nm^[104]. In addition to production of polymer nanoparticles^[105], films^[106, 107], nanocapsule compounds^[108], high-solid content lattices^[109, 110] and polymeric hybrids^[111], miniemulsion has already been used for the efficient encapsulation of water-insoluble materials in hydrophobic polymers to obtain hybrid particles as reported for the encapsulation of CaCO₃^[112], carbon nanotubes^[113], nanoparticles, such as SPIONs^[114-117], TiO₂^[116, 118-120], SiO₂^[121, 122] and CdS just as CdSe^[123].

The encapsulating material is dispersed in the monomer phase prior to emulsification, using methods such as ultrasonic dispersing or conditioning with ultraturax. The obtained solution is added under high shear conditions to the continuous phase, in which emulsifier, hydrophobe, and initiator are present. In this way, the emulsifier concentration is maintained below the critical micelle concentration to avoid micellar nucleation^[124]. Anionic, cationic, and non-ionic emulsifiers, as well as combinations of these can be utilized. The emulsifier can simultaneously act as monomer and as bearer of functional groups (surfmere). Thus a subsequent purification step can be avoided.

Initially, the achieved droplets, which are kinetically stabilized but thermodynamically unstable show a certain particle size distribution. Based on the Lifshitz-Slezov-Wagner (LSW) theory^[125] of Ostwald ripening and Kabalnov's extension^[126], the drop size distribution can be predicted^[127].

Admittedly a growth process appears, in which larger droplets will grow at the expense of the smaller droplets, due to the fact that smaller droplets have higher vapour pressures than those of larger droplets. This process is called Ostwald ripening^[128] and can be suppressed by a hydrophobe which is a monomer-soluble and continuous phase insoluble compound. The presence of the hydrophobe acts to reduce substantially the rate of diffusion of monomers from smaller to larger droplets. It decreases the Gibbs free energy of droplets, thereby decreasing the driving force for diffusion. Typical hydrophobes are for example hexadecane, dodecyl alcohol and cetyl alcohol (CA)^[129-131]. In addition to Ostwald ripening coalescence can occur^[127].

In addition to the droplet nucleation mechanism^[132], delineated above, homogenous nucleation is a second possible mechanism for miniemulsion polymerization. The latex seeds are created from oligomers in the continuous phase, and the monomer is brought to the nucleation site by diffusion^[133].

The initiation of the polymerization can be carried out thermally, photochemically, or by redox-initiators or radical-initiators, such as azo- or peroxy-initiators. Initiators such as the cationic initiator 2,2'-azobis(2-amidinopropane) dihydrochloride (V-50) provide an opportunity to achieve emulsifier-free emulsion polymerizations via ultrasonic irradiation. V-50 polymerizes the slightly water-soluble monomers, such as styrene, in aqueous phase to form oligomeric radicals with sulfate end groups, which are surface active and form droplets or micelles^[134, 135].

1.2.5.2 Microemulsion

Microemulsions are, from a macroscopic viewpoint, a homogenous composite of water, oil-phase, and emulsifier^[136]. They are characterized by an emulsifier/monomer ratio of >1 and are both thermodynamically and kinetically stable. The reaction rate is contingent upon the concentration of the initiator. Contrary to (macro-)emulsion polymerizations, phases one and three appear, while phase two, with a constant reaction rate, is missing. Also no gel-effect (Trommsdorff-Norrish-Smith effect) appears^[137]. Commonly a maximum of the polymerization speed is found at 20-25% conversion.

According to Chamberlain *et al.*^[138] the first phase represents the particle generation period, in which new reaction loci are generated and in which the reaction rate ascends with the number of particles. The reaction rate depends on the concentration of monomers and radicals inside of the particle^[137]. Accordingly maximum reaction rate occurs when a maximal particle number is engaged in the reaction. Guo *et al.*^[137] showed that in case of a microemulsion the nucleation proceeds throughout the whole reaction process. At the beginning of the reaction the radicals generated in the aqueous phase enter the monomer micelles and initiate thereby the polymerization. At the same time, the monomer is transferred from droplets into the creating particle causing the droplets to impoverish on monomer. A mixture of 1-pentanol and monomer filled micelles remains, which compete for any remaining radicals. This mechanism is called droplet nucleation.

Due to the small mean particle diameter (10-30 nm^[104]), however, just one radical is active per particle. If a second radical enters a particle termination occurs immediately. In case of the microemulsion polymerization of styrene, transmission of the radical from the reacting chain to a monomer molecule with subsequent transfer of the monomer radical from the droplet into the aqueous phase is more probable than termination^[137]. Asua *et al.*^[139] demonstrated that the rate of emission of one monomer radical out of a droplet increases with decreasing droplet diameter. Hence, it is anticipated that the emission rate from droplets in a microemulsion is extremely high.

In order to limit the growth of the polymer particles, it is essential to induce polymerization at temperatures below the microemulsion instability temperature^[140]. For polymerization of water-soluble monomers in w/o microemulsions, Candau adapted the cohesive energy ratio (CER) concept for optimizing the polymerization system^[141].

1.3 Biological applications

In the field of medical application^[1-5] the unique physical properties of nanoparticles are attracting more and more interest. The combination of their physical properties with the versatility of their coating allows the development of diverse nanocomposites with a high application spectrum. An overview is given in figure 3.

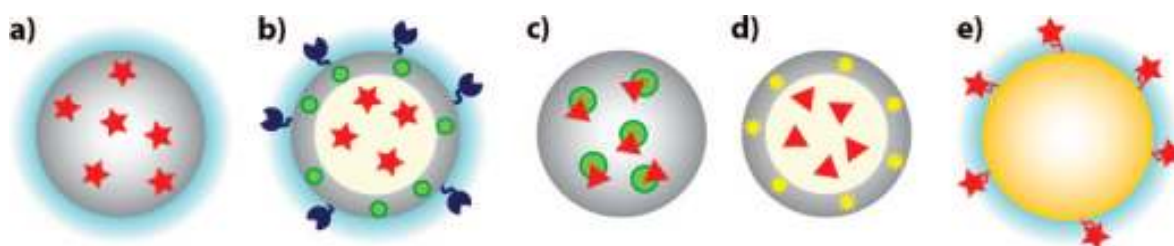


figure 3: illustration of nanocomposites^[142].

(a) Organic fluorophores (red) are embedded in a calcium phosphate matrix (gray), and the resulting composite particles are stabilized by PEO molecules (light blue) on their surfaces. (b) Polyelectrolyte capsules comprise a multilayer wall (gray) in which magnetic particles (green) can be incorporated for magnetic targeting. The cavity of the capsules can be loaded with analyte-sensitive fluorophores (red). Though most practical capsule systems thus far have diameters of 1-5 μm , their size can be reduced to 100-200 nm. The capsule assembly technology also enables immobilizing ligands for active targeting (dark blue) and stabilization (light blue) on the capsule surface. (c) Magnetic NPs (green) are embedded in a dextran matrix (gray). Through magnetic targeting, an anticancer drug (red), which is adsorbed on the particles, can be delivered to the tumour tissue. (d) Gold NPs (yellow) can be integrated in the wall of polyelectrolyte capsules (gray), which surrounds an anticancer drug (red) inside the cavity. Light-induced heating of the gold particles locally disintegrates the capsule wall and releases the anticancer drug. (e) A photosensitizer (red) can be excited *via* energy transfer from a quantum dot NP (yellow) to produce a radical oxygen species. In this case, the particle is also the carrier matrix. The NP is stabilized by ligands on the particle surface (light blue).

The stability against photobleaching^[21], large molar extinction coefficients, and high quantum yield^[26] make quantum dots superior to organic fluorophores in detection sensitivity as well as in long-term tracking of biological processes. A further advantage is the wide span of emission wavelengths covered by quantum dots. This is notable, because theoretical modelling studies have indicated that two spectral windows are available for *in vivo* quantum dot imaging (one at 700 – 900 nm and another at 1200 – 1600 nm)^[143].

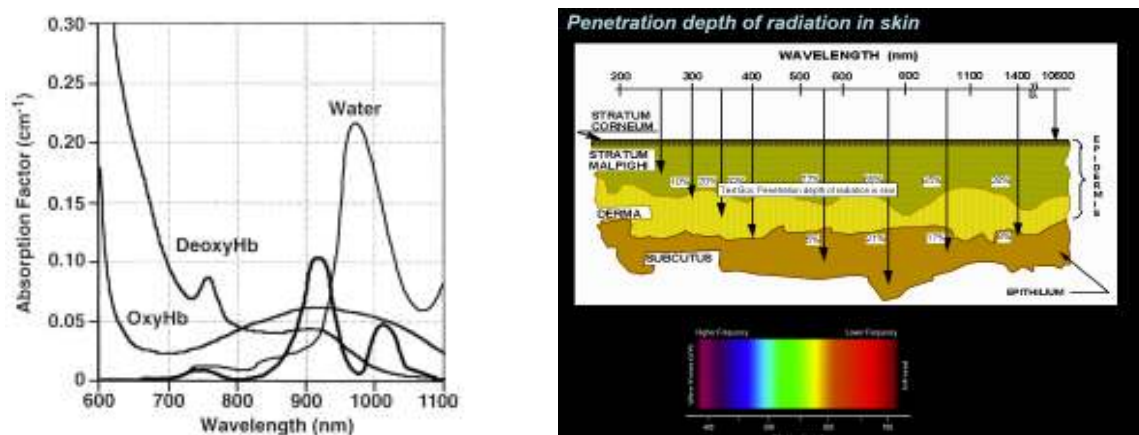


figure 4: (left) background absorption, which occur in *in vivo* imaging, (right) penetration depth of radiation in skin^[144].

Those windows are important for deep tissue imaging (figure 4), because they are separated from the major absorption peaks of blood and water^[145]. At a wavelength of around 770 nm the penetration depth of radiation in skin has its highest level (figure 4). CdTe/ZnS and InP/ZnS nanoparticles cover this range.

Intense multicolour up-converting nanoparticles such as NaYF₄ nanoparticles doped with lanthanide ions (Yb³⁺ and Er³⁺ or Yb³⁺ and Tm³⁺) are an alternative^[146] and have already found biological applications^[147, 148]. The term 'up-conversion fluorescence' reflects their capability of converting absorbed near infrared light into shorter wavelengths (visible light). In these materials the excitation light is primarily absorbed by Yb³⁺, showing a higher absorption at 975 nm (4f state → ⁴F_{7/2} in case of two photons). In the case of Yb³⁺/Er³⁺ co-doping, the energy of two excited Yb³⁺ states is then transferred to one Er³⁺ ion, resulting in emission mainly in the green and the red spectral region. In the case of Yb³⁺/Tm³⁺ the energy of four excited Yb³⁺ states is transferred to one Tm³⁺ ion and emission of blue and violet light is observed.

Nonetheless Gao *et al.*^[92] substantiate the use of CdSe quantum dots with emission maxima of 640 nm for *in vivo* imaging by using spectral unmixing algorithms. Thus it was viable to separate the autofluorescence from the quantum dot emission. In addition they were able to demonstrate along with Chang *et al.*^[149] the advantages of quantum dots relative to genetically

encoded fluorescent proteins such as green fluorescent protein (GFP), which is also applied for cancer imaging^[150]. Due to the 10-50 times larger molar extinction coefficient ($0.5 - 0.2 \cdot 10^6 \text{ M}^{-1}\text{cm}^{-1}$) of quantum dots relative to those of organic dyes ($5 - 10 \cdot 10^4 \text{ M}^{-1}\text{cm}^{-1}$) the quantum dots absorption rates are 10-50 times faster than those of organic dyes at the same excitation photon flux^[92]. This makes quantum dots appear 10-20 times brighter than organic dyes^[22, 26, 151, 152].

Using two-photon technology a high three dimensional handling ability and extremely high resolution imaging ability can be achieved in the application of quantum dots like CdSe as biolabels^[153]. In a two-photon excitation process, the ground state atom jumps to the excited state and emits a photon after absorbing two photons, so that the excitation energy is lower than that of the emission. Moreover, because of the inverse relationship between solution scattering and laserwavelength^[154, 155], two-photon excitation can cause lower sample scattering, smaller optical bleaching and stronger sample penetrability than one-photon excitation^[156, 157]. This technology has been pursued heavily in tumour detection recently^[92, 158, 159].

On account of these advantages ZnS-capped CdSe nanoparticles are often used for biolabelling e.g. proteins or DNA^[2, 160-164]. Results from multicolour labelling of fixed mouse 3T3 fibroblasts^[152] and breast cancer marker Her on the surface of fixed and live cancer cells^[21, 165], have proved that quantum dots can be very effective in cellular imaging and offer substantial advantages over organic dyes.

Further established applications of nanoparticles in biochemistry include colorimetric sensing^[25, 166], whereby oligonucleotides in the sub-picomolar level can be detected without the assistance of PCR^[167]. Förster resonance energy transfer (FRET)-based biosensors^[168] for example for fluorescence competition assays in case of DNA detection^[169] and array-based sensing^[170] in the field of fluorescence sensing but also electrochemical sensing^[171, 172] and surface enhanced Raman scattering (SERS) has been successfully exploited in biological sensing using nanoparticles^[173]. Further work was done on real-time tracking of embryonic development^[22], cell transfection^[174], fluorescent blood tracer to image small vasculatures^[153], fluorescent tracers for nonspecific uptake studies and lymph node mapping in living animals^[68, 175], and real-time imaging and tracking of single receptor molecules^[176, 177].

However, combined targeting and imaging *in vivo* studies of quantum dots upon systemic injection into the blood serum^[68, 92, 149, 178] are still rare and often suffer from instability^[22, 69]. Quantum dots have also been reported to aggregate non-selectively on the surface of cell membranes^[152, 179, 180].

Superparamagnetic iron oxide nanoparticles (SPIONs), which have been extensively studied as an magnetic resonance imaging (MRI) contrast agent^[181-186], are in particular utilized in cell sorting/separation^[187-191], and for tumour thermotherapy, e. g. hyperthermia^[192-195]. In this regard the non toxic properties of SPIONs are an obvious advantage. Other nanoparticles used for magnetic resonance imaging are GdPO₄ nanoparticles, which allow an even higher contrast^[196].

SPIONs have also found application in drug delivery systems^[197-199] site-specific drug delivery tissue engineering^[200] and nucleic acids concentration^[201, 202]. Electromagnetic fields in the 350 - 400 kHz frequency range can produce local heat via induction and cause the targeted release of bound drugs. They also provide an opportunity to be magnetically guided to a selected part of the body, for example, into a tumour^[203-205]. Simultaneously, the nanoparticles can transport anticancer drugs to the the tumour tissue^[206]. Gupta *et al.*^[207-209], Zhang *et al.*^[210], and Berry *et al.*^[211] determined the interaction of differently coated SPIONs with cells. Their results indicate that the nanoparticle surface appears to be more important than the composition of its core.

Gold nanoparticles show an intense absorption peak from 500 to 550 nm^[212] arising from surface plasmon resonance. Surface plasmon resonance occurs from the collective oscillation of the conductive electrons owing to the resonant excitation by the incident photons, although the fundamental physical principles of surface plasmon resonance are very complex. The surface plasmon resonance is sensitive to the surrounding environment, signalling changes in solvent and binding. Particularly useful is the red-shift up to around 650 nm and broadening of the plasmon band due to the interparticle plasmon coupling^[213]. This phenomenon leads to the popular and widely applicable colorimetric sensing for oligonucleotides. Hereby gold nanoparticles are functionalized with single-stranded DNA. Upon addition of the target sequence the particles aggregate, resulting in a change of the colour of the solution^[25, 167].

Huang *et al.*^[214] could demonstrate *in vitro* the use of gold nanorods as novel contrast agents for both molecular imaging and photothermal cancer therapy. The specific binding of anti-EGFR antibody-conjugated nanorods to the surface of the malignant-type cells (HSC, HOC) in opposite to non-malignant type cells (HaCaT) could be diagnosed due to the strongly scattered red light from gold nanorods in dark field (figure 5). The photothermal degradation could be achieved by laser-excitation at a wavelength of 800 nm.

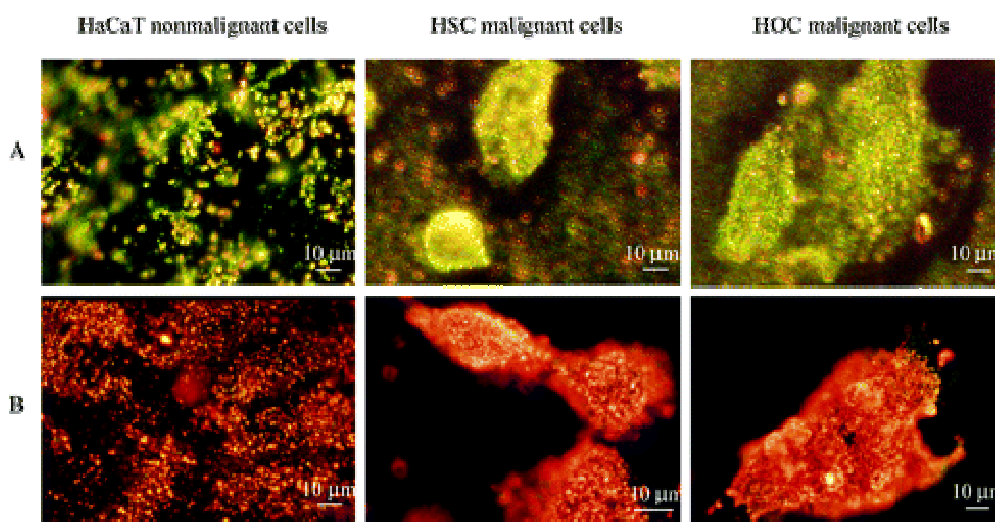


figure 5: Cancer therapy using gold nanorods^[214].

A Light scattering images of anti-EGFR/Au nanospheres after incubation with cells for 30 min at room temperature. **B** Light scattering images of anti-EGFR/Au nanorods after incubation with cells for 30 min at room temperature.

Gold nanoparticles also find application in electrochemical sensing^[171] or together with fluorescent nanoparticles like CdSe in fluorescence sensing^[168]. Gold nanoparticles are also used for drug delivery systems^[215], whereas the gold nanoparticles can function simultaneously as active agent. At a distinct size of 1.4 nm, bare Au₅₅ clusters coordinate irreversibly in the major grooves of DNA (figure 6), which making Au₅₅ an even more effective chemotherapeutic than cisplatin^[216]. Gold nanoparticles interact hereby with the negatively charged phosphates of the DNA and inhibit the transcription of the DNA.

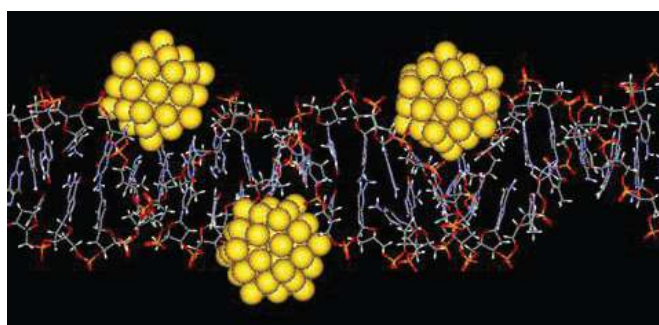


figure 6: Molecular model of B-DNA combined with Au₅₅ clusters irreversibly attached to the major grooves^[216].

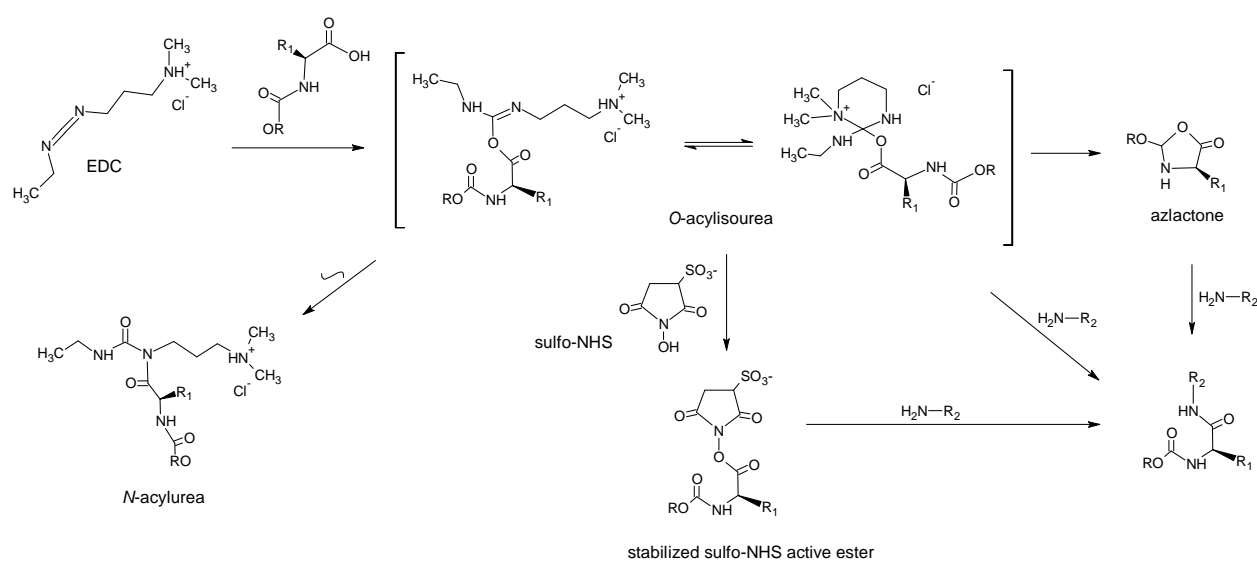
Amongst the numerous other nanoparticles and multifarious bioapplications, which are not mentioned in this chapter, silica nanoparticles owing to their non-toxic character are a further interesting class of nanoparticle. They are regularly synthesised by a sol-gel process (Stober's process)^[217] or microemulsions^[218] and possess a porous structure. Because of the optical transparency of silica nanoparticles they offer a system to stabilise dyes and/or drugs, thus having the potential i.a. to act as fluorescence label.

1.3.1 Protein (antibody) coupling

For vectored targeting of nanocomposites, molecules that show a high specificity to the respective, desired destination-motif are attached. An example are antibodies, containing a for binding responsible paratope, and which can be easily selected against all kind of molecules and molecule-fragments (epitopes, antigenic determinant) e.g. via phage display and then amplified by existing methods.

In contrast to other molecules, proteins are less stable and have to be coupled in aqueous media (buffer solutions). A widespread coupling method for bio-molecules in aqueous media is via the ‘zero-length’ cross-linker EDC/sulfo-NHS, which does not generate any toxic by-product in the matrix^[219].

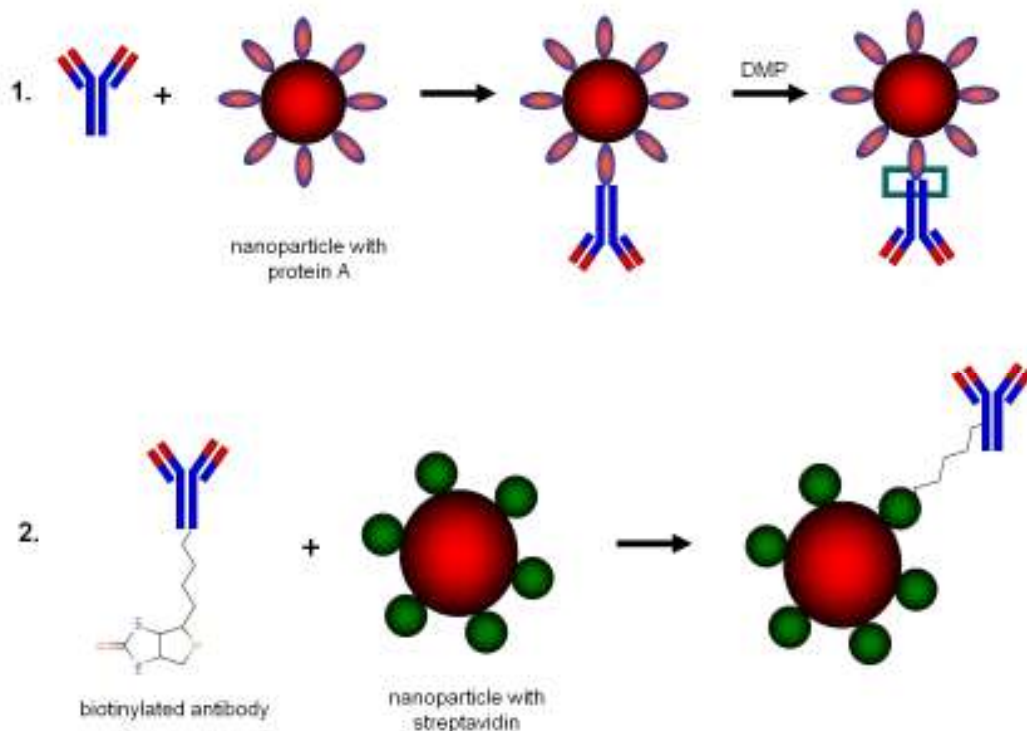
The activation proceeds similarly to other carbodiimide couplings (schema 3). An *O*-acylisourea intermediate is formed by the reaction of a carboxylic acid and the carbodiimide. The *O*-acylisourea is a highly reactive species that readily reacts with amines, peptide coupling additives or reducing agents. However, the *O*-acylisourea can rearrange irreversibly to an *N*-acylurea and also racemise the α -carbon of the amino acid via formation of an oxazol-4(5H)-one (azlactone). *N*-Acylurea formation and racemisation may be reduced by using intermediate nucleophiles like sulfo-NHS, which convert the *O*-acylurea to an activated ester containing the nucleophile. This species is more stable at $\text{pH} \leq 6$, wherefore the nanoparticle solution was dialysed against water, pH 6. Buffer solutions, containing 2-(*N*-morpholino)ethanesulfonic acid (MES), were shown to have an effect on the solubility of PEO.



schema 3: peptide bond formation catalyzed by EDC/sulfo-NHS.

Unreacted EDC can be quenched by addition of 2-mercaptoethanol. During coupling reaction EDC is transformed to the corresponding urea, which can be removed from the reaction mixture by dialysis against water, pH 6. The subsequent antibody coupling was carried out in PBS, pH 7.4. Aminolysis of the ester due to the reaction with amines of the antibody liberates the additive. The reaction can be discontinued by the addition of hydroxylamine in up to two-fold excess relative to NHS. In this way unreacted sulfo-NHS was hydrolyzed and the carboxylic group regained. The elimination products were separated by dialysis against PBS or ddH₂O.

Antibodies show benefits compared to antibody-fragments like scFv, Fab, and F(ab)₂ fragments. The presence of the Fc part of the antibody features amines, which are not primarily involved in the antigen binding. Also the Fc part can be modified. For example an amine rich tag reduces the probability that a lysine, for example in the antigen binding domain of the antibody, is coupled, which has an affect on the binding behaviour of the antibody. Another possible strategy involves the prior binding of the antibody to an immobilized antigen, which would shield the antigen binding domain of the antibody during the coupling reaction.



schema 4: illustration of antibody coupling.

1. protein A immobilized on a nanoparticle surface binds the Fc part of an antibody. DMP allows a further crosslinkage. 2. A biotinylated antibody is getting bound by streptavidin, which is immobilized on the surface of a nanoparticle.

For controlled antibody-coupling the nanoparticles can be coupled with a protein, which binds selectively to the antibody. Protein A, a 42 kD polypeptide from the cell wall of the bacterium *S. Aureus*, can bind antibody on the Fc part, thus keeping the Fab part unaffected^[220]. The binding strength of $K_a = 10^9/\text{M}$ can be increased by a coupling reaction with dimethyl pimelimidate (DMP) (schema 4, 1.). A further option is the tetrameric protein streptavidin (53 kD), purified from the bacterium *streptomyces avidinii*. This protein has a high affinity to biotin. The dissociation constant (K_d) of the biotin-streptavidin complex is on the order of $\sim 10^{-15}$ mol/L. Owing to the strong non-covalent interaction, biotinolyated antibodies can be bound (schema 4, 2.).

2 Results and Discussion

Concerning (bio-)applications of nanoparticles in aqueous media, the following aspects regarding the ligands, which provide the water-solubility are significant: 1. the ligand must be strongly bound to the nanoparticle surface to ensure the ligand remains attached to the nanoparticle surface to prevent loss of solubility, to prevent agglomeration, and to reduce the potential toxicity of the metal core. 2. the polymer should offer a functional group towards the aqueous solution, which should not lead to a crosslink between different nanoparticles, but on the other hand allow mild coupling reactions, for instance in protein essential buffer solutions.

2.1 Synthesis and characterization of PEO-*b*-PCL-*b*-PEI

To combine all of the requirements of a biocompatible ligand, an amphiphilic triblock polymer was designed, consisting of an poly(ethylene oxide) (PEO), an poly(ϵ -caprolactone) (PCL) and an poly(ethylene imine) (PEI) block.

Vesicle formation and biocompatibility to the point of drug delivery of *branched*-poly(ethylene imine)-*graft*-poly(ethylene oxide) (PEO-*b*-PEI) block copolymers has been demonstrated [221-223]. This polymer has already been applied for phase transfer of CdSe/CdS core/shell nanoparticles [224]. The PEI block allows the interference of the polymer with the nanoparticle surface while PEO permits water solubility.

In the process of work it was determined that a higher degree of protection was required to stabilize quantum dots in water. Therefore the block copolymer was expanded by a hydrophobic segment. Poly(ϵ -caprolactone) (PCL) was chosen, since it has been utilized in various biomedical applications due to its biodegradability and biocompatibility. Poly(ethylene oxide)-*block*-poly(ϵ -caprolactone) (PEO-*b*-PCL) diblock polymers have been proven to be excellent drug carriers [225-231]. In aqueous solution these amphiphilic polymers form micellar structures, in which the crystalline hydrophobic PCL core stabilizes the micelle structure and acts as a micro reservoir for the incorporation of lipophilic drugs, while the hydrophilic PEO corona, which can feature functional groups [225, 232], serves as the stabilizer. Concerning the insolubility of PCL in aqueous solution, the micellar core can be treated like a quasi-solid, which promotes a very low critical micelle concentration [233].

The synthesis of the PEO-*b*-PCL back-bone was achieved by anionic and catalytic ring opening polymerisation (figure 7). This method allows a precise control over the respective block length that is a crucial parameter for self assembly processes of amphiphilic molecules. The back-bone consists of a poly(ethylene oxide) segment (PEO), one hydrophobic poly(ϵ -caprolactone) block (PCL) and a hyper-branched poly(ethylene imine) (PEI₇₀₀), possessing on an average six to eight primary amines.

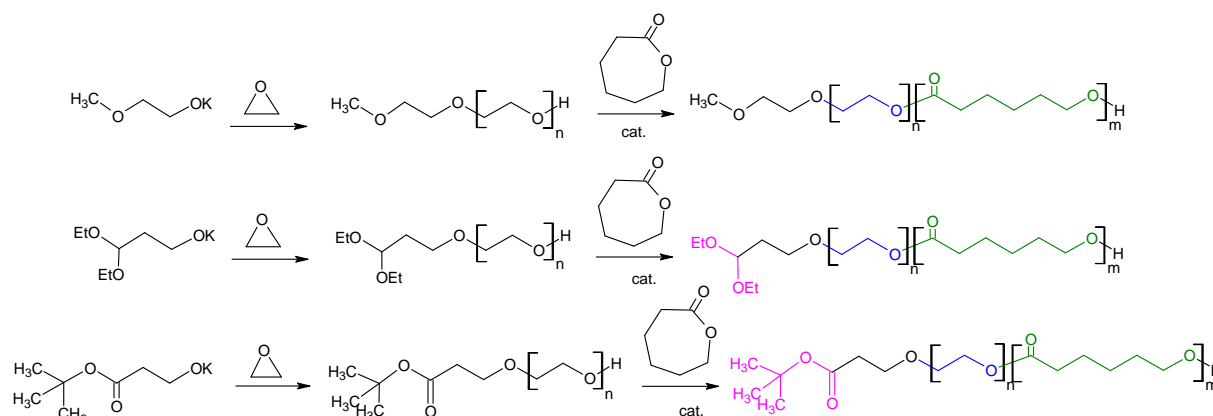
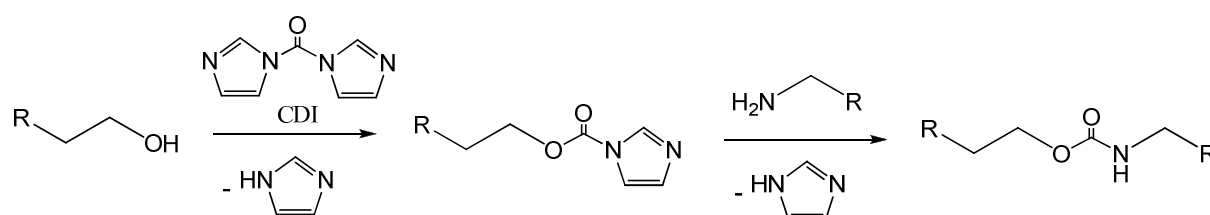


figure 7: synthesis strategy of the polymer back-bone.

The PEO-*b*-PCL polymer strain was synthesized by polymerisation of the respective monomers, while PEI was coupled via CDI activation of the terminal hydroxylic group of PEO-*b*-PEI-OH (reaction equation 1).



reaction equation 1: CDI coupling.

¹H-NMR analysis of the CDI coupling of a mono methoxylated PEO₁₁₀₀ with tris(2-aminoethyl)amine showed evidence of a quantitative reaction (figure 8), which indicates the stability of the imidazolyl intermediate during the hydrolysis of the CDI excess.

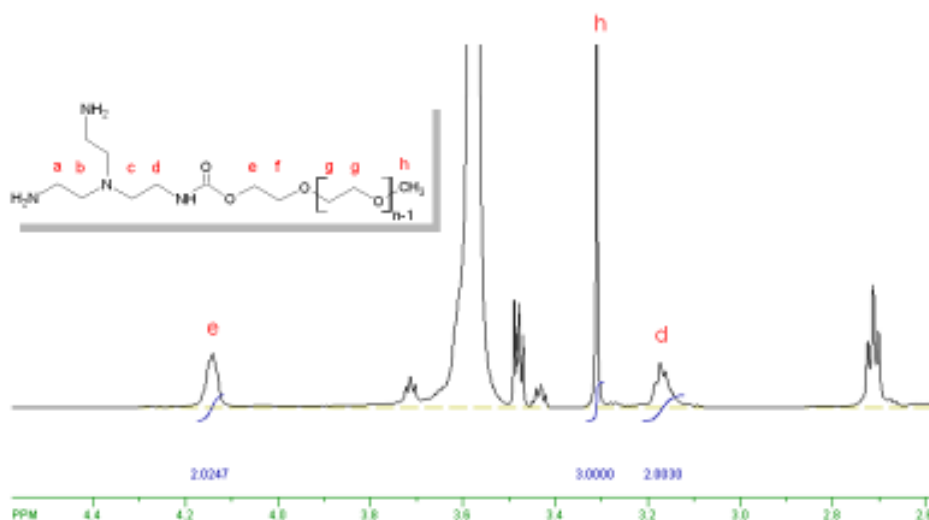
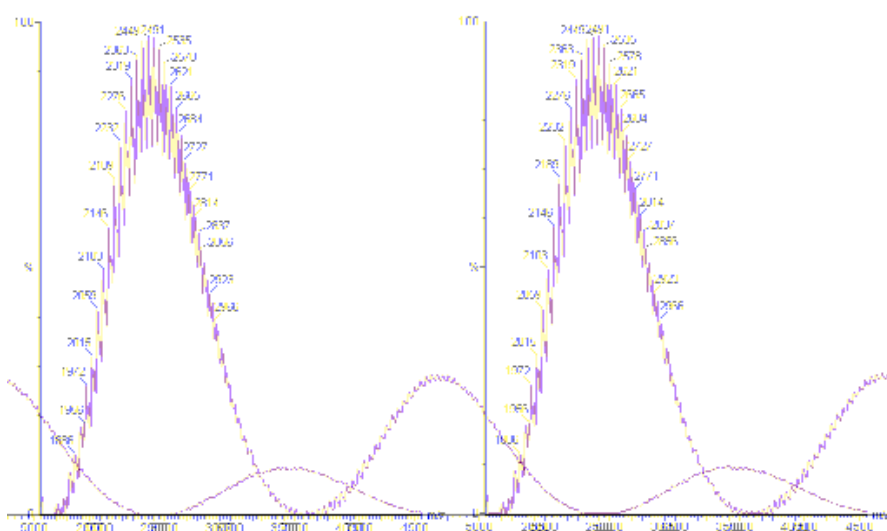


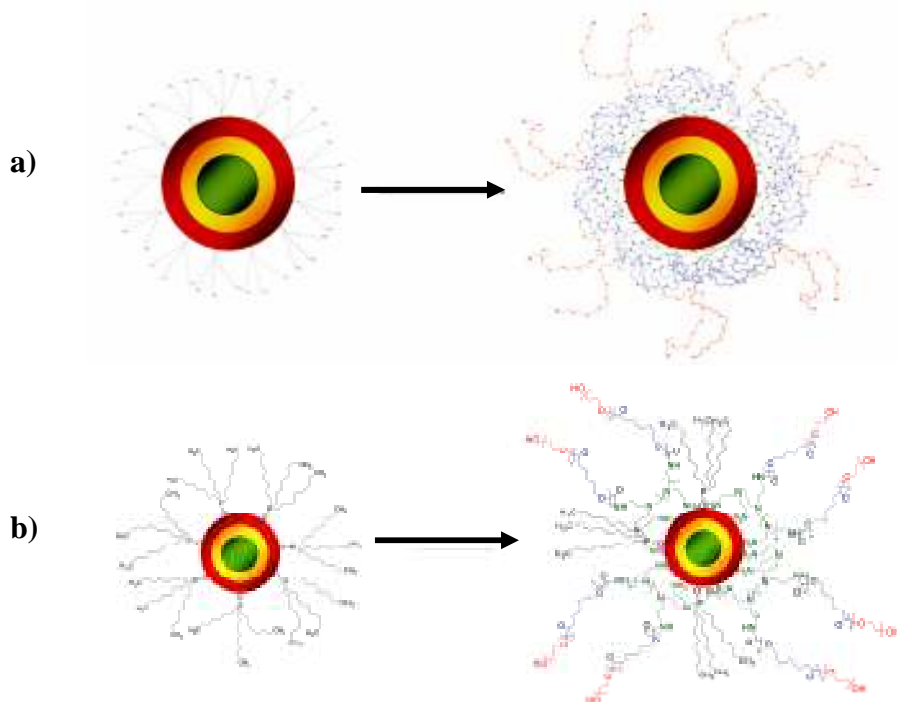
figure 8: $^1\text{H-NMR}$ (400 MHz, CDCl_3) of M-PEO-N4.

To guarantee a micellar assembly of the ligand, a maximum of three PEO-b-PCL chains were attached per PEI, so that the PCL segment had a molecular weight of $< 1/3$ compared to the molecular weight of the PEO block. The CDI attachment of the polymer chain to the PEI binding block leads to a distribution in the number of polymer chains coupled to PEI. In figure 30 a matrix assisted laser desorption/ionization time of flight mass spectrum (MALDI-TOF) of $(\text{M-PEO}_{2000})_2\text{-PEI}_{700}$ (**20**) is shown, which reveals the distribution. In case of the triblock polymers no matrix was found to desorb the ligand, so no MALDI-TOF measurements could be performed on these polymers.



1100 g/mol. Typically PEO with a mass of 2000 g/mol was used. No significant advantage was achieved by enlarging the PEO to a mass of 5000 g/mol.

By using different initiators, different block lengths, and different PEO-*b*-PCL to PEI ratios, a variety of triblock polymers could be synthesized. Their abbreviations (1 - 16) are listed in chapter 7.2.1.2.5.



schema 5: illustration of CdSe/CdS/ZnS nanoparticles coated by PEO-*b*-PCL-*b*-PEI. a) packing b) clarification of ligand-attachment.

Nanoparticles, which feature a hydrophobic ligand coating after synthesis, were encapsulated during self-assembly of the triblock polymer by avoiding usual ligand exchange procedures, which usually involve harsh procedures such as precipitation of the nanoparticles to remove the prior ligands. Throughout the coating procedure presented here the nanoparticles stay in solution, which simplifies the process and also makes the transfer of nanoparticles to water a controllable act. An illustration of the packing and a clarification of the ligand-attachment is shown in schema 5. A more detailed explanation of the ligand coating is given in 2.2.

2.1.1 Terminal functionalisation of PEO-*b*-PCL-*b*-PEI

By selecting the initiator for the PEO-synthesis a variety of different functional groups (inert or protected terminal endgroups) can be inserted (figure 7). Sterically unprotected esters are an exception because they would be vulnerable to attack by the living anionic end of the growing

PEO chain. So polymers were provided with acetals (DP-), vinyl groups (V-), and *tert*-butyl-protected carboxylic-groups (*t*C-) ($^1\text{H-NMR}$ spectra are shown in figure 10 and figure 11).

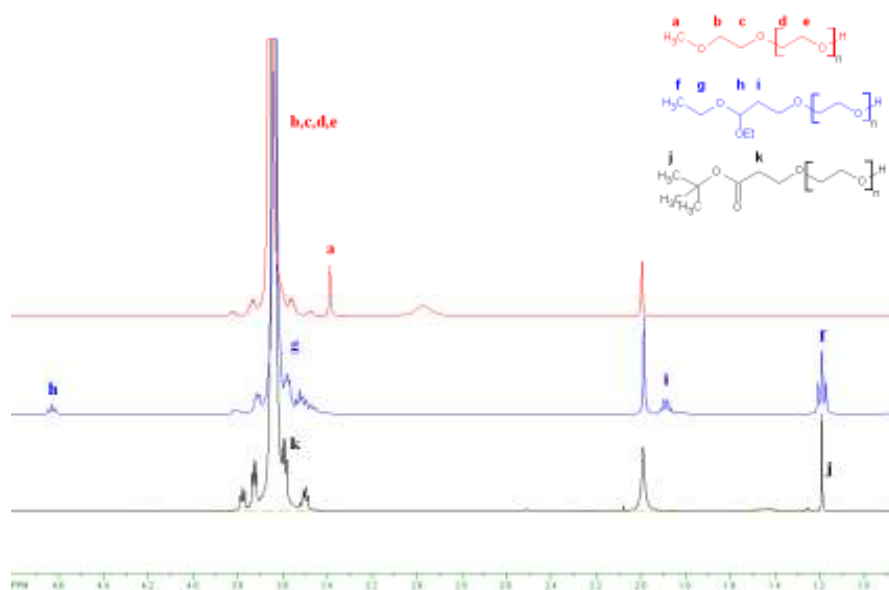


figure 10: $^1\text{H-NMR}$ (400 MHz, CDCl_3) of M-PEO (red), DP-PEO (blue), *t*C-PEO (black).

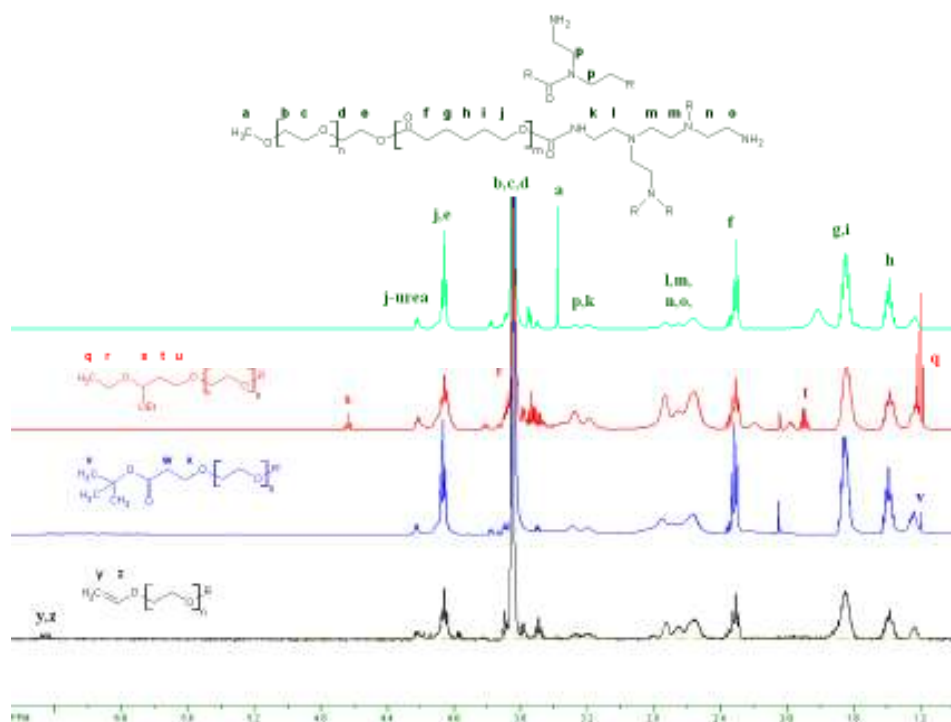


figure 11: $^1\text{H-NMR}$ (400 MHz, CDCl_3) of M-PEO-*b*-PCL-*b*-PEI (green), DP-PEO-*b*-PCL-*b*-PEI (red), *t*C-PEO-*b*-PCL-*b*-PEI (blue), V-PEO-*b*-PCL-*b*-PEI (black).

In figure 12 a MALDI-TOF spectrum of DP-PEO-OH is presented. The polymer strand consists of 18 to 44 units. The polydispersity of the PEO was determined by SEC to be 1.108 ($M_n = 1203$ g/mol, $M_w = 1334$ g/mol), which is satisfactory for a short polymer. The

distribution of the PEO-length has the advantageous that terminal functional groups of longer PEO chains protrude on the nanoparticle coating. Hence, they are easier accessible, considering steric requirements.

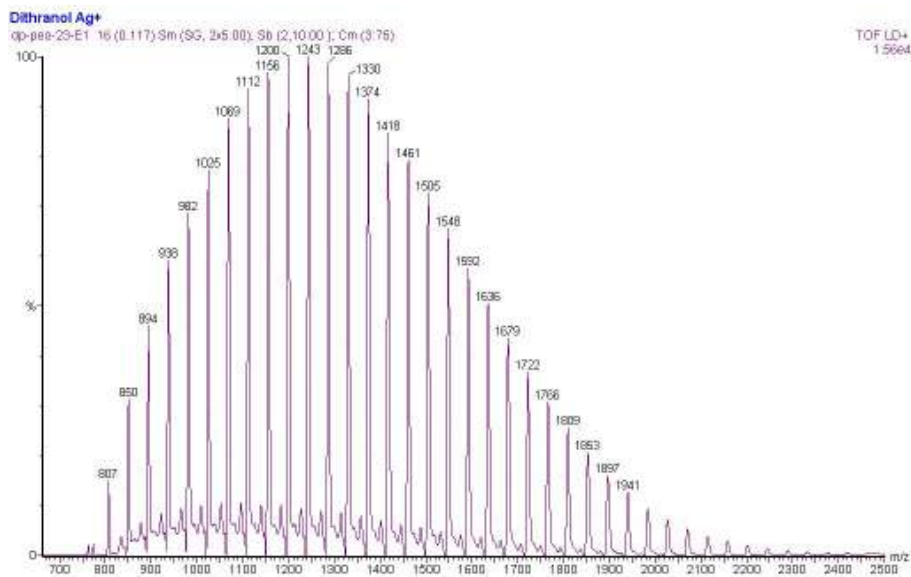
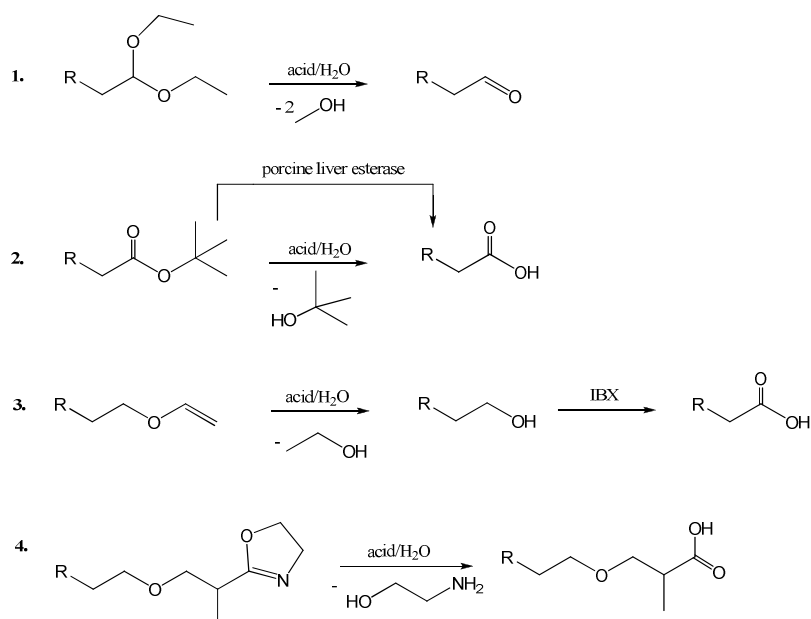


figure 12: MALDI-TOF of DP-PEO-OH.

In a final step the endgroups of the PEO blocks (tC , DP or V) were deprotected and oxidized (see schema 6) to form terminal functional groups, e.g. hydroxyl (-OH), aldehyde (-CHO) or carboxylic groups (-COOH), which allow further coupling chemistry to biomolecules. An alternative approach, which is also shown in schema 6 is the integration of an oxazoline, which produces a carboxylic function by acid cleavage.



schema 6: functionalisation of PEO-*b*-PCL-*b*-PEI.

1. cleavage of an acetal,
2. cleavage of a *t*-butyl ester,
3. cleavage & oxidation of a vinyl terminated PEO,
4. cleavage of an oxazoline.

The basic activation of the initiator preliminary to the PEO synthesis constrains the use of esters. Most esters are labile to basic solvents. The bulky *t*-butyl group shields the ester functionality from hydrolysis. The deprotection of the carboxylic group can be achieved in different ways. The *t*-butyl esters are cleaved by moderately acidic hydrolysis (< pH 4)^[234-236]. But even enzymatic cleavage using porcine liver esterase (PLE; EC 3.1.1.1)^[237] or a thermitase^[238] offers an option. The mild conversion of the aldehyde of the DP-ligands by oxidation with sodium chlorite to the corresponding acid is another possible alternative^[239].

In addition to those mentioned above, a vinyl (allyl) terminated PEO, purchased from Clariant Functional Chemicals, was produced with the PCL and PEI blocks via the same procedure stated in the experimental section. The double bond, which can be verified by NMR spectroscopy (figure 13) opens the field of click chemistry and cycloadditions as well as transition metal catalyzed reactions (e.g. Heck reaction, metathesis) as promising chemical coupling routes. The electrophilic bromination of the terminal alkene, permitting Suzuki coupling using catecholborane, is a selective reaction, where other functional groups are not effected.

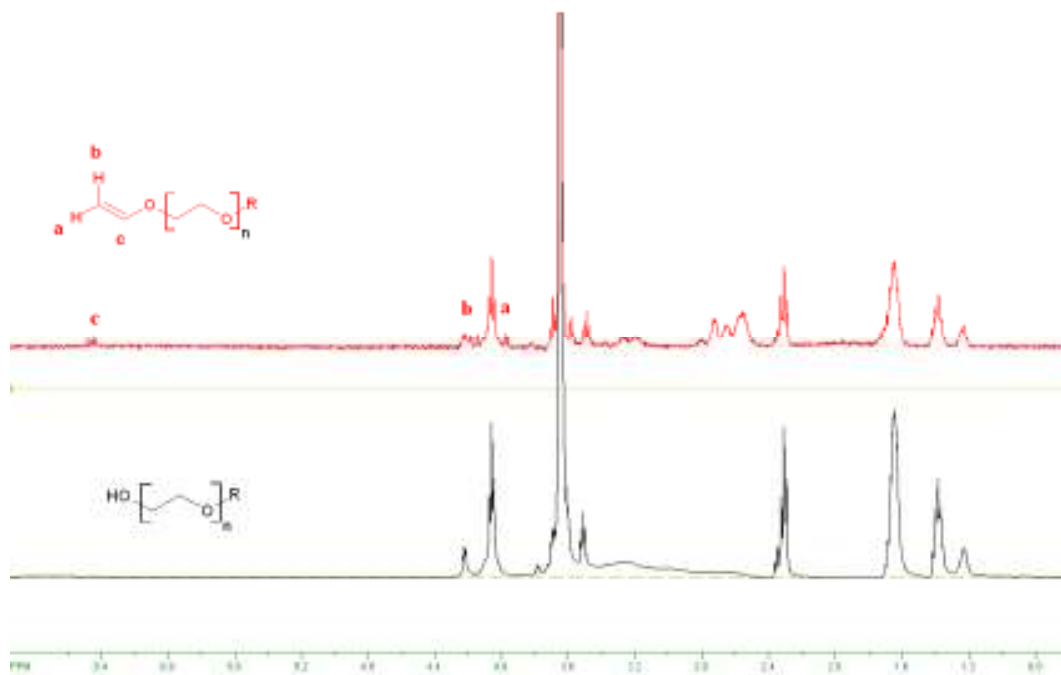


figure 13: ¹H-NMR (400 MHz, CDCl₃) of V-PEO-*b*-PCL-*b*-PEI (red) and after hydrolysis (black).

Supplemental acidic treatment of the vinyl group in an aqueous solution generates a hydroxylic group, whilst the urethane group is buried in a protecting, hydrophobic environment. This terminal functionality allows *inter alia* reaction with succinic acid to obtain a carboxylic group and CDI or epichlorohydrin activation. Also the oxidation of the hydroxylic group by *o*-iodoxybenzoic acid (IBX) in water was attempted. IBX is an oxidant in water-miscible organic solvent^[240], which can be generated from 2-iodobenzoic acid (2IBAcid)^[241]. The reduced form of IBX iodosobenzoic acid (IBA) is oxidized back to the active state using oxone®. In these conditions, oxone® oxidizes not only IBA (the reduced formed of IBX), but also the aldehyde intermediates into acids. In the presence of 0.6 eq 2IBAcid and 1.3 eq oxone® a quantitative cleavage of the vinyl group could be achieved, which yielded the oxidation to the hydroxylic group.

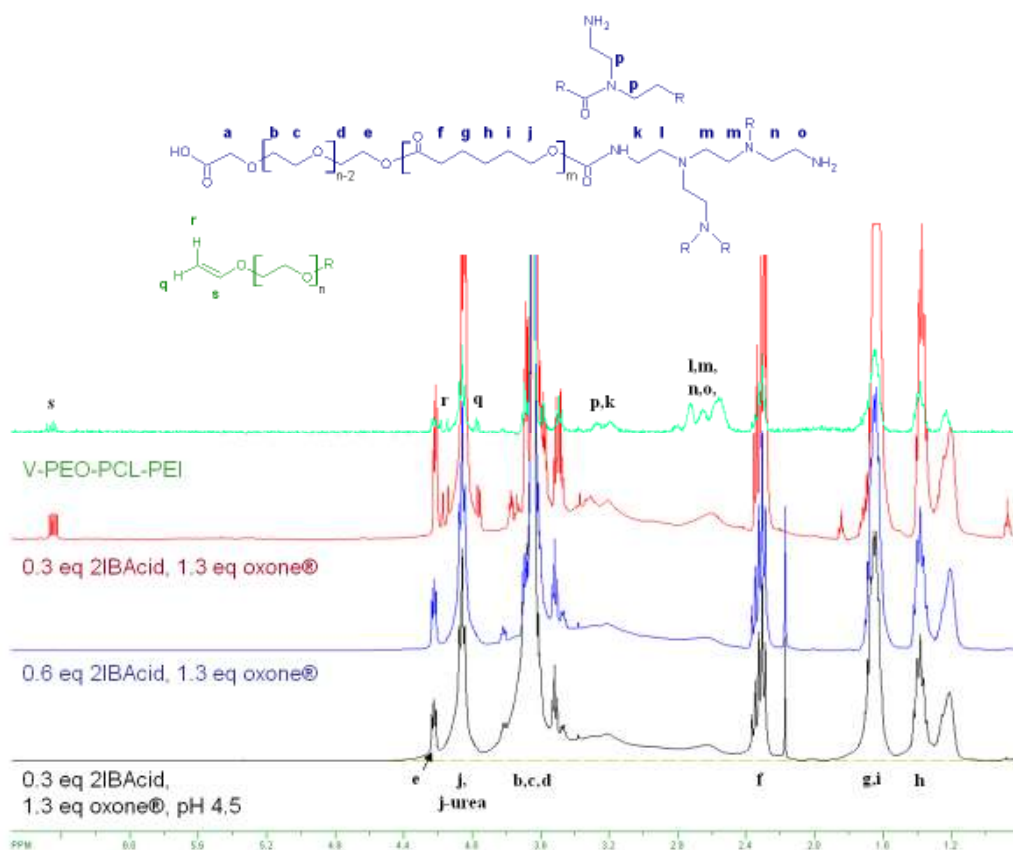


figure 14: $^1\text{H-NMR}$ (400 MHz, CDCl_3) of V-PEO-*b*-PCL-*b*-PEI (green) after IBX oxidation I (red), IBX oxidation II (blew), and), IBX oxidation II (black).

The oxidation was conducted under different amounts of oxidants. In the presence of 0.3 eq 2IBAcid, $^1\text{H-NMR}$ measurements (see figure 14) reveal that according to the integrals ~ 50% of the vinyl groups are still attached to the polymer. The yield is here a rough dimension, because the size distributions and the overlap of signals complicate the comparison of the integrals. It can be concluded that to a certain extent an oxidation could be achieved, while the urea bond remained unaffected and the iodobenzoic-species was separated by purification. Since it is not necessary to have a carboxylic group on every polymer on the micelle surface, the results are satisfactory. By increasing the amount of 2IBAcid to 0.6 eq or lowering the pH value to 4.5 respectively a higher reaction yield was achieved, regarding the priorcleavage of the vinyl bound.

But the carboxylic function was not assigned distinctively in a $^1\text{H-NMR}$ analysis (see figure 14). Calculations based on the increment system^[242] presume the signal of the methylene group next to the carboxylic group to be at 3.55 ppm. Thus, the signal is overlaid by the broad PEO signal. Since the proton exchange is slower in DMSO a signal at 8.24 ppm in an $^1\text{H-NMR}$ measurement (see figure 15) could represent a carboxylic group, concerning the polyether matrix. $^{13}\text{C-NMR}$ measurements show signals at 162.8, 173.6, and also a signal at 183.8 ppm. In a HMBC the signal of 173.6 could be ascribed to the ester carbon atoms of PCL. The signal

at 162.8 ppm could represent the urea carbon atom whilst the signal of 183.8 ppm might document the carboxylic carbon atom.

Unfortunately the proof via FT-IR measurements is complicated by the presence of further carbonyl species of the polymer. Nevertheless, the oxidation of the free hydroxylic group must have been accomplished, because IBX offers a high reactivity, while the partial coiled state of PEO allows the accessibility of the hydroxylic groups.

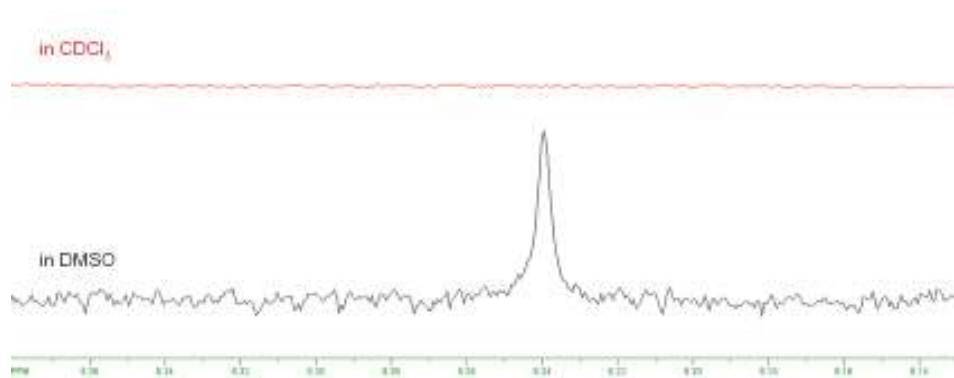
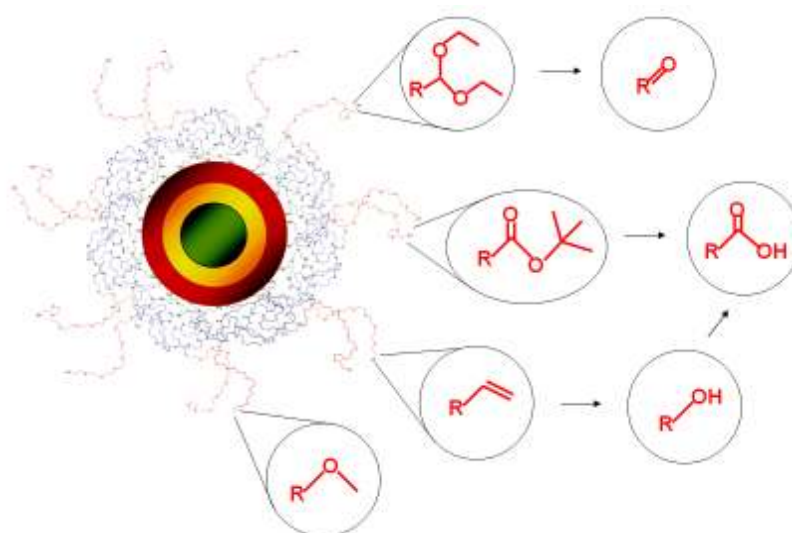


figure 15: $^1\text{H-NMR}$ (500 MHz, CDCl_3 & DMSO) of $\text{HOOC-PEO-}b\text{-PCL-}b\text{-PEI}$.

The functionalisation of $\text{PEO-}b\text{-PCL-}b\text{-PEI}$ enables a plethora of coupling reactions to biomolecules. A few examples include peptide coupling and Suzuki coupling. Since the functional groups are terminal in the hydrophilic polymer segment and due to the physical behaviour of PEO they are been presented toward the aqueous phase of the micelle (schema 7). This allows the coupling to further (bio-)molecules.



schema 7: functionalisation of $\text{PEO-}b\text{-PCL-}b\text{-PEI}$.

The length of the PEO-segment promotes the flexibility and accessibility of the protruding protein, which is conformationally restricted while interacting with biological molecules such as antibodies.

2.2 Ligand exchange with PEO-*b*-PCL-*b*-PEI

As described in the experimental section (7.2.1.3), ligand addition with the triblock polymer is a very easy and versatile procedure, which involves only ligand and water addition and the removal of THF. The driving force for this exchange reaction is strongly enhanced by amphiphilic interactions of the ligands in the final biocompatible particles.

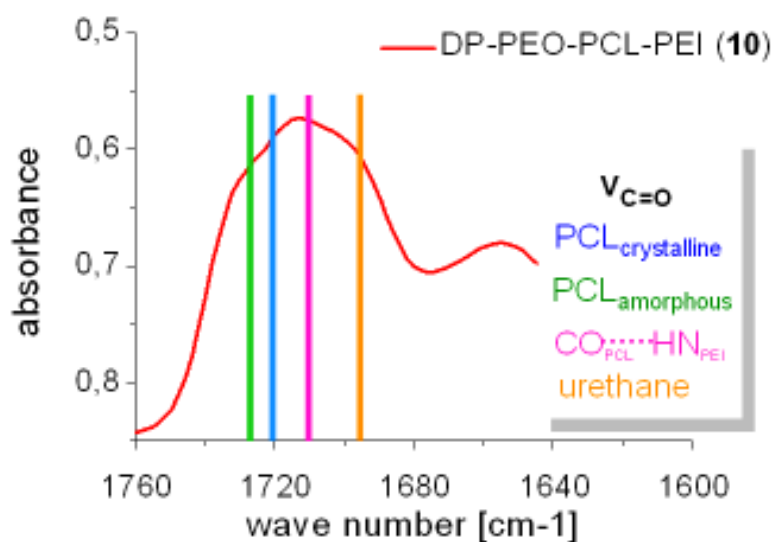


figure 16: FT-IR measurements.

The new ligand produces a robust coating not only by the multi-attachment of the amines on the nanoparticle surface due to *inter alia* electrostatic interactions^[243], but also by hydrophobic interactions of the PCL segments of different chains, as well as with the octylchains of TOPO ligands, which are present on the nanoparticle surface. Additional hydrogen bonds between the ester groups of the PCL part with the amines of PEI (figure 16) as well as the tendency of the PCL-segment to reduce its surface area towards the aqueous solution support the rigidity of the polymeric coating. Its endurance is mirrored in the absence of degradation in the presence of lithium borohydride (LiBH₄) even at elevated temperatures^[244]. Shuai *et al.*^[245] have already demonstrated inter- and intramolecular cross-linkage between the hydrophobic PCL part with PEI in vesicles, reflected by higher glass transition temperature (T_g) values in DSC

measurements. Like the research group of Shuai *et al.* the FT-IR measurements of DP-PEO-*b*-PCL-*b*-PEI (**10**) presented here feature a stretching absorption band of the PCL ester carbonyl groups, which are hydrogen-bonded to the amine of PEI^[246].

The tight packing of the TOPO/PCL-part around the nanoparticle surface in turn utilizes the mentioned interactions and protects the nanoparticles from the outer milieu. In this way the amines are also protected. Unbound ligands also form micelles, thus affecting the size distribution of the hydrophilic to hydrophobic block. The PCL-*b*-PEI fragment has a size of ~1/3 of the whole polymer. PEO has an increased volume due to its stretched coiled state and solvation shell. Considering the nucleophilic character of amines, the shielding prevents the amines from undesired interference during, for example, peptide coupling reactions.

To understand the effect of the triblock polymer on the nanoparticle, ligand addition to CdSe/CdS/ZnS core/shell/shell nanoparticles was followed by nuclear magnetic resonance (NMR) experiments. To observe changes, unbound TOPO ligand from the prior nanoparticle solution had to be removed. Therefore the nanoparticles were purified of TOPO ligands as much as possible by repeated precipitation with methanol. However, a certain amount of TOPO and TOP ligands on the nanoparticle surface are necessary for solubility of the nanoparticles in CDCl₃, so the purification was done carefully. To avoid signal overlaps a new ligand with a M-PEO₁₁₀₀ chain and tris(2-aminoethyl)amine (-N4) as anchor group had to be prepared. The corresponding ¹H-NMR spectrum is shown in figure 137.

¹H-NMR measurements were performed with the purified nanoparticles (figure 17, bottom). The signal broadening and partial overlap of the methylene groups close to the P atom at 1.5 ppm of the TOP and TOPO ligands arises from the steric hindrance to relaxation^[247]. After each addition of a 25 fold excess of MPEO-N4 ligand (**18**) and incubation time of 20 minutes a further ¹H-NMR spectrum was measured.

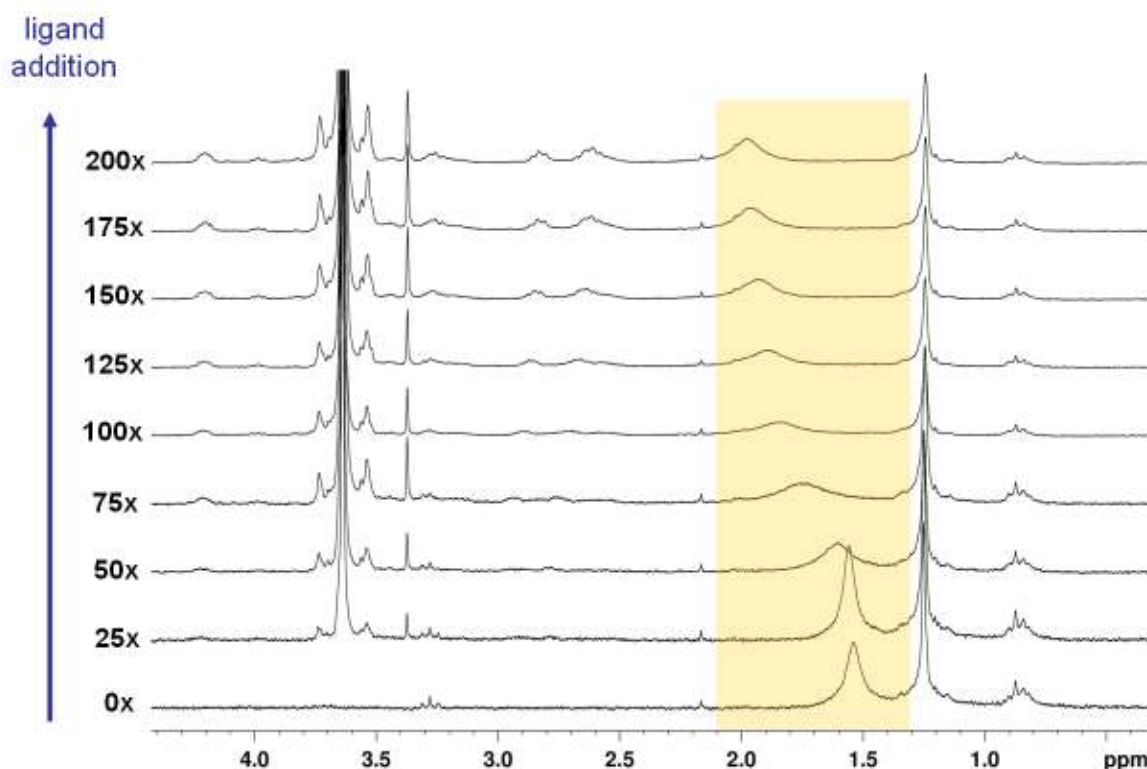


figure 17: ¹H-NMR (200 MHz, CDCl₃) of CdSe/CdS/ZnS coated by TOP/TOPO in the process of M-PEO-N4 ligand (**18**) addition. In each step a 25 fold excess of ligand proportional to the amount of quantum dots was added. The bottom spectrum (0x) shows TOP/TOPO coated quantum dots.

In the procedure of ligand addition, the TOP/TOPO signal shifts from 1.5 to 1.9 ppm (figure 17, yellow highlighted), accompanied with a broadening of the signal.

The NMR measurements were performed in solution. The movement of the TOPO molecules relative to the particle movement leads to averaging. Causes for this effect might include changes in temperature, pH, diffusion and concentration. Changes in the equilibrium of the ligand binding could also lead to a shift of the signal. Exchange spectroscopy (EXSY) to analyse proton exchange and diffusion ordered spectroscopy (DOSY) to analyse ligand-attachment must be made for a more detailed explanation.

The fact that the separate signals of the methylene protons next to the P atom do not emerge implies that the TOP/TOPO molecules do not detach from the surface. The broadening of the signal related to the impeded relaxation, which might be due to the steric requirements, corroborates this conclusion.

The steric oppression of the TOP/TOPO ligands might crowd the alkyl-chains into the less shielded region of the magnetically anisotropic phosphine oxide (schema 8), thus causing nearby protons to shift downfield (to higher δ -values).



schema 8: structure of TOPO.

The contribution σ to the shielding of a nucleus by induced paramagnetic circle currents parallel to the axis of the double bond can have positive or negative values. The dependence is clarified in formula 25 and divided in three factors: the angle θ between the assembly vector connecting nucleus to neighbour group and the axis of the neighbour group, the magnetic susceptibility χ parallel and perpendicular to the axis of the neighbour group, and the distance r from the nucleus to the neighbour group.

$$\sigma(\text{neighbour}) \propto (\chi_{\parallel} - \chi_{\perp}) \left(\frac{1 - 3\cos^2\theta}{r^3} \right) \quad (28)$$

Formula 25 entails an angle-dependence of $54^{\circ} < \theta < 144^{\circ}$ in which the term $1 - 3\cos^2\theta$ is positive, otherwise negative. In accordance with the results, free TOPO molecules show a θ of $55\text{-}60^{\circ}$. A compression of the alkyl chains ($< 54^{\circ}$) therefore leads to a notable negative shielding of the nearest methylene protons, whereby less excitation energy (higher frequencies) is required. Consequently a signal-shift to higher ppm values is observable.

This effect could be supported by changes in the binding behaviour of TOPO. The dative bond of $\text{P}=\text{O}$ to the nanoparticle surface could be stretched. This might increase the double bond character of $\text{P}=\text{O}$ and in turn increase the anisotropy (schema 9).



schema 9: TOPO binding to zinc atom.

These results point to a close assembly of TOP/TOPO molecules and new ligand on the surface of the quantum dots. The more densely packed arrangement increases the van der Waals forces

between the polymethylene chains of the TOP/TOPO ligands, described by Young *et al.*^[248], as well as with the new polymeric coating. Transferring these concepts to the ligand addition of PEO-*b*-PCL-*b*-PEI to a nanoparticle surface, where even more TOPO is present, a really close hydrophobic polymeric barrier around the nanoparticle can be assumed. Along with an increased stability of the nanocomposites the polymeric coating should assure a reduced cytotoxicity. The inert PEO ensures the steadiness of the structure against biological degradation. This is highly relevant, because the PCL-segment is biodegradable. Furthermore, the PCL block next to the TOPO layer also shields proteins or other molecules, for example, coupled to the PEO block from adsorption at the nanoparticle surface. In case of antibodies an interference with the metal surface could lead to a denaturation of the antibody.

Thermogravimetry (TG) measurements of dialysed CdSe/CdS/ZnS quantum dots encapsulated by M-PEO-*b*-PCL-*b*-PEI (1) (QD/P 1:200) indicate a high rigidity of the ligand at temperatures below 200 °C. In this range no loss of mass was detected. Degradation is initiated above 240 °C.

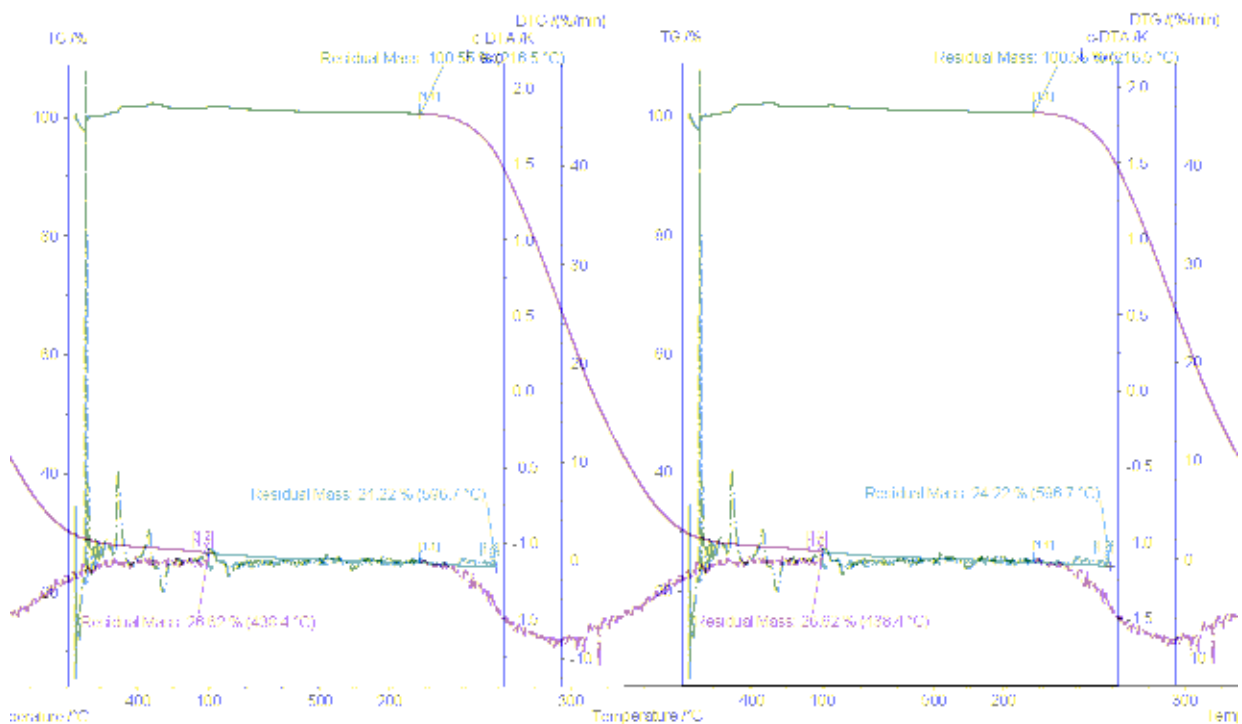


figure 18: TG measurements of CdSe/CdS/ZnS QDS coated with M-PEO-*b*-PCL-*b*-PEI (1) (QD/P 1:200).

According to the TG measurements 76% of the mass is lost up to a temperature of 600 °C. The residual 24% should mainly belong to inorganic material. With the assumption that the core/shell/shell nanoparticles, which have an average diameter of 5 nm (volume = 65.4 nm³), are individually encapsulated and consist of mainly CdSe (density = 5.67 g/cm³), the remaining ligand to quantum dot ratio can be calculated. The nanoparticles have a weight of $3.71 \cdot 10^{-19}$

g. Based on the 76% loss of mass observed, the organic material per nanoparticle has a mass of $11.7 \cdot 10^{-19}$ g. One ligand **1** ($M = 6700$ g/mol) has a mass of $0.11 \cdot 10^{-19}$ g. Thus each nanoparticle possesses 106 ligands. This number is just a benchmark, because of the above made approximation and negligence of the remaining hydrophobic ligands (TOP/TOPO) from the nanoparticle synthesis.

2.2.1 Fluorescence and stability in water

The tight packing of the PEO-*b*-PCL-*b*-PEI ligand on the surface of nanoparticles results in highly fluorescent quantum dots in aqueous solutions. In figure 19 are the absorption and emission spectra of CdSe/CdS/ZnS nanoparticles coated with ligand **8** and ligand **9** (abbreviations are listed in chapter 7.2.1.2.5) in different quantum dot to ligand ratios (1:200, 1:250, 1:350). The exciton peak in UV-vis spectroscopy was observed at 580 nm and the emission maximum at 594 nm. During the ligand addition and phase transfer to aqueous solution the first absorption maximum stays constant, showing no amine etching [249]. At the same time, the emission maximum shifts 7 nm to the red, thus increasing the Stokes shift from 14 to 21 nm.

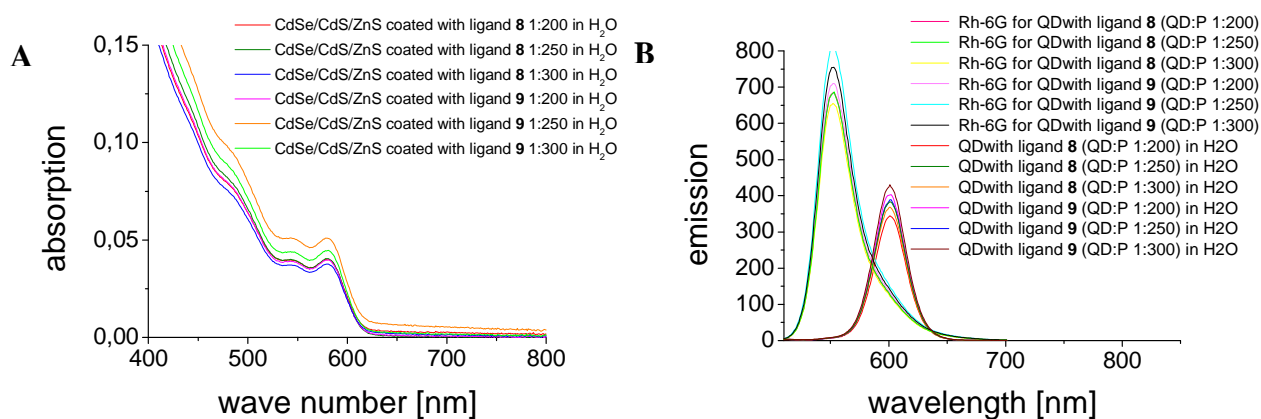


figure 19: CdSe/CdS/ZnS (QD) coated by *t*C-PEO-*b*-PCL-*b*-PEI (**8** & **9**) in water. a) absorbance spectra b) emission spectra. QD:P abbreviates the quantum dot to polymer ratio.

CdSe nanocrystals have been shown to exhibit solvatochromism^[37], where local dielectric properties and interactions with the surrounding matrix influence the nanoparticles optical transition energy. In the present system this effect is minimized because the micelles provide a local chemical environment similar to that of the initial organic solvent.

Electrostatic interactions compounded by changes in the dielectric constant surrounding the nanoparticle may result from THF, which is also present inside of the micelle. THF is a more

polar solvent than chloroform and can therefore better stabilize electrons in trap states, thus leading to longer dark-states of the nanoparticle. Indeed, compared to the TOP/TOPO coated nanoparticle in chloroform the ligand addition and the transfer in aqueous solution resulted in a small drop in quantum yield of up to 20% (figure 20). This is the same value which is been observed by transferring TOP/TOPO coated quantum dots from chloroform to THF (stabilizer & contamination in THF have a high effect on the quantum yield of quantum dots). A further drop in the process of phase transfer from THF to water was not observed.

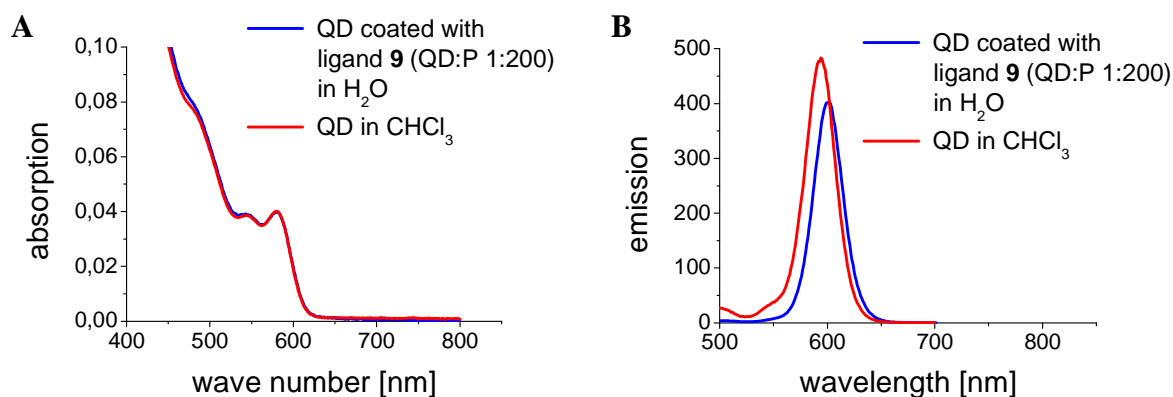


figure 20: comparison of CdSe/CdS/ZnS (QD) after synthesis in chloroform and coated by *t*C-PEO-*b*-PCL-*b*-PEI (**9**) in water. a) absorbance spectra b) emission spectra.

To examine the stability of the nanocomposites a dilution series was performed. The dilution leads to a change in the equilibrium of the ligands between the bond and unbond state. With increasing dilution more and more ligands go over into the unbond state, unless the ligand binds strongly to the nanoparticle surface. The loss of ligand correlates with the loss in quantum yield. Does the ligand shell stay unaffected the quantum yield should stay constant.

Dilution of a 124 pmol/mL concentrated solution down to 2 pmol/mL (figure 21 A) and a 197 pmol to 3 pmol dilution series (figure 21 B) showed no decrease of the quantum yield even after a time period of three hours. Since the absolute quantum yield fluctuates between different ligand additions, two different ligand additions were performed and the intensities of each sample were compared to that of the highest concentration, which was set equal to 1. The results for both dilution series are identical. The nanoparticle stayed in solution even in the lowest concentration.

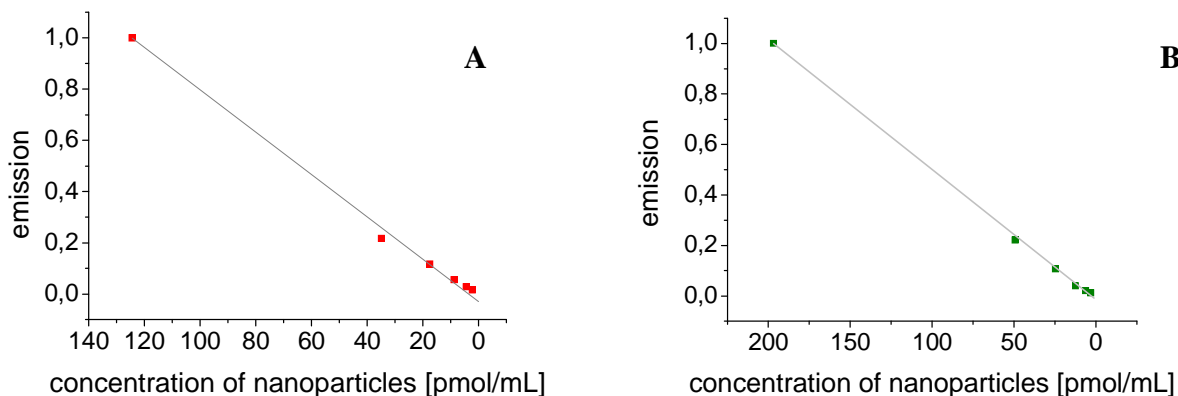


figure 21: Emission spectra of CdSe/CdS/ZnS coated by *tC*-PEO-*b*-PCL-*b*-PEI (**8**) in water. The dilution was arranged in 10 mL volumetric flasks. The inspections of the used cuvettes with pure water showed no emission at all.

The lowest concentration yielded a colourless solution. Under UV-light the uniformly distributed fluorescence in the cuvette could be seen. This illustrates the rigidity of the triblock polymer shell.

2.2.2 Fluorescence in biological buffers

In a further set of experiments the fluorescence stability in typical cell buffers and media was investigated. In buffer solutions salts and surfactants like SDS, EDTA and EGTA are present, and these could have an impact on the solubility or the optical behaviour of the nanocomposites. Therefore CdSe/CdS/ZnS quantum dots were encapsulated via a 200 fold excess of the respective ligand (**1**, **2**, **6**, **7**, **8**, **9**, **12**, **13**, and **17**; abbreviations are listed in chapter 7.2.1.2.5) and transferred into water. The solution was cleaned by use of a 0.2 μm PTFE-filter. From this stock solution the same amount of nanoparticles (50 μL) was redissolved in several different buffer solutions (1 mL). These were incubated for three hours. In figure 22 the fluorescence intensities are compared for different ligands in different buffer solutions. The integral of the emission of the nanoparticles in ddH₂O is set equal to 1.

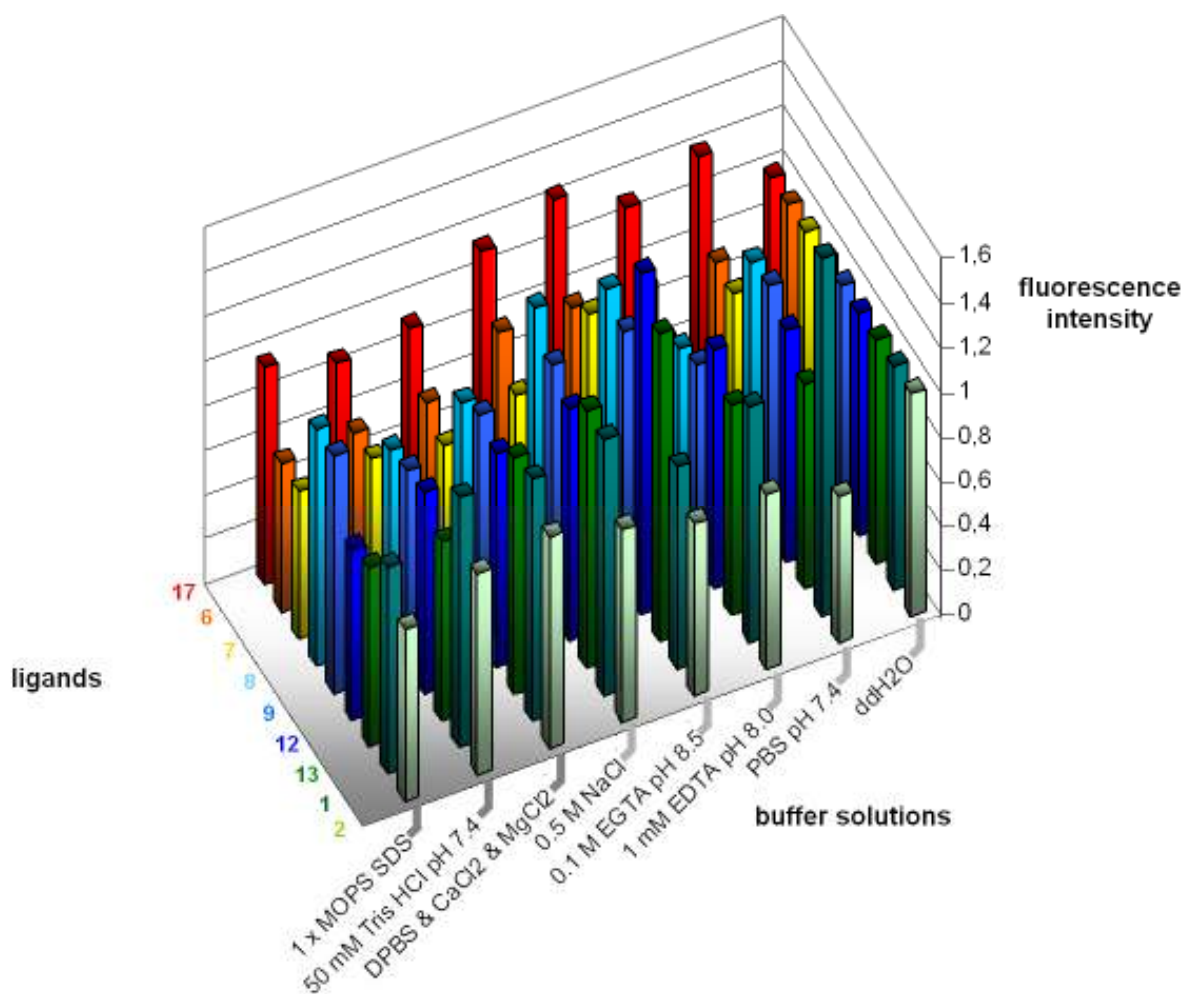


figure 22: Buffer test of CdSe/CdS/ZnS nanoparticles, with different coatings.

Repeat determination of the area of the emission peaks of CdSe/CdS/ZnS nanoparticles coated by M-PEO-*b*-PCL-*b*-PEI (**1**, **2**), DP-PEO-*b*-PCL-*b*-PEI (**12**, **13**), *t*C-PEO-*b*-PCL-*b*-PEI (**6**, **7**, **8**, **9**) and M-PEO-*b*-PEI-DDA (**17**) in water, 1xMOPS SDS, 50 mM Tris HCl pH 7.4, DPBS & CaCl₂ & MgCl₂, 0.5 M NaCl, 0.1 M EGTA pH 8.5, 0.1 M EDTA pH 8.5, PBS pH 7.4. Abbreviations are listed in chapter 7.2.1.2.5.

The results clearly indicate that the particles are remarkably stable in all buffer solutions. Only in some cases a slight decrease in fluorescence efficacy occurs. As expected no influence of the terminal endgroup at the PEO moiety is observed. It is further recognized that the PCL to PEO ratio can be modified over a rather broad range (1 : 3 for ligand **2** to 1 : 14 for ligand **6** and **7**) without significant changes in the stability. In some cases the quantum yield is even higher in the presence of buffer solutions like ethylene glycol tetraacetic acid (EGTA) as compared to water.

To further evaluate the impact of the PCL block on the fluorescence properties of the quantum dots, control experiments with PEI-*b*-PEO diblock-copolymer ligands **18** – **22** were performed, in a manner very similar to those described in a former publication^[224]. Ligands **18** – **22** are the analogues to ligands **1** – **5**, but do not contain the hydrophobic PCL segments. The ligands were

added to the quantum dots in a QD/P ratio of 1 to 300 in chloroform. After precipitation with heptane the nanoparticles were dissolved in water.

figure 23 shows the results of the respective buffer tests. Whereas these particles exhibit high fluorescence intensities in water, which are comparable to those of the triblock-copolymer they lose a significant fraction of their luminescence. These experiments impressively demonstrate the importance of the hydrophobic PCL moiety within the ligand shell for biostability of quantum dots.

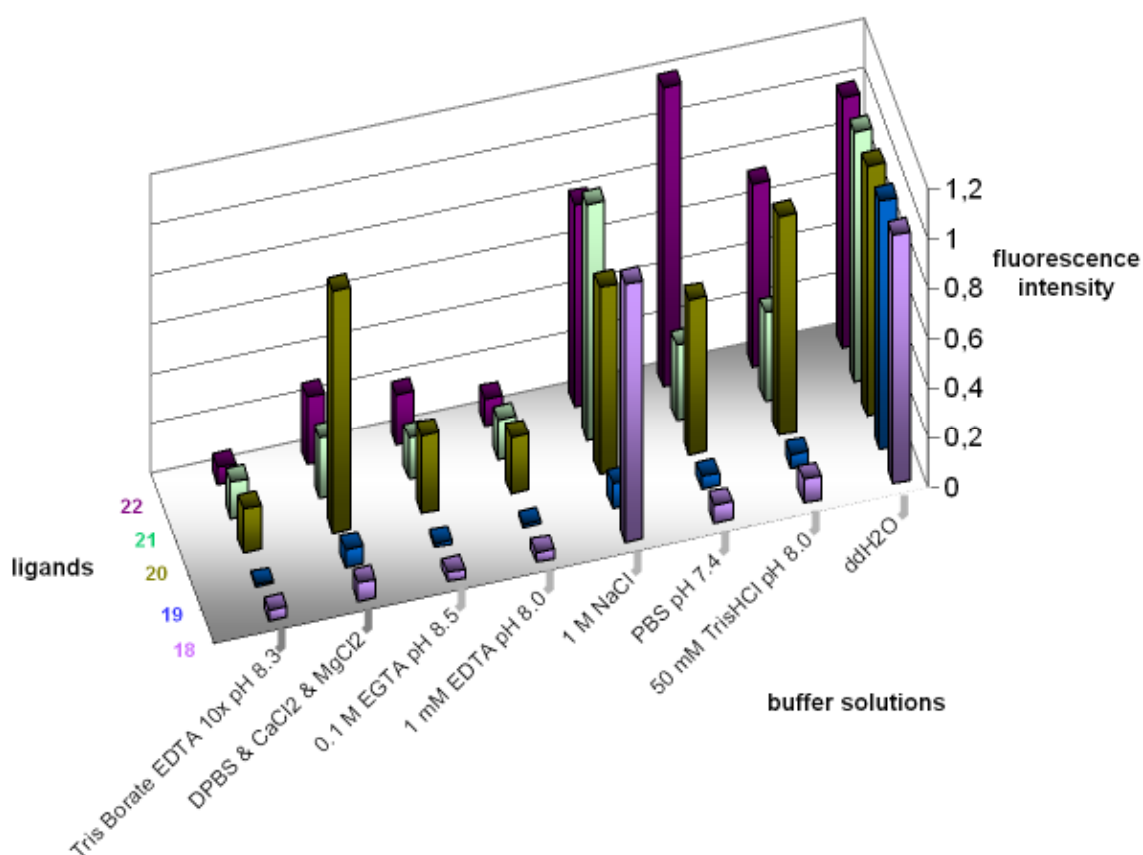


figure 23: Buffer test of CdSe/CdS/ZnS nanoparticles, with different coatings.

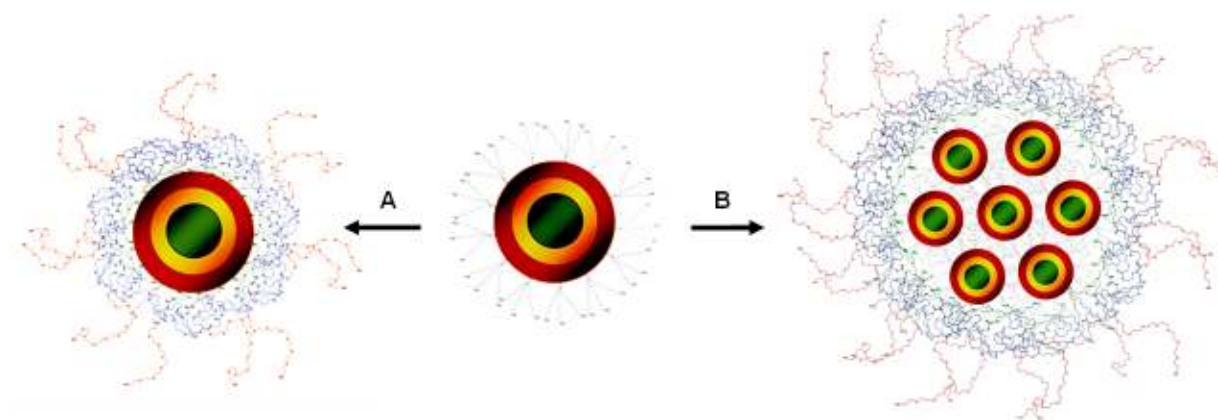
Repeat determination of the area of the emission peaks of CdSe/CdS/ZnS nanoparticles coated by (M-PEO₁₁₀₀-N₄) (**18**), (M-PEO₂₀₀₀)₃-PEI₇₀₀ (**19**), (M-PEO₂₀₀₀)₂-PEI₇₀₀ (**20**), (M-PEO₂₀₀₀)₂-PEI₄₂₃ (**21**), and (M-PEO₁₁₀₀)₂-PEI₇₀₀ (**22**) in water, tris borate EDTA 10x pH 8.3, DPBS & CaCl₂ & MgCl₂, 0.1 M EGTA pH 8.5, 1 M EDTA pH 8.5, 1 M NaCl, PBS pH 7.4, 50 mM Tris HCl pH 8.0. Abbreviations are listed in chapter 7.2.1.2.5.

The reason for the quenching is the absence of the hydrophobic shielding and the far lower stability of the arranged nanocomposites due to the unhindered displacement of the ligands. The ligand containing only two primary amines per ligand exhibits (M-PEO₁₁₀₀)₁-N₄ (**18**) the lowest bond strength to the nanoparticle surface of the applied ligands.

2.2.3 Self assembly to multifunctional beads

As recently demonstrated, amphiphilic nanoparticles with outermost PEO blocks can undergo thermodynamically driven self assembly processes like amphiphilic molecules^[250]. In particular, the formation of cylinder micelles, γ -branched networks and vesicular structures was observed by controlling the packing parameter which reflects the ratio of the volume fractions of hydrophobic and hydrophilic moieties. The triblock-copolymers used here can also undergo self assembly to micellar structures in the absence of nanoparticles due to their amphiphilic properties. When hydrophobic nanoparticles are present they will be encapsulated and may even serve as nucleation site for small micelles by binding the PEI block of the triblock-copolymer at its surface.

The formation of these individually encapsulated particles (beneath empty micelles) is favoured by a large polymer to particle ratio (route A in schema 10). If, however, this ratio is gradually decreased the amount of ligand will finally no longer be sufficient to encapsulate each particle individually. In this case, larger micelles will be formed, each encapsulating several particles (route B in schema 10).



schema 10: encapsulation of nanoparticles in one PEO-*b*-PCL-*b*-PEI micelle.

Representative TEM images of M-PEO-*b*-PCL-*b*-PEI (2) micelles are shown in figure 24. The raspberry-like micelles contain on average twenty nanoparticles.

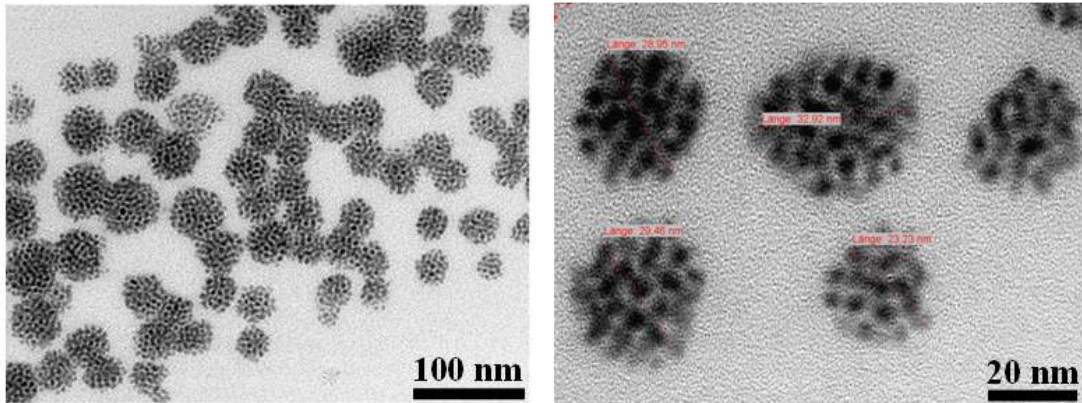


figure 24: CdSe/CdS/ZnS coated by ligand M-PEO-*b*-PCL-*b*-PEI (2) in water.

Contrary by increasing the nanoparticle to ligand ratio the total PEO surface, which is directed to the aqueous medium, declines. At a certain amount not enough ligands are available to stabilize the total surface of all present nanoparticles. Accordingly the nanoparticles close ranks to minimize the surface toward the solvent. The new structure could be promoted by the ligand, through the hyperbranched binding side, which allows a single ligand to bind to more than one nanoparticle. This effect is illustrated in figure 24. The TEM image shows CdSe/CdS/ZnS quantum dots encapsulated in M-PEO-*b*-PCL-*b*-PEI (2). Obtained micelles show a diameter of the hydrophobic segment of ~30 nm, wherein ~30 nanoparticles are embedded. By decreasing the quantum dot to ligand ratio from 1:400 to 1:50 the micelles increase their hydrodynamic diameter from 27 nm to 117 nm (intensity application) according to dynamic light scattering (DLS) measurements (figure 25).

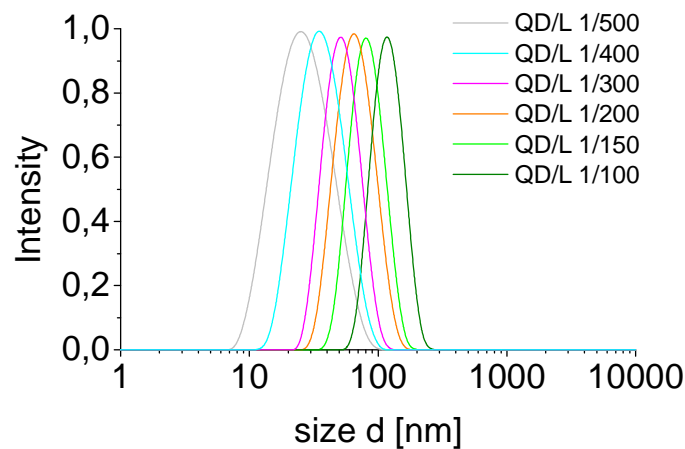


figure 25: DLS-Intensity distribution of CdSe/CdS/ZnS coated by PEO-*b*-PCL-*b*-PEI (10) with different quantum dot to ligand ratios (QD/L) in water.

This size range is reasonable considering the expansion of the ligand in water and the additional solvation shell. TEM images corroborate the presumption of single nanoparticles concerning a quantum dot to ligand ratio of 1:400 (figure 26). Some domains of aggregates on the grid may be ascribed to evaporation effects of water. Decreasing the nanoparticle to ligand ratio of 1:300, 1:200, and finally to 1:100 demonstrates the growth of micelles and the increasing number of nanoparticles encapsulated in a single micelle (figure 26).

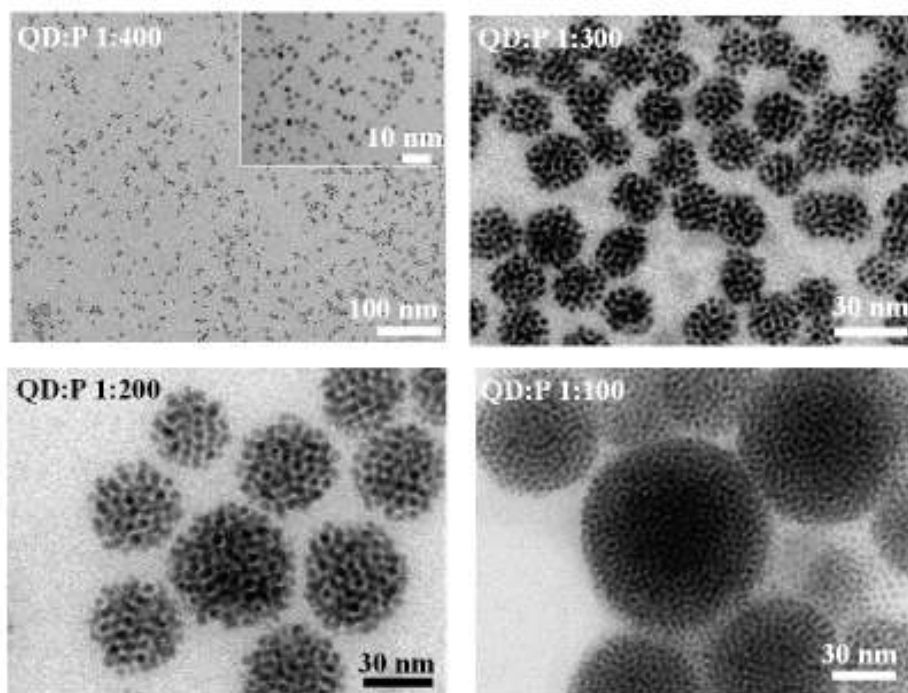


figure 26: TEM images of CdSe/CdS/ZnS nanoparticles coated with ligand **10** after evaporation of the previous solvent water.

The rate of water addition to THF solution, in which the nanoparticles and the triblock polymers are present, during phase transfer as well as the concentration of the THF/nanoparticle solution offers a secondary control of the size of the micellar structures. Schabas *et al.*^[251] determined that the faster water is added the faster self-assembly occurs, which results in a corresponding decrease in mean particle diameter. Same results were achieved using the triblockpolymer.

The versatile options of the unique ligand have also been demonstrated in case of InP (synthesized by Tim Strupeit), PbS (synthesized by Constanze Schliehe), Au (synthesized by Michael Ijeh), FePt (synthesized by Hauke Heller), FeO_x (synthesized by Ulrich Tromsdorf), NiPt (synthesized by Dr. Kirsten Ahrensdoerf) GdPO₄ and NaYF₄ particles (both synthesized by Dr. Volker Bachmann). Single as well as multi nanoparticle micelles could be formed by varying of the nanoparticle/polymer ratio during ligand addition (figure 27).

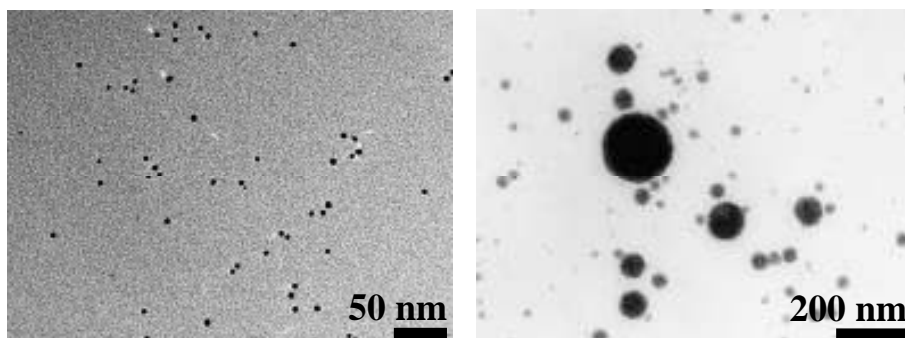


figure 27: TEM images of NiPt nanoparticles coated with the triblock polymer after evaporation of the prior solvent water.

The conclusion can be made, that the ligands don't make demands in terms of nanoparticles. In the ambit of fluorescent nanoparticles the ligand is compatible with a wide range of different shell materials of the cores. Thus a diverse selection of CdSe as well as CdSe/CdS or CdSe/CdS/ZnS nanoparticles could be solubilised in water easily and quantitatively.

It has been reported that clustering of superparamagnetic magnetite nanoparticles results in higher saturation magnetization than that of individual ones because of the interaction between the assembled nanoparticles^[252]. TEM-images of encapsulated magnetite nanoparticles (figure 28) show the versatility of the triblock-polymer as a ligand for such purposes.

Magnetite nanoparticles are a promising material as magnetic resonance imaging (MRI) contrast agents as well as for applications like magnetic separation, drug delivery, and cancer hyperthermia^[253-257]. The controlled packing of magnetite nanoparticles is therefore an important achievement.

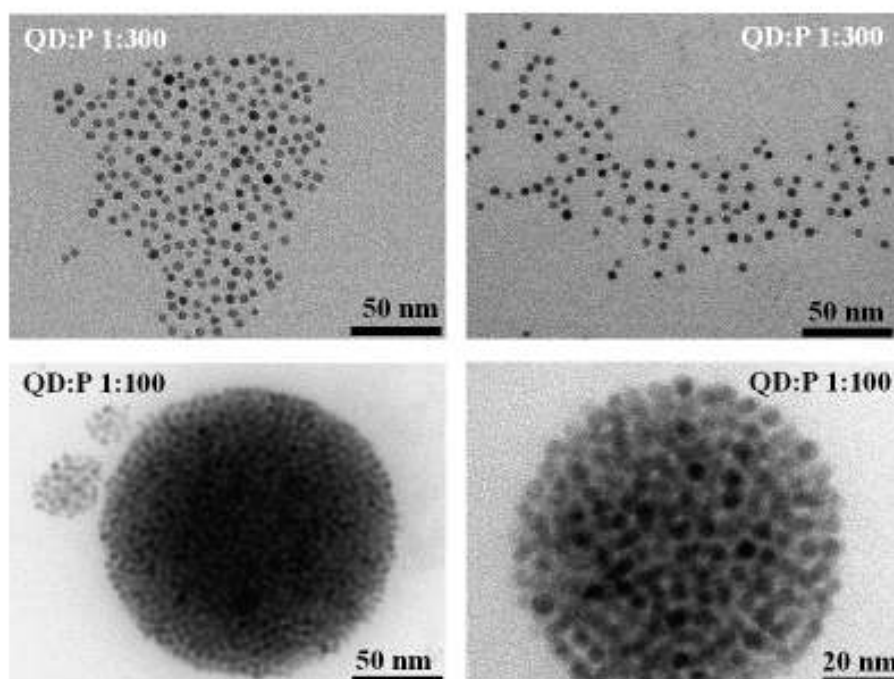
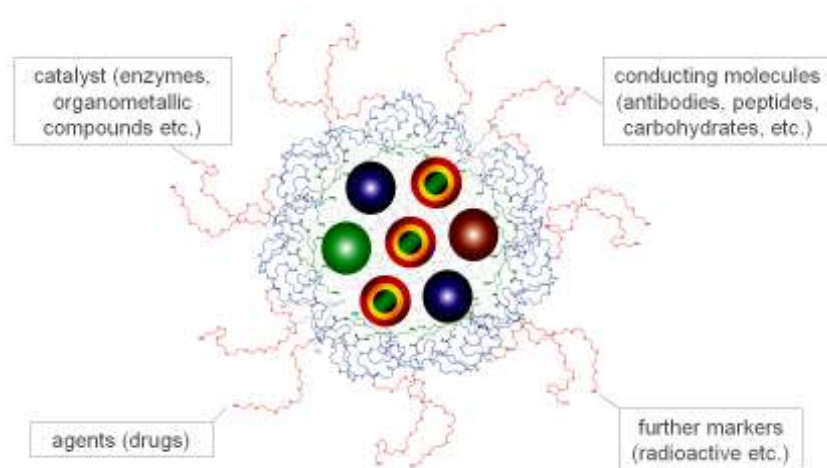


figure 28: magnetite nanoparticles coated by ligand 2 after evaporation of the prior solvent water.

Park *et al.*^[258] published prospects using PEO-phospholipid micelles, which contain multiple different kind of nanoparticles, whereby a combination of properties is achieved. In the case of quantum dots with their optical properties and SPIONs with their superparamagnetic properties, a nanocomposite is created that is simultaneously detectable via fluorescence spectroscopy and magnetic resonance imaging (MRI)^[259-264]. Those multifunctional nanoparticles open up a wide field of application for biomedical imaging *in vivo* and *in vitro*, even having the potential to integrate therapeutic and diagnostic functions into a single nanodevice^[197, 256, 265-271]. Previous *in vitro* studies have demonstrated that drug molecules and magnetic particles can be incorporated within a micelle to enable the corroboration of drug delivery by MRI^[43, 45].



schema 11: PEO-b-PCL-b-PEI micelles containing different nanoparticles.

Micellar structures were also obtained, which contain different nanoparticles like quantum dots in combination with FeO_x , NiPt_x or GdPO_4 particles (schema 11).

Since the ligand encapsulation is a rather general approach it can also be applied for the formation of multifunctional beads. In order to demonstrate this 22 nm large FeO_x and 8 nm NiPt_x nanoparticles were co-encapsulated into micellar nanobeads using DP-PEO-*b*-PCL-*b*-PEI (12). Due to the difference in size and contrast the loading of micelles with a mixture of these particles is easily recognizable in TEM (figure 29).

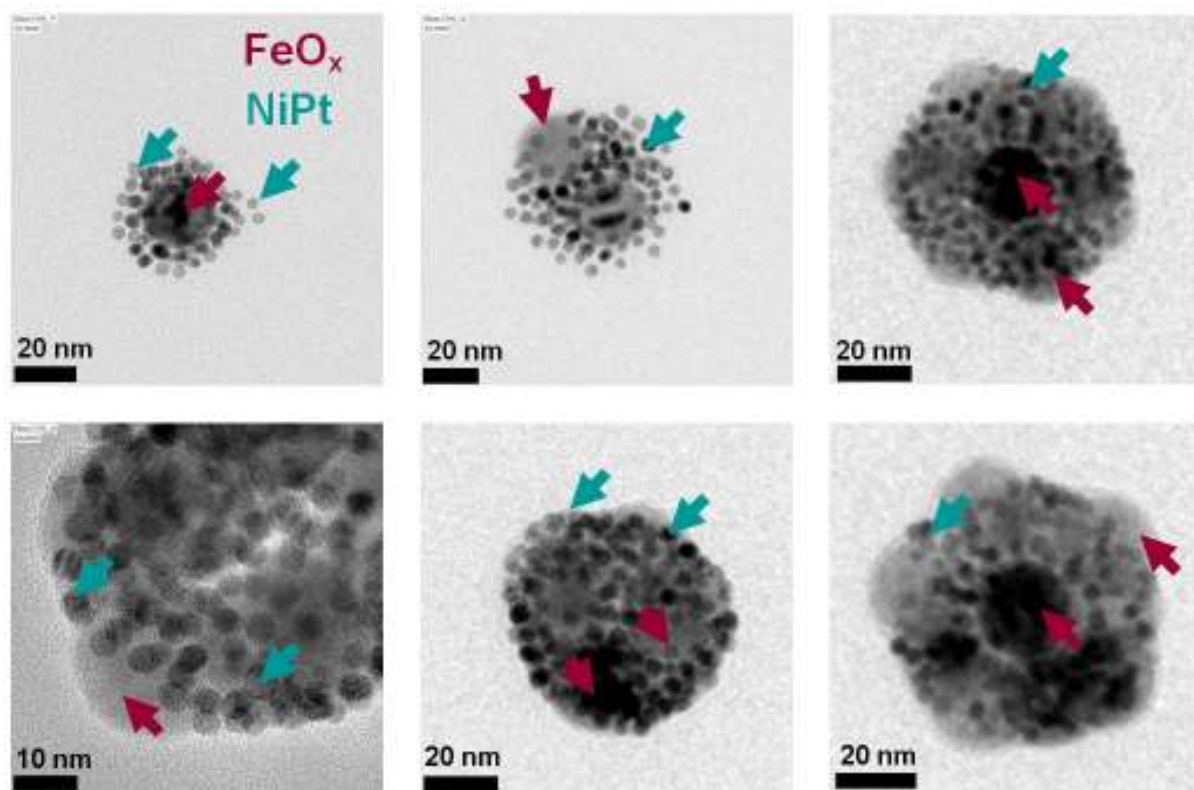


figure 29: TEM images of FeO_x (diameter ~ 22 nm) and NiPt (diameter ~ 8 nm) nanoparticles coated with ligand **12** after evaporation of the prior solvent water.

Other combinations of particles are, of course, also accessible by the described procedure. TEM images of DP-PEO-*b*-PCL-*b*-PEI (**12**) micelles containing CdSe/CdS/ZnS (QDs) and NiPt nanoparticles are shown in figure 30. From the differences in the lattice and the contrast it is easy to distinguish the presence of both kinds of nanoparticles in each micelle. The raspberry shape of the micelles was not maintained on the TEM grid. The reason for this might be the major difference of the FeO_x and NiPt nanoparticles, their different surface ligands and the different affinities of the amines of triblock ligand **12** to the different nanoparticle surfaces.

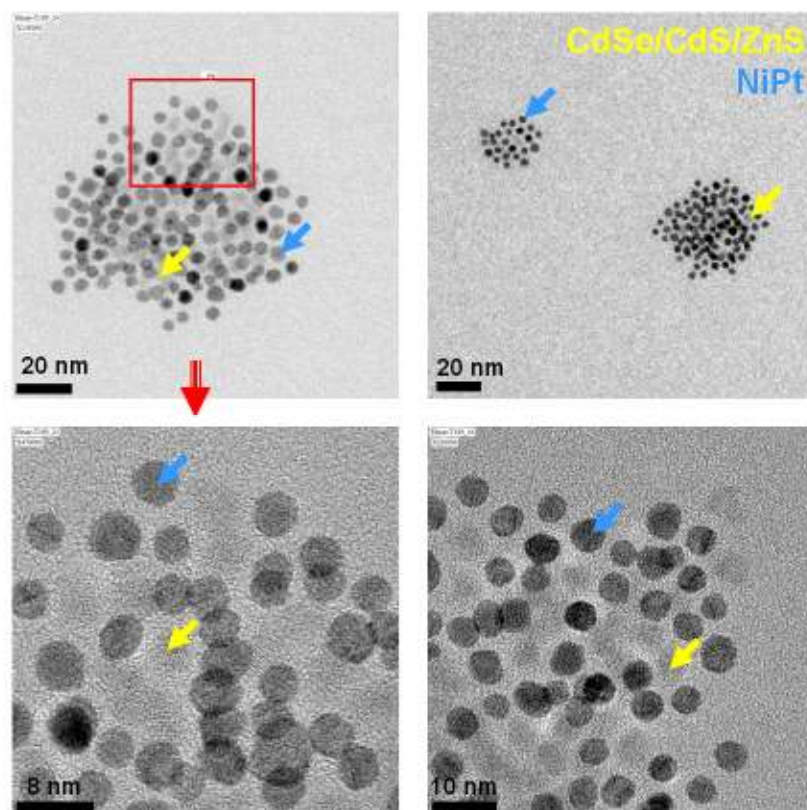
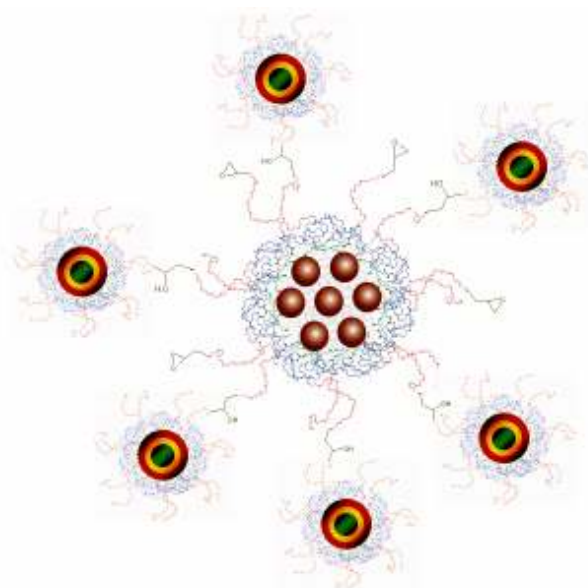


figure 30: TEM images of CdSe/CdS/ZnS and NiPt nanoparticles coated with ligand **12** after evaporation of the prior solvent water.

The fluorescence quenching of CdSe/ZnS nanoparticles in the presence of superparamagnetic FeO_x, which has been debated in literature^[263], could also be observed in the case of CdSe/CdS/ZnS, which were packed together with FeO_x nanoparticles inside the micelles. This is an indication that the inorganic shells of the CdSe nanoparticles, viz. CdS and ZnS shells, can be further improved and underlines the challenge of the ligands to stabilize the quantum yield.

Using triblock-polymers and coupling strategies, not only is encapsulation within one micelle possible (schema 11), but it also spacing at certain distances from the surface is feasible by coupling strategies (schema 12). Such multifunctional nanocomposites should overcome the obstacle of other hybrid nanosystems, owing to their high stability. In particular in vivo cancer imaging and hybrid therapy nanosystems have shown low stability or short systemic circulation times^[272, 273]. First attempts involved the subjection of SPIONs to a ligand addition with a carboxylic-functionalised triblock ligand and esterification with quantum dot containing micelles with terminal hydroxylic group. Another ligand (chapter 2.3), which offers a higher multiplicity of functionalisation and consequently coupling strategies, was used for this objective.



schema 12: nanocomposite of magnetic nanoparticles and quantum dots.

The new triblock polymer not only allows a simple strategy to achieve a phase transfer of nanoparticles from organic into aqueous media, but also accomplishes a dense and stable coating, which offers functional groups access to the aqueous medium. In the domain of nano-architecture among the constructing of superior structures all the way to meta-structures the multifunctional nanocomposites can certainly be equipped with further markers like radioactive compounds (^{18}F), conducting molecules, catalysts, and drugs (schema 11).

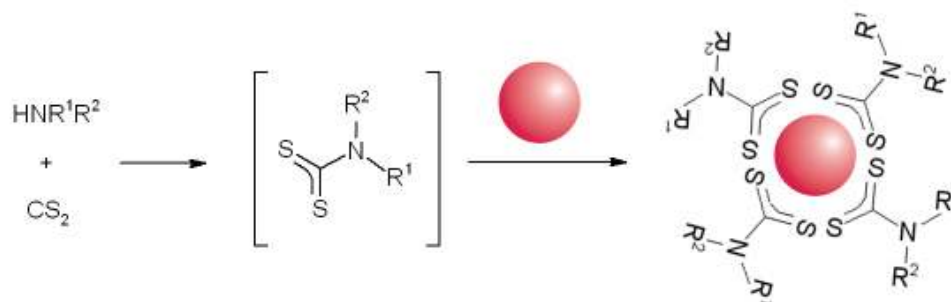
Multifunctional beads offer easy route to molecular imaging combinations like e.g. fluorescence imaging and MRI or MRI and positron emission tomography (PET). Such combinations are currently under development since the striking features of each technique like high sensitivity, high special resolution or high temporal resolution can be combined into a new quality of imaging.

Moreover, such multifunctional nanobeads open up the possibility to integrate therapeutic and diagnostic functions in a single nanodevice^[197, 256, 265-271]. Previous in vitro studies have demonstrated that drug molecules and magnetic particles can be incorporated within a micelle to enable the combination of drug delivery with MRI^[43, 45].

2.2.4 Binding motif $\text{R}^1\text{R}^2\text{N}(-\text{C}(\text{S})\text{S}^-)$

The bond strength to the nanoparticle surface can be advanced easily by amplifying a part of the amines with carbon disulfide (CS_2), which is illustrated in schema 13. The obtained bidentate chelating carbodithioate ($-\text{C}(\text{S})\text{S}^-$) exhibit a significant enhanced stability against

photooxidation, which is a handicap of other thiol ligands^[274-276]. The photooxidation is accompanied by the formation of disulfides, which leads to the precipitation of the nanoparticle^[277].

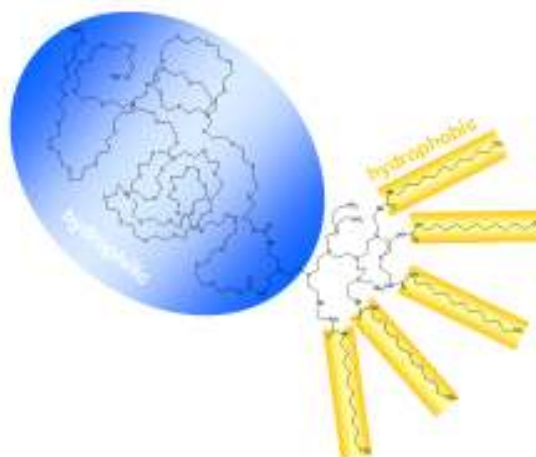


schema 13: CS₂ approach.

According to the amount of amines per ligand the ligand was incubated with carbon disulfide in an eight fold excess for one to five minutes until the nanoparticles were added. The results show especially in the case of PEO-*b*-PEI ligands a better stabilization of CdSe/CdS nanoparticles.

2.2.5 Binding motif PEI-(DDA)₇₋₈

The binding motif of PEO-*b*-PCL-*b*-PEI can be converted into single alkyl chains. A ligand (-DDA) has been developed by coupling dodecylamines over the amines on M-PEO-PEI via urea bonds. The aliphatic dodecylchains act as fingers, which grasp into the TOPO-surface of the nanoparticles (schema 14). Consequently this ligand contains hardly any primary amines. This modification is also adapted for the PEO-*b*-PCL-*b*-PEI ligand.



schema 14: illustration of ligand M-PEO-PEI-DDA (17).

The comparison of the DDA modified ligand with the prior PEO-*b*-PEI ligand in $^1\text{H-NMR}$ measurements indicates the absence of primary amines and the presence of the dodecyl chains.

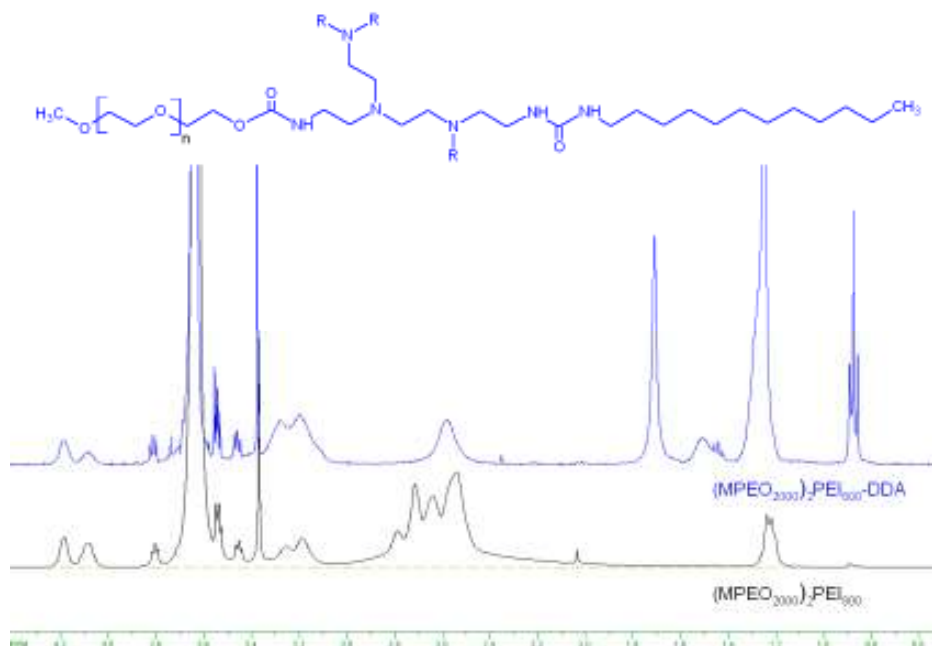


figure 31: $^1\text{H-NMR}$ (400 MHz, CDCl_3) of PEO-*b*-PEI in comparison with PEO-*b*-PEI-(DDA)_{7,8}

The ligand addition was achieved in the same way as with the triblock polymers. A highly close packing occurs by using this new M-PEO-*b*-PEI-DDA ligand (figure 32). The TEM images document the stable architecture of the micellar formation, which obviously is rugged under high vacuum. The packing is so close that even packing layers can be seen (figure 32, picture 1). This documents the firmness of hydrophobic interactions and van der Waals forces between the polymethylene layers of the ligand and TOPO, which needn't be removed like in typical ligand exchange procedures.

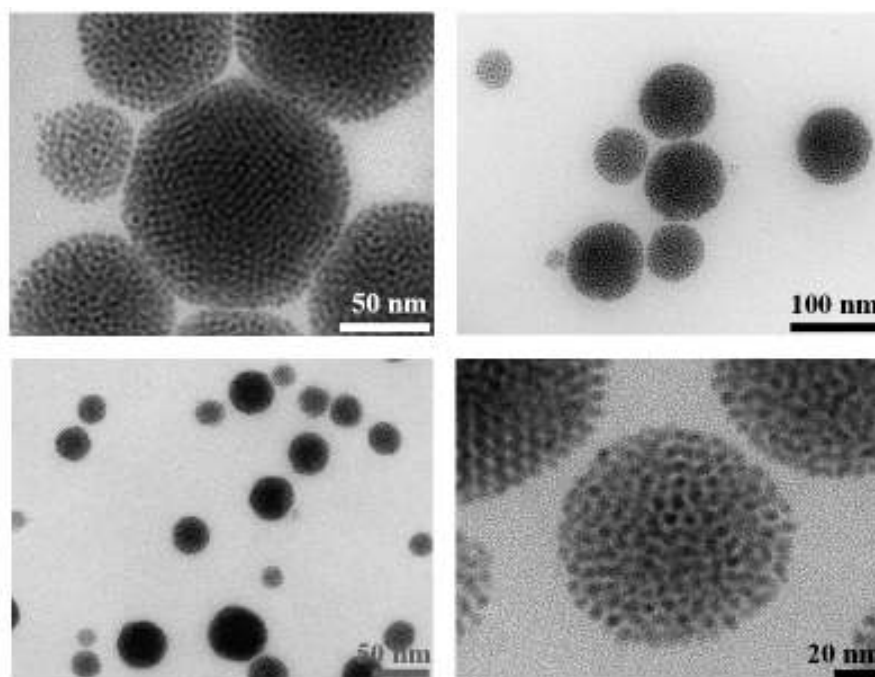


figure 32: TEM images of CdSe/CdS/ZnS nanoparticles coated by M-PEO-PEI-DDA (**17**) in water.

Similar to the ligand addition with *t*C-PEO-*b*-PCL-*b*-PEI (**6-9**) the new M-PEO-*b*-PEI-DDA (**17**) coating and the transfer to water produces an increase of the Stokes shift from 14 to 20 nm. The exciton peak in UV-vis spectroscopy (figure 33) remained at 580 nm and the emission maximum shifted from 594 nm to 600 nm, which can be attributed to the change due to the dielectric constant of the solvent ($\text{CHCl}_3 \rightarrow \text{THF}$) in the environment of the nanoparticles.

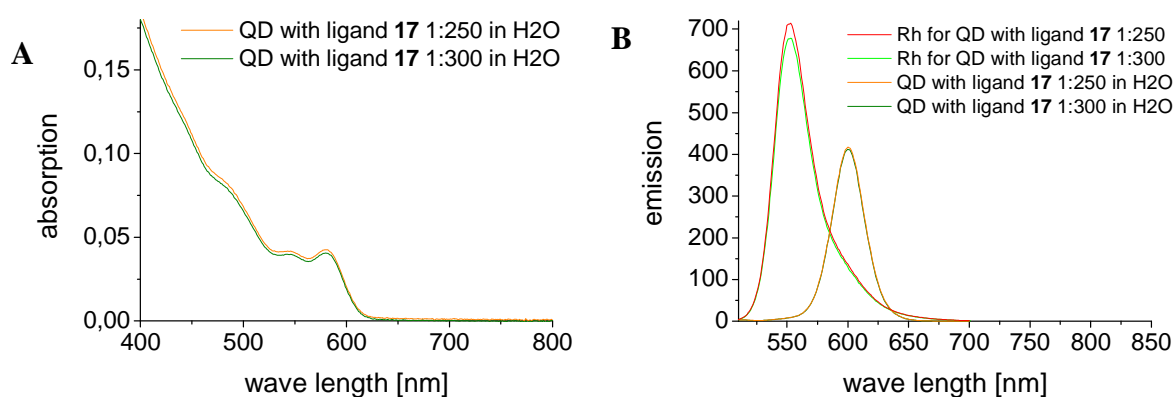


figure 33: absorbance spectra (a) and emission spectra (b) of CdSe/CdS/ZnS quantum dots (QD) coated by M-PEO-PEI-DDA (**17**) in water.

DLS measurements show a hydrodynamic radius of more than 70 - 180 nm (figure 34). Diminishing the polydispersity of the polymers and modifying the phase transfer should lead to micellar structures of smaller sizes and size ranges.

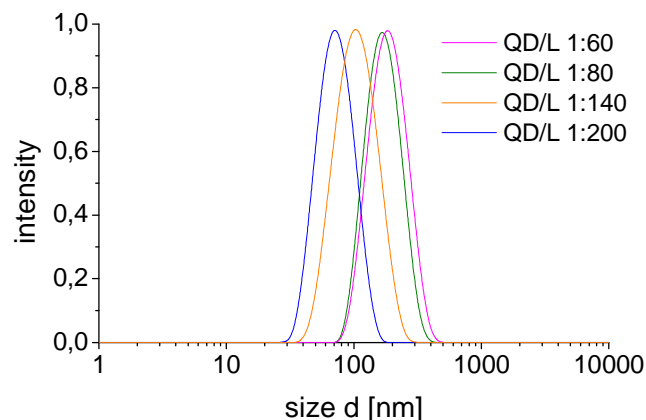


figure 34: DLS-Intensity distribution of CdSe/CdS/ZnS coated by ligand M-PEO-PEI-DDA (**17**) with different quantum dot to ligand ratios (QD/L) in water.

It is noteworthy that the close packing does not degrade the remarkable quantum yields of the nanoparticles. Thus, the nanoparticles exhibit a packing which isn't identical with agglomeration. Agglomeration appears in the absence of a certain amount of ligands., This is a drawback which can arise, for example, when TOPO ligands are removed during ligand exchanges in which the binding group of the new ligand has to interfere with the nanoparticle surface. The direct contact of the nanoparticles leads to a darkening of the sample, a quenching of the fluorescence.

This ligand has already been equipped with functional groups like carboxygroups (tC^-) to yield the opportunity for applications in case of coupling reactions. An additional PCL segment can be introduced, which supplements the dodecyl-fingers.

Hence, the multilateral accoutrement and transferability of the ligand to various nanoparticles opens a potential and manifold way to implement nanoparticles not only in biological systems.

2.2.6 MMA polymerization in the presence of QDs

For cryogenic temperature measurements quantum dots have to be embedded in a polymer. CdSe/CdS/ZnS quantum dots were coated with the ligands **8**, **9**, **12**, and **17**. The hydrophilic ligand shell allowed the dissolving in methyl methacrylate (MMA) and polymerisation in blocks (figure 35). The radical polymerisation resulted in no decrease in quantum yield.

The anionic ring polymerisation leads to a PI block mainly consisting of the isoprene units of the isomers 3.4 and 1.2. Such units offer a terminal double bond. In figure 37 the $^1\text{H-NMR}$ of PI-OH and PI-*b*-PEO-OH are shown. The generation of the 1.4 isomer is mostly not observable. Due to signal-overlay the presence of the 1.4 isomer couldn't be excluded totally. Thus the 1.4 PI units were also stated in the NMR analyses in the experimental section.

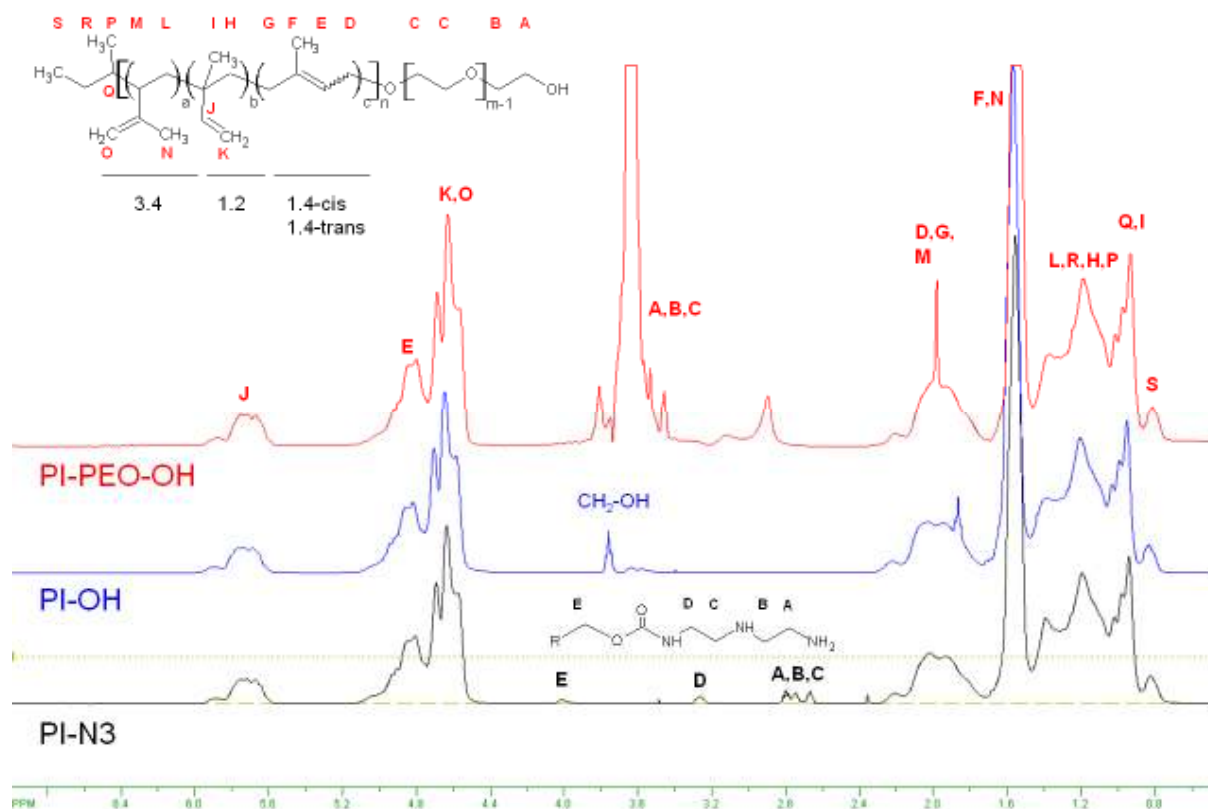


figure 37: $^1\text{H-NMR}$ (400 MHz, CDCl_3) of $\text{PI}_{61}\text{-}b\text{-PEO}_{212}\text{-OH}$ (red), $\text{PI}_{61}\text{-OH}$ (blue), and $\text{PI}_{30}\text{-N}_3$ (black).

Such lipid-like block copolymers form micelles^[279-281] in dilute solutions via self-assembly. Their shape depends on the aspect ratio of the two blocks. Large hydrophilic weight fractions ($f_{\text{phil}} < 60\%$), represented by the PEO-block, form the desired spherical micelles in water. This structure is adopted because it minimizes the contact area between non-polar tails and water and thus reduces the positive free energy associated with the hydrophobic effect^[282]. Their size depends on the aggregation number (Z), i. e., the number of block copolymers in a micelle, which is determined by the length of the polymer blocks^[283]. This is governed by the scaling law^[284, 285] $Z = Z_0 N_A^\alpha N_B^{-\beta}$, where $\alpha = 2$ and $\beta = 0.8$. In this equation N typifies the degree of polymerisation of the appropriate block, a stands for the soluble block, and b for the insoluble block. Z_0 mainly depends on the enthalpy of mixing between the insoluble polymer block A and the solvent.

2.3.1 Terminal functionalisation of PI-*b*-PEO

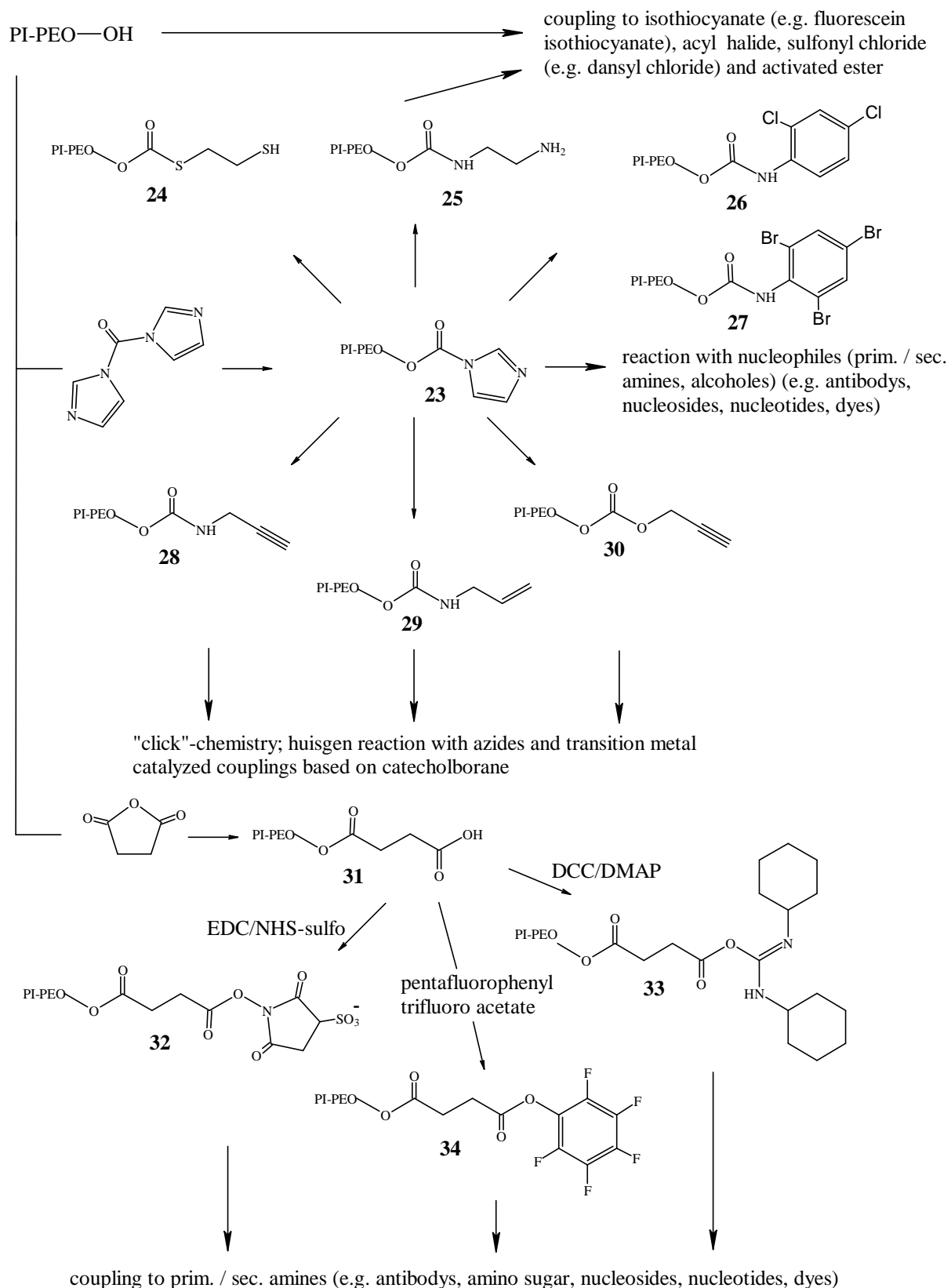
Among the tailoring of size and composition of the micellar structures, the characteristics of the new ligand allow manifold functionalisation strategies, which will be subsequently discussed. The integrated terminal functional groups allow miscellaneous functions for the attachment of further molecules (additives) such as drugs, dyes, catalysts a.s.o.. Because of the large variety of functional groups which could be attached, the additives can be coupled before ligand addition as well as after micelle formation via self assembly, which facilitates coupling routes in organic and inorganic solvents. This provides a plurality of chemical reaction routes. Moreover, the use of different functional groups enables the selective and simultaneous attachment of different molecules via different coupling strategies.

The functional groups also lead to diverse interactions in biological media. Different charges may be incorporated on nanoparticle and micelles respectively under physiological conditions. For instance positive charges assist the uptake by lymphocytes.

For functionalisation the presence of just one terminal hydroxylic group of PI-*b*-PEO-OH on the block copolymer is preferable. This allows the straightforward attachment of a multiplicity of functional groups without the integration of protection groups and without an influence on later ligand addition procedures with nanoparticles during self-assembly. Common PEO functionalisation strategies can be adopted^[286, 287]. Implementation of an assortment of functional groups is shown in figure 38.

During the synthesis of the block copolymer carboxylic groups were inserted into the PI-*b*-PEO ligand as protected ethyl esters in the process of polymerisation abruption by aborting the polymerisation with ethyl 2-bromoacetate. The ethylester can be hydrolyzed before ligand addition by hydrolysis in 0.5 M NaOH at room temperature. Alternatively the hydrolysis can be catalyzed enzymatically by pig liver esterase^[237] or thermitase^[238].

The hydroxylic group, which is gained by termination of the polymerisation via an acid, allows modifications (figure 38), which again allow the attachment of molecules before and after ligand addition.



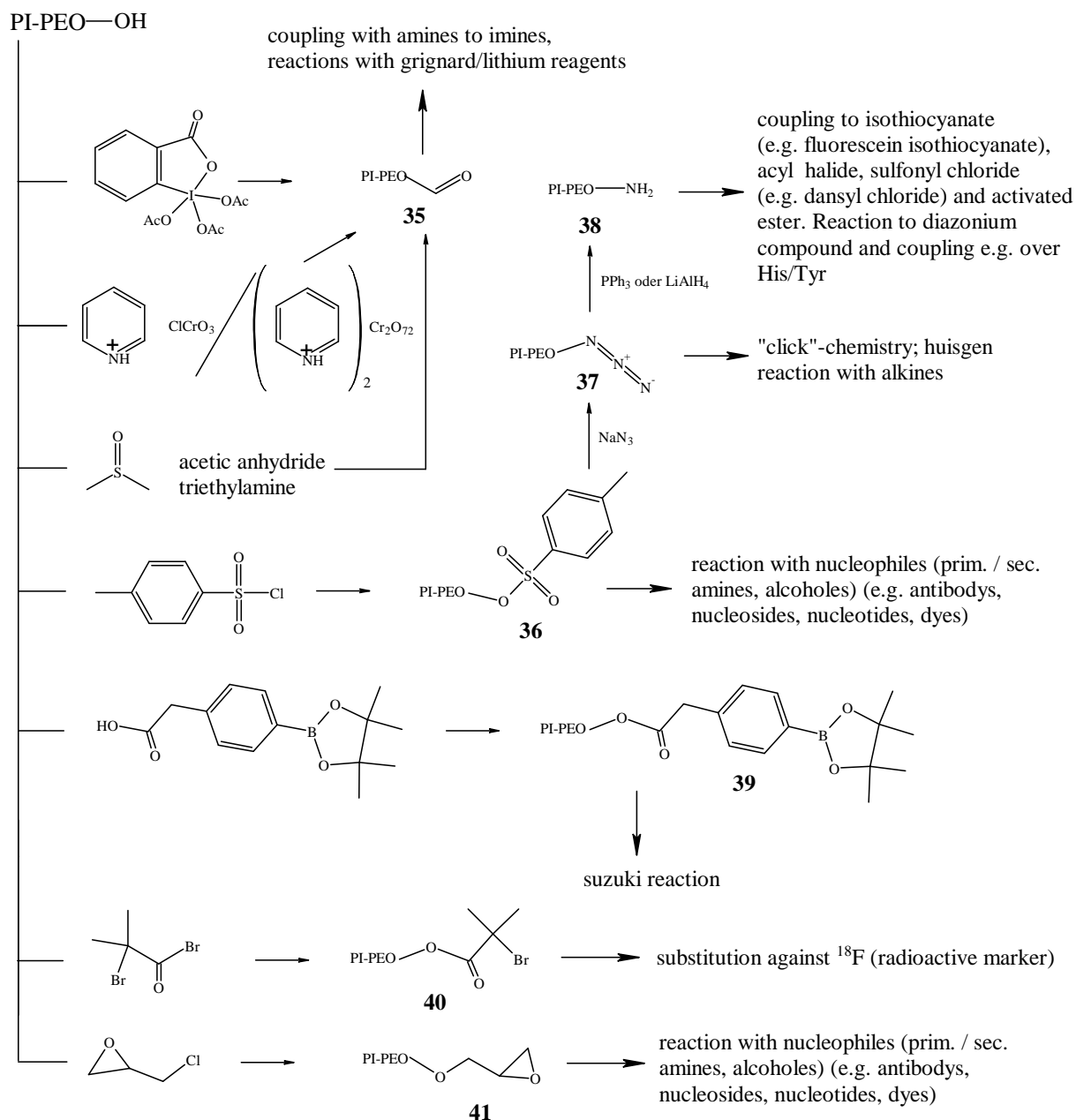


figure 38: assortment of functionalisation strategies.

One alternative to attach a carboxylic group on the PEO block was achieved via the reaction with succinic anhydride^[288-291]. The nucleophilic ring opening reaction of the PI₆₁-*b*-PEO₂₁₂-OH with succinic anhydride was catalysed by the Steglich-Höfle catalyst 4-Dimethylaminopyridine (DMAP). Based on proton migration the proton of the carboxylic group is hardly detectable in nmr spectroscopy in the range of 11 ppm. Nevertheless, the methylene protons could be detected (figure 39-1.).

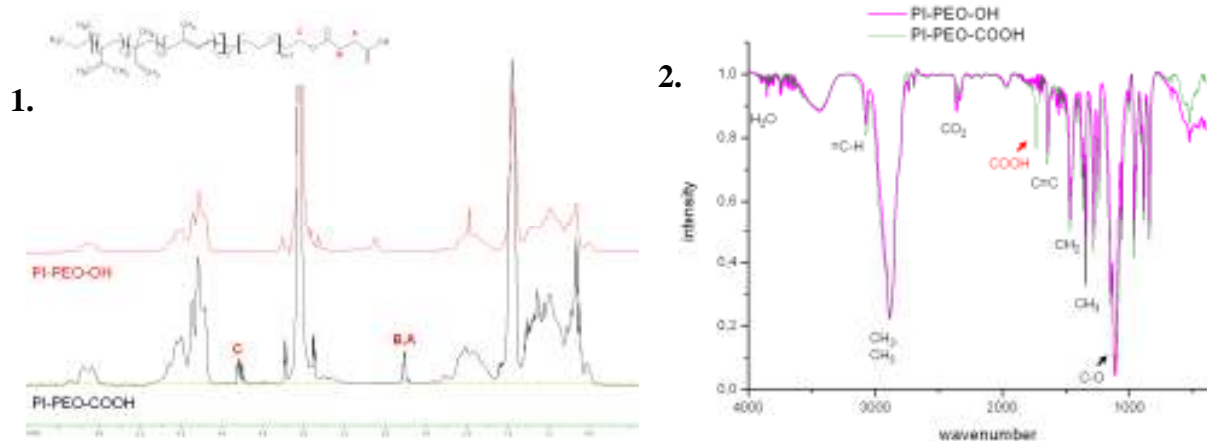


figure 39: 1. $^1\text{H-NMR}$ of $\text{PI}_{61}\text{-}b\text{-PEO}_{212}\text{-OH}$ in comparison to $\text{PI}_{61}\text{-}b\text{-PEO}_{212}\text{-COOH}$ (500 MHz, CDCl_3).

2. FT-IR of $\text{PI}_{61}\text{-}b\text{-PEO}_{212}\text{-OH}$ in comparison to $\text{PI}_{61}\text{-}b\text{-PEO}_{212}\text{-COOH}$.

The methylene stretches of poly(ethylene oxide) and methylene and methyl stretches of poly(isoprene) appear between $2,983$ and $2,780\text{ cm}^{-1}$, while additional deformations of methylene emerge at $1,466$ and methyl at $1,340\text{ cm}^{-1}$. Also prominent is the $=\text{C-H}$ out-of-plane wag at 844 cm^{-1} . Smaller but distinctive peaks exist at $3,076\text{ cm}^{-1}$ for the $=\text{C-H}$ stretch, $2,745\text{ cm}^{-1}$ for the overtone of the methyl deformation and $1,642\text{ cm}^{-1}$ for the $\text{C}=\text{C}$ stretch. The C-O stretch, regarding poly(ethylene oxide) is strong and appears at $1,114\text{ cm}^{-1}$, whereas the methylene stretches appear at 2790 cm^{-1} .

Fourier transform spectroscopy (FT-IR) shows a characteristic vibration at 1735 cm^{-1} , which can be assigned to the carboxylic group evoked by H-bridging with the ether functions of poly(ethylene oxide) (figure 39-2.).

Carboxylic groups are chelating agents which for example can interact with magnetite surfaces. In this case the hydrophobic, crosslinkable PI-segment and the prior encapsulation in $\text{PI}_{30}\text{-N3}$ shows an advantage over other ligands due to the fact that the hydrophilic PEO segment is always exposed to the aqueous phase and an interaction of the carboxylate with the nanoparticle surface is prevented by the PI segment.

In connection with coupling strategies in organic solvents a pentafluorophenyl active ester was synthesized from $\text{PI}_{61}\text{-}b\text{-PEO}_{212}\text{-COOH}$ using pentafluorophenyl trifluoroacetate. The product could be identified by $^1\text{H-}$ and $^{19}\text{F-NMR}$ (figure 40-1.). The $^1\text{H-NMR}$ spectrum shows separation of the methylene multiplet of the polymeric succinic acid segment from 2.6-2.7 ppm to two triplets at 3.0 and 2.8 ppm. At the same time, the $^{19}\text{F-NMR}$ spectrum shows the expected signals of the five fluorine atoms attached to the aromatic ring at -152.5 ppm, -157.8 ppm and -162.4 ppm that can be assigned to the fluorine atoms in ortho, para and meta position, respectively, with a peak integration ratio of 2:1:2.

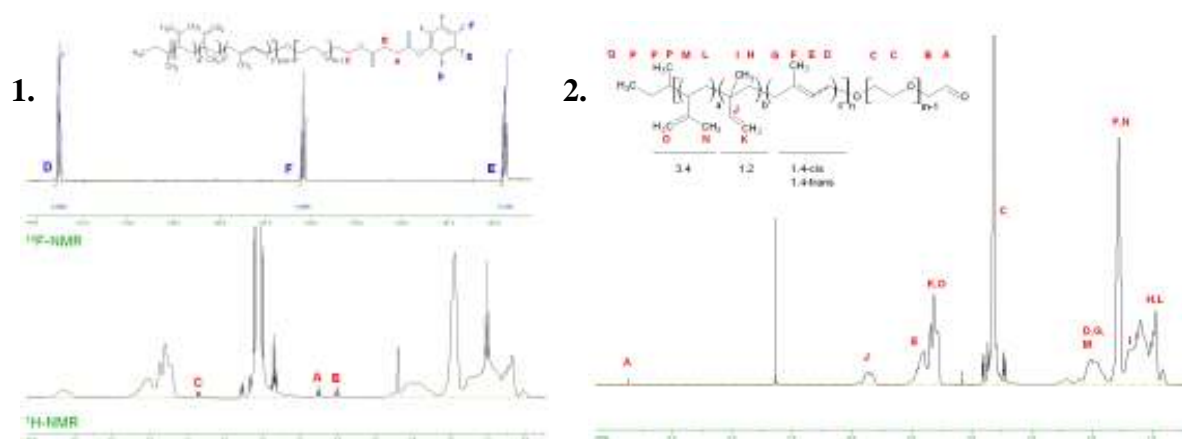


figure 40: 1. ^1H - & ^{19}F -NMR (400 MHz, CDCl_3) of $\text{PI}_{61}\text{-}b\text{-PEO}_{212}$ -pentafluorophenyl ester.
2. ^1H -NMR (400 MHz, CDCl_3) of $\text{PI}_{61}\text{-}b\text{-PEO}_{212}$ -aldehyde.

The Dess-Martin periodinane (DMP) oxidation of the primary PEO-terminal alcohol, which was performed by interrupting the polymerisation using acetic acid, runs under very mild conditions at room temperature with high yields. The aldehyde could be verified using ^1H -NMR (figure 40-2.).

In comparison to chromate based oxidants DMP shows a lower toxicity and shorter reaction times^[292]. Moreover other functional groups like $\text{C}=\text{C}$ double bounds, ethers, enolethers, epoxides, furanes, sulfides, thiols and secondary amines stay unaffected. Meyer *et al.*^[293] report that marginal amounts of water have a catalytic affect on the oxidation.

The Pfitzner-Moffatt oxidation^[294] is an additional mild and selective oxidation of primary and secondary alcohols by dimethyl sulfoxide. The resulting PEO-alkoxysulfonium ylide rearranges in this case to generate an aldehyde with no trace of the corresponding acid. This reaction is a rapid oxidation at room temperature, which is even attractive for labile compounds.

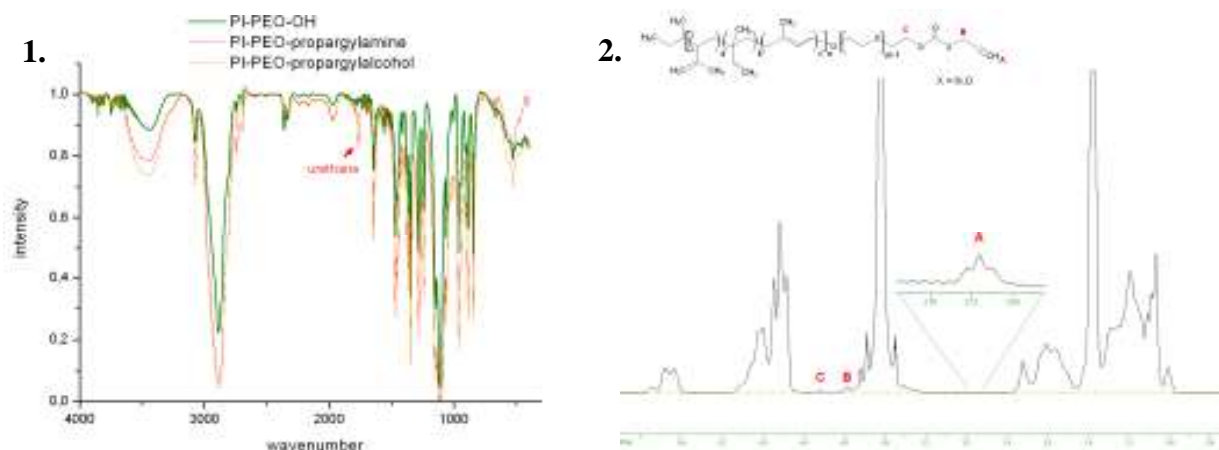


figure 41: 1. FT-IR of $\text{PI}_{61}\text{-}b\text{-PEO}_{212}\text{-OH}$ in comparison to $\text{PI}_{61}\text{-}b\text{-PEO}_{212}\text{-alkine}$.
2. ^1H -NMR (500 MHz, CDCl_3) of $\text{PI}_{61}\text{-}b\text{-PEO}_{212}\text{-alkine}$.

In the hope of permitting of click chemistry based on the Huisgen-[2_s+4_s]-cycloaddition, a terminal alkyne was introduced by CDI coupling. The characteristic urethane stretch at 1767 cm⁻¹ in the FT-IR spectrum (figure 41-1.) and nmr spectroscopy (figure 41-2.) confirmed the successful coupling.

Additionally, the reduction to an olefin over catecholborane and transition metal catalyzed coupling is possible. Alternatively, CDI coupling of allylamine allows the integration of an alkene function (figure 42-1.). Regrettably the overlap of the ¹H-NMR signals impeded the assignment of the characteristic signals of the allyl group. The same reaction channel allowed the insertion of a terminal thiol group. But the generation of disulfides was a limiting factor.

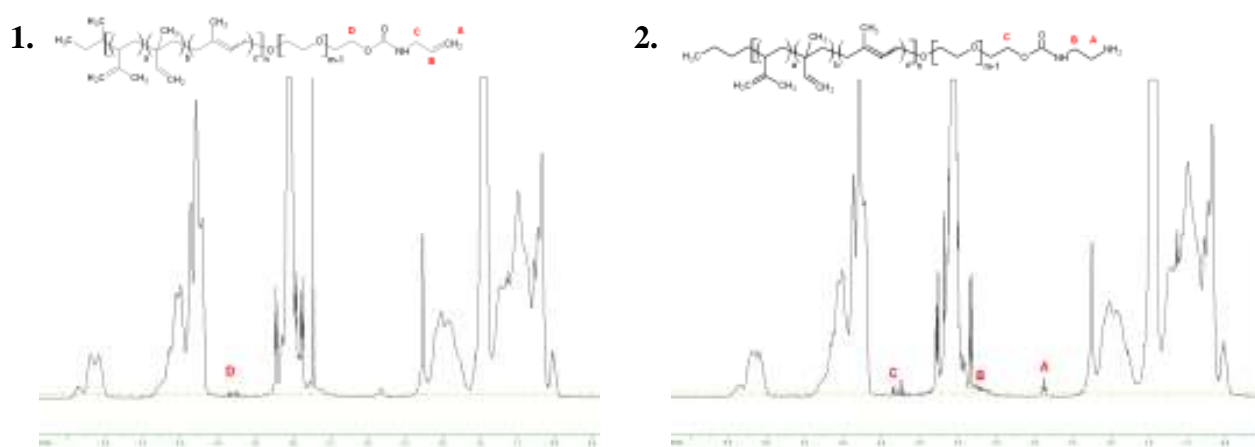


figure 42: 1. ¹H-NMR (500 MHz, CDCl₃) of PI₆₁-b-PEO₂₁₂-alkene.
2. ¹H-NMR (400 MHz, CDCl₃) of PI₆₁-b-PEO₂₁₂-ethylenediamine.

A further modification of the PI₆₁-b-PEO₂₁₂-OH permitted incorporation of an azide function. The reaction involved the activation of the hydroxylic group with tosylchloride and the reaction with sodium azide.

The azid was also reduced to an amine group by triphenylphosphine and lithium aluminium hydride respectively. Both reagents allow the selective reduction of the azid to an amine, without reacting with the double bounds. The amine function could be identified by the use of ninhydrin. The blue colour of the produced Ruhemann's purple was considered as verification of the presence of the amine. But there are easier terminal NH₂-functionalisation alternatives. For instance an amine can be introduced by attaching ethylenediamine via CDI coupling (figure 42-2.).

The amine allows further activation steps by bifunctional homo and hetero molecules like α,ω sulfo-NHS active esters. Secondary is the reaction with aldehydes forming imines which can be reduced using sodium cyanoborohydride. Also the conversion of amines to diazonium ions, which react in aqueous media with tyrosine and histidine, has to be mentioned. Those amino

acids are rare and the simple attachment of a his-tag to a protein offers a control of the binding site.

The enabling of Miyaura-Suzuki coupling reactions, which is feasible in aqueous media, was attained over the esterification of phenylacetic acid-4-boronic acid pinacol ester with PI₆₁-*b*-PEO₂₁₂-OH by activation with DCC and DMAP in pure DMF. Hereby reacts the Steglich-Höfle catalyst DMAP with the labile *O*-acylisourea active ester, which can rearrange in a side reaction irreversibly to an *N*-acylurea, forming a more stable active ester.

The boronic acid can be activated, for example with a base. This activation of the boron atom enhances the polarisation of the organic ligand and facilitates transmetallation.

Functionalizing PI₆₁-*b*-PEO₂₁₂-OH with a halide wasn't possible with α -bromoisobutyryl bromide in the Einhorn-variant of the Schotten-Baumann reaction. The alcoholysis of the acyl halide in pyridine didn't yield an ester. The reaction was modified as listed in the experimental part to achieve the attachment. The corresponding FT-IR measurement is shown in figure 43-1. The bromide provides a good leaving group so that nucleophilic substitution with ¹⁸F fluoride should enable positron emission tomography (PET)^[295]. PET is an imaging method in nuclear medicine.

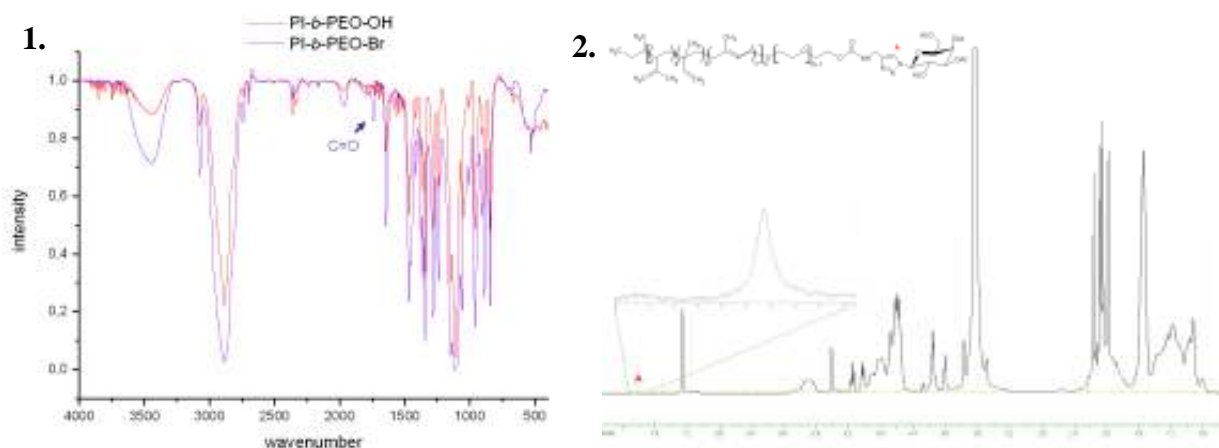


figure 43: 1. FT-IR of PI₆₁-*b*-PEO₂₁₂-Br.
2. ¹H-NMR (400 MHz, CDCl₃) of PI₆₁-*b*-PEO₂₁₂-galactopyranosid.

But halogens can also be introduced by for example CDI coupling as was attempted with 2,4-dichloroaniline (DCA) and 2,4,6-tribromoaniline (TBA). ¹H-NMR measurements reveal the presence of the urea bond and 2,4,6-tribromoaniline by a signal of 7.51 ppm. The signals of 2,4-dichloroaniline which are calculated according to the increment system^[242] to be 7.13 ppm for H_C, 7.25 ppm for H_D, and 7.34 ppm H_B couldn't be detected since the chloroform signal overlays the weak signals.

Furthermore an epoxide was introduced to the terminal PEO segment using epichlorohydrine. The characteristic ^1H signals of the epoxide group could not be identified by $^1\text{H-NMR}$ definitely due to signal overlap. But the high reactivity of epichlorohydrine must have granted the conversion of the $-\text{OH}$ group. The species is to be perceived as an intermediate for a coupling step. The partial hydrolysis of the epoxide can lead to allow superposes of the hydroxylic functions with the ethylene signals of PEO.

The presence of the epoxide function could be verified by nucleophilic addition of the amine of rhodamine 110 (figure 48). The coupling reaction was performed at a neutral pH value, whereby the preference of the nucleophilic attack of the most substituted carbon atom under acidic conditions and reaction with the least substituted carbon atom under basic conditions is not so pronounced. Afterward a quintet at 4.15 ppm and at 4.39 ppm of the proton of the formed tertiary carbon atom could confirm the successful coupling of the dye.

To verify the possibilities of the modified ligands certain bio molecules were coupled via different coupling strategies.

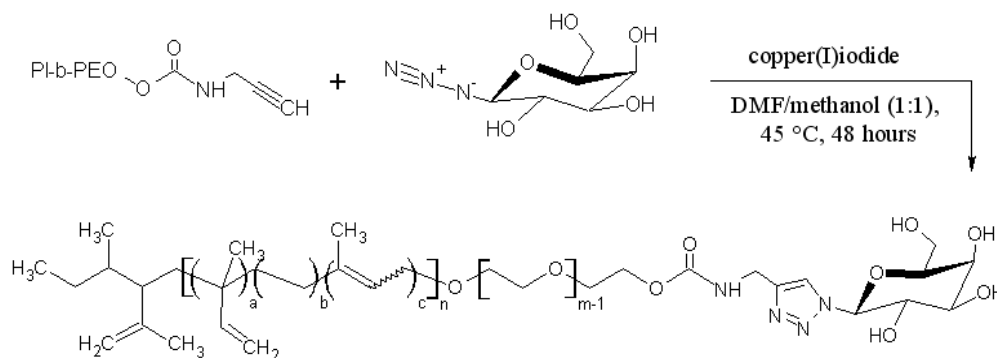
2.3.1.1 Coupling of carbohydrates, drugs, and dye molecules

Using the various terminal functional groups different coupling strategies can be used to attach (bio-)molecules.

2.3.1.1.1 Carbohydrate attachment

The azide and alkyne ligands allow for the use of the Huisgen cycloaddition (“click chemistry”)^[296], which is viable in polar solvents such as acetonitrile, methanol, DMF, and water. The copper(I) species can be isolated using affinity chromatography. Scavenger-columns, for example, can be placed directly in the solution.

In this way 2,3,4,6-tetra-O-acetyl-1-azido-1-deoxy- β -D-galactopyranose (GalAc- N_3) and 2,3,4,6-tetra-O-acetyl-1-azido-1-deoxy- β -D-glucopyranose (GluAc- N_3), both synthesized by Dr. Herwig Berthold, were coupled with $\text{PI}_{61-b}\text{-PEO}_{212}$ -alkyne (schema 15). The acetyl protective group was removed beforehand or subsequently by basic catalyzed ester interchange via sodium ethoxide (Zemplén deacetylation)^[297]. The solely presence of the 1,4-regioisomer of 1,2,3-triazol could be identified by $^1\text{H-NMR}$ spectroscopy (figure 43-2.). The chemical shift of the single ring-proton to 7.82 ppm can be distinctly seen^[298, 299].



schema 15: Huisgen cycloaddition.

The carboxylic functionalised PI-*b*-PEO block copolymer opens an option for peptide coupling to differently modified disaccharides. Therefore PI₆₁-*b*-PEO₂₁₂-COOH was coupled after EDC/sulfo-NHS activation to amino-functionalised cellobiose (**xviii**), maltose (**xix**), melibiose (**xx**), and gentiobiose (**xxi**) respectively (disaccharides analoga were synthesized by Matthias Wulff from the research group of professor Vill). The ¹H-NMR spectra are shown in figure 44.

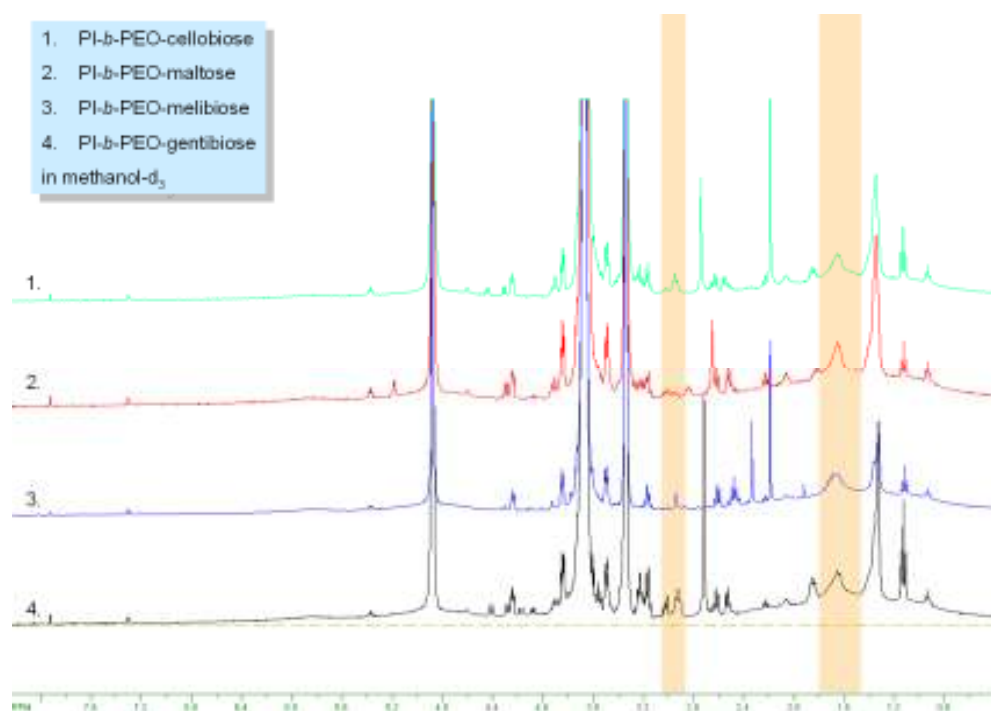


figure 44: ¹H-NMR (400 MHz, methanol-*d*₄) of PI₆₁-*b*-PEO₂₁₂-cellobiose (**1.**), PI₆₁-*b*-PEO₂₁₂-maltose (**2.**), PI₆₁-*b*-PEO₂₁₂-meliobiose (**3.**), PI₆₁-*b*-PEO₂₁₂-gentiobiose (**4.**).

¹H-NMR measurements of the polymer products versus the ¹H-NMR measurements of the disaccharide units (figure 45) reveal a shift of the methylene protons of the CH₂-NH₂ group of the saccharides from 2.75 ppm to 2.98 ppm, commensurate with the reaction to a peptide bond.

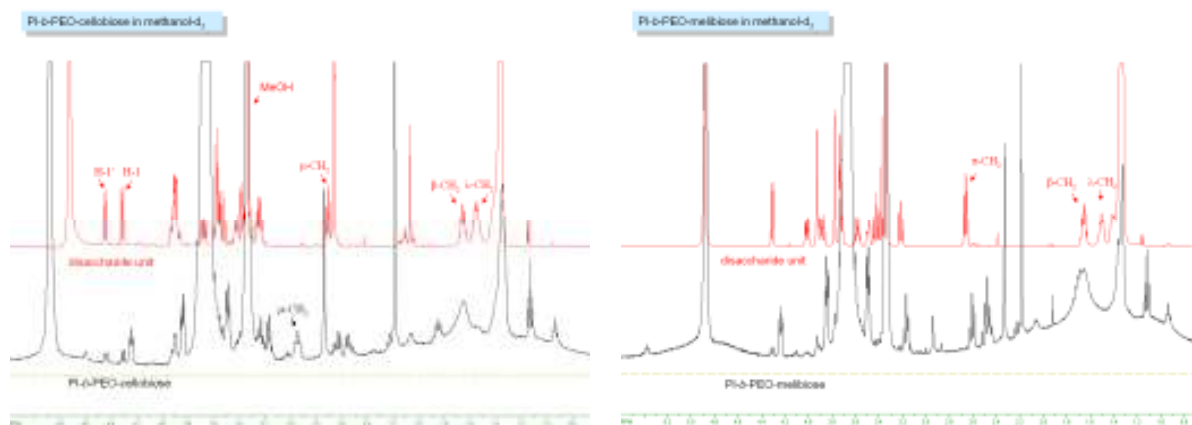


figure 45: (left) $^1\text{H-NMR}$ (400 MHz, methanol- d_4) of $\text{PI}_{61}\text{-}b\text{-PEO}_{212}\text{-cellobiose}$.
(right) $^1\text{H-NMR}$ (400 MHz, methanol- d_4) of $\text{PI}_{61}\text{-}b\text{-PEO}_{212}\text{-meliobiose}$.

The amino-functionalised cellobiose (**xviii**), maltose (**xix**), melibiose (**xx**), and gentibiose (**xxi**) feature an alkyl chain and thereby have an amphiphilic character. The EDC/sulfo-NHS was still efficient due to the longer reaction time.

2.3.1.1.2 Dye attachment

Various dyes could be coupled using different functionalised ligands. Alexa Fluor®594 could be coupled to $\text{PI-}b\text{-PEO-NH}_2$, rhodamine 110 to $\text{PI-}b\text{-PEO-epoxid}$, and cresyl violet to $\text{PI-}b\text{-PEO-COOH}$ (figure 46). Unbound dye had to be removed via dialysis over many days. The synthesized $\text{PI-}b\text{-PEO-dye}$ ligands are shown under daylight and under UV- excitation in figure 47.

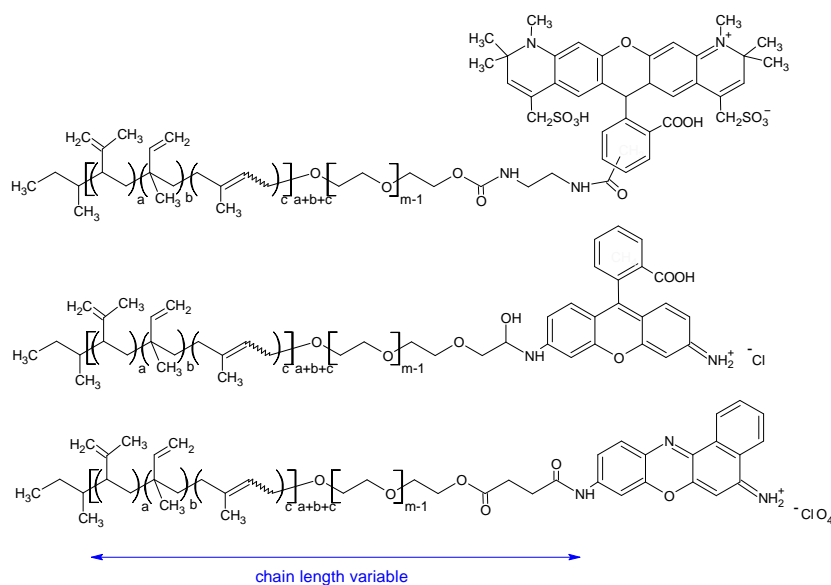


figure 46: dyes coupled to $\text{PI-}b\text{-PEO}$.

$\text{PI}_{61}\text{-}b\text{-PEO}_{212}\text{-Alexa Fluor® 594}$, $\text{PI}_{61}\text{-}b\text{-PEO}_{212}\text{-rhodamine 110}$, and $\text{PI}_{61}\text{-}b\text{-PEO}_{212}\text{-CONH-cresyl violet}$.



figure 47: On PI-*b*-PEO coupled organic dyes in different solutions.

1. rhodamine 110 chloride (left), cresyl violet perchlorat (central), Alexa Fluor®594 (right) each coupled to PI₆₁-*b*-PEO₂₁₂, picture was made after lyophilisation.
2. Alexa Fluor®594 after coupling to PI₆₁-*b*-PEO₂₁₂-NH₂ in DMF at daylight.
3. 1.5 mg rhodamine 110 labelled PI₆₁-*b*-PEO₂₁₂-epoxid and 13.5 mg unlabelled PI₆₁-*b*-PEO₂₁₂-OH in 1.5 mL EtOH (left) and 10 mg cresyl violet labelled PI₆₁-*b*-PEO₂₁₂-OH
4. Alexa Fluor®594 after coupling to PI-*b*-PEO-NH₂ in DMF under UV-excitation.
5. 1.5 mg rhodamine 110 labelled PI₆₁-*b*-PEO₂₁₂-epoxid and 13.5 mg unlabelled PI₆₁-*b*-PEO₂₁₂-OH in 1.5 mL EtOH under UV-excitation.
6. Alexa Fluor®594 after coupling to PI-*b*-PEO-NH₂ in H₂O under UV-excitation.

Due to the high price of Alexa Fluor®594 and the small amount of the ligand-conjugate no NMR spectrum was measured. Instead the product of the coupling reaction of rhodamine 110 with PI₆₁-*b*-PEO₂₁₂-epoxide is shown in figure 48.

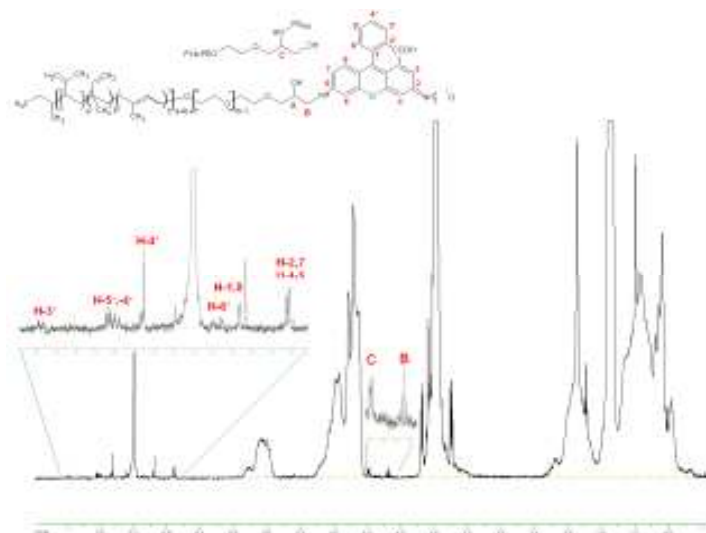


figure 48: $^1\text{H-NMR}$ (400 MHz, CDCl_3) of $\text{PI}_{61}\text{-}b\text{-PEO}_{212}\text{-CONH-rhodamine-110}$.

The attachment of organic dyes has no effect on the micelle self-assembly as will be shown in chapter 2.4.4. This allows the production of fluorescent micelles, which can contain for example non-fluorescent nanoparticles.

Information about the density and width of the polymer shell can be realised due to the covalent attachment of dyes, on the basis of (Förster-) fluorescence resonance energy transfer (FRET) measurements (see chapter 2.4.4).

2.3.1.1.3 Drug attachment

6-*O*-(4'-(*cis*-diaminoplatin(II)malonat)-butyl)- α/β -galactopyranose, a *cis*-platin containing monosaccharide analogue (synthesized by Janina Möker from the research group of professor J. Thiem in the organic chemistry department of the university of Hamburg, Germany), was coupled to $\text{PI}_{61}\text{-}b\text{-PEO}_{212}\text{-COOH}$ via DCC/DMAP activation of the carboxylic group. For NMR-analysis (figure 49) the chemotherapeutic agent bearing ligand was measured in CDCl_3 and in D_2O . The latter solvent displayed the signals, which are overlaid in CDCl_3 measurements due to the solubility of the poly(isoprene) block. The analysis reveals that the coupling wasn't achieved over the anomeric carbon, but over the C2, C3, or C4, which can be seen in figure 49 as the dd signal at 4.14 ppm, emphasized by X. Signals of H-2, -3, -4, -5, -6a, and -6b are between 3.40 and 3.83 ppm, thus overlaid by the broad signal of PEO.

Hydrolysis of the *cis*-platin complex was not observed. The unchelated ligand would show a signal of H-5' 2.9 ppm. In the presence of platin the signal should be at 3.6 ppm and thereby overlaid by the broad PEO signal^[300].

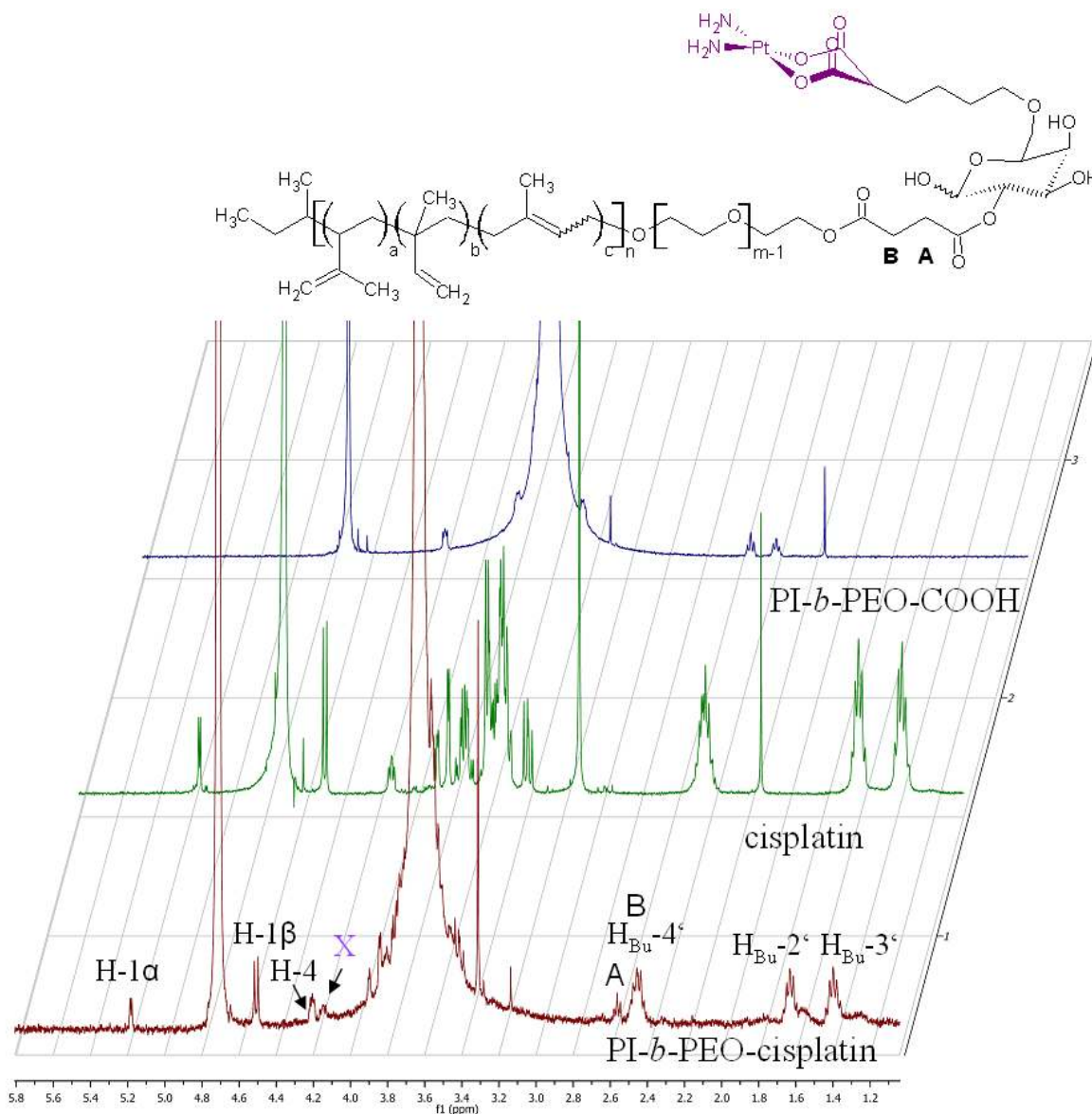


figure 49: $^1\text{H-NMR}$ (400 MHz, D_2O) of $\text{PI}_{61}\text{-}b\text{-PEO}_{212}\text{-COOH}$ (**1**), 6-*O*-(4'-(*cis*-diaminoplatin(II)malonat)-butyl)- α/β -galactopyranose (**2**) and $\text{PI}_{61}\text{-}b\text{-PEO}_{212}\text{-6-}O\text{-}(4'\text{-}(\textit{cis}\text{-diaminoplatin(II)malonat})\text{-butyl})\text{-}\alpha/\beta\text{-galactopyranose}$ (**3**).

Also zidovudine (AZT) could be converted into a $\text{PI}_{61}\text{-}b\text{-PEO}_{212}$ -ester analogue by DCC/DMAP coupling strategy. The achievement of the reaction was confirmed by $^1\text{H-NMR}$ measurements (figure 50). From comparing the integrals a reaction yield of 65% can be estimated.

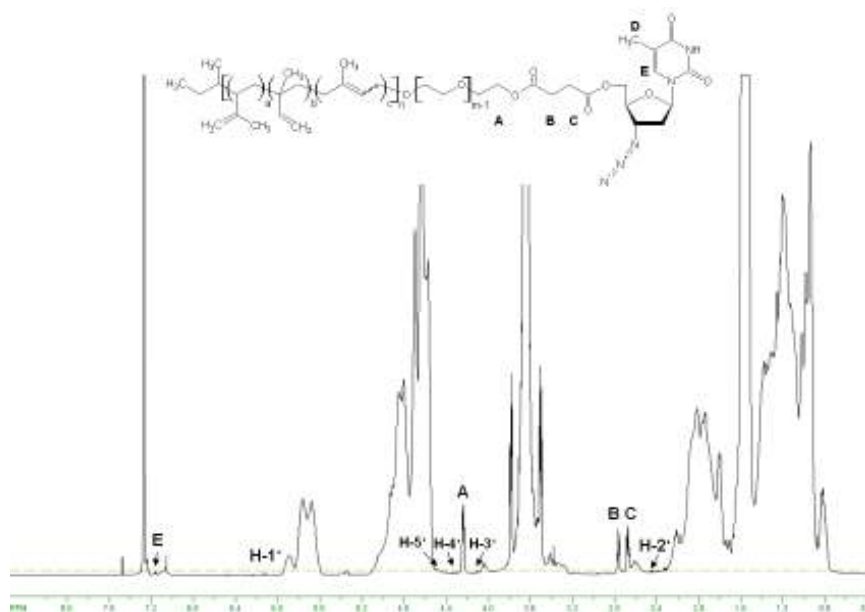
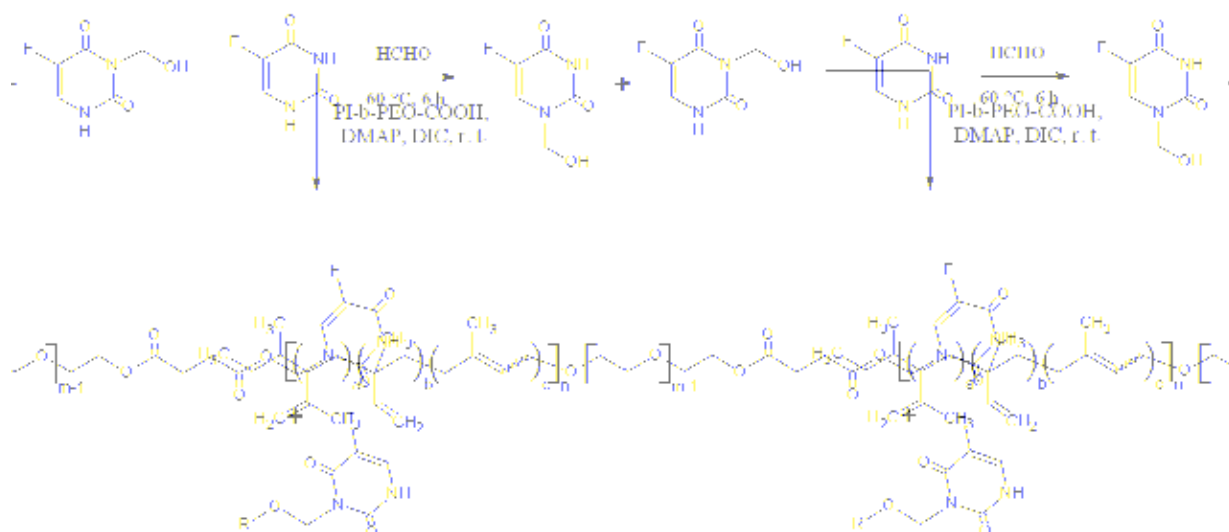


figure 50: $^1\text{H-NMR}$ (500 MHz, CDCl_3) of $\text{PI}_{61}\text{-}b\text{-PEO}_{212}\text{-AZT}$.

One of the antitumour agents frequently used for treating solid tumours such as breast, colorectal and gastric cancers is 5-fluorouracil (5-Fu)^[301]. 5-Fu was reacted with formaldehyde to form a mixture of N^1 -hydroxymethylene-5-fluorouracil, N^3 -hydroxymethylene-5-fluorouracil and N^1, N^3 -dihydroxymethylene-5-fluorouracil. The synthesis of N^1, N^3 -dihydroxymethylene-5-fluorouracil was reduced by using an excess of 5-Fu in the synthesis of the hydroxymethylene-5-fluorouracil.



schema 16: synthesis of $\text{PI}_{61}\text{-}b\text{-PEO}_{212}\text{-5-Fu}$.

Without separation, the mixture was directly esterified with $\text{PI}_{61}\text{-}b\text{-PEO}_{212}\text{-COOH}$ via N, N' -diisopropylcarbodiimide (DIC) activation^[302] (schema 16). The $^1\text{H-NMR}$ is in agreement with

the results of Tian *et al.*^[302]. The ¹H-NMR spectrum is shown in figure 51. At 5.55 ppm the signal of the methylene protons (D) reveal the success of the reaction.

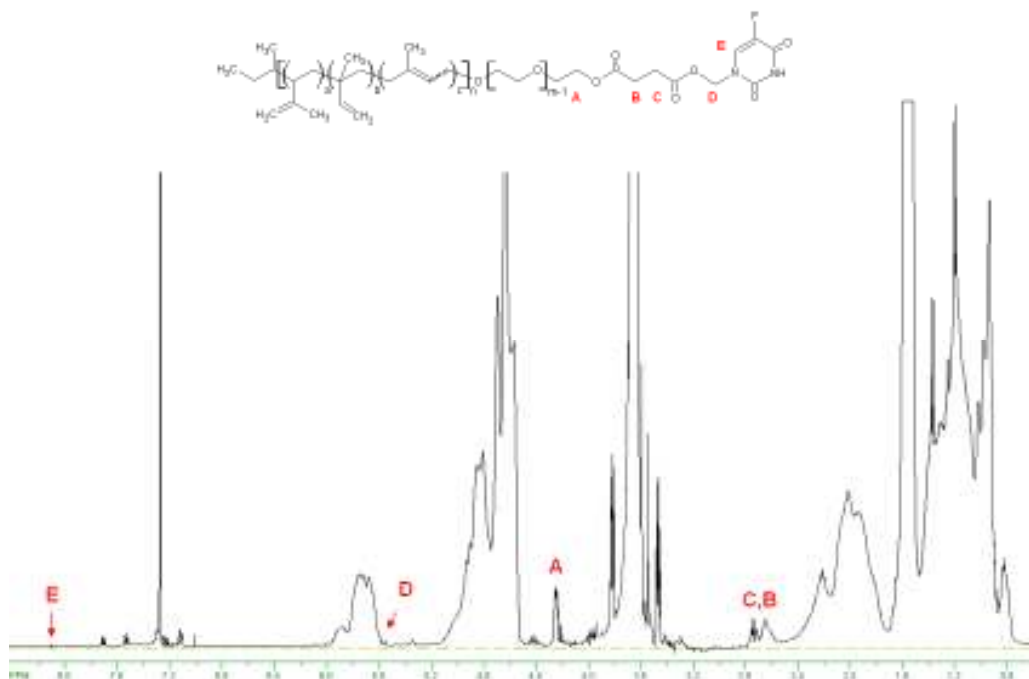


figure 51: ¹H-NMR (400 MHz, CDCl₃) of PI₆₁-b-PEO₂₁₂-5Fu.

The anthracycline antibiotic doxorubicin (Adriamycin) is used in antimitotic chemotherapy. Via EDC/NHS-sulfo coupling strategy it could be coupled to PI₆₁-b-PEO₂₁₂-COOH (figure 52). An alternative approach over a hydrazone linker is shown by Yoo *et al.*^[303], which permits acid cleavage of the cancer drug. Besides medical application doxorubicine features fluorescence properties^[304].

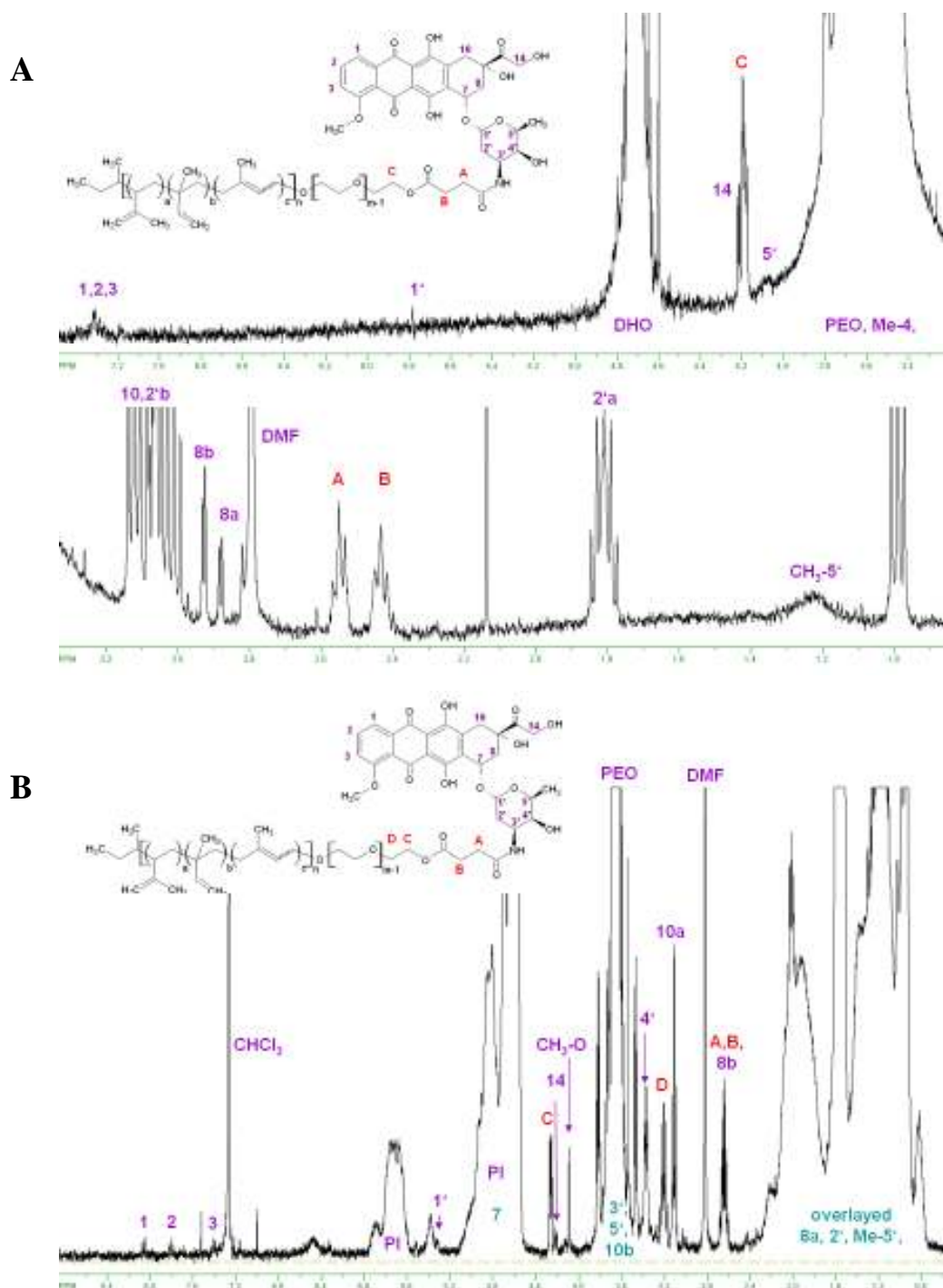


figure 52: $^1\text{H-NMR}$ (400 MHz, D_2O (**A**), CDCl_3 (**B**)) of $\text{PI}_{61}\text{-}b\text{-PEO}_{212}\text{-doxorubicin}$.

The implementation of various functional groups and the unique characteristics of the block copolymer facilitates not only the use of further coupling reactions in organic and inorganic solvents to attach further molecules but also allows the coupling before or after micelle formation (encapsulation of nanoparticles). Therefore nanoparticles can be equipped with different hydrophilic drugs in the process of ligand self-assembly. Carboxylic functionalized ligands can be also integrated to allow antibody-coupling after micelle formation.

2.3.1.1.4 Biomolecule attachment

Due to the presence of a carboxylic group in biotin, Fmoc-glycine and (\pm)- α -lipoic acid, the molecules could be esterified with PI₂₇-*b*-PEO₉₃-OH based on the coupling reagents DCC in combination with DMAP.

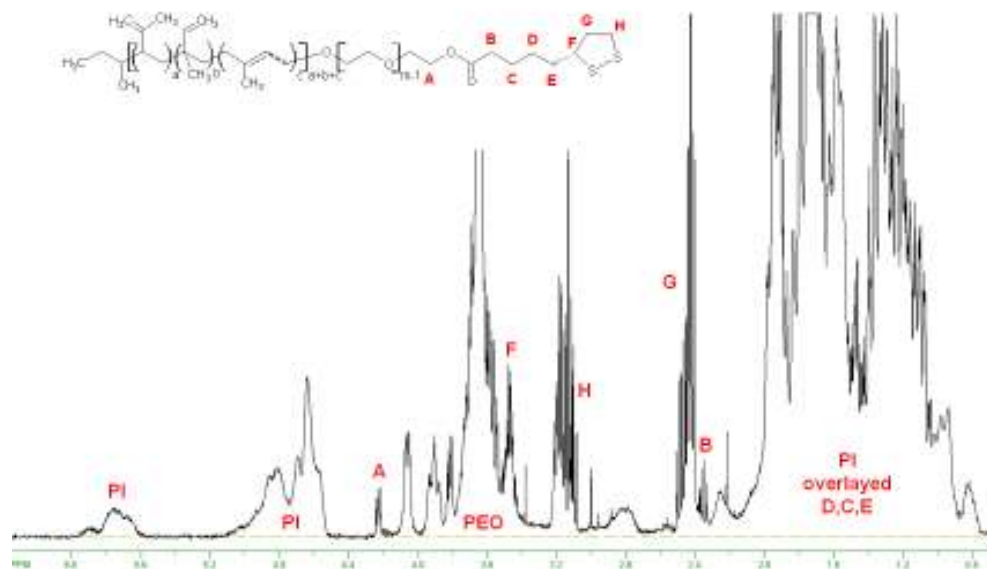


figure 53: ¹H-NMR (400 MHz, CDCl₃) PI₂₇-*b*-PEO₉₃-lipoic acid.

The NMR analysis of the products are shown in figure 53 and figure 54. The achievement of the coupling reaction could be documented. The active ester can form a 1,3-dicyclohexylurea (DCU) through an 1,3-rearrangement. DCU could be removed mainly by dialysis.

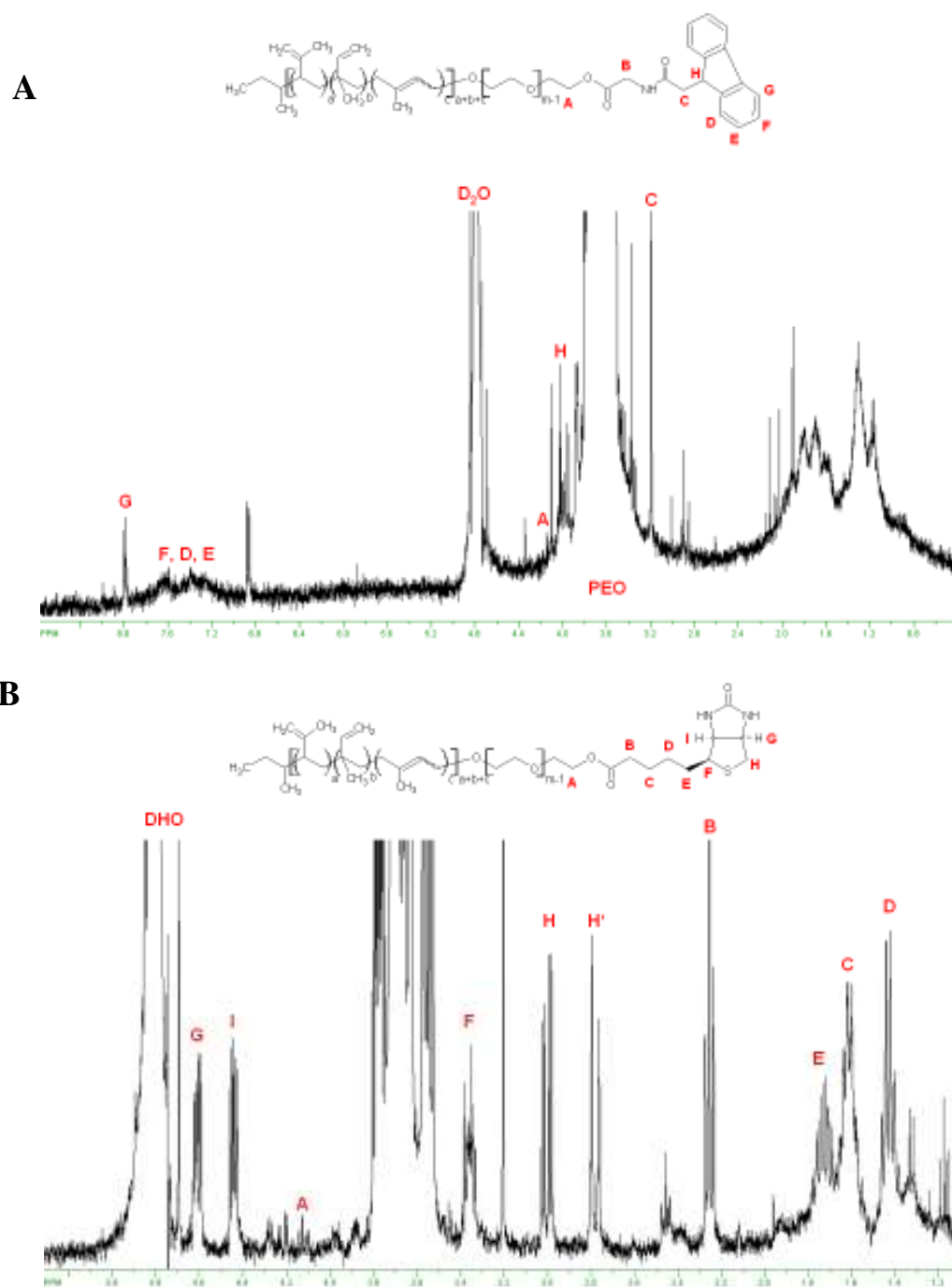


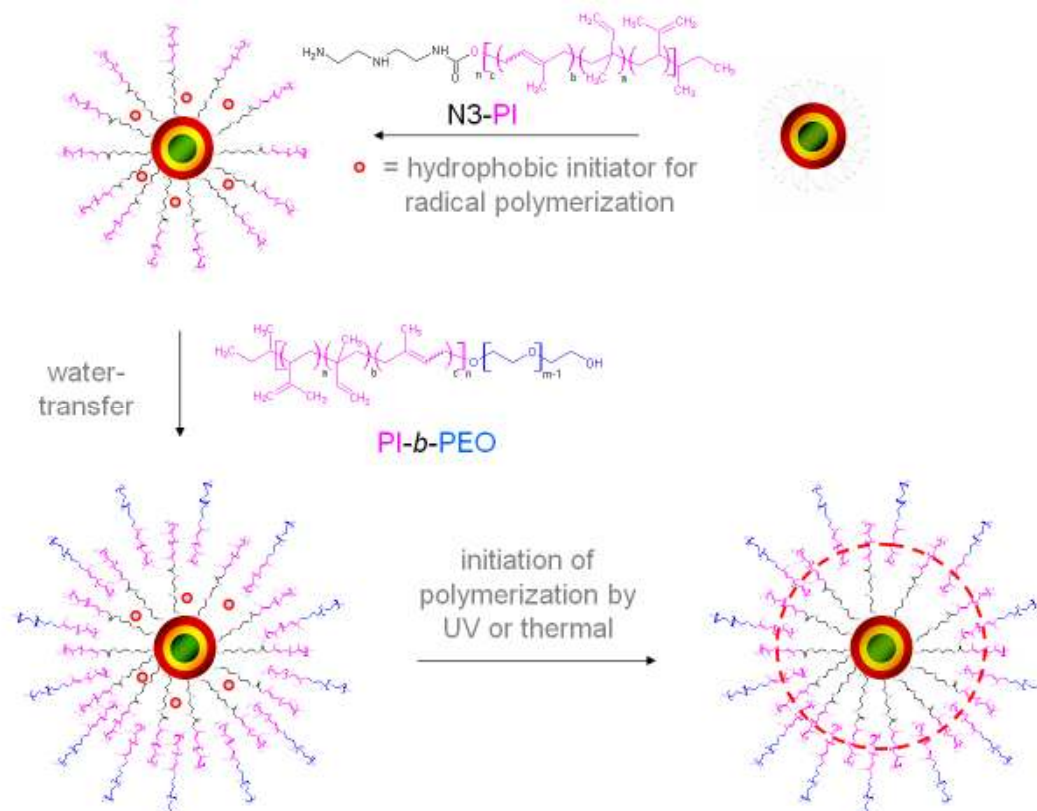
figure 54: $^1\text{H-NMR}$ (400 MHz, D_2O) $\text{PI}_{27}\text{-}b\text{-PEO}_{93}\text{-FMOC-glycin}$ (**A**) and $\text{PI}_{27}\text{-}b\text{-PEO}_{93}\text{-biotin}$ (**B**).

Next to the above presented biomolecules the biopolymer arabinogalactan was coupled via DCC/DMAP esterification of $\text{PI}_{61}\text{-}b\text{-PEO}_{212}\text{-COOH}$. The polymer was isolated from *larix occidentalis* – Western Larch and consists of arabinose and galactose monosaccharids. Due to its high size distribution of 30 to 130 kD no NMR was measured.

2.4 Ligand exchange with PI-*b*-PEO

In the following the main work was done with a PI₆₁-*b*-PEO₂₁₂-OH, containing a hydrophilic weight fraction of 70% and a total mass of 13500 g/mol. The PI blocks possess mainly 3.4 and 1.2 PI-units, which feature terminal -C=C- double bonds. The *trans* 1.4-isomer is also present, due to the polymerization in THF. The coblock polymer was applied in combination with a short poly(isoprene) pre-ligand (PI-N3), with a terminal amine function (2,2'-diaminodiethylamine, -N3) and a total mass of 2000 g/mol, achieving a dense packing around a nanocrystal and a high degree of passivation.

By adding the above discussed block copolymer above the critical micelle concentration (cmc), to PI-N3 coated nanocrystals in THF and injecting this solution in water, spherical micelles can be prepared, and these micelles have a dense hydrophobic packing around the nanocrystal (schema 17). The PI₃₀-N3 prepolymer-ligand serves on the one hand as organic passivation of trap states and on the other hand the conservation of the nanoparticles. Additional hydrophobic ligands, which are still present from the synthesis, are not prejudicial.



schema 17: illustration of nanoparticle transfer from organic solvents into water. The prior ligand exchange with PI-N3 is followed by the addition of radical initiator (like AIBN, benzoyl peroxide, IRGACUR) and PI-*b*-PEO ligands. The micelle assembly occurs by injection the solution in water, whereupon the crosslinkage is initiated by dissociation of the initiator.

When a hydrophobic initiator is present during in the process of micelle self-assembly, co-encapsulation occurs, and a linkage between the terminal -C=C- double bonds can be formed by subsequent initiation. The initiation can be achieved, depending on the initiator, thermally or by UV-light, although in the case of quantum dots the use of UV-light should be avoided. Best results were achieved with AIBN. Already it was shown that the process of polymerization of MMA in the presence of QDs led to no remarkable changes in the optical behaviour of the QDs (chapter 2.2.6). The degree of covalent crosslinkage can be conveyed by prior swelling of the micelles with isoprene.

Wegrzyn *et al.*^[305] has previously demonstrated in AFM studies that the crosslinkage of PI-*b*-PEO micelles in solution provides the integrity of the micellar structure upon the removal of water. An additional crosslinkage could be facilitated by a hydrophilic, interfacial poly(acrylic acid) (PAA) block with a hydrophilic diamine using EDC chemistry^[263, 306-308].

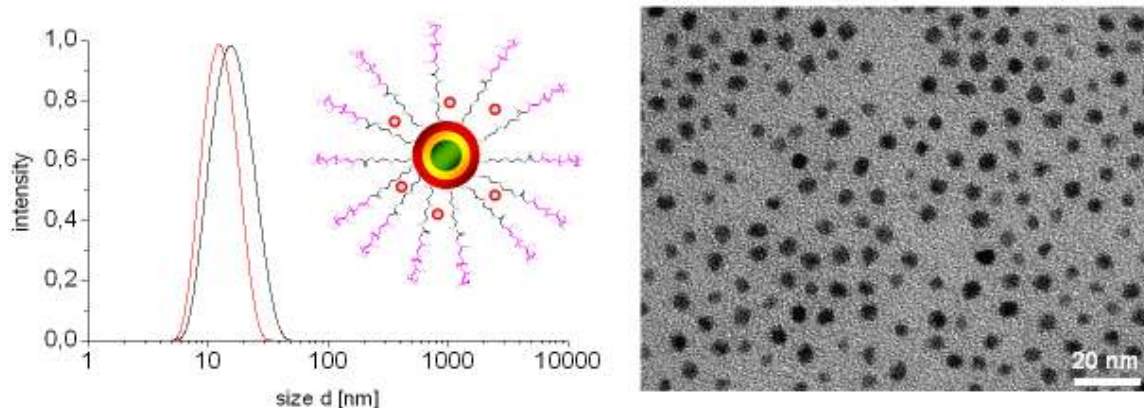


figure 55: dynamic light scattering of PI₃₀-N3 (red) and PI₆₆-N3 (black) coated CdSe/CdS/ZnS in chloroform and the corresponding TEM image of PI₃₀-N3 coated CdSe/CdS/ZnS quantum dots.

Several nanoparticles especially CdSe/CdS/ZnS core/shell/shell nanocrystals with average diameters of 5 to 6 nm, contingent upon the synthesis, and adequate thick outer ZnS shells were equipped with the PI₃₀-N3 ligands and incubated with an initiator. Hydrophobic ligands on the nanoparticle-surface, which remain from nanoparticle synthesis, were partially exchanged against PI-N3. The main work was done with a preligand, which contained thirty isoprene units. Changes in the length of the poly(isoprene) polymer leads to different quantities of PI-N3 ligands on the nanoparticle surface, considering sterical requirements. The shorter the PI polymer the higher the number of preligands, that can coordinate. Considering a high passivation grade and numerous interactions with the final PI-*b*-PEO ligands the main work was done with PI₃₀-N3.

Dynamic light scattering (DLS) measurements of stock solutions in chloroform show hydrodynamic radii with maxima in the intensity PSD distribution between 10 and 17 nm, primarily depending on the chain length of PI (figure 55).

The addition of the PI₆₁-*b*-PEO₂₁₂-OH ligands and the injection in stirred water, increases the size to >40 nm in size distribution (figure 56). Considering the solvation shell and the stretching of the PEO segment in water compared with chloroform, the increase in size is to be expected. The strong hydration of PEO is due to a very favourable fitting of the ethylene oxide monomer into the hydrogen bridging network of water^[309-311]. Due to the high graft density at the core/corona interface in copolymer micelles, the hydrophilic chains are expected to be flatter than in the favourable, coiled state^[312]. Each PEO-monomer unit can be solvated with 2-3 water molecules^[313], which results in a high radius of gyration and a repulsion between the PEO-chains.

Especially in case of the PI-*b*-PEO micelles the discrepancy between the DLS intensity distribution and the TEM images becomes evident. In case of single nanoparticle containing PI₆₁-*b*-PEO₂₁₂-OH micelles TEM images assume sizes of 15-20 nm in diameter. In contrast the intensity distribution in DLS shows often larger sizes of 40-50 nm. Certainly the stretching of the PEO chains in water and the additional solvate shell result in larger sizes, but nevertheless the sizes obtained by DLS intensity PSD are to large.

The DLS volume and number distribution factor the radius, r , with r^3 , while DLS intensity PSD the radius includes with r^6 . Hence they show smaller sizes, which correlate more with TEM images. But they disguise larger peaks, which can indicate agglomeration, and the possible inconsistency of the probe. Therefore always the intensity PSD distribution is shown in this doctor thesis.

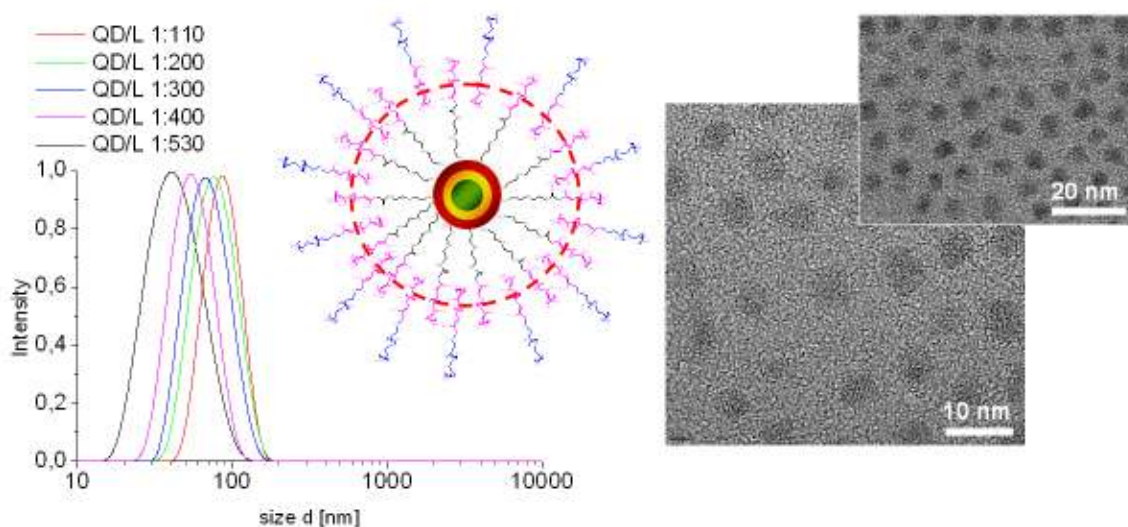


figure 56: dynamic light scattering of PI-N3 & PI-*b*-PEO-OH coated CdSe/CdS/ZnS in water and the corresponding TEM image of the quantum dot to ligand (QD/L) ratio 1:530.

The higher density of PI, related to the unfavourable hydrophilic vicinity, as well as the addition of isoprene seconds the crosslinking during the decay of AIBN. According to Flory's gelation theory, the proportion of crosslinkage is remarkably small for the onset of gelation when crosslinking a polymer. The presence of the solvated, non-crosslinkable PEO block prevents the formation of macrogels and leads to the formation of nanoparticles.

The polymerisation can be initialised by radical initiators. ESR, IR and NMR measurements of poly(isoprene) after UV-irradiation reveal the presence of unpaired electrons, which underlie magnetic dipole/dipole interactions which lead to a loss of double bounds, hydrogen formation, and crosslinking^[314, 315]. Using a mini emulsion polymerisation, the polymerisation can also be initiated in the aqueous phase in the presence of isoprene and a hydrophilic initiator like VA044 (WAKO). The higher the temperature, the lower is the half-life of the radical initiator. It takes 13 hours for 10% of the AIBN to decompose at a temperature of 50 °C, but in contrast only 2 minutes at 90 °C.

Certain factors dominate the size of the micelles (DLS, figure 56): the aforementioned properties of the block copolymer, the nanocrystal to ligand ratio, added cosolvents, and the concentration of the THF solution before injection in water as well as the speed of injection. Schabas *et al.*^[251] determined that the faster water is added the faster self-assembly occurs, which results in a corresponding decrease in mean particle diameter. This means that the faster the transfer of the ligand, which is in a non-aggregated state, to water is accomplished, the shorter the time is to form micelles and the smaller the particle diameter will be. Therefore, a slow addition speed and a high stirring rate of water are beneficial because the amount of added THF is smaller and disperses faster, so the ligand comes into contact with water faster.

The presence of water, which is a selective solvent for PEO, constrains the monomers to self-assemble in micelles. The bigger the average distance between the nanoparticles is in the THF solution, the more likely the micelles will be to have just one nanoparticle inside. Along with concentration, temperature can be used to vary the block copolymer self-assembly. The hydration of PEO is temperature dependent. With the increase of the temperature up to the upper critical solution temperature (UCST) the hydrogen bonding decreases and PEO attains a less polar configuration^[316, 317]. The Flory-theta temperature for PEO in water is close to 100 °C.

The size of the PI-*b*-PEO ligands has a certain impact on the size of the nanocomposites. In figure 57 DLS measurements are presented, which document the size distribution of PI_x-*b*-PEO_y micelles, containing PI-N3 coated CdSe/ZnS/CdS quantum dots.

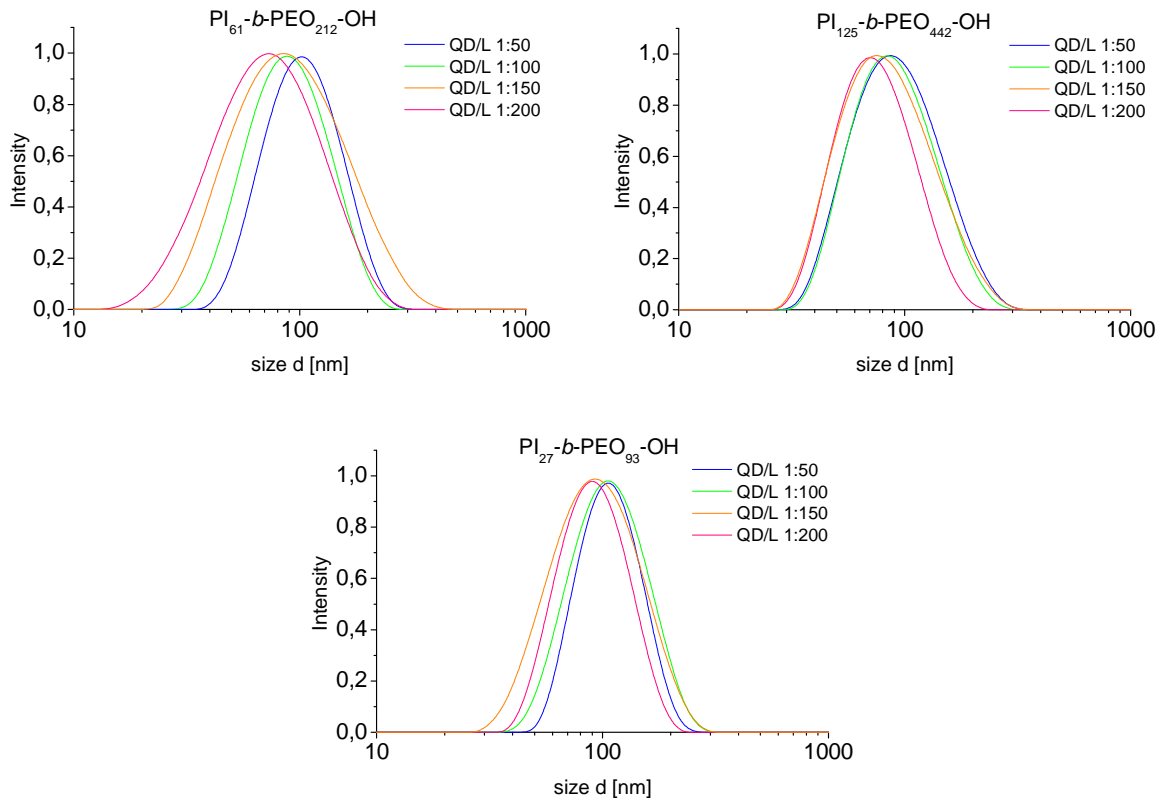


figure 57: DLS measurements (intensity PSD) of PI_{61} - b - PEO_{212} -OH, PI_{125} - b - PEO_{442} -OH, and PI_{27} - b - PEO_{93} -OH coated PI-N3 CdSe/CdS/ZnS quantum dots

According to the DLS measurements, PI_{61} - b - PEO_{212} -OH, PI_{125} - b - PEO_{442} -OH, and PI_{27} - b - PEO_{93} -OH assemble in the presence of nanoparticles to smaller micelles with increasing quantum dot to ligand ratio (QD/L). Comparing the same QD/L ratios different sizes are achieved due to different large block copolymers. In figure 58 the size average (intensity PSD) is plotted against the QD/L ratios of the different PI_x - b - PEO_y block copolymers. Remarkably PI_{27} - b - PEO_{93} -OH, the smallest used ligand forms the micelles with the largest diameter. The presumption that smaller PI - b - PEO block copolymers, with the same PI to PEO block ratio, assemble in smaller nanoparticle containing micelles, need not be correct. Depending on the steric dimension, the volume ratio of the two blocks is an important factor. A further aspect is the number of ligands that form the micelle and the packing of the hydrophobic segment.

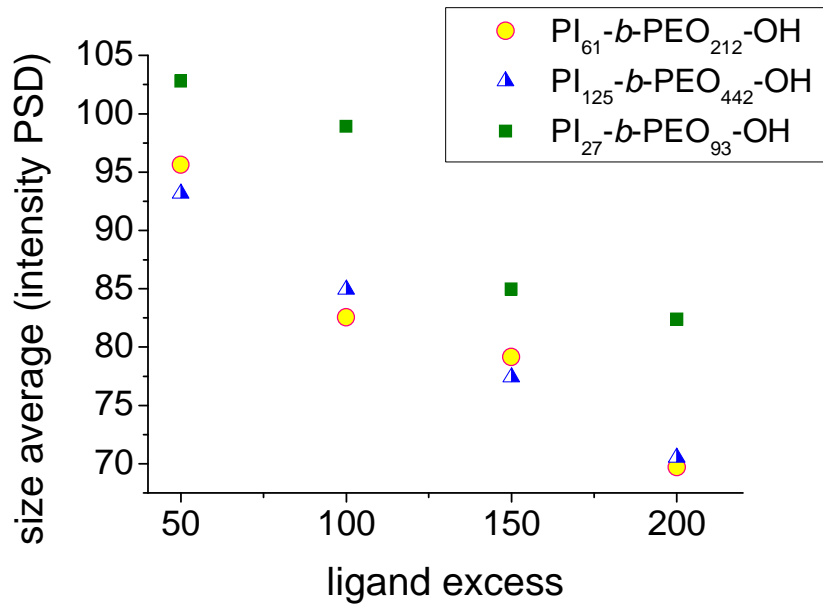


figure 58: size average (intensity PSD) plotted against QD/L ratios of PI_x-b-PEO_y micelles, containing PI-N3 coated CdSe/CdS/ZnS quantum dots.

The numerous parameters by which the sizes and the amount of encapsulated nanoparticles per micelle can be varied allow the average in the size distribution using PI₆₁-b-PEO₂₁₂-OH to be maintained between 30 and 200 nm according to the size distribution application measured by dynamic light scattering.

The assembly occurs also in the absence of nanoparticles. DLS measurements of different PI₆₁-b-PEO₂₁₂-X (X = CHO, glucose, imdazolyl (CDI), and NH₂) are shown in figure 59.

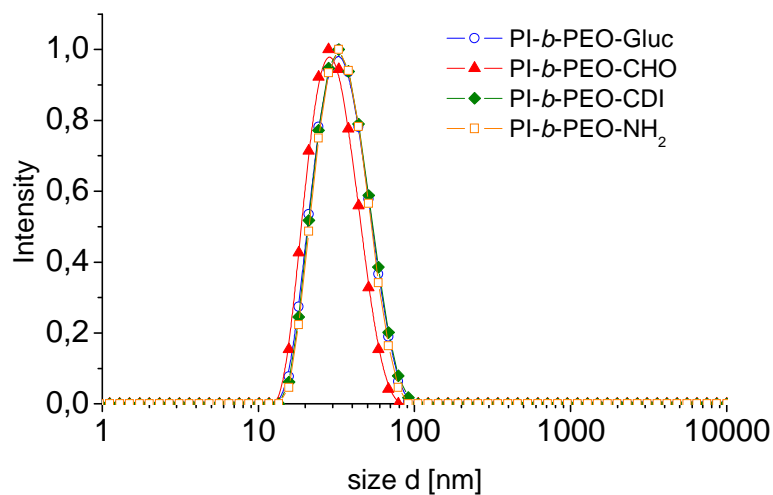
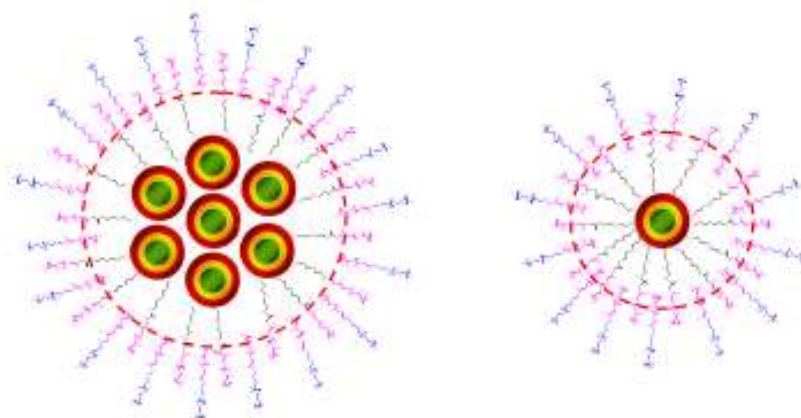


figure 59: DLS measurements of PI₆₁-b-PEO₂₁₂-OH micelles in water.

The micellar structure can be imposed on on all kind of nanoparticles including quantum dots. Their unique optical and electronic properties, such as size- and composition-tunable fluorescence emission from visible to infrared wavelengths, large absorption coefficients across a wide spectral range and very high levels of brightness and photostability make them superior to organic fluorophores^[160, 318].

2.4.1 Self Assembly to Multifunctional Beads

A feature of the ligand is that, subject to the nanocrystal to ligand ratio during ligand addition, those ligands can form micellar structures, which contain more than one particle (schema 18). This can be explained by the fact that the smaller the amount of ligand the smaller the total surface, which can be covered by ligands. The nanocrystals act hereby as simple hydrophobic solutes and are therefore distributed between the micelles. During the injection into water, hydrophobic attractive interactions force the packing of more than one nanocrystal into each micelle, simultaneously avoiding precipitation. Thereby up to one hundred nanoparticles could be encapsulated into one micelle.



schema 18: illustration of PI-*b*-PEO micelles containing PI-N3 coated core/shell/shell quantum dots.

The determined clustering of nanoparticles consists of different options. It has been reported that clustering of superparamagnetic magnetite nanoparticles results in higher saturation magnetization than that of individual ones because of the interaction between the assembled nanoparticles^[319]. Next to magnetic separation, drug delivery and cancer hyperthermia magnetite nanoparticles are a promising material to work as magnetic resonance imaging (MRI) contrast agents^[253, 254, 256, 257, 320, 321]. The achievement of controlled packing of magnetite nanoparticles is therefore a strong facility.

However, the prospects are multifaceted. Since the encapsulation doesn't depend chiefly on specific polymer-surface interactions, different kind of nanoparticles can be clustered in one micelle. The assembly of nanoparticles depends only on simultaneous desolvation of nanoparticles and amphiphilic block copolymers and offers thereby an option to co-encapsulate different sizes and/or kind of nanocrystals in one micelle, whereby interactions of nanocrystals can appear. For instance, the presence of magnetic nanoparticles quench the luminescence of CdSe/ZnS quantum dots by dynamic quenching^[262, 263, 322], concordantly with reports of dynamic quenching of fluorophores by magnetic nanoparticles^[322, 323]. Those interactions can be minimized through prior encapsulation with PI-N3. The length of the poly(isoprene) chain constitutes the interspace between two nanoparticles. The broad excitation profiles and narrow, symmetric emission spectra of high quality quantum dots make them suitable for multicolor imaging^[92] and optical multiplexing, in which multiple colors and intensities are combined to encode genes, proteins, and small-molecule libraries^[5, 324, 325]. The finding of Kim *et al.*^[263, 326], that the amount of nanocrystals in each polystyrene-*block*-poly(acrylic acid) (PS-*b*-PAA) micelle followed a roughly Gaussian distribution, is consistent with our results. On account of this, at limiting nanoparticle concentrations a large section of micelles containing single nanoparticles are obtained (figure 60).

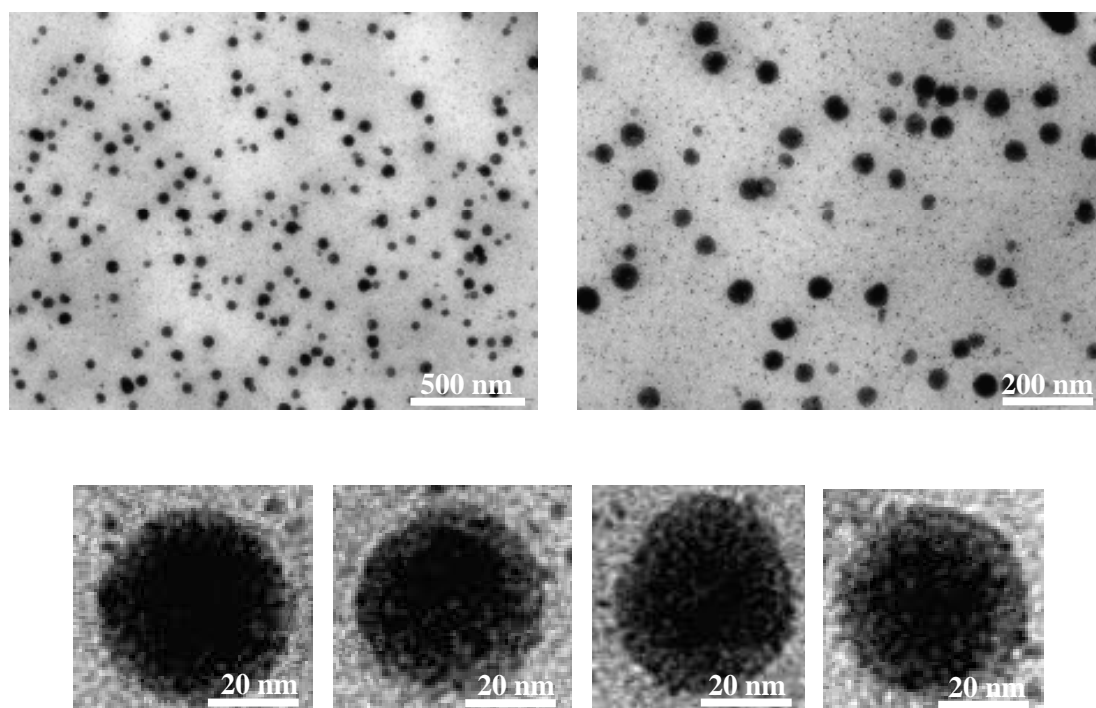


figure 60: TEM images of PI-N3 & PI-*b*-PEO-OH coated CdSe/CdS/ZnS in larger micelles.

The consistency of the ligand shell was determined by a dilution series (figure 61). For polymers, the cmc, below which there are no longer micelles but only monomers in solution, is

generally much lower in comparison to other surfactants and often it is impossible to determine it experimentally. Stocco *et al.*^[327] verified for PI-*b*-PEO block copolymers with a molecular weight (M_w) of 20 – 60 kg/mol, astronomically low values for the cmc, estimated from trends of low molecular weight surfactants. This is been reflected in the stability of the micellar nanocomposites.

2.4.2 Dilution stability of PI-*b*-PEO nanocomposites

For comparison one dilution was performed with an uncrosslinked shell (figure 61 A) and one with a crosslinked shell (figure 61B). Since the absolute quantum yield fluctuates between different ligand additions each absolute quantum yield of the highest concentrated probe was equated with one. Dilution of a 290 pmol/mL concentrated solution down to 50 fmol/mL (figure 61 B) showed no decrease and change of the quantum yield at all. Just in case of uncrosslinked micellar compounds in the range of fmol/mL a blueshift and a broadening of the emission peak was detectable (figure 61A). Nevertheless the uncrosslinked shell shows low exchange kinetics. The residence time of a single amphiphile in its micelle rises exponentially with the free energy (G) of micellization^[328]. On the basis of published values for the standard free energies of micelle formation ($G_{mic}(-CH_2-) \approx -1.15k_B T$ & $G_{mic}(-CH_2-CH_2-O-) \approx +0.32k_B T$ at 25 °C, where k_B is the Boltzmann constant and T is the temperature)^[282], leads to the anticipation that the residence time is so high that the strong amphiphilicity locks the block copolymer in an aqueous solution and dominates any other mechanism like micelle fusion/fission^[329-331] or even concerted cooperative exchange^[328, 330, 332, 333] for redistribution of the amphiphilic molecule

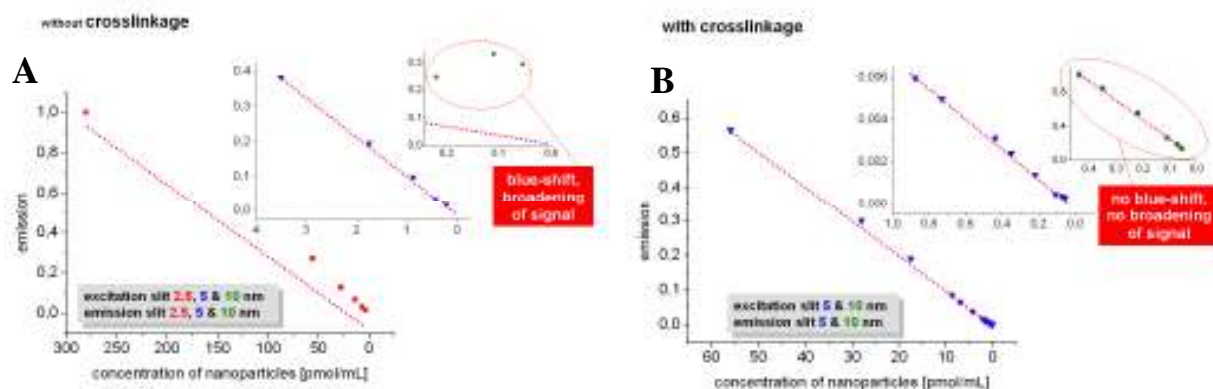


figure 61: The dilution was arranged in 10 mL volumetric flasks. The inspections of the used cuvettes with pure water showed no emission at all.

Whereas the uncrosslinked shell is already quite strong, the crosslinked shell was even more remarkable. The nanoparticle remained stable even at the lowest concentration. Due to the hydrophobic, crosslinked PI-layer the nanoparticles show a steady quantum yield in water. This indicates that hardly any ligand has been removed from the surface and a crosslinkage has been accomplished.

These results are getting confirmed on the basis of stability tests. The nanocrystal-micelles were lyophilized and resuspended either in THF or chloroform. In those solvents the hydrophobic PI-block is also soluble and a nanoparticle coated with an uncrosslinked shell would be dismantled. In figure 62 changes in the size distribution in DLS measurements are graphical shown. Concerning the crosslinked micelle solely a marginal swelling was detectable, while the uncrosslinked fraction already showed the formation of larger structures. The dissolving of a PI-*b*-PEO ligand is kinetically and thermodynamically hindered, for this reason the change in structure are getting more obvious over a time range of 74 hours.

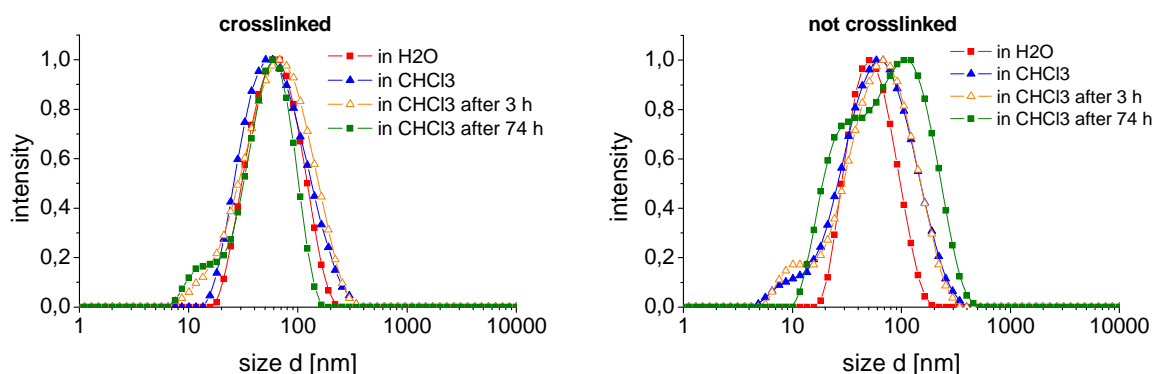


figure 62: DLS measurements of CdSe/CdS/ZnS quantum dots encapsulated in PI-*b*-PEO micelles. The micelles were prepared in water, frozen in liquid nitrogen and lyophilized. The resuspension was done in chloroform.

The loss of ligands and the formation of larger structures finally leads to the precipitation of the nanoparticles as pictured in figure 63, where un- and crosslinked PI-*b*-PEO-OH micelles containing ferric oxide nanoparticles after ten days in chloroform are compared. While the uncrosslinked micelles precipitated, the crosslinking inhibited the detachment of ligand.



figure 63: FeO nanoparticles in uncrosslinked (left) and crosslinked (right) PI-*b*-PEO-OH micelles in chloroform.

The results indicate a high stability of the organic shell around the nanoparticles, which is the root for biological application. A loss of ligand would lead to irreversible precipitation and agglomeration.

2.4.3 Stability in biological buffers

Also crosslinked micelles and uncrosslinked micelles containing CdSe/CdS/ZnS core/shell/shell nanoparticles were exposed with ddH₂O at pH 2, 5% bovine serum albumin (BSA), 20% BSA, and 1% SDS and the summed normalized quantum yield (crosslinked 4, not crosslinked 2) was measured with time (figure 64). In this experiment the uncrosslinked micelles showed the same behaviour as the crosslinked micelles. After a drop of the emission in the first four days the quantum yield stayed nearly constant. The quantum yield of the crosslinked micelles was 1/3 higher than the quantum yield of the uncrosslinked ones.

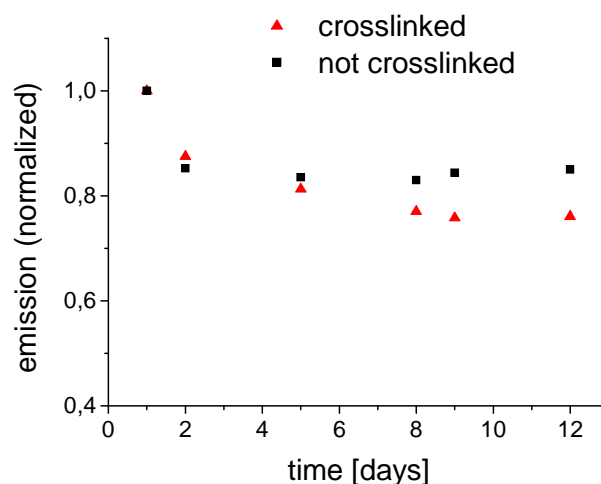


figure 64: graphical application of changes in the normalized quantum yield with time of quantum dot containing PI-*b*-PEO-OH micelles in the presence of ddH₂O at pH 2, 5% bovine serum albumin (BSA), 20% BSA, and 1% SDS.

To further determine the rigidity, a series of stability tests were performed. Relying on the acidic condition inside the tumour and the inflamed tissues (pH ~ 6.8) and cellular compartments including endosomes (pH ~ 5.5-6) and lysosomes (pH ~ 4.5-5)^[334] the pH values were varied between four and nine and certain surfactants in high concentrations above average were added. It is known, that in the presence of surfactants interactions emerge with micelles. The non-ionic surfactant pentaethylene glycol dodecyl ether was found to interact strongly with the interface between the hydrophilic shell and hydrophobic core of polybutadiene-poly(ethylene oxide) (PB-PEO) copolymers, yielding characteristic changes in the geometry of the block copolymer micelles. Like spines the surfactant molecules that diffuse into the block copolymer create more space for each hydrophilic segment to get into a thermodynamically favourable coiled state^[335].

Cationic and anionic surfactants like sodium dodecyl sulfate (SDS) and dodecyltrimethylammonium bromide (DTAB) also adsorb on the interface due to their amphiphilic character. Some of the spherical PB-PEO micelles transformed due to stretching of the PB block into large micellar clusters or vesicles especially in case of those copolymers, which have long PB blocks^[336].

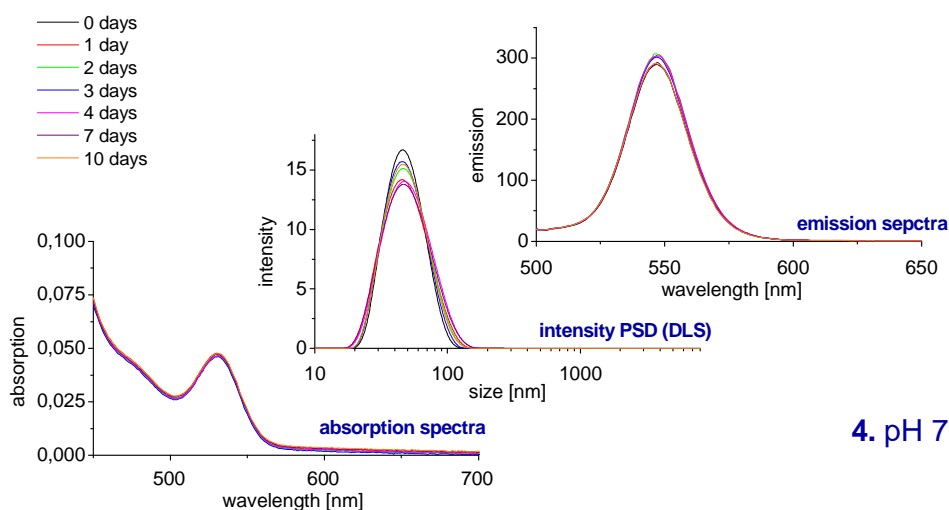


figure 65: absorption, emission, and dynamic light scattering of different nanoparticle solutions over the period of 10 days at pH 7.

Those results were observed in PI_{61} -*b*-PEO₂₁₂-OH micelles containing quantum dots. CdSe/CdS/ZnS core/shell/shell nanoparticles with a diameter of < 3.5 nm and correspondingly high surface to volume ratio were used. The high surface area makes these nanoparticles more sensitive to environmental changes, because the surface is more relevant.

In each case $1.7 \cdot 10^{-9}$ mol of the nanoparticles (QD to PI₆₁-*b*-PEO₂₁₂-OH ratio: 1 to 250) were dissolved in 3 mL of an aqueous solution containing surfactants (DTAB, and SDS), NaCl or different pH (4-9) values. Changes were followed by DLS measurements, as well as absorption- and emission-spectroscopy over a time period of ten days. In figure 65 the results are summarized for the micelle solution at pH 7.

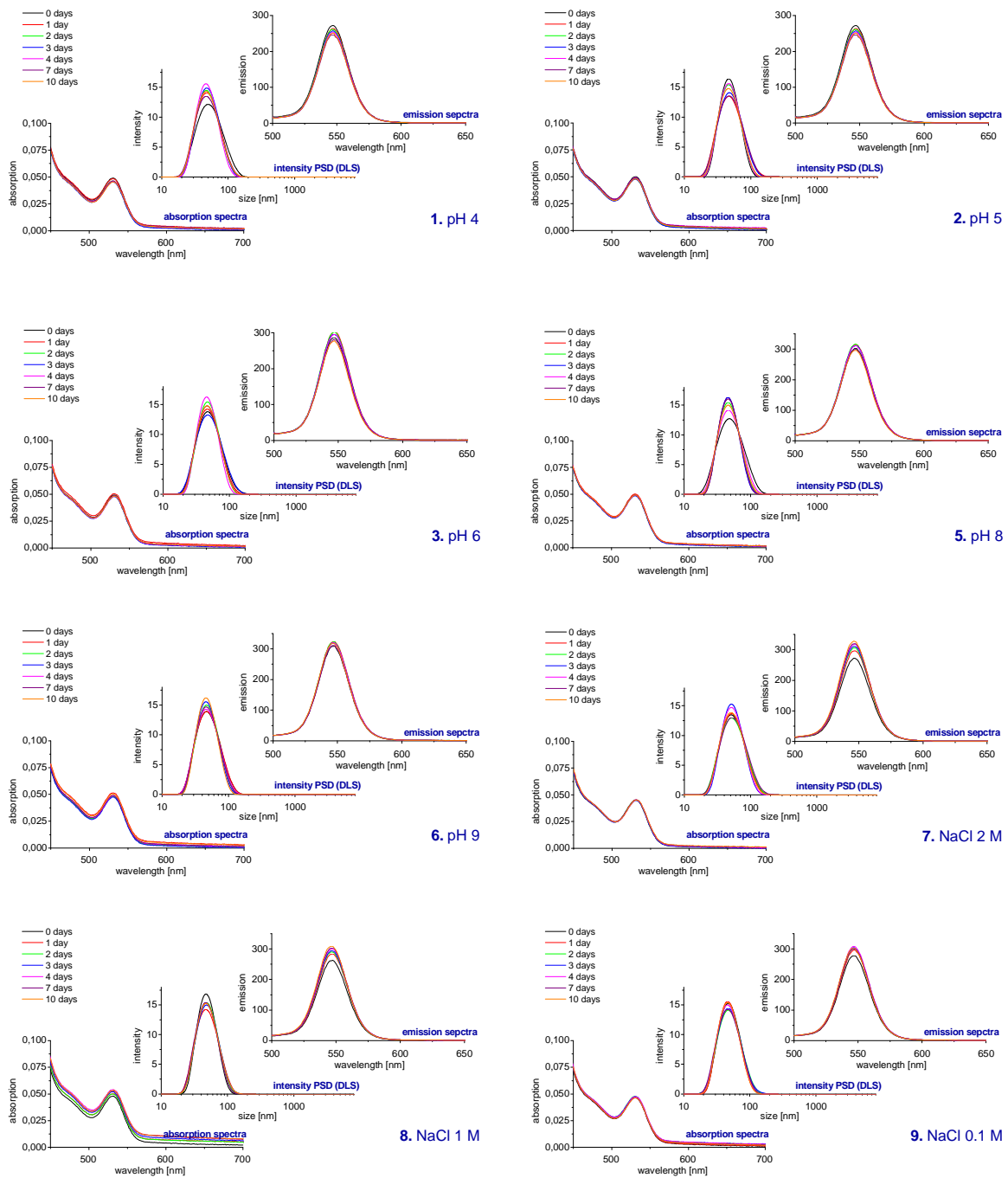


figure 66: absorption, emission, and dynamic light scattering of different nanoparticle solutions over the period of 10 days.

1. pH 4, 2. pH 5, 3. pH 6, 4. pH 7 (see figure 65), 5. pH 8, 6. pH 9, 7. 2.0 M NaCl, 8. 1.0 M NaCl, 9. 0.1 M NaCl.

The pH variation within the studied range produces no changes in the optical properties (absorption maxima 530 nm, emission maxima 547 nm) of the nanoparticles and a steady size distribution (45 ± 3 nm) according to the DLS measurements (figure 65 and figure 66).

CdSe nanocrystals have shown to exhibit solvatochromism^[37], where local dielectric properties and interactions with the surrounding matrix influence the nanoparticles optical transition energy. This is getting minimized, by reason that the micelles provide a local chemical environment similar to that of the initial organic solvent. The inert PEO ensures the steadiness of the structure against biological degradation.

Variation of the emission quantum yield with time is graphical depicted in figure 67. The quantum yield of the probe pH 7 was equated with 1. The figure shows that the lower the pH value (from 9 to 4) the lower the quantum yield is initially. The variance to the quantum yield at pH 7 is 6%. With the exception of the probe at pH 4 the quantum yield increases in the first two days, which can be understood as increased passivation due to the hydrophobic PI-N3 shell. After this initial increase, the quantum yield shows a nearly constant behaviour. This trend is especially evident in the samples containing 0.1, 1 and 2 M NaCl, where the increase in emission is more distinctive.

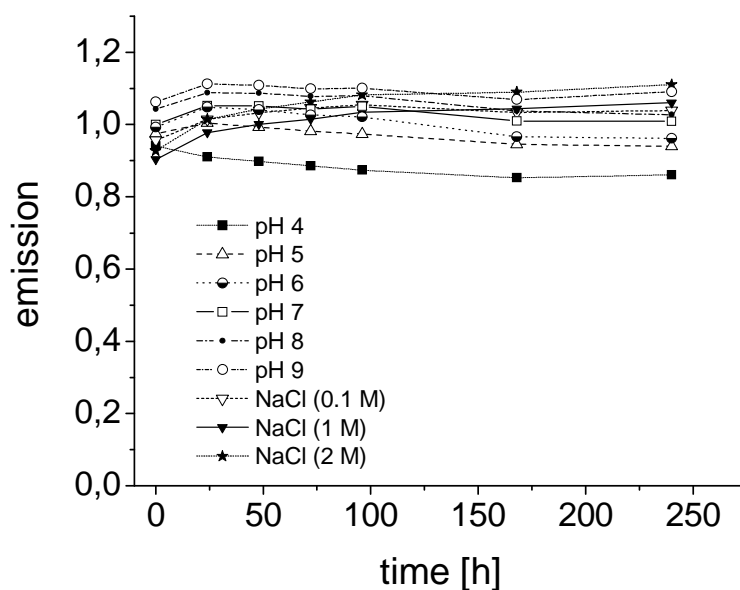


figure 67: graphical application of changes in emission of quantum dot containing PI-*b*-PEO micelles over a time period of 10 days.

In the presence of surfactants like one weight per cent SDS, one and five weight per cent DTAB no significant change in the physical characteristics of the micellar nanocomposites is detectable. So, to increase the strain on the micellar nanocomposites the micelles were subjected to 3 mL ddH₂O with ten weight per cent SDS (600000 fold excess of SDS per

nanoparticle). In the presence of the surfactant a proportionate change in structure was observable, which led to a lower solubility, concluding with the precipitation of a small amount of nanoparticles after 24 hours. This is been reflected in a drop of the emission maximum. Nevertheless, the precipitate was easily redissolvable and showed no significant change in the fluorescence intensity. The micelles, which stayed unaffected in solution showed a steady emission as shown in figure 68. This behavior is partly associated with the solubility of PI-b-PEO micelles and with the degree of crosslinking. The sample could, for example, exhibit an incomplete cross polymerisation between the terminal $-C=C-$ double bounds of poly(isoprene). This is contingent on the quantity and kind of initiator, the temperature of polymerisation, and the amount of additional crosslinking molecules like isoprene.

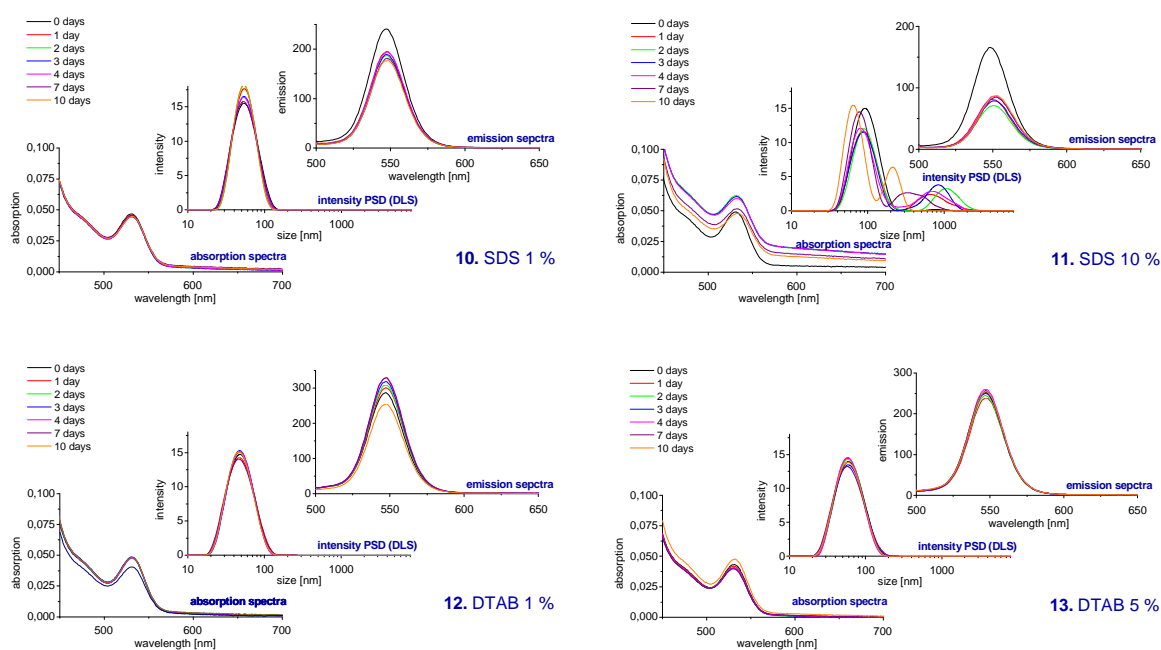


figure 68: absorption, emission, and dynamic light scattering of different nanoparticle solutions over the period of 10 days.

10. SDS 1%, **11.** SDS 10%, **12.** DTAB 1%, **13.** DTAB 5%.

On the following picture (figure 69) the luminescence of the nanoparticles buffer solutions after eleven days can be seen. Those, which contain 10% SDS, show a lower luminescence due to their lower concentration in solution.



figure 69: luminescence after eleven days.

1. pH 4, 2. pH 5, 3. pH 6, 4. pH 7, 5. pH 8, 6. pH 9, 7. 2.0 M NaCl, 8. 1.0 M NaCl, 9. 0.1 M NaCl, 10. SDS 1 %, 11. SDS 10 %, 12. DTAB 1 %, 13. DTAB 5 %.

The tightness of the ligand shell and the associated stability of nanoparticles in high dilutions should be reflected in a lower cytotoxicity. Many research groups found cytotoxicity to be dose dependent. Higher concentrations of nanoparticles result in significantly higher cell death^[67, 337-339].

2.4.4 (Förster-) fluorescence resonance energy transfer (FRET) measurements

With the purpose of collecting information on the coverage of the PI₆₁-*b*-PEO₂₁₂ ligand shell and distances between quantum dot and micelle surface in aqueous media, (Förster-) fluorescence resonance energy transfer (FRET) measurements were employed in cooperation with Klaus Boldt (research group of prof. H. Weller).

FRET is a non-radiative dipole-dipole energy transfer, the efficiency of which depends on:

- distance between donor and acceptor
- spectral overlap of the donor emission spectrum and the acceptor absorption spectrum
- relative orientation of the donor emission dipole moment and the acceptor absorption dipole moment.
- refractive index of the medium and quantum yield of the donor

An illustration of FRET is shown in figure 70. A donor absorbs a photon $h\nu_1^D$, whereupon an electron is excited from the ground state (S_0) to the S_1 state. In the progress of relaxation instead of fluorescence ($h\nu_{em}^D$) the energy is transferred non-radiatively via dipole-dipole-interactions from the donor to the acceptor. Depending on the acceptor either the acceptor emits a photon ($h\nu_{em}^A$) or the excited electron relaxes non-radiatively.

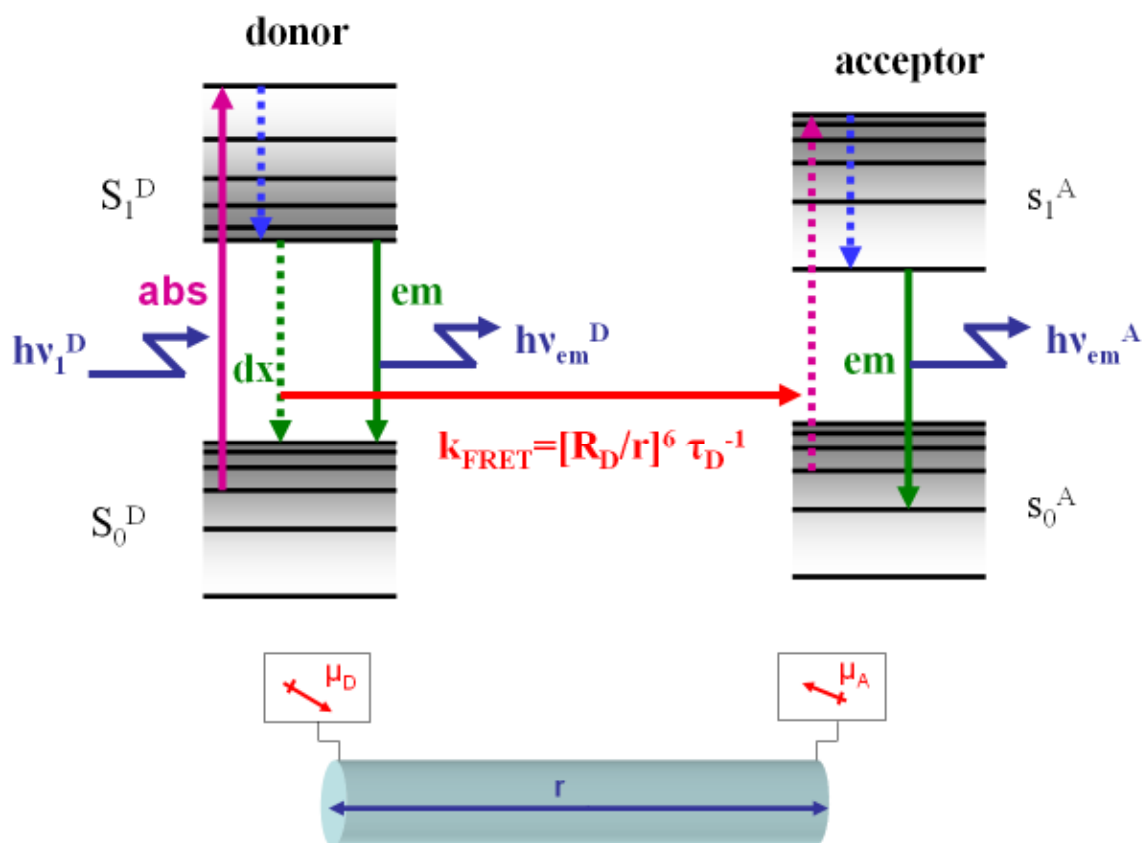


figure 70: illustration of FRET.

The donor is here a nanoparticle, while the acceptor is an organic dye.

In figure 70 the fluorescence lifetime τ_D of the donor has been noted down. τ refers to the mean time the molecule stays in its excited state before emitting a photon. Fluorescence typically follows first-order kinetics: $[S_1] = [S_1]_0 e^{-\Gamma t}$, where $[S_1]$ is the concentration of excited state molecules at time t , $[S_1]_0$ is the initial concentration and Γ is the decay rate or the inverse of the fluorescence lifetime. This is an example of exponential decay. Various radiative and non-radiative processes can de-populate the excited state. In such a case the total decay rate is the sum over all rates: $\Gamma_{tot} = \Gamma_{rad} + \Gamma_{non-rad}$, where Γ_{tot} is the total decay rate, Γ_{rad} the radiative decay rate and $\Gamma_{non-rad}$ the non-radiative decay rate.

The process takes place from the material with the higher band gap to the material with the lower band gap. Due to the fact that energy is lost rapidly after transfer through vibrational relaxation, this process is unidirectional.

The corresponding equation for the FRET-energy transfer efficiency is:

$$E = \frac{1}{1 + (r/R_0)^6} \quad , \quad (29)$$

whereby R_0 is the so called “Förster radius”, *i.e.* the distance where the probability of energy-transfer is 50% and r is the distance between acceptor and donor.

Different organic dyes were therefore attached to PI₆₁-*b*-PEO₂₁₂ (figure 46), whereby Alexa Fluor®594 was suited best for FRET measurements owing to its emission properties and its solubility in water.

Considering a sufficient spectral overlap of Alexa Fluor®594 with a quantum dot, CdSe/CdS/ZnS nanoparticles with an absorption maximum of 540 nm and an emission maximum of 553 nm were employed and encapsulated in micelles in such a manner that in each micelle one quantum dot was present. The Alexa Fluor®594 modified ligand was integrated in the micelle in quantum dot to dye ratios 1:0, 2:1, and 1:1. Best results were obtained with a ratio of 1:1. The corresponding HR-TEM images are shown in figure 71.

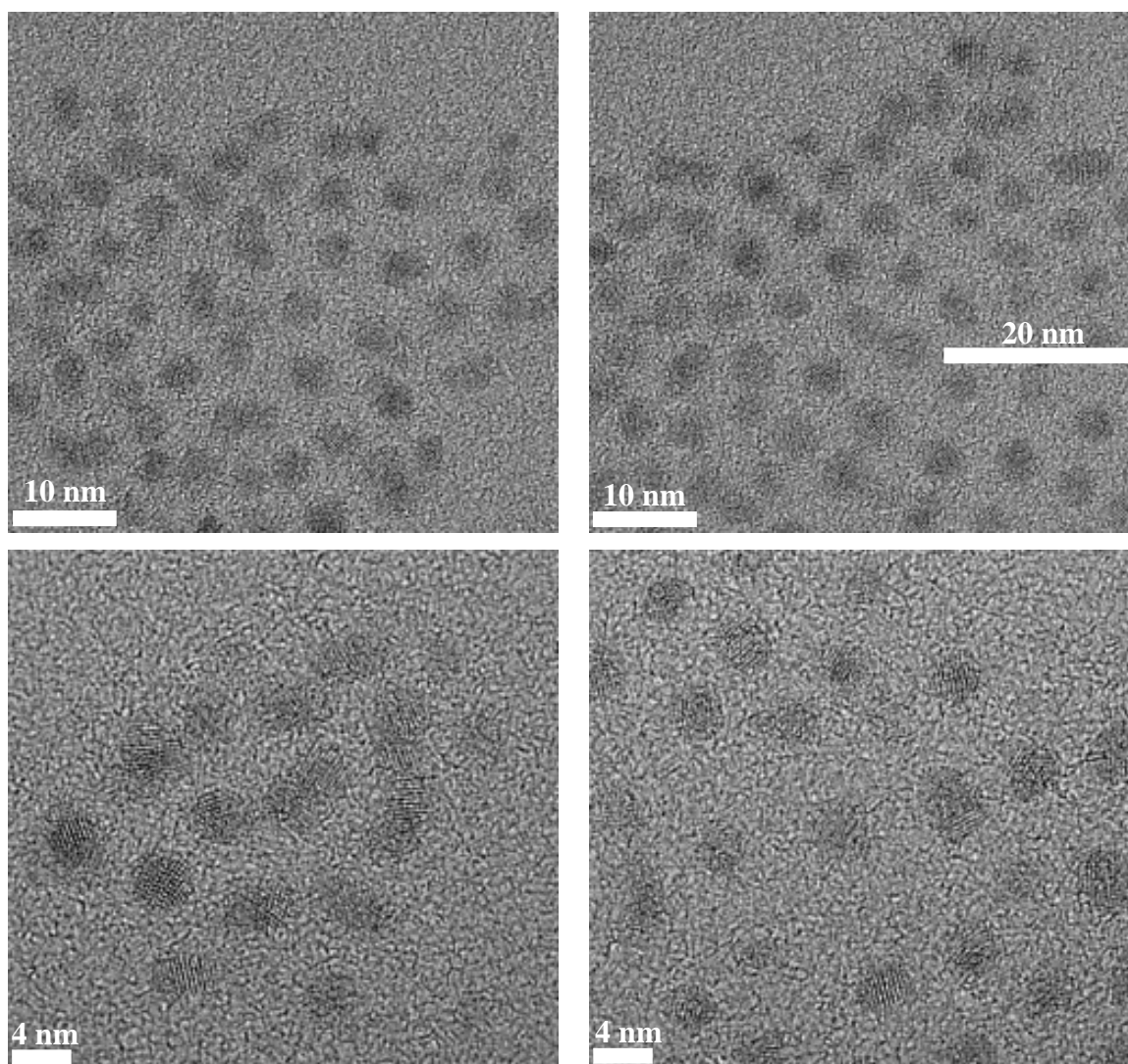


figure 71: HR-TEM images.

$1.084 \cdot 10^{-9}$ mol PI₃₀-N3 coated CdSe/CdS/ZnS encapsulated with PI₆₁-*b*-PEO₂₁₂-Alexa Fluor®594 & PI₆₁-*b*-PEO₂₁₂-OH (QD/P ration 1:573, QD/ PI₆₁-*b*-PEO₂₁₂-Alexa Fluor®594 1:1) in water.

The concentration of the QD solution was determined via UV-vis spectroscopy according to Yu *et al.*^[340] (figure 72). A pulsed diode laser with an emission wavelength of 438 nm was used. The organic dye was chosen so that the excitation (absorption) of the dye (acceptor) at this wavelength was minimal.

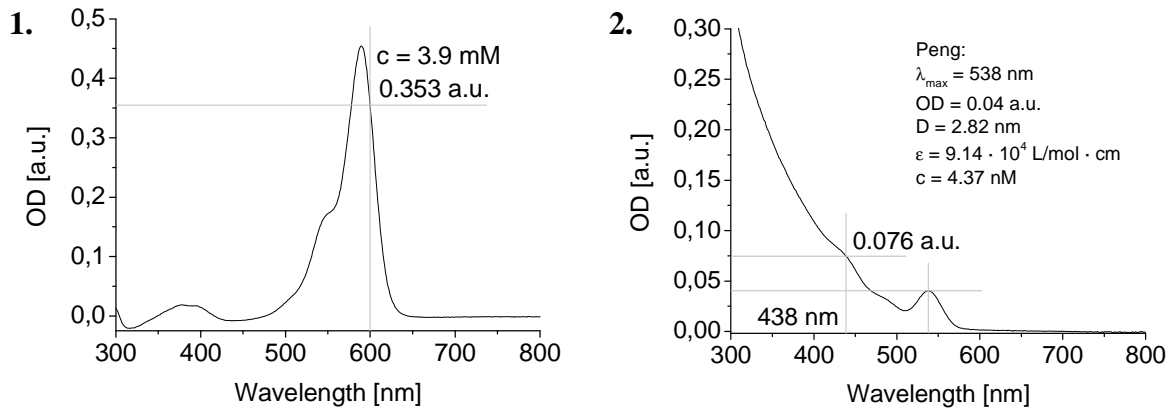


figure 72: 1. determination of the concentration of Alexa Fluor® 594. 2. determination of the concentration of CdSe/CdS/ZnS nanoparticles in water.

From the UV-vis spectrum of the coupled QD-dye solution (figure 73) the ratio was determined to be 1:2.

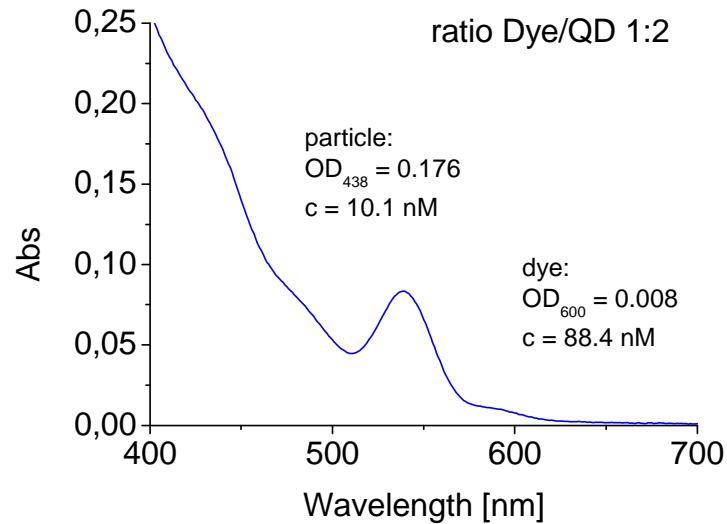


figure 73: absorption of QD-Alexa Fluor®594 nanocomposite in water.

The extinction coefficient ϵ of the organic dye was determined experimentally (figure 74).

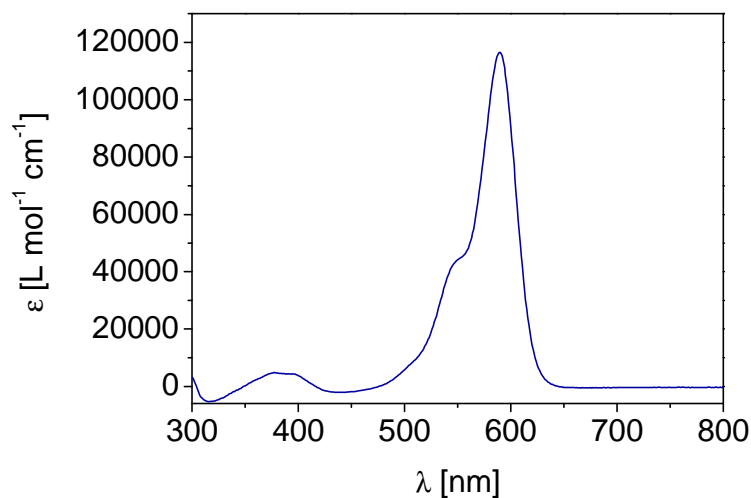


figure 74: molar extinction coefficient of Alexa Fluor®594 experimental determined.

The Förster radius R_0 was calculated based on the equation:

$$R_0^6 = \frac{(9 \cdot Q_0 \cdot \ln 10 \cdot \kappa^2 \cdot J)}{128 \cdot \pi^5 \cdot n^4 \cdot N_A} \quad , \quad (30)$$

in which Q_0 is the quantum yield of the donor (20%), κ^2 is the orientation factor (2/3), J the overlap integral ($5.5 \cdot 10^{15}$), n the refractive index of water, and N_A Avogadro's number.

The overlap J is a measure for the dipole-dipole interaction.

$$J = \int_0^{\infty} \epsilon_A(\lambda) \cdot f_D(\lambda) \cdot \lambda^4 d\lambda \quad , \quad (32)$$

f_D is the normalized emission spectrum and proportional to the donor oscillator strength.

$$\int_0^{\infty} f_D(\lambda) d\lambda = 1 \quad , \quad (31)$$

The extinction coefficient of the acceptor ϵ_A contributes to the strength of the dipole-dipole interaction of the acceptor and donor. ϵ_A is proportional to the optical density divided by the concentration and density (OD/cd).

The Förster radius R_0 was 5.1 nm. FRET-efficiency was determined to be 11%, using the equation:

$$E = 1 - \frac{\tau'}{\tau}, \quad (33)$$

wherein τ' is the lifetime of the QD-dye micelle and τ the lifetime of the quantum dot micelles.

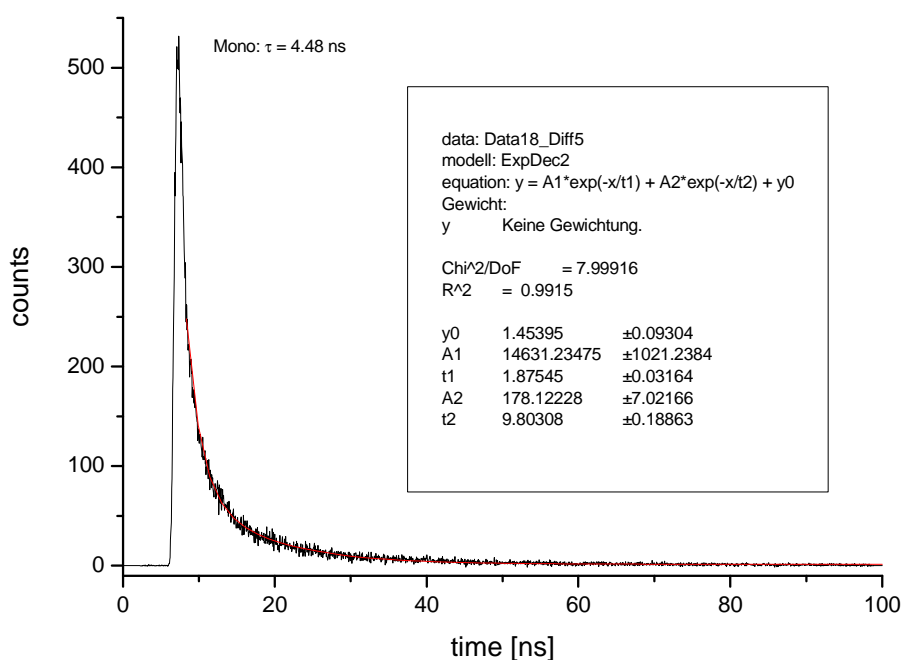


figure 75: biexponential fit of fluorescence lifetime of the QD-dye nanocomposite.

Using a biexponential fit to analyze the decay curve of the donor (figure 75) two different lifetimes were measured, which represent two distinctive species in solution. Calculations were performed with the longer lifetime.

$$\tau_1 = 1.9 \text{ ns}$$

$$\tau_2 = 9.8 \text{ ns}$$

In the process of excitation at 438 nm also the organic dye is being excited by the laser, because of a minimal absorption. This is shown in figure 76.

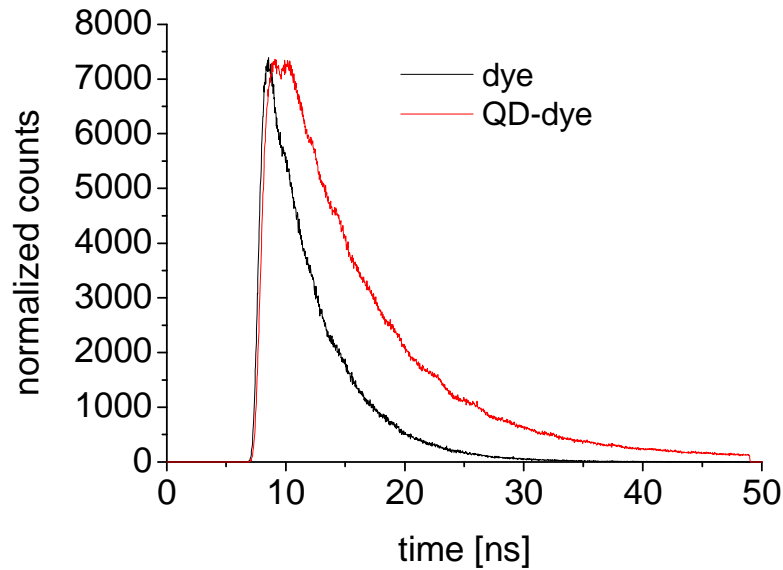


figure 76: comparison of dye with a mixture of dye and QD-dye.

To subtract the direct excitation of the organic dye the decay rate of the dye (times a factor f) was subtracted from the decay rate of the QD-dye composite. The residual shows the quality of the fit (figure 77). Thereby the amount of excitation of the acceptor evoked by the laser could be eliminated and the assumption can be made that the remaining emission of the acceptor is caused by FRET.

Consequently the mean distance from dye to quantum dot is 7 nm, with an error of ± 1 nm, based on the following equation:

$$E = \frac{R_0^6}{R_0^6 + r^6} \Leftrightarrow r^6 = \frac{R_0^6}{E + R_0^6} \quad (34)$$

The Förster radius R_0 was calculated with R_0^6 based on the assumption that the energy transfer occurs between point-dipoles. Due to their size nanoparticles can't be regarded as point-dipoles. So far there is no exact theory according to nanoparticles.

In case of plane surfaces the Förster radius would be included with R_0^3 . But the nanoparticle is spherical, whereby the Förster radius has to be calculated between R_0^3 and R_0^6 . Nevertheless,

with a nanoparticle size of 4 nm in diameter the total size of the nanocomposites is 18 ± 2 nm. This size agrees with TEM images.

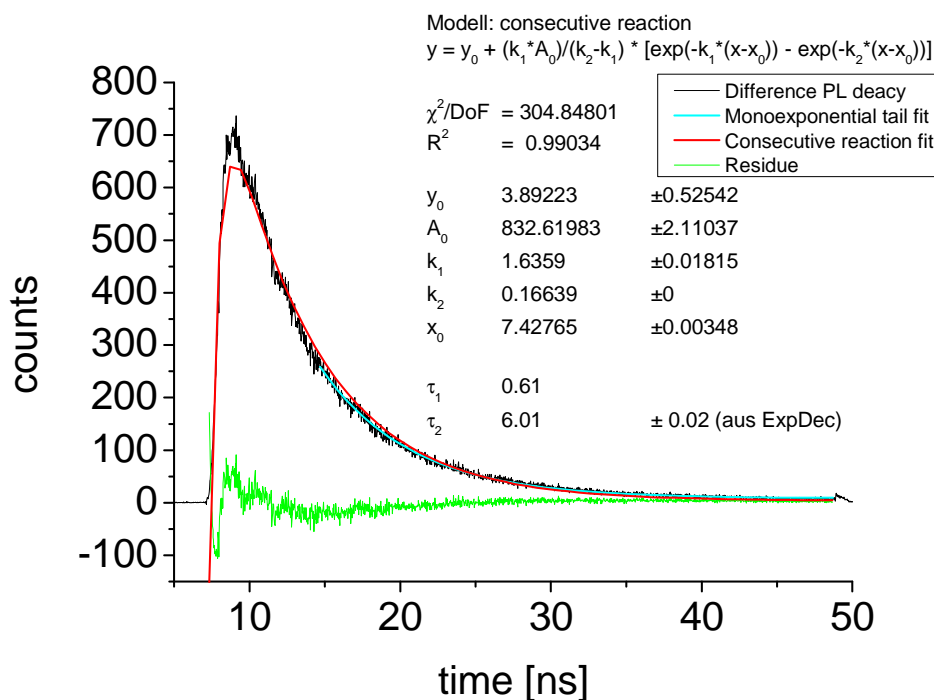


figure 77: kinetic of consecutive reaction $A \rightarrow B \rightarrow C$ specifies the acceptor.

The results are just an estimate, because the FRET rate couldn't be confirmed in the build up time of the acceptor. This is due to the poor time resolution of the used photomultiplier tube. However, the FRET measurements document the presence of the organic dye outside of the hydrophobic segment, thus no interaction with the nanoparticle surface occurs. This indicates a dense package of the ligand system around the nanoparticle.

2.5 Phase-transfer based on emulsionpolymerisation

This chapter describes the potential of emulsion polymerization in the range of nanotechnology. In contrast to complex ligand systems which have to be first synthesized and then attached to the nanoparticle, in this approach any nanoparticles can be encapsulated into a cross-linked polymer-shell by a simple procedure based on (micro)emulsion techniques. Microemulsion was expected by theoretical considerations to show better performance than miniemulsion in terms of emulsion stability and prevention of contact between nanoparticles and water.

The field of application for the composite particles depends predominantly on three characteristics: first on the applied metallic nanoparticle, second on the polymer shell, and finally on the functional groups at the edge of the polymer shell.

2.5.1 Emulsifier approach

To enlarge the wide field of application for nanoparticles, especially to aqueous systems, the approach of emulsion polymerization was implemented in cooperation with the research group of Prof. Dr. H. U. Moritz from the department of technical and macromolecular chemistry. In this method the nanoparticles are co-dissolved in solution with monomers, and these monomers and nanoparticles are stabilized by surfactants. Amphiphilic molecules like SDS are present at the water/oil periphery. Lower alcohols work as cosurfactants. They lower the interfacial tension between oil and water sufficiently for almost spontaneous formation of the microheterogeneous systems^[341].

The following radical polymerization is initiated by thermally activated initiators and constructs polymer particles, in which the nanoparticles are embedded. Styrene and divinylbenzene (DVB) were used as monomers. Polymerization of these monomers builds up a three dimensional meshwork (figure 78).

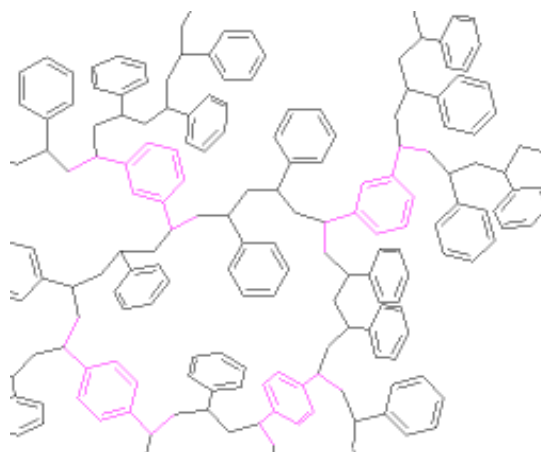


figure 78: Meshwork of styrene and DVB units.

Those organic-inorganic hybrid materials and polymeric nanocomposites present the properties of both the inorganic nanoparticles and the polymer by combining thermal stability, mechanical strength, or electronic and optical properties with flexibility and the ability to form films^[106, 107]. Further these inorganic nanoparticles can possess functions such as magnetic susceptibility, electrical conductivity, catalytic activity, or electroactivity, and so they may possibly form functional composites (or nanocomposites)^[342, 343].

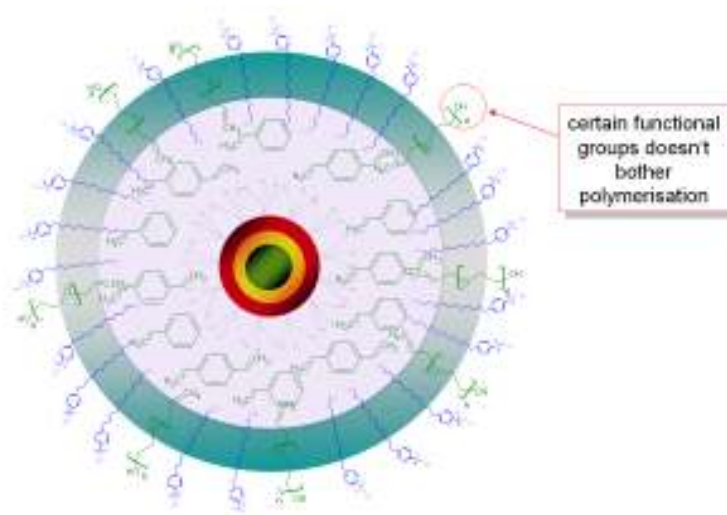


figure 79: nanoparticle in an emulsion micelle.

Nanosphere copolymerization was implemented to introduce reactive functional groups to the composite. The copolymerization was performed with hydrophilic monomers to ensure water solubility even in highly diluted systems, in which emulsifier based approaches might be problematic due to desorption of the emulsifier from the polymer particles. Styrene and divinylbenzene should build up the crosslinked core, while acrylic acid served as functional monomer. By introducing vinyl-terminated poly(ethylene oxide) (V1100 PEG) for copolymerization also hydroxy groups along with carboxylic groups could be incorporated as functional groups. Due to the high amount of divinylbenzene the performed polymerisations could be called “tripolymerisation”.

With this approach polymer nanoparticles of the styrene-V1100 PEG copolymer can be produced in a particle range of 27 nm up to 61 nm (figure 80 a) and styrene-acrylic acid copolymer particles in a range of 23 nm up to 80 nm (figure 80 b). Regarding size distribution in dynamic light scattering (DLS) measurements polydispersity indices (pdi) around 0.1 were observed.

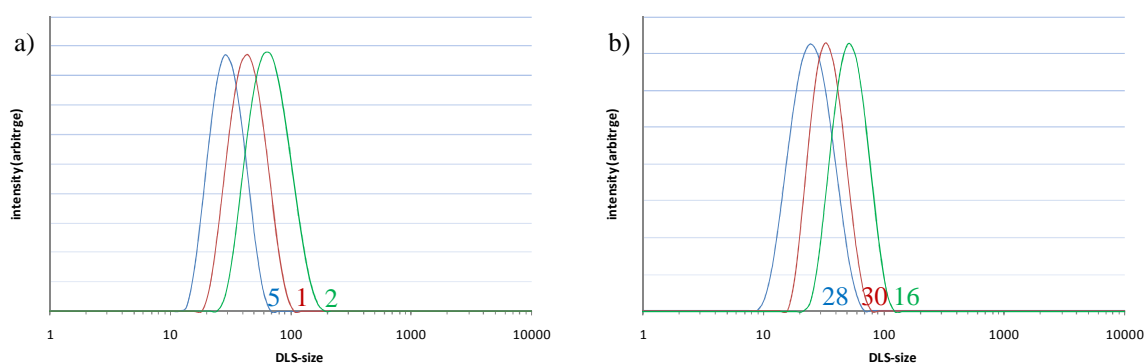


figure 80: DLS measurements of a) styrene-V1100 PEG copolymer particles and b) styrene-acrylic acid copolymer particles. The number refers to the emulsion approaches listed in table 9.

By reason that the solubility of polyacrylic acid is limited and a large amount of functional groups are buried in the polymer during polymerization with only a small part left on the surface^[344, 345], the acrylic acid was added after a certain time, customarily 10 - 60 minutes after the polymerization has been started by addition of initiator. While the advantage of this delay is that the hydrophilic polymer will be located precisely at the surface, the drawback is the number of double bonds at the surface, which is reduced with the start of the reaction. This has to be compensated by a higher amount of monomer or a longer reaction time.

In figure 81 a ¹H-NMR spectrum of CdSe QDs in DVB/styrene/acrylic acid particles is presented. At 4.7 ppm the signal of H₂O/HOD can be seen. The broad signals at 7.1 and 7.6 ppm arise from the aromatic protons of styrene and DVB units. A broad multiplet from 0.9 to 1.5 ppm indicates, as expected, that the polymerisation leads to an atactic polymer. In case of syndio- and isotactic polymers the methylene protons should have separated signals.

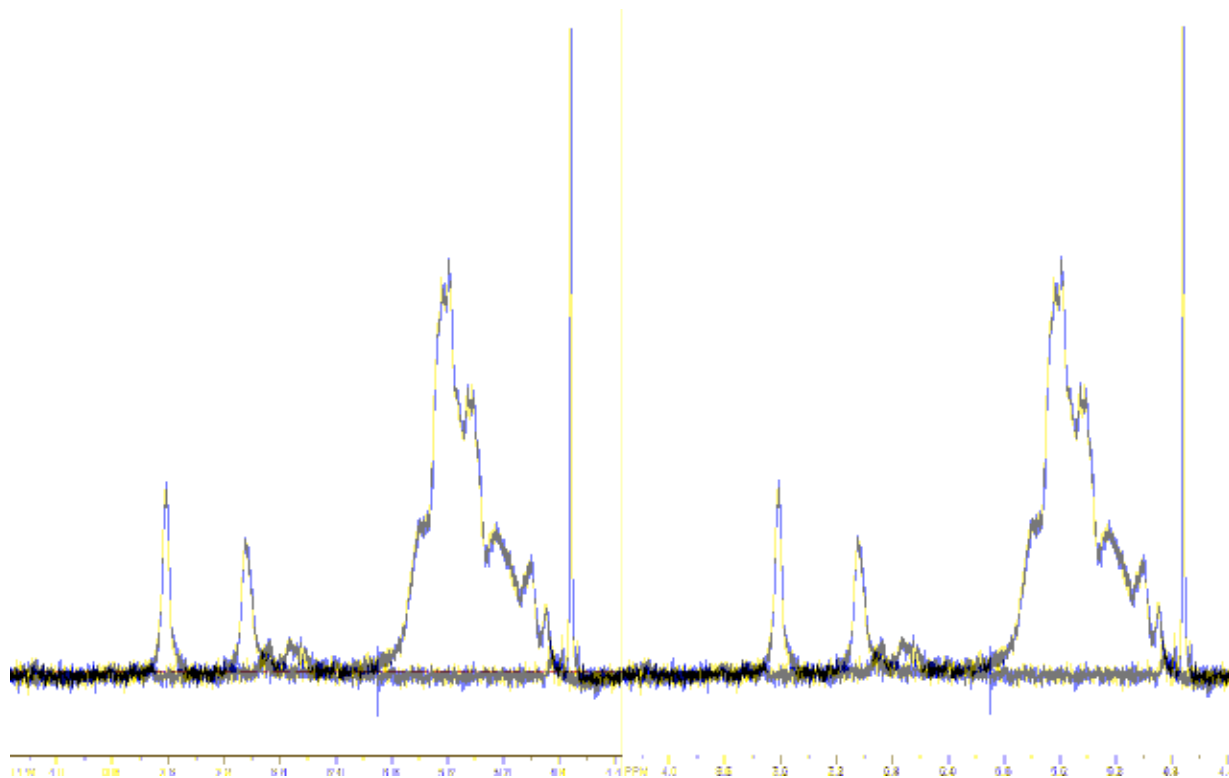


figure 81: ¹H-NMR (400 MHz, D₂O) of an emulsion polymerisation approach (0.65 g styrene, 106 mg DVB, 60 μL acrylic acid, 1.23 g SDBS, 75 mg pentanol, 14 g water, 15.9 mg WAKO VA44, 2 nmol CdSe, temperature of polymerisation 45 °C)

To examine the evolution of the emulsion polymerization, a calorimetric measurement (figure 82) was performed on the SDS, styrene and DVB system in the research group Prof. Dr. H. U. Moritz. The thermal flow, indicated in yellow (figure 82), can be interpreted as follows. After the temperature settled to 45 °C the initiator dissolved in water was injected. Because the water was at room temperature, which was of course lower than 45 °C both curves show a negative

thermal flow. The thermal flow then increases rapidly, due to the ensuing polymerization, which starts immediately after the injection of the initiator. The monomer concentration decreased as it was converted to polymer, resulting in a lower heat flow and rate of the reaction. The initiator concentration can be assumed to be constant. After around 30 minutes the reaction has finished. During that time an cumulative thermal flow of 3.82 kJ was observed. In a rough approximation, ascribing the same reaction enthalpy to styrene and DVB, a value of 4.55 kJ would be expected for 100% conversion. Accordingly a yield of 84% is calculated.

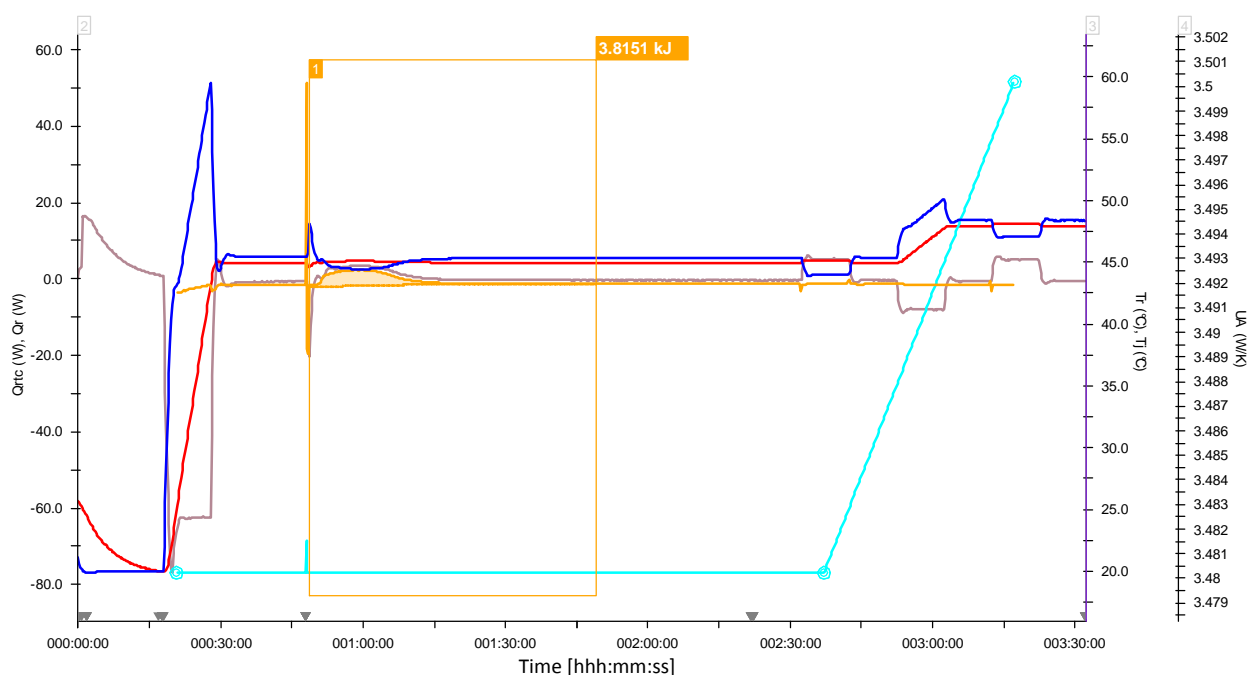


figure 82: calorimetric data of emulsion polymerizations performed with styrene, DVB and SDS. Temperature developing of cooling/heating jacket (dark-blue), heat transfer coefficient (light blue), temperature developing in the reactor (red), heat flow across the wall of the reactor (beige) and heat of reaction (yellow).

Great attention has to be taken in the completeness and uniformity of the polymer shell around the nanoparticles. An incomplete polymer shield would disturb the positive character of reduced heavy metal exposure and stimulate agglomeration. Next to shells, which were able to be produced for all kind of nanoparticles (see figure 83 for examples of CdSe, CdSe/CdS/ZnS and Fe₃O₄ nanoparticles), it can also happen quite easily that the monomer and thereby also the polymer builds up droplets on the surface.

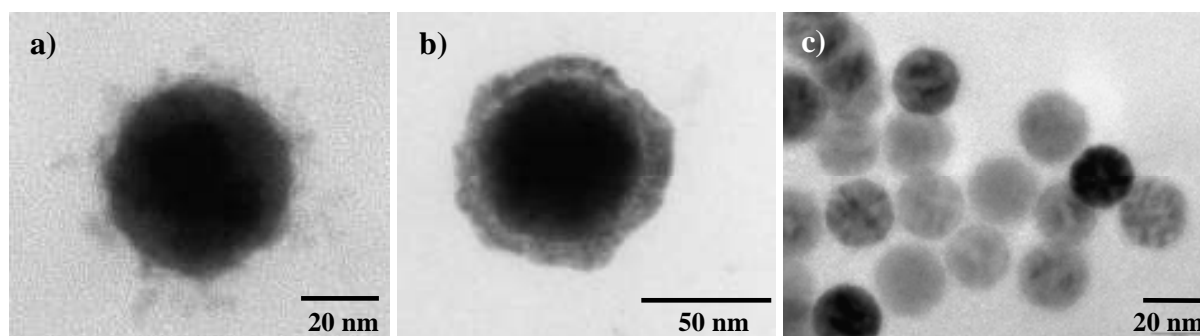


figure 83: TEM images of experiment a) 5 (CdSe), b) 11 (CdSe/CdS/ZnS) and c) 32 (Fe_3O_4). The number refers to the emulsion approaches listed in table 9.

As shown in figure 83 a) and b) the hydrophilic polymer in, a) V1100 PEG and in b) polyacrylic acid, around the particle core are visible. The polyacrylic acid shell seems to be more compact than the V1100 PEG shell, which is more diffuse.

This allows application-specific density control of the shell under similar reaction conditions. The high contrast of the core is based on the presence of the metallic nanoparticles. This indicates that the nanoparticles are completely surrounded by polymer (see figure 83 a - c). Especially in case of toxic nanoparticles in bioapplications this will be an extraordinary advantage for reducing toxicity. In figure 83 c) iron oxide containing nanoparticles are shown. Referring to Park *et al.*^[346] the synthesized large particles exist in the form $(\text{Fe}_2\text{O}_3)_{1-x}(\text{Fe}_3\text{O}_4)_x$, in which $\gamma\text{-Fe}_2\text{O}_3$ (maghemite) and Fe_3O_4 (magnetite) are both present. Spotted particles show that also partial oxidation is possible. As another remarkable fact it can be seen that these particles show water solubility even though the hydrophilic organic shell is very thin. That leads us to conclude that water solubility can be already obtained with a small, but strongly-bonded hydrophilic polymer on the surface. When hydrophobic initiators are used in the process of encapsulation of magnetite nanoparticles a change in colour is detectable. The change of colour from black to brown was possibly due to partial oxidation of Fe_3O_4 to $\gamma\text{-Fe}_2\text{O}_3$ on the surface due to the presence of radicals. The observation that the change in colour also occurred in case of hydrophilic initiators suggests that during the polymerization the radical marches from the droplet surface to the inside. So polymerization was partly terminated on the nanoparticle surface in the inside of the droplet.

Homogenous nucleation leads to the formation of polymer particles without nanoparticles inside. The number of such pure polymer particles can be minimized by adding a higher amount of nanoparticles in the solution, to attain more polymerization seeds. However, homogenous nucleation can never be fully suppressed, particularly when using a water-soluble initiator^[347]. Accordingly a purification step is required. In the case of magnetic particles they can be sedimented by a magnet and the water phase, in which homogenous polymer particles

are present, can be easily removed. Other nanoparticles can be precipitated via centrifugation in the presence of a hydrophobic solvent.

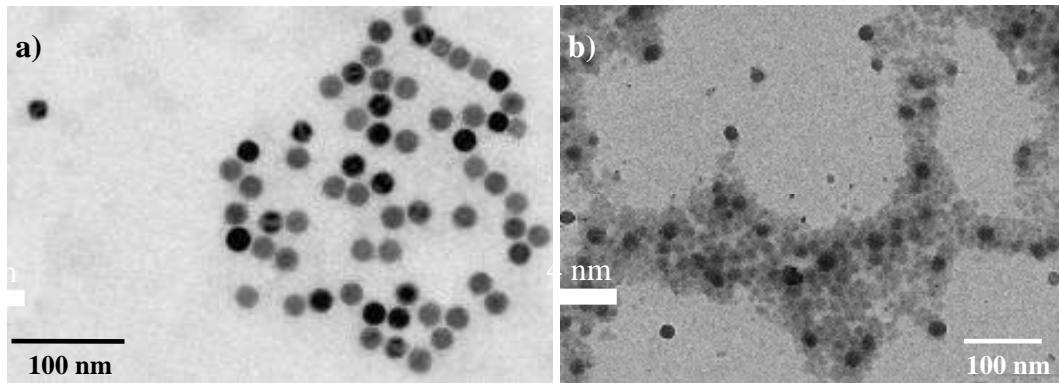


figure 84: TEM images with separated (a) and deliquesced particles (b).

In figure 84 a) particles which are nicely separated are shown. On the other hand the particles in figure 84 b) are deliquesced. Coalescence of polymer particles can always be observed if they are dried and close by. In case of wall paint this effect is necessary for the quality of the paint. In general soft particles coalesce more easily than stiff particles, but also very stiff particles can show coalescence. Due to this fact particles were not dried during or after the synthesis to ensure separated particles. Referring to Reynhout *et al.*^[348] styrene / acrylic acid lattices show coalescence and aggregation already in solution, beginning at 35 °C. At 80 °C massive coalescence and aggregation takes place. Deprotonation of the acrylic acid (pH 12) increases the stability due to the presence of negative charges at the surface. High electrolyte concentrations lower the stabilizing effect. On that account all experiments were regularly performed at 40 °C performed to minimize coalescence and aggregation.

Another interesting effect, evident from TEM images, is the ordering of nanoparticles inside the polymer particle. In figure 85 a bright TEM image of a multi nanoparticle containing polymer particle is shown as an example. Referring to the TEM image a pronounced order can be observed. Similar to a crystal lattice the nanoparticles are ordered in close-packed arrangement. This might become very important in case of particles which contain different nanoparticles.

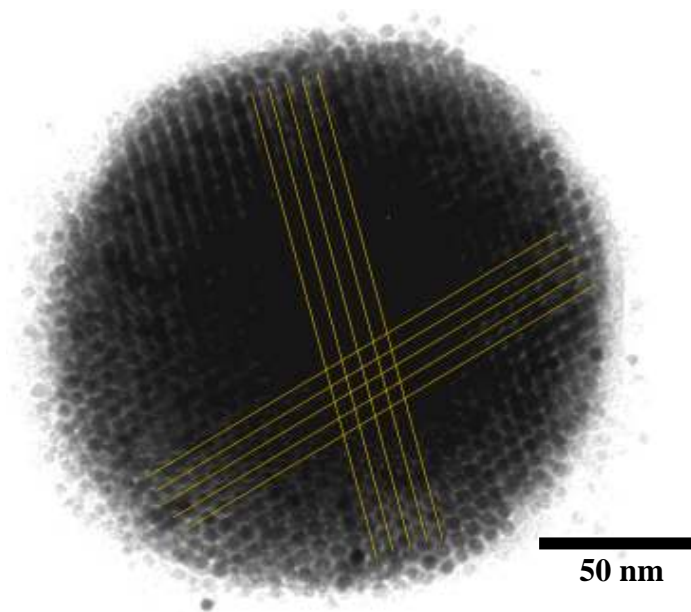


figure 85: TEM images (brightened) with indication of lattice.

Like the particle inside, the imbedding monomer can be selected based on the application needs. To demonstrate the versatility of the system, experiments with squalene, which is used as solvent in continuous flow production of CdSe nanoparticles, and methyl methacrylate (MMA) were performed. With both monomers similar results compared with the styrene based emulsion polymerizations were achieved.

For encapsulation of CdSe nanoparticles poly(*n*-butyl acrylate) (PBA) proved to be a suitable potential polymer matrix^[349]. But it must be noted that in this process the nanoparticles are exposed to the emulsifier and to a certain extent to the solvent. Since ionic emulsifiers and polar solvents quench the fluorescence of quantum dots, it is necessary to use an inverse emulsion and non-ionic emulsifier. Additionally, a monolayer of an alkylamine with a terminal double bond, established on the nanoparticle surface by ligand exchange, could assist the polymerization and the rigidity, which leads to a faster burial of the nanoparticle in the polymer. For this the ligand PI-N3 (chapter 2.3) was introduced.

2.5.2 Surfmer approach

The challenge of the coemulsion is the hydrophilic compound: acrylic acid polymerises in the aqueous phase. The emulsifier and the hydrophilic properties of acrylic acid constrain the attachment of polyacrylic acid on the particle surface. A higher degree of DVB and styrene derivatives, which are more likely found on the phase barrier could make functional groups

available, which allow an increased attachment of the hydrophilic polymer strains. But there is a further option.

In addition to the aforementioned problems, the denaturation of proteins via the emulsifier SDBS or SDS is a problem for biomedical applications. It requires attentive removal of the emulsifier, for example by dialysis. An option to minimize or eliminate the use of emulsifier respectively is the adoption of reactive surface-active substances like initiators (inipars)^[350, 351] and monomers (surfmers)^[352-358], achieving polymer colloidal systems with strong aggregative and sedimentation stability^[359-363].

In general the application of an excess of surfmer should be constrained to avoid homopolymerization of the surfmer in the aqueous phase especially concerning smaller surfmers, which can lead to bridging flocculation^[364]. Certainly, homopolymerization can also appear in an adsorbed surfmer layer on the polymer interface^[365]. The presence of unreacted surfactants may worsen adhesion, water sensitivity, and optical properties^[359]. However, a highly reactive surfmer, which would limit the amount of unreactive surfactants, would be consumed at the beginning of the polymerization and would result in surfmer burial^[366] during particle growth. Thus, the optimal surfmer should have intermediate reactivity ratios^[367]. Due to the generation of secondary and tertiary radicals chain transfer to surfmers is reported to appear in the process of copolymerization of allylic surfmers^[368] and block copolymers containing PEO groups^[369, 370], while the double bond of the surfmer remains unaffected.

Mandal *et al.*^[322] tried to avoid complex classical ligand systems^[371] by using a surfmer (NP10) approach which allows the nanoparticles to be encapsulated in a protective shell^[21, 22, 92] for transfer into aqueous media. Using fluorescent and magnetic nanoparticles such composite materials have interesting potential applications since they combine the property of purely magnetic micrometer sized beads that are used for a variety of biotechnology applications including cell sorting^[372, 373], sensing^[374] and assay separations^[375] and the properties of purely fluorescent labels for macromolecule detection^[376] and multiplex optical coding for biomolecules^[377]. Compared to organic fluorophores quantum dots show excellent photostability and the emission wavelength is directly correlated (through quantum confinement) to their size. Consequently different colours can be obtained just by changing the size of the quantum dots the polymer-particles contain.

Based on the results of Mandal *et al.*^[322] several approaches implementing surfmers were performed. Along with NP10 which was used by Mandal *et al.* Ralumer, Lutensol, Pluronic and Tween[®]80 (polyethoxysorbitan mono-oleate) were adopted for application. This amphiphilic molecule is a non-ionic surfactant comprised of a sorbitan ring and about twenty ethylene oxide

units. The surfactant is excellent for use in the formulation of miniemulsions. The surfactant is known as a non-toxic surfactant with excellent physiological properties and is widely used in biochemical applications including emulsifying and dispersing substances for pharmaceuticals, cosmetics and food products.

In contrast to the emulsifier approaches the surfmer has to be present in the monomer solution in the process of the addition to the aqueous phase^[356]; an observation that has also been seen with other emulsifiers.

In accord with the results of Mandal *et al.*, it was possible to produce nanocomposites with fluorescent and magnetic properties with different reaction conditions in a range of 50 - 105 nm (average size distribution). Particles containing both fluorescent nanoparticles and magnetic oxide particles are a very powerful tool for many applications. The fluorescence shown by the particles can be used for fluorescence detection methods which are orders of magnitude more sensitive than e.g. UV/VIS spectroscopy, which is commonly used for labelling in bio applications. The magnetic properties can be used for imaging contrast, but there is also a possibility for magnetic manipulation. The properties of both nanoparticles together with the availability of a functional group of the outer side of the shell offer the chance to tune the particle through specific coupling to e.g. antibodies to a target and then detect them via different method, depending on the applicable analytical method.

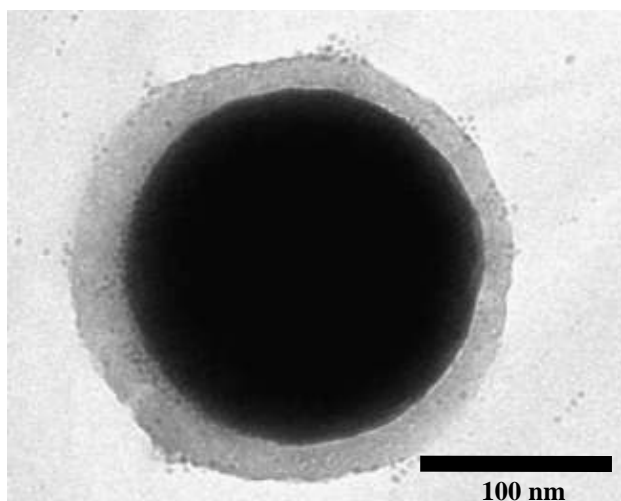


figure 86: TEM image of NP10 particles synthesized according to Mandal *et al.*

Next to establishment of the emulsion, a crosslinkage during polymerization was achieved. In figure 86 TEM image of a NP10 particle is shown, synthesised according to Mandal *et al.*, but with cross linking via thermally induced polymerization. The shell can be seen with a thickness of around 10 nm. It's been assumed that there is crosslinking presence due to several

indications. First a high amount of the cross linker DVB was used. Second the particles show excellent stability also in high dilution, and third the non cross linked particles show always a slightly higher diameter than the cross linked ones. The decrease of the diameter might be caused by reduction in the mobility of the surfmer NP10 caused by cross linked bonds.

2.5.3 Surfmer approach using Tween[®]80

As mentioned in the results from Mandal *et al.* a lower fluorescence intensity was observed compared with pure fluorescent nanoparticles, mainly caused by the absorption of fluorescence by the magnetic nanoparticles. To afford higher quantum yields, attempts were made to minimize negative effects associated with the NP10 approach like presence of water or oxygen. Concerning this matter Tween[®]80 seemed to be ideal, because of the presence of three hydrophilic (PEO) chains to one hydrophobic chain and hence the more conical space requirement. In comparison Tween[®]80 should build up a more closed shell than the more cylindrical NP10. Aside from the structure, Tween[®]80 also provides a higher density of functional groups that allows a following modification of the micelle surface. Further Tween[®]80 has a food and drug administration (FDA, code number 433).

With this approach Tween[®]80 emulsified polystyrene particles were achieved in a range of 31 nm up to 88 nm (figure 87 a). The stability of the interaction between styrene and Tween[®]80 could be demonstrated by dilution series (figure 87 b). Hereby no significant decrease in particle size and no drop out was detected, which would be expected if the emulsifier (Tween[®]80) would be desorbed from the particle surface. Again a slight decrease in particle size comparing the diameter before and after the reaction was observed.

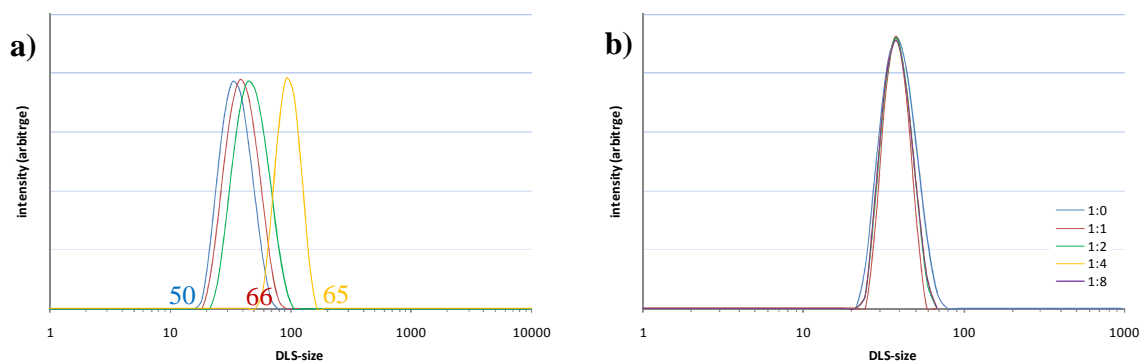


figure 87: a) DLS measurements of Tween[®]80 styrene particles; b) Tween[®]80 styrene particles thinned 1:0, 1:1, 1:2, 1:4, 1:8 (experiment 60).

By this emulsion approach hydrophobic nanoparticles like gold, FeO_x and QDs can be encapsulated easily (figure 88, 1.-3.). The presence of stabilizers in styrene and DVB like for example the polymerization inhibitor 4-tert-butylbrenzcatechin results in quenching of the luminescence of quantum dots. Therefore the monomers have to be distilled, what permits the establishing of solutions, containing CdSe/CdS/ZnS nanoparticles with satisfying quantum yields (figure 88, 4.).

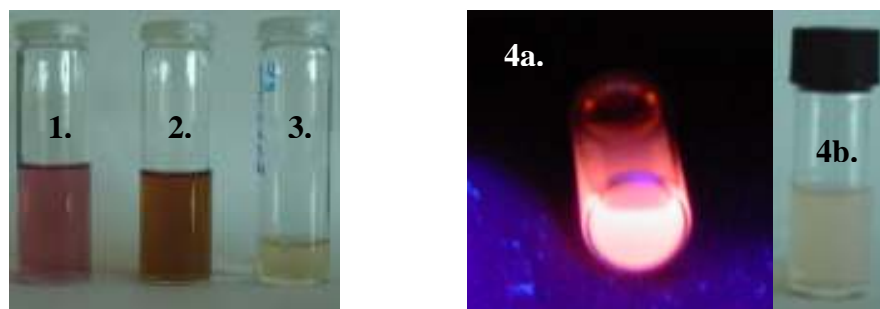


figure 88: Tween[®]80 emulsified polystyrene composite particles. **1.** goldnanoparticle in water, **2.** FeO_x in water, **3.** CdSe/CdS/ZnS QDs in water, **4.** CdSe/CdS/ZnS QDs in water under UV excitation (**a**) and under daylight (**b**).

TEM images of the FeO_x and CdSe/CdS/ZnS nanoparticle solutions show single encapsulated nanoparticles (figure 89). The excess of polymer is also apparent, which can be removed via heptane.

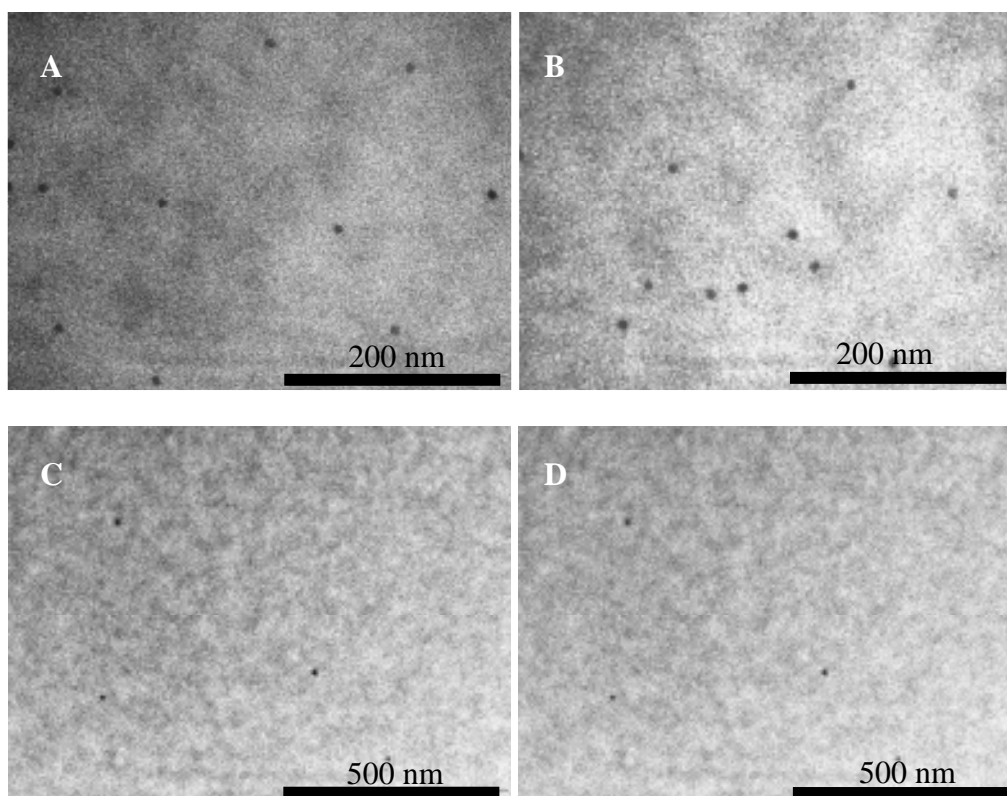


figure 89: TEM images of CdSe/CdS/ZnS (**A-B**) and FeO_x (**C-D**) containing Tween[®]80 emulsion-particles.

Concerning fluorescence a low level of fluorescence looking at the Tween[®]80 emulsified polystyrene particles carrying QDs and FeO_x nanoparticles was observed (figure 90), which was too low for reasonable quantification, however in general fluorescence was observable. The low quantum yield might be due to three factors. First, the absorption of fluorescence by the magnetic nanoparticles which was already mentioned as a general problem of composite particles of this kind. Second, water might have entered the hydrophobic phase, causing now quenching by being present at the nanoparticle surface. And third, which might have the greatest influence, free radicals which are provided in a large number by the initiator may also cause quenching effects by reacting with the nanoparticle surface. So the amount of radicals has an immense impact on the quantum yield of the quantum dots. A prior encapsulation of the nanoparticles with a tighter ligand shell could shield the radicals from the nanoparticle surface.

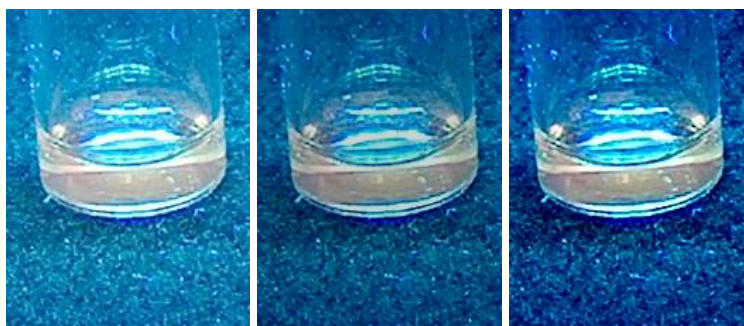


figure 90: Fluorescence of Tween[®]80 emulsified polystyrene composite particles, containing fluorescing and magnetic nanoparticles.

To examine the evolution of Tween[®]80 based emulsion polymerizations, a calorimetric measurement (figure 91) was performed with styrene, DVB and Tween system. Changes in the thermal flow, indicated in yellow (figure 91), can be interpreted as follows. After the temperature settled down to 45 °C the initiator dissolved in water was injected. Because the water was at room temperature, which was of course lower than 45 °C, both curves show a negative thermal flow. With the injection of the initiator the polymerization starts immediately and the thermal flow increases. However, here a massive delay between a prepolymerization and the main polymerization (two maxima on the yellow curve) was observed. It has been assumed that first the monomers in the aqueous phase react. Because Tween[®]80 builds up a very compact shell the oligomer radicals are not able to enter the micelles easily, compared to SDS emulsified micelles. Thus a shift of approximately five minutes was measured between the start of the polymerization in the aqueous phase and in the micelles. After 30 minutes this reaction has finished. During that time a cumulative thermal flow of 2.84 kJ was observed. In a rough approximation, ascribing styrene and DVB the same reaction enthalpy and neglecting the

enthalpy offered by Tween[®]80, for 100% conversion 4.55 kJ are expected. Accordingly a conversion of 62% is calculated.

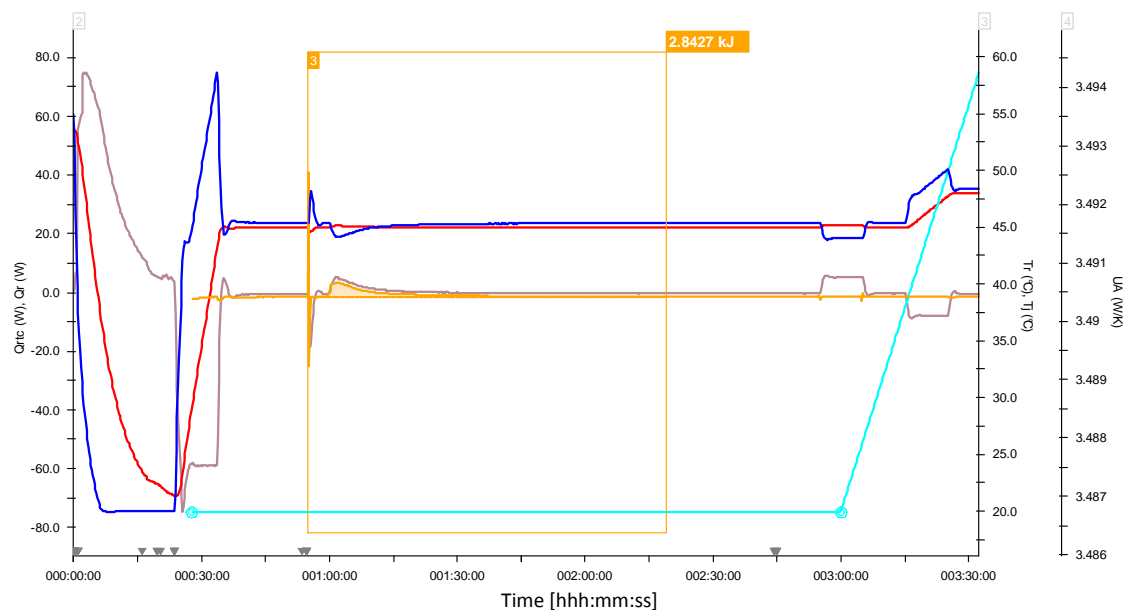


figure 91: calorimetric data of emulsion polymerizations performed with styrene, DVB and Tween[®]80 . Temperature developing of cooling/heating jacket (dark-blue), heat transfer coefficient (light blue), temperature developing in the reactor (red), heat flow across the wall of the reactor (beige) and heat of reaction (yellow).

In a gravimetric experiment where free monomer was removed from the polymer by evaporation in vacuum at 80 °C, a ratio of solid matter of 80% was found. Tween[®]80 provides a high mass, a low reaction enthalpy and will not be removed during the drying. The solid matter ratio of 80% is consistent with the calorimetric measurements. From a previous reaction the amount of free monomer was analyzed via gas chromatography (GC) with the result that no free monomer was detected. That suggests that the polymer shell is complete. Free monomer is, if the conversion is smaller than 100%, inside and does not negatively affect on particle stability.

The lower conversion in comparison with SDS emulsified micelles might come from the closer shell, buildup by Tween[®]80. Even if a low conversion might seem negative from the first point of view, it demonstrated in combination with the delay between the polymerization in solution and into the micelles, that Tween[®]80 provides an effective screen separating nanoparticles and aqueous phase. This was primary the reason for implementing Tween[®]80. By using another initiator system or other reaction conditions (e.g. temperature) it should be possible to increase the conversion, too.

The set of all results observed by dynamic light scattering (DLS, DTS Nano) are shown in table 1. The DLS size is given as the average diameter calculated.

number	DLS-size [nm]						
1	61	21	72	41	59	61	88
2	41	22	42	42	42	62	36
3	30	23	48	43	342	63	39
4	39	24	47	44	245	64	50
5	27	25	57	45	650	65	83
6	39	26	24	46	5700	66	38
7	30	27	55	47	106	67	41
8	63	28	23	48	98	68	35
9	43	29		49	93	69	33
10	26	30	32	50	33	70	80
11	31	31		51	31		
12	30	32	43	52	38		
13	40	33	22	53	38		
14		34	32	54	39		
15	48	35	59	55	40		
16	49	36	39	56	41		
17	44	37	106	57	59		
18	44	38	220	58	43		
19	52	39	44	59	48		
20	58	40		60	38		

table 1: DLS-results. The number refers to the emulsion approaches listed in table 9.

Based on the results important parameters to control the size of the particles could be identified, shown on Tween[®]80 containing experiments. This becomes very important, especially for bio applications, because in some cases the particle size has to be limited and therefore carefully tuned.

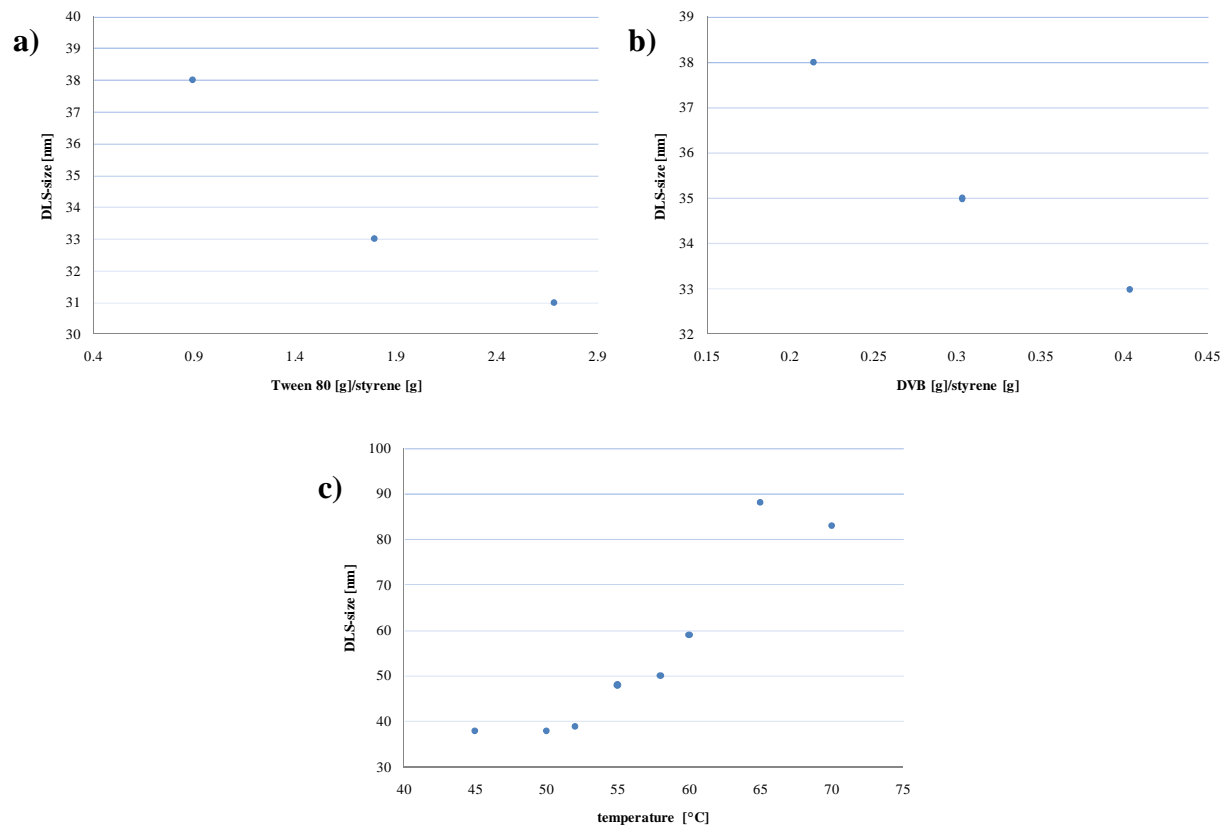


figure 92: a) influence of the amount of Tween[®]80 on DLS-size (in each case 28.0 g water, 615 μ L styrene, 132 μ L DVB, 32 μ g VA044, 120 μ L pentanol, 45 $^{\circ}$ C); b) influence of DVB ratio on DLS-size size (in each case 28.0 g water, 615 μ L styrene, 32 μ g VA044, 120 μ L pentanol, 0.50 g Tween[®]80, 45 $^{\circ}$ C); c) influence of the temperature on DLS-size (in each case 28.0 g water, 615 μ L styrene, 132 μ L DVB, 32 μ g VA044, 150 μ L pentanol, 0.50 g Tween[®]80).

figure 92 a) shows an obvious relationship between the amount of Tween[®]80 and the recorded DLS-size. If more Tween[®]80 is used the DLS-size decreases. This fact confirms one of the best known relationships in emulsion polymerization that says that the particle size can be reduced by enlarging the amount of emulsifier. Referring to figure 92 b) it was observed that the particle size rises up with higher temperature. This might be caused by lower density of the monomer and stronger movement of the oligomers. Hence the mesh width could increase, causing density of the polymer to be lower. However this effect should be smaller than the observed values. The solubility of water in the monomer micelles might rise up which also results in bigger sized particles. Concerning the ratio between DVB and styrene it was observed that enlarging the ratio of DVB the particle size goes down. It can be reasoned that the higher ratio of DVB results not only in higher cross linked particles but also to particles with higher density.

Additionally it was observed that the thickness of the polymer shell can be varied by the amount of additional monomer. Even different shells can be polymerised onto the surface subsequently. Size tunability is given by the amount of emulsifier and the ratio of monomer to nanoparticle.

2.5.4 Stabilitytests of Tween[®]80 emulsion particles

To document the stability of the outer Tween[®]80 shell a dilution series was carried out. In figure 93 DLS measurements are shown, which present the hydrodynamic diameters of the emulsion approach 52 and 58 (table 9). With increasing dilution no significant changes of the Tween[®]80 emulsion particles were observable. The particles were also stored for 24 hours, since the loss of Tween[®]80 could be kinetically hindered. But no degree in size was detected. Further no swelling was observed.

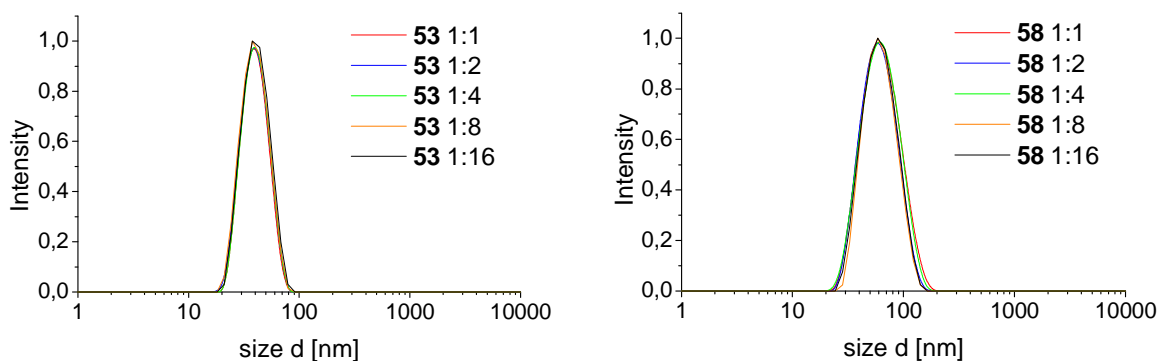


figure 93: DLS measurements of dilution series. The numbers refer to the emulsion approaches listed in table 9.

For a better overview the results are presented graphically in figure 94. Additionally the approach 69 (table 9) is appended to show the behaviour of particles with a larger hydrophobic diameter. The concentration of the emulsion particles was not known. It should range in the μM range. Nevertheless, the used emulsion approaches have similar initial concentrations. The highest concentration of all solutions was set equal to 1.

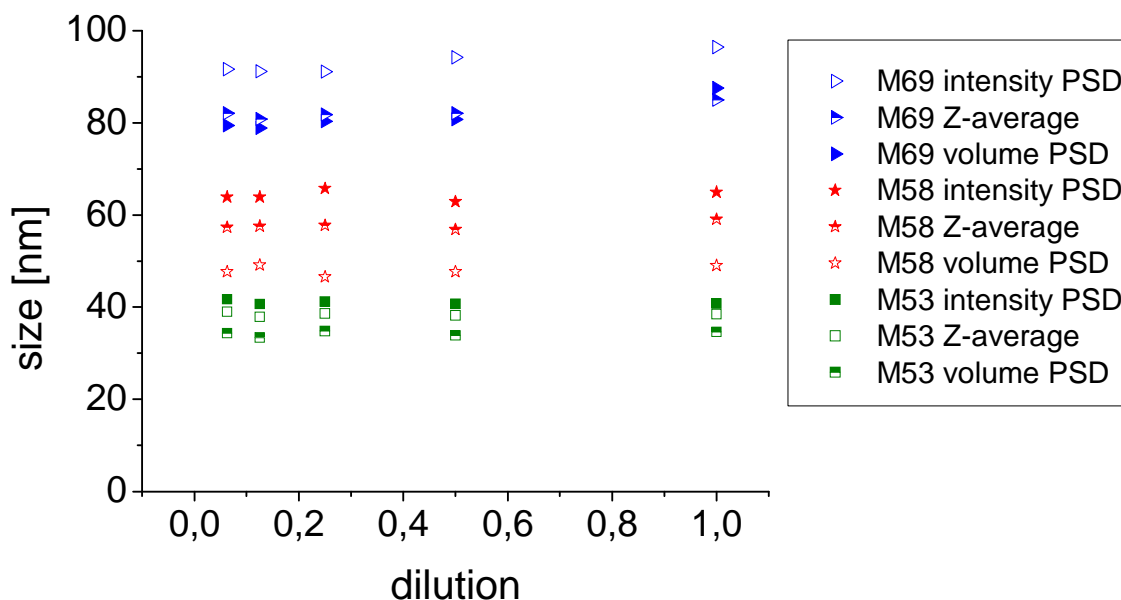


figure 94: results of the dilution series. The numbers refer to the emulsion approaches listed in table 9.

The results reveal the preservation of size and thus the maintenance of Tween[®]80 on the particle surface.

2.5.5 Functionalization of Tween[®]80

A variety of nanoparticles can be coated in the same polymer particle and a great bandwidth of functional groups can be thereby integrated by modifying the surface with different chemicals. Because Tween[®]80 showed to be one of the most competitive surfmers the hydroxy groups were converted to other functional groups, which can be used for various number of coupling strategies. The terminal hydroxylic group can be transformed e.g. into a carboxylic -, carbonyl- or alkyne- group (figure 95). The functionalisation was achieved with preservation of the double bond, which is fundamental for the copolymerisation.

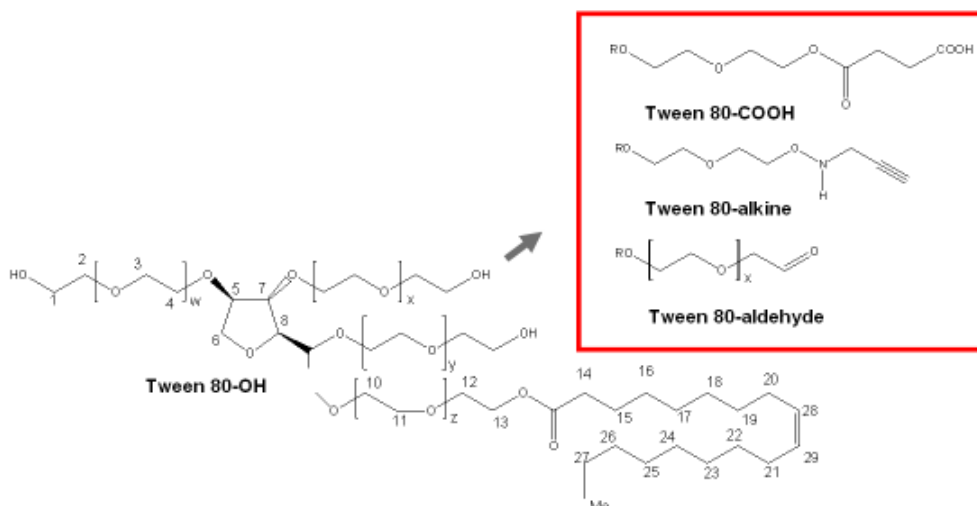


figure 95: Structure of Tween[®]80 and functionalisation.

In figure 96 the ¹H NMR-spectra of Tween[®]80 -OH is shown in comparison with that of the modified Tween. The assignment of the signals was achieved by ¹H, ¹³C, and two-dimensional NMR (HMBC, HSQC, HHQC), since Tween[®]80 has a low mass of ~ 1300 g/mol in comparison with above discussed ligands.

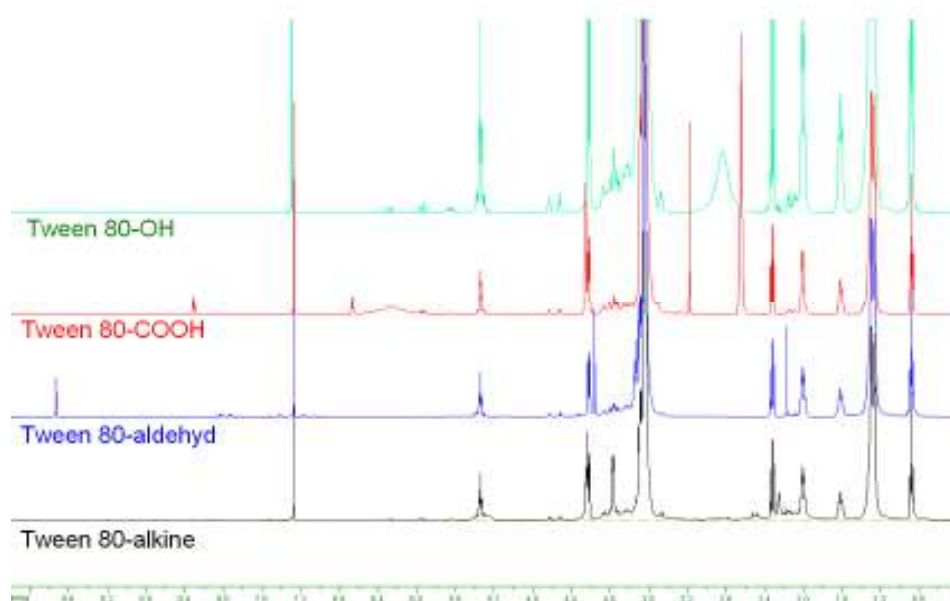


figure 96: ¹H-NMR (400 MHz, CDCl₃) spectra of Tween[®]80 -OH in comparison with modifications.

The HHCOSY of the carboxylic functionalized Tween[®]80 shows a coupling of the methylene protons vicinal to the carboxylic group at 2.63 ppm with the terminal methylene protons of the PEO chain at the ester function at 4.24 ppm (figure 97). The weak coupling can be assigned to the coupling over five bonds (⁵J coupling).

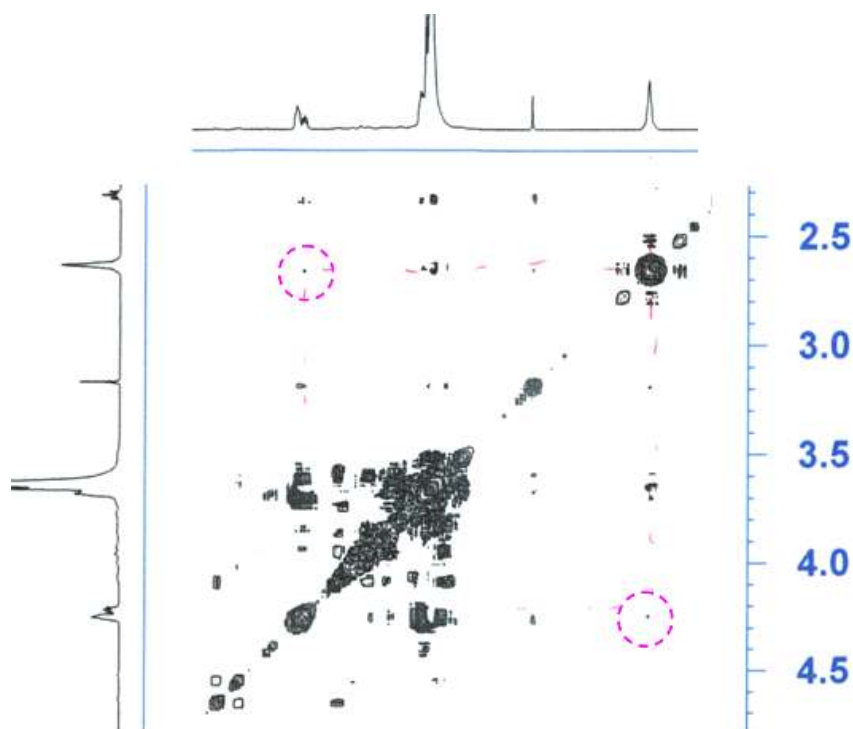
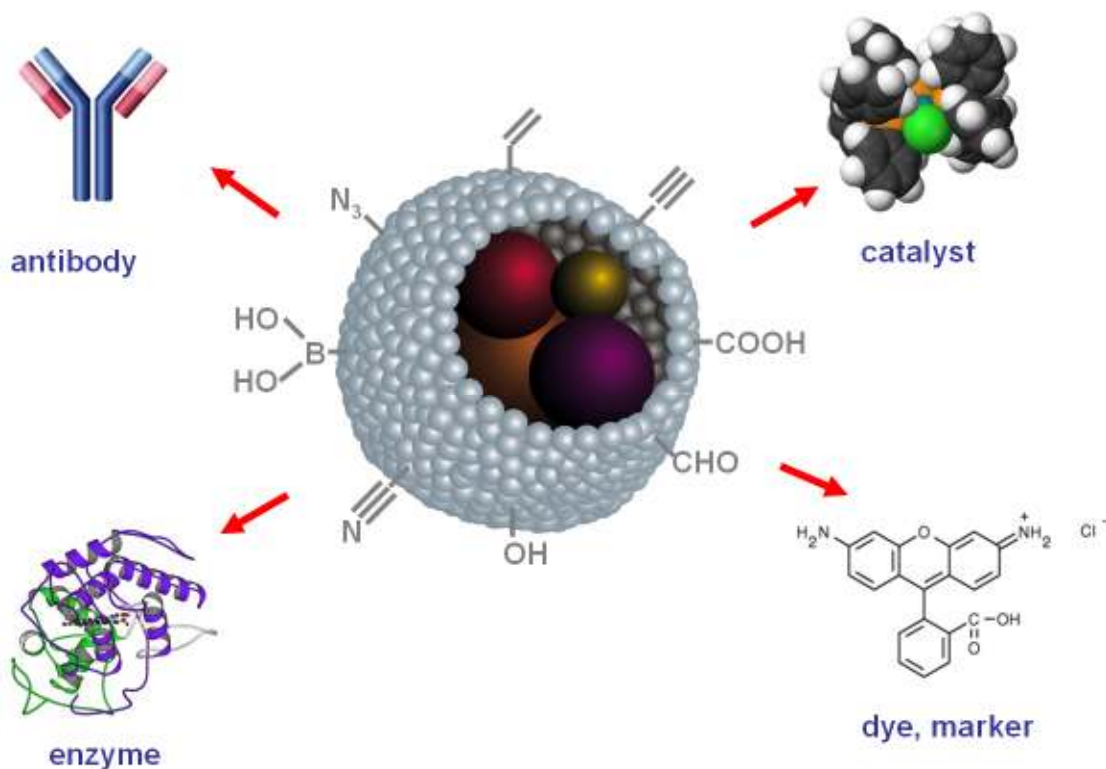


figure 97: HHCOSY (500 MHz, CDCl_3) of Tween[®]80-COOH.

The synthesized polymer particles can be further modified as exemplified with surfmers like V1100, which possesses a PEO chain, Tween[®]80 or acrylic acid. The polymer shell, shell thickness, degree of cross-linking, solubility through surface-functionalisation, and chemical resistance can be optionally varied.

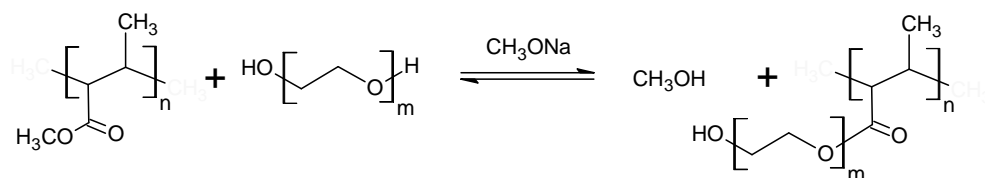
In the field of molecular labelling further detection components can be applied, which assist the detection. Antibodies, enzymes, further dyes, carbohydrates, radioactive markers a.s.o. can be added. Polymer particles equipped with functional groups can now be coupled in a suitable coupling reaction with biomolecules, catalysts, or dyes (schema 19).



schema 19: Accoutrement of emulsion micelles with further molecules.

Biomolecules generally require mild coupling reactions to prevent degradation. Thus it is necessary to be able to offer a wide range of functional groups on the polymer particle surface. PMA e.g. provides carboxylic groups, which can be activated by EDC and sulfo-NHS^[219], which is an established procedure in biochemistry. The yield for the formation of DNA-*b*-PPO micelles produced by this method was 72%^[378].

Surface modification with poly(ethylenoxide) can be achieved in case of poly(MMA-DVB) nanospheres by a transesterification reaction in the presence of sodium methoxide as the catalyst, as shown in the following equation^[117]:



The terminal hydroxyl group can be coupled for example nucleophilically to isothiocyanates or halogen-containing compounds under alkaline conditions. In coupling PEO by this method, not only was the functional group changed, but also a spacer was incorporated to achieve good solubility as well as other properties.

The ligands can be amplified by certain chemicals, which show broad specificities or general specificity for biomolecules. For instance, Cibacron Blue F3G-A has the group specificity for albumin, dehydrogenase, and lysozyme^[379]. The coupling between the terminal hydroxylic group of poly(ethylenoxide) and Cibacron Blue F3G-A can be achieved in the presence of sodium hydroxide. Since both compounds are negatively charged, the reaction is performed under repulsive conditions. So the concentration of electrolyte can be used to control the dye immobilization^[380, 381].

The characterization of surface group contents is strongly hampered by the fact that the amounts of both surface groups and elements are close to the limit of detection owing to the relatively large contribution of the polymer core. A conductometric titration is often used to determine the content of carboxylic and aldehyde groups^[382]. With this technique (titration with NaOH) it was possible to calculate the number carboxy group on a polyacrylic acid coating of around 1.5 carboxy groups per nm².

2.5.6 Fluorescence quenching by (Förster-) fluorescence resonance energy transfer (FRET)

To prove the thickness and density of the polymer shell Förster energy transfer between a donor and acceptor pair, due to dipole-dipole interactions, was studied in cooperation with Aliaksandr Yaravy during his stay in the group of Prof. Dr. H. Weller.

The fluorescence dye rhodamine 110 was coupled by EDC/NHS activation over the carboxylic groups of polyacrylic acid of encapsulated gold nanoparticles. After dialysis over three days, FRET measurements were performed.

The nonradiative energy transfer strongly depends on the chromophores center-to-center separation distance^[383]. The gold nanoparticles functioned as acceptors, while the donor was a fluorescent dye, which features a required non-zero integral of the spectral overlap between donor emission and acceptor absorption^[384].

and leads in the case of gold nanoparticles to a quenched donor photoemission.

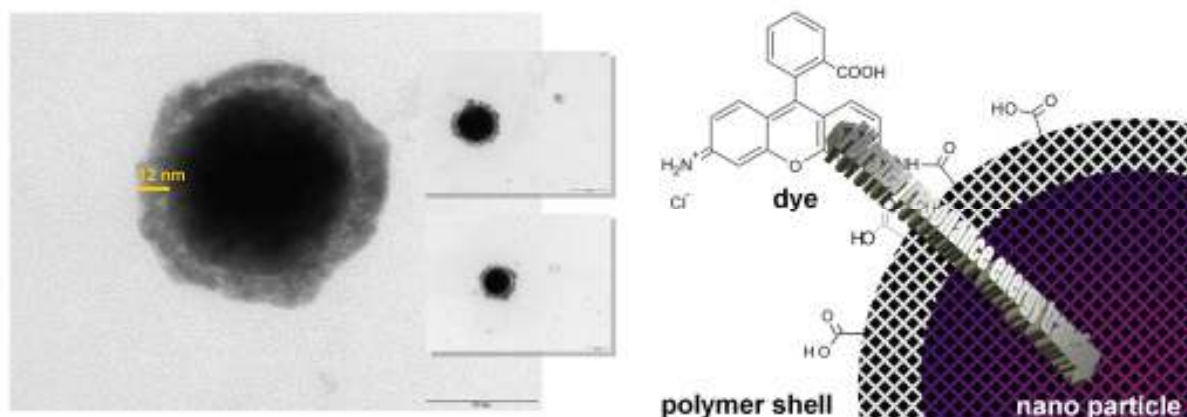


figure 98: TEM image showing the thickness of the polymer shell and scheme polymer particle with dye.

TEM images of the obtained nanocomposites, containing gold nanoparticles, are shown in figure 98. The shown emulsion particles are composed of approximately 50 gold nanoparticles. The gold particles act as acceptor, while rhodamine 110 represents the donor.

The spectral overlap (figure 99, overlap integral) of the fluorescence of the donor and the absorption of the acceptor is described by $J(\lambda)$. The energy transfer is optimal if the fluorescence spectrum of the donor corresponds totally with the long wave band of the absorption spectrum of the acceptor.

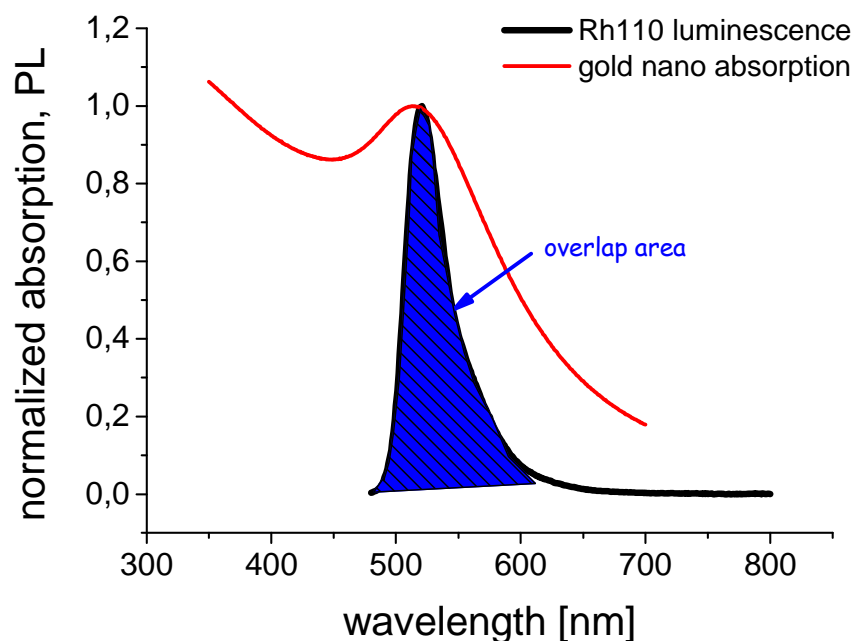


figure 99: Spectral overlap illustration.

Corresponding fluorescence measurements (figure 82) indicate a decline of the quantum yield in case of attached gold-nanocomposites. The FRET efficiency was $E = 78\%$ (figure 100).

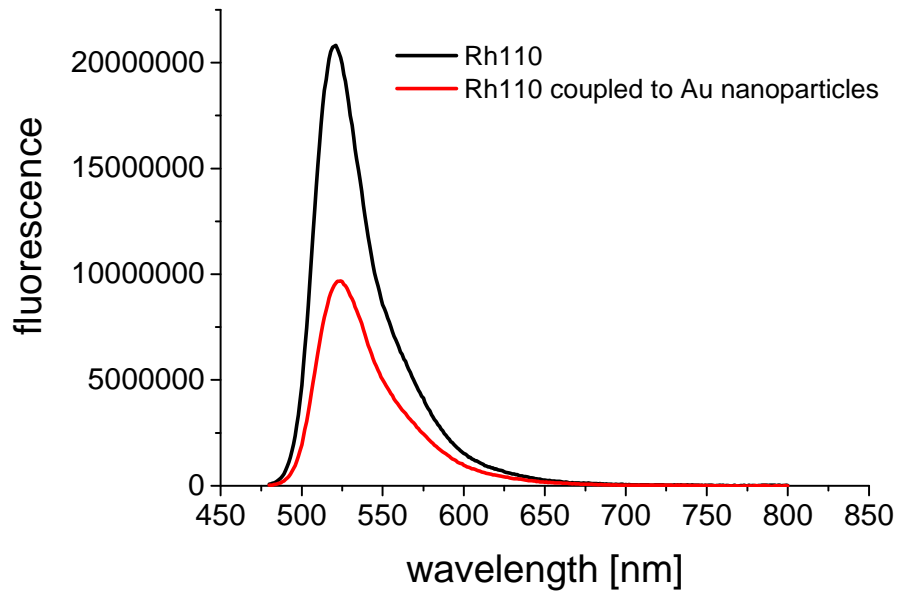


figure 100: Rh110 photoluminescence quenching by Au nanoparticles.

On the basis of the FRET efficiency a distance of 13.2 nm was calculated, which corresponds with the shell, shown on the TEM image in figure 98. This result reflects a tight and thick polymer shell and underlines the quality of the crosslinked shell.

But like mentioned in chapter 2.4.4 the assumption was made, that the energy transfer occurs between point-dipoles. Due to the presence of approximately 50 nanoparticles in one emulsion particle the Förster radius R_0 has to be calculated with $R_0^{4.5}$.

2.6 Relaxivity of clustered SPIONs

Clustering of superparamagnetic magnetite nanoparticles results in higher saturation magnetization than that of individual ones because of the interaction between the assembled nanoparticles^[252]. But the spin-spin relaxation rate R_2 ($= 1/T_2$) does not always increase linear and echo time (time between 90° and 180° pulse, τ_{CP}) independent with the diffusion correlation time (τ_D), and thus particle size.

To observe the relaxation rate R_2 depending on the clustering rate, FeO_x nanoparticles (~10 nm) were encapsulated and clustered in polymer shells in cooperation with Ulrich

Tromsdorf^[385]. Via *t*C-PEO-*b*-PCL-*b*-PEI (7) triblockligands diameters of 83 to 182 nm (intensity PSD) were obtained (figure 101).

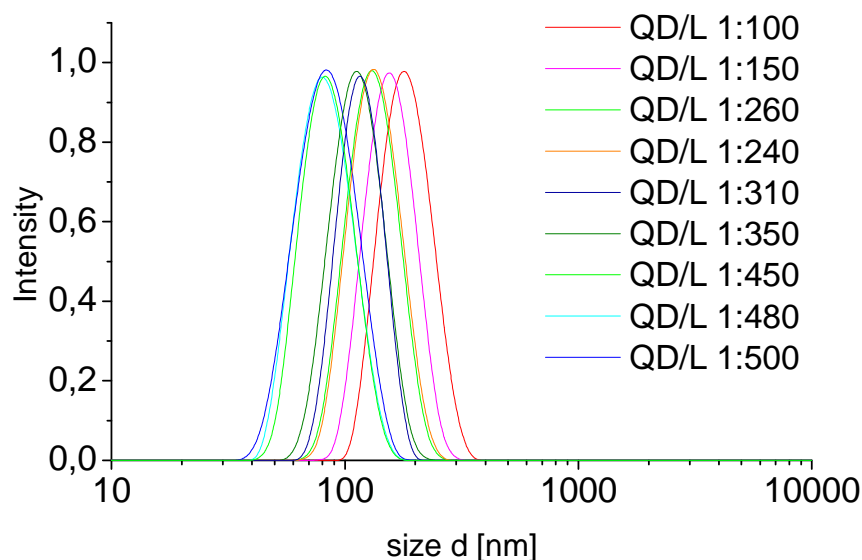


figure 101: DLS measurements (intensity PSD) of the SPIONs with a *t*C-PEO-*b*-PCL-*b*-PEI (7) coating in water.

The T_2 relaxivities of the nanocomposites were measured at 1.41 Tesla with pulse spacing, τ_{CP} , ranging from 0.05 to 1 ms. The results are shown in figure 102. At a hydrodynamic particle size of up to 90 nm no echo time dependency of the relaxivity was measured. At hydrodynamic sizes above 118 nm a clear echo time (τ_{CP}) dependence and a decrease in relaxivity was measured. Owing to the ligand shell thickness and the measured solvent shell, the metallic core is at least 20-40 nm smaller than the particle sizes presented in figure 102.

The results agree with the results of Gillis *et al.*^[386]. At smaller sizes (figure 102, 1.) a linear dependency of relaxation rate R_2 on particle size and no echo time dependency is measurable. This is due to signal loss arising from diffusion (disordered process). But the influence of diffusion decreases with size.

Due to dependence of the relaxation rate on particle magnetization and diffusion times ($\tau_D = r^2/D$, where r is the particle radius and D the water diffusion coefficient) a maximum is reached at a certain size or clustering rate (figure 102, 2.). The measurements indicate a T_2 -relaxivity maximum at hydrodynamic sizes of ~ 80 nm, corresponding to FeO_x clusters of ~ 40 nm. In this size range the static dephasing regime begins, in which diffusion shows no effects on R_2 .

By further increasing of the particle size the refocusing pulses rephrase the spins. Thus the transverse relaxation T_2 increases, consequently $R_2 (= 1/T_2)$ decreases. In this regime there is a clear echo time dependency. The longer the time between the refocusing pulses, so the longer

the echo time (time between 90° and 180° pulse, τ_{CP}) is, the less echo appears. This shortens T_2 and increases R_2 (for more detailed information see chapter 9.4.1).

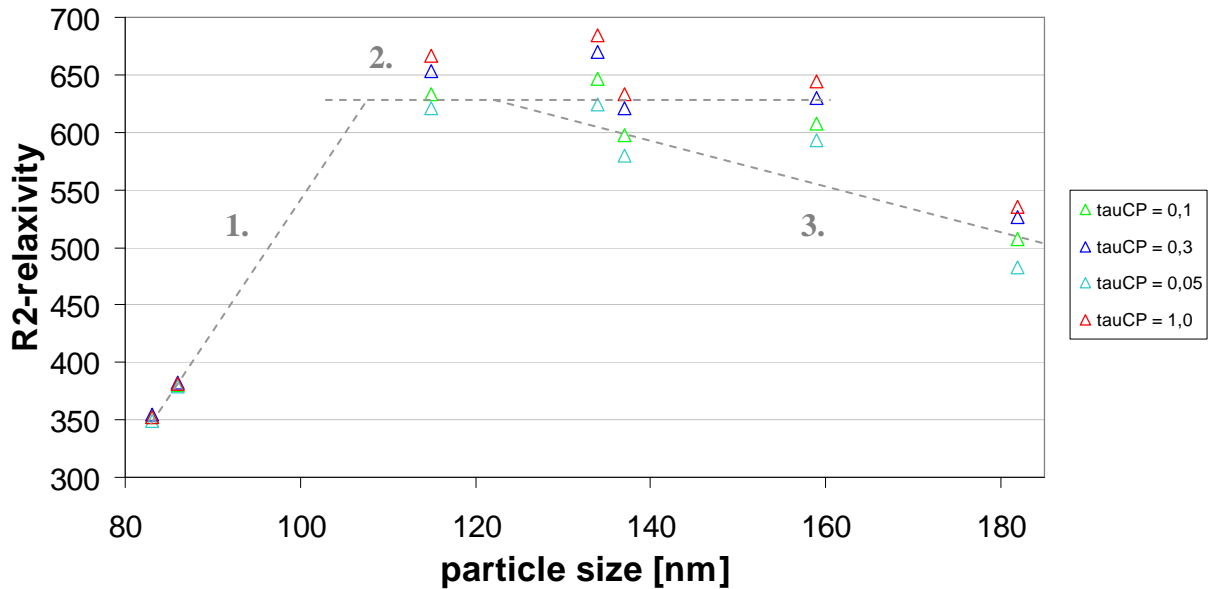


figure 102: R_2 -relaxivity dependency on hydrodynamic diameter of FeO_x (diameter 10 nm) containing nanocomposites. The relaxivity was measured using a Bruker mq60 MR relaxometer (1.41 Tesla).
1. In this region, in which a linear dependency is observable, the influence of diffusion decreases,
2. static dephasing regime, **3.** decrease in R_2 due to refocusing pulses.

Gillis *et al.*^[386] calculated a maximum of the relaxivity rate at a diffusion time (τ_D) of $1 \cdot 10^{-4}$ to $5 \cdot 10^{-4}$ ms. The diffusion time depends on the particle radius, r , and the water diffusion coefficient, D , as follows: $\tau_D = r^2/D$. The calculations of Gillis *et al.*^[386] were based on a water diffusion coefficient of $2.5 \cdot 10^6$ nm²/ms, corresponding to a particle radius of 16 nm (10^{-4} ms) to 35 nm ($5 \cdot 10^{-4}$ ms) and corresponding to a hydrodynamic diameter of 32 nm to 71 nm. Hence, the highest measured T_2 relaxivity in figure 102 of a particle with a hydrodynamic radius of 70 nm and in particular with a metallic core of a diameter of ~ 40 nm correlates with the theory of Gillis *et al.*^[386].

2.7 Relaxivity of $GdPO_4$ nanoparticles

The relaxivity of $GdPO_4$ nanoparticles in water (CAN09-0026) was studied in cooperation with Volker Bachmann from the Center for Applied Nanotechnology (CAN, Hamburg).

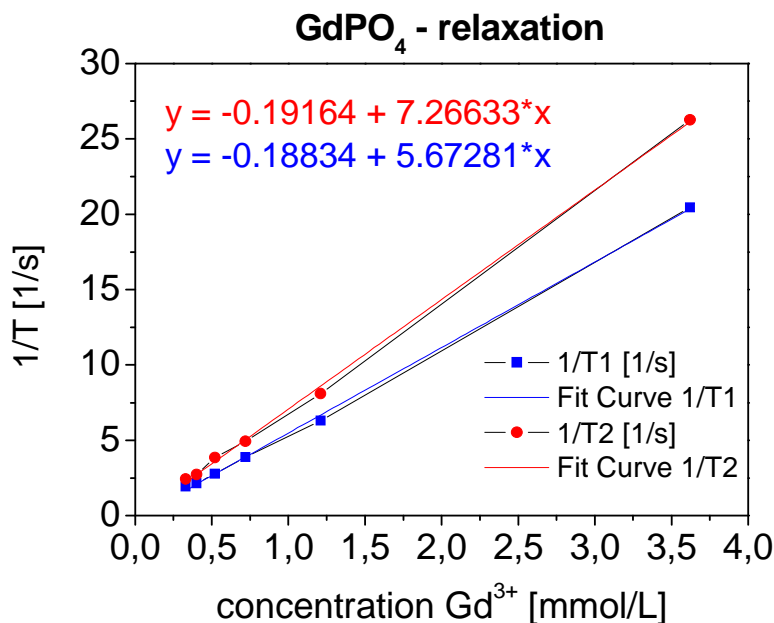


figure 103: relaxivity of GdPO₄ nanoparticles with a PI₆₁-*b*-PEO₂₁₂-OH coating in water.

The water-transfer of the nanoparticles, which possessed tributyl phosphate and trioctylamine as stabilizer, was achieved with a coating of PI₆₁-*b*-PEO₂₁₂-OH. A crosslinkage and the PI-N3 preligand was avoided, since the T₁ relaxivity depends on *inter alia* dipole-dipole interaction, which relies on $E_{dd} \sim 1/r^6$. A close ligand shell is therefore not required.

A dilution series was prepared, whereupon the relaxivity of the nanoparticles was measured at 1.41 Tesla. Results are shown in figure 103. In comparison to Magnevist[®] with a measured T₁ relaxivity of 3.6 L/(mmol·s), the Gd³⁺ atoms of the GdPO₄ nanoparticles feature a higher relaxivity of 5.7 L/(mmol·s). The measured T₂ relaxivity is 7.3 L/(mmol·s).

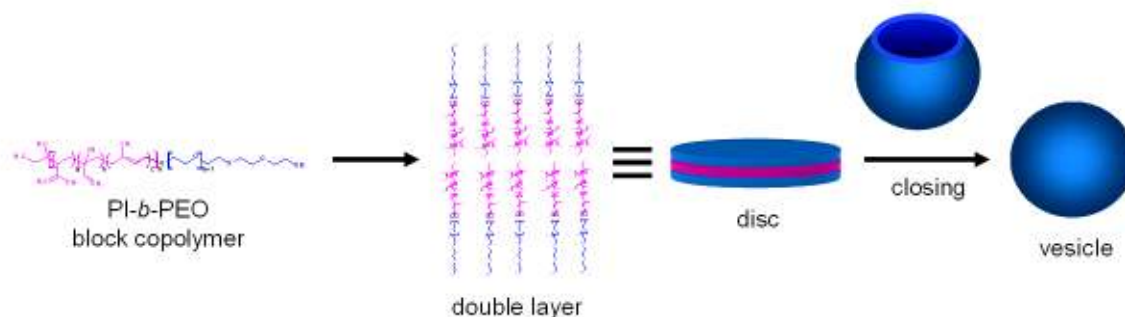
2.8 Vesicle formation

By equalising the block length of the hydrophobic (PI) and hydrophilic blocks (PEO), block copolymers are obtained which form vesicles when they are dissolved in a THF solution and injected quickly into water. The amphiphilic block copolymers associate in a bilayer membrane, forming a hollow sphere in which the aqueous phase is present.

The formation of such colloidal structures starts above the critical micelle concentration (CMC). Above the CMC spherical micelles, cylindrical micelles or vesicles form at first. By further increasing of the concentration of the amphiphile, lyotropic liquid crystalline phases are

found, to which the sphere packing, the hexagonal packed cylinder, bicontinuous, three dimensional structures (gyroid), and a variety of lamellar structures belong^[387].

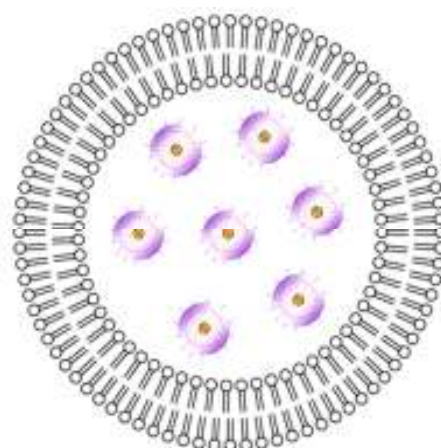
Self-assembly of lipids and amphiphilic block copolymers, yielding the formation of vesicles, occurs in two steps^[388]. At the beginning the amphiphiles align to a double layer, which constantly grows in radius. Once a certain radius is reached, the disc is energetically unfavourable. This induces a flexion of the disc and the energetically favourable vesicle closes (schema 20).



schema 20: illustration of vesicle formation.

As mentioned in chapter 2.3, the structure of the block copolymer depends on the length and volume of the blocks and the composition of the medium (salt concentration, temperature, pH)^[389]. For the formation of a vesicle should be the hydrophilic volume fraction of the polymer should be at $35 \pm 10\%$ ^[390].

Volkan Filiz of the research group of Stephan Förster (University of Hamburg, Germany) could demonstrate the encapsulation of the micellar PI-*b*-PEO coated quantum dots in vesicles^[391]. Vesicle formation was achieved in cooperation with Volkan Filiz by injecting PI₃₂-*b*-PEO₂₇-OH (molecular mass of 3350 g/mol), dissolved in THF, in water. Any molecules present may get sealed inside of the vesicle (schema 21).



schema 21: illustration of nanoparticle containing micelles inside of a vesicle.

The amount of encapsulated molecules, e.g. water-soluble nanoparticles, depends on their concentration and distribution in water. Accordingly the non-encapsulated nanocomposites have to be removed by syringe filter.

A confocal microscopy image is shown in figure 104 of an unpurified solution. The same section is presented with and without laser-excitation. The luminescence demonstrates that the concentration of PI₆₁-*b*-PEO₂₁₂-OH coated CdSe/CdS/ZnS quantum dots inside of the PI₃₂-*b*-PEO₂₇-OH vesicles is much higher than in the surrounding aqueous medium.

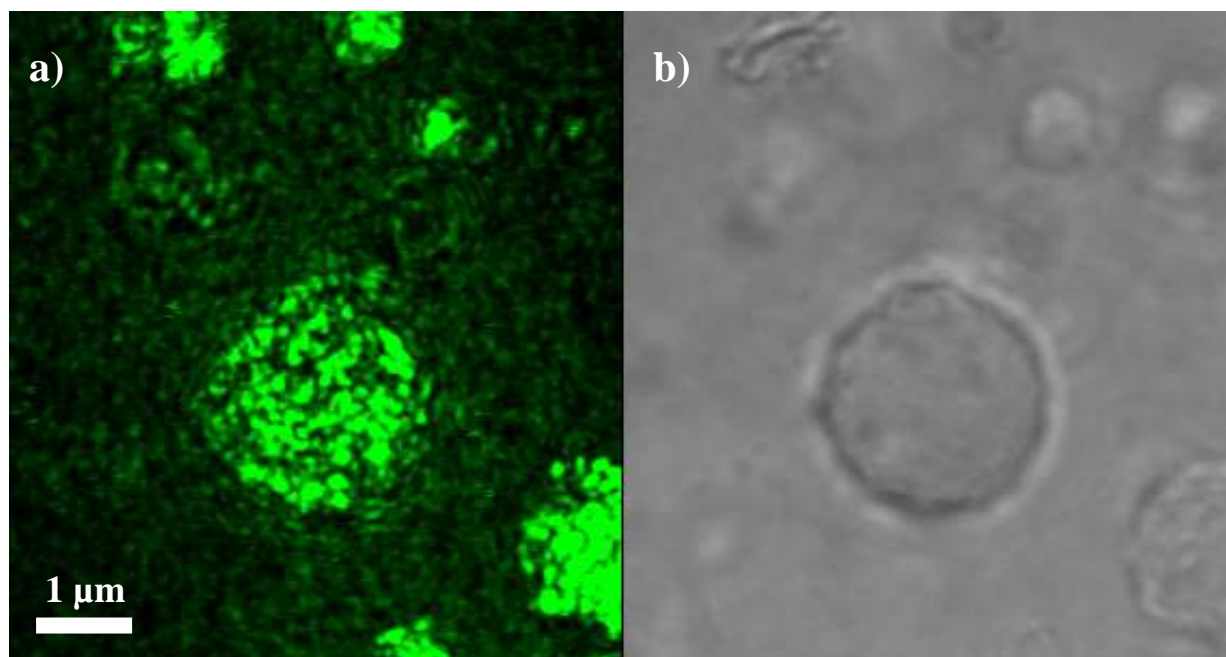


figure 104: confocal microscopy image of PI₃₂-*b*-PEO₂₇-OH vesicles, containing PI₆₁-*b*-PEO₂₁₂-OH coated CdSe/CdS/ZnS quantum dots. The same section is shown under a) excitation and b) via transmitted light.

In a 3D scan of the same unpurified solution (figure 105) a cross-section of a vesicle demonstrates the presence of the quantum dots inside of the vesicle. In the framed box a part of the lower semisphere of a vesicle is shown.

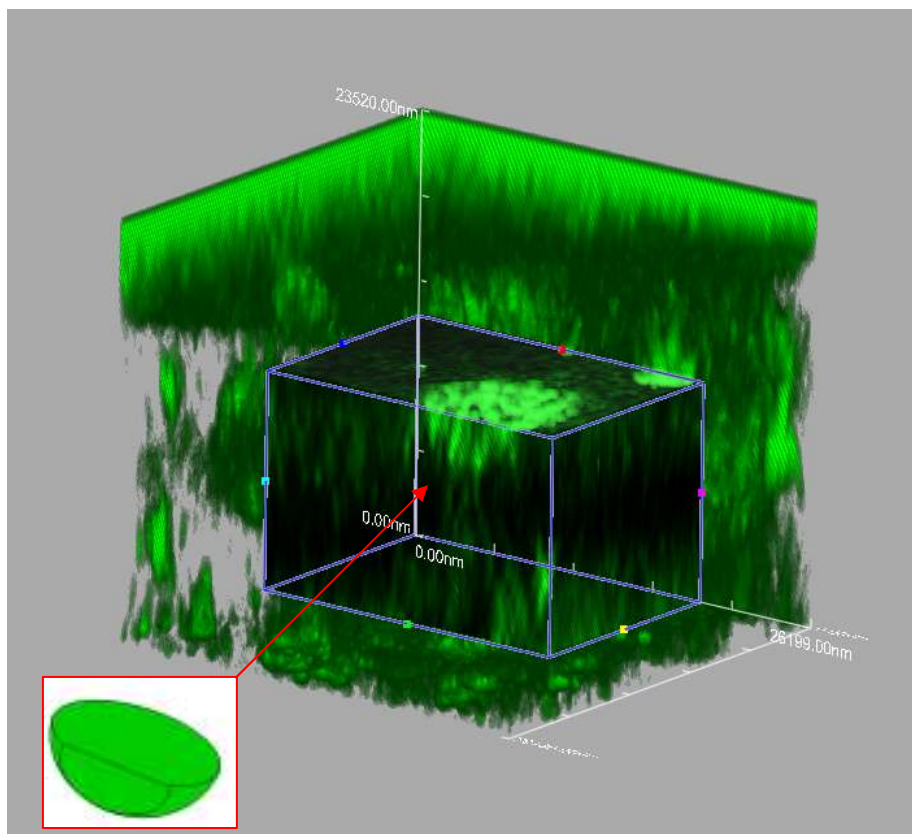


figure 105: confocal microscopy image (3D scan) of $PI_{32}\text{-}b\text{-}PEO_{27}\text{-}OH$ vesicles, containing $PI_{61}\text{-}b\text{-}PEO_{212}\text{-}OH$ coated CdSe/CdS/ZnS quantum dots. A cross-section of a vesicle shows the presence of the quantum dots inside of the vesicle.

Integration of different nanoparticles in vesicular systems allows more secure transport of nanoparticles in biological environments and can increase cellular uptake. The outer vesicle membrane can be equipped easily with further molecules (e.g. antibodies) in the same process that has been described in the experimental section.

The use of vesicles as superior transport vehicles permits guided and controlled release. Either the use of a biodegradable polymer-block such as poly(ϵ -caprolactone) (PCL), poly(dimethylsiloxane) (PDMS), and poly(lactide) (PLA) or the use of polymers, which are degradable by outside influences (e.g. pH value, optical excitation), can enable controlled release of the vesicle content. Hydrophobic nanoparticles can be embedded in the vesicle membrane and can convey the release. Similarly, gold nanoparticles, integrated in the vesicle wall, can photothermally destroy the carrier matrix^[392]. The released content could be e.g. nanocomposites for multitargeting and drugs.

2.9 Bioapplication

Debating the adoption of nanoparticles in clinical studies the consideration of the cytotoxicity of the nanoparticles is of particular importance. The possibility of interaction of metal nanoparticles with biological systems, agglomeration, which can affect cellular uptake, and *inter alia* the release of metal ions depends strongly on the rigidity and kind of coating that stabilizes the nanoparticles in aqueous media. While for example bare superparamagnetic iron oxide nanoparticles (SPIONs) induced a dose-dependent loss in fibroblast viability^[209, 393], PEG coated SPIONs were found to be relatively nontoxic^[394]. Tkachenki et al.^[395] and Goodman *et al.*^[396] show, that also in case of gold nanoparticles the surface coating can play an important role in the cytotoxicity.

2.9.1 Cytotoxicity

A cell is the smallest unit of an organism that is classified as living and its complexity allows the appraisal of the effects of different agents onto organisms. Not only the cellular uptake, which depends strongly on the size of the nanocomposite and correspondingly the possibility of agglomeration as well as the surface of the nanocomposites (present molecules, structure, and charges) have an impact, but also the accretion on the plasma membrane with its diverse responsibilities. Due to their low baseline expression of adhesion molecules^[397], A549 cells were selected as a source of alveolar epithelial cells for the present study.

To demonstrate the quality of the crosslinkable PI-N3/PI-*b*-PEO ligand shell cadmium containing CdSe nanoparticles were adopted. Their implementation in cell solutions should reflect conspicuously the effect of our ligand shell. Hence the results should be conferrable to other nanoparticles which are been known to be less toxic.

Known cytotoxic effects of CdSe nanoparticles are imputed to the release of Cd²⁺ ions^[337] and formation of free hydroxyl radicals^[398, 399], generated by holes by virtue of the valence band edge of 1.6 eV^[400], is a handicap. Hence, multishell nanocrystals^[401-403] concerning higher quantum yields due to inorganic passivation of the nanocrystals surface, ensuring radiative electron and hole recombination^[7, 401], robustness against chemical degradation or photo-oxidation^[7] and the reduction of cytotoxicity^[69, 337, 338, 404-406] came to the fore.

The human alveolar epithelial cell line A549 was treated with different terminally functionalised PI-*b*-PEO-X (X = -OH, -CHO, -COOH, -N₃, and -NH₂) ligands and PI-*b*-PEO-

X micelles respectively, containing CdSe/CdS/ZnS^[403] quantum dots with an PI-N3 shell (figure 106). Presentation of different functional groups and charges to the outer milieu could have an impact on the cytotoxicity, since negative charges are believed to increase the blood circulation time^[92], whereas positive charges lead to increased cellular uptake.



figure 106: For toxicity tests applied 1 μ M solutions (DMEM + 10% HEPES) of CdSe/CdS/ZnS multishell quantum dots with different PI-*b*-PEO ligand shells under UV light excitation. The solutions were previous dialysed two days to remove any salts from the nanoparticle synthesis as well as further contaminations. All solutions were autoclaved.

To pursue changes in the cell vitality, different cytotoxicity assays were employed. The lactate dehydrogenase assay (LDH-assay) is a method for quantitating cytotoxicity based on the measurement of activity of lactate dehydrogenase (LDH) released from damaged cells due to plasma membrane damage. Unlike many other cytoplasmic enzymes which exist in many cells either in low amount (e.g., alkaline and acid phosphatase) or unstable, LDH is a stable cytoplasmic enzyme present in all cells and rapidly released into the cell culture supernatant upon damage of the plasma membrane. LDH activity can be determined by a coupled enzymatic reaction: LDH oxidizes lactate to pyruvate which then reacts with tetrazolium salt INT to form formazan. The increase in the amount of formazan produced in culture supernatant directly correlates to the increase in the number of lysed cells. The formazan dye is water-soluble and can be detected by spectrophotometer at 500 nm.

The outcome of the LDH-assay is graphed in figure 107. figure 107 A represents the values for the ligands and figure 107 B the quantum dot offering micelles. For this experiment a control via CdCl₂ is not relevant, since the interaction between CdCl₂ and the enzyme takes place. Except for the quantum dot containing micelles, which feature ligands functionalised with aldehydes, no appreciable biological fluctuations appear. This finding indicates a high homogeneity of the probes. The high initial value of the outlier is in all likelihood caused by a dilution failure during sample preparation (in a repeat LDH-assay PI-*b*-PEO-CHO coated nanoparticles didn't show this behaviour, see 9.5.1). This conjecture is been supported by figure 107 B, in which the same sample lies outside of the biological variance-range. It should

be noted that in both cases a decline of the toxicity at higher concentration values is recorded, which further supports the stated presumption. First in the third window at a concentration of more than 0.1 μM of the nanocomposites a minimal increase of the LDH release is adumbrated. This test was accompanied by a Wst-assay, measuring the metabolic activity of viable cells. This test was accompanied by a Wst-assay, measuring the metabolic activity of viable cells. This colorimetric assay is based on the cleavage of the cell proliferation reagent Wst-8 (a tetrazolium salt) to a formazan-class dye by mitochondrial succinate-tetrazolium reductase in viable cells^[407]. As the cells proliferate, more Wst-8 is converted to the formazan product. The quantity of formazan dye is directly related to the number of metabolically active cells, and can be quantified by measuring the absorbance at 420-480 nm (A_{max} 450 nm) in a multiwell plate reader.

Results of the Wst-assay are shown in figure 107. In figure 107 C the plain ligands and in figure 116 D the quantum dot containing micelles are shown against CdCl_2 .

The developing of the CdCl_2 control in the Wst-assay (figure 107 D) is suggestive of a successful accomplishment of the tox-tests, arising from the decrease of the cell proliferation reagent Wst-8 due to the toxic effect of CdCl_2 . The first concentration window, which is located between 0.001 and 0.01 μM QD-nanocomposites (figure 107 D), represents a non-toxic domain, since the probes are subject to a biological variance, which lies between 80 and 100%. In the second as well as in the third concentration window all nanocomposites except the CdCl_2 control exhibit a positive cell vitability. The different coated core/shell/shell quantum dots feature no toxic effects on the alveolar epithelial cell line A549 in the concentration range between 0.001 and 1.000 μM .

It has to be pointed out, that in both assays the molare concentration of nanoparticles is compared with the molare concentration of Cd^{2+} ions. Due to the presence of approximately 1000 cadmium atoms per nanoparticle the Cd^{2+} control has to be 1000 fold higher. Thus the Cd^{2+} control would show already toxic effects in the lowest molar concentration of nanoparticles used. This highlights the low toxicity of the nanocomposites.

In addition to the toxic effects of the QD-nanocomposites themselves, it is important to understand the toxic effects of the different functionalised ligands, which could be released from the micelle-compartment (figure 107 C). Again, the results from the CdCl_2 control in the conducted Wst-assay is suggestive of a successful accomplishment of the tox-tests. As in case of the quantum dot containing micelles, the Wst-assay shows a non-toxic range in the first concentration window between 0.001 and 0.01 μM ligand, though the solutions are subject to biological variance, which range between 80 and 100%. The following two windows depict for

all ligands except for CdCl_2 a positive trend in the vitality of the alveolar epithelial cell line A549.

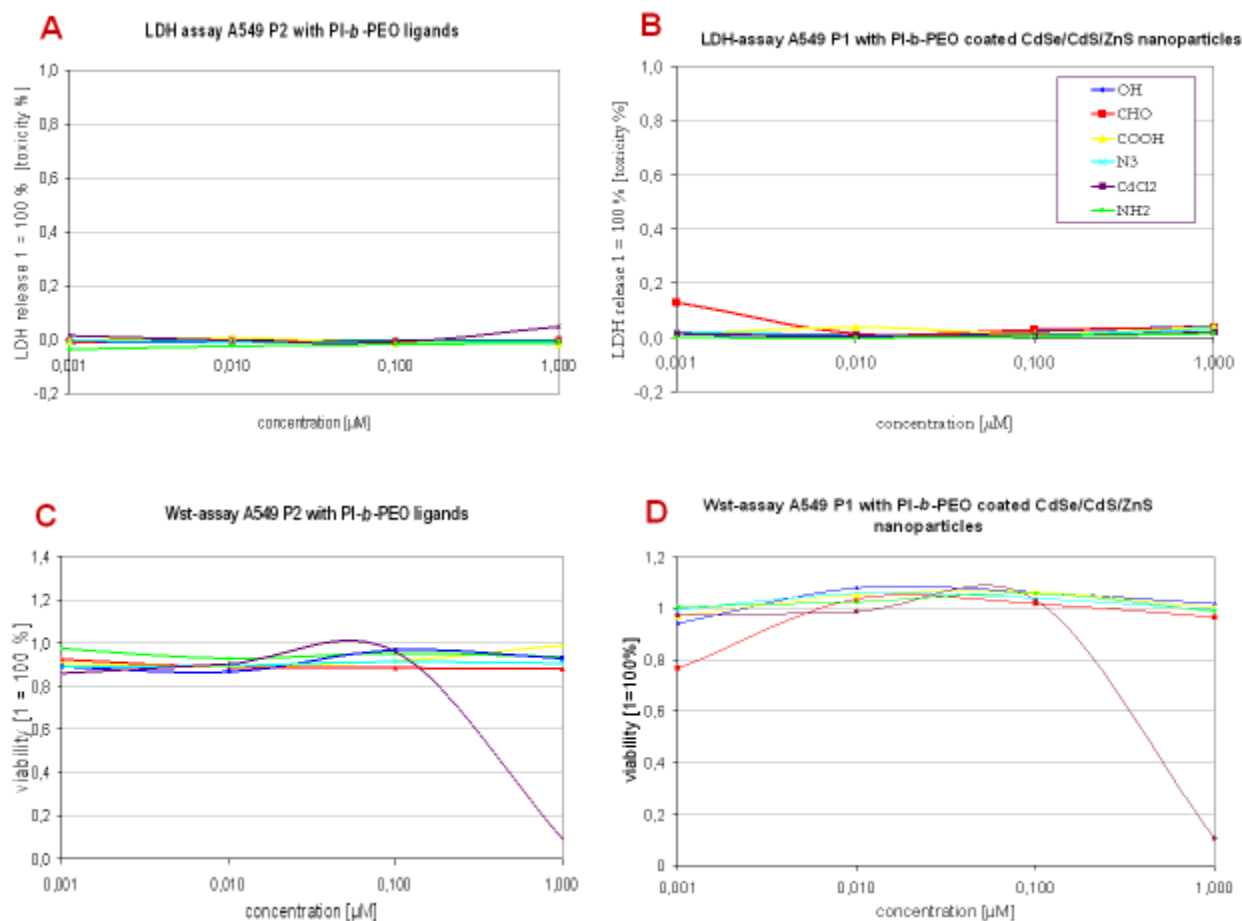


figure 107: LDH assay & Wst assays.

A LDH assay A549 with PI-*b*-PEO ligands, which possessed terminal azids, amines, hydroxyl- and carboxylic - groups as functional groups. **B** LDH assay A549 with PI-*b*-PEO coated CdSe/CdS/ZnS nanoparticles. **C** Wst-assay A549 with PI-*b*-PEO ligands. **D** Wst-assay A549 with PI-*b*-PEO coated CdSe/CdS/ZnS nanoparticles. Measurements were achieved at the centre for applied nanotechnology (CAN, Hamburg, Germany).

Toxicity mediated by reactive oxygen species (ROS-TOX) was also investigated by the Centre for Applied Nanotechnology (CAN, Hamburg, Germany). The progression of the FeCl_3 - and diethoxymethane (DEM) control of the ROS-assay indicates a successful realization of the tox-test, in consideration of the clear appraisal of oxidative stress for the cells (figure 108).

For all nanocomposites the concentration of the reactive oxygen species was very low, and even decreased further in the progress of the test. The decay of the relative ROS-concentration with time could be interpreted by the absence of UV-excitation, as all probes remain in the gadget during the measurement time. Creation of photochemical induced radicals by semiconductors is thus excluded, which should allay ROS-generation.

That the cells by reason of the toxicity of the particles perish and accordingly no oxidative stress is evolved, is highly improbable, since in all previous tox-tests no cytotoxicity of the

particle was observable. Furthermore all photochemical generated radicals on the surface of the quantum dot would interact primarily with the double bonds of the PI block, which could function like β -carotene as a radical interceptor.

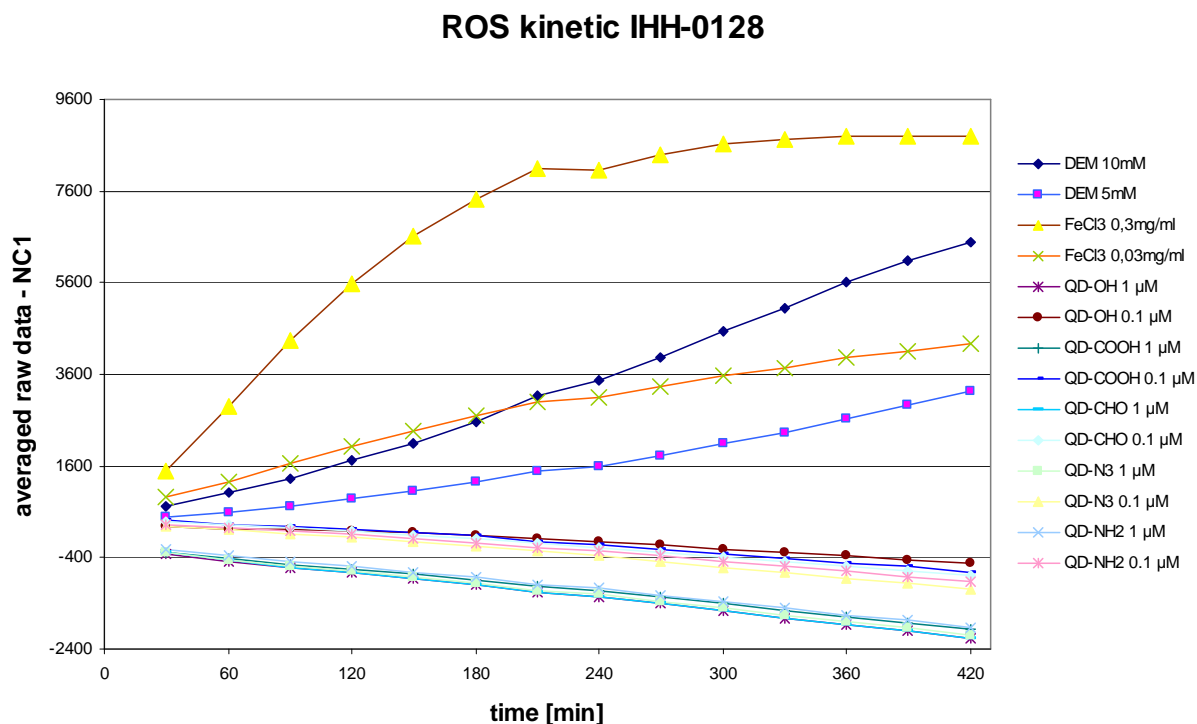


figure 108: ROS assay.

Quantum dots (QD) coated with $\text{PI}_{61}\text{-}b\text{-PEO}_{212}\text{-OH}$ (QD-OH), -COOH (QD-COOH), -CHO (QD-CHO), -N_3 (QD- N_3), and -NH_2 (QD- NH_2). Control samples were made with FeCl_3 and diethoxymethane (DEM).

Neither Wst- nor LDH-assays identified any toxic effects of the analysed samples in the concentration range of 0.001 and 1.000 μM QD-micelles. The quality of the inorganic ZnS shell due to the CdS interlayer, the passivation of the quantum dot surface by PI- N_3 and the additional coating via amphiphilic PI- b -PEO-diblock polymers next to the crosslinkage minimized both oxidative stress and cytotoxicity, corroborating the grade of quality of the encapsulation.

The Wst-, LDH- and ROS-assays were repeated without dialysis of the nanoparticle solutions (9.5.1, 9.5.2, 9.5.3). The possible presence of sideproducts and educts from the nanoparticle synthesis, THF or excess of ligand had no remarkable effect on the experiments. The results could be validated. Since the ROS assay depends strongly on the cell count, the assay was followed via a Cellomics Reader (9.5.4). A cytotoxicity kit II was used to distinguish between necrosis and apoptosis. Results are shown in chapter 9.5.5. In case of apoptosis the mitochondrial potential changes, which can be visualized as a red colouration. Appearance of a

green colour signals the increasing permeability of the membrane and could identify necrosis. The A549 cell nucleus is stained blue.

Valinomycin, CdCl_2 (9.5.5.1) and FeCl_3 (9.5.5.2) in a concentration range of 10 to 100 μM were used as controls. The ionophore valinomycin chelates K^+ ions and makes them membrane-permeable. Thus the membrane potential collapses and cell-death is induced. The onset of apoptosis (red-colour) was already observed in the lowest applied concentration of 10 to 20 μM . With the increase in concentration the cell number declines, due to cell-death.

The same unpurified solution from the ROS-assay was tested. CdSe/CdS/ZnS nanoparticles, coated with PI_{61} -*b*-PEO₂₁₂-CHO (9.5.5.3), -OH (9.5.5.4), and -COOH (9.5.5.5) were used in a lower concentration range, which correlates with concentrations used for *in vivo* applications. A549 cells were incubated seventeen hours at concentrations of 0.1 to 1 μM . Cellomics pictures of cells, exposed to the highest concentration of quantum dots, are shown in figure 109. A green staining indicates an increased membrane-permeability. The cell count stayed constant and verifies the ROS-assay.

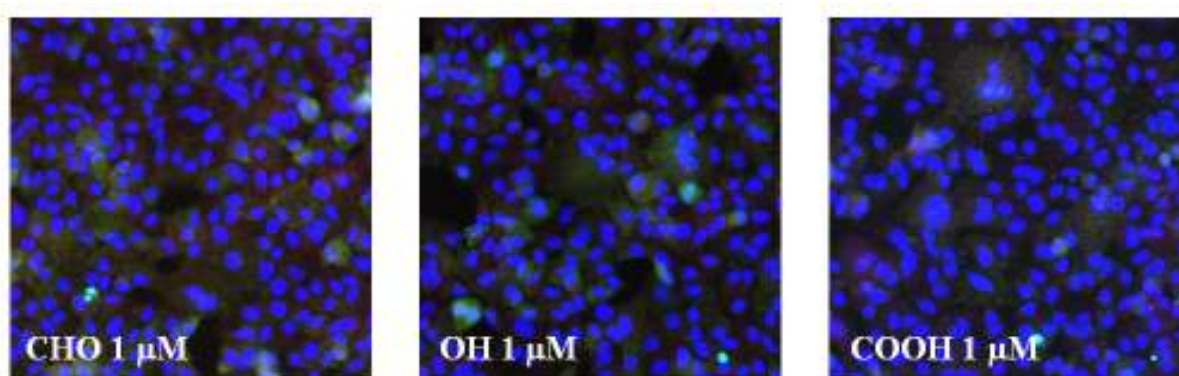


figure 109: A549 cells in the presence of PI_{61} -*b*-PEO₂₁₂-CHO, -OH, and -COOH coated quantum dots and a cytotoxicity kit II. The incubation time was 17 hours. The pictures were made using a Cellomics Reader

Under the assumption that 80 pmol CdSe/CdS/ZnS nanoparticles are applied *in vivo* in a mouse model for tumour targeting the maximal amount of 64 nmol (7.2 μg) of Cd^{2+} ions (presumption: 800 cadmium atoms per nanoparticle) would be inserted. Under the assumption that all particles agglomerate and remain inside of the body the cadmium ions would assuredly not be released all of a sudden. The process should span at least over many days. For applications in humans a larger amount of quantum dots is necessary, which should be in the range of 1 mg. In case of tumour-targeting a certain amount of QDs could be removed by surgery.

The disposal of cadmium should be set in relation with daily contamination. Exposure to Cd^{2+} can occur from food, water, smoking or occupational. Urban agglomeration with its density of

traffic and smoking increase such values. Tobacco carried by workers can become contaminated and may contribute up to 10 times more cadmium to the daily uptake than under normal conditions^[408].

According to the environmental health criteria 134, published under the joint sponsorship of the United Nations Environment Programme, the International Labour Organisation, and the World Health Organization in the year 1992, in the US, the average person consumes about 33-45 μg cadmium (294-400 nmol) in food daily^[409-412]. In Japan, the mean dietary intake of Cd^{2+} by nonsmokers women is 31-49 $\mu\text{g}/\text{day}$ (276-436 nmol). So, for an average person of 60 kg, the total daily intake of Cd^{2+} from food, water and air in North America and Europe is estimated to be about 10 to 40 $\mu\text{g}/\text{day}$ equivalent to 0.16 to 0.65 $\mu\text{g}/\text{kg}$ body weight/day using an average human body weight of 60 kg. Having regard to those findings, the release of small amounts of cadmium per day ($< 30 \mu\text{g}/\text{day}$) is of no significant consequence. This analysis suggests the possibility of applications beyond medical research.

2.9.2 *in vitro* & *in vivo* experiments

The aforementioned cytotoxicity tests suggest the applicability of PI-*b*-PEO in combination with PI-N3 as a nanoparticle-coating in biological systems, permitting the implementation of different functional groups and accordingly expansion of the nanocomposite.

A requisite arising from the lability of the proteins is, that the PI-*b*-PEO ligands have to be already assembled in a micelle dialysed to avoid any contamination. Representative TEM images of the $\text{PI}_{61}\text{-}b\text{-PEO}_{212}\text{-COOH}$ encapsulated magnetite nanoparticles are shown in figure 110 after evaporation of the prior solvent water. The images reveal that the nanoparticles are mainly separately distributed on the grid. Dense areas may be caused by the slow evaporation of the solvent water. These results cannot exclude the possibility that more than one particle is encapsulated in one micelle, nor is that the intent. Clustered particles subject to a certain size wouldn't be obstructive for biological applicants since an enhancement of the signal is involved.

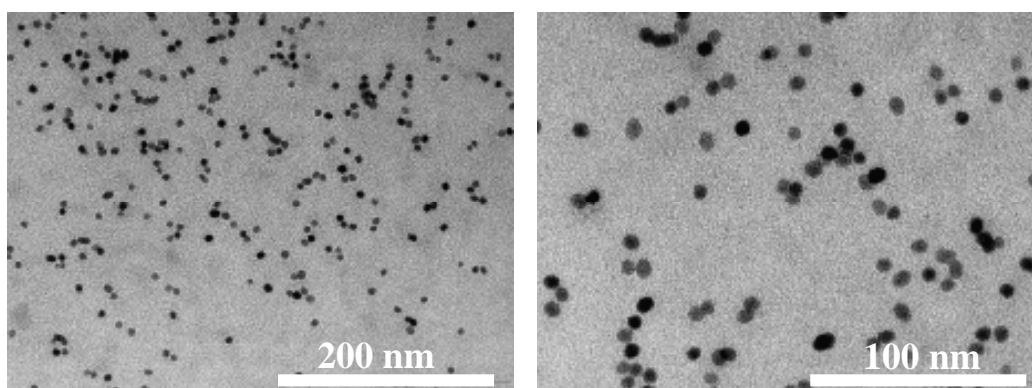


figure 110: TEM images of PI₃₀-N3 coated SPIO nanoparticles encapsulated in PI₆₁-*b*-PEO₂₁₂-COOH and PI₆₁-*b*-PEO₂₁₂-OH (QD/P 1:400, PI₆₁-*b*-PEO₂₁₂-OH / PI₆₁-*b*-PEO₂₁₂-COOH 1:1).

Nevertheless, best results were achieved by activation of the carboxylic group in water, pH 5-6, and coupling in PBS, pH 7.4 with an > 30 fold excess of EDC/sulfo-NHS (1:2.5). The possibility of multibinding to one antibody has to be acknowledged.

Special diligence has to be taken in the separation of uncoupled antibodies. Their unmodified structure offers them a higher binding affinity compared with the antibody-containing nanocomposites. Consequently free antibody would block the binding motifs in further experiments. Therefore magnetic nanocomposites were purified from unbound antibody after coupling via a magnet, while quantum dots were purified via dialyses.

The coupling of the micelles in buffer solutions is affected by the reduced solubility of PEO in the presence of high salt concentrations. The addition of salts leads to a decrease of the lower critical solution temperature for the PEO/water system^[413]. This phase transition temperature is called the 'cloud point.' Under conditions of reduced solubility, the PEO chains are subject to reversible phase transitions due to loss of the solvation shell. Consequently the chains need a reduced volume and a closer packing is arranged instead of the solvated random coil package. This certainty raises the question, is the functional group embedded in the polymer or does it stay outside maybe supported by a better solvation. To prove the efficiency of the selected coupling strategy, answering the question, did the antigen-binding site stay unaffected to the most part, enzyme-linked immunosorbent assays (ELISA), fluorescence activated cell sorting (FACS), and Biacore measurements are promising tools.

2.9.3 *in vitro* cell experiments

The terminal functional groups of the triblock ligands have been shown to have no degrading effect on the protection of the nanoparticles from the outer medium in the applied buffer tests

(see 2.1). However it could have an impact on biological systems, considering the contact of the polymer coating with cell membranes.

It has been observed that living cells ingest nanoparticles. If cells are exposed to a culture medium that contains nanoparticles, they start to take up the nanoparticles by endocytosis^[26, 337, 414-416]. Nanoparticles are then transported to vesicular compartments around the nucleus of the cell where they remain^[414, 415, 417, 418]. Receptor-mediated uptake^[177, 337] and non-specific uptake are alternative modes of cellular uptake of nanoparticles that have been discussed in literature.

To determine the effect of the quantum dot containing triblock micelles cell experiments were arranged. In collaboration with Andrea Salcher from the Center for Applied Nanotechnology (CAN, Hamburg, Germany), carcinomic human alveolar basal epithelial A549 cells were stained with Hoechst (blue). In a cell count per well of 10000/1 the cells were incubated for three days with 20 μL of the 10 μM nanoparticle solutions (7.4.1.4.4) in a Lab-Tek™ Chamber Slide™ system (200 μL medium with phenol red, without FCS, 10% HEPES).

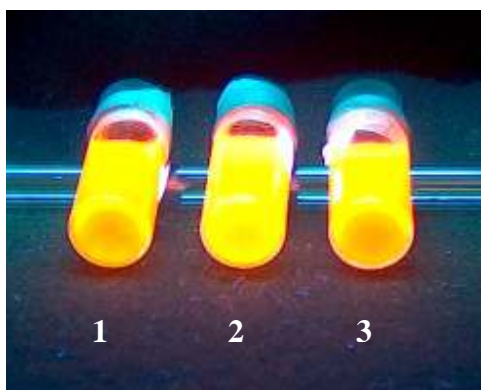


figure 111: Solutions of CdSe/CdS/ZnS nanoparticles, stabilized by ligand **8** (1), **10** (2), and **12** (3) in water.

The applied solutions of CdSe/CdS/ZnS nanoparticles, stabilized with PEO-*b*-PCL-*b*-PEI ligands **8**, **10**, and **12** in water, are shown under UV-excitation in figure 111. Ligand **8** has a *tert*butyl protected carboxylic function, ligand **10** a methoxy group and ligand **12** an acetal function. Each solution showed an average particle size of 50 nm.

The nanoparticles with terminal *tert*butyl-carboxylic groups entered the cells (figure 112). The green color of the cells before incubation is due to autofluorescence. A lambda-scan of the probe after the addition of nanoparticles (location shown by a red line in the second confocal picture) substantiates the presence of the quantum dots, which emit in the range of 600 nm.

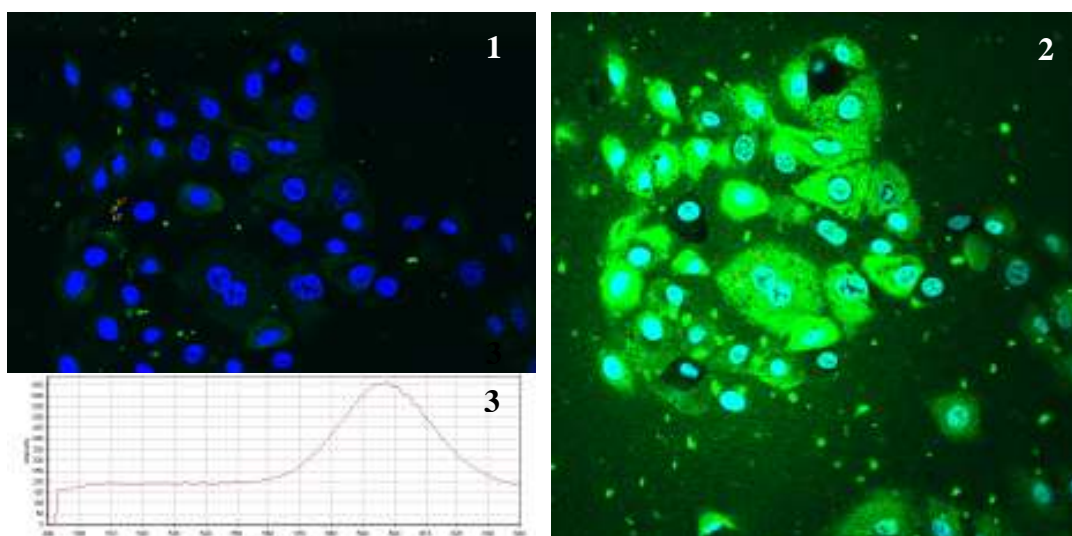


figure 112: A549 cells incubated with CdSe/CdS/ZnS nanoparticles, with *tC*-PEO-*b*-PCL-*b*-PEI (**8**) ligands. Confocal microscopes, 4% laser output. 1. cells before incubation, 2. cells after incubation, 3. Lambda scan.

Those nanoparticle compounds, which contained acetal groups at the end of the PEO block just adsorb at the cell membrane (figure 113). In comparison, methoxy functionalised nanoparticles show now specificity (figure 114). They are distributed in the cell medium, and also cell uptake occurs. As a result of the size distribution there might be the presence of nanocomposites with different sizes, which leads to an uptake of a certain amount of nanoparticles by cells.

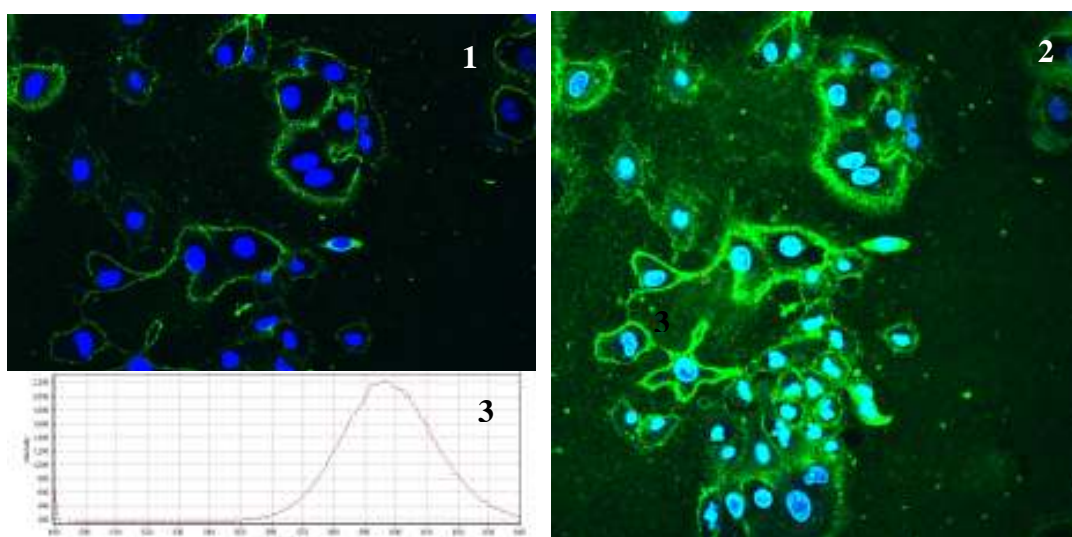


figure 113: A549 cells incubated with CdSe/CdS/ZnS nanoparticles, with DP-PEO-*b*-PCL-*b*-PEI (**12**) ligands. Confocal microscopes, 4% laser output. 1. cells before incubation, 2. cells after incubation, 3. Lambda scan.

Certainly the cell-interaction can be reduced by the extension of the PEO segment. But still there are applications, in which unspecific interaction in *in vitro* experiments could be of interest. One example could be gene therapy.

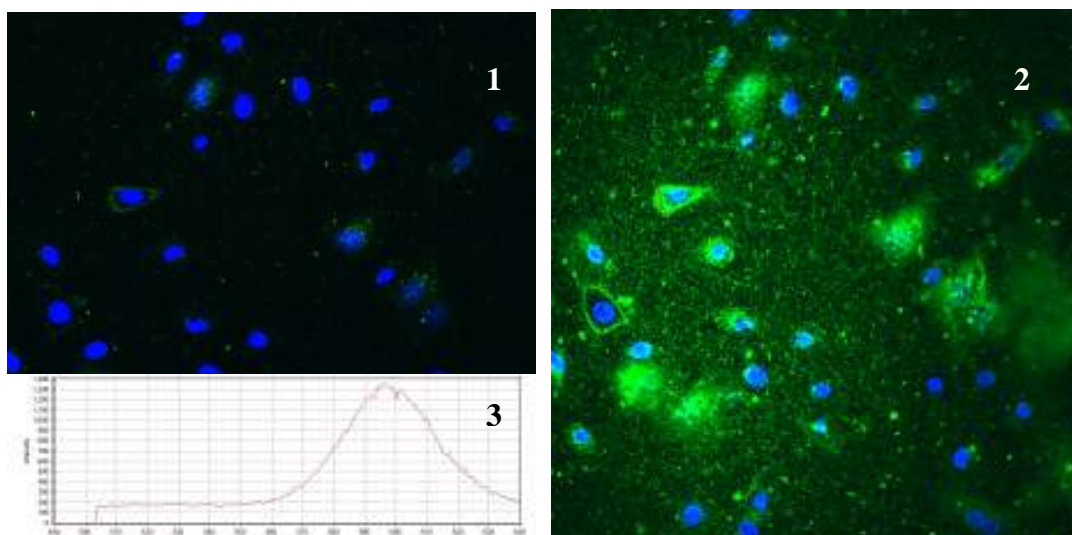
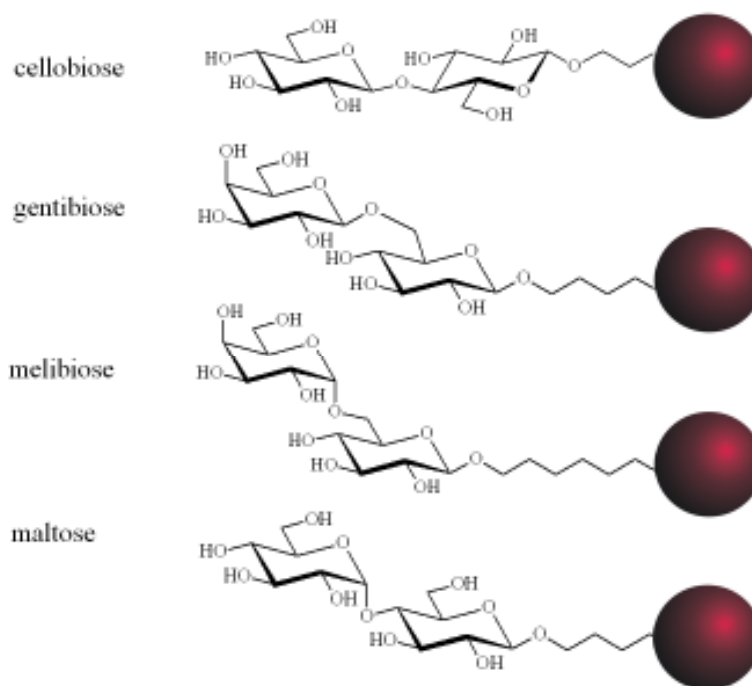


figure 114: A549 cells incubated with CdSe/CdS/ZnS nanoparticles, with M-PEO-*b*-PCL-*b*-PEI (**1**) ligands. Confocal microscopes, 4% laser output. 1. cells before incubation, 2. cells after incubation, 3. Lambda scan.

Instead CdSe/CdS/ZnS nanoparticles, coated with PI₆₁-*b*-PEO₂₁₂-CHO (figure 115), do not enter the cells. Same results were obtained in studies of cellular uptake of human colonic adenocarcinoma HT29 cells by Dr. Kersten Peldschus at the university hospital of Hamburg. Hydroxylic and carboxylic functionalized PI₆₁-*b*-PEO₂₁₂ coated CdSe/CdS/ZnS quantum dots were compared with those, which were modified with cellobiose, gentibiose, melibiose and maltose (disaccharides analoga were synthesized by Matthias Wulff from the research group of professor Vill) (schema 22, see also chapter 2.3.1.1.1).



schema 22: illustration of cellobiose, gentibiose, melibiose and maltose modified nanocomposites.

Neither the disaccharide modified nanocomposites nor the hydroxylic and carboxylic functionalized nanocomposites let in the space of 12 hours of incubation to a cellular uptake. Also no agglomeration at the cell membrane was observed.

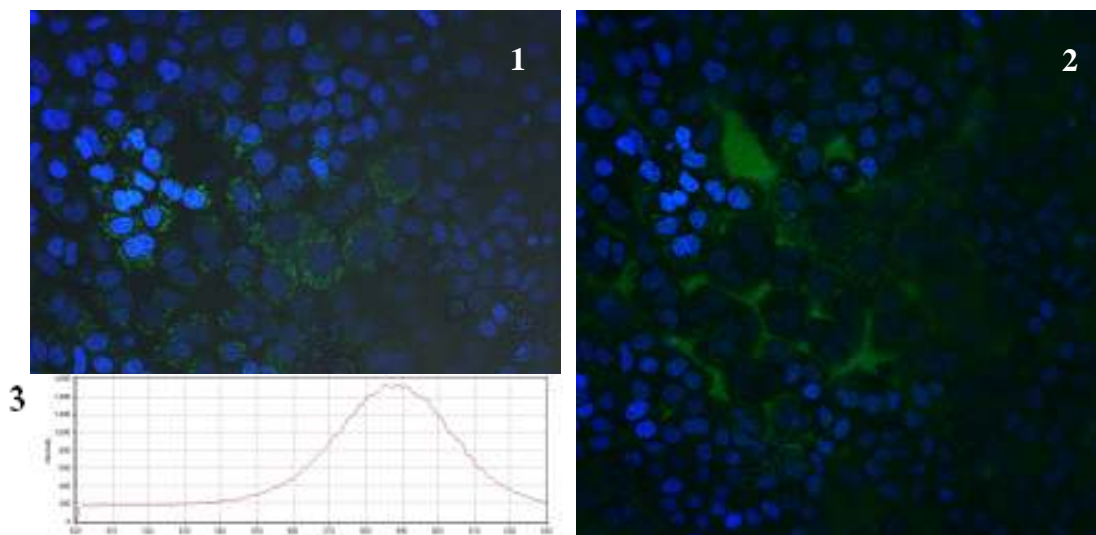


figure 115: A549 cells incubated with CdSe/CdS/ZnS nanoparticles, with PI_{61} -*b*-PEO₂₁₂-CHO ligands. Confocal microscopes, 4% laser output. 1. cells before incubation, 2. cells after incubation, 3. Lambda scan.

The surface of the polymer shell has a high effect on biological environment. By variation of the terminal group the cell uptake can be controlled. Certainly the occurrences have to be analysed in more detail, but they highlight the versatility of the compounds for biological applications. It is still unclear if active, passive, or membrane dislocating (like endocytose) transport is the dominant passage for nanoparticle uptake and what causes it.

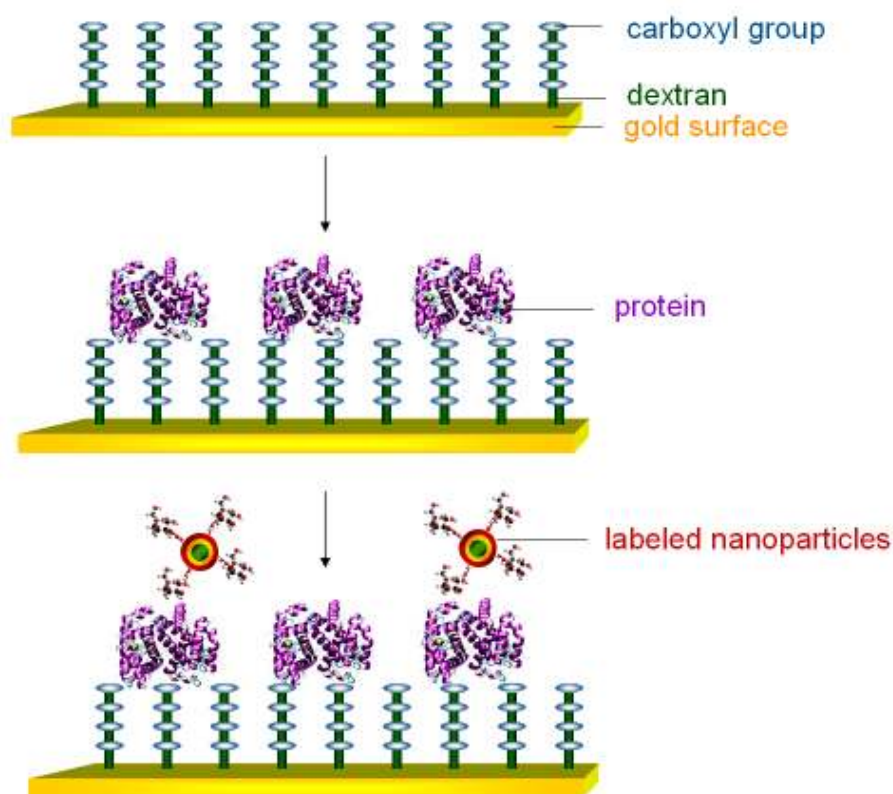
A further observation, which couldn't be clarified in detail, is that the quantum dots in the cell medium first start emitting after 5-10 minutes of laser excitation.

The applied PI_{61} -*b*-PEO₂₁₂ comprising nanocomposites showed no specific and unspecific uptake. Their biological inert properties in cell culture make them an interesting vehicle for *in vivo* application.

2.9.3.1 Biacore technique

The presence of carbohydrates on the surface of the *PI-b*-PEO polymer shell, coupled via Huisgen cycloaddition, was revised by Biacore measurements (schema 23) in cooperation with Sebastian Kopitzki (research group of Prof. Dr. J. Thiem). The grounding of Biacore is the surface plasmon resonance, which gives information about the occupancy rate of a gold coated

sensor chip CM5. To this surface carboxymethylated dextran is covalently bonded. Via a NHS-activated carboxylic group R-type lectin *ricinus communis* agglutinin I (RCA₁₂₀) was coupled. This tetrameric hemagglutinin (120 kD protein), comprising two ricin-like dimers held together by non-covalent forces^[419-421], bears a β -galactose specificity. Due to its high affinity for glycans containing non-reducing terminal β Gal residues, RCA₁₂₀ has been widely used as a versatile tool to detect sugar structures such as those found in complex-type N-linked glycans^[422-424]. The profit of this coating was verified by unbound β -D-galactose.



schema 23: principle of biacore.

A dilution series of HEPES buffer containing different amounts of nanoparticles carrying β -D-galactose, β -D-glucose and plain quantum dots were prepared and eluted on a CM5-chip, on which RCA₁₂₀ was immobilized. The corresponding adjusted sensorgrams are shown in figure 116. After 20 s the injection of the QDs was arranged, whereupon an increased response was observable.

Biomolecular binding events at a sensor surface cause changes in an SPR signal which are expressed in resonance units, RU (one RU is equivalent to one picogram of protein per square millimetre on the sensor surface).

Upon the abandonment of the nanoparticle containing running buffer after 250 s the dissociation of the protein-sugar complex is induced by a run of pure running buffer. The blank

nanoparticles (figure 116 C) showed hereby already at first sight of the adjusted sensorgram no binding behaviour to RCA₁₂₀, by reason that the response drops instantly to zero, when no more nanoparticles are present in the buffer.

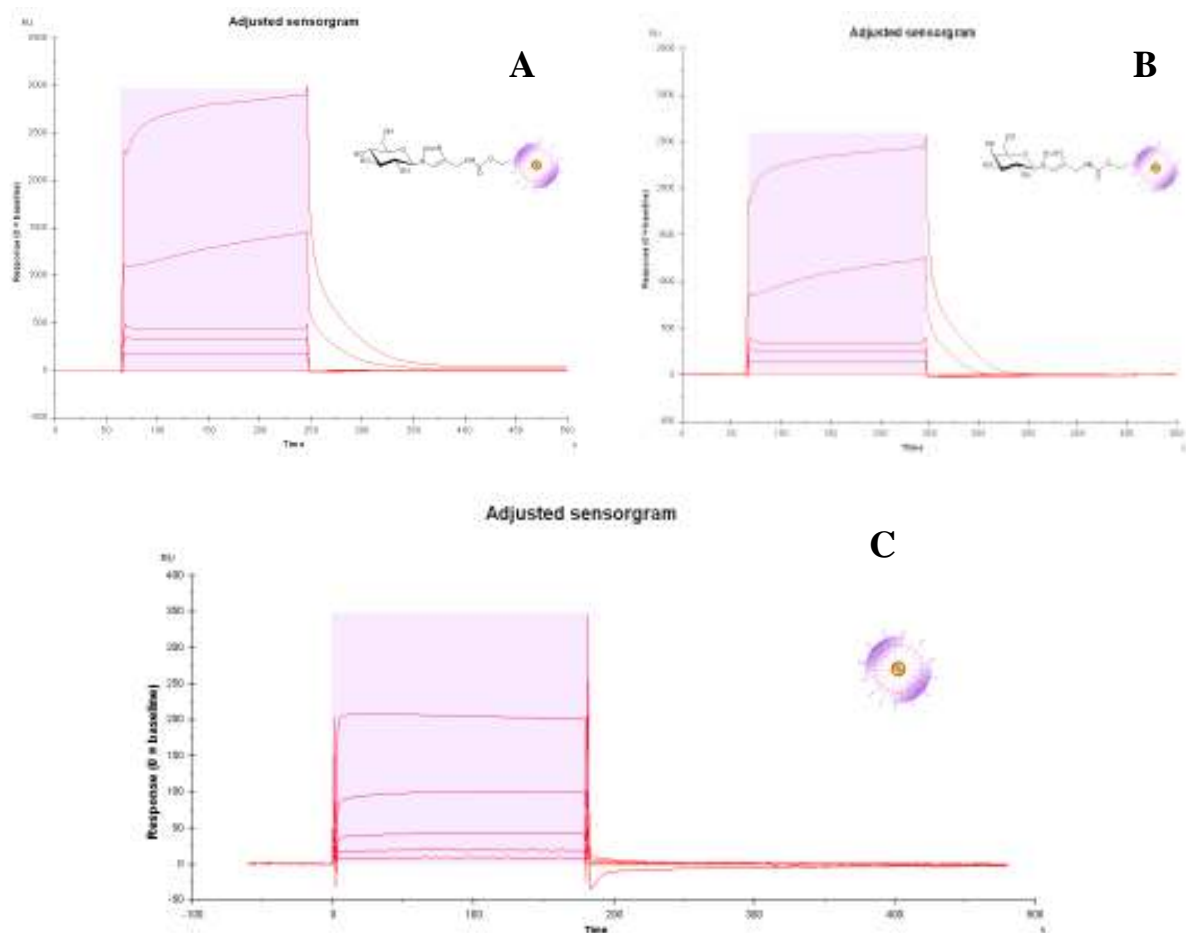


figure 116: biacore measurements.

Layered SPR-sensorgrams of β -D-glucose (A), β -D-galactose coated (B), and blank nanoparticles (C). The measurements were achieved using an Biacore T100 automate; the software used was Biacore T100 Evaluation Software version 1.1.

The sensorgrams depart from an idealized SPR-sensorgram, why it was prescind from a kinetic appraisal. Under the definite concentration dependence of the sensorgram a thermodynamic analysis was made based on the one-side binding model. The values, attained in the performed measurements, of on-rates (k_a) and off-rates (k_d) of protein interactions are directly related to equilibrium binding affinities ($K_D = k_d/k_a$).

For determination of the thermodynamic dissociation constant K_D the steady-state obtained RU response was plotted against the concentration of the quantum dots containing HEPES-buffer solutions (figure 117).

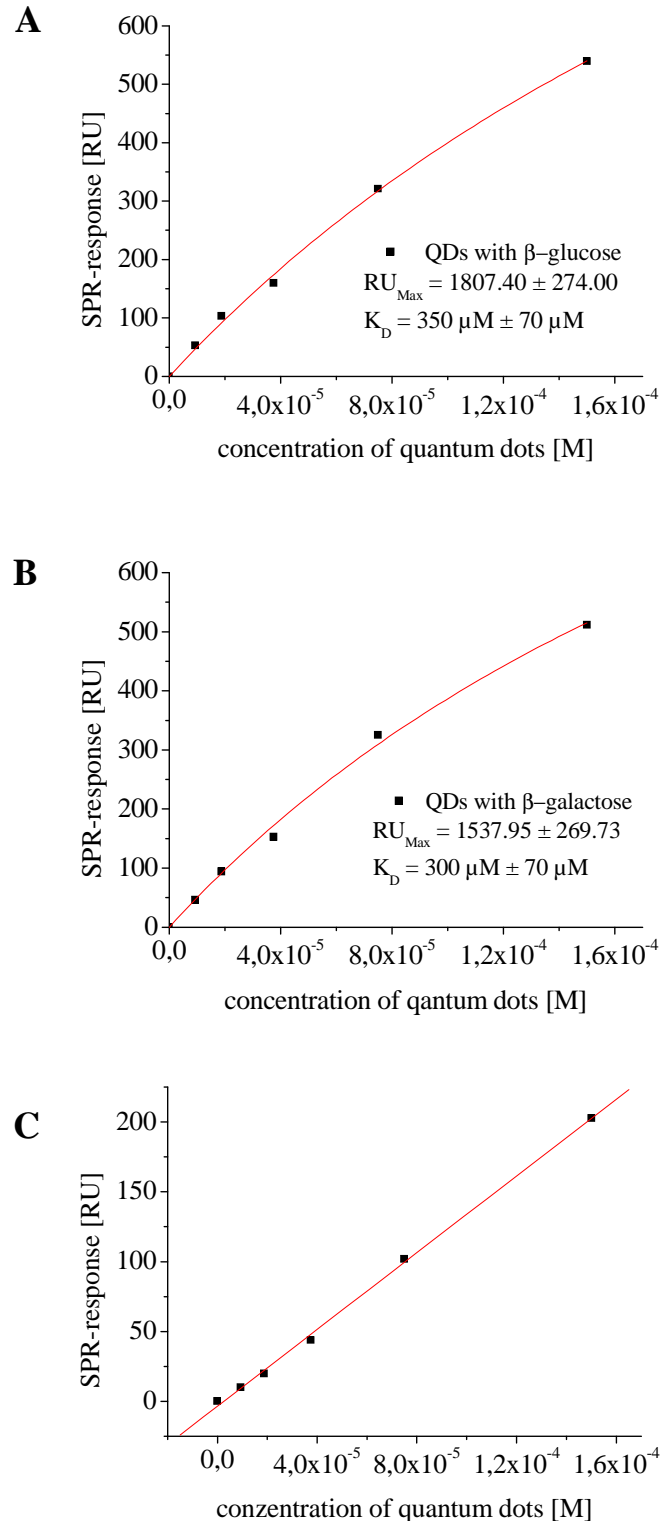


figure 117: RU difference response of the quantum dots as a function of concentration in the running buffer.

Layered SPR-sensorgrams of β -D-glucose coated (A), β -D-galactose nanoparticles (B), and of QDs without monosaccharides (C). The data points were by dint of the software Origin adjusted to the one-site binding model.

In the event of the RU difference response as a function of the quantum dots, offering no monosaccharides on the PEO surface, in the running buffer a linear correlation was determined.

Whilst in case of the glycosylated nanoparticles in terms of their RU difference response as a function of the concentration a definite curve, which approaches saturation, was gained. RCA₁₂₀ showed therefore a binding affinity for the glycosylated nanoparticles, whereby with Biacore T100 evaluation software as well as calculations with Origin under consideration of the one side binding model a higher binding affinity ($K_D = 285 \mu\text{M}$), which is expressed by lower K_D -value, was found for the β -D-galactose-QDs compared with β -D-glucose-QDs ($K_D = 400 \mu\text{M}$) (table 2).

β -D-glucopyranosyl	K_D [μM]	RU_{Max}
Biacore	450	2125.00
Origin (calculated)	350	1807.40
average value	400	1966.20
β -D-galactosepyranosyl		
Biacore	270	1441.50
Origin (calculated)	300	1537.95
average value	285	1489.73

table 2: comparison of obtained and calculated K_D - and RU_{Max} -values.

An integrated alkyl chain between the sugar molecule and the 1,2,3-triazole ring could diminish the influence of the 1,2,3-triazole ring, hence assuring an unobstructed binding behaviour and thus higher binding affinities.

The results comply with the expectation on the SPR-experiment by which the availability of the saccharide on the quantum dot coating and accessibility by lectines could be substantiated. Owing to the high molecular mass of the nano-composite ($M > 1000 \text{ kD}$) high RU responses could be detected, which could permit the determination of lesser molecular interactions.

The results reflect the effectual presentation of a hydrophilic molecule on the polymer surface. Certainly the coupling of the molecule doesn't have to be accomplished ere the ligand is assembled in a micelle, depicted subsequent.

2.9.3.2 Cell culture experiments with anti-CEACAM specific SPIONs

The evidence of the achievement of antibody-coupling and the accessibility and preservation of the antigen binding site of the antibody was arranged by cell culture experiments in cooperation with Dr. Kersten Peldschus and Dr. Peter Nollau from the university hospital Hamburg Eppendorf. As a model for tumour cell targeting the monoclonal antibody T84.1 binding to

carcinoembryonic antigen related cell adhesion molecules (CEACAM) and the CEACAM expressing human colon carcinoma cell line HT29 were used. CEACAM are involved in intercellular adhesion and signal transduction events in a number of epithelia and are frequently dysregulated in many carcinoms.

Carboxylic functionalised SPIONs with a hydrodynamic radius of 50 nm were coupled to the antibody T84.1. Resulting from the antibody-coupling the hydrodynamic diameter of the PI₆₁-*b*-PEO₂₁₂-COOH stabilized SPIONs increased from 50 nm to 90 nm in water (figure 118) according to DLS measurements (DLS, intensity PSD).

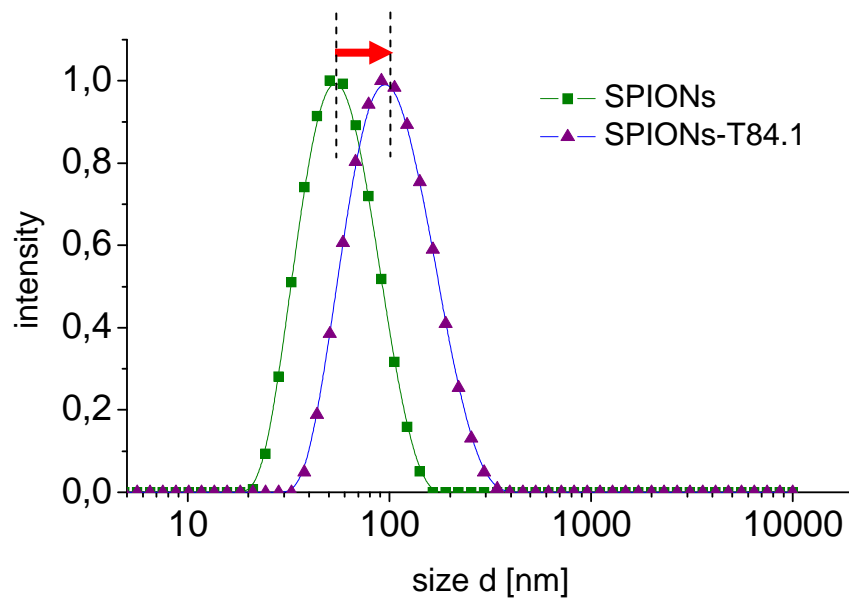


figure 118: DLS measurements (intensity PSD) of the SPIONs before and after coupling to T84.1 antibodies.

Unbound antibody was isolated by using a column surrounded by a magnet. Cell suspensions of HT29 cells were incubated with purified anti-CEACAM specific SPIONs and SPIONs coupled to IgG1, SPIONs coupled to anti-CEACAM in combination with unbound anti-CEACAM antibody and PBS as appropriate controls. After incubation, cells were washed and pelleted in Eppendorf tubes on a layer of polyacrylamide (for more detailed information see chapter 7.4.1.4). Cellular probes underwent magnetic resonance imaging on a 3.0T scanner and a small solenoid coil in a custom made rack of acrylic glass containing water (figure 119).

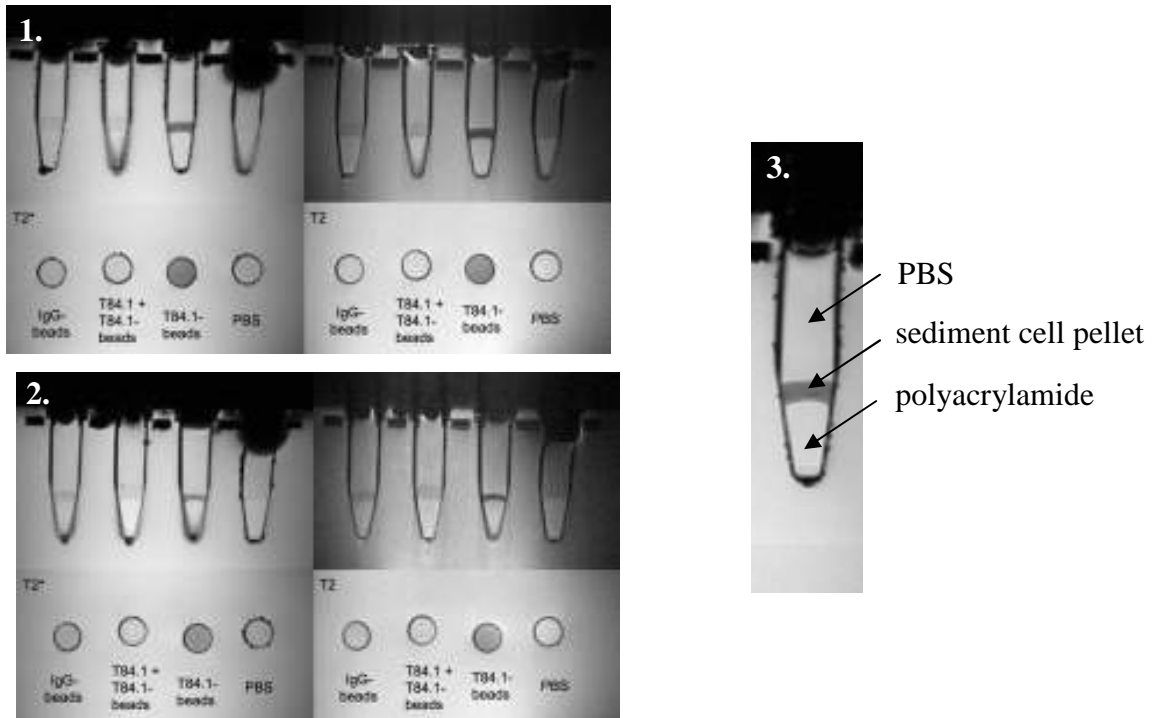


figure 119: 1. Magnetic resonance imaging of HT29 cells incubated with 50 μL SPION-A (c_1). 2. MR imaging of HT29 cells incubated with 25 μL SPION-A (c_2). 3. Explanation. (see also chapter 7.4.1.4).

The T2*- and T2-weighted images demonstrated a clear signal loss of cell pellets incubated with anti-CEACAM specific SPIONs and weak signal loss for all controls indicating a negligible unspecific binding. In the presence of unbond anti-CEACAM the antigen was blocked due to the higher concentration of the unbond antibody.

Coronal and axial images of both sets show darkening of the samples treated only with T84.1-SPION-A and no signal loss of controls with IgG-SPION-A and pretreated with mAb T84.1.

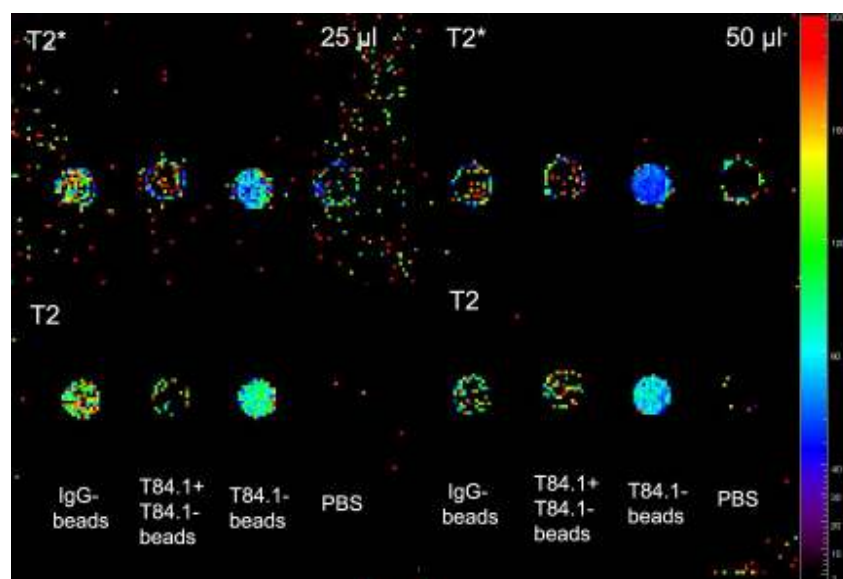


figure 120: Quantitative magnetic resonance measurements of HT29 cell pellets incubated with 50 μL (c_1) and 25 μL SPIONs (c_2).

Quantitative measurements (figure 120) of cell pellets treated with anti-CEACAM specific SPIONs revealed dose depended relaxation rates up to $R_2^* = 0.022 \pm 0.005 \text{ s}^{-1}$ and $R_2 = 0.010 \pm 0.002 \text{ s}^{-1}$ (c_1) ($R_2^* = 0.015 \pm 0.00 \text{ s}^{-1}$ and $R_2 = 0.008 \pm 0.002 \text{ s}^{-1}$ (c_2)). In contrast to SPIONs purchased *inter alia* from Micromod, unspecific binding was nearly undetectable. The results are getting corroborated by the cell tests (chapter 2.9.3).

These results proved the biological functionality of antibody-coupled SPIONs and demonstrated the preservation of the antibody affinity after coupling. The weak unspecific binding promise a low biological interaction and presumably beneficial pharmacokinetic properties for *in vivo* experiments.

2.9.4 *in vivo* applications

To further prove the biological applications antibody-coupled nanoparticles were tested in a mouse tumour model.

In contrast to other labelling techniques, where proteins e.g. biotinylated antibodies are getting immobilized over streptavidin^[177], directly conjugated^[425], attached to a polymethacrylic acid sterically complex beneath PEO chains close to the nanoparticle surface^[92], which are in some extend applied in biological *in vivo* systems, in this work the antibodies were attached terminal of a long PEO polymer chain. Thus presenting them at the outside of the shell while conserving the flexibility and accessibility of the full antibody. The new ligand system and functionalisation strategies were published previously. It has to be emphasized that the coupling reaction with the functional group is unimpeded due to the presence at the micelle-surface, which allows the reaction with an antibody. Furthermore, the antibody is blocked from the nanoparticle surface, where it could coordinate and thereby be denatured.

2.9.4.1 Anti-CEACAM specific SPIONs

Based on the results of chapter 2.9.3.2 carcinoembryonic antigen related cell adhesion molecules (CEACAM) were chosen as a target for *in vivo* studies. CEACAM molecules are differentially expressed in epithelial cells or in leucocytes. In tumours of epithelial origin overexpression of CEACAM-5 occurs, while CEACAM-1 expression is down-regulated in many tumours indicating a tumour-suppressive function.

To verify the results the coupling of anti-CEACAM (T84.1) antibodies to PI₆₁-*b*-PEO₂₁₂-COOH coated SPIONs and cell culture experiments were repeated in cooperation with Dr. K. Peldschus and Dr. P. Nollau from the university hospital Hamburg Eppendorf. The new antibody-nanocomposites had a hydrodynamic diameter of 94 nm according to DLS (intensity PSD) measurements.

Instead of HT29 cells the human melanoma cell line FEMX-I expressing the carcino embryonic antigen related cell adhesion molecules (CEACAM) 1, 5 and 6 were used. This cell line, originating from a lymph node metastasis in a patient, uniquely and selectively produces extrapulmonary metastases.

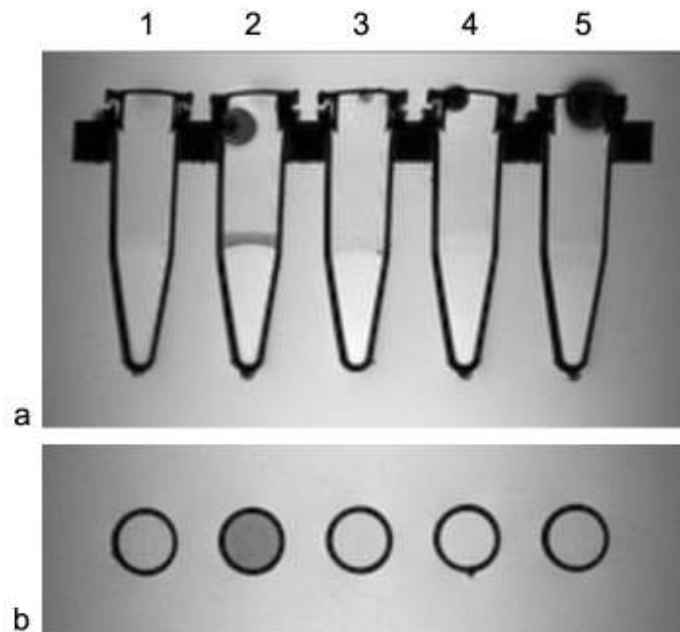


figure 121: Magnetic resonance imaging of FEMX-I cells incubated with SPION-CEACAM. T2 weighted coronal (a) and axial (b) turbo spin-echo (TSE) sequences of cell phantoms incubated with SPIONs.

1. PBS, **2.** T84.1-SPIONs, **3.** T84.1 & T84.1-SPIONs, **4.** SPIONs, **5.** cells without SPIONs.

Incubation of cells: cells of the human melanoma cell line FEMX-I expressing the carcino embryonic antigen related cell adhesion molecules (CEACAM) 1, 5 and 6 were trypsinized and washed three times in PBS. Cells were counted and split onto 11 round bottom tubes with 1.9×10^7 cells in 500 μ L PBS supplemented with 1% BSA, respectively. Three samples were pre-incubated with un-conjugated monoclonal antibody (mAb) T84.1 (10 μ g/mL) for 15 minutes at 4 °C to block specific binding sites. Cell suspensions were then supplemented with T84.1-conjugated SPIONs and un-conjugated SPIONs at a dose of 50 μ g/mL. Cells were incubated for 1 hour at 4 °C. Afterwards, cells were washed twice and re-suspended in 300 μ L PBS.

MR imaging of cell phantoms: Cell phantoms were prepared of 200 μ L polyacrylamide in 0.5 mL Eppendorf tubes. Cell suspensions were transferred in to the Eppendorf tubes and phantoms were kept 2 hours at 4 °C for sedimentation. Cell phantoms were then examined on a 3.0 T magnetic resonance scanner (Intera, Philips, Best, The Netherlands) using a small solenoid receiver coil. Phantoms were placed in a custom made device of acrylic glas contacting that fit into the receiver coil. The imaging protocol consisted of coronal and axial T2 turbo spin echo (TSE) and T2* gradient echo (GRE) sequences.

Cell suspensions of FEMX-I cells were incubated with purified anti-CEACAM specific SPIONs and SPIONs coupled to anti-CEACAM in combination with unbond anti-CEACAM antibody and PBS as appropriate controls. After incubation, cells were washed and pelleted in Eppendorf

tubes on a layer of polyacrylamide. Cellular probes underwent magnetic resonance imaging on a 3.0 T scanner and a small solenoid coil in a custom made rack of acrylic glass containing water. In figure 121 T2-weighted coronal (figure 121 a) and axial (figure 121 b) turbo spin-echo (TSE) sequences of cell phantoms incubated with SPIONs are shown (probe 2-4). Probe 1 contained PBS as control. Considerable signal decrease (darkening) of the cell pellet in probe 2 demonstrated detection of T84.1-SPIONs by MR imaging. Cells pre-incubated by T84.1 followed by incubation with T84.1-SPIONs in probe 3 as well as cells incubated with unconjugated SPIONs in probe 4 showed no signal decrease compared to cells without incubation of SPIONs in probe 5 indicating the target specific binding of T84.1 SPION in probe 2.

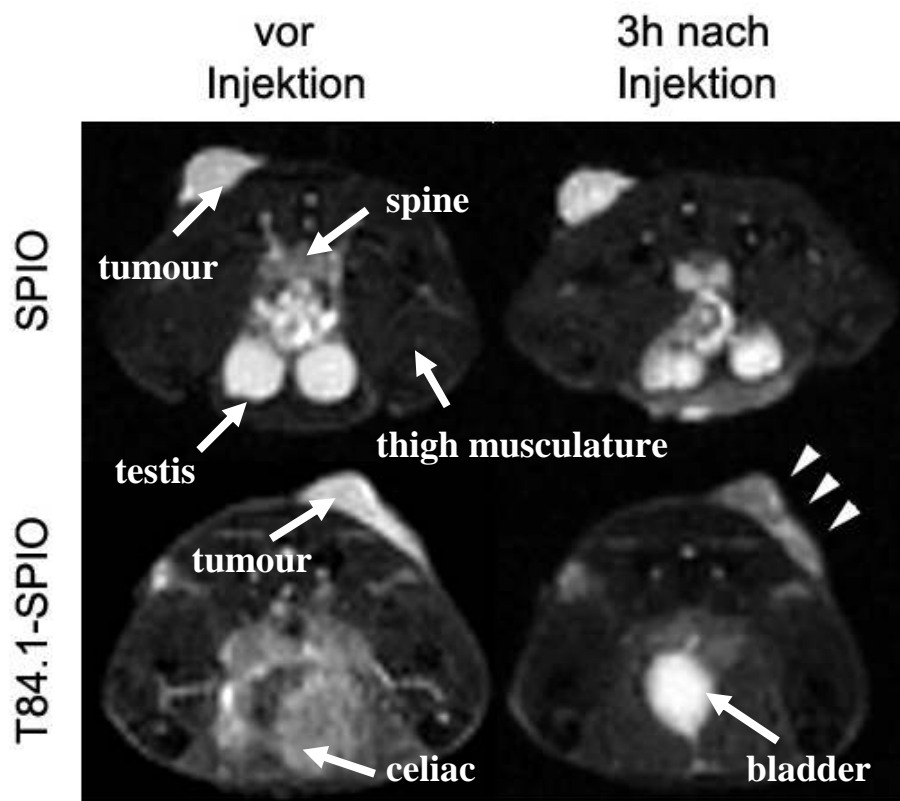


figure 122: MR imaging (T2 weighted) of mice before and 3 h after administration of SPIONs (transverse section in region of the pelvis).

For *in vivo* application served ten weeks old male severe combined immunodeficiency (SCID) mice as clinical relevant xenograft tumour model. 10^6 cells of the human melanoma cell line FEMX-I were subcutaneously inoculated in the flanks of their pelvis. After 21 days of tumour growth mice showed well palpable tumours at the injections sites. The tumour tissue had a size of 2-3 mm. At this size the tumour is vascularised sufficiently.

The mice received intravenous administration of SPIONs, whereby T84.1-SPIONs and unconjugated SPIONs as control were injected at a dose of 700 μg Fe respectively. MR images

(T2 weighted axial turbo spin echo (TSE) sequence) of the tumour bearing mice before and 3 hours after injection are shown in figure 122. After injection of the contrast material the mouse treated with T84.1-SPION (lower row) shows a signal decrease (darkening) of the tumour (arrow heads) where as the mouse treated with unconjugated SPIONs (upper row) reveals no signal change of the tumour. Signal changes in the area of the celiac are due to changes of the position of the bowels and the amount of liquid in the bladder. Further mice can move their testis in and out of the body.

The results indicate a successful tumour-targeting and -imaging. Circulation times of up to 12 hours could be detected. In comparison, dextran coated SPIONs were just detectable for five minutes in previous *in vivo* experiments. This again points out the outstanding quality of the ligand shell and its facility to be bio-functionalized.

2.9.4.2 Anti-YKL-40 specific SPIONs and QDs

Several types of solid tumour (breast, colon, lung, kidney, ovary, prostate, uterine, pancreas, osteosarcoma, thyroid, oligodendroglioma, glioblastoma, and germ cell tumours) express YKL-40, a protein, which belongs to the glycosyl hydrolase family 18. This excretory protein is often found in the blood of cancer patients and maybe plays a role in the growth of different tumours, *inter alia* the human melanomic cell line LOX. There are suggestions that YKL-40 plays a role in the proliferation and differentiation of malignant cells, protects the cancer cells from undergoing apoptosis, stimulates angiogenesis, has an effect on extracellular tissue remodelling, and stimulates fibroblasts surrounding the tumour. Nevertheless, the actual biological function of YKL-40 in cancer is not known^[426].

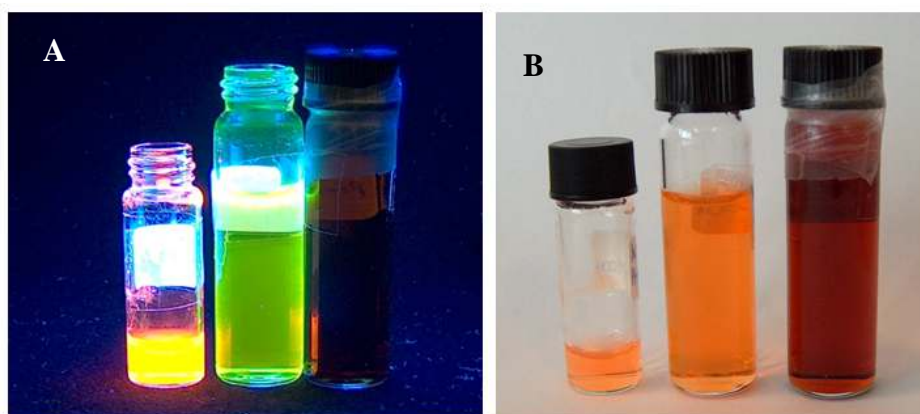


figure 123: CdSe/CdS/ZnS probe N17, CdSe/CdS/ZnS probe N25, and γ -Fe₂O₃ coated with PI₆₁-b-PEO₂₁₂-COOH after 80 days of storage in water. **A** under UV-light, **B** under daylight.

For targeting of YKL-40 *in vivo* murine IgG2b κ anti-YKL-40 (146 kD protein), and mouse IgG2b isotype (146 kD protein) were coupled with CdSe/CdS/ZnS quantum dots and magnetite nanoparticles. The used nanoparticle-PI₆₁-*b*-PEO₂₁₂-COOH stock solutions after 80 days of storage in water are shown in figure 123.

The proof of the effectual coupling was done by an *in vivo* experiment in cooperation with Kersten Peldschus and Johannes Salamon from the research group of Prof. Dr. U. Schumacher in the university hospital Hamburg Eppendorf.

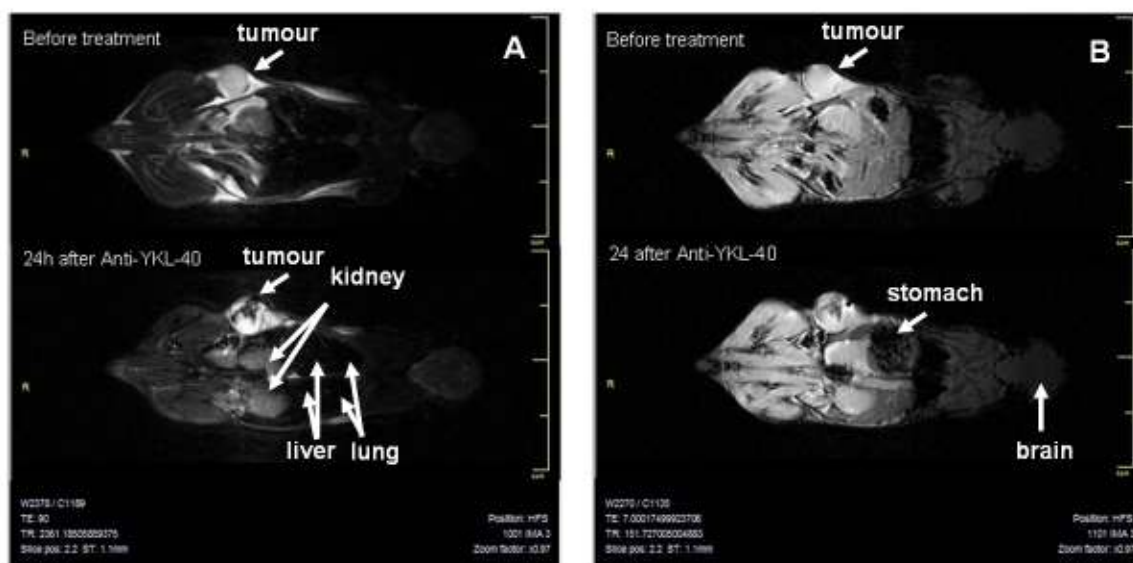


figure 124: MR images of a mouse exposed to the anti-YKL-40-quantum dot and -SPION conjugates.
A: T2 weighted measurement before injection (top) and after injection (bottom).
B: T2* weighted measurement before injection (top) and after injection (bottom).

10^6 cells of the YKL-40 expressing human melanoma cell line LOX were subcutaneously inoculated in the left flank of four female C57Bl/6 SCID mice and served as clinical relevant xenograft tumour model. After 2 weeks of tumour growth 86 pmol of the constructed anti-YKL-40-QD conjugates in combination with 300 pmol anti-YKL-40-SPIONs conjugates were intravenously injected. Magnetic resonance imaging of tumour bearing mice was carried out before and 24 hours after application of the antibody-conjugates. In mice treated with the anti-YKL-40 antibody conjugates magnetic resonance imaging revealed a substantial signal loss of the tumour tissue in T2- and in the T2*-weighted images (figure 124).

As a negative control 170 pmol IgG2b-isotype-QD conjugate along with 170 pmol IgG2b-isotype- SPION conjugate in 200 μ L PBS, pH 7.4, were injected into another four cancer bearing mice. At this juncture no signal loss of tumour tissue was observed, thus no binding could be identified, whilst the tumour grows unaffected (figure 125). This result is coinciding with the anticipation, that the antibody-conjugates exhibit only negligible unspecific binding.

Upon administration of the coupled iso-antibody at the most a light darkening in the liver but no variance in the tumour tissue was detectable. This result coincides with expectations because the mouse IgG2b isotype shows no specificity to the tumour tissue.

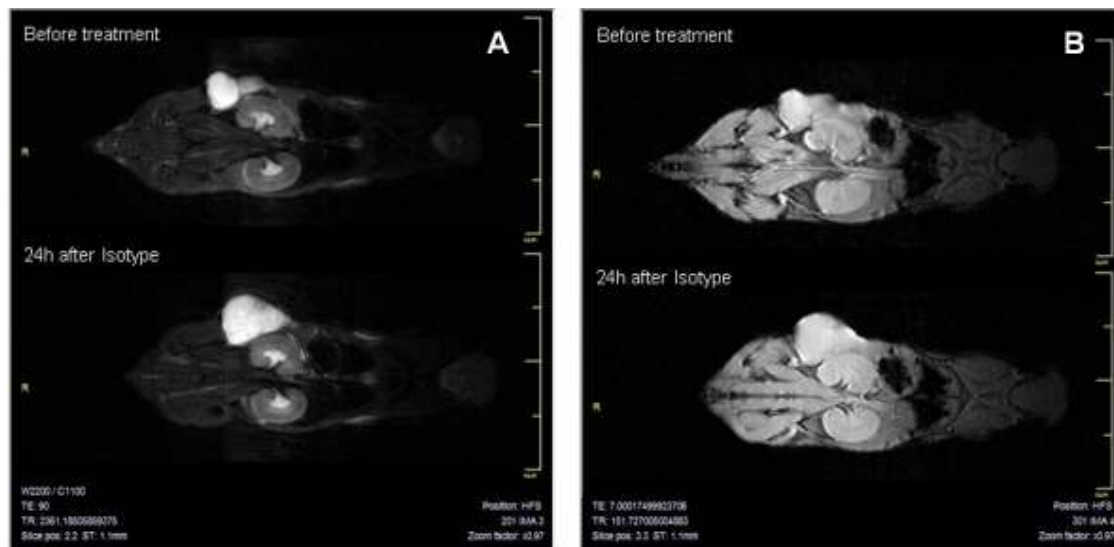


figure 125: MRI pictures of a mouse exposed to the IgG2b-isotype-quantum dot and -SPION conjugates.
A: T2 weighted measurement before injection (top) and after injection (bottom).
B: T2* weighted measurement before injection (top) and after injection (bottom).

Histological analysis of tumours confirmed magnetic resonance imaging findings by detection of anti-YKL-40-QDs (figure 126 A & B) within the tumour tissue. Notably high accumulations of anti-YKL-40-QDs were found in the vicinity of vessels which supports the assumption that the antibody-conjugates could leave the vasculature and bound to the extracellular tumour matrix which contained YKL-40. The absence of IgG2b-isotype-QD conjugates in tumours of the control group (figure 126 C & D) confirmed the observation of no unspecific binding.

In spite of the low concentration of nanoparticles (in the range of pmol) targeting of tumour tissue could be documented. The dosage of 86 pmol quantum dots is remarkable, compared to other systems, which require quantum dots in the high nanomolar to micromolar range^[21, 415, 427]. The small amount of nanoparticles and their inorganic and organic coatings should minimize toxic effects, which are mainly attributed to the release of surface cations (Cd^{2+}), assisted by metallothioneins, and the formation of photoinitiated radicals^[428]. These toxic effects can be observed, when water comes in contact with the nanoparticles. But this is getting circumvented by the double PI layer, which simultaneously can act as a remarkable radical interceptor. Indeed, no toxic effects were observed in treated mice. Nevertheless detailed investigations are pending.

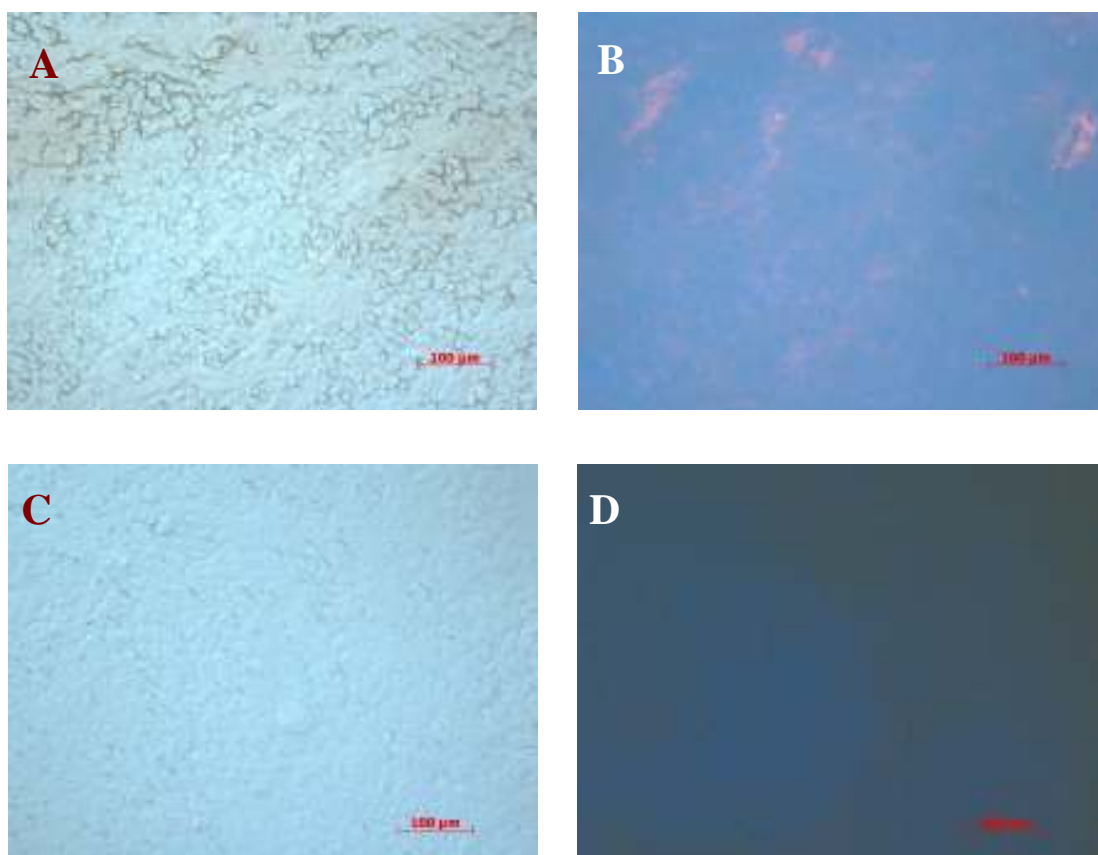


figure 126: superimposed confocal microscope images of the tumour tissues.

- A:** treated tumour tissue with anti-YKL-40-nanoparticles. Normanski-contrast (200x enhanced)
B: treated tumour tissue with anti-YKL-40-nanoparticles. Excitation at 365 nm (200x enhanced)
C: treated tumour tissue with the isotype control. Normanski-contrast (200x enhanced)
D: treated tumour tissue with the isotype control. Excitation at 365 nm (200x enhanced)

In addition to the observed active targeting, quantum dot probes can also be delivered to the tumour by a mechanism referred to as passive targeting^[429]. Macromolecules and nanometer-sized particles accumulate preferentially at tumour sites through an enhanced permeability and retention (EPR) effect^[430-432]. This is due to some peculiarities of tumour cells, which can be harnessed for targeting: some cancerous cells can promote the synthesis of new blood vessels (vasculature) by secreting growth factors. Such neovasculature, which perfuse the tumour tissue, exhibit hyperpermeable tumour-associated walls. As a result, compared to normal blood capillaries' wall-leakage most tumours lack an effective lymphatic drainage system. On that account nanocomposites preferentially accumulate in the tumour interstitial space.

This passive targeting wasn't observed in our experiment (figure 126 C & D). This could be due to the low dose and/or the excess negative charges supplied by free carboxylic acid groups on the polymer coating^[92]. Negative charges are known to reduce the rate of probe extravasation and its subsequent accumulation into tumour xenografts^[433]. In contrast, positively charged amino groups on quantum dot-immunoliposomes are suggested to lower the circulation time^[434].

The established auspicious route opens new possibilities to understand the function of the protein YKL-40 and shows the circuitousness of applicability of nanoparticles in biochemistry^[88, 435, 436].

The findings verify the prosperous coupling of the antibodies to the nanoparticle coating with preservation, for the most part, of the binding capability and accordingly flexibility of the antigen binding domain of the antibody. Moreover, long circulation times were ascertained. But these deliverables allow additional conclusions: the PI₆₁-*b*-PEO₂₁₂-COOH ligand remains on the nanoparticle and the PEO chain circumvents interactions with the blood serum. Hence the ligand system allows the use of diverse nanoparticles, what could not only be proved with QDs and SPIONs but also with GdPO₄ nanoparticles.

2.9.4.3 GdPO₄ nanoparticles in comparison with Magnevist[®]

The high relaxivity of the GdPO₄ (CAN09-0026) nanoparticles (see chapter 2.7) was the reason to examine their applicability in biological environments.

GdPO₄ nanoparticles, which were coated by PI₆₁-*b*-PEO₂₁₂-OH in absence of the preligand PI-N3 and without a radical crosslinkage, were compared *in vivo* with the clinical approved contrast agent Magnevist[®]. 1.44 μmol GdPO₄ nanoparticles dissolved in 400 μL ddH₂O and 2.00 μmol Magnevist[®] dissolved in 50 μL ddH₂O were intravenously injected in mice and investigated by magnetic resonance angiography (MRA).

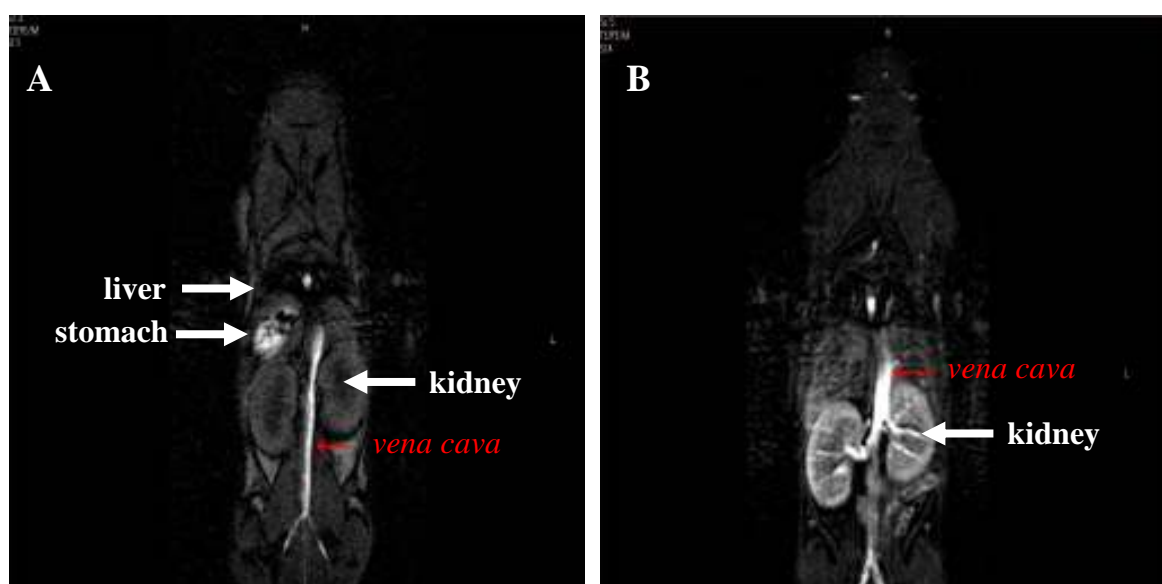


figure 127: magnetic resonance angiography images of GdPO₄ nanoparticles (A) and Magnevist[®] (B).

The results are shown in figure 127. In both cases the *vena cava* is contrasted considerably. Major difference is the renal elimination (over the kidney) of Magnevist®. The GdPO₄ nanoparticles caused a slight signal in the liver which could be seen after 7 minutes (figure 128).

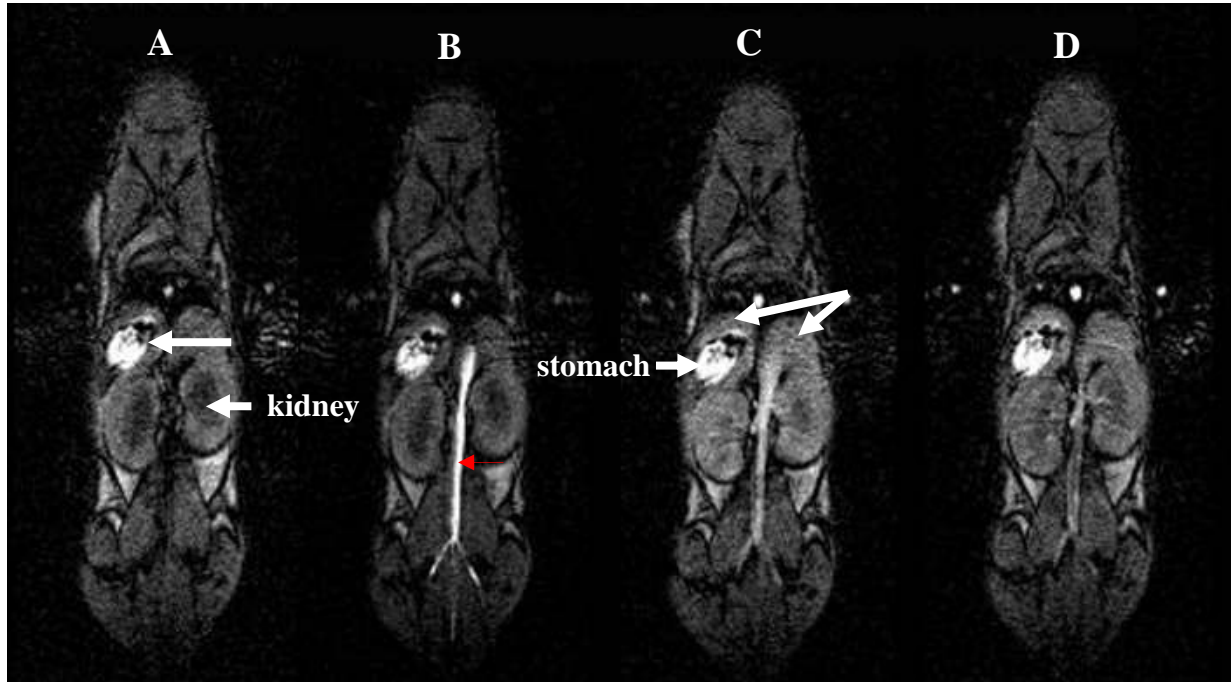


figure 128: magnetic resonance angiography images of GdPO₄ nanoparticles.

- A** MRT angiography before contrast agent administer
- B** MRT angiography 30 seconds after contrast agent administer
- C** MRT angiography 2 minutes after contrast agent administer
- D** MRT angiography 7 minutes after contrast agent administer

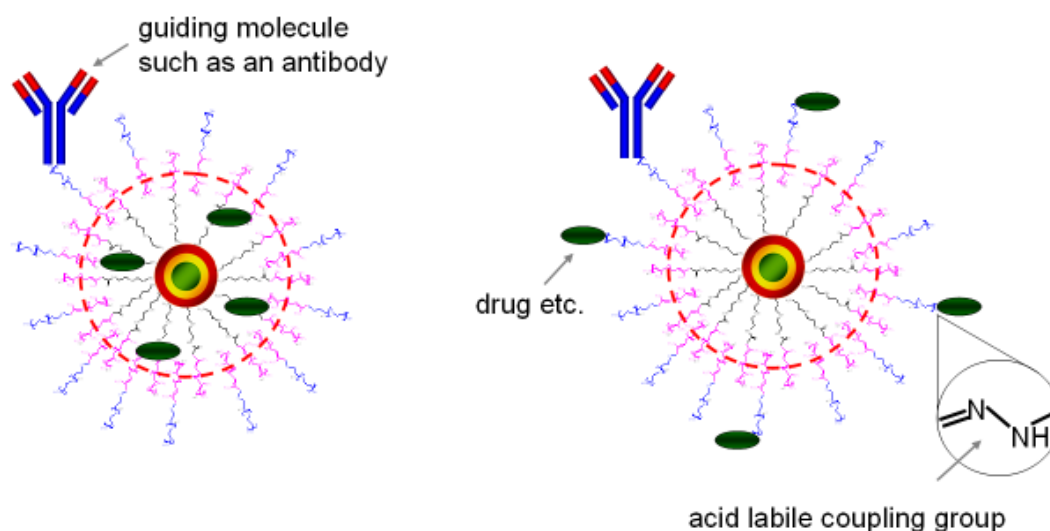
The nanocomposites had a size of 80 nm (intensity PSD application) according to dynamic light scattering (DLS) measurements. The large size and the avoidance of a crosslinkage might be the main reasons for their agglomeration in the liver. However, this effect can be reduced by reducing the size of the nanocomposites.

This experiment was just a proof of concept and was not repeated. The research group of Prof. U. Schumacher at the university hospital Hamburg Eppendorf was provided with carboxylic functionalized, crosslinked GdPO₄ nanocomposites of a size <50 nm (intensity PSD) for further biochemical uses.

2.9.5 Drug delivery systems

Occasionally, the nanoparticle-antibody system can be expanded by co-molecules like for example radioactive markers, further dyes, and even drugs. They can be coupled either to the terminal functional PEO group (chapter 2.3.1.1) or, if they are hydrophobic, ensured by the hydrophobic PI layer (schema 24). Like AIBN they can be embedded in the progress of self-assembly. Further molecules like antibodies and cell-penetrating peptides (CPPs) procure the accumulation of the drug-vehicle at the desired destination. Pujals *et al.*^[437] report the tumour cell uptake of gold nanoparticles, which were conjugated to amphipathic proline-rich peptides (sweet arrow peptides, SAP).

The guided and “safe” delivery of these biomolecules in such a drug delivery system (DDS)^[197, 438] provides access to gene therapy as well as protein-based therapeutic approaches. Such systems are known to improve solubility, *in vivo* stability, pharmacokinetics, biodistribution, and to enhance the efficacy of the attached drug^[439]. The covalent functionalisation, for example with doxorubicin (DOX), an anticancer drug, through an acid labile hydrazone linker releases the drug in the cancer tissue^[440].



schema 24: drug delivery system.

The adjustability of the size allows the formation of multifunctional micelles with sizes smaller than 40 nm. Promising drug delivery vehicles of immunoliposome-antibody conjugates, which were loaded with quantum dots, have in contrast diameters of 212 ± 32 nm in size distributions measured by dynamic light scattering^[434].

As an often intravenously applied cytostatic drug, cisplatin is an effective chemical compound to treat various types of cancers. Cellular uptake results from passive diffusion and active transport by the copper transporter Ctr1P^[441], after which intracellular hydrolysis of the prodrug occurs. Cisplatin (cisplatinum) inhibits DNA syntheses by chelating two bases, in preference with the nucleophilic N-7 positions of the purine bases adenine and guanine, upon displacement of the previous ligands^[442, 443]. This leads either to a DNA adduct, if the lesion affects just one DNA strand, or to a DNA cross-link. The main adduct is a 1,2 intrastrand-d(GpG) cross-link^[444]. Also interference with cell division by mitosis occurs. The activation of apoptosis is procured in turn via the elicitation and failure of DNA repair mechanisms^[445, 446]. Side effects are nephrotoxicity (kidney damage), neurotoxicity (nerve damage), ototoxicity (hearing loss), alopecia (hair loss), electrolyte disturbance, nausea, and vomiting. Next to the mentioned toxic effects cisplatin resistance can emerge. Proposed mechanisms include changes in cellular uptake and efflux, as well as increased detoxification of the drug, inhibition of apoptosis and increased DNA repair^[446, 447].

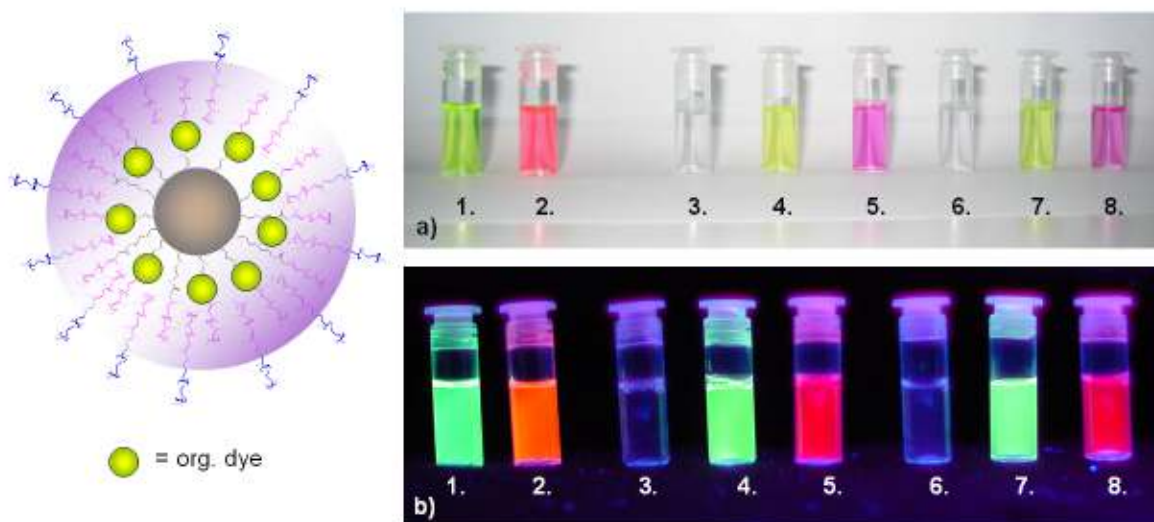


figure 129: GdPO₄ (3-5) and NaYF₄ (6-8) nanoparticles encapsulated via PI₆₁-*b*-PEO₂₁₂-OH (QD/L 1:300) in the presence of nile red and hostasol yellow in water. (a) under daylight, (b) under UV excitation).

1. hostasol yellow dissolved in THF; 2. Nile red dissolved in THF; 3. GdPO₄ nanoparticles in PI₆₁-*b*-PEO₂₁₂-OH micelles in water; 4. GdPO₄ nanoparticles and hostasol yellow in PI₆₁-*b*-PEO₂₁₂-OH micelles in water, 5. GdPO₄ nanoparticles and nile red in PI₆₁-*b*-PEO₂₁₂-OH micelles in water, 6. NaYF₄ nanoparticles in PI₆₁-*b*-PEO₂₁₂-OH micelles in water; 7. NaYF₄ nanoparticles and hostasol yellow in PI₆₁-*b*-PEO₂₁₂-OH micelles in water, 8. NaYF₄ nanoparticles and nile red in PI₆₁-*b*-PEO₂₁₂-OH micelles in water.

To evidence lower toxicity and diminishment of incidence of cisplatin resistance conditional upon the exigency of smaller dosages by the administration of specific “guided” cisplatin^[444], a diamminoplatinmalonat (a carboplatin-analoga) was introduced to the PI-*b*-PEO ligand (chapter 2.3.1.1.3). Carboplatin shows a reduction of nephrotoxicity, while the activity of the mono- and diaqua complexes is comparable with cisplatin^[448], and has additional uses as an

intracavitary chemotherapeutic agent and as a radiosensitizer^[449, 450]. The stronger binding of the leaving group to platinum(II) decreases for cisplatin-analoga plasma protein binding and increases renal elimination^[444].

The thymidine analogue zidovudine (INN), also called azidothymidine (AZT) represents a nucleoside reverse transcriptase inhibitor (NRTI). This type of antiretroviral drug combined with cisplatin enhances cytotoxicity and oxidative stress in human head and neck cancer cells via a thiol-dependent mechanism^[451]. Zidovudine could be therefore converted into a PI₆₁-*b*-PEO₂₁₂-ester analogue by DCC/DMAP coupling strategy (chapter 2.3.1.1.3).

Hydrophobic organic molecules are simultaneously assembled in the micelle. This effect can be visualized with organic dyes, which show no solubility and emission in water. GdPO₄ (CAN08-0040) and NaYF₄ (CAN-BAY-0711) nanoparticles were both embedded in the hydrophobic segment of PI₆₁-*b*-PEO₂₁₂-OH micelles in combination with the organic compounds Nile red and hostasol yellow. Such hydrophobic organic dyes are not soluble in water. In figure 129 the solutions shown are the aqueous solutions. The luminescence of the organic compounds is predicated on the presence of the dye in the hydrophobic segment of the micelles.

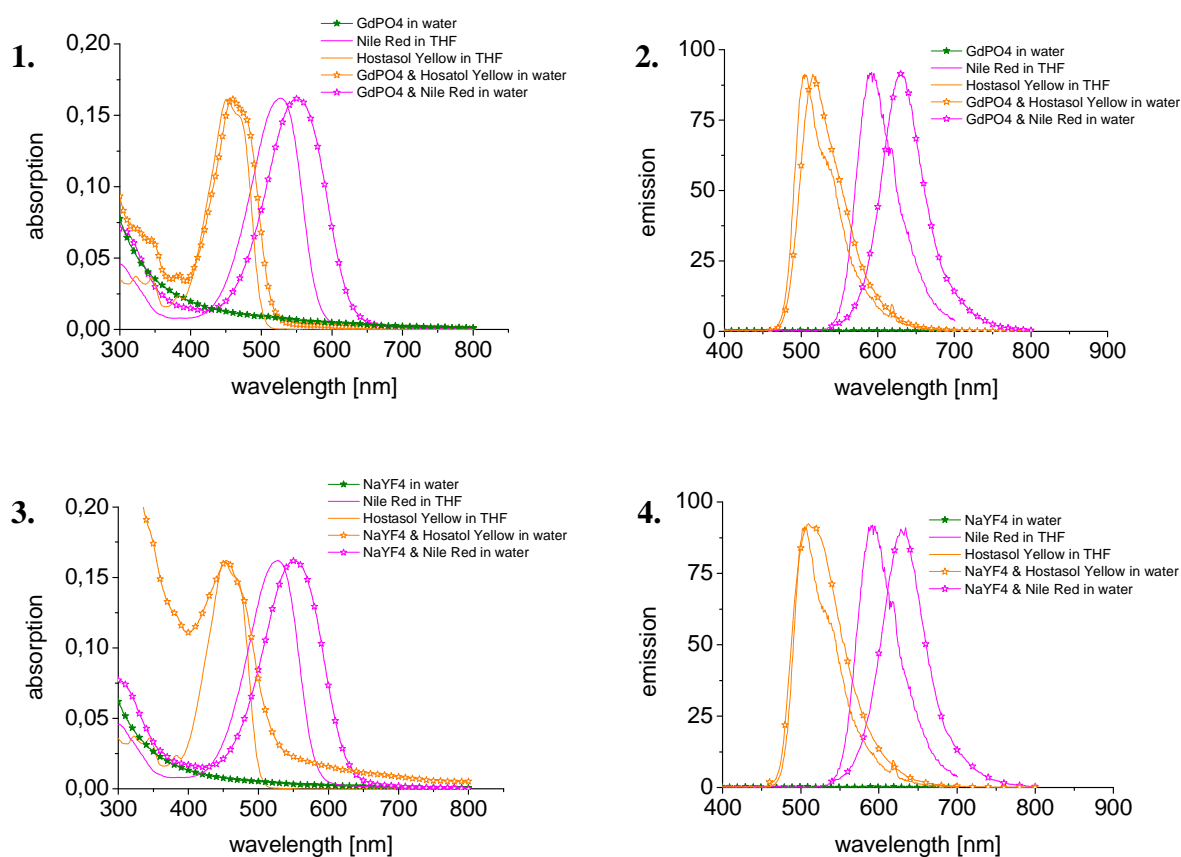


figure 130: Absorption and emission spectra of GdPO₄ (1. & 2.) and NaYF₄ (3. & 4.) encapsulated in PI₆₁-*b*-PEO₂₁₂-OH (QD/L 1:300) in the presence of Nile red and Hostasol yellow in water. The absorption and emission spectra of the used dyes in THF are also shown.

The corresponding absorption and emission spectra of the nanoparticle and organic dye containing micelles in water are shown in figure 130. A red shift of the emission and absorption maxima of the organic dyes was detectable and can be ascribed to the micellar environment in the presence of the nanoparticles.

The results verify the feasibility to co-encapsulate further hydrophobic molecules. Hence, on the one hand drug-delivery systems and on the other hand multitargeting using other molecules, such as radioactive compounds, can be established.

2.9.6 Multi-targeting

For *in vivo* imaging distinct documentation of the location of nanoparticles in spite of a high background is essential. The parallel detection of nanoparticles, using different analysis methods, is a chance to provide objective evidence that a signal can be assigned to nanoparticles. The co-encapsulation of different kind of nanoparticles in one micelle like it's been shown in chapter 2.1 and chapter 2.5 is hereby beneficial. Two different sizes of quantum dots for example permit fluorescence intensity multiplexing^[452]. The coencapsulation of nanoparticles like GdPO₄, a T1 contrast agent, and hydrophobic dyes (see chapter 2.9.5) is also an example for a multidiagnosable nanocomposite. Position emission tomography (PET) isotopes such as ¹¹¹In or ⁶⁴Cu, which emit gamma rays from their decay, could be used for trimodal imaging. Such radioactive compounds or radioactive nanoparticles (containing for example the radioactive isotope ⁵⁹Fe) can also be co-encapsulated.

Another perspective is the attachment of hydrophilic molecules on the micelle surface. Functional groups grant the appending of further analytical compounds like organic fluorophores, radioactive markers, and drugs. An example is the equipment of SPIONs with the organic dye Alexa Fluor® 594 by using the ligands PI₆₁-*b*-PEO₂₁₂-OH and PI₆₁-*b*-PEO₂₁₂-Alexa Fluor® 594 in a 10 to 1 ratio. The obtained solution and an illustration of the nanocomposites are shown in figure 131.

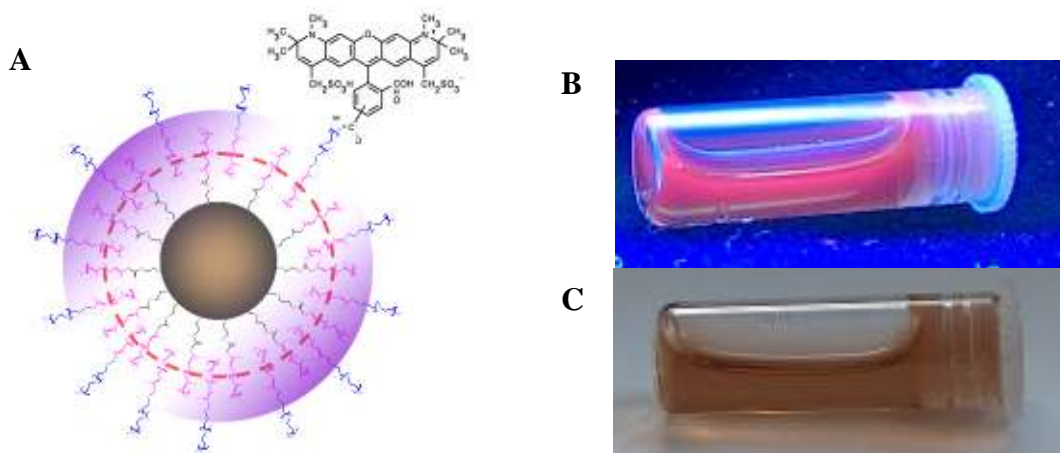


figure 131: SPIONs with a PI_{61} - b - PEO_{212} -OH and PI_{61} - b - PEO_{212} -Alexa Fluor® 594 (ratio 10 to 1) coating in water. **A** illustration, **B** under UV excitation, **C** at day light.

In this context, it has to be mentioned that different nanoparticles can also be coupled to each other. The PEO based polymer ligands offer various functional groups to achieve the syntheses of such substructures. Concerning multimodal imaging, the combination of MRI and optical imaging was achieved by EDC/sulfo-NHS coupling of magnetic FeO_x nanoparticles, coated with PI_{61} - b - PEO_{212} - NH_2 , to CdSe/CdS/ZnS quantum dots, coated with PI_{61} - b - PEO_{212} - NH_2 , were coupled to CdSe/CdS/ZnS quantum dots, coated with PI_{61} - b - PEO_{212} -COOH. In figure 132 are TEM images of the obtain QD- FeO_x -nanocomposites shown.

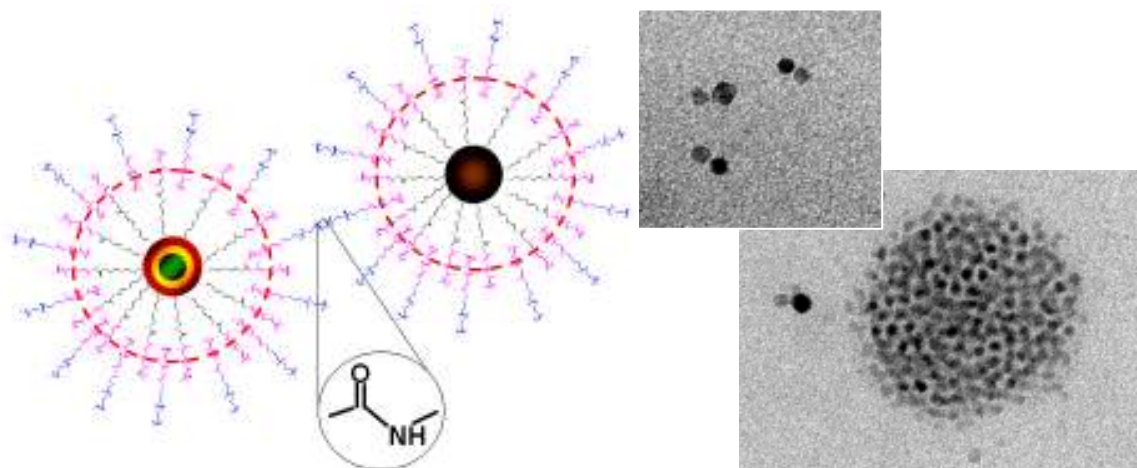


figure 132: QD- FeO_x -nanocomposites.

The efficacy of the coupling reaction was clarified by coupling gold nanoparticles to quantum dots. In cooperation with Dr. Neus Gomez Bastus, carboxylic functionalized gold nanoparticles were coupled with amino functionalized CdSe/CdS/ZnS nanoparticles. Results are shown in figure 133. In the absence of EDC/sulfo-NHS the gold and CdSe/CdS/ZnS nanoparticles are

distributed over the grid. In the process of increasing the amount of EDC/sulfo-NHS from 0/0 over 2 eq/1 eq up to 10 eq/ 5 eq an agglomeration is observable. This is due to the activation of more than one carboxylic group per gold nanoparticle.

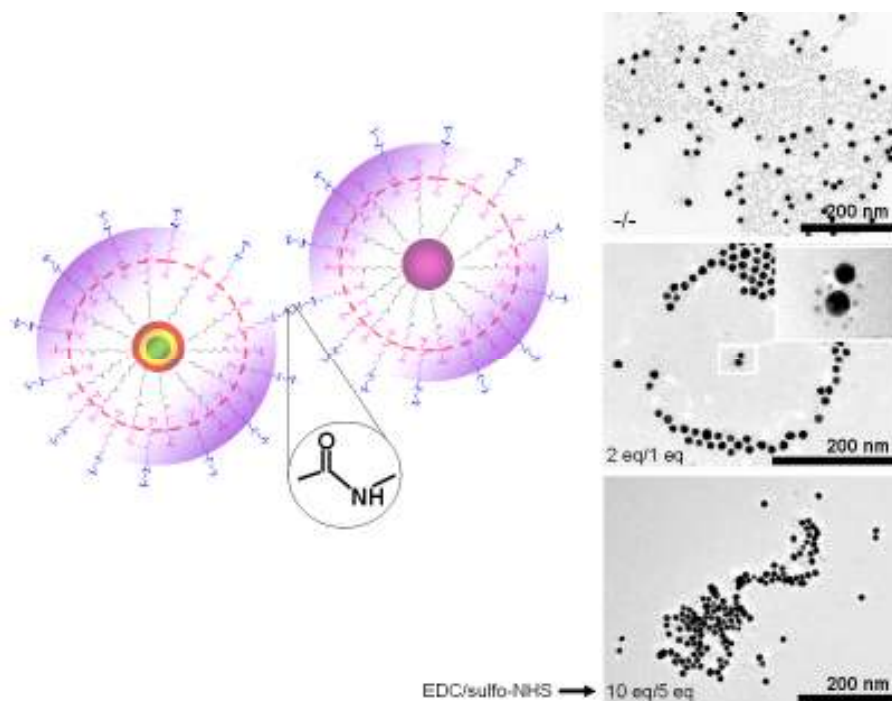


figure 133: QD-gold-nanocomposites.

The results, in combination of the results of the FRET measurements, (2.4.4 and 2.5.6) are valuable for the production of FRET based biosensors^[168, 453]. An approach of Chang *et al.*^[454] is the use of quantum dots bound to gold nanoparticles via a proteolytically degradable peptide sequence. Upon enzymatic proteolysis of the peptide linker, the quenching of the quantum dot is abrogated. Admittedly, for such conceivable *in vitro* and *in vivo* applications is the exploration of the effects of such nanocomposites on living organisms required.

3 Conclusions

This study deals with aspects around the use of nanoparticles for biomedical applications. Herein some of the main results and possible extensions of some of the problems addressed in the previous chapters are concluded. Although specific conclusions are presented along the work, here are a compilation of those presented, which are considered to be most relevant.

3.1 Ligand shell

In this doctor thesis, variants of promising, polymer based ligand coatings are disclosed, which show remarkable robustness, versatility, and perpetuation of physical properties of nanoparticles, opening manifold simultaneous appendages for further functionalisation strategies. The work comprises ligand synthesis and exchange procedures, regarding the nanoparticle coating, as well as functionalisation strategies. Multifarious modification strategies with further functional groups could be demonstrated, which allow manifold coupling strategies to couple molecules onto the ligand. They effect the arrangement of multilateral micellar structures up to substructures. Methods for scaling-up of the coating procedure are been demonstrated by emulsion polymerisation all the way to in vitro and in vivo applications of nanoparticles.

Ligand-systems were evolved based on poly(ethylene oxide) (PEO), which minimizes non-specific adsorption and allows conjugation of enzymes and other biomolecules with preservation of their biological activity^[90, 91]. By attachment of a binding motif like a Lewis base (e.g. amine, thiols) to PEO, the polymer can coordinate to the nanoparticle surface and a ligand is created.

The PEO-NH₂/-SH ligands suffer from instability. Due to the low binding strength of the Lewis base and the hydrophilic properties the attachment-detachment equilibrium of the ligand on the nanoparticle surface shifts to the detachment side by dilution. Changes on the ligand, which can also be nanoparticle-catalysed, intensify the shift. Consequently the contact with water occurs, which can minimize the nanoparticle properties and lead to agglomeration. Ligands with just one amine or thiol group showed an especially low binding affinity to CdSe/CdS/ZnS quantum dots. It has been presumed that the sulphur atoms of the outer ZnS shell dominate at the surface.

To stabilize the ligand shell, the detachment of ligand has to be impeded. This can be achieved by increasing the binding strength of the ligand to the nanoparticle surface. One option is the presence of more than one binding group per ligand, what allows a multi-binding. Another possibility is the modification of the nanoparticle surface. The outer ZnS shell-thickness was increased to stabilize the quantum yield, and zinc-precursor was added after H₂S was removed from the CdSe/CdS/ZnS nanoparticle synthesis. Therefore the quantum dots exhibited more atoms, which can coordinate ligands with Lewis bases.

The ligand-disposition can be further compounded by ligand-ligand interactions. A hydrophobic ligand-segment allows complex interaction with other ligands and the nanoparticle surface as well as the prior stabilizers from nanoparticle synthesis. An insertion of the hydrophobic segment between the ligand segment responsible for water-solubility and binding motif bears the trait to shield the nanocrystal surface from water. Furthermore the ligand-coating gets more robust, which is reflected in the stabilization of quantum yield in buffer solutions and minimisation of the cytotoxicity of particles. The most stable ligand shell is accordingly a covalent crosslinked shell, which achieves a cage around the nanoparticle.

Ligands, which consist of a hydrophobic and hydrophilic block show amphiphilic character. The ligand exchange as customary, which involves the precipitation of nanoparticles to remove the prior ligands from nanoparticle synthesis, had to be modified. Thus, the ligand-coating of nanoparticles was achieved by self-assembly of the ligands in the progress of water-transfer. This “ligand addition” procedure is controllable and has the advantage that the process can be up scaled and automatated, because the nanoparticles stay in solution continuously. The nanoparticle to ligand ratio, the concentration of the nanoparticle and ligand solution previous to the water addition, pH, temperature, and the speed of the water addition are options to control the micellar assembly. Supplemental hydrophobic molecules can be co-encapsulated.

The formation of micellar structures via *branched-PEI-b-PCL-b-PEI* triblock polymers facilitates not only the transfer of hydrophobic nanoparticles like TOP/TOPO coated CdSe/CdS/ZnS^[403] in aqueous solution, but also accomplishes high rigidity of the nanocomposite. The multi-dentate poly(ethylene imine) (PEI) binding motif provides higher binding strength to the nanoparticle surface, while the hydrophobic poly(ϵ -caprolactone) segment (PCL) leads to hydrophobic interactions and hydrogen bonding of the PCL ester with the amines of PEI (figure 121). Thus a high stability of the ligand coating is generated. At the same time, the polymers can bear protected functional groups for coupling reactions, which are shielded from nanoparticle surface due to the hydrophobic shielding of the nanoparticle.

In addition to the strategy of emulsion polymerization^[455] this method accomplishes a simple and versatile strategy to achieve water-solubility of nanoparticle.

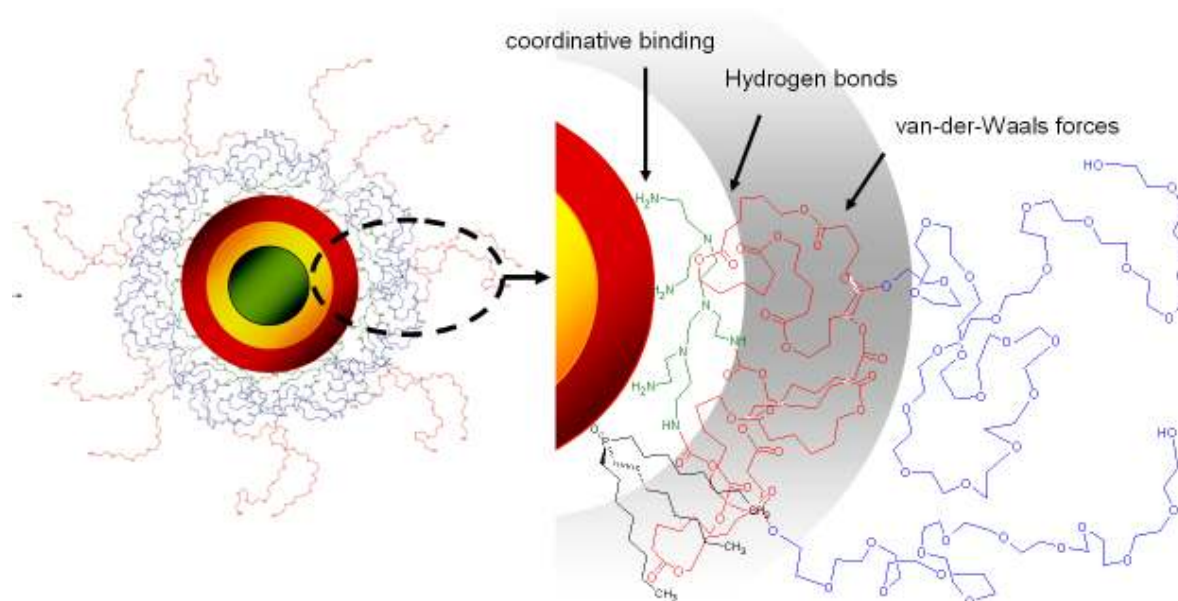


figure 134: interaction of PEI-*b*-PCL-*b*-PEO on nanoparticle surface.

A further improvement was the design of a duplex, covalent crosslinkable ligand-system. The system combines the coordinative binding of an amino-functionalized poly(isoprene) preligand (PI-N3), hydrophobic encapsulation in an amphiphilic poly(isoprene)-*block*-poly(ethylene oxide) (PI-*b*-PEO) ligand, and crosslinkage. The interactions are illustrated in figure 135. They achieve a stabilization of the ligand and extract the ligand from the equilibrium between attachment and release.

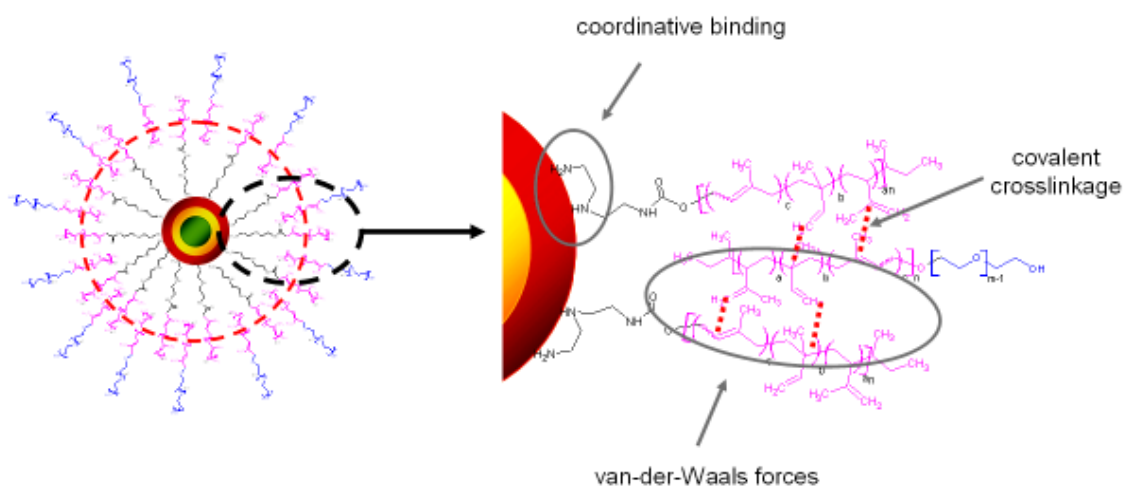


figure 135: interaction of PI-N3 and PI-*b*-PEO ligands on nanoparticle surface.

The large PEO block with a mass of > 6000 g/mol achieves a high water solubility and biocompatibility, while the inner, rigid, hydrophobic shell protects the nanoparticles against contact with the outer medium. Thus, the new ligands conserve the physical properties of the nanocrystals, among preservation of flexibility of the outer PEO shell. The use of the amphiphilic ligand permits not only the encapsulation of nanoparticles but also the co-encapsulation of hydrophobic molecules (e.g. drugs, further nanoparticles) as well as the formation of “empty” micelles.

3.2 Emulsionpolymerization

Emulsionpolymerisation allows the upscaling and simplification of the ligand exchange. This technique has attracted interest in a wide variety of industries such as coatings, adhesives, biomedicine, and biotechnology^[116, 134, 135]. Coming from classical microemulsions using SDBS as emulsifier it could be demonstrated that with this technique a dense shell can be built up, which offers competitive results in comparison with classical ligand systems. To force the properties concerning water stability surfmers were implemented to make sure that desorption of emulsifier and therewith loss of water stability cannot occur even in highly diluted systems. For Tween[®]80 it could be shown exemplarily, that transformation of the functional groups can be achieved, fitting for almost every coupling requirement.

In contrast to other nanoparticles, quantum dots are affected due to the presence of stabilizers in monomer solutions or due to the contact with water. Therefore a high degree of inorganic passivation is necessary. A further pre-ligand can to stabilize the quantum yield in the process of polymerization.

3.3 Functionalisation of the ligand shell

For biofunctionalisation of nanoparticles, functional groups are required, which are accessible from the aqueous phase. Such are e.g. carboxylic groups and amines. Such terminal groups can lead to an inter- or intraparticulate crosslinkage. Hence, a hydrophobic or crosslinked shielding from the nanoparticle surface is essential.

The PI-*b*-PEO block copolymer features just one nucleophilic group, by virtue of the lack of an anchor group, giving a competitive edge for further functionalisation. The hydrophobicity of the inner crosslinked hinders the binding of the new functional group (e.g. NH₂, COOH) on the surface of nanoparticles, while the persistency of the ligand coating ensures the disposition of the ligand. This is important, when further molecules like antibodies or dyes are to be attached.

3.4 Integretion and coupling of (bio-)molecules

Due to the assortment of functional groups of the ligands routine coupling procedures can be used to provide nanoparticles with antibodies, carbohydrates, DNA- & RNA-fragments, drugs or other chemical molecules.

Depending on the chemical characteristic of the molecule the coupling can be arranged not only after the ligand exchange, but also preceding. The attachment of dye molecules previous to the ligand exchange with PI-*b*-PEO and following FRET measurements demonstrated the presence of the new molecule at the micelle surface and verify the density of the shell. FRET measurements were also conducted to specify the density of the polymer shell induced by emulsion polymerization. The results correspond with TEM images and confirm the excellent quality of the polymer shell. To provide evidence that an attached molecule is accessible, Biacore measurements were run with nanocomposites offering carbohydrates on the surface. Results show the accessibility of the presented molecule on the micelle surface.

In case of coupling after the formation of the nanocomposites, an excess of ligand, which also offers functional groups has to be avoided or rather minimized. The ligand systems, presented in this doctor thesis show the benefit that they can be used in a ratio of 1 to 50 up to 1 to 400. Thus, the excess of ligand is low. In case of the coupling of molecules which can lead to a crosslinkage, because they bear more than one functional group, they have to be used in an excess. This can be seconded by reducing the amount of functionalized ligand by using a mixture of un- and functionalized ligand in the process of ligand exchange.

For antibody labelling, EDC/sulfo-NHS coupling^[219] under sterile conditions was adopted, since the educts and side products of EDC/sulf-NHS activation show a low toxicity. But due to the steric hindrance and the accessibility of the lysine at the antibody surface a low reaction yield of approximately 20% was observed. The increase of EDC/sulf-NHS to > 5 eq. per nanocomposite can lead to a crosslinkage between antibodies and nanocomposites. This

entails a far lower blood circulation time in *in vivo* experiments and the agglomeration in organs such as liver and lung. An approach could be a lys-taq at the Fc part of the antibody. The presence of too many uncoupled nanocomposites can be avoided by two to threefold repeat of the activation procedure. Also the prior binding of the antibody to immobilized antigen can avoid the peptide coupling to the antigen binding domain of the antibody, which would have a negative influence on the binding ability of the antibody.

An alternative approach could be the conversion of terminal amines to diazonium ions, which react in aqueous media with tyrosine and histidine. Those amino acids are rare and the simple attachment of a his-tag to a protein offers a control of the binding site.

Uncoupled antibody must be removed completely because of its higher binding affinity, which would block antigen binding sites. This can be done via dialysis or in case of SPIONs via purification using a magnet.

Anti-YKL-40 antibodies, labelled with SPIONs and quantum dots, were used in *in vivo* applications and could be detected in the tumour tissue. Their long circulation time due to low unspecific interactions was remarkable and of high significance for targeting approaches, where a long disposition in the bloodstream is fundamental.

3.5 *in vivo* applications

Not only the reduced disposition of ligand, but also the thick and dense PEO shells reduce the toxic effects of nanoparticles on cells. Several cytotoxicity tests indicated a low toxicity of the nanoparticles, which are securely encapsulated in a PEO shell.

Many research groups found cytotoxicity to be dose dependent^[67, 337-339]. The ligand systems presented in this doctor thesis realise the feasibility to use low concentration of e.g. antibody-nanoparticle nanocomposites in *in vivo* applications, contingent upon the preservation of the antibody and its specificity. Consequently the cytotoxicity is further diminished.

These satisfying results and the evidence of the preservation of antigen-specificity in the progress of antibody-coupling (anti-CEACAM specific SPIONs) next to the non-appearance of unspecific interactions marked the cornerstone for *in vivo* applications of antibody containing nanocomposites. The potential of the ligands to cluster SPIONs was adjuvant, since the detectability was higher in case of clusters with a diameter of >40 nm. Quantum dots proved to be conducive when they are used in combination with other labels e.g. SPIONs. The

in vivo experiments indicate that they can be applied in combination with SPIONs. A coupling or coencapsulation of QDs and SPIONs seems to be not necessary.

3.6 Properties of nanoparticles

The versatility of the different ligand systems could be asserted with a wide range of different nanoparticles. In case of quantum dots like CdSe, CdTe and InP, a high degree of inorganic passivation is necessary to gain high and stable quantum yields and to lower the cytotoxicity. At a thickness of the ZnS shell of more than three atom layers a small reduction of the quantum yield in case of CdSe is discussed in literature. However, on such quantum dots THF has no influence, which serves as solvent for the transfer to water.

The ligand systems achieve the stabilization of any hydrophobic quantum dot. Thus a wide bandwidth of emission-wavelength can be permitted by the choice of the appropriate quantum dots (figure 136).

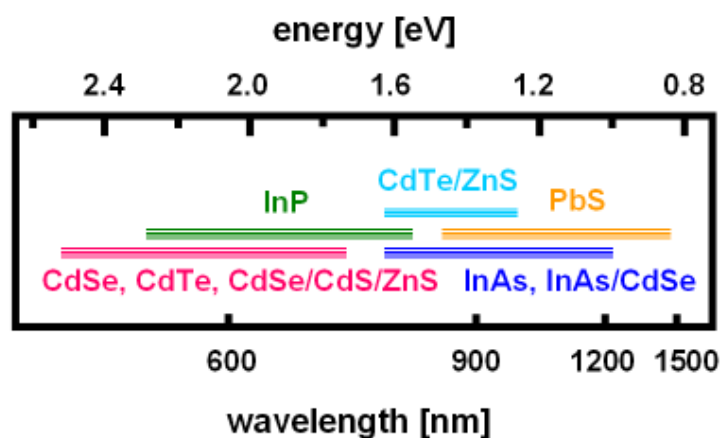


figure 136: overview of the emission-wavelength of different quantum dots.

It was also verified with NaYF₄, GdPO₄, PbS, Au, FePt, FeO_x, and NiPt_x nanoparticles very satisfying (schema 25, 1.). In summary, any hydrophobic nanoparticle can be encapsulated and functionalized by this method. It isn't constrained by the shape of the nanoparticle. The transfer from an organic solvent to water is also possible with rods, dots, tetrapods, tubes a.s.o..

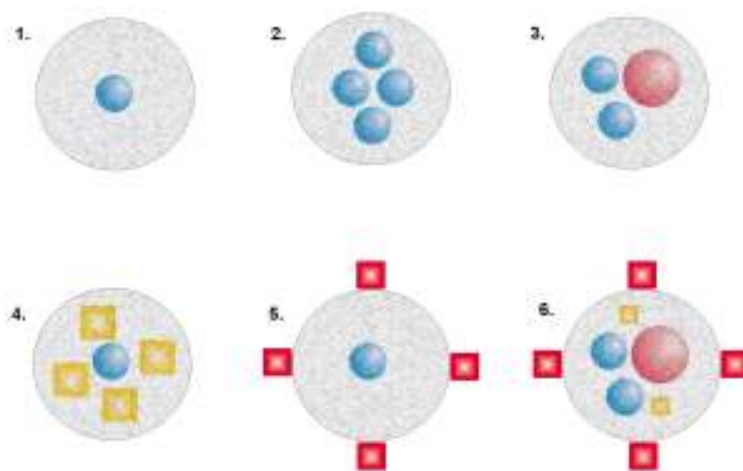
Quantum dots showed to be applicable especially in *in vitro* experiments. Also *in vitro* experiments are fundamental and necessary previous to *in vivo* applications. Due to the

universalism of the ligand shell the quantum dots can be changed against any other nanoparticle like for example SPIONs. In *in vivo* experiments the use of quantum dots in combination with SPIONs proved to be an interesting application.

3.7 Self assembly to multifunctional beads

For *in vivo* imaging, the simultaneous use of different diagnostic methods is beneficial. Arising from the multitude of ligand-interactions with the nanoparticle and its hydrophobic ligand shell the developed ligands can coencapsulate more than one nanoparticle (schema 25, 2.) as well as different nanoparticles (schema 25, 3.) and further hydrophobic molecules (schema 25, 4.) in one micelle in a controllable manner.

The combination of QDs and SPIONs results in a decline of the quantum yield. Pre-ligands, which increase the distance of the clustered nanoparticles, are convenient to prevent a loss in fluorescence.



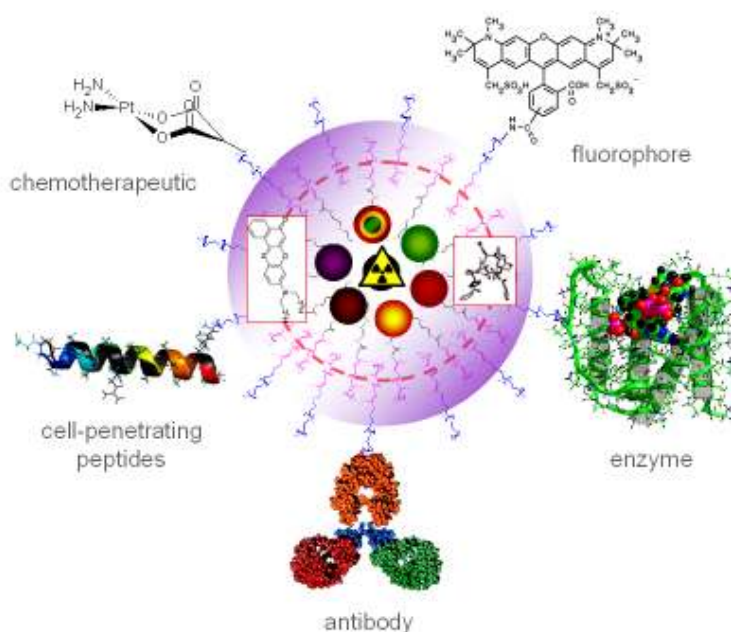
schema 25: illustration of nanocomposites.

1. nanocomposite containing one nanoparticle; **2.** nanocomposite containing clustered nanoparticles; **3.** nanocomposite containing different nanoparticles; **4.** nanocomposite containing nanoparticle and further hydrophobic molecules; **5.** nanocomposite with attached hydrophilic molecules; **6.** nanocomposite containing different nanoparticles and hydrophobic molecules and attached hydrophilic molecules.

Either via protected functional groups during polymerisation or later functionalisation strategies, ligands and emulsion particles were expanded by functional groups, which in turn allowed a plurality of coupling strategies for the attachment of further molecules (schema 25, 5.). The transferability of the developed ligands to various nanoparticles opens a potential and manifold way to implement nanoparticles in biological systems. The insertion of diverse

nanocrystals in one micelle and further modifications allow the architecture of multifaceted composites (schema 25, 6.) and the formation of nanoparticle substructures like diverse linked nanoparticles. Thus, SPIONs and QDs can be coupled with a distance of >10 nm, which minimizes the loss in quantum yield.

The potential to implement chemical molecules in the hydrophobic segment (schema 25, 4.) or in the hydrophilic PEO segment (schema 25, 5.) to convey them unaffected from the blood serum to the target region is feasible. Combinations of both approaches achieve nanocomposites, which merge detection possibilities (schema 25, 6.).



schema 26: garnished nanocomposite for multi-diagnoses and drug delivery.

Multiple diagnostic imaging applications such as multiplexing, PET, MRI and drug delivery systems, which e.g. can be guided in a magnetic field in case of integrated SPIONs, have a great potential in medicine. The package and tailored transport can be used even for gene therapy.

4 Zusammenfassung

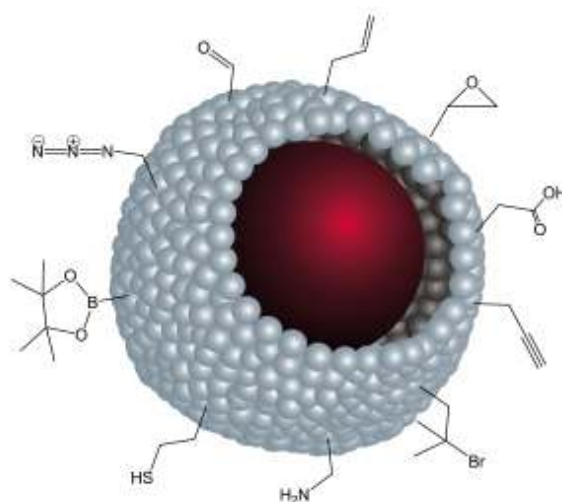
Unter dem Begriff Nanoteilchen werden Strukturen wie z.B. Metallcluster zusammengefasst, die in der Größenordnung von 1 bis 100 nm liegen. Aufgrund ihrer diskreten Anzahl an Atomen verfügen sie über einzigartige, größenabhängige, optische, magnetische und elektronische Eigenschaften. Ihre geringe Größe und das daraus folgende Volumen zu Oberflächen Verhältnis führt allerdings zu einer thermodynamischen Instabilität. Eine kinetische Stabilisierung wird durch Liganden erzielt, die an die Oberfläche der Nanoteilchen koordinieren und infolge einer Agglomeration entgegenwirken. In der Synthese von Nanoteilchen sind sperrige Liganden meist hydrophoben Charakters für ein kontrolliertes Wachstum verantwortlich.

Zu den Anwendungsbereichen von Nanoteilchen gehört die medizinische Forschung, in der Nanoteilchen vielfältige Ansätze in der Diagnostik und Therapie ermöglichen. Für solche Anwendungen müssen Nanoteilchen unter Erhalt ihrer physikalischen Eigenschaften in wässrige Systeme überführt und stabilisiert werden. Diese sogenannte Biofunktionalisierung von Nanoteilchen umfasst auch die Ermöglichung von Kopplungsreaktionen von z.B. Antikörper(fragmenten) und zeigt gewisse Anforderungen auf das dazu dienliche Ligandensystem.

Hinsichtlich der gewünschten Bioanwendungen muss neben der Rigidität und Biokompatibilität der Ligandenschale ein hoher Grad der Abgrenzung gegen das äußere Milieu gewährleistet sein. Liganden, die ausschließlich über ein hydrophiles Fragment und eine Lewis Base („Ankergruppe“), die der Anlagerung des Liganden an der Nanoteilchenoberfläche dient, verfügen, konnten sich nicht zur Stabilisierung von Nanoteilchen in Wasser bewähren. Das Ligandengleichgewicht zwischen dem ungebundenen und gebundenen Zustand ist anfällig gegenüber Verdünnungen und wird durch chemische Prozesse, die teils auch durch Nanoteilchen katalysiert werden, auf die Seite des ungebundenen Zustandes hin verschoben. Ein solcher Verlust an Liganden hat die unmittelbare Agglomeration der Nanoteilchen zur Folge. Zwecks der Stabilisierung der Ligandenschale wurde an einer höheren Bindungsstärke des Liganden zur Nanoteilchenoberfläche und attraktiven Wechselwirkungen bishin zur kovalenten Quervernetzung der Liganden geforscht.

Diesbezüglich konnten in der vorliegenden Doktorarbeit unterschiedliche amphiphile Liganden synthetisiert werden. Als gemeinsames Strukturmotiv verfügen die hier

dargestellten Liganden allesamt über einen Polyethylenoxid (PEO) Block, auch unter der Bezeichnung Polyethylenglycol (PEG) geläufig, der aufgrund seiner Biokompatibilität und Repressionen von unspezifischen Wechselwirkungen in biologischen Medien gewählt wurde. Die terminale Funktionalisierung der Liganden wurde durch Wahl eines entsprechenden Initiators für die Initiation der Polymerisation von Ethylenoxid oder durch spätere chemische Modifikation erzielt (schema 27).



schema 27: Illustration eines Nanoteilchens innerhalb einer micellulären, nach außen hin funktionalisierten Ligandenschale.

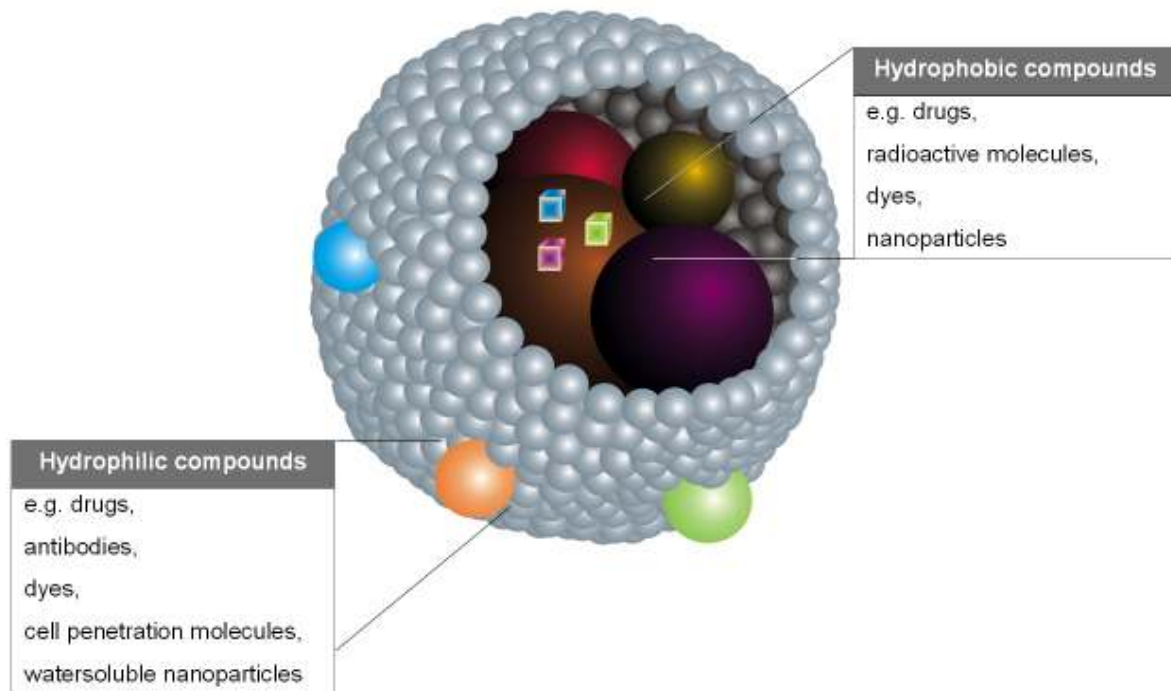
Unter den Ankergruppen zeichnete sich verzweigtes Polyethylenimin (PEI) aus, das je nach durchschnittlichem Molekulargewicht über eine hohe Anzahl an Aminen verfügt. Durch die Mehrfach-Bindung an die Nanoteilchenoberfläche konnte eine verbesserte Stabilität erzielt werden. Die primären Amine lassen sich zudem durch Carbondisulfid in Dithiocarbamate überführen, die als Ankergruppen fungieren können und aufgrund der Mesomerie-Stabilisierung im Vergleich zu einfachen Thiol-Gruppen eine höhere Stabilität gegen Oxidation besitzen. Die Oxidation von Thiolgruppen führt zur Bildung von Disulfiden, die bis auf Goldnanoteilchen keine hohe Bindungsstärken zu Nanoteilchen aufweisen.

Zwecks weitere Interaktionen, die der Stabilisierung der Ligandenschale zuträglich sind, zu ermöglichen, wurde als weiterer Polymerblock zwischen PEI und PEO Polycabrolacton (PCL) gewählt. Das somit synthetisierte Triblockpolymer zeichnet sich durch einen hohen Grad an Wechselwirkungen aus. Einerseits kommt es zu vielseitigen hydrophoben Interaktionen zwischen den hydrophoben PCL Blöcken des Triblockpolymer sowie zwischen den Triblockpolymeren und den aus der Nanoteilchensynthese stammenden Liganden, andererseits treten Wasserstoffbrückenbindungen zwischen den Aminen des PEI und den Estergruppen von PCL auf. Diese Interaktionen werden durch eine enge Packung des

hydrophoben Segments geschürt, welches die Grenzfläche zum wässrigen Millieu zu verringern trachtet. Die Integration eines hydrophoben Ligandensegments ermöglicht hierbei nicht nur Stabilisierung der Ligandenschale sondern verhindert die Diffusion von Wasser an die Nanoteilchenoberfläche.

Mittels der Kombination eines aminofunktionalisierten Polyisopren (PI) Liganden mit einem amphiphilen Liganden, bestehend aus einem PI und einem PEO Block, konnte eine Passivierung der Nanoteilchen und eine kovalente Quervernetzung der Ligandenschale bewirkt werden. Somit konnte die Beständigkeit der Ligandenschale noch gesteigert werden.

Die Ligandenanlagerung wurde durch Selbstorganisation der amphiphilen Liganden erreicht und bietet die Möglichkeit der Verkapselung unterschiedlichster hydrophober Komponenten. Somit konnten nicht nur unterschiedlichste Nanoteilchen durch die Liganden verkapselt werden, sondern auch weitere hydrophobe, organische Komponenten miteingebettet werden. Dazu gehören Fluoreszenzfarbstoffe, Wirkstoffe und radioaktive Moleküle (schema 28).



schema 28: Illustration eines Nanokomposits, welches hydrophobe Moleküle und Nanoteilchen im Inneren aufweist, während die äußere, hydrophile Schale mit hydrophilen Moleküle versehen ist.

Die vielfältigen, funktionellen Gruppen der hydrophilen, äußeren Schale ermöglichen unterschiedlichste Kopplungsreaktionen. Es konnten dadurch nicht nur hydrophile Moleküle wie Chemotherapeutika, Fluoreszenzfarbstoffe und Biomoleküle gekoppelt werden, sondern auch weitere Nanoteilchen. Aufgrund der Möglichkeit, dass hydrophobe Moleküle miteingekapselt und hydrophile Moleküle vor und/oder nach der Ligandenanlagerung

gekoppelt werden können, konnten Nanokomposite hergestellt werden, die vielfach detektierbar sind und zugleich als Vehikel für Medikamente oder für die Gentherapie dienen können (Theragnostik).

Die PI-*b*-PEO Verkapselung von Nanoteilchen wies eine sehr geringe Cytotoxizität und keine unspezifische Aufnahme von HT29 Zellen auf. Mithilfe der Modifikation der Nanokomposite durch Antikörper konnte anhand von Zellexperimenten *in vitro* das Ausbleiben von unspezifischen Wechselwirkungen dokumentiert werden. Auch in der Tumordiagnostik *in vivo* bewährten sich die Nanokomposite mit einem hydrodynamischen Durchmesser <60 nm (entsprechend DLS, Intensity PSD) durch hohe Zirkulationszeiten und konnten trotz Applikation von Mengen <100 pmol im Tumor nachgewiesen werden.

In Bezug auf Vereinfachung und Hochskalierung des Phasen-transfer von Nanoteilchen konnte die Emulsionpolymerisation mit dem Emulgator Tween[®]80 entwickelt werden. Auf diesem Wege kann die Ligandenschale von Nanoteilchen direkt in Wasser durch Polymerisation in Emulsionspartikel erzielt werden.

Somit konnte nicht nur der Medizin die Verwendung von Nanoteilchen zugänglich gemacht und Nanokomposite mit vielfältigen Eigenschaften generiert, sondern auch Möglichkeiten der Vereinfachung des Phasentransfers aufgezeigt werden.

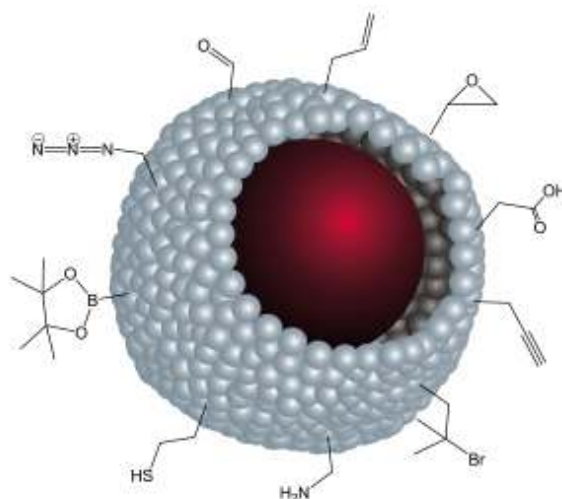
5 Summary

The term nanoparticle outlines structures such as metal clusters, which are in the size-range of 1 to 100 nm. Due to the discrete number of atoms they possess unique, size-dependent, optical, magnetic, and electronic properties. Their small size and the resulting surface to volume ratio lead to a thermodynamic instability. A kinetic stabilization is gained by ligands, which coordinate to the surface of the nanoparticle and in consequence counteract the process of agglomeration. During the synthesis of nanoparticles bulky ligands of hydrophobic character are used for a controlled growth.

To the range of applications of nanoparticles belong medical sciences, in which nanoparticles offer manifold approaches in diagnostics and therapy. For such applications nanoparticles have to be transferred and stabilized in water under preservation of their physical properties. This so called bio-functionalisation of nanoparticles includes also the activation of coupling reactions with for example antibody (-fragments) and depicts certain requirements for the appropriate ligand system.

Regarding the desired bio-application a high degree of boundary to the outer milieu next to rigidity and biocompatibility of the ligand shell must be assured. Ligands, which solely consist of a hydrophilic fragment and a Lewis base (anchor group) was not suited as stabilizers in aqueous systems. The ligand equilibrium between unbound and bound state is susceptible to dilution and can be shifted via chemical processes to the unbound state, which can partly be catalyzed by the nanoparticles. Such a loss of ligands implicates instantaneous agglomeration. For the purpose of stabilizing the ligand shell a higher binding strength of the ligand to the nanoparticle surface and attractive interactions up to covalent crosslinkage of the ligands was requested.

Concerning this matter different amphiphilic ligands could be synthesized in this doctoral PhD thesis. As common structural motif possess all here depicted ligands of a poly(ethylene oxide) (PEO) block. This polymer is also known as poly(ethylene glycol) (PEG) and was chosen, because of the high degree of biocompatibility and repressions of unspecific interactions in biological media. The terminal functionalisation of the ligands was attained by an appropriate initiator for the initiation of the polymerization of ethylene oxid or by subsequent chemical modification (schema 29).



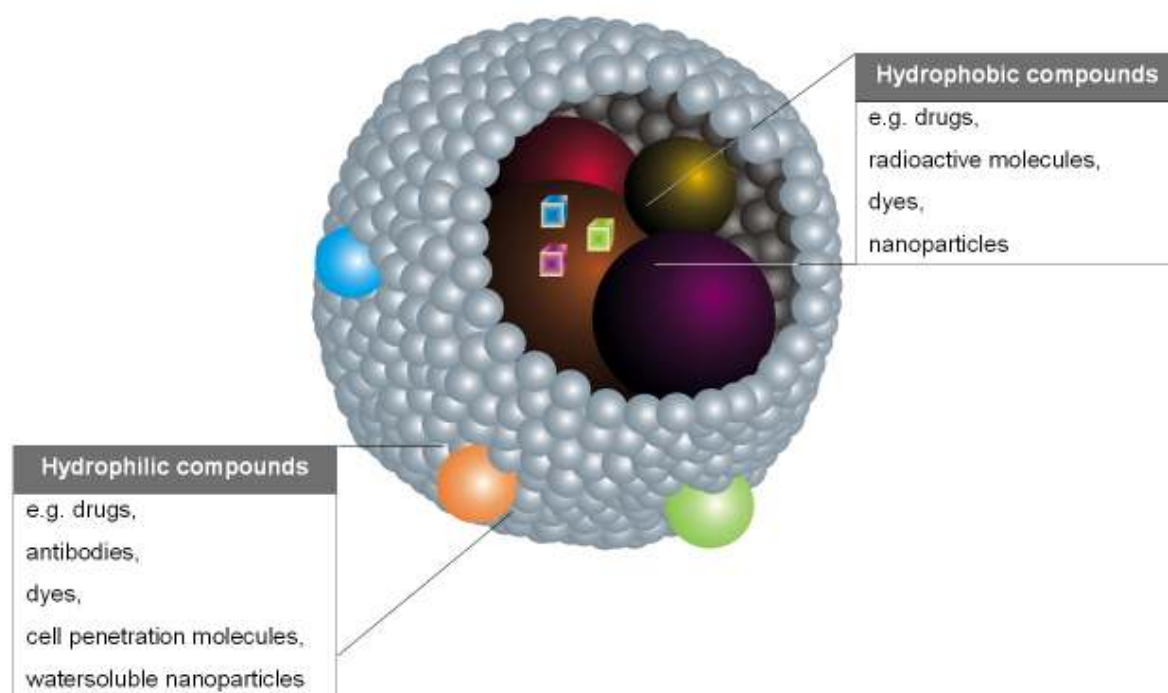
schema 29: illustration of a nanoparticle inside of a micellelike, to the outer sphere functionalised ligand shell.

Concerning the anchor group poly(ethylene imine) (PEI) shows an outstanding performance due to the high number of amines subject to its average molecular weight. As a result of multi-binding to the nanoparticle surface an enhanced stabilization of the ligand shell is achieved. The primary amines can be converted via carbondisulfid to dithiocarbamates, which function as anchor groups. Due to the mesomerism dithiocarbamates feature a higher stability against oxidation in opposite to other thiols. The oxidation of thiols leads to the formation of disulfids, which have no high binding strength to metal nanoparticle surfaces except for gold nanoparticles.

Concerning further interactions, which are beneficial for the stabilization of the ligand shell, as further polymer segment poly(ϵ -caprolactone) (PCL) was integrated between PEI and PEO. This synthesized triblockpolymer features a high degree of interactions with nanoparticle surfaces. On the one hand versatile hydrophobic interactions occur between the hydrophobic PCL blocks of the triblockpolymer with further triblockpolymers and the hydrophobic ligands from nanoparticle synthesis; on the other hand hydrogen bonds are formed between the amines of PEI and the ester groups of PCL. These interactions are forced by a dense package of the hydrophobic segments, which strive to minimize the interface to the aqueous milieu. The integration of a hydrophobic ligand segment allows hereby not only the stabilization of the ligand shell, but also circumvents the diffusion of water to the nanoparticle surface.

Using the combination of an amino-functionalized polyisoprene (PI) ligand with an amphiphilic ligand, consisting of a PI and PEO block, a passivation of the nanoparticle and a covalent crosslinkage of the ligand shell could be produced. Thus the consistency of the ligand shell was increased considerably.

The ligand attachment was achieved by self-assembly of the amphiphilic ligands and offers the possibility to encapsulate different hydrophobic compounds. Thereby not only different nanoparticles can be encapsulated, but also further hydrophobic, organic compounds co-encapsulated (schema 30). Among those organic dyes, drugs and/or radioactive molecules can be.



schema 30: illustration of a nanocomposite, which possesses inside hydrophobic molecules and nanoparticles, while the outer, hydrophilic shell is equipped with hydrophilic molecules.

The multifaceted, functional groups of the hydrophilic, outer shell facilitate various coupling reactions. Thus not only hydrophilic molecules such as chemotherapeutics, dyes and biomolecules could be attached, but also further nanoparticles. Because of the option to coencapsulate hydrophobic compounds and the possibility that hydrophilic molecules before and/or after ligand attachment can be coupled, nanocomposites could be generated, which are multiple detectable and can serve simultaneously as vehicles for drugs or gene therapy (theragnostics)

The PI-*b*-PEO packing of nanoparticles yielded in a very low cytotoxicity and no unspecific uptake by HT29 cells was detectable. Via the modification of the nanocomposites with antibodies and their application in the basis of cellincubation experiments *in vitro* the absence of unspecific interactions could be documented. Also in tumour-diagnostics *in vivo* the nanocomposites (amount of <100 pmol) with a hydrodynamic diameter <60 nm (according to DLS, intensity PSD) featured long circulation times and could be detected in the tumour.

For upscaling and simplification of the ligand exchange emulsion polymerisation using Tween[®]80 as emulsifier could be implemented. In this approach the polymer-shell is created in emulsion particles around the nanoparticles directly in water.

Accordingly manifold ways for bio-functionalisation of nanoparticles could be demonstrated, generating nanocomposites with multifaceted properties. Thereby nanoparticles could be made accessible for biochemical approaches and their applicableness expanded extensively.

6 Danksagung

Ich habe vielen Menschen für ihre Beiträge und Hilfen zu dieser Doktorarbeit zu danken. An erster Stelle ist hier **Herr Professor Dr. Horst Weller** zu nennen, dem ich für die freundliche Aufnahme in seinen Arbeitskreis, die Überlassung meines Doktorarbeitsthemas und die gewährten Freiheiten bei der Durchführung danken möchte.

Im gleichen Zuge möchte ich mich bei **Herrn Professor Dr. Stephan Förster** bedanken, in dessen Arbeitskreis ich umfangreiche Arbeiten für meine Doktorarbeit verrichten konnte und der mich dabei sehr unterstützt hat.

Frau Pakula danke ich für ihre entgegenkommende und unkomplizierte Art, mit der sie sämtliche bürokratischen Schranken überwand und trotz der vieler Arbeit immer ein offenes Ohr für mich hatte.

Mein besonderer Dank gilt **Steffen Fischer** (Arbeitsgruppe Prof. Dr. S. Förster), der mir während meiner Doktorarbeit mit Rat und Tat an der Seite stand und die PI-*b*-PEO Blockcopolymere synthetisierte, und meinem alten Schulfreund und Diplomanten **Chrisitan Schmidtke**, mit dem ich so einige produktive Labor-Wochenenden verbrachte und mir stets zur Seite stand.

Volkan Filiz und **Stephanie Domes** (Arbeitsgruppe Prof. Dr. S. Förster) gilt mein Dank für die anregenden Gespräche und stets zuvorkommende Hilfsbereitschaft. **Volkan Filiz** habe ich darüber hinaus für die Zusammenarbeit im Bereich der Vesikelverkapselung und der Funktionalisierung der PI-*b*-PEO Liganden zu danken. Hierbei möchte ich mich auch besonders bei **Martin Kehden** bedanken, der mir bei der PEO Synthese half.

Armin Tröger (Arbeitskreis Prof. Dr. W. Francke), meinem Spezialisten für alle organisch-chemischen Fragestellungen danke ich für seine kompetente Hilfe.

Dem **gesamten Arbeitskreis** von Prof. Dr. H. Weller danke ich für die Aufnahme und Mithilfe. Besonders möchte ich mich bei **Marc Thiery**, für die Gespräche im Bereich der Biofunktionalisierung von Nanoteilchen, **Ulrich Tromsdorf** für die Bereitstellung von FeO_x-Nanoteilchen bedanken, bei **Dr. Tobias Vossmeier** und **Michael Ijeh** für die Bereitstellung von Goldnanoteilchen sowie bei **Klaus Bolt**, der die vielen FRET Messungen durchgeführt hat und **Dr. Neus Bastos** für die aufmunternden und tollen Gespräche und der Zusammenarbeit im Bereich der Goldnanoteilchen. Für die schönen after-labor Abende möchte ich mich sehr bei **Sebastian Jander** bedanken.

Für die Bereitstellung von weiteren Nanoteilchen möchte ich mich unter anderem bei **Dr. Tim Strupeit** für die Bereitstellung von InP Nanoteilchen, **Constanze Schliehe** für die PbS Nanoteilchen, **Hauke Heller** für die FePt Nanoteilchen, **Ulrich Tromsdorf** für die FeO_x und **Dr. Kirsten Ahrendorf** Nanoteilchen für die NiPt Nanoteilchen bedanken.

Besonderer Dank gilt **Dr. Kathrin Hoppe** für die Einrichtung sowie Instandsetzung meines Computers, der Auswahl an zugeschickten Journals und die Einarbeitung in die IR-Spektroskopie, sowie **Sylvia Bartholdi-Nawrath** für die vielen TEM Aufnahmen und **Frank Bürli**, der bei technischen Proben mir stets hilfreich zur Seite stand.

Für die engagierte und vertrauensvolle Zusammenarbeit möchte ich meinen Kooperationspartnern dem Assistenzarzt **Dr. Kersten Peldschus** aus der Abteilung Radiologie, sowie **Johannes Salamon** und **Dr. Markus Heine** und ihrem Professor **Prof. Dr. U. Schumacher** aus der Abteilung Anatomie, sowie **Dr. Peter Nollau** aus der Abteilung klinische Chemie (Arbeitskreis Prof. Dr. C. Wagener) vom Universitätsklinikum Hamburg-Eppendorf danken, die die Zellinkubationsversuche und das Tumortargeting *in vivo* ermöglichten.

Außerdem möchte ich mich für die Zusammenarbeit und die Unterstützung im Bereich der Emulsionspolymerisation bei **Herrn Prof. Dr. H. U. Moritz**, **Dr. Werner Pauer**, **Christian Fuhrmann** und **Sascha Kappen** bedanken.

Ein weiterer Dank geht an **Dr. Herwig Berthold, Janina Möker** (Arbeitskreis Prof. Dr. J. Thiem) und **Matthias Wulf** (Arbeitskreis Prof. Dr. V. Vill), die mir Saccharide zur Verfügung stellten und mir mit Rat und Tat zur Verfügung standen.

Zu Dank verpflichtet bin ich **Anna-Winona Struck** (Arbeitskreis Prof. Dr. B. Meyer), **Sebastian Kopitzki** und **Sebastian Meinke** (Arbeitskreis Prof. Dr. J. Thiem), die mir den Zugang zu Biacore-Messungen möglich machten und hilfsbereit Rede und Antwort standen.

Meinen Dank möchte ich auch an die Mitarbeiter der CAN GmbH richten, wobei namentlich **Volker Bachmann**, der mir GdPO_4 und NaYF_4 Nanoteilchen zur Verfügung gestellt hatte, und **Dr. Thomas Frahm, Dr. Andrea Salcher** und **Charis Schlundt** die die Cytotoxizitäts-Assays durchgeführt haben.

Prof. Dr. Greg van Patten (Ohio University) danke ich für die Bereitstellung von CdTe Nanoteilchen sowie der Durchsicht meiner Doktorarbeit.

Für die viele NMR-Spektroskopie und die weiterführenden Gespräche danke ich **Herrn Dr. E. Haupt** und **Herrn Dr. V. Sinnwell**.

Melanie Bartels (Arbeitsgruppe Prof. Dr. S. Förster) danke ich für die unterhaltsamen Gespräche während der Praktikumsbetreuung.

Zu guter letzt möchte ich mich bei all meinen Praktikanten bedanken: **Hauke Kloust, Patrizia Leccese, Knut Peetz, Christian Bernstein, Conny Bothe, Jan Dilcher, Tobias Brimah, Svenja Kunze, Christopher Schulz, Christian Retusch, Alexey Petrov, Natalia Rheim, Lena Skok, Elvira Huber, Rassa Faryamman, Frederic Michelly, Ilona Kobielus** und **Stephanie Ruser**.

7 Experimental Section

7.1 Preparation of nanoparticles

Trioctylphosphine oxid (TOPO) and partially trioctylphosphine (TOP) capped CdSe/CdS/ZnS core/shell/shell nanoparticles were synthesized by methods reported previously^[249, 403]. The nanoparticles were precipitated twice with methanol to remove excess of TOPO and were stored in chloroform. Size selective precipitation was also adopted by the stepwise addition of methanol and following centrifugation. Each precipitate was stored separately.

Lanthanide phosphat nanoparticles (GdPO_4) were prepared in organic solution, containing diphenyl ether, phosphoric acid, and dihexyl ether, according to published procedures^[456]. The nanoparticle was washed in an ultrafiltration cell with a 5 kD membrane with methanol. This purification step was repeated three times. After the methanol was evaporated the dry nanoparticles were stored at room temperature. The centre of applied nanoparticles (CAN, Hamburg, Germany) placed tributyl phosphate and trioctylamine coated nanoparticles CAN08-0040, -0042, and -0043 with a diameter of 3-4 nm at the disposal.

Fe_3O_4 nanoparticles, which were coated with sodium oleate, were obtained by a ultra-large-scale synthesis^[346] and synthesis in high-boiling ether solvents^[319]. The procedure of the purification involved the same ligand exchange conformable with the purification of GdPO_4 nanoparticles.

Gold nanoparticles coated with dodecylamine were synthesized in a water and toluene two phase reaction referring Leff *et al.*^[457].

7.1.1 General preparation of CdSe/CdS/ZnS core/shell/shell nanoparticles

For the synthesis of the nanoparticles the following stock solutions were prepared in a glove box under nitrogen atmosphere:

- a) 1.58 g selenium (99.99%, ChemPur) in 20 mL tri-*n*-octylphosphine (TOP, 90%, Fluka)
- b) 0.80 g cadmium acetate (99.99%, ChemPur) in 20 mL TOP

In a 50 mL three-necked flask were 8.00 g tri-*n*-octylphosphine oxide (TOPO, > 98%, Merck) at 50 °C 12 hours and two hours at 180 °C dried and degassed under vacuum. After cooling

TOPO down to 100 °C 5.00 g hexadecylamine (HDA, > 92%, Merck) and 0.20 g *n*-tetradecylphosphonic acid (TDPA, 99%, Alfa Aesar) were added. The drying process was pursued for one hour at 120 °C under vacuum.

Subsequent 2 mL of the selenium stock solution were injected under nitrogen flow and the reaction mixture was heated up to 300 °C. Once the nucleation-temperature has been reached 3 mL of the cadmium stock solution was rapidly injected using a Hamilton syringe. Nearly simultaneous the solution was cooled down to 260 °C with a wet cloth. At this temperature the CdSe upgrowth period was maintained for 1-60 minutes, depending on the desired size of the quantum dots. After the expiration of this term the solution was quickly cooled down to 130 °C, where the temperature was kept constant for another hour.

For the growth of the CdS shell were under intermittence of the nitrogen flow at a temperature of 220 °C through a diaphragm 10 mL H₂S gas injected in 2 mL/10 minutes steps. Subsequent to a further half hour of stirring the nitrogen flow was engaged and the solution kept stirring for one hour at 130 °C.

For the last shell were either 3 mL of a 0.2 M zinc stearate/TOP or 3 mL of a 0.2 M zinc acetate/TOP solution injected. The reaction temperature was increased to 220 °C, the nitrogen flow suspended and 20 mL H₂S gas in 4 mL/10 minute steps injected. The solution was stirred for 17 hours. After 2 hours of stirring under nitrogen further 1.5 mL of the zinc stock solution was added to ensure an outer zinc layer on the nanoparticle surface. Finally after 3 hours of stirring the reaction temperature was lowered below 100 °C. Thereon, for purification 20 mL toluene were injected and side products as well as educts centrifuged. The precipitate was discarded and the solution precipitated one to three times with methanol. In case of the last precipitation addition of methanol and following centrifugation was done stepwise to achieve a size selective precipitation. Each precipitate was dissolved in chloroform, filtered through a syringe filter (PTFE, 0.2 μm) and stored separately in the dark at room temperature.

7.2 Preparation of ligands

The preparation of ligands was accomplished by synthesis of polymers and further modification.

7.2.1 PEO-*b*-PCL-*b*-PEI based ligands

The hydrophilic PEO block and the hydrophobic PCL block were synthesised via polymerisation, while PEI was purchased and coupled via CDI coupling.

7.2.1.1 Polymer synthesis

The synthesis of the PEO-PCL back-bone was achieved by catalytic ring opening polymerisation (figure 7).

7.2.1.1.1 Synthesis of poly(ethylene oxide) (PEO)

Under argon atmosphere 2.1 g naphthaline (16.0 mmol) and 567.0 mg potassium (14.5 mmol) were dissolved in 20 mL THF and stirred over night. The appropriate initiator (16.0 mmol) was added and the reaction was kept stirring for another two days. As initiator for the anionic ring opening polymerisation the following agents officiated as initiator: *tert*-butyl-3-hydroxypropionate (*t*C-), 3,3-dieethoxy-propanol (DP-), 2-methoxyethanol (M-).

To 500 mL THF and 16 mL, in a three step procedure purified, ethylenoxide in a 1 L flask 14.5 mmol of the initiator was injected and the reaction was stirred at 40 °C for three days. The purification of poly(ethylene oxide) (PEO) was achieved by precipitation of the product in diethyl ether. Analysis involved ¹H- and ¹³C-NMR, HMBC, HHCosy, HSQC, TOCSY, Maldi-TOF, SEC, FT-IR and TG measurements.

Additional a vinyl and allyl terminated PEG was purchased from Clariant Functional Chemicals.

7.2.1.1.2 Synthesis of PEO-*b*-PCL block copolymers

The diblock copolymers were synthesized by ring-opening polymerization of ϵ -caprolactone using the polyethylenoxide as a macroinitiator^[458]. Dried PEO was weighed into a dry flask and ϵ -caprolactone (different amounts according to different M/I ratios) was subsequently added. The reaction mixture was heated up to 130 °C before one drop of stannous octanoate as a catalyst was added^[231]. The polymerisation was performed for 3 h. The resulting viscous solution was rapidly cooled, upon which it solidified. The crude polymer was dissolved in dichloromethane and precipitated twice into heptane. Afterwards the product was dialysed. Analysis involved ¹H- and ¹³C-NMR, HMBC, HHCosy, HSQC, TOCSY, SEC, FT-IR and TG measurements.

7.2.1.2 Ligand synthesis

The coupling to the amines, which serve as anchor group, was achieved by activation with 1,1'-carbonyldiimidazol (CDI).

7.2.1.2.1 Synthesis of PEO-*b*-PCL-*b*-PEI

The diblock polymer was equipped with poly(ethylene imine) by activation of the hydroxylic group of PEO-PCL-OH by a fifteen fold excess of 1,1'-carbonyldiimidazol (CDI) in dry chloroform. After two hours of stirring at room temperature, the excess of CDI was hydrolysed by a twofold extraction each with 5 mL water and instant drying over sodium sulfate. The solid phase was filtered out and branched polyethylenimine with a mass of ~700 g/mol (PEO-PCL to PEI ratio 1-3 to 1) was added. The reaction mixture was stirred for five hours at a temperature of 55 °C. The product was precipitated in diethyl ether and dialysed to remove imidazole, which would prejudicial interfere with the nanoparticle surface. Finally the product was lyophilized. Analysis involved ¹H- and ¹³C-NMR, HMBC, HHCosy, HSQC, TOCSY, SEC, FT-IR and TG measurements.

Ligands with different block length and terminal groups were applied, which have the abbreviation M-PEO-*b*-PCL-*b*-PEI (1-5), *t*C-PEO-*b*-CL-*b*-PEI (6-9), DP-PEO-*b*-PCL-*b*-PEI (10-13), V-PEO-*b*-PCL-*b*-PEI (14-16), (see 2.3.4 chapter, wherein the average molecular masses of the polymer blocks are quoted). Each ligand bears on average two to three PEO-PCL chains and has a total mass of at least 6000 g/mol.

7.2.1.2.2 Synthesis of PEO-*b*-PEI and PEO-N4

One equivalent of tris(2-aminoethyl)amine was reacted with a 1.3 fold excess of CDI activated poly(ethylene oxide) monomethyl ether (M = 1100 g/mol, M-PEO₁₁₀₀, Sigma Aldrich) in dry chloroform for 12 hours at 55 °C. The product was precipitated three times in diethyl ether to remove side-products. After dialyses against water the product M-PEO-N4 (18) was subsequent lyophilized.

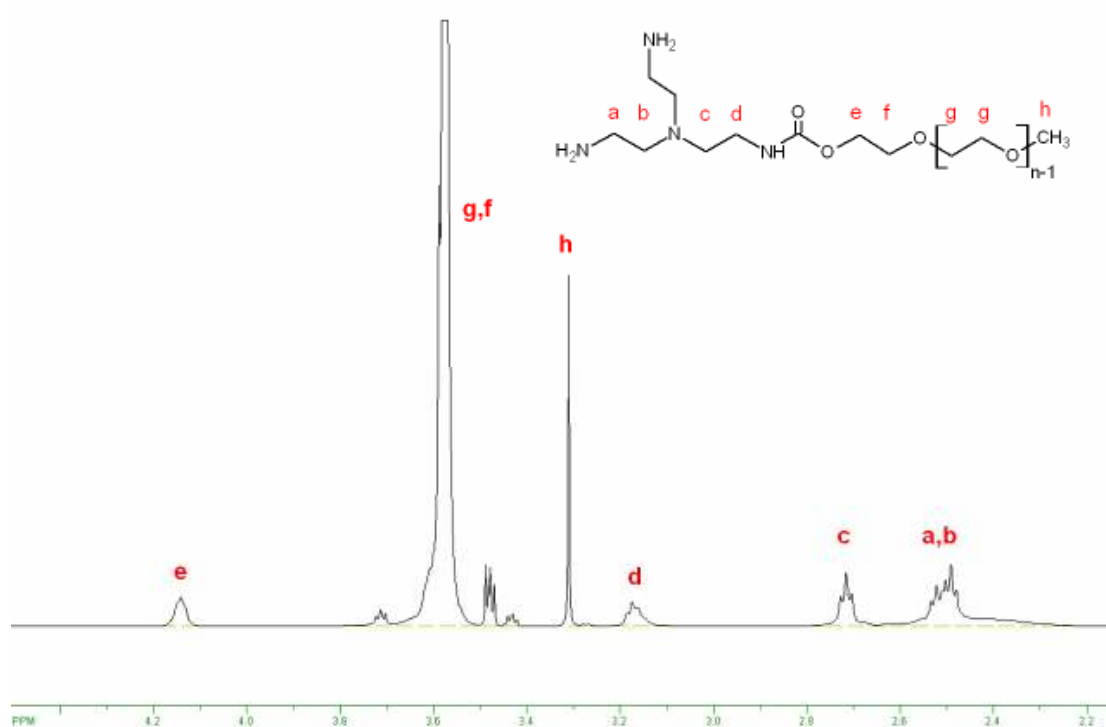


figure 137: ¹H-NMR NMR (400 MHz, CDCl₃) of M-PEO-N4.

Analogue poly(ethylene oxide) polymers (molecular weight 500 to 5000 g/mol) were coupled to polyethylenimine (PEI, 0.3 - 0.6 eq according to PEO).

7.2.1.2.3 Binding motif $R^1R^2N(-C(S)S^-)$

Ligands comprising an amine group for binding were dissolved in pure chloroform in a glove box. The solution was cooled down in the fridge of the glove box. At a temperature below 10 °C one equivalent carbon disulfide (CS_2) was added. After incubation time of 5 minutes the solution was added to the nanoparticles in the respective quantum dot to ligand ratio. The nanoparticles were transferred into the glove box as a solid. Therefore the nanoparticles had to be redissolved in dry chloroform previously. The following procedure agrees with chapter 7.2.1.3 and 7.2.1.4.

7.2.1.2.4 Binding motif PEI-(DDA)₇₋₈

Poly(ethylene oxide) monomethyl ether ($M = 1100$ g/mol, M-PEO₁₁₀₀, Sigma Aldrich) was coupled to PEI₇₀₀ in the same procedure described in 7.2.1.2.2. In dry chloroform the (M-PEO)₂₋₃-PEI product was added to a 9 fold excess of *n*-dodecylamine, which was activated with CDI (50 °C, three hours). The solution was stirred for 12 hours at 55 °C. For purification of the product M-PEO-PEI-DDA (17) was precipitated three times in diethyl ether (7 °C), dialysed against water and finally lyophilized.

7.2.1.2.5 Summary of ligands and abbreviations

Applied ligands are listed in the following tables.

M-PEO- <i>b</i> -PCL- <i>b</i> -PEI-ligands	abbreviation	
[Methoxy-PEO ₂₀₀₀ -PCL ₄₅₀] ₂ -PEI ₇₀₀	CP1 (= CP10)	1
[Methoxy-PEO ₂₀₀₀ -PCL ₆₈₀] ₂ -PEI ₇₀₀	CP2	2
[Methoxy-PEO ₂₀₀₀ -PCL ₄₅₀] ₂ -PEI ₄₂₃	CP3	3
[Methoxy-PEO ₂₀₀₀ -PCL ₆₈₀] ₂ -PEI ₄₂₃	CP4	4
[Methoxy-PEO ₅₀₀₀ -PCL ₁₇₀₀] ₁ -PEI ₇₀₀	CP5	5

table 3: synthesized M-PEO-*b*-PCL-*b*-PEI-ligands.

<i>t</i> C-PEO- <i>b</i> -PCL- <i>b</i> -PEI-ligands	abbreviation	
[<i>tert</i> -butylcarboxyl-PEO ₈₀₀₀ -PCL ₅₇₀] ₂ -PEI ₇₀₀	CP6	6
[<i>tert</i> -butylcarboxyl-PEO ₈₀₀₀ -PCL ₅₇₀] ₂₋₃ -PEI ₇₀₀	CP7	7
[<i>tert</i> -butylcarboxyl-PEO ₈₀₀₀ -PCL ₉₀₀] ₂ -PEI ₇₀₀	CP8	8
[<i>tert</i> -butylcarboxyl-PEO ₈₀₀₀ -PCL ₉₀₀] ₂₋₃ -PEI ₇₀₀	CP9	9

table 4: synthesized *t*C-PEO-*b*-PCL-*b*-PEI-ligands

DP-PEO- <i>b</i> -PCL- <i>b</i> -PEI-ligands	abbreviation	
[3,3-Dieethoxy-propanyl-PEO ₁₆₀₀ -PCL ₄₀₀] ₂ -PEI ₇₀₀	DPA1	10
[3,3-Dieethoxy-propanyl-PEO ₁₆₀₀ -PCL ₆₀₀] ₂ -PEI ₇₀₀	DPA2	11
[3,3-Dieethoxy-propanyl-PEO ₁₆₀₀ -PCL ₄₀₀] ₂₋₃ -PEI ₇₀₀	DPA3	12
[3,3-Dieethoxy-propanyl-PEO ₁₆₀₀ -PCL ₆₀₀] ₂₋₃ -PEI ₇₀₀	DPA4	13

table 5: synthesized DP-PEO-*b*-PCL-*b*-PEI-ligands

V-PEO- <i>b</i> -PCL- <i>b</i> -PEI-ligands	abbreviation	
[Vinyl-PEO ₁₁₀₀ -PCL ₄₀₀] ₂₋₃ -PEI ₇₀₀	VPA1	14
[Vinyl-PEO ₁₁₀₀ -PCL ₄₀₀] ₂₋₃ -PEI ₇₀₀	VPA2	15
[Vinyl-PEO ₁₁₀₀ -PCL ₆₀₀] ₂ -PEI ₇₀₀	VPA3	16

table 6: synthesized V-PEO-*b*-PCL-*b*-PEI-ligands.

M-PEO- <i>b</i> -PEI-DDA ligands	abbreviation	
[Methoxy-PEO ₁₁₀₀] ₂₋₃ -PEI ₇₀₀ -[<i>n</i> -dodecylamine] ₅₋₇	E14-DDA	17

table 7: synthesized M-PEO-*b*-PEI-DDA ligands.

M-PEO- <i>b</i> -PEI ligands	abbreviation	
[Methoxy-PEO ₁₁₀₀]-N4	E15	18
[Methoxy-PEO ₂₀₀₀] ₃ -PEI ₇₀₀	E14	19
[Methoxy-PEO ₂₀₀₀] ₂ -PEI ₇₀₀	E12	20
[Methoxy-PEO ₂₀₀₀] ₂ -PEI ₄₂₃	E11	21
[Methoxy-PEO ₁₁₀₀] ₂ -PEI ₇₀₀	E10	22

table 8: synthesized PEO-*b*-PEI-ligands.

7.2.1.3 Ligand-addition (“exchange”) with PEO-*b*-PCL-*b*-PEI

The concentration of the nanoparticle/chloroform stock solution was defined by UV-Vis absorbance^[459]. A certain amount of nanoparticles, usual amounts range from 0.5 to 10 nmol, was dehumidified in nitrogen flow and resuspended in 100 μ L of tetrahydrofuran (THF). A one hundred to five hundred molar excess of ligand was dissolved furthermore in THF and incubated with the nanoparticles at temperatures from 20 to 50 $^{\circ}$ C. The incubation time varied from one minute up to four hours. After the edition of \sim 400 to 1000 μ L of water (dropwise to abruptly injection) using an Eppendorf pipette or injection in water using a syringe the THF

was evaporated first in nitrogen flow and afterwards in vacuum. A purification step over a 0.2 μm syringe filter is feasible. Photos of obtained solutions are shown below in figure 138.

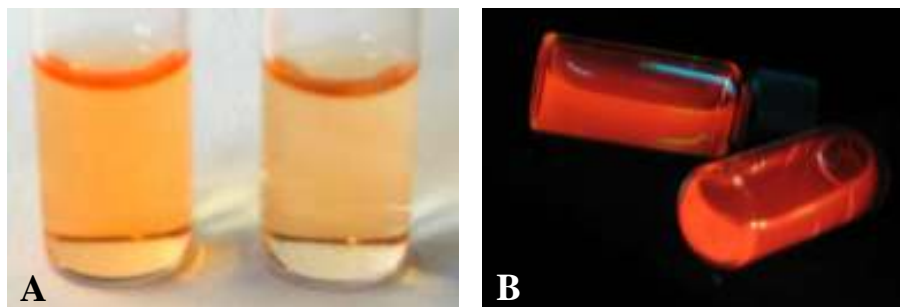


figure 138: Example of CdSe/CdS/ZnS nanoparticles coated with ligand 8 in water under daylight (A) and UV-excitation (B).

7.2.1.4 Ligand exchange with PEO-N4 and PEO-*b*-PEI

Ligands PEO-N4 (17) and PEO-*b*-PEI (18-22) were exchanged according to Nikolic *et al.*^[224]. The nanoparticles were incubated with the respective ligand in a quantum dot to ligand ratio of 1 to 50-400. After precipitation with heptane the nanoparticles were dried and redissolved in water.

7.2.1.5 Functionalisation

The removal of the protecting groups was done via acidic cleavage (schema 6). The *t*-butyl esters and DP functionalized PEOs were hydrolyzed at pH 1-4^[234-236] yielding the respective carboxylate or aldehyde endgroup. Alternatively enzymatic cleavage using porcine liver esterase (PLE; EC 3.1.1.1)^[237] was performed.

Vinyl terminated PEO was oxidized by *o*-iodoxybenzoic acid (IBX) after acidic cleavage. Therefore 900 mg V-PEO-*b*-PCL-*b*-PEI ($1.50 \cdot 10^{-4}$ mol) was dissolved in THF and injected in 5 mL water to achieve micelle formation. 10 mL acetonitrile, 120 mg oxone® ($1.95 \cdot 10^{-4}$ mol, 1.3 eq), and 11.1 mg 2-iodobenzoic acid (2IBAcid, $4.50 \cdot 10^{-5}$ mol, 0.6 eq) were added. The solution was stirred twelve hours at 40 °C and six hours at 70 °C. In the process of cooling the solution in an ice bath the complete precipitation occurred of the insoluble hypervalent iodine by-product, which was then removed by filtration. The solvent was

concentrated at lower pressure to 3 mL. 2 mL chloroform were added, and the product was precipitate in 7 °C cold diethyl ether, whereon a dialysis against water for three days followed. Finally the product was lyophilized.

The reaction was repeated with 0.3 eq 2IBAcid and once with 0.3 eq 2IBAcid at pH 4.5 (presence of acetic acid).

7.2.1.6 Buffer tests

Stock-solutions of CdSe/CdS/ZnS quantum dots in water were prepared by using ligand **1**, **2**, **6**, **7**, **8**, **9**, **12**, **13**, and **17** (quantum dot to ligand ratio of 1 to 200) respectively. In each case 50 µL of the stock-solution was added to 1 mL of buffer solution. After 3 hours the fluorescence intensities were recorded with a multiplate reader.

The following buffer solutions were prepared using ddH₂O: 1x MOPS SDS, 50 mM Tris HCl pH 7.4, 0.5 M NaCl, 0.1 M EGTA pH 8.5, 0.1 M EDTA pH 8.5, PBS pH 7.4, and Tris Borate EDTA 10x pH 8.3. Dulbecco's Phosphate-Buffered Saline (D-PBS) with CaCl₂ & MgCl₂ and phosphate buffered saline (PBS) were purchased from Invitrogen.

7.2.1.7 MMA polymerization in the presence of QDs

Methyl methacrylate (MMA) was extracted threefold with 1 M KOH to remove the stabilizer. After neutralization via threefold washing with water and drying over calcium chloride MMA was distilled at 100 °C.

CdSe/CdS/ZnS quantum dots (2.5 nmol) were coated with ligand **8** (QD/P 1:500), **9**, **12** (QD/P 1:200), and **17** (QD/P 1:300). The aqueous solution was lyophilized and the orange solid in the presence of 0.5 mg AIBN dissolved in 3 mL MMA and cast into a glass cuvette. To remove oxygen, which would abort the polymerisation, argon was conducted through the solution. Additionally the solution was freeze-dried by placing the cuvettes to the half in liquid nitrogen. The gas phase was removed by applying vacuum. After melting of the probe the procedure was repeated two more times. Finally the polymerization carried out under nitrogen at 60 °C for 20 hours.

7.2.2 PI-*b*-PEO based ligands

7.2.2.1 Polymer synthesis

Synthesis of PI and PI-*b*-PEO was done by Steffen Fischer. The synthesis of the PI block was achieved by anionic polymerisation and the PEO back-bone by anionic ring opening polymerisation, which is an ideal method for the synthesis of block copolymers with a narrow molecular weight distribution and well-defined block structure^[278].



figure 139: cohesive glass apparatus for anionic polymerisation.

7.2.2.1.1 Synthesis of poly(isoprene) (PI)

The synthesis of PI has been applied with dry argon as cover gas. 156 mL isoprene (107 g, 1.57 mol) was purified in two steps in a cohesive glass apparatus (picture 1), wherein the siccative in flasks are integrated and the isoprene is been distilled from on flask to the next. First isoprene was dried with CaH₂ and after distillation in a second flask with di-*n*-butylmagnesium. With a final distillation step it was transferred in a reactor containing 1.3 L dried THF. As initiator 30.0 mL *sec*-butyllithium (1.30 mol/L, 39.0 mmol) was used. The solution reaction was stirred for 6 h at -60 °C. The polymerisation was terminated with

4.00 mL (3.60 g, 82.0 mmol) ethylene oxide to achieve a hydroxyl end group. After adding 5.00 mL of acetic acid (5.30 g, 87.0 mmol) the polymere was purified by precipitation in methanol.

¹H-NMR (400 MHz, CDCl₃):

δ (ppm) = 0.76-0.88 (m, 3H of *sec*-butyl, CH₃-CH₂-), 0.88-1.06 (m, 1H of *sec*-butyl, -CH(-CH₃)-; 2H per unit of 1,2-PI, -C(-CH₃)-), 1.06-1.48 (m, 3H of *sec*-butyl, -CH(-CH₃)-; 2H per unit of 1,2-PI, -C(-CH₃)-CH₂-; 2H of *sec*-butyl, CH₃-CH₂-; 2H per unit of 3,4-PI, CH-CH₂-), 1.48-1.74 (m, 3H per unit of 3,4-PI, C-CH₃; 3H per unit of 1.4-PI, -CH(-CH₃)=), 1.74-2.34 (m, 1H per unit of 3.4-PI, -CH-; 2H per unit of 1.4-PI, -HC=CH-CH₂-; 2H per unit of 1.4-PI, -CH₂-CH(-CH₃)=), 3.76 (t, 2H, -CH₂-OH), 4.51-4.76 (m, 2H per unit of 3,4-PI, -C=CH₂, 2H per unit of 1,2-PI, -HC=CH₂), 4.76-5.10 (m, 1H per unit of 1,4-PI, C=CH-), 5.57-6.00 (m, 1H per unit of 1,2-PI, -HC=CH₂).

7.2.2.1.2 Synthesis of PI-*b*-PEO block copolymers

46.0 g PI (11.0 mmol) was solved in 1.3 L dry THF. Under argon atmosphere 110 mL ethylene oxide (98.0 g, 2.22 mol) was purified in a three step procedure. Ethylene oxide was dried with CaH₂, sodium mirror and *n*-butyllithium. Finally it was distilled to the a solution of PI in THF. 9.00 mL of a solution of diphenylmethylpotassium (~ 1 mol/L. 9.00 mmol) in cyclohexane was added. The solution was stirred 72 h at 40 °C and terminated with 4.00 mL acetic acid (90.0 mmol). The PI-*b*-PEO was purified by precipitation in cold acetone.

All PI-*b*-PEO ligands were stored under argon at 4 °C in the dark.

¹H-NMR (400 MHz, CDCl₃):

δ (ppm) = 0.76-0.88 (m, 3H of *sec*-butyl, CH₃-CH₂-), 0.88-1.06 (m, 1H of *sec*-butyl, -CH(-CH₃)-; 2H per unit of 1,2-PI, -C(-CH₃)-), 1.06-1.48 (m, 3H of *sec*-butyl, -CH(-CH₃)-; 2H per unit of 1,2-PI, -C(-CH₃)-CH₂-; 2H of *sec*-butyl, CH₃-CH₂-; 2H per unit of 3,4-PI, CH-CH₂-), 1.48-1.74 (m, 3H per unit of 3,4-PI, C-CH₃; 3H per unit of 1.4-PI, -CH(-CH₃)=), 1.74-2.34 (m, 1H per unit of 3.4-PI, -CH-; 2H per unit of 1.4-PI, -HC=CH-CH₂-; 2H per unit

of 1,4-PI, $-CH_2-CH(-CH_3)=$), 3.44-3.84 (m, 4H per unit of PEO; 4H, $-CH_2-CH_2-OH$; 4.51-4.76 (m, 2H per unit of 3,4-PI, $-C=CH_2$, 2H per unit of 1,2-PI, $-HC=CH_2$), 4.76-5.10 (m, 1H per unit of 1,4-PI, $C=CH-$), 5.57-6.00 (m, 1H per unit of 1,2-PI, $-HC=CH_2$).

7.2.2.2 Synthesis of PI-DETA (PI-N3)

The poly(isoprene) polymer was equipped with 2,2'-diaminodiethylamine (DETA, -N3) by activation of the hydroxylic group of PI by a twenty fold excess of 1,1'-carbonyldiimidazol (CDI) in dry chloroform. After fourteen hours of stirring at room temperature, the excess of CDI was hydrolysed by twofold extraction the solution with 5 mL water. Subsequent the solution was dried with sodium sulfate. A twenty fold excess of 2,2'-diaminodiethylamine (DETA) was added slowly to the solution. The reaction mixture was stirred for further twelve hours at a temperature of 55 °C. The product was precipitated twice in ethanol.

All PI-N3 prepolymer-ligands were stored under argon at -10 °C in the dark.

¹H-NMR (400 MHz, CDCl₃):

δ (ppm) = 0.76-0.88 (m, 3H of *sec*-butyl, CH_3-CH_2-), 0.88-1.06 (m, 1H of *sec*-butyl, $-CH(-CH_3)-$); 2H per unit of 1,2-PI, $-C-(CH_3)-$), 1.06-1.48 (m, 3H of *sec*-butyl, $-CH(-CH_3)-$); 2H per unit of 1,2-PI, $-C-(CH_3)-CH_2-$; 2H of *sec*-butyl, CH_3-CH_2- ; 2H per unit of 3,4-PI, $CH-CH_2-$), 1.48-1.74 (m, 3H per unit of 3,4-PI, $C-CH_3$; 3H per unit of 1,4-PI, $-CH(-CH_3)=$), 1.74-2.34 (m, 1H per unit of 3,4-PI, $-CH-$; 2H per unit of 1,4-PI, $-HC=CH-CH_2-$; 2H per unit of 1,4-PI, $-CH_2-CH(-CH_3)=$), 2.62-2.86 (m, 6 H, $-CH_2-NH-CH_2-CH_2-NH_2$), 3.18-3.32 (m, 2H, $-O-C(=O)-NH-CH_2-CH_2-$), 3.80-4.10 (m, 2 H, $-CH_2-O-C(=O)-NH-CH_2-$), 4.51-4.76 (m, 2H per unit of 3,4-PI, $-C=CH_2$, 2H per unit of 1,2-PI, $-HC=CH_2$), 4.76-5.10 (m, 1H per unit of 1,4-PI, $C=CH-$), 5.57-6.00 (m, 1H per unit of 1,2-PI, $-HC=CH_2$).

7.2.2.3 Ligand exchange

The stock solution of nanoparticles was achieved by incubation the nanoparticles with a three hundred to six hundred excess of PI₃₀-N3 ligand and three fold precipitation of the

nanoparticles with ethanol out of tetrahydrofuran (THF). The nanoparticles were stored in toluene or chloroform.

7.2.2.4 Ligandaddition

The concentration of the nanoparticle/chloroform stock solution was defined by UV-Vis absorbance^[459]. A certain amount of nanoparticles, usual amounts range from 0.5 to 2 nmol, was dehumidified in nitrogen flow and resuspended in 100 to 300 μL of THF (99+%, A.C.S reagent, Aldrich), which contained a fifty fold to five hundred fold molar excess of PI-*b*-PEO and a 50 to 100 hundred molar excess of azobisisobutyronitrile (AIBN). Functional modified PI-*b*-PEO ligands were used together with unmodified PI-*b*-PEO in a percentage range of one to one hundred. The incubation time after accurate mixing varied from one minute up to four hours, whereby customarily five minutes of incubation was performed. Afterwards the solution was injected very slowly in 1000 μL of water, which was present in a glass jar of 1 cm in diameter, coeval with stirring (1200 rpm) and a steady nitrogen flow from above of the water surface area, which removes the THF. Nitrogen blisters have to be avoided, since it influences the self-assembly of the micelles. In case of amounts of water (> 2 mL) glass jars with larger diameters were used to take advantage of the larger water surface area, considering the removal of THF.

After the removal of THF the solution was heated up for 30 minutes to 70 °C to initiate the crosslinkage. A purification step over a 0.2 μm syringe filter is feasible.

Higher concentrations were achieved by using more THF and slowly injection of 100 to 200 μL portions of the quantum dot/THF/ligand/AIBN-solution, whereupon between each portion 10 minutes were waited to secure the remove most of the THF by the nitrogen flow. The solution could be easily further concentrated in the progress of crosslinkage by perpetuation the nitrogen flow. According to the crosslinkage ultracentrifugation is a further simple feasibility to concentrate the probe.

7.2.2.5 Ligand functionalisation

The field of application is getting expanded by the supplement of functional groups. Different methods were proved to modify the terminal hydroxylic group of the poly(ethylene oxide) under conservation of the double bounds of poly(isoprene). Concerning the accessibility of the hydroxyl function, which is sterically reduced, the reaction times had to be increased to achieve satisfying reaction yields.

The identification of the respective terminal group via nuclear spin resonance spectroscopy (NMR) proves to be difficult, by reason that the coblockpolymer possess a large, average size of > 13500 g/mol and to some extent are composed of inhomogeneous block length. As for NMR-analysis typical amount of 5 mg/mL of a substance with a molecular weight of 500 mg/mol correlates with 135 mg of the applied PI-*b*-PEO polymer, which constitutes a problem of solubility as well as the mass-concentration. Thence just NMR-active nuclei with very high isotopic abundance (^1H , ^{19}F) can be analysed, whereby ^{13}C -NMR and two dimensional NMR experiments are inapplicable. Further problems are lower reaction yields and the often overlay of characteristic signals for the terminal functional group by multiplets of the PI-*b*-PEO polymer.

Similarly problematic proves to be infrared radiation based analysis, since the ratio between the large polymer blocks against the functional group immense (factor ~450) is. For instance is the apart from that intense carbonyl vibration band in IR-spectra of coblock polymers for the most part weak and difficult identifiable.

All PI-*b*-PEO ligands as well as the functionalised ligands were stored under argon at 4 °C.

7.2.2.5.1 Synthesis of an aldehyde

The synthesis of an aldehyde was achieved via three different reactions.

7.2.2.5.1.1 Dess-Martin oxidation

200 mg of the ligand PI₆₁-*b*-PEO₂₁₂-OH ($1.48 \cdot 10^{-5}$ mol) dissolved in 6 mL dichloromethan (DCM) were added to a solution, containing 7.50 mg Dess-Martin periodinane (DMP) ($1.78 \cdot 10^{-5}$ mol, 1.2 eq) in 3 mL DCM. After stirring at room temperature for 48 hours the modified PI-*b*-PEO ligand was precipitated in cold acetone and filtrated. After a dialysis against water for 48 hours, the ligand was lyophilized.

7.2.2.5.1.2 Oxidation via PDC

Under inert conditions 200 mg PI₆₁-*b*-PEO₂₁₂-OH ($1.48 \cdot 10^{-5}$ mol) and 0.1 g activated, pulverized molecular sieve Å4 were dissolved in 10 mL dry DCM. At a temperature of -10 °C under stirring 7.20 mg pyridinium dichromate (PDC) ($1.92 \cdot 10^{-5}$ mol) were added in portions. The reaction mixture was allowed to reach room temperature slowly, whereupon the reaction kept going for another 60 hours. In a final step the reaction mixture was diluted with 5 mL DCM and purified by filtration over 4 g of silica. The solvent of the filtrate was evaporated and the product was precipitated in 40 mL cold diethyl ether. This purification step was repeated after redissolving the product in 1 mL DCM.

7.2.2.5.1.3 Pfitzner-Moffatt oxidation

1.00 g PI₆₁-*b*-PEO₂₁₂-OH ($7.41 \cdot 10^{-5}$ mol) were dissolved in 5 mL dry DMSO and were stirred at a temperature of 60 °C until the solution was clear. After cooling down to room temperature a solution, containing 1.50 mL acetic anhydride (15.9 mmol) and 5 mL dry DMSO, was added and the reaction mixture was kept stirring for 24 hours. In portions 1.50 mL acetic anhydride (15.9 mmol) in 2.5 mL triethylamine were added and the solution was stirred for another 24 hours. The solution was diluted with 25 mL diethyl ether and 25 mL ethylacetate. The purification was achieved by precipitation of the product in diethyl ether at 4 °C. The residuum was washed three times with cold diethyl ether^[460].

IR (KBr):

$\tilde{\nu}$ [cm^{-1}] = 3074, 2890, 2741, 2695, 1792, 1970, 1734, 1644, 1468, 1413, 1375, 1361, 1343, 1282, 1243, 1101, 1060, 1004, 962, 906, 886, 842, 742.

 $^1\text{H-NMR}$ (400 MHz, CDCl_3):

δ (ppm) = 0.76-0.88 (m, 3H of *sec*-butyl, $\text{CH}_3\text{-CH}_2\text{-}$), 0.88-1.06 (m, 1H of *sec*-butyl, $\text{-CH(-CH}_3\text{)-}$; 2H per unit of 1,2-PI, $\text{-C(-CH}_3\text{)-}$), 1.06-1.48 (m, 3H of *sec*-butyl, $\text{-CH(-CH}_3\text{)-}$; 2H per unit of 1,2-PI, $\text{-C(-CH}_3\text{)-CH}_2\text{-}$; 2H of *sec*-butyl, $\text{CH}_3\text{-CH}_2\text{-}$; 2H per unit of 3,4-PI, $\text{CH-CH}_2\text{-}$), 1.48-1.74 (m, 3H per unit of 3,4-PI, C-CH_3 ; 3H per unit of 1.4-PI, $\text{-CH(-CH}_3\text{)=}$), 1.74-2.34 (m, 1H per unit of 3.4-PI, -CH- ; 2H per unit of 1.4-PI, $\text{-HC=CH-CH}_2\text{-}$; 2H per unit of 1.4-PI, $\text{-CH}_2\text{-CH(-CH}_3\text{)=}$), 3.44-3.84 (m, 4H per unit of PEO; 2H, $\text{-CH}_2\text{-CHO}$; 4.51-4.76 (m, 2H per unit of 3,4-PI, -C=CH_2 , 2H per unit of 1,2-PI, HC=CH_2), 4.76-5.10 (m, 1H per unit of 1,4-PI, C=CH-), 5.57-6.00 (m, 1H per unit of 1,2-PI, -HC=CH_2), 9.73 (t, -CHO).

7.2.2.5.2 Synthesis of a terminal epoxid

At a temperature of 0 °C to 7.30 mg sodium hydride (60% in paraffin) ($1.85 \cdot 10^{-4}$ mol, 5 eq) in 5 mL THF were 510 mg of $\text{PI}_{61}\text{-}b\text{-PEO}_{212}\text{-OH}$ ($3.78 \cdot 10^{-5}$ mol, 1 eq) slowly added. After one hour stirring at room temperature the temperature was decreased again to 0 °C and 17.1 mg epichlorohydrin ($1.85 \cdot 10^{-4}$ mol, 5 eq) were added dropwise. That followed stirring at 40 °C for further 21 hours. Purification embraced the separation of NaCl and surplus NaH via centrifugation and the precipitation of the product in diethyl ether (5 °C). Subsequent to the dissolving of the product in a small amount of chloroform the precipitation was repeated. The precipitate was finally dried in vacuum.

 $^1\text{H-NMR}$ (400 MHz, CDCl_3):

δ (ppm) = 0.76-0.88 (m, 3H of *sec*-butyl, $\text{CH}_3\text{-CH}_2\text{-}$), 0.88-1.06 (m, 1H of *sec*-butyl, $\text{-CH(-CH}_3\text{)-}$; 2H per unit of 1,2-PI, $\text{-C(-CH}_3\text{)-}$), 1.06-1.48 (m, 3H of *sec*-butyl, $\text{-CH(-CH}_3\text{)-}$; 2H per unit of 1,2-PI, $\text{-C(-CH}_3\text{)-CH}_2\text{-}$; 2H of *sec*-butyl, $\text{CH}_3\text{-CH}_2\text{-}$; 2H per unit of 3,4-PI, $\text{CH-CH}_2\text{-}$), 1.48-1.74 (m, 3H per unit of 3,4-PI, C-CH_3 ; 3H per unit of 1.4-PI, $\text{-CH(-CH}_3\text{)=}$), 1.74-2.34 (m, 1H per unit of 3.4-PI, -CH- ; 2H per unit of 1.4-PI, $\text{-HC=CH-CH}_2\text{-}$; 2H per unit of

1.4-PI, $-\text{CH}_2\text{-CH}(\text{-CH}_3)=$; 1H, epoxidic-H), 2.63 (m, 1H, epoxidic-H), 3.44-3.84 (m, 4H per unit of PEO; 4H, $\text{CH}_2\text{-epoxid}$), 4.51-4.76 (m, 2H per unit of 3,4-PI, $-\text{C}=\text{CH}_2$, 2H per unit of 1,2-PI, $-\text{HC}=\text{CH}_2$), 4.76-5.10 (m, 1H per unit of 1,4-PI, $\text{C}=\text{CH-}$), 5.57-6.00 (m, 1H per unit of 1,2-PI, $-\text{HC}=\text{CH}_2$).

7.2.2.5.3 Synthesis of a terminal carboxylic acid function

To 1.00 g $\text{PI}_{61}\text{-}b\text{-PEO}_{212}\text{-OH}$ ($7.41 \cdot 10^{-5}$ mol), dissolved in 10 mL chloroform, 0.9 mg of the nucleophilic Steglich-Höfle catalyst 4-dimethylaminopyridine (DMAP) ($7.41 \cdot 10^{-6}$ mol, 0.1 eq) were added. After the addition of 14.8 mg succinic anhydride ($1.48 \cdot 10^{-4}$ mol, 2 eq), in 3 mL chloroform dissolved, the reaction mixture was stirred for 48 hours at room temperature, concluding with the evaporation of the solvent, and suspension of the yellow, viscous pellet in a water and ethanol (3:2, 5 mL), solution. The raw product was dialysed for two days and lyophilized^[289]. The reaction was also repeated in an alternative procedure in pyridine, with an 1.7 fold excess of DMAP^[288].

IR (KBr):

$\tilde{\nu}$ [cm^{-1}] = 3074, 2889, 2741, 2695, 1968, 1734, 1645, 1559, 1468, 1413, 1375, 1361, 1343, 1282, 1242, 1150, 1108, 1061, 963, 886, 842.

$^1\text{H-NMR}$ (500 MHz, CDCl_3):

δ (ppm) = 0.76-0.88 (m, 3H of *sec*-butyl, $\text{CH}_3\text{-CH}_2\text{-}$), 0.88-1.06 (m, 1H of *sec*-butyl, $-\text{CH}(\text{-CH}_3)\text{-}$; 2H per unit of 1,2-PI, $-\text{C}(\text{-CH}_3)\text{-}$), 1.06-1.48 (m, 3H of *sec*-butyl, $-\text{CH}(\text{-CH}_3)\text{-}$; 2H per unit of 1,2-PI, $-\text{C}(\text{-CH}_3)\text{-CH}_2\text{-}$; 2H of *sec*-butyl, $\text{CH}_3\text{-CH}_2\text{-}$; 2H per unit of 3,4-PI, $\text{CH-CH}_2\text{-}$), 1.48-1.74 (m, 3H per unit of 3,4-PI, C-CH_3 ; 3H per unit of 1,4-PI, $-\text{CH}(\text{-CH}_3)=$), 1.74-2.34 (m, 1H per unit of 3,4-PI, $-\text{CH-}$; 2H per unit of 1,4-PI, $-\text{HC}=\text{CH-CH}_2\text{-}$; 2H per unit of 1,4-PI, $-\text{CH}_2\text{-CH}(\text{-CH}_3)=$), 2.58-2.65 (m, 4H, $\text{CH}_2\text{-CH}_2\text{-COOH}$), 3.44-3.84 (m, 4H per unit of PEO), 4.18-4.26 (m, 2H, $-\text{CH}_2\text{-O-C(=O)-}$) 4.51-4.76 (m, 2H per unit of 3,4-PI, $-\text{C}=\text{CH}_2$, 2H per unit of 1,2-PI, $-\text{HC}=\text{CH}_2$), 4.76-5.10 (m, 1H per unit of 1,4-PI, $\text{C}=\text{CH-}$), 5.57-6.00 (m, 1H per unit of 1,2-PI, $-\text{HC}=\text{CH}_2$).

7.2.2.5.4 Synthesis of a terminal azide

In 5 mL ethyl acetate were 500 mg PI₆₁-*b*-PEO₂₁₂-OH ($3.70 \cdot 10^{-5}$ mol) and 8.30 mg 1,4-diazabicyclo[2.2.2]octane (DABCO) ($7.41 \cdot 10^{-5}$ mol, 1 eq) dissolved and cooled to 0 °C. Slowly 10.6 mg tosylchloride ($5.56 \cdot 10^{-5}$ mol, 1.5 eq) were added. The reaction mixture was allowed to warm up to room temperature and was stirred for 48 hours. The solvent was evaporated and the solid was subsequent to dissolving in 4 mL chloroform precipitated in 20 mL acetone. After centrifugation the solid phase was redissolved in 4 mL chloroform and again precipitated with acetone to isolate the tosylated product.

250 mg tosylated PI₆₁-*b*-PEO₂₁₂-OH ($1.85 \cdot 10^{-5}$ mol), 3.40 mg tetrabutylammoniumiodide (TBAI) ($9.2 \cdot 10^{-6}$ mol), and 15.0 mg sodium azide ($2.31 \cdot 10^{-4}$ mol, 12.5 eq) were dissolved in 10 mL pure DMF. The reaction mixture was stirred 2 hours at 65 °C and stirring continued for three days at 50 °C. The raw product was processed by repeated precipitation in 20 mL cold acetone (four times). The precipitate was always dissolved in chloroform before precipitation, whereby after the first precipitation, the white solid, mainly sodium azide, which was not soluble in chloroform, was separated by centrifugation and rejected. The colourless solid matter, which was obtained by purification, was dissolved in water and lyophilized.

¹H-NMR (500 MHz, CDCl₃) PI₆₁-*b*-PEO₂₁₂-tosylat:

δ (ppm) = 0.76-0.88 (m, 3H of *sec*-butyl, CH₃-CH₂-), 0.88-1.06 (m, 1H of *sec*-butyl, -CH(-CH₃)-; 2H per unit of 1,2-PI, -C(-CH₃)-), 1.06-1.48 (m, 3H of *sec*-butyl, -CH(-CH₃)-; 2H per unit of 1,2-PI, -C(-CH₃)-CH₂-; 2H of *sec*-butyl, CH₃-CH₂-; 2H per unit of 3,4-PI, CH-CH₂-), 1.48-1.74 (m, 3H per unit of 3,4-PI, C-CH₃; 3H per unit of 1,4-PI, -CH(-CH₃)=), 1.74-2.34 (m, 1H per unit of 3,4-PI, -CH-; 2H per unit of 1,4-PI, -HC=CH-CH₂-; 2H per unit of 1,4-PI, -CH₂-CH(-CH₃)=; 3H, benzene-CH₃), 3.44-3.84 (m, 4H per unit of PEO, 2H, CH₂-O-S), 4.51-4.76 (m, 2H per unit of 3,4-PI, -C=CH₂, 2H per unit of 1,2-PI, -HC=CH₂), 4.76-5.10 (m, 1H per unit of 1,4-PI, C=CH-), 5.57-6.00 (m, 1H per unit of 1,2-PI, -HC=CH₂, 7.80 (m, 4H, H_{ar}).

IR (KBr) PI₆₁-*b*-PEO₂₁₂-N₃:

$\tilde{\nu}$ [cm⁻¹] = 3072, 2888, 2740, 1967, 1643, 1467, 1412, 1374, 1360, 1343, 1281, 1242, 1148, 1110, 1061, 1004, 963, 907, 887, 843.

¹H-NMR (500 MHz, CDCl₃) PI₆₁-*b*-PEO₂₁₂-N₃:

δ (ppm) = 0.76-0.88 (m, 3H of *sec*-butyl, CH₃-CH₂-), 0.88-1.06 (m, 1H of *sec*-butyl, -CH(-CH₃)-; 2H per unit of 1,2-PI, -C(-CH₃)-), 1.06-1.48 (m, 3H of *sec*-butyl, -CH(-CH₃)-; 2H per unit of 1,2-PI, -C(-CH₃)-CH₂-; 2H of *sec*-butyl, CH₃-CH₂-; 2H per unit of 3,4-PI, CH-CH₂-; 2H, CH₂-CH₂-N₃), 1.48-1.74 (m, 3H per unit of 3,4-PI, C-CH₃; 3H per unit of 1,4-PI, -CH(-CH₃)=), 1.74-2.34 (m, 1H per unit of 3,4-PI, -CH-; 2H per unit of 1,4-PI, -HC=CH-CH₂-; 2H per unit of 1,4-PI, -CH₂-CH(-CH₃)=), 3.44-3.84 (m, 4H per unit of PEO; 2H, CH₂-CH₂-N₃), 4.51-4.76 (m, 2H per unit of 3,4-PI, -C=CH₂, 2H per unit of 1,2-PI, -HC=CH₂), 4.76-5.10 (m, 1H per unit of 1,4-PI, C=CH-), 5.57-6.00 (m, 1H per unit of 1,2-PI, -HC=CH₂).

7.2.2.5.5 Synthesis of a terminal amine

a) 80.0 mg of the PI₆₁-*b*-PEO₂₁₂-N₃ ($5.93 \cdot 10^{-6}$ mol) and 6.20 mg triphenylphosphine ($2.37 \cdot 10^{-5}$ mol) in 10 mL THF dissolved. The reaction mixture was stirred for 24 hours at room temperature. Successive to the addition of 0.5 mL water the reaction mixture was further stirred for 24 hours, concluding with the evaporation of the solvent and redissolving the product in 25 mL water. The precipitated triphenylphosphine oxide was filtered out. By lyophilisation a colourless, powdery product was obtained.

b) In an additional reaction 120 mg PI₆₁-*b*-PEO₂₁₂-N₃ ($8.89 \cdot 10^{-6}$ mol) and 6.7 mg lithium aluminium hydride ($1.77 \cdot 10^{-4}$ mol) were, after dissolving in 10 mL THF, stirred for 24 hours at room temperature. The surplus lithium aluminium hydride was neutralized by the addition of 20 mL water. The resulting white precipitate of aluminium hydroxide was removed by filtering, whereupon the filtrate was concentrated to 5 mL, dialysed over 2 days against water to remove LiOH and finally lyophilized.

¹H-NMR (500 MHz, CDCl₃):

δ (ppm) = 0.76-0.88 (m, 3H of *sec*-butyl, CH₃-CH₂-), 0.88-1.06 (m, 1H of *sec*-butyl, -CH(-CH₃)-; 2H per unit of 1,2-PI, -C(-CH₃)-), 1.06-1.48 (m, 3H of *sec*-butyl, -CH(-CH₃)-; 2H per unit of 1,2-PI, -C(-CH₃)-CH₂-; 2H of *sec*-butyl, CH₃-CH₂-; 2H per unit of 3,4-PI, CH-CH₂-), 1.48-1.74 (m, 3H per unit of 3,4-PI, C-CH₃; 3H per unit of 1,4-PI, -CH(-CH₃)=), 1.74-

2.34 (m, 1H per unit of 3,4-PI, -CH-; 2H per unit of 1,4-PI, -HC=CH-CH₂-; 2H per unit of 1,4-PI, -CH₂-CH(-CH₃)=), 2.82 (m, 2H, CH₂-CH₂-NH₂), 3.44-3.84 (m, 4H per unit of PEO; 2H, CH₂-CH₂-NH₂), 4.51-4.76 (m, 2H per unit of 3,4-PI, -C=CH₂, 2H per unit of 1,2-PI, -HC=CH₂), 4.76-5.10 (m, 1H per unit of 1,4-PI, C=CH-), 5.57-6.00 (m, 1H per unit of 1,2-PI, -HC=CH₂).

c) A third variant was achieved by CDI activation of PI-*b*-PEO. Therefore at first 2040 mg PI₆₁-*b*-PEO₂₁₂-OH ($15.11 \cdot 10^{-5}$ mol) were dissolved in 15 mL pure chloroform under inert conditions. The obtained solution was added drop wise under stirring in a solution, consisting of 480 mg CDI ($14.81 \cdot 10^{-4}$ mol, 20 eq) in 10 mL chloroform. After 24 hours stirring at room temperature the mixture was extracted three times with always 20 mL water to hydrolyse unreacted CDI. Having dried the solution of sodium sulfate and removing the solid phase by filtering, the solvent of the filtrate was evaporated. The residue was redissolved in 15 mL chloroform and added to a solution of 178 mg ethylenediamine (2.963 mmol, 0.198 mL, 20 eq) in 5 mL chloroform. The reaction mixture was stirred for further 41 hours at a temperature of 45 °C. Subsequent to concentration by evaporation of the solvent the product was precipitated twice in 60 mL acetone. According the precipitation was repeated three times in acetone and three times in diethyl ether. Finally the product was dissolved in water and lyophilized.

IR (KBr):

$\tilde{\nu}$ [cm⁻¹] = 3072, 2888, 2741, 2695, 1967, 1785, 1643, 1468, 1412, 1374, 1360, 1343, 1281, 1242, 1120, 1061, 1004, 962, 907, 887, 843.

¹H-NMR (400 MHz, CDCl₃):

δ (ppm) = 0.76-0.88 (m, 3H of *sec*-butyl, CH₃-CH₂-), 0.88-1.06 (m, 1H of *sec*-butyl, -CH(-CH₃)-; 2H per unit of 1,2-PI, -C(-CH₃)-), 1.06-1.48 (m, 3H of *sec*-butyl, -CH(-CH₃)-; 2H per unit of 1,2-PI, -C(-CH₃)-CH₂-; 2H of *sec*-butyl, CH₃-CH₂-; 2H per unit of 3,4-PI, CH-CH₂-), 1.48-1.74 (m, 3H per unit of 3,4-PI, C-CH₃; 3H per unit of 1,4-PI, -CH(-CH₃)=), 1.74-2.34 (m, 1H per unit of 3,4-PI, -CH-; 2H per unit of 1,4-PI, -HC=CH-CH₂-; 2H per unit of 1,4-PI, -CH₂-CH(-CH₃)=), 2.70 (t, 2H, -CH₂-NH₂), 3.44-3.84 (m, 4H per unit of PEO), 4.20 (dd, 2H, CH₂-O-C(=O)-NH-), 4.51-4.76 (m, 2H per unit of 3,4-PI, -C=CH₂, 2H per unit of

1,2-PI, $-HC=CH_2$), 4.76-5.10 (m, 1H per unit of 1,4-PI, $C=CH-$), 5.57-6.00 (m, 1H per unit of 1,2-PI, $-HC=CH_2$).

7.2.2.5.6 Synthesis of a terminal alkyne

After dissolving 0.721 g *N,N*-carbonyl dimidazole (CDI) ($44.4 \cdot 10^{-4}$ mol, 20 eq) in 5 mL of pure chloroform under inert conditions, the reaction mixture was complemented with a solution of 300 mg PI₆₁-*b*-PEO₂₁₂-OH ($2.22 \cdot 10^{-4}$ mol) in 5 mL pure chloroform. The reaction mixture was kept stirring for 12 hours at room temperature. Subsequent the organic phase was washed twice with 5 mL H₂O to hydrolyze the excess of CDI. Thereby, imidazole gets separated in the aqueous phase. The organic phase was dried over sodium sulfate and filtrated. Either 100 mg 2-propin-1-ol ($17.84 \cdot 10^{-4}$ mol) or 100 mg propargylamine ($18.16 \cdot 10^{-4}$ mol) were added to the filtrate. The reaction mixture was kept stirring at a temperature of 55 °C for 72 hours. Afterwards the solution was concentrated to ¼ of the primal volume, precipitated in 15 mL cold acetone (0 °C) and filtered off. The precipitate was washed twice with 15 mL cold acetone (0 °C). For further removal of imidazole, the white solid was dissolved again in 10 mL chloroform and the precipitation and washing was repeated. In a final step the product was dissolved in water and lyophilized.

Via propargylamine: **IR** (KBr):

$\tilde{\nu}$ [cm⁻¹] = 3072, 2888, 2741, 1968, 1763, 1644, 1559, 1467, 1412, 1374, 1360, 1343, 1281, 1242, 1148, 1111, 1061, 1004, 963, 887, 843.

Via propargylalcohol: **IR** (KBr):

$\tilde{\nu}$ [cm⁻¹] = 3072, 2888, 2741, 2695, 1968, 1763, 1644, 1559, 1467, 1412, 1374, 1360, 1343, 1281, 1242, 1149, 1108, 1061, 1004, 963, 907, 887, 843.

¹H-NMR (500 MHz, CDCl₃):

δ (ppm) = 0.76-0.88 (m, 3H of *sec*-butyl, CH_3-CH_2-), 0.88-1.06 (m, 1H of *sec*-butyl, $-CH(-CH_3)-$); 2H per unit of 1,2-PI, $-C(-CH_3)-$), 1.06-1.48 (m, 3H of *sec*-butyl, $-CH(-CH_3)-$); 2H per unit of 1,2-PI, $-C(-CH_3)-CH_2-$; 2H of *sec*-butyl, CH_3-CH_2- ; 2H per unit of 3,4-PI, $CH-$

CH_2-), 1.48-1.74 (m, 3H per unit of 3,4-PI, C- CH_3 ; 3H per unit of 1,4-PI, -CH(- CH_3)=), 1.74-2.34 (m, 1H per unit of 3,4-PI, -CH-; 2H per unit of 1,4-PI, -HC=CH- CH_2- ; 2H per unit of 1,4-PI, - CH_2 -CH(- CH_3)=), 2.71 (t, 1H, alkene-H), 3.44-3.84 (m, 4H per unit of PEO), 3.97 (m, 2H, -O-C(=O)-X- CH_2 -alkene), 4.24 (m, 2H, CH_2 -O-C(=O)-X, X = N or O), 4.51-4.76 (m, 2H per unit of 3,4-PI, -C=CH $_2$; 2H per unit of 1,2-PI, -HC=CH $_2$), 4.76-5.10 (m, 1H per unit of 1,4-PI, C=CH-), 5.57-6.00 (m, 1H per unit of 1,2-PI, -HC=CH $_2$).

7.2.2.5.7 Synthesis of a terminal alkene

Under nitrogen atmosphere 1.01 g PI $_{61}$ -*b*-PEO $_{212}$ -OH ($7.48 \cdot 10^{-5}$ mol) were dissolved in 5 mL of pure chloroform, in which 241 mg CDI ($1.49 \cdot 10^{-3}$ mol, 20 eq) were present. Upon stirring for 22 hours the mixture was washed three times with each time 5 mL of water. The organic phase was dried over sodium sulfate and filtrated. The filtrate was added to a solution of 113 μ L allylamine (85.8 mg, $1.50 \cdot 10^{-3}$ mol, 20 eq.) in 5 mL chloroform. The reaction mixture was stirred for 43 hours at a temperature of 45 °C, whereon the solvent was evaporated. The residue was dissolved in 60 mL acetone and precipitated by cooling to a temperature of -15 °C. The precipitate was again dissolved in 2 mL chloroform and the precipitation was repeated three times in acetone and three times in diethyl ether. The product was finally dissolved in water and lyophilized.

IR (KBr):

$\tilde{\nu}$ [cm^{-1}] = 3072, 2885, 2741, 2695, 1967, 1791, 1643, 1467, 1412, 1374, 1360, 1343, 1281, 1242, 1102, 1061, 1004, 963, 907, 887, 843.

1H -NMR (500 MHz, CDCl $_3$):

δ (ppm) = 0.76-0.88 (m, 3H of *sec*-butyl, CH $_3$ -CH $_2-$), 0.88-1.06 (m, 1H of *sec*-butyl, -CH(-CH $_3$)-; 2H per unit of 1,2-PI, -C(-CH $_3$)-), 1.06-1.48 (m, 3H of *sec*-butyl, -CH(-CH $_3$)-; 2H per unit of 1,2-PI, -C(-CH $_3$)-CH $_2-$; 2H of *sec*-butyl, CH $_3$ -CH $_2-$; 2H per unit of 3,4-PI, CH-CH $_2-$), 1.48-1.74 (m, 3H per unit of 3,4-PI, C-CH $_3$; 3H per unit of 1,4-PI, -CH(-CH $_3$)=), 1.74-2.34 (m, 1H per unit of 3,4-PI, -CH-; 2H per unit of 1,4-PI, -HC=CH-CH $_2-$; 2H per unit of 1,4-PI, -CH $_2$ -CH(-CH $_3$)=), 3.44-3.84 (m, 4H per unit of PEO; 2H, O-C(=O)-NH-CH $_2$), 4.19

(dd, 2H, $\text{CH}_2\text{-O-C(=O)-NH-}$), 4.51-4.76 (m, 2H per unit of 3,4-PI, $-\text{C}=\text{CH}_2$, 2H per unit of 1,2-PI, $-\text{HC}=\text{CH}_2$), 4.76-5.10 (m, 1H per unit of 1,4-PI, $\text{C}=\text{CH-}$; 2 H, terminal $\text{CH}=\text{CH}_2$), 5.57-6.00 (m, 1H per unit of 1,2-PI, $-\text{HC}=\text{CH}_2$; 1 H, terminal $\text{CH}=\text{CH}_2$).

7.2.2.5.8 Synthesis of a terminal boronic acid ester

23.3 mg phenylacetic acid-4-boronic acid pinacol ester ($8.89 \cdot 10^{-5}$ mol) were dissolved in 5 mL pure DMF. 22.0 mg *N,N'*-dicyclohexylcarbodiimide (DCC) ($1.07 \cdot 10^{-4}$ mol, 1.2 eq) and 2.20 mg 4-(dimethylamino)pyridine (DMAP) ($1.8 \cdot 10^{-5}$ mol, 0.17 eq) were added. After ten minutes of stirring 500 mg $\text{PI}_{61}\text{-}b\text{-PEO}_{212}\text{-OH}$ ($3.70 \cdot 10^{-5}$ mol), dissolved in 5 mL DMF, were added. The reaction mixture was stirred for 77 hours at room temperature. Subsequently the solvent was evaporated, and the remaining film dissolved in 5 mL water and dialysed against water for two days. The product was lyophilized, dissolved in 5 mL chloroform and precipitated in 25 mL acetone. After centrifugation the liquid phase was discarded. This purification step was repeated twice. Finally the colourless residue was dissolved in 8 mL water and lyophilized.

IR (KBr):

$\tilde{\nu}$ [cm^{-1}] = 3072, 2889, 2741, 2695, 1967, 1734, 1670, 1644, 1559, 1507, 1467, 1413, 1374, 1360, 1343, 1281, 1242, 1149, 1111, 1061, 1004, 963, 907, 887, 843.

$^1\text{H-NMR}$ (500 MHz, CDCl_3):

δ (ppm) = 0.76-0.88 (m, 3H of *sec*-butyl, $\text{CH}_3\text{-CH}_2\text{-}$), 0.88-1.06 (m, 1H of *sec*-butyl, $-\text{CH}(\text{-CH}_3)\text{-}$; 2H per unit of 1,2-PI, $-\text{C}(\text{-CH}_3)\text{-}$), 1.06-1.48 (m, 3H of *sec*-butyl, $-\text{CH}(\text{-CH}_3)\text{-}$; 2H per unit of 1,2-PI, $-\text{C}(\text{-CH}_3)\text{-CH}_2\text{-}$; 2H of *sec*-butyl, $\text{CH}_3\text{-CH}_2\text{-}$; 2H per unit of 3,4-PI, $\text{CH-CH}_2\text{-}$; 12H, $\text{B-O-C}(\text{-CH}_3)_2\text{-C}(\text{-CH}_3)_2$), 1.48-1.74 (m, 3H per unit of 3,4-PI, C-CH_3 ; 3H per unit of 1,4-PI, $-\text{CH}(\text{-CH}_3)=$), 1.74-2.34 (m, 1H per unit of 3,4-PI, $-\text{CH-}$; 2H per unit of 1,4-PI, $-\text{HC}=\text{CH-CH}_2\text{-}$; 2H per unit of 1,4-PI, $-\text{CH}_2\text{-CH}(\text{-CH}_3)=$), 3.44-3.84 (m, 4H per unit of PEO; $\text{O-C(=O)-CH}_2\text{-}$), 4.25 (dd, 2H, $\text{CH}_2\text{-O-C(=O)-}$), 4.51-4.76 (m, 2H per unit of 3,4-PI, $-\text{C}=\text{CH}_2$, 2H per unit of 1,2-PI, $-\text{HC}=\text{CH}_2$), 4.76-5.10 (m, 1H per unit of 1,4-PI, $\text{C}=\text{CH-}$), 5.57-6.00 (m, 1H per unit of 1,2-PI, $-\text{HC}=\text{CH}_2$), 7.14-7.19 (m, 4H, H_{ar}).

7.2.2.5.9 Synthesis of a terminal halogen

a) In 10 mL THF 34.1 mg α -bromoisobutyryl bromide (18.0 μ L, $1.48 \cdot 10^{-4}$ mol) were dissolved and cautiously mixed with a solution of 500 mg PI₆₁-*b*-PEO₂₁₂-OH ($3.70 \cdot 10^{-5}$ mol, 1 eq) in 5 mL THF. The reaction mixture was stirred at room temperature for 18 hours and afterwards in 30 mL cold diethyl ether converted. In the process the ester precipitated as a colourless, floccose deposit. After secession of the filtrate and redissolving the pellet in 2 mL chloroform a threefold precipitation in acetone was accomplished; closing with the dissolving of the halogenated product in water and lyophilisation.

IR (KBr):

$\tilde{\nu}$ [cm^{-1}] = 3072, 2888, 2741, 2695, 1967, 1740, 1643, 1467, 1412, 1374, 1360, 1343, 1281, 1242, 1111, 1061, 1004, 963, 907, 887, 843.

¹H-NMR (400 MHz, CDCl₃):

δ (ppm) = 0.76-0.88 (m, 3H of *sec*-butyl, CH₃-CH₂-), 0.88-1.06 (m, 1H of *sec*-butyl, -CH(-CH₃)-; 2H per unit of 1,2-PI, -C(-CH₃)-), 1.06-1.48 (m, 3H of *sec*-butyl, -CH(-CH₃)-; 2H per unit of 1,2-PI, -C(-CH₃)-CH₂-; 2H of *sec*-butyl, CH₃-CH₂-; 2H per unit of 3,4-PI, CH-CH₂-), 1.48-1.74 (m, 3H per unit of 3,4-PI, C-CH₃; 3H per unit of 1,4-PI, -CH(-CH₃)=), 1.74-2.34 (m, 1H per unit of 3,4-PI, -CH-; 2H per unit of 1,4-PI, -HC=CH-CH₂-; 2H per unit of 1,4-PI, -CH₂-CH(-CH₃)=; 6H, -C(-Br)(-CH₃)₂), 3.44-3.84 (m, 4H per unit of PEO), 4.32 (dd, 2H, CH₂-O-C(=O)-), 4.51-4.76 (m, 2H per unit of 3,4-PI, -C=CH₂, 2H per unit of 1,2-PI, -HC=CH₂), 4.76-5.10 (m, 1H per unit of 1,4-PI, C=CH-), 5.57-6.00 (m, 1H per unit of 1,2-PI, -HC=CH₂).

b) Under nitrogen atmosphere 1.00 g PI₆₁-*b*-PEO₂₁₂-OH ($7.48 \cdot 10^{-5}$ mol) were dissolved in 5 mL of pure chloroform, in which 241 mg CDI ($1.49 \cdot 10^{-3}$ mol, 20 eq) were present. Upon stirring for 48 hours the mixture was washed three times with each time 5 mL of water. The organic phase was dried over sodium sulfate and filtrated. The filtrate was added to a solution of 48.9 mg 2,4,6-tribromoaniline ($1.48 \cdot 10^{-4}$ mol, 2 eq.) in 5 mL chloroform. The reaction mixture was stirred for 43 hours at a temperature of 55 °C, whereon the solvent was evaporated. The residue was dissolved in 60 mL acetone and precipitated by cooling to a

temperature of $-15\text{ }^{\circ}\text{C}$. The precipitate was again dissolved in 2 mL chloroform and the precipitation was repeated three times in acetone and three times in diethyl ether. The product was finally dissolved in water and lyophilized.

$^1\text{H-NMR}$ (500 MHz, CDCl_3):

δ (ppm) = 0.76-0.88 (m, 3H of *sec*-butyl, $\text{CH}_3\text{-CH}_2\text{-}$), 0.88-1.06 (m, 1H of *sec*-butyl, $\text{-CH(-CH}_3\text{)-}$); 2H per unit of 1,2-PI, $\text{-C(-CH}_3\text{)-}$), 1.06-1.48 (m, 3H of *sec*-butyl, $\text{-CH(-CH}_3\text{)-}$); 2H per unit of 1,2-PI, $\text{-C(-CH}_3\text{)-CH}_2\text{-}$; 2H of *sec*-butyl, $\text{CH}_3\text{-CH}_2\text{-}$; 2H per unit of 3,4-PI, $\text{CH-CH}_2\text{-}$), 1.48-1.74 (m, 3H per unit of 3,4-PI, C-CH_3 ; 3H per unit of 1,4-PI, $\text{-CH(-CH}_3\text{)=}$), 1.74-2.34 (m, 1H per unit of 3,4-PI, -CH- ; 2H per unit of 1,4-PI, $\text{-HC=CH-CH}_2\text{-}$; 2H per unit of 1,4-PI, $\text{-CH}_2\text{-CH(-CH}_3\text{)=}$), 3.44-3.84 (m, 4H per unit of PEO), 4.28 (dd, 2H, $\text{CH}_2\text{-O-C(=O)-}$), 4.51-4.76 (m, 2H per unit of 3,4-PI, -C=CH_2 , 2H per unit of 1,2-PI, -HC=CH_2), 4.76-5.10 (m, 1H per unit of 1,4-PI, C=CH-), 5.57-6.00 (m, 1H per unit of 1,2-PI, -HC=CH_2), 7.51 (m, 2H, H_{ar}).

c) 1.00 g $\text{PI}_{61}\text{-}b\text{-PEO}_{212}\text{-OH}$ ($7.48 \cdot 10^{-5}$ mol) were dissolved under nitrogen atmosphere in 5 mL of pure chloroform, in which beforehand 241 mg CDI ($1.49 \cdot 10^{-3}$ mol, 20 eq) were dissolved. Upon stirring for 48 hours the mixture was washed three times with each time 5 mL of water. The organic phase was dried over sodium sulfate and filtrated. The filtrate was added to a solution of 24.0 mg 2,4-dichloroaniline ($1.48 \cdot 10^{-4}$ mol, 2 eq.) in 5 mL chloroform. The reaction mixture was stirred for 43 hours at a temperature of $55\text{ }^{\circ}\text{C}$, whereon the solvent was evaporated. The residue was dissolved in 60 mL acetone and precipitated by cooling to a temperature of $-15\text{ }^{\circ}\text{C}$. The precipitate was again dissolved in 2 mL chloroform and the precipitation was repeated three times in acetone and three times in diethyl ether. The product was finally dissolved in water and lyophilized.

$^1\text{H-NMR}$ (500 MHz, CDCl_3):

δ (ppm) = 0.76-0.88 (m, 3H of *sec*-butyl, $\text{CH}_3\text{-CH}_2\text{-}$), 0.88-1.06 (m, 1H of *sec*-butyl, $\text{-CH(-CH}_3\text{)-}$); 2H per unit of 1,2-PI, $\text{-C(-CH}_3\text{)-}$), 1.06-1.48 (m, 3H of *sec*-butyl, $\text{-CH(-CH}_3\text{)-}$); 2H per unit of 1,2-PI, $\text{-C(-CH}_3\text{)-CH}_2\text{-}$; 2H of *sec*-butyl, $\text{CH}_3\text{-CH}_2\text{-}$; 2H per unit of 3,4-PI, $\text{CH-CH}_2\text{-}$), 1.48-1.74 (m, 3H per unit of 3,4-PI, C-CH_3 ; 3H per unit of 1,4-PI, $\text{-CH(-CH}_3\text{)=}$), 1.74-2.34 (m, 1H per unit of 3,4-PI, -CH- ; 2H per unit of 1,4-PI, $\text{-HC=CH-CH}_2\text{-}$; 2H per unit

of 1,4-PI, $-CH_2-CH(-CH_3)=$), 3.44-3.84 (m, 4H per unit of PEO), 4.28 (dd, 2H, $CH_2-O-C(=O)-$), 4.51-4.76 (m, 2H per unit of 3,4-PI, $-C=CH_2$, 2H per unit of 1,2-PI, $-HC=CH_2$), 4.76-5.10 (m, 1H per unit of 1,4-PI, $C=CH-$), 5.57-6.00 (m, 1H per unit of 1,2-PI, $-HC=CH_2$)).

7.2.2.5.10 Synthesis of a terminal thiol

Under nitrogen atmosphere 1.01 g $PI_{61}-b-PEO_{212}-OH$ ($7.48 \cdot 10^{-5}$ mol) were dissolved in 5 mL chloroform, in which 241 mg CDI ($1.49 \cdot 10^{-3}$ mol, 20 eq) were present. Upon stirring for 22 hours the mixture was washed three times with each time 5 mL of water. The organic phase was dried over sodium sulfate and filtrated. The filtrate was added to a solution of 126 μ L 1,2-ethanedithiol (142 mg, $1.50 \cdot 10^{-3}$ mol, 20 eq.) in 5 mL chloroform. The reaction mixture was stirred for 43 hours at a temperature of 45 °C, whereon the solvent was evaporated. The residue was dissolved in 60 mL acetone and precipitated by cooling to a temperature of -15 °C. The precipitate was again dissolved in 2 mL chloroform and the precipitation was repeated three times in acetone and three times in diethyl ether. The product was finally dissolved in water and lyophilized.

1H -NMR (500 MHz, $CDCl_3$):

δ (ppm) = 0.76-0.88 (m, 3H of *sec*-butyl, CH_3-CH_2-), 0.88-1.06 (m, 1H of *sec*-butyl, $-CH(-CH_3)-$; 2H per unit of 1,2-PI, $-C(-CH_3)-$), 1.06-1.48 (m, 3H of *sec*-butyl, $-CH(-CH_3)-$; 2H per unit of 1,2-PI, $-C(-CH_3)-CH_2-$; 2H of *sec*-butyl, CH_3-CH_2- ; 2H per unit of 3,4-PI, $CH-CH_2-$), 1.48-1.74 (m, 3H per unit of 3,4-PI, $C-CH_3$; 3H per unit of 1,4-PI, $-CH(-CH_3)=$), 1.74-2.34 (m, 1H per unit of 3,4-PI, $-CH-$; 2H per unit of 1,4-PI, $-HC=CH-CH_2-$; 2H per unit of 1,4-PI, $-CH_2-CH(-CH_3)=$), 2.72 (m, 2H, $-CH_2-CH_2-SH$), 3.44-3.84 (m, 4H per unit of PEO), 4.10 (dd, 2H, $CH_2-O-C(=O)-S-$), 4.51-4.76 (m, 2H per unit of 3,4-PI, $-C=CH_2$, 2H per unit of 1,2-PI, $-HC=CH_2$), 4.76-5.10 (m, 1H per unit of 1,4-PI, $C=CH-$), 5.57-6.00 (m, 1H per unit of 1,2-PI, $-HC=CH_2$)).

7.2.2.5.11 Synthesis of a terminal pentafluorophenyl ester

1.00 g PI₆₁-*b*-PEO₂₁₂-COOH ($7.41 \cdot 10^{-5}$ mol) were dissolved in 10 mL of a pyridine/DMF (1:10) solution. To this solution were added in 1 mL DMF dissolved 298 mg pentafluorophenyl trifluoroacetate ($7.41 \cdot 10^{-4}$ mol). The reaction mixture was stirred for 20 hours at room temperature. After evaporation of the solvent the residue was dissolved in 1 mL chloroform and precipitated in acetone. The precipitate was dissolved again in 1 mL chloroform and the precipitation was repeated three times in acetone and three times in diethyl ether. The product was finally dissolved in water and lyophilized.

¹⁹F-NMR (470 MHz, CDCl₃):

δ (ppm) = -162.4, -157.8, -152.5.

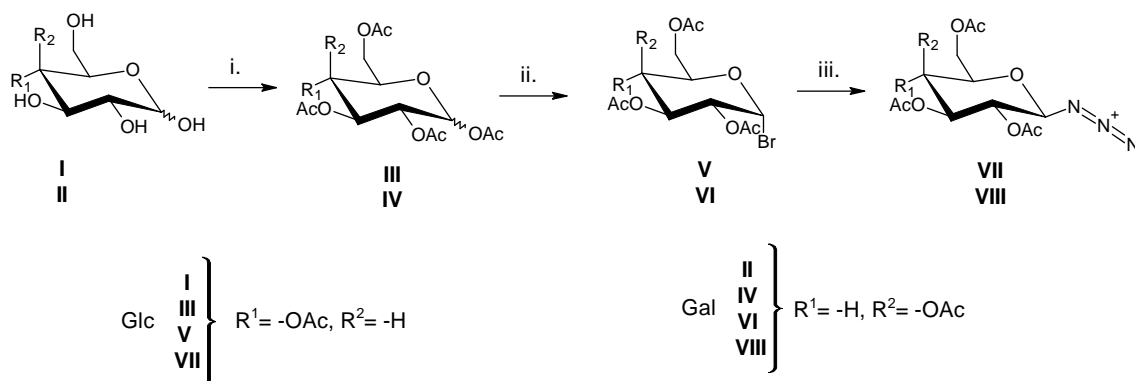
¹H-NMR (400 MHz, CDCl₃):

δ (ppm) = 0.76-0.88 (m, 3H of *sec*-butyl, CH₃-CH₂-), 0.88-1.06 (m, 1H of *sec*-butyl, -CH(-CH₃)-); 2H per unit of 1,2-PI, -C-(CH₃)-), 1.06-1.48 (m, 3H of *sec*-butyl, -CH(-CH₃)-); 2H per unit of 1,2-PI, -C-(CH₃)-CH₂-; 2H of *sec*-butyl, CH₃-CH₂-; 2H per unit of 3,4-PI, CH-CH₂-), 1.48-1.74 (m, 3H per unit of 3,4-PI, C-CH₃; 3H per unit of 1,4-PI, -CH(-CH₃)=), 1.74-2.34 (m, 1H per unit of 3,4-PI, -CH; 2H per unit of 1,4-PI, -HC=CH-CH₂-; 2H per unit of 1,4-PI, -CH₂-CH(-CH₃)=), 2.79 (t, 2H, ³J = 6.8 Hz, -CH₂-CH₂-COOC₆F₅), 2.98 (t, 2H, ³J = 6.8 Hz, -CH₂-CH₂-COOC₆F₅), 3.44-3.84 (m, 4H pro per unit of PEO; 4H, -CH₂-CH₂-OH; 4.51-4.76 (m, 2H per unit of 3,4-PI, -C=CH₂, 2H per unit of 1,2-PI, -HC=CH₂), 3.80 (t, 2H, -O-CH₂-CH₂-OC(O)R, ³J = 4.8 Hz), 4.27 (t, 2H, -O-CH₂-CH₂-OC(O)R, ³J = 4.8 Hz), 4.76-5.10 (m, 1H per unit of 1,4-PI, C=CH-), 5.57-6.00 (m, 1H per unit of 1,2-PI, -HC=CH₂).

7.2.2.5.12 Modification of carbohydrates

The synthesis of glycosyl azides was performed by Dr. Herwig Berthold from the research group of professor J. Thiem in the organic chemistry department of the university of Hamburg, Germany.

Peracetylated azides of glucose **VII** and galactose **VIII** (schema 31) were synthesized via triazole-coupling in a subsequent 1,3-dipolar-cycloaddition reaction as described in the literature^[461, 462].



schema 31: Synthesis of peracetylated azides of glucose **VII** and galactose **VIII**: i.) Py., Ac₂O, r.t., 24 h, 99%; ii.) 33% HBr/HOAc, r.t., 17 h, 65%;^[463, 464] iii.) DMF, NaN₃, 50 °C, 2 h, 85%.^[465]

7.2.2.6 Coupling strategies

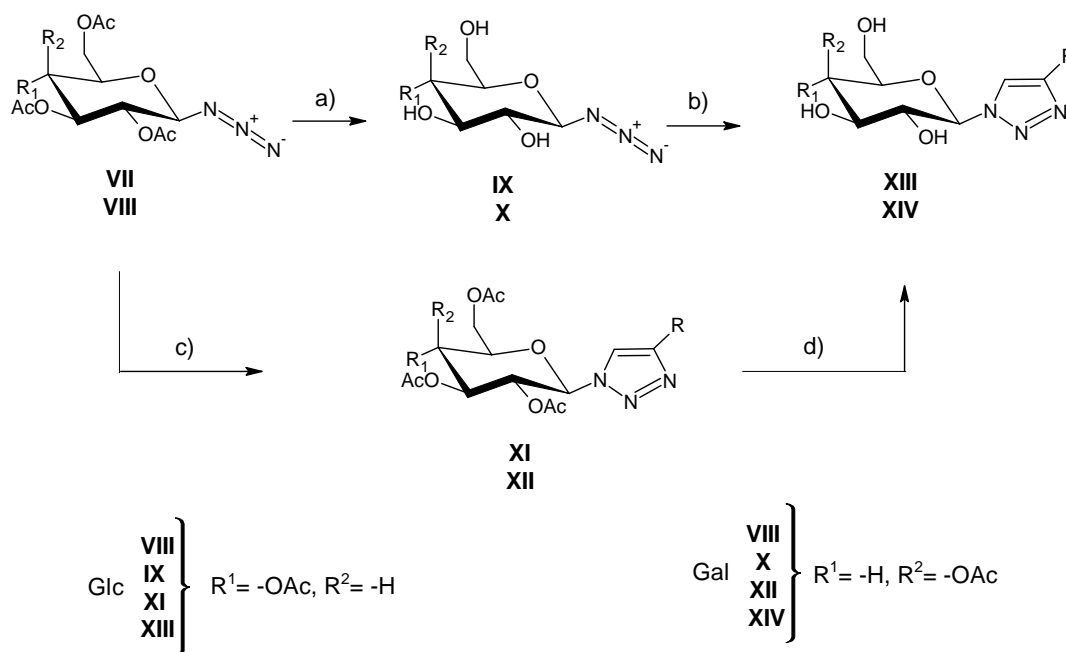
The coupling strategies were focused on synthesis in aqueous media.

7.2.2.6.1 Biofunctionalisation with carbohydrates

Mono- and disaccharides were provided by the research group of professor J. Thiem and the research group of professor V. Vill, both belonging to the department of organic chemistry, Hamburg, Germany.

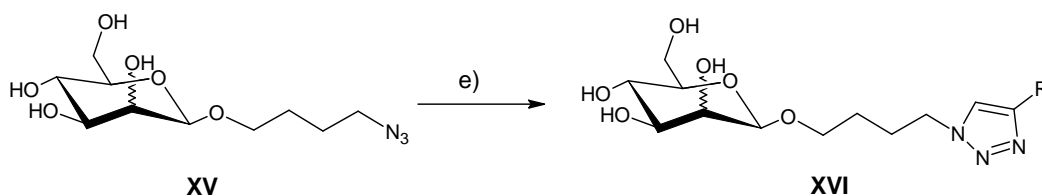
7.2.2.6.1.1 Huisgen cycloaddition (“click-chemistry”)

After dissolving the PI₆₁-*b*-PEO₂₁₂-alkyne in DMF/MeOH, 0.2 M CuI and 1 äq of the azid compound were added. The solution was stirred at a temperature of 45 °C for two days (schema 32). For purification a dialysis against water was performed over a time period of three days.



schema 32: Performed synthesis route for coupling PI-*b*-PEO-C≡CH with 2,3,4,6-tetra-*O*-acetyl-β-*D*-gluco- & galactopyranosyl azide. The abbreviation R stands for the PI-PEO segment of the alkyne functionalized PI₆₁-*b*-PEO₂₁₂-OH.

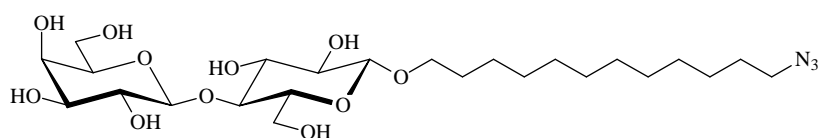
a+d) Upon dissolving 100 mg 2,3,4,6-tetra-*O*-acetyl-β-*D*-gluco- & galactopyranosyl azide (**vii** & **viii**) ($6.68 \cdot 10^{-4}$ mol), and 2,3,4,6-tetra-*O*-acetyl-β-*D*-gluco- & galactopyranosyl-triazolyl-PI₆₁-*b*-PEO₂₁₂ (**xi** & **xii**) respectively, in 10 mL dry methanol under argon atmosphere a small amount of 50 mg sodium ethoxide was added. The obtained reaction mixture was stirred for 48 hours, whereupon the solution was neutralized by adding the ion exchanger Amberlite® IR 120 (H⁺). Subsequent the ion exchanger was filtered out and the solvent evaporated. The brown, amorphous product was without further purification used in the next reaction step. In case of the terminal modified PI₆₁-*b*-PEO₂₁₂ (d) a dialysis was carried out.



schema 33: Performed synthesis route for coupling PI-*b*-PEO-C≡CH with 1-*O*-(4'-azidbutyl)-β-*D*-glucopyranose. This was provided by Sebastian Kopitzki from the research group of professor J. Thiem (department of organic chemistry, Hamburg, Germany)

b+c+e) 300 mg PI₆₁-*b*-PEO₂₁₂-alkine ($2.22 \cdot 10^{-5}$ mol), 10.0 mg 2,3,4,6-tetra-*O*-acetyl- β -D-galactopyranosyl azide (**xii**) ($2.68 \cdot 10^{-5}$ mol, 1.2 μ q) (equimolar amounts of 2,3,4,6-tetra-*O*-acetyl- β -D-glucopyranosyl azide (**xi**), β -D-glucopyranosyl azide (**ix**), β -D-galactopyranosyl azide (**x**), and 1-*O*-(4'-azidbutyl)- β -D-glucopyranose (**xv**) respectively), and 0.85 mg copper(I) iodide ($4.44 \cdot 10^{-6}$ mol, 0.2 μ q) were dissolved in 5 mL pure DMF/methanol (1:1). The solution was stirred at a temperature of 45 °C for two days. The product was dissolved in 5 mL water and one drop of methanol. For purification a dialysis against water was performed over a time period of three days.

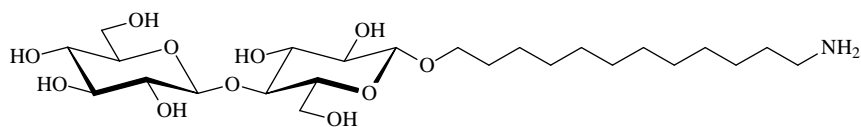
Further disaccharide with an azide function, provided from M. Wulf of the research group of professor V. Vill was (12''azido-dodecyl)-4-*O*-(β -D-galactopyranosyl)- β -D-glucopyranoside (**xvii**).



XVII
 (12''Azido-dodecyl)-4-*O*-(β -D-galactopyranosyl)- β -D-glucopyranoside
 (Lactose-C₁₂-N₃)
 C₂₄H₄₇NO₁₁
 525.64
 Probe MW51

7.2.2.6.1.2 EDC & sulfo-NHS coupling

Regarding biological applications coupling of amino-functionalised disaccharides cellobiose-C₁₂-NH₂ (**xviii**), maltose-C₁₂-NH₂ (**xix**), melibiose-C₁₂-NH₂ (**xx**), and gentibiose-C₁₂-NH₂ (**xxi**) was achieved via in biochemistry well-established EDC and sulfo-NHS activation of PI-*b*-PEO-COOH. It has been reported that the EDC/NHS is a 'zero-length' cross-linker, and does not generate any toxic by-product in the matrix^[219].

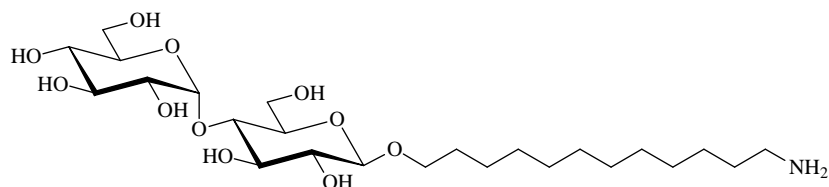
**XVIII**

(12''-Amino-dodecyl)-4-*O*-(β-D-glucopyranosyl)-β-D-glucopyranoside
(Cellobiose-C₁₂-NH₂)

C₂₄H₄₇NO₁₁

525.64

Probe MW61

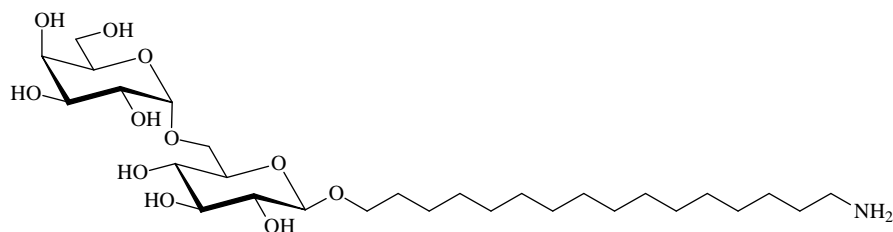
**XIX**

(12''-Amino-dodecyl)-4-*O*-(α-D-glucopyranosyl)-β-D-glucopyranoside
(Maltose-C₁₂-NH₂)

C₂₄H₄₇NO₁₁

525.64

Probe MW163

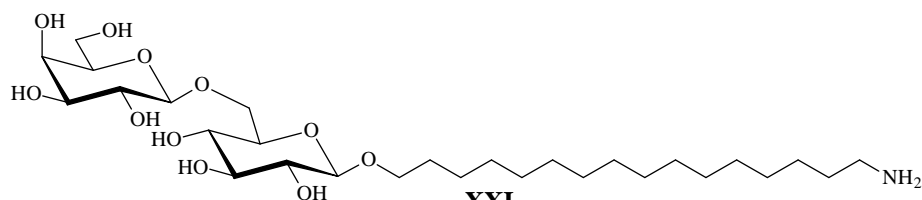
**XX**

(16''-Amino-hexadecyl)-6-*O*-(α-D-galactopyranosyl)-β-D-glucopyranoside
(Melibiose-C₁₆-NH₂)

C₂₈H₅₅NO₁₁

581.74

Probe MW426

**XXI**

(16''-Amino-hexadecyl)-6-*O*-(β-D-glucopyranosyl)-β-D-glucopyranoside
(Gentibiose-C₁₆-NH₂)

C₂₈H₅₅NO₁₁

581.74

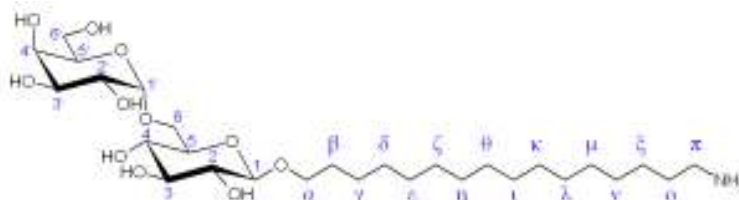
Probe MW422

Per reaction 200 mg PI₆₁-*b*-PEO₂₁₂-COOH ($1.48 \cdot 10^{-5}$ mol) were dissolved in 8 mL ddH₂O. In each flask were added 3.97 mg *N*-(3-dimethylaminopropyl)-*N'*-ethylcarbodiimide hydrochloride (EDC) ($2.07 \cdot 10^{-5}$ mol, 1.4 eq) and 4.50 mg *N*-hydroxysulfosuccinimide (sulfo-NHS) ($2.07 \cdot 10^{-5}$ mol, 1.4 eq). After stirring at room temperature for 10 minutes 8.57 mg (12''-amino-dodecyl)-4-*O*-(β-D-glucopyranosyl)-β-D-glucopyranoside (**XVIII**) ($1.63 \cdot 10^{-5}$ mol,

1.1 eq), 8.57 mg (12''amino-dodecyl)-4-*O*-(α -D-glucopyranosyl)- β -D-glucopyranoside (**xix**) ($1.63 \cdot 10^{-5}$ mol, 1.1 eq), 9.48 mg (16''amino-hexadecyl)-6-*O*-(α -D-galactopyranosyl)- β -D-glucopyranoside (**xx**) ($1.63 \cdot 10^{-5}$ mol, 1.1 eq), and 9.48 mg (16''amino-hexadecyl)-6-*O*-(β -D-galactopyranosyl)- β -D-glucopyranoside (**xxi**) ($1.63 \cdot 10^{-5}$ mol, 1.1 eq) respectively were added per synthesis. The reaction mixture was kept stirring for 96 hours at room temperature at high shear forces, regarding the accessibility of the amines due to the micelle formation of the saccharide educts. The purification of the product was achieved by dialysis against water and closing lyophilisation.

$^1\text{H-NMR}$ (400 MHz, methanol- d_4):

Denotation of signals shown exemplarily for the melibiose derivate:



(12''amino-dodecyl)-4-*O*-(β -D-glucopyranosyl)- β -D-glucopyranoside (**xviii**)

δ (ppm) = 1.28-1.44 (m, 16H, alkyl- CH_2), 1.46-1.58 (m, 2H, λ - CH_2), 1.60-1.72 (m, 2H, β - CH_2), 2.48-2.58 (m, 2H, O-C(O)- CH_2 - CH_2 -C(O)-N), 2.59-2.69 (m, 2H, O-C(O)- CH_2 - CH_2 -C(O)-N), 2.84 (dd, 2H, μ - CH_2 -NH-C(O)), 3.12-3.88 (m, 9H, H-2, H-2', H-3, H-3', H-4, H-4', H-5, H-5', H-6b', H- α b; 4H per EO unit), 3.88-3.96 (m, 4H, H-6a, H-6b, H-6a', H- α a), 4.24 (dd, 2H, CH_2 -O-C(O)- CH_2 - CH_2 -C(O)-N), 4.30 (d, 1H, $^3J_{\text{H-1,H-2}} = 8.1$ Hz, H-1), 4.44 (d, 1H, $^3J_{\text{H-1',H-2'}} = 8.1$ Hz, H-1'), 4.88 (PI).

(12''amino-dodecyl)-4-*O*-(α -D-glucopyranosyl)- β -D-glucopyranoside (**xix**)

δ (ppm) = 1.27-1.47 (m, 18H, alkyl- CH_2), 1.47-1.56 (m, 2H, λ - CH_2), 1.56-1.64 (m, 2H, β - CH_2), 2.47-2.57 (m, 2H, O-C(O)- CH_2 - CH_2 -C(O)-N), 2.58-2.70 (m, 2H, O-C(O)- CH_2 - CH_2 -C(O)-N), 2.84 (dd, 2H, μ - CH_2), 3.12-3.88 (m, H-2, H-2', H-3, H-3', H-4, H-4', H-5, H-5', H-6b', H- α b; 4H per EO unit), 3.88-3.97 (m, 4H, H-6a, H-6b, H-6a', H- α a), 4.21-4.27 (m, 2H, CH_2 -O-C(O)- CH_2 - CH_2 -C(O)-N), 4.29 (d, 1H, $^3J_{\text{H-1,H-2}} = 7.6$ Hz, H-1), 4.88 (PI), 5.19 (d, 1H, $^3J_{\text{H-1',H-2'}} = 3.4$ Hz, H-1').

(16''amino-hexadecyl)-6-*O*-(α -D-galactopyranosyl)- β -D-glucopyranoside (**xx**)

δ (ppm) = 1.26-1.46 (m, 24H, alkyl- CH_2), 1.51-1.77 (m, 4H, β - CH_2 , o- CH_2), 2.42-2.54 (m, 2H, O-C(O)- CH_2 - CH_2 -C(O)-N), 2.57-2.65 (m, 2H, O-C(O)- CH_2 - CH_2 -C(O)-N), 2.90-2.96 (m, 2H, π - CH_2), 3.16 (dd, 1H, $^3J_{H-1,H-2} = 8.4$ Hz, $^3J_{H-2,H-3} = 8.4$ Hz, H-2), 3.26-3.88 (m, H-3, H-3', H-4, H-4', H-5, H-6b, H-6'a, H-6'b, H- α b; 4H per EO unit), 3.88-3.95 (m, 3H, H-2', H-5', H- α a), 3.98 (dd, 1H, $^3J_{H-5,H-6a} = 4.5$ Hz, $^3J_{H-6a,H-6b} = 10.7$ Hz, H-6a), 4.24 (dd, 2H, CH_2 -O-C(O)- CH_2 - CH_2 -C(O)-N), 4.31 (d, 1H, $^3J_{H-1,H-2} = 7.6$ Hz, H-1), 4.88 (PI, H-1').

(16''amino-hexadecyl)-6-*O*-(β -D-galactopyranosyl)- β -D-glucopyranoside (xxi)

δ (ppm) = 1.26-1.46 (m, 24H, alkyl- CH_2), 1.58-1.78 (m, 4H, β - CH_2 , o- CH_2), 2.49-2.56 (m, 2H, O-C(O)- CH_2 - CH_2 -C(O)-N), 2.58-2.68 (m, 2H, O-C(O)- CH_2 - CH_2 -C(O)-N), 2.93 (dd, 2H, $^3J_{H-\pi,H-0} = 7.0$ Hz, π - CH_2), 3.17 (dd, 1H, $^3J_{H-1,H-2} = 7.8$ Hz, $^3J_{H-2,H-3} = 9.0$ Hz, H-2), 3.23 (dd, 1H, $^3J_{H-1',H-2'} = 7.8$ Hz, $^3J_{H-2',H-3'} = 9.0$ Hz, H-2'), 3.28-3.87 (m, H-3, H-3', H-4, H-4', H-5, H-5', H-6b, H-6'a, H-6'b, CH_2 - α b; 4H per EO unit), 3.87-3.95 (m, 1H, CH_2 - α a), 4.17 (dd, 1H, $^3J_{H-5,H-6a} = 1.6$ Hz, $^3J_{H-6a,H-6b} = 11.5$ Hz, H-6a), 4.24 (dd, 2H, CH_2 -O-C(O)- CH_2 - CH_2 -C(O)-N), 4.28 (d, 1H, $^3J_{H-1,H-2} = 8.0$ Hz, H-1), 4.41 (d, 1H, $^3J_{H-1,H-2} = 8.0$ Hz, H-1'), 4.88 (PI).

7.2.2.6.2 Dyes accoutrement

a) In 8 mL ddH₂O 50.0 mg PI₆₁-*b*-PEO₂₁₂-COOH ($3.70 \cdot 10^{-6}$ mol) were dissolved. The addition of 781 μ g *N*-(3-dimethylaminopropyl)-*N'*-ethylcarbodiimide hydrochloride (EDC) ($4.07 \cdot 10^{-6}$ mol, 1.1 eq) and 643 μ g *N*-hydroxysulfosuccinimide (sulfo-NHS) ($2.96 \cdot 10^{-6}$ mol, 0.8 eq) was followed by a reaction time of ten minutes. After the addition of 1.48 mg cresyl violet ($3.70 \cdot 10^{-6}$ mol, 1.0 eq), purchased from Radiant Dyes (article number 095), the reaction mixture was kept stirring for 48 hours. The purification of the product was achieved by dialysis against water and lyophilisation.

b) 82.9 mg PI-PEO-NH₂ ($6.10 \cdot 10^{-6}$ mol) and 0.50 mg ($6.10 \cdot 10^{-7}$ mol, 0.1 eq) of the succinimidyl active ester Alexa Fluor®594 were dissolved in 6 mL pure DMF. After stirring the reaction mixture 44 hours at room temperature, the solvent was evaporated and the residue dissolved in 1 mL H₂O. The product was dialysed for 4 days, subsequently lyophilized, and stored under argon atmosphere and exclusion of light.

c) In 10 mL pure chloroform were under nitrogen atmosphere 121 mg PI₆₁-*b*-PEO₂₁₂-epoxid ($8.96 \cdot 10^{-6}$ mol) reacted with 329 μ g rhodamine 110 chloride ($8.96 \cdot 10^{-7}$ mol, 0.1 eq) at 55 °C. After 14 hours of stirring the solvent was evaporated und the product purified by dialysis against water. Finally the product was lyophylized.

7.2.2.6.3 Coupling of chemotherapeutics

The synthesis of 6-*O*-(4'-(*cis*-diaminoplatin(II)malonat)-butyl)- α/β -galactopyranose was performed by Janina Möker from the research group of professor J. Thiem in the organic chemistry department of the university of Hamburg, Germany.

7.2.2.6.3.1 Coupling of *cis*-platin

Under inert conditions were 150 mg PI₆₁-*b*-PEO₂₁₂-COOH ($1.11 \cdot 10^{-5}$ mol, 1 eq) dissolved in 10 mL pure DMF and exposed to 2.72 mg DCC ($1.33 \cdot 10^{-5}$ mol, 1.2 eq) and 271 μ g DMAP ($2.22 \cdot 10^{-6}$ mol, 0.2 eq). After ten minutes of stirring 7.50 mg 6-*O*-(4'-(*cis*-diaminoplatin(II)malonat)-butyl)- α/β -galactopyranose ($1.33 \cdot 10^{-5}$ mol, 1.2 eq), dissolved in 5 mL DMF, were added. The reaction mixture was stirred for 48 hours at room temperature. Subsequently the solvent was evaporated, and the remaining film dissolved in 3 mL chloroform, whereupon precipitation twice in cold diethyl ether followed. The white residue was finally dissolved in 2 mL of water and lyophilised.

¹H-NMR (400 MHz, D₂O):

δ (ppm) = 1.42-1.38 (m, 2H, H-3'), 1.60-1.67 (m, 2H, H-2'), 2.43-2.48 (m, 2H, H-4'), 2.54-2.58 (m, 4H, C(=O)-CH₂-CH₂-COO), 3.41 (dd, 1H, $^3J_{H_2-H_3} = 11.6$ Hz, H-2), 3.57-3.90 (m, 4H per unit of PEO, H-1', H-5', H-3, H-4, H-5, H-6a, H-6b), 4.19-4.23 (m, 2H, CH₂-O-C(=O)-CH₂), 4.13-4.16 (m, CH₂-O-C(=O)-CH_{gal}), 4.51 (d, 1H, $^3J_{H_{1\beta}-H_2} = 7.9$ Hz, H-1 β), 4.64-4.66 (m, PI), 4.70 (s, D₂O), 5.19 (d, 1H, $^3J_{H_{1\alpha}-H_2} = 3.5$ Hz, H-1 α).

¹H-NMR *cis*-platin edukt (400 MHz, D₂O):

δ (ppm) = 1.33-1.41 (m, 2H, H_{Bu}-3), 1.57-1.64 (m, 2H, H_{Bu}-2), 2.38-2.48 (m, 2H, H_{Bu}-4), 3.37-3.41 (dd, $^3J_{H_2-H_3} = 9.9$ Hz, 1H, H-2), 3.48-3.64 (m, 6H, H-3, H-5, H-6b, H_{Bu}-1, CH),

3.73 (dd, $^2J_{\text{H6a-H6b}} = 10.4$ Hz, 1H, H-6a), 3.85 (dd, $^3J_{\text{H4-H5}} = 1.3$ Hz, 1H, H-4), 4.48 (d, $^3J_{\text{H1}\beta\text{-H2}} = 7.7$ Hz, 1H, H-1 β), 5.16 (d, $^3J_{\text{H1}\alpha\text{-H2}} = 3.8$ Hz, 1 H, H-1 α).

7.2.2.6.3.2 Coupling of azidothymidine (AZT)

In 19 mL pure DMF were 300 mg PI₆₁-*b*-PEO₂₁₂-COOH ($2.22 \cdot 10^{-5}$ mol, 1 eq) dissolved and exposed to 8.16 mg DCC ($3.99 \cdot 10^{-5}$ mol, 1.8 eq) and 2.71 mg DMAP ($2.22 \cdot 10^{-5}$ mol, 1 eq) under inert conditions. After ten minutes of stirring 7.12 mg azidothymidine ($2.66 \cdot 10^{-5}$ mol, 1.2 eq), dissolved in 1 mL DMF, were added. The reaction mixture was stirred for 48 hours at room temperature. Subsequently the solvent was evaporated, and the remaining film dissolved in 3 mL chloroform, whereupon precipitation twice in cold diethyl ether followed. The white residue was finally dissolved in 2 mL of water and lyophilised.

¹H-NMR (500 MHz, CDCl₃):

δ (ppm) = 0.76-0.88 (m, 3H of *sec*-butyl, CH₃-CH₂-), 0.88-1.06 (m, 1H of *sec*-butyl, -CH(-CH₃)-; 2H per unit of 1,2-PI, -C-(CH₃)-), 1.06-1.48 (m, 3H of *sec*-butyl, -CH(-CH₃)-; 2H per unit of 1,2-PI, -C-(CH₃)-CH₂-; 2H of *sec*-butyl, CH₃-CH₂-; 2H per unit of 3,4-PI, CH-CH₂-), 1.48-1.74 (m, 3H per unit of 3,4-PI, C-CH₃; per unit of 1,4-PI, -CH(-CH₃)=), 1.74-2.34 (m, 3H, thymine-C5-CH₃, 1H per unit of 3,4-PI, -CH; 2H per unit of 1,4-PI, -HC=CH-CH₂-; 2H per unit of 1,4-PI, -CH₂-CH(-CH₃)=), 2.45 (t, 2H, $^3J = 5.95$ Hz, C-2'H), 2.67 (t, 2H, $^3J = 6.5$ Hz, -CH₂-CH₂-COO-AZT), 2.77 (t, 2H, $^3J = 6.5$ Hz, -CH₂-CH₂-COO-AZT), 3.44-3.84 (m, 4H per unit of PEO), 4.08-4.13 (m, 1H, C-3'H), 4.42 (d, 2H, $^3J = 3.83$ Hz, C-5'H), 4.51-4.76 (m, 2H per unit of 3,4-PI, -C=CH₂, 2H per unit of 1,2-PI, -HC=CH₂), 4.24 (t, 2H, $^3J = 4.8$ Hz, -O-CH₂-CH₂-OC(O)R), 4.28-4.34 (m, 1H, C-4'H), 4.76-5.10 (m, 1H per unit of 1,4-PI, C=CH-), 5.57-6.00 (m, 1H per unit of 1,2-PI, -HC=CH₂), 6.13 (t, 1H, $^3J = 6.49$ Hz, C-1'H), 7.24 (m, 1H, C-6H).

7.2.2.6.3.3 Coupling of 5-fluorouracil (5-Fu)

6.78 mg 5-Fu ($5.21 \cdot 10^{-5}$ mol), 3.88 mg formaldehyde (37 wt.%, aq., $4.76 \cdot 10^{-5}$ mol) and 0.75 mL water were added to a round-bottom flask. The solution was stirred at 60 °C for six

hours. The product solution was concentrated under reduced pressure to give a white residue. The oil was dissolved in 1 mL dry acetonitrile, and 300 mg PI₆₁-*b*-PEO₂₁₂-COOH ($2.22 \cdot 10^{-5}$ mol), 5.07 mg DMAP ($4.15 \cdot 10^{-5}$ mol) and 6.53 μ L *N,N'*-diisopropylcarbodiimide (DIC, $4.15 \cdot 10^{-5}$ mol) were added and the mixture was stirred at room temperature for 72 hours. The white precipitate was filtered off and the solvent was removed by evaporation. The residue was dissolved in 5 mL water, dialysed against water and finally lyophilised.

¹H-NMR (500 MHz, CDCl₃):

Significant peaks: δ (ppm) = 5.55 (s, 2H, 5Fu-CH₂O), 8.10 (m, 1H, CH=CF),

7.2.2.6.3.4 Coupling of doxorubicin (DXR, Adriamycin[®])

To a solution, containing 100 mg PI₆₁-*b*-PEO₂₁₂-COOH ($7.41 \cdot 10^{-6}$ mol) in 3 mL water, 2.30 mg EDC ($1.48 \cdot 10^{-5}$ mol) and 1.70 mg NHS-sulfo ($1.48 \cdot 10^{-5}$ mol) were added. The solution was stirred for 10 minutes. After the addition of 1 mg doxorubicin hydrochlorid (Sigma 44583, $1.85 \cdot 10^{-6}$ mol) the solution was stirred for 72 hours. Finally the solution was dialysed and lyophilised.

7.2.2.6.4 Coupling of bio-molecules

7.2.2.6.4.1 Coupling of antibodies (-fragments) via a terminal active ester

Prior all vessels, solutions, and materials like Eppendorf pipette tip were autoclaved. To one equivalent of in ligand embedded nanoparticles in water, pH 6, was added two equivalent of 1-ethyl-3-(3-dimethylaminopropyl)carbodiimide (EDC) and five equivalent of *N*-hydroxysulfosuccinimide (Sulfo-NHS). After one hour of stirring the nanoparticles were dialysed against water, pH 6, for half hour. Afterwards the dialysis chamber was placed in phosphate buffered saline (PBS) buffer or ddH₂O respectively, pH 7.4. The solution was transferred into vessels and subjected with three equivalent of antibodies (-fragments). After ten hours of stirring at room temperature the solution was again dialysed against PBS or

ddH₂O respectively, pH 7.4. Depending on the antibody the reaction was achieved at 4 °C. The final nanoparticle solutions had an antibody concentration between 0.2 to 0.4 mg/mL.

7.2.2.6.4.2 Coupling of Fmoc-glycine

Under nitrogen atmosphere 18.1 mg Fmoc-glycine ($6.10 \cdot 10^{-5}$ mol, 1 eq), dissolved in 2 mL pure DMF, were converted with 16.5 mg DCC ($8.00 \cdot 10^{-5}$ mol, 1.3 eq) and 9.76 mg DMAP ($8.00 \cdot 10^{-5}$ mol, 1.3 eq) into an active ester. After ten minutes 183 mg PI₂₇-*b*-PEO₉₃-OH ($3.05 \cdot 10^{-5}$ mol, 0.5 eq) were added. The reaction mixture was stirred for 48 hours at room temperature. Subsequently the solvent was evaporated, and the remaining film dissolved in 3 mL chloroform, whereupon precipitation twice in cold diethyl ether followed. The white residue was finally dissolved in 2 mL of water and lyophilised.

7.2.2.6.4.3 Coupling of biotin

In 2 mL of pure DMF 19.2 mg biotin (approx 99% (TLC)) ($7.84 \cdot 10^{-5}$ mol, 1 eq) were dissolved under nitrogen atmosphere. To this solution 16.5 mg DCC ($8.00 \cdot 10^{-5}$ mol, 1 eq) and 9.76 mg DMAP ($8.00 \cdot 10^{-5}$ mol, 1 eq) was added. After ten minutes of stirring 235 mg PI₂₇-*b*-PEO₉₃-OH ($3.92 \cdot 10^{-5}$ mol, 0.5 eq) were added. The reaction mixture was stirred for 48 hours at room temperature. Subsequently the solvent was evaporated, and the remaining film dissolved in 3 mL chloroform, whereupon precipitation twice in cold diethyl ether followed. The white residue was finally dissolved in 2 mL of water and lyophilised.

7.2.2.6.4.4 Coupling of (±)-α-lipoic acid

12.4 mg (±)-α-lipoic acid (99%) ($6.02 \cdot 10^{-5}$ mol, 1 eq) were dissolved in 2 mL of pure DMF under nitrogen atmosphere. To this solution 16.5 mg DCC ($8.00 \cdot 10^{-5}$ mol, 1.3 eq) and 9.76 mg DMAP ($8.00 \cdot 10^{-5}$ mol, 1.3 eq) was added. After ten minutes of stirring 301 mg PI₂₇-*b*-PEO₉₃-OH ($5.02 \cdot 10^{-5}$ mol, 0.8 eq) were added. The reaction mixture was stirred for 48 hours at room temperature. Subsequently the solvent was evaporated, and the remaining film

dissolved in 3 mL chloroform, whereupon precipitation twice in cold diethyl ether followed. The white residue was finally dissolved in 2 mL of water and lyophilised.

7.2.2.6.4.5 Coupling of arabinogalactan

In 5 mL pure DMF and 3 mL pure DMSO were 200 mg PI₆₁-*b*-PEO₂₁₂-COOH ($1.48 \cdot 10^{-5}$ mol, 1 eq) dissolved and exposed to 3.37 mg *N,N'*-diisopropylcarbodiimide (DIC, 4.18 μ L, $2.67 \cdot 10^{-5}$ mol, 1.8 eq) and 2.35 mg DMAP ($1.92 \cdot 10^{-5}$ mol, 1.3 eq) under inert conditions. After ten minutes of stirring 1.24 g arabinogalactan (FEMA 3254, from *larix occidentalis* – Western Larch (~ 60 kD), $2.08 \cdot 10^{-5}$ mol, 1.4 eq), dissolved in 1 mL DMF, were added. The reaction mixture was stirred for 48 hours at room temperature. Subsequently the solvent was evaporated, and the remaining film dissolved in 3 mL chloroform, whereupon precipitation twice in cold diethyl ether followed. The white residue was finally dissolved in 2 mL of water and lyophilised.

7.2.3 Emulsion polymerization

7.2.3.1 Materials

The predominant number was performed by using styrene (Merck), divinylbenzene (DVB, Merck) as a crosslinker, acrylic acid (Merck) or vinyl-terminated polyethylene glycol (V1100 PEG, DEGE139780, Clariant GmbH) as hydrophilic monomers, and sodium dodecyl benzene sulfonate (SDBS, Aldich) as emulsifier. In other systems methyl methacrylate (Aldrich), and squalene (Fluka) were used. The reactions were initiated by using sodium persulfate (Aldrich) for reactions at 80 °C, 2,2'-Azobis[2-(2-imidazolin-2-yl)propane]dihydrochloride (VA044, WAKO) for reactions at 45 °C and Azo-bis-(isobutyronitril) (AIBN, Fluka). As surfmers were established Ralumer (BASF), Lutensol T07 (BASF), Lutensol (BASF), Pluronic (BASF), nonyl phenol ethoxylate (NP10, Aldrich) and Tween[®]80 (Merck).

7.2.3.2 Polymerization

Concerning the emulsifiers it was distinguished between ones, which don't take part at the polymerization (2.1.1) and ones which are bonded during the polymerization, the so called surfmeres (2.1.2).

7.2.3.2.1 Emulsifier approach

The emulsions were typically prepared as shown in the following section. First emulsifier was dissolved in water and *n*-pentanol was added. Then nanoparticles were dried in vacuum and dissolved in the hydrophobic monomers. The typical number of nanoparticles applied was varied between 6 and $9 \cdot 10^{-8}$ mol. While stirring the aqueous solution (1200 rpm) the hydrophobic monomers were added dropwise. After devolatilization via nitrogen flow, the mixture was heated up to a temperature of 44 - 80 °C. After reaching a constant temperature the initiator, dissolved in some droplets of water, in case of hydrophobic initiators dissolved in the hydrophobic monomers, was injected after 5 - 10 minutes. Finally hydrophilic monomers were added after a time period of 10 - 60 minutes. Typically the reaction period was 24 h. The amount of substances used is shown in table 9.

number	solvens		hydrophobic monomers				hydrophilic monomers		emulsifier	alcohol	initiator		Nanos
	water [g]	styrene [g]	DVB [g]	squalene [g]	MMA [g]	V1100 PEG [g]	acrylic acid [g]	SDBS [g]	1-pentanol [g]	NaPS [g]	VA 044		
1	12.1	1.11	0.09				0.14		1.5	0.08	0.010	CdSe	
2	11.5	1.11	0.09				0.47		1.5	0.08	0.010	CdSe	
3	12.1	1.08	0.16				0.14		1.7	0.08		CdSe	
4	12.1	1.15	0.05				0.14		1.3	0.09	0.016	CdSe	
5	20.1	1.05	0.16				0.60		1.7	0.08		CdSe	
6	40.1	1.05	0.16				1.00		1.7	0.09	0.016	CdSe	
7	11.0	0.74	0.11				0.90		1.2	0.06		CdSe	
8	15.0	0.75	0.11				1.40	0.095	1.2	0.00	0.016	CdSe	
9	14.0	0.65	0.11					0.057	1.2	0.08	0.016	CdSe	
10	14.0	0.55	0.11					0.048	1.2	0.20	0.016	CdSe/CdS/ZnS	
11	14.0	0.28	0.06					0.029	1.2	0.08	0.016	CdSe/CdS/ZnS	
12	20.1	1.05	0.16					0.057	1.7	0.09	0.016	CdSe	
13	20.1	0.90	0.15					0.095	1.7	0.09	0.016	CdSe	
14	98.3	4.55	0.74					0.400	1.7	0.57	0.110	CdSe	
15	20.1	1.05	0.16					0.057	1.7	0.09	0.016	Gold	
16	14.0	0.65	0.11					0.057	1.2	0.08	0.016	Gold	
17	20.1	0.81	0.13					0.057	1.7	0.09	0.016	Fe ₃ O ₄	
18	20.1	0.81	0.13					0.057	1.7	0.09	0.016	Fe ₃ O ₄	
19	20.2	1.05	0.17					0.057	1.7	0.09	0.017	Gold	
20	20.2	1.05	0.17					0.057	1.7	0.09	0.017	Gold	
21	20.1	0.70	0.13					0.057	1.2	0.09	0.016	Fe ₃ O ₄	
22	25.2	1.05	0.16					0.057	1.7	0.09	0.017	Gold	
23	20.1	0.91	0.13					0.057	1.8	0.09	0.016	Fe ₃ O ₄	
24	10.0	0.45	0.80					0.029	0.9	0.05	0.008	Fe ₃ O ₄	
25	10.0	0.35	0.70					0.029	0.9	0.05	0.008	Fe ₃ O ₄	
26	10.0	0.45	0.80					0.029	1.4	0.05	0.008	Fe ₃ O ₄	
27	10.0	0.45	0.80					0.029	0.9	0.09	0.008	Fe ₃ O ₄	
28	20.0	0.45	0.80					0.029	0.9	0.05	0.008	Fe ₃ O ₄	
29	10.0	0.45	0.80					0.048	0.9	0.05	0.008	Fe ₃ O ₄	
30	25.2	1.05	0.16					0.057	1.7	0.09	0.017	CdSe	
31	20.0	1.05	0.16					0.057	1.7	0.09	0.017	Gold	
32	12.6	0.53	0.08					0.029	0.9	0.05	0.017	Fe ₃ O ₄	
33	12.6	0.30	0.30					0.048	0.9	0.05	0.017	Fe ₃ O ₄	
34	20.1	0.81	0.13					0.057	1.7	0.09	0.016	Fe ₃ O ₄	
35	20.1	0.81	0.13					0.057	1.7	0.09	0.016	Giga-Fe ₃ O ₄	
36	20.1	0.81	0.13					0.095	1.7	0.09	0.016	Giga-Fe ₃ O ₄	
37	20.1			1.07				0.095	1.7	0.09	0.016	CdSe	
38	20.1			1.20				0.067	1.7	0.09	0.016	CdSe	
39	25.2				1.03			0.057	1.8	0.09	0.017	CdSe	
40	25.2		0.16		1.03			0.057	1.8	0.09	0.017	CdSe	
41	6.3		0.04		0.26			0.014	0.4	0.02	0.004	Fe ₃ O ₄	

table 9: amount of substance used for the reactions.

7.2.3.2.2 Surfmer approach

The emulsions using surfmeres were typically prepared as standard emulsions with use of VA044 as initiator. The amount of substance used is shown in table 10. The surfmer was partial to fully present in the monomer solution upon addition to the aqueous phase.

A comparison between NP10 and Tween[®]80 was performed according to Mandal *et al.*^[322] Tween[®]80 was used as a 4 wt% aqueous solution. Some reactions with NP10, NP10 and Tween[®]80 (1:1) and Tween[®]80 were performed with and without adding initiator to examine the effect of polymerisation on the micelles.

number	styrene [g]	DVB [g]	surfmer [g]	l-pentanol [g]	water [g]	temperature [°C]	initiator [g]
42	0.75	0.12	1.2 Ralumer	0.07	14	45	0.016
43	1.05	0.16	1.0 Lutensol T07	0.09	25	45	0.017
44	1.05	0.16	0.5 Lutensol T07	0.09	25	45	0.017
45	1.05	0.16	1.0 Lutensol	0.09	25	45	0.017
46	1.05	0.16	1.0 Pluronic	0.09	25	45	0.017
47	0.56	0.12	0.3 oleic acid	0.15	28	50	0.032
48	0.56	0.12	1.0 oleic acid	0.15	28	50	0.032
49	0.56	0.12	0.6 oleic acid	0.15	28	50	0.032
50	0.56	0.12	1.0 Tween 80	0.15	28	45	0.032
51	0.56	0.12	1.5 Tween 80	0.15	28	45	0.032
52	0.56	0.12	0.5 Tween 80	0.15	28	45	0.032
53	0.56	0.12	1.0 Tween 80	0.15	28	45	0.032
54	0.56	0.12	1.0 Tween 80	0.15	28	45	0.032
55	0.56	0.20	1.0 Tween 80	0.15	28	45	0.032
56	0.56	0.30	1.0 Tween 80	0.15	28	45	0.032
57	0.56	0.12	0.5 Tween 80	0.15	28	60	0.032
58	0.56	0.12	0.5 Tween 80	0.15	28	60	0.032
59	0.56	0.12	0.5 Tween 80	0.15	28	55	0.032
60	0.56	0.12	0.5 Tween 80	0.15	28	50	0.032
61	0.56	0.12	0.5 Tween 80	0.15	28	65	0.032
62	0.56	0.12	2.0 Tween 80	0.15	28	65	0.032
63	0.56	0.12	0.5 Tween 80	0.15	28	52	0.032
64	0.56	0.12	0.5 Tween 80	0.15	28	58	0.032
65	0.56	0.12	0.5 Tween 80	0.15	28	70	0.032
66	0.56	0.12	1.3 Tween 80	0.15	28	45	0.032
67	0.56	0.12	0.8 Tween 80	0.15	28	45	0.032
68	0.53	0.16	0.5 Tween 80	0.15	28	45	0.032
69	0.50	0.20	0.5 Tween 80	0.15	28	45	0.032
70	0.56	0.12	0.5 Tween 80	0.15	28	70	0.032 (AIBN)

table 10: amount of substance used for the reactions with surfmers.

7.2.3.2.3 Purification of emulsion particles

Purification of the polymer / nanoparticles composites, if necessary, was performed by means of syringe filters (450 nm, Roth) to cut off agglomerates and dialysis to separate emulsifier. Magnetic particles were picked out by magnetic forces.

Separation of polymer/nanoparticles composites from polymer particles was achieved by addition of heptane. After mixing and centrifugation the polymer particles are located in the organic phase, while the nanoparticle containing composites are present in the aqueous phase.

7.2.3.3 Functionalisation of emulsifier

A further functionalization of the particles (e.g. for biolabelling) requires functional groups on the surface of the particles. Tween[®]80 offers a terminated hydroxylic groups which can be used for such reactions. In favour this reaction should take place in water, to allow functionalization even after the polymerization. In many cases the hydroxylic group might not

be the “ideal” functional group. Thus it is necessary to find ways to transform the hydroxylic group into functional groups required (figure 140).

The analytic was based on nuclear magnetic resonance spectroscopy (NMR). $^1\text{H-NMR}$, $^{13}\text{C-NMR}$, and two-dimensional NMR spectra (H,H-COSY, HSQC, and HMBC) were recorded in CDCl_3 using tetramethylsilane as the internal standard or in D_2O using the solvent peak as the internal standard. An AMX400 spectrometer with a test frequency of 400 MHz and a DRX500 Avance spectrometer with a test frequency of 500 MHz, both fabricated by Bruker, were used. The spectra were evaluated using the SpinWorks software version 2.5.5.

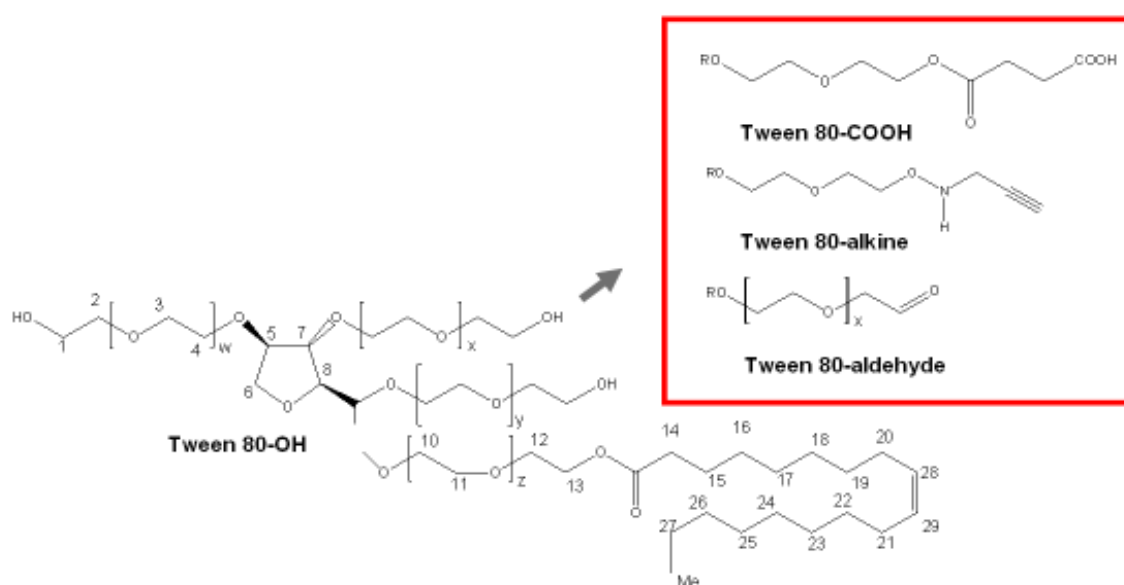


figure 140: Modification of functional group of Tween[®]80 .

7.2.3.3.1 Synthesis of *w*-carboxyl-polyoxyethylenesorbitan monooleate

To 2.00 g Tween[®]80 (1.53 mmol), dissolved in 10 mL chloroform, 37.4 mg of the nucleophilic Steglich-Höfle catalyst 4-dimethylaminopyridine (DMAP) (306 μmol , 0.2 eq) were added. After the addition of 764 mg succinic anhydride (7.64 mmol, 5 eq), in 3 mL chloroform dissolved, the reaction mixture was stirred for 48 hours at room temperature, concluding with the evaporation of the solvent, and resuspension of the yellow, viscous pellet in a water and ethanol solution. The raw product (TWEEN[®]80-COOH) was dialysed for two days and lyophilized^[289].

¹H-NMR (500 MHz, CDCl₃):

δ (ppm) = 0.88 (t, 3 H, ³J_{Me, H-27} = 7.3 Hz, Me), 1.20-1.22 (m, 20 H, CH₂-16-19 und CH₂-22-27), 1.62 (quin., 2 H, ³J_{H-15, H-14} = 7.8 Hz, ³J_{H-15, H-16} = 6.9 Hz, CH₂-15), 2.0 (q, 4 H, ³J_{H, H} = 6.3 Hz, CH₂-20-21), 2.32 (t, 2 H, ³J_{H-14, H-15} = 7.8 Hz, CH₂-14), 2.63 (m, 10 H, C-CH₂-CH₂-COOH), 3.56-3.76 (m, 65, PEO, CH₂-5-9), 4.22 (dd, 2 H, CH₂-13, ³J_{H, H} = 5.2 Hz), 5.30-5.39 (m, 2 H, CH-28-29).

¹³C-NMR (126 MHz, CDCl₃):

δ (ppm) = 14.00 (Me), 24.90 (C-15), 27.18, 27.22 (C-20-21), 29.11 - 29.76 (C-16-19 und C-22-27), 31.90 (C-CH₂-CH₂-COOH), 34.20 (C-14), 63.36 (C-1), 63.81 (C-13), 69.01, 69.20, 70.52 (PEO und C-5-9), 129.75, 130.00 (C-28 und C-29).

7.2.3.3.2 Implementation of aldehyde terminated Tween[®]80

1.16 g dimethylaminopyridine (DMP, $2.75 \cdot 10^{-3}$ mol, 1.2 eq.) were dissolved in 5 mL dichlormethane. To this solution 1 g ($7.64 \cdot 10^{-4}$ mol) of Tween[®]80 in 10 mL dichlormethane were added. The reaction mixture was stirred for 48 h, than centrifugated and the dissolved aldehyd precipitate from acetone. After evaporation the product (TWEEN[®]80-CHO) was dissolved in water and lyophilised.

¹H-NMR (500 MHz, CDCl₃):

δ (ppm) = 0.88 (t, 3 H, ³J_{Me, H-27} = 7.3 Hz, Me), 1.20-1.22 (m, 20 H, CH₂-16-19 und CH₂-22-27), 1.62 (quin., 2 H, ³J_{H-15, H-14} = 7.8 Hz, ³J_{H-15, H-16} = 6.9 Hz, CH₂-15), 2.0 (q, 4 H, ³J_{H, H} = 6.3 Hz, CH₂-20-21), 2.32 (t, 2 H, ³J_{H-14, H-15} = 7.8 Hz, CH₂-14), 3.56-3.76 (m, 65, PEO, CH₂-5-9), 4.15 (m, 2 H, CH₂-CHO), 4.22 (dd, 2 H, ³J_{H, H} = 5.2 Hz, CH₂-13), 5.30-5.39 (m, 2 H, CH-28-29), 9.72 (s, 1 H, CHO).

¹³C-NMR (126 MHz, CDCl₃):

δ (ppm) = 14.08 (Me), 22.64 (C-27), 24.88 (C15), 27.15, 27.20, (C-20, C-21), 29.74 – 29.09 (C-16-19, C-22-25), 31.87 (C-26), 34.18 (C-14), 63.33 (C-13), 69.19 – 71.23 (PEO, C-5-9), 76.84 (CH₂-CHO), 129.72, 129.98 (C-28, C-29), 173.00 (COOR), 196.00 (CHO).

7.2.3.3.3 Implementation of epoxid terminated Tween[®]80

76.6 mg (1.91 mmol) (5 eq.) sodium hydride (60% in paraffin) were dissolved in 5 mL tetrahydrofuran (THF). To this solution 500 mg Tween[®]80 ($3.82 \cdot 10^{-4}$ mol, 1 eq.) in 5 mL THF was injected at 0°C. After stirring 1 h at room temperature the mixture was cooled down again to 0°C and 177 mg (1.91 mmol) (5 eq.) epichlorohydrine was added. Further 48 h stirring at 40 °C results again in two times precipitation from diethylether.

The product could not be isolated. Instead, as an intermediate the reaction could be achieved with a primary amine.

7.2.3.3.4 Implementing of an alkine group into Tween[®]80

To 7.429 g (45.81 mmol) 1,1'-carbonyldiimidazole (CDI) (60 eq.) dissolved in 10 mL dichlormethane 1 g ($7.64 \cdot 10^{-4}$ mol) Tween[®]80 dissolved in 10 mL dichlormethane was added. After stirring 48 h the organic solution was washed three times with water to hydrolyse the excess of CDI. The organic phase was dried with sodium sulphate, and concentrated up to a volume of 20 mL.

To 1.262 g imidazole-activated Tween[®]80 (22.91 mmol) propargylamine was added and stirred 48 h at 55 °C. The crude product (TWEEN[®]80-C≡CH) was precipitated three times from acetone, and then lyophilised.

¹H-NMR (500 MHz, CDCl₃):

δ (ppm) = 0.88 (t, 3 H, $^3J_{\text{Me, H-27}} = 7.3$ Hz, Me), 1.20-1.22 (m, 20 H, CH₂-16-19 und CH₂-22-27), 1.62 (quin., 2 H, $^3J_{\text{H-15, H-14}} = 7.8$ Hz, $^3J_{\text{H-15, H-16}} = 6.9$ Hz, CH₂-15), 2.0 (q, 4 H, $^3J_{\text{H, H}} = 6.3$ Hz, CH₂-20-21), 2.24 (m, 1 H, NH), 2.32 (t, 2 H, $^3J_{\text{H-14, H-15}} = 7.8$ Hz, CH₂-14), 3.56-3.76 (m, 65, PEO, CH₂-5-9), 3.95-4.00 (m, 4 H, CH₂-alkine), 4.22 (dd, 2 H, $^3J_{\text{H, H}} = 5.2$ Hz, CH₂-13), 5.30-5.39 (m, 2 H, CH-28-29).

¹³C-NMR (126 MHz, CDCl₃):

δ (ppm) = 27.45 (C-20-21), 28.78 – 29.62 (C-16-19 und C-22-27), 62.43 (C-13), 69.31 – 70.52 (PEO und C-5-9), 129.24, 129.86 (C-28 und C-29).

7.2.3.3.5 Implementing of an bromide into Tween[®]80

To 1.05g (0.550 mL, 4.86 mmol) 2-Bromopropionylbromide (6 eq.) dissolved in 5 mL tetrahydrofuran (THF) 1.00 g ($7.64 \cdot 10^{-4}$ mol) Tween[®]80 in 5 mL THF were added slowly. Further 18 h stirring at room temperature results in the try of precipitation from diethylether. However the product could not be isolated.

7.2.3.4 Calorimetric Measurements

The calorimetric measurements were performed by means of an isoperibolic calorimeter (Mettler). Experiment a): 45 °C, 280.3 g water, 1.5 g 1-pentanol, 5.6 g styrene, 1.2 g DVB, 5.0 g Tween[®]80 ; b): 45°C, 280.4 g water, 1.5 g 1-pentanol, 5.6 g styrene, 1.2 g DVB, 1.1 g sodium dodecyl sulfate (SDS).

7.2.3.5 (Förster-) fluorescence resonance energy transfer (FRET)

The probes for fluorescence resonance energy transfer (FRET) measurements were prepared as listed in table 11. To assure the presence of just one nanoparticle per micelle a quantum dot to ligand ratio of 1:573 was used, abandoning a crosslinkage to avoid a thermal degradation of the dye. The ratio of quantum dot to dye (Alexa Fluor[®] 594) was 1:0, 2:1, and 1:1. In each case $1.08 \cdot 10^{-9}$ mol CdSe/CdS/ZnS nanoparticles with an absorption maximum of 540 nm and an emission maximum of 553 nm were applied.

approach	PI- <i>b</i> -PEO-OH	PI- <i>b</i> -PEO-Alexa Fluor® 594	THF [μL]	H ₂ O [μL]
1.	8.14 mg, 603 nmol	-	350	1000
2.	8.14 mg, 603 nmol	73.0 μg, 5.4 nmol (10% coupled with dye)	350	1000
3.	8.14 mg, 603 nmol	146 μg, 10.8 μmol (10% coupled with dye)	350	1000

table 11: parameter of ligand-addition.

7.3 Vesicle formation

A solution of 1-3 nmol nanoparticles coated by PI₆₁-*b*-PEO₂₁₂-OH in 1 mL water was heated to 60 °C. Under stirring 10 mg PI₃₂-*b*-PEO₂₇, dissolved in 100 μL THF, was injected quickly via a 1 mL syringe. After the evaporation of THF the solution was analysed using a light microscope.

To remove nanoparticle micelles, which were not located inside of the vesicle, the solution was cleaned by a syringe filter 1.2 μm (FP 30 1.2 cellulose acetate (CA), Schleicher & Schuell, Dassel, Germany).

To 20 μL of the vesicle solution was 20 μL liquefied (microwave) agarose added. Fixed on a glas plate confocal microscopy was arranged.

7.4 Biological applications

7.4.1 Cell culture

Tumour cells HT29 and LOX were cultivated in vented 250 mL (75 cm² growth space) culture-bottles (Sarstedt AG & Co Nümbrecht, Deutschland) at standard conditions (37 °C, 100% relative air moisture, 5% CO₂/75% air) in a hera cell cellculture-cupboard (Heraeus Instruments GMBH, Hanau, Germany). The culture-medium consists of GIBCO® RPMI-medium 1640 1x (+) L-glutamine (invitrogen™ corporation / Carlsbad, CA, U.S.), which were added with 10% fetal bovine serum (50 mL, GIBCO® FCS, invitrogen™ corporation / Carlsbad, CA, U.S.) plus penicillin and streptomycin (5 mL, 10.000 U/mL penicillin G-

sodium + 10000 µg/mL streptomycin-sulfate in 0.85% NaCl, GIBCO™, invitrogen corporation / Carlsbad, CA, U.S.). For detaching of the adherend growing cells the cells were brood-conditions for 5 minutes trypsinized (0.5% trypsin-EDTA Gibco, invitrogen™ corporation / Carlsbad, CA, U.S.).

7.4.1.1 Determination of the cell count

The cell count was determined using a Neubauer-count chamber (Marienfeld GmbH Lauda-Königshofen, Germany) with 0.1 mm depth and 0.0025 mm² plane. After resuspension of the cell suspension 10 µL were pipetted on the object holder. Under a Axiovert 35 microscope (Carl Zeiss AG, Germany) were four large-quadrates (each 16 small-quadrates with each 0.1 µL volume) counted out.

$$\text{counted cells} / 4 \times \text{dilution factor} \times 10000 = \text{cells/mL}$$

In case of more than 40 cells per large-quadrant a dilution with PBS of a factor of 10 conducted to achieve a cell count of 20-40 cells / large-quadrant. By means of dilution or concentration of the stock solution the required cell count / volume ratio was regulated.

7.4.1.2 Laboratory animals

SCID (severe combined immunodeficiency disorder) mice were exhibit subcutaneous with 10⁶ cells in 200 µL serum-free medium (GIBCO® RPMI-medium 1640 1x (+) L-glutamine invitrogen™ corporation / Carlsbad, CA, U.S.) upside of the right flank. For injection were 26 G cannula (Microlance 0.45 x 13 mm Becton Dickinson GmbH, Heidelberg, Germany) and 1000 µL plastic-insulin-syringes (Becton Dickinson GmbH, Heidelberg, Germany) used. HT29 was fourteen, LOX seven days let adhere, than the experiment accomplished.

7.4.1.3 Application

Intravenous application of the antibodies-nanoparticle constructs was carried out employing 30 G expendable-injection-cannula (Sterican, B. Braun Melsungen AG, Melsungen, Germany) and 250 μL Hamilton glass-syringes (Hamilton Bonaduz AG, Bonaduz, Switzerland). The antibody-labelled nanoparticles, dissolved in 100 μL PBS (Dulbeccos Phosphat Buffer Saline, Gibco[®] Life Technologies Ltd., Pasley, Scotland), were in the caudal-vein injected. As a control were equivalent amounts of nanoparticles, coupled with IgG1 iso-antibodies, applied.

7.4.1.4 Cellincubation experiments

7.4.1.4.1 Incubation of cells

HT29 cells were trypsinized and washed three times in PBS. Cells were counted and split into round bottom tubes resulting in twelve samples of 1.5×10^7 cells, each in a volume of 500 μL PBS supplemented with 30 μL human AB-serum to block unspecific binding (Biotest AG, Dreieich, Germany). The cell suspensions were supplemented with unconjugated, IgG-conjugated or T84.1-conjugated equal mixtures of magnetite and quantum dot particles at different amounts of 10 μL (c_1), 25 μL (c_2) and 50 μL (c_3). In addition, three aliquots were pre-treated with unconjugated mAb T84.1 (40 $\mu\text{g}/\text{mL}$) for 15 minutes to block specific binding sites (T84.1-magnetite nanoparticles). Cells were incubated for 1 hour at room temperature on a rolling device to prevent cell adherence and aggregation. Subsequently, cells were washed three times in PBS and re-suspended in 300 μL PBS. Flow cytometry was performed with 20 μL of the cell suspension (approximately 1×10^6 cells) and phantoms for MR imaging were prepared from the remaining suspension.

7.4.1.4.2 Incubation of cells with anti-CEACAM specific SPIONs

HT29 cells were trypsinized and washed three times in PBS. Cells were counted and split into round bottom tubes as nine samples of 1.5×10^7 cells, each in a volume of 500 μL PBS supplemented with 30 μL human AB-serum to block unspecific binding (Biotest AG, Dreieich, Germany). Cell suspensions were supplemented with IgG-conjugated and T84.1-conjugated particles at two sets with different amounts of 25 μL (c_1) and 50 μL (c_2) SPION-A.

One sample of each set was pre-treated with unconjugated mAb T84.1 (40 $\mu\text{g}/\text{mL}$) for 15 minutes to block specific binding sites. Cells were incubated for 1 hour at room temperature on a rolling device. Afterwards, cells were washed twice and re-suspended in 300 μL PBS for preparation of MR imaging phantoms (0.5 mL Eppendorf tubes). These consist of a layer of polyacrylamid at the bottom covered by the cell pellet and PBS.

Results from MR imaging and MR relaxometry are listed below. Considerable darkening of cell pellets indicates a positive detection of SPION by MR imaging. MR relaxometry indicates T_2^* and T_2 relaxation times. The reciprocal values R_2^* and R_2 are quantitative measures of SPION accumulation.

7.4.1.4.3 Magnetic resonance imaging (MRI)

Imaging phantoms of cells were prepared in 0.5 mL Eppendorf tubes on a layer of 200 μL of 10% polyacrylamide gel. The tubes were filled up with 280 μL of cell suspension and samples were kept for 2 hours at 4 $^\circ\text{C}$ for sedimentation.

MR imaging was performed on a whole-body 3.0T MR scanner (Philips, Best, Netherlands) equipped with a gradient system providing a maximal amplitude of 30 mT/m and a slew rate of 150 T/m/s. All measurements were conducted with a small animal solenoid coil of 10 cm length and 7 cm inner diameter. The tubes were positioned in the coil using a custom made rack of acrylic glass containing water at room temperature.

A T_2 -weighted multi-echo spin-echo sequence was used for MR relaxometry. Imaging parameters were as follows: TR 1307 ms, first TE 8.2 ms, echoes 22, echo spacing 7.8 ms, NSA 1, FOV 100 mm, matrix 192×134 , slice thickness 0.7 mm, slices 3, effective voxel size

$0.52 \times 0.52 \times 0.7 \text{ mm}^3$, acquisition time 6:03 minutes. Image data were analyzed using a specific software tool (RelaxFit, Philips Research Laboratories, Hamburg, Germany) based on the interactive data language (IDL). The program employed a mono-exponential fit to estimate T_2 relaxations times in a region of interest ($n = 50$ pixel) within the cell pellets and to calculate reciprocal R_2 relaxation rates. Results were also presented as T_2 and R_2 parametric maps.

7.4.1.4.4 Cell experiments in cooperation with CAN

Each 10 nmol CdSe/CdS/ZnS nanoparticles were dried and in 1 mL THF, in which the respective ligand (QD/P 1:256), listed in table 12, was previously been dissolved. To 200 μL of this stock solution 1 mL water was injected quickly, whereby instantly the solution was vortexed and the THF amount was removed in nitrogen flow. With the next (4 x) 200 μL stock solution it was proceeded accordingly to the first step.

samples
23 mg M-PEO- <i>b</i> -PCL- <i>b</i> -PEI CP10 (2.56 μmol)
23 mg <i>t</i> C-PEO- <i>b</i> -PCL- <i>b</i> -PEI CP8 (2.56 μmol)
15 mg DP-PEO- <i>b</i> -PCL- <i>b</i> -PEI DPA3 (2.56 μmol)

table 12: amount of used ligands.

7.4.1.5 Fluorescence activated cell sorting (FACS)

The required concentration of the QD-antibody solutions was 400 $\mu\text{g/mL}$ ($4 \cdot 10^{-9}$ mol/mL). Accordant 10 nmol CdSe/CdS/ZnS nanoparticles, coated with $\text{PI}_{30}\text{-N3}$, were subsequent to drying dissolved in 800 μL THF, in which 240 μg AIBN ($1.46 \cdot 10^{-6}$ mol) and 75.0 mg $\text{PI}_{61}\text{-}b\text{-PEO}_{212}\text{-COOH}$ ($5.56 \cdot 10^{-6}$ mol) were present, which is consistent with a quantum dot to ligand ratio of 1:556, gaining micelles with an average of one particle embedded. From this stock solution stepwise 200 μL were very slowly injected in 2.5 mL of water under stirring (800 rpm) and a nitrogen flow unto the water surface area.

For half an hour the solution was heated up to 60 $^{\circ}\text{C}$ under continuing nitrogen flow to concentrate the solution to 2 mL. This clear, orange solution was dialysed against water for

24 hours using a membrane with a MWCO of 5000. The solution was diluted to 2.4 mL and partitioned to twelve 200 μ L samples, containing 833 pmol QD-micelles.

The attachment of the antibodies anti CEA T84.1 (AB1) and IgG2b-isotype (AB2) was carried out like it is specified in table 13. All equivalents shown in table 1 are in reference to 833 pmol QD-micelles.

Following the addition of EDC and sulfo-NHS at pH 7 in terms of sample 1-4 the addition of the respective antibody was done after 5 minutes of stirring. In case of the activation of the carboxylic function at pH 6 the samples 5-12 were dialysed for half an hour against dH₂O (MWCO 5000), pH 6, transferred in glass jars, wherein the activation of the carboxylic groups was performed. After 15 minutes of stirring the EDC/sulfo-NHS activated micelles were dialysed for 10 minutes against dH₂O, pH 6, and subsequent against dH₂O, pH 7, for 10 minutes. The respective antibody was added in glass jars. A final dialysis to remove reacted sulfo-NHS and EDC couldn't be achieved, since the amounts of the samples were too low.

sample	EDC	sulfo-NHS	pH	dialysis	AB1	AB2
1.	155 ng, 1.2 eq, 1.00 nmol	90.4 ng, 0.5 eq, 417 pmol	7	-	117 μ g, 1.4 eq, 1.17 nmol	
2.	155 ng, 1.2 eq, 1.00 nmol	90.4 ng, 0.5 eq, 417 pmol	7	-		117 μ g, 1.4 eq, 1.17 nmol
3.	155 ng, 1.2 eq, 1.00 nmol	181 ng, 1.0 eq, 833 pmol	7	-	117 μ g, 1.4 eq, 1.17 nmol	
4.	155 ng, 1.2 eq, 1.00 nmol	181 ng, 1.0 eq, 833 pmol	7	-		117 μ g, 1.4 eq, 1.17 nmol
5.	155 ng, 1.2 eq, 1.00 nmol	90.4 ng, 0.5 eq, 417 pmol	6	+	117 μ g, 1.4 eq, 1.17 nmol	
6.	155 ng, 1.2 eq, 1.00 nmol	90.4 ng, 0.5 eq, 417 pmol	6	+		117 μ g, 1.4 eq, 1.17 nmol
7.	155 ng, 1.2 eq, 1.00 nmol	181 ng, 1.0 eq, 833 pmol	6	+	117 μ g, 1.4 eq, 1.17 nmol	
8.	155 ng, 1.2 eq, 1.00 nmol	181 ng, 1.0 eq, 833 pmol	6	+		117 μ g, 1.4 eq, 1.17 nmol
9.	155 ng, 1.2 eq, 1.00 nmol	90.4 ng, 0.5 eq, 417 pmol	6	+	100 μ g, 1.2 eq, 1.00 nmol	
10.	155 ng, 1.2 eq, 1.00 nmol	90.4 ng, 0.5 eq, 417 pmol	6	+		100 μ g, 1.2 eq, 1.00 nmol
11.	155 ng, 1.2 eq, 1.00 nmol	181 ng, 1.0 eq, 833 pmol	6	+	100 μ g, 1.2 eq, 1.00 nmol	
12.	155 ng, 1.2 eq, 1.00 nmol	181 ng, 1.0 eq, 833 pmol	6	+		100 μ g, 1.2 eq, 1.00 nmol

table 13: parameter of ligand-addition.

Finally, following the reaction time of one hour, the solutions of the IgG-conjugated quantum dots and T84.1-conjugated equals stored at 4 °C in a fridge. The final concentrations of the solutions are listed in table 14.

sample	concentration	
1.	833 pmol QDs, 1.17 nmol ABs, 375 μ L dH ₂ O, 312 μ g/mL ABs	222 μ g/mL QD-ABs
2.	833 pmol QDs, 1.17 nmol ABs, 361 μ L dH ₂ O, 324 μ g/mL ABs	231 μ g/mL QD-ABs
3.	833 pmol QDs, 1.17 nmol ABs, 375 μ L dH ₂ O, 312 μ g/mL ABs	222 μ g/mL QD-ABs
4.	833 pmol QDs, 1.17 nmol ABs, 362 μ L dH ₂ O, 323 μ g/mL ABs	230 μ g/mL QD-ABs
5.	833 pmol QDs, 1.17 nmol ABs, 375 μ L dH ₂ O, 312 μ g/mL ABs	222 μ g/mL QD-ABs
6.	833 pmol QDs, 1.17 nmol ABs, 361 μ L dH ₂ O, 324 μ g/mL ABs	231 μ g/mL QD-ABs
7.	833 pmol QDs, 1.17 nmol ABs, 375 μ L dH ₂ O, 312 μ g/mL ABs	222 μ g/mL QD-ABs
8.	833 pmol QDs, 1.17 nmol ABs, 362 μ L dH ₂ O, 323 μ g/mL ABs	230 μ g/mL QD-ABs
9.	833 pmol QDs, 1.00 nmol ABs, 365 μ L dH ₂ O, 274 μ g/mL ABs	228 μ g/mL QD-ABs
10.	833 pmol QDs, 1.00 nmol ABs, 352 μ L dH ₂ O, 284 μ g/mL ABs	237 μ g/mL QD-ABs
11.	833 pmol QDs, 1.00 nmol ABs, 363 μ L dH ₂ O, 275 μ g/mL ABs	229 μ g/mL QD-ABs
12.	833 pmol QDs, 1.00 nmol ABs, 353 μ L dH ₂ O, 283 μ g/mL ABs	236 μ g/mL QD-ABs

table 14: concentration of samples.

7.4.1.6 Biacore technique

For the surface plasmon resonance measurements was an immobilization buffer (acetate buffer) and a running buffer (HEPES buffer) were freshly prepared, sterile filtered and degassed.

A measuring cell and a reference cell were parallel charged with the same reagents with the exemption that in the reference flow cell no analyt (lectin) was immobilized.

For immobilization of the lectrin RCA₁₂₀ a CM5 chip with carboxylated dextran matrix was applied. The carboxylat groups of the dextran coating was via EDC/NHS (4:1) transformed in an active ester. For this purpose at flow rate of 10 μ L/min a solution of 0.4 M EDC and 0.1 NHS in ddH₂O was run over the chip.

After 10-minute activation for washing the running buffer was let at the same flow rate for two minutes over the dextran surface. The chip was subsequent incubated with a solution of 50 μ M lectin RCA₁₂₀ in acetate buffer at a flow rate of 5 μ L/min for 20 minutes. After further wash steps capping was achieved with 200 μ L ethanolamine, which was injected over a time period of 20 minutes.

Nanoparticle-containing solutions in HEPES buffer with ascending concentration (0 μM , 9.38 μM , 18.75 μM , 37.5 μM , 75 μM , and 150 μM) were run over the chip at a flow rate of 20 $\mu\text{L}/\text{min}$ 3 minutes respectively. Following each concentration was the conditioning with running buffer for regeneration.

7.4.1.6.1 Coating of nanoparticles

PI-N3 featuring CdSe/CdS/ZnS-nanoparticles were coated with PI-*b*-PEO-OH at a quantum dot / polymer ratio of 1:142. In case of sugar-nanoparticles 20% of the ligand featured galactose or glucose respectively. The parameters of the ligand addition are shown in table 15.

approach	PI- <i>b</i> -PEO-OH	PI- <i>b</i> -PEO-saccharide	AIBN [mg]	THF [μL]	H ₂ O [μL]	PI-N3 coated QDs [mol]
1.	115 mg, 8.52 μmol	0	7	800	10000	$6 \cdot 10^{-8}$
2.	92 mg, 6.8 μmol	23 mg, 1.7 μmol (galactoside)	7	800	10000	$6 \cdot 10^{-8}$
3.	92 mg, 6.8 μmol	23 mg, 1.7 μmol (glucoside)	7	900	10000	$6 \cdot 10^{-8}$

table 15: parameter of ligand-addition.

The nanoparticles were purified and concentrated by ultrafiltration and finally dialysed against HEPES-buffer.

7.5 Analytic

7.5.1 Nuclear magnetic resonance spectroscopy (NMR)

^1H -NMR, ^{13}C -NMR, ^{19}F -NMR, and two-dimensional NMR spectra were recorded in CDCl_3 using tetramethylsilane as the internal standard or in D_2O using the solvent peak as the internal standard. An AMX400 spectrometer with a test frequency of 400 MHz and a DRX500 Avance spectrometer with a test frequency of 500 MHz, both fabricated by Bruker, were used. The spectra were evaluated using the SpinWorks software version 2.5.5.

7.5.2 Fourier transformed infrared spectroscopy (FTIR)

FTIR spectroscopy was carried out on a Bruker FT-Infrared spectrometer type Equinox 55, using the geometry for attenuated total reflectance measurements (ATR). A solution of the sample was dropped onto the crystal surface and allowed to dry before the measurement. Otherwise KBr pellets were prepared.

7.5.3 UV-Vis- and fluorescence spectroscopy

The absorption spectra were recorded on Cary 50, Cary 100 or Cary 500 spectrometers (Varian). The data obtained from the absorption spectra were used to calculate the size and extinction coefficients of nanoparticles using published calibration curves^[466].

The luminescence measurements were performed on a FluoroMax-2 or a FluoroLog-3 spectrometer (Instruments SA) or an Eclipse spectrometer (Varian). Except for the quantum yield measurements, the fluorescence spectra were recorded between 470 and 800 nm at room temperature using an excitation wavelength of 450 nm. Estimates of quantum yield were obtained by comparing the integrated emission from Rhodamine 6G (Fluka, 83697) in ethanol with that of the nanoparticles. The sample and Rhodamine 6G were excited at the wavelength obtained at the cross-over of the absorption spectra of both samples. Literature data for the luminescence efficiency of the dye was used. The obtained values for the quantum yield were

not corrected for the refractive indices of the solvents. However, the error was smaller than 5%.

7.5.4 Transmission electron microscopy (TEM)

A Philips CM-300 microscope operating at 300 kV was used for the TEM measurements. Samples were prepared by placing a drop of a dilute chloroform or water solution on a carbon-coated copper grid. The excess solution was removed with filter paper and the grids were dried in air.

7.5.5 Powder X-ray diffraction measurements (XRD)

XRD measurements were performed on a Philips X'Pert diffractometer (Cu K α -radiation, variable entrance slit). The samples for these measurements were prepared by dropping a toluene solution of the nanoparticles on a standard single crystal Si support and evaporating the solvent.

7.5.6 Dynamic light scattering (DLS)

Dynamic light scattering analysis was performed on a Malvern Zetasizer Nano ZS system equipped with a single angle 173° backscatter system using He-Ne laser illumination at 633 nm. For each measurement, the autocorrelation function was the average of three runs of 30 s, and for each sample three measurements were performed. All the solutions were filtered through 0.2 μm PTFE membrane filter. The hydrodynamic radii were obtained using Dispersion Technology Software (DTS) Version 4.00 (Malvern Instruments).

7.5.7 Matrix assisted laser desorption/ionisation time of flight mass spectrometry (MALDI-TOF)

Sample preparation was done as follows. 10 μL of a solution of 2 mg/mL ligand in THF, 10 μL of the matrix solution (10 mg/mL dithranol in THF), and 1 μL of a solution, consisting of 1-2 mg/mL silver trifluoroacetate in THF, were mixed and applied on the MALDI disk.

MALDI-TOF measurements were performed using a M@ldi L spektrometer, produced by Micromass Ltd. (now Waters), equipped with a nitrogen laser ($\lambda = 337 \text{ nm}$). The source voltage was 15000 V and pulse-tension 2000 V. Interpretation was done using the software MassLynx 4.0.

7.5.8 (Förster-) fluorescence resonance energy transfer (FRET)

FRET measurements were measured using a pulsed diode laser PDL 800-D (Pico Quant GmbH) with a wavelength of 438 nm and a pulserate of 73-78 ps. Next to a single photon counter (EG&G ORTEC) a photomultiplier tube R2658P (Hamamatsu) was utilized.

7.5.9 Biacore

The SPR-measurements were proceeded using a Biacore® T100 apparatus. Interpretation of the corresponding sensorgram was achieved via T100 evaluation software and parallel with origin software.

7.5.10 Light microscopy

For light microscopy an Axiovert S100 with an AxioCam HRc camera (Zeiss) was used.

7.5.11 Biological applications

The biological experiments were done in the research group of Prof. Schumacher in the university hospital Eppendorf, Hamburg.

7.5.11.1 Magnetic resonance imaging (MRI)

The measurements were performed with a solenoid-shaped small animal reception coil and a 3.0 tesla apparatus (Philipps, Hamburg, Germany), shown in figure 141.

The therefore necessary anaesthesia of the mice was carried out weight-adopted with a mixture of 1.2 mL Ketasol-100 (agent: ketamine, Gräub, Bern, Switzerland), 0.8 mL Rompun (agent: xylazine, Bayer HealthCare AG, Berlin, Germany) and 8.0 mL 0.9% NaCl (Bayer HealthCare AG, Berlin, Germany).



figure 141: cohesive glass apparatus for anionic polymerisation.
3.0 Tesla MRT, Philips Medizin Systeme GmbH, Hamburg, Germany

7.5.11.2 Cryo-transection-technique

After sacrifice of the animals the tumours were taken out and embedded in tissue-Tek (polyvinyl alcohol < 11%, carbowax < 5%, nonreactive ingredients > 85% Sakura Finetek Germany GmbH, Heppenheim, Germany). This was frozen in by liquid nitrogen cooled 2-methyl butane (Merk KGaA, Darmstadt, Germany).

Of the tissue-blocks were in each case four 7 μm thick transaction established (Leica Microsystems GmbH Wetzlar, Germany) and on Histo Bond[®] (75x25x1 mm, Marienfeld, Marienfeld GmbH Lauda - Königshofen, Germany) fused (figure 142). Following the examination under the microscope were the cuttings in 0.2 molar phosphate buffer, containing four-percent paraformaldehyde, for 20 minutes fixing.

For this 14.2 g $\text{Na}_2\text{HPO}_4 \times 2 \text{H}_2\text{O}$ and 2.76 g $\text{NaH}_2\text{PO}_4 \times 1 \text{H}_2\text{O}$ (Merk, Darmstadt, Germany) were dissolved in 500 mL dH_2O , adjusting in the 0.2 molar phosphate buffer a pH value of 7.2 – 7.4. Secondary, 4 g perfluoroalkoxy (PFA, Merk, Darmstadt, Germany) in 45 mL dH_2O were heated up to a temperature of 80 °C and dissolved under stirring and slowly addition of 1 N NaOH. Finally 50 mL of the 0.2 molar phosphate buffer were added.

Concerning the sealing of the of the probes were a drop Dako Fluorescent Mounting Medium (Dako, Glostrup, Denmark) put on the tissue and with a 21 × 26 mm cover-glass (Marienfeld GmbH Lauda-Königshofen, Germany) obturated.

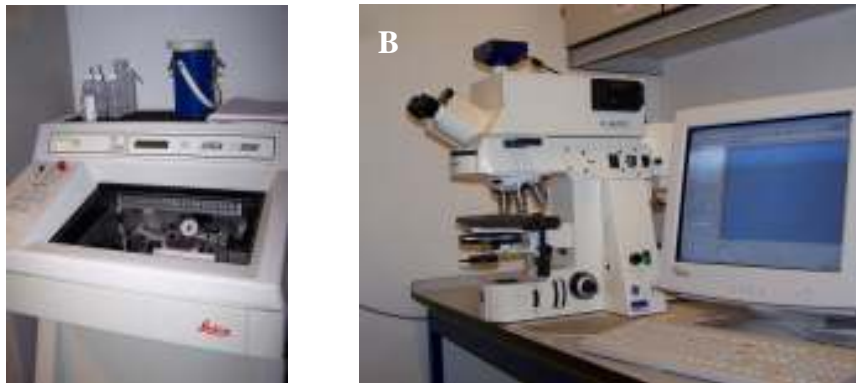


figure 142: A Leica Cryostat Microsystems GmbH Wetzlar, Germany
B Axio Phot2, AxioCamMRc5 Carl Zeiss MicroImaging GmbH, Göttingen, Germany

7.5.11.3 Fluorescence microscopy

The transections were unfixed after excitation at 365 nm as well as under transmitted light with Nomarski-contrast with a two hundred fold enhancement examined under the microscope and photographed (Axio Phot2, AxioCamMRc5 Carl Zeiss MicroImaging GmbH, Göttingen, Germany).

7.5.11.4 Fluorescence activated cell sorting (FACS)

Flow cytometry was performed on a FACScan Calibur using CellQuest Pro software (Becton Dickinson, Franklin Lakes, NJ, USA). The twelve cell aliquots were washed and resuspended in flow cytometry buffer. Results of fluorescence measurements were given as geometric mean of 10000 events for each probe and plotted as diagrams.

7.5.11.5 Confocal fluorescence microscopy

Point-scanning, point-detection, and confocal laser scanning were achieved using an Olympus FluoView™ FV1000 confocal microscope with an IX81 inverted microscope.

8 Literature

- [1] P. Alivisatos, *Nature Biotechnology* **2004**, 22, 47.
- [2] N. L. Rosi, C. A. Mirkin, *Chemical Reviews (Washington, DC, United States)* **2005**, 105, 1547.
- [3] X. Michalet, F. F. Pinaud, L. A. Bentolila, J. M. Tsay, S. Doose, J. J. Li, G. Sundaresan, A. M. Wu, S. S. Gambhir, S. Weiss, *Science (Washington, DC, United States)* **2005**, 307, 538.
- [4] I. L. Medintz, H. T. Uyeda, E. R. Goldman, H. Mattoussi, *Nature Materials* **2005**, 4, 435.
- [5] M. Han, X. Gao, J. Z. Su, S. Nie, *Nature Biotechnology* **2001**, 19, 631.
- [6] D. E. Gomez, M. Califano, P. Mulvaney, *Physical Chemistry Chemical Physics* **2006**, 8, 4989.
- [7] X. Peng, M. C. Schlamp, A. V. Kadavanich, A. P. Alivisatos, *Journal of the American Chemical Society* **1997**, 119, 7019.
- [8] P. S. Chowdhury, A. Patra, *Physical Chemistry Chemical Physics* **2006**, 8, 1329.
- [9] C. Burda, S. Link, M. B. Mohamed, M. El-Sayed, *Journal of Chemical Physics* **2002**, 116, 3828.
- [10] L. Qu, X. Peng, *Journal of the American Chemical Society* **2002**, 124, 2049.
- [11] A. P. Alivisatos, *Journal of Physical Chemistry* **1996**, 100, 13226.
- [12] A. L. Rogach, A. Kornowski, M. Gao, A. Eychmueller, H. Weller, *Journal of Physical Chemistry B* **1999**, 103, 3065.
- [13] X. Peng, J. Thessing, *Structure and Bonding (Berlin, Germany)* **2005**, 118, 79.
- [14] C. B. Murray, C. R. Kagan, M. G. Bawendi, *Annual Review of Materials Science* **2000**, 30, 545.
- [15] N. Pradhan, D. Reifsnnyder, R. Xie, J. Aldana, X. Peng, *Journal of the American Chemical Society* **2007**, 129, 9500.
- [16] F. Wang, R. Tang, W. E. Buhro, *Nano Letters* **2008**, 8, 3521.
- [17] A. M. Smith, H. Duan, M. N. Rhyner, G. Ruan, S. Nie, *Physical Chemistry Chemical Physics* **2006**, 8, 3895.
- [18] M.-Q. Zhu, E. Chang, J. Sun, R. A. Drezek, *Journal of Materials Chemistry* **2007**, 17, 800.
- [19] W. P. Faulk, G. M. Taylor, *Immunochemistry* **1971**, 8, 1081.
- [20] E. L. Romano, C. Stolinski, N. C. Hughes-Jones, *Immunochemistry* **1974**, 11, 521.
- [21] X. Wu, H. Liu, J. Liu, K. N. Haley, J. A. Treadway, J. P. Larson, N. Ge, F. Peale, M. P. Bruchez, *Nature Biotechnology* **2003**, 21, 41.
- [22] B. Dubertret, P. Skourides, D. J. Norris, V. Noireaux, A. H. Brivanlou, A. Libchaber, *Science (Washington, DC, United States)* **2002**, 298, 1759.
- [23] R. C. Doty, T. R. Tshikhudo, M. Brust, D. G. Fernig, *Chemistry of Materials* **2005**, 17, 4630.
- [24] C. A. Mirkin, R. L. Letsinger, R. C. Mucic, J. J. Storhoff, *Nature (London)* **1996**, 382, 607.
- [25] R. Elghanian, J. J. Storhoff, R. C. Mucic, R. L. Letsinger, C. A. Mirkin, *Science* **1997**, 277, 1078.
- [26] W. C. W. Chan, S. Nile, *Science* **1998**, 281, 2016.

- [27] F. Patolsky, R. Gill, Y. Weizmann, T. Mokari, U. Banin, I. Willner, *Journal of the American Chemical Society* **2003**, *125*, 13918.
- [28] C. Xu, K. Xu, H. Gu, R. Zheng, H. Liu, X. Zhang, Z. Guo, B. Xu, *Journal of the American Chemical Society* **2004**, *126*, 9938.
- [29] J. Xie, C. Xu, Z. Xu, Y. Hou, K. L. Young, S. X. Wang, N. Pourmond, S. Sun, *Chemistry of Materials* **2006**, *18*, 5401.
- [30] V. Ramamurthy, *Organic Photochemistry, Vol. 1*, CRC Press, **1997**.
- [31] C. F. Landes, M. Braun, M. A. El-Sayed, *Journal of Physical Chemistry B* **2001**, *105*, 10554.
- [32] G. Kalyuzhny, R. W. Murray, *Journal of Physical Chemistry B* **2005**, *109*, 7012.
- [33] C. Landes, C. Burda, M. Braun, M. A. El-Sayed, *Journal of Physical Chemistry B* **2001**, *105*, 2981.
- [34] V. V. Breus, C. D. Heyes, G. U. Nienhaus, *Journal of Physical Chemistry C* **2007**, *111*, 18589.
- [35] A. M. Munro, I. J.-L. Plante, M. S. Ng, D. S. Ginger, *Journal of Physical Chemistry C* **2007**, *111*, 6220.
- [36] W. R. Algar, J. Krull Ulrich, *Chemphyschem FIELD Full Journal Title: Chemphyschem : a European journal of chemical physics and physical chemistry* **2007**, *8*, 561.
- [37] C. A. Leatherdale, M. G. Bawendi, *Physical Review B: Condensed Matter and Materials Physics* **2001**, *63*, 165315/1.
- [38] P. Suppan, N. Ghoneim, *Solvatochromism*, **1997**.
- [39] H. Fan, E. W. Leve, C. Scullin, J. Gabaldon, D. Tallant, S. Bunge, T. Boyle, M. C. Wilson, C. J. Brinker, *Nano Letters* **2005**, *5*, 645.
- [40] W. W. Yu, E. Chang, J. C. Falkner, J. Zhang, A. M. Al-Somali, C. M. Sayes, J. Johns, R. Drezek, V. L. Colvin, *Journal of the American Chemical Society* **2007**, *129*, 2871.
- [41] Z. Gao, A. N. Lukyanov, A. Singhal, V. P. Torchilin, *Nano Letters* **2002**, *2*, 979.
- [42] V. P. Torchilin, A. N. Lukyanov, Z. Gao, B. Papahadjopoulos-Sternberg, *Proceedings of the National Academy of Sciences of the United States of America* **2003**, *100*, 6039.
- [43] T. K. Jain, M. A. Morales, S. K. Sahoo, D. L. Leslie-Pelecky, V. Labhasetwar, *Molecular Pharmaceutics* **2005**, *2*, 194.
- [44] H. Ai, C. Flask, B. Weinberg, X. Shuai, M. D. Pagel, D. Farrell, J. Duerk, J. Gao, *Advanced Materials* **2005**, *17*, 1949.
- [45] N. Nasongkla, E. Bey, J. Ren, H. Ai, C. Khemtong, J. S. Guthi, S.-F. Chin, A. D. Sherry, D. A. Boothman, J. Gao, *Nano Letters* **2006**, *6*, 2427.
- [46] Z. Liu, W. Cai, L. He, N. Nakayama, K. Chen, X. Sun, X. Chen, H. Dai, *Nature Nanotechnology* **2007**, *2*, 47.
- [47] Y. Tu, X. Wan, D. Zhang, Q. Zhou, C. Wu, *Journal of the American Chemical Society* **2000**, *122*, 10201.
- [48] M. Svensson, P. Alexandridis, P. Linse, *Macromolecules* **1999**, *32*, 637.
- [49] V. Buetuen, S. P. Armes, N. C. Billingham, *Macromolecules* **2001**, *34*, 1148.
- [50] S. Liu, N. C. Billingham, S. P. Armes, *Angewandte Chemie, International Edition* **2001**, *40*, 2328.
- [51] J.-F. Gohy, S. Antoun, R. Jerome, *Macromolecules* **2001**, *34*, 7435.
- [52] C. Wu, A. Niu, L. M. Leung, T. S. Lam, *Journal of the American Chemical Society* **1999**, *121*, 1954.
- [53] A. Harada, K. Kataoka, *Macromolecules* **1995**, *28*, 5294.

- [54] A. V. Kabanov, T. K. Bronich, V. A. Kabanov, K. Yu, A. Eisenberg, *Macromolecules* **1996**, *29*, 6797.
- [55] H. Duan, D. Chen, M. Jiang, W. Gan, S. Li, M. Wang, J. Gong, *Journal of the American Chemical Society* **2001**, *123*, 12097.
- [56] M. Wang, G. Zhang, D. Chen, M. Jiang, S. Liu, *Macromolecules* **2001**, *34*, 7172.
- [57] W. Liu, M. Howarth, A. B. Greytak, Y. Zheng, D. G. Nocera, A. Y. Ting, M. G. Bawendi, *Journal of the American Chemical Society* **2008**, *130*, 1274.
- [58] H. Wu, H. Zhu, J. Zhuang, S. Yang, C. Liu, Y. C. Cao, *Angewandte Chemie, International Edition* **2008**, *47*, 3730.
- [59] D. Chen, H. Peng, M. Jiang, *Macromolecules* **2003**, *36*, 2576.
- [60] V. Buetuen, X. S. Wang, M. V. d. P. Banez, K. L. Robinson, N. C. Billingham, S. P. Armes, Z. Tuzar, *Macromolecules* **2000**, *33*, 1.
- [61] Q. Zhang, E. E. Remsen, K. L. Wooley, *Journal of the American Chemical Society* **2000**, *122*, 3642.
- [62] V. Buetuen, N. C. Billingham, S. P. Armes, *Journal of the American Chemical Society* **1998**, *120*, 12135.
- [63] Y. Kakizawa, A. Harada, K. Kataoka, *Journal of the American Chemical Society* **1999**, *121*, 11247.
- [64] J. Tao, G. Liu, J. Ding, M. Yang, *Macromolecules* **1997**, *30*, 4084.
- [65] A. Guo, G. Liu, J. Tao, *Macromolecules* **1996**, *29*, 2487.
- [66] F. Checot, S. Lecommandoux, Y. Gnanou, H.-A. Klok, *Angewandte Chemie, International Edition* **2002**, *41*, 1339.
- [67] J. P. Ryman-Rasmussen, J. E. Riviere, N. A. Monteiro-Riviere, *Journal of Investigative Dermatology* **2007**, *127*, 143.
- [68] B. Ballou, B. C. Lagerholm, L. A. Ernst, M. P. Bruchez, A. S. Waggoner, *Bioconjugate Chemistry* **2004**, *15*, 79.
- [69] M. E. Akerman, W. C. W. Chan, P. Laakkonen, S. N. Bhatia, E. Ruoslahti, *Proceedings of the National Academy of Sciences of the United States of America* **2002**, *99*, 12617.
- [70] C. Allen, D. Maysinger, A. Eisenberg, *Colloids and Surfaces, B: Biointerfaces* **1999**, *16*, 3.
- [71] G. S. Kwon, K. Kataoka, *Advanced Drug Delivery Reviews* **1995**, *16*, 295.
- [72] A. V. Kabanov, V. A. Kabanov, *Advanced Drug Delivery Reviews* **1998**, *30*, 49.
- [73] P. Kingshott, H. J. Griesser, *Current Opinion in Solid State & Materials Science* **1999**, *4*, 403.
- [74] K. Holmberg, J. M. Harris, *International Congress on Adhesion Science and Technology, Invited Papers, Festschrift in Honor of Dr. K. L. Mittal on the Occasion of his 50th Birthday, 1st, Amsterdam, Oct. 16-20, 1995* **1998**, 443.
- [75] J. M. Harris, S. Zalipsky, Editors, *Polyethylene glycol: Chemistry and Biological Applications. (Proceedings of a Symposium at the 213th National Meeting of the American Chemical Society, held 13-17 April 1997, in San Francisco, California.) [In: ACS Symp. Ser., 1997; 680]*, **1997**.
- [76] F. M. Veronese, *Biomaterials* **2001**, *22*, 405.
- [77] S. Zalipsky, *Advanced Drug Delivery Reviews* **1995**, *16*, 157.
- [78] C. Foa, M. Soler, A. M. Benoliel, P. Bongrand, *Journal of Materials Science: Materials in Medicine* **1996**, *7*, 141.
- [79] J. D. Andrade, V. Hlady, S. I. Jeon, *Advances in Chemistry Series* **1996**, *248*, 51.
- [80] S. I. Jeon, J. D. Andrade, *Journal of Colloid and Interface Science* **1991**, *142*, 159.

- [81] S. I. Jeon, J. H. Lee, J. D. Andrade, P. G. De Gennes, *Journal of Colloid and Interface Science* **1991**, *142*, 149.
- [82] J. H. Lee, H. B. Lee, J. D. Andrade, *Progress in Polymer Science* **1995**, *20*, 1043.
- [83] I. Szleifer, *Physica A: Statistical and Theoretical Physics (Amsterdam)* **1997**, *244*, 370.
- [84] T. McPherson, A. Kidane, I. Szleifer, K. Park, *Langmuir* **1998**, *14*, 176.
- [85] S. Dreborg, E. B. Aakerblom, *Critical Reviews in Therapeutic Drug Carrier Systems* **1990**, *6*, 315.
- [86] M. C. Woodle, D. D. Lasic, *Biochimica et biophysica acta* **1992**, *1113*, 171.
- [87] E. W. Merrill, *Springer Verlag* **1992**, 199.
- [88] P. Ghosh, G. Han, M. De, C. K. Kim, V. M. Rotello, *Advanced Drug Delivery Reviews* **2008**, *60*, 1307.
- [89] B. J. Jordan, R. Hong, B. Gider, J. Hill, T. Emrick, V. M. Rotello, *Soft Matter* **2006**, *2*, 558.
- [90] M. Malmsten, B. Lassen, K. Holmberg, V. Thomas, G. Quash, *Journal of Colloid and Interface Science* **1996**, *177*, 70.
- [91] J. A. Neff, K. D. Caldwell, P. A. Tresco, *Journal of Biomedical Materials Research* **1998**, *40*, 511.
- [92] X. Gao, Y. Cui, R. M. Levenson, L. W. K. Chung, S. Nie, *Nature Biotechnology* **2004**, *22*, 969.
- [93] X. L. Xu, Z. C. Zhang, X. W. Ge, M. W. Zhang, *Colloid and Polymer Science* **1998**, *276*, 534.
- [94] W. D. Harkins, R. S. Stearns, *Journal of Chemical Physics* **1946**, *14*, 215.
- [95] W. D. Harkins, *Journal of the American Chemical Society* **1947**, *69*, 1428.
- [96] M. Nomura, *Journal of Industrial and Engineering Chemistry (Seoul, Republic of Korea)* **2004**, *10*, 1182.
- [97] W. D. Harkins, *Journal of Chemical Physics* **1945**, *13*, 381.
- [98] N. Yanase, H. Noguchi, H. Asakura, T. Suzuta, *Journal of Applied Polymer Science* **1993**, *50*, 765.
- [99] G. Xie, Q. Zhang, Z. Luo, M. Wu, T. Li, *Journal of Applied Polymer Science* **2003**, *87*, 1733.
- [100] K. Wormuth, *Journal of Colloid and Interface Science* **2001**, *241*, 366.
- [101] Y. Deng, L. Wang, W. Yang, S. Fu, A. Elaissari, *Journal of Magnetism and Magnetic Materials* **2003**, *257*, 69.
- [102] L. Shen, P. E. Laibinis, T. A. Hatton, *Langmuir* **1999**, *15*, 447.
- [103] L. P. Ramirez, K. Landfester, *Macromolecular Chemistry and Physics* **2003**, *204*, 22.
- [104] R. G. Gilbert, *Emulsion Polymerization*, **1995**.
- [105] D. Crespy, K. Landfester, *Macromolecules* **2005**, *38*, 6882.
- [106] N. Naderi, N. Sharifi-Sanjani, B. Khayyat-Naderi, R. Faridi-Majidi, *Journal of Applied Polymer Science* **2006**, *99*, 2943.
- [107] M. Zhang, G. Gao, C.-Q. Li, F.-Q. Liu, *Langmuir* **2004**, *20*, 1420.
- [108] A. J. P. Van Zyl, R. F. P. Bosch, J. B. McLeary, R. D. Sanderson, B. Klumperman, *Polymer* **2005**, *46*, 3607.
- [109] K. Ouzineb, C. Graillat, T. F. McKenna, *Journal of Applied Polymer Science* **2005**, *97*, 745.
- [110] L. Lopez de Arbina, J. M. Asua, *Polymer* **1992**, *33*, 4832.
- [111] C. Wang, F. Chu, C. Graillat, A. Guyot, C. Gauthier, J. P. Chapel, *Polymer* **2005**, *46*, 1113.

- [112] N. Bechthold, F. Tiarks, M. Willert, K. Landfester, M. Antonietti, *Macromolecular Symposia* **2000**, 151, 549.
- [113] H. T. Ham, Y. S. Choi, N. Jeong, I. J. Chung, *Polymer* **2005**, 46, 6308.
- [114] Z. Z. Xu, C. C. Wang, W. L. Yang, Y. H. Deng, S. K. Fu, *Journal of Magnetism and Magnetic Materials* **2004**, 277, 136.
- [115] W. Zheng, F. Gao, H. Gu, *Journal of Magnetism and Magnetic Materials* **2005**, 288, 403.
- [116] R. Faridi-Majidi, N. Sharifi-Sanjani, *Journal of Applied Polymer Science* **2007**, 105, 1244.
- [117] X. Liu, Y. Guan, Z. Ma, H. Liu, *Langmuir* **2004**, 20, 10278.
- [118] B. Erdem, E. D. Sudol, V. L. Dimonie, M. S. El-Aasser, *Journal of Polymer Science, Part A: Polymer Chemistry* **2000**, 38, 4431.
- [119] B. Erdem, E. D. Sudol, V. L. Dimonie, M. S. El-Aasser, *Journal of Polymer Science, Part A: Polymer Chemistry* **2000**, 38, 4441.
- [120] B. Erdem, E. D. Sudol, V. L. Dimonie, M. S. El-Aasser, *Journal of Polymer Science, Part A: Polymer Chemistry* **2000**, 38, 4419.
- [121] S.-W. Zhang, S.-X. Zhou, Y.-M. Weng, L.-M. Wu, *Langmuir* **2005**, 21, 2124.
- [122] F. Tiarks, K. Landfester, M. Antonietti, *Langmuir* **2001**, 17, 5775.
- [123] M. Peres, L. C. Costa, A. Neves, M. J. Soares, T. Monteiro, A. C. Esteves, A. Barros-Timmons, T. Trindade, A. Kholkin, E. Alves, *Nanotechnology* **2005**, 16, 1969.
- [124] M. F. Cunningham, *Progress in Polymer Science* **2002**, 27, 1039.
- [125] I. M. Lifshits, V. V. Slezov, *Zhurnal Eksperimental'noi i Teoreticheskoi Fiziki* **1958**, 35, 479.
- [126] A. S. Kabalnov, A. V. Pertsov, E. D. Shchukin, *Journal of Colloid and Interface Science* **1987**, 118, 590.
- [127] K. Tauer, *Polymer* **2005**, 46, 1385.
- [128] C. D. Anderson, E. D. Sudol, M. S. El-aasser, *Journal of Applied Polymer Science* **2003**, 90, 3987.
- [129] J. A. Alduncin, J. M. Asua, *Polymer* **1994**, 35, 3758.
- [130] C. S. Chern, T. J. Chen, Y. C. Liou, *Polymer* **1998**, 39, 3767.
- [131] K. Landfester, *Abstracts of Papers, 224th ACS National Meeting, Boston, MA, United States, August 18-22, 2002* **2002**, PMSE.
- [132] G. W. Poehlein, *Polymer Reaction Engineering* **2003**, 11, 955.
- [133] N. Bechthold, K. Landfester, *Macromolecules* **2000**, 33, 4682.
- [134] R. Faridi-Majidi, N. Sharifi-Sanjani, F. Agend, *Thin Solid Films* **2006**, 515, 368.
- [135] T. Tanrisever, O. Okay, I. C. Sonmezoglu, *Journal of Applied Polymer Science* **1996**, 61, 485.
- [136] R. Strey, *Colloid and Polymer Science* **1994**, 272, 1005.
- [137] J. S. Guo, E. D. Sudol, J. W. Vanderhoff, M. S. El-Aasser, *ACS Symposium Series* **1992**, 492, 99.
- [138] B. J. Chamberlain, D. H. Napper, R. G. Gilbert, *Journal of the Chemical Society, Faraday Transactions 1: Physical Chemistry in Condensed Phases* **1982**, 78, 591.
- [139] J. M. Asua, M. E. Adams, E. D. Sudol, *Journal of Applied Polymer Science* **1990**, 39, 1183.
- [140] C. Larpent, T. F. Tadros, *Colloid and Polymer Science* **1991**, 269, 1171.
- [141] C. Holtzscheler, F. Candau, *Colloids and Surfaces* **1988**, 29, 411.
- [142] P. R. Gil, W. J. Parak, *ACS Nano* **2008**, 2, 2200.

- [143] Y. T. Lim, S. Kim, A. Nakayama, N. E. Stott, M. G. Bawendi, J. V. Frangioni, *Molecular Imaging* **2003**, *2*, 50.
- [144] T. Thepen, S. Barth, Fraunhofer Institut, Molekularbiologie und Angewandte Oekologie, LUNA Verbundtreffen in Düsseldorf, **2009**.
- [145] V. Ntziachristos, C. Bremer, R. Weissleder, *European radiology* **2003**, *13*, 195.
- [146] S. Heer, K. Koempe, H.-U. Gudel, M. Haase, *Advanced Materials (Weinheim, Germany)* **2004**, *16*, 2102.
- [147] F. Auzel, *Chemical Reviews (Washington, DC, United States)* **2004**, *104*, 139.
- [148] D. R. Gamelin, H. U. Gudel, *Topics in Current Chemistry* **2001**, *214*, 1.
- [149] S. S. Chang, V. E. Reuter, W. D. Heston, P. B. Gaudin, *Urology* **2001**, *57*, 801.
- [150] M. Yang, E. Baranov, J.-W. Wang, P. Jiang, X. Wang, F.-X. Sun, M. Bouvet, A. R. Moossa, S. Penman, R. M. Hoffman, *Proceedings of the National Academy of Sciences of the United States of America* **2002**, *99*, 3824.
- [151] W. C. W. Chan, D. J. Maxwell, X. Gao, R. E. Bailey, M. Han, S. Nie, *Current Opinion in Biotechnology* **2002**, *13*, 40.
- [152] M. Bruchez, Jr., M. Moronne, P. Gin, S. Weiss, A. P. Alivisatos, *Science* **1998**, *281*, 2013.
- [153] D. R. Larson, W. R. Zipfel, R. M. Williams, S. W. Clark, M. P. Bruchez, F. W. Wise, W. W. Webb, *Science* **2003**, *300*, 1434.
- [154] J. Mertz, C. Xu, W. W. Webb, *Optics Letters* **1995**, *20*, 2532.
- [155] P. Schwille, U. Haupts, S. Maiti, W. W. Webb, *Biophysical Journal* **1999**, *77*, 2251.
- [156] J. L. Swift, R. Heuff, D. T. Cramb, *Biophysical Journal* **2006**, *90*, 1396.
- [157] T. P. Thomas, M. T. Myaing, J. Y. Ye, K. Candido, A. Kotlyar, J. Beals, P. Cao, B. Keszler, A. K. Patri, T. B. Norris, J. R. Baker, Jr., *Biophysical Journal* **2004**, *86*, 3959.
- [158] M. Stroh, J. P. Zimmer, D. G. Duda, T. S. Levchenko, K. S. Cohen, E. B. Brown, D. T. Scadden, V. P. Torchilin, M. G. Bawendi, D. Fukumura, R. K. Jain, *Nature Medicine (New York, NY, United States)* **2005**, *11*, 678.
- [159] X. Yu, L. Chen, Y. Deng, K. Li, Q. Wang, Y. Li, S. Xiao, L. Zhou, X. Luo, J. Liu, D. Pang, *Journal of Fluorescence* **2007**, *17*, 243.
- [160] C. M. Niemeyer, *Angewandte Chemie, International Edition* **2001**, *40*, 4128.
- [161] M. Sastry, M. Rao, K. N. Ganesh, *Accounts of Chemical Research* **2002**, *35*, 847.
- [162] E. Katz, I. Willner, *Angewandte Chemie, International Edition* **2004**, *43*, 6042.
- [163] T. Pellegrino, S. Kudera, T. Liedl, A. M. Javier, L. Manna, W. J. Parak, *Small* **2005**, *1*, 48.
- [164] A. Verma, V. M. Rotello, *Chemical Communications (Cambridge, United Kingdom)* **2005**, 303.
- [165] O. Minet, C. Dressler, J. Beuthan, *Journal of Fluorescence* **2004**, *14*, 241.
- [166] J. J. Storhoff, A. D. Lucas, V. Garimella, Y. P. Bao, U. R. Mueller, *Nature Biotechnology* **2004**, *22*, 883.
- [167] R. A. Reynolds, III, C. A. Mirkin, R. L. Letsinger, *Journal of the American Chemical Society* **2000**, *122*, 3795.
- [168] K. E. Sapsford, L. Berti, I. L. Medintz, *Angewandte Chemie, International Edition* **2006**, *45*, 4562.
- [169] L. Dyadyusha, H. Yin, S. Jaiswal, T. Brown, J. J. Baumberg, F. P. Booy, T. Melvin, *Chemical Communications* **2005**, 3201.
- [170] R. L. Phillips, O. R. Miranda, C.-C. You, V. M. Rotello, U. H. F. Bunz, *Angewandte Chemie, International Edition* **2008**, *47*, 2590.
- [171] E. Katz, I. Willner, J. Wang, *Electroanalysis* **2004**, *16*, 19.

- [172] S.-J. Park, T. A. Taton, C. A. Mirkint, *Science* **2002**, 295, 1503.
- [173] R. F. Aroca, R. A. Alvarez-Puebla, N. Pieczonka, S. Sanchez-Cortez, J. V. Garcia-Ramos, *Advances in Colloid and Interface Science* **2005**, 116, 45.
- [174] W. B. Tan, S. Jiang, Y. Zhang, *Biomaterials* **2007**, 28, 1565.
- [175] S. Kim, Y. T. Lim, E. G. Soltesz, A. M. De Grand, J. Lee, A. Nakayama, J. A. Parker, T. Mihaljevic, R. G. Laurence, D. M. Dor, L. H. Cohn, M. G. Bawendi, J. V. Frangioni, *Nature Biotechnology* **2004**, 22, 93.
- [176] M. Dahan, S. Levi, C. Luccardini, P. Rostaing, B. Riveau, A. Triller, *Science* **2003**, 302, 442.
- [177] D. S. Lidke, P. Nagy, R. Heintzmann, D. J. Arndt-Jovin, J. N. Post, H. E. Grecco, E. A. Jares-Erijman, T. M. Jovin, *Nature Biotechnology* **2004**, 22, 198.
- [178] G. Soltesz Edward, S. Kim, G. Laurence Rita, M. DeGrand Alec, P. Parungo Cherie, M. Dor Delphine, H. Cohn Lawrence, G. Bawendi Mounqi, V. Frangioni John, T. Mihaljevic, *The Annals of thoracic surgery* **2005**, 79, 269.
- [179] S. Pathak, S.-K. Choi, N. Arnheim, M. E. Thompson, *Journal of the American Chemical Society* **2001**, 123, 4103.
- [180] E. L. Bentzen, I. D. Tomlinson, J. Mason, P. Gresch, M. R. Warnement, D. Wright, E. Sanders-Bush, R. Blakely, S. J. Rosenthal, *Bioconjugate Chemistry* **2005**, 16, 1488.
- [181] J. W. M. Bulte, D. L. Kraitchman, *NMR in Biomedicine* **2004**, 17, 484.
- [182] C. Corot, P. Robert, J.-M. Idee, M. Port, *Advanced Drug Delivery Reviews* **2006**, 58, 1471.
- [183] L. J. Thorek Daniel, K. Chen Antony, J. Czupryna, A. Tsourkas, *Annals of biomedical engineering* **2006**, 34, 23.
- [184] A. K. Gupta, R. R. Naregalkar, V. D. Vaidya, M. Gupta, *Nanomedicine (London, United Kingdom)* **2007**, 2, 23.
- [185] P. Wunderbaldinger, L. Josephson, R. Weissleder, *Academic radiology* **2002**, 9 Suppl 2, S304.
- [186] P. Wunderbaldinger, L. Josephson, R. Weissleder, *Bioconjugate Chemistry* **2002**, 13, 264.
- [187] J. Ugelstad, A. Berge, T. Ellingsen, R. Schmid, T. N. Nilsen, P. C. Moerk, P. Stenstad, E. Hornes, O. Olsvik, *Progress in Polymer Science* **1992**, 17, 87.
- [188] R. S. Molday, S. P. Yen, A. Rembaum, *Nature* **1977**, 268, 437.
- [189] A. Rembaum, W. J. Dreyer, *Science* **1980**, 208, 364.
- [190] Y. Haik, V. Pai, C.-J. Chen, *Journal of Magnetism and Magnetic Materials* **1999**, 194, 254.
- [191] K. Sugibayashi, Y. Morimoto, T. Nadai, Y. Kato, *Chemical & Pharmaceutical Bulletin* **1977**, 25, 3433.
- [192] D. C. F. Chan, D. B. Kirpotin, a. P. A. Bunn, Jr., *Journal of Magnetism and Magnetic Materials* **1993**, 122, 374.
- [193] C. C. Berry, A. S. G. Curtis, *Applied Physics* **2003**, 36, R198.
- [194] P. Tartaj, M. d. P. Morales, S. Veintemillas-Verdaguer, T. Gonzalez-Carreno, C. J. Serna, *Journal of Physics D: Applied Physics* **2003**, 36, R182.
- [195] Q. A. Pankhurst, J. Connolly, S. K. Jones, J. Dobson, *Journal of Physics D: Applied Physics* **2003**, 36, R167.
- [196] Z. P. Xu, N. D. Kurniawan, P. F. Bartlett, G. Q. Lu, *Chemistry--A European Journal* **2007**, 13, 2824.
- [197] A. M. Derfus, G. von Maltzahn, T. J. Harris, T. Duza, K. S. Vecchio, E. Ruoslahti, S. N. Bhatia, *Advanced Materials* **2007**, 19, 3932.

- [198] E. Viroonchatapan, M. Ueno, H. Sato, I. Adachi, H. Nagae, K. Tazawa, I. Horikoshi, *Pharmaceutical Research* **1995**, *12*, 1176.
- [199] P. K. Gupta, C. T. Hung, *Life Sciences* **1989**, *44*, 175.
- [200] D. K. Kim, Y. Zhang, W. Voit, K. V. Rao, J. Kehr, B. Bjelke, M. Muhammed, *Scripta Materialia* **2001**, *44*, 1713.
- [201] M. Uhlen, *Nature (London, United Kingdom)* **1989**, *340*, 733.
- [202] A. Elaissari, M. Rodrigue, F. Meunier, C. Herve, *Journal of Magnetism and Magnetic Materials* **2001**, *225*, 127.
- [203] T. Kubo, T. Sugita, S. Shimose, Y. Nitta, Y. Ikuta, T. Murakami, *International Journal of Oncology* **2000**, *17*, 309.
- [204] T. Kubo, T. Sugita, S. Shimose, Y. Nitta, Y. Ikuta, T. Murakami, *International Journal of Oncology* **2001**, *18*, 121.
- [205] R. Jurgons, C. Seliger, A. Hilpert, L. Trahms, S. Odenbach, C. Alexiou, *Journal of Physics: Condensed Matter* **2006**, *18*, S2893.
- [206] C. Alexiou, W. Arnold, R. J. Klein, F. G. Parak, P. Hulin, C. Bergemann, W. Erhardt, S. Wagenpfeil, A. S. Lubbe, *Cancer Research* **2000**, *60*, 6641.
- [207] A. K. Gupta, A. S. G. Curtis, *Biomaterials* **2004**, *25*, 3029.
- [208] A. K. Gupta, M. Gupta, *Biomaterials* **2005**, *26*, 3995.
- [209] K. Gupta Ajay, M. Gupta, *Biomaterials* **2005**, *26*, 1565.
- [210] Y. Zhang, N. Kohler, M. Zhang, *Biomaterials* **2002**, *23*, 1553.
- [211] C. C. Berry, S. Wells, S. Charles, A. S. G. Curtis, *Biomaterials* **2003**, *24*, 4551.
- [212] P. K. Jain, K. S. Lee, I. H. El-Sayed, M. A. El-Sayed, *Journal of Physical Chemistry B* **2006**, *110*, 7238.
- [213] K. H. Su, Q. H. Wei, X. Zhang, J. J. Mock, D. R. Smith, S. Schultz, *Nano Letters* **2003**, *3*, 1087.
- [214] X. Huang, I. H. El-Sayed, W. Qian, M. A. El-Sayed, *Journal of the American Chemical Society* **2006**, *128*, 2115.
- [215] M. A. Polizzi, N. A. Stasko, M. H. Schoenfish, *Langmuir* **2007**, *23*, 4938.
- [216] M. Tsoli, H. Kuhn, W. Brandau, H. Esche, G. Schmid, *Small* **2005**, *1*, 841.
- [217] W. Stoeber, A. Fink, E. Bohn, *Journal of Colloid and Interface Science* **1968**, *26*, 62.
- [218] F. J. Arriagada, K. Osseo-Assare, *Journal of Colloid and Interface Science* **1995**, *170*, 8.
- [219] Z. Grabarek, J. Gergely, *Analytical Biochemistry* **1990**, *185*, 131.
- [220] B. Akerstrom, L. Bjorck, *The Journal of biological chemistry* **1986**, *261*, 10240.
- [221] H. Petersen, P. M. Fechner, D. Fischer, T. Kissel, *Macromolecules* **2002**, *35*, 6867.
- [222] K. Kunath, A. von Harpe, H. Petersen, D. Fischer, K. Voigt, T. Kissel, U. Bickel, *Pharmaceutical Research* **2002**, *19*, 810.
- [223] E. Kleemann, M. Neu, N. Jekel, L. Fink, T. Schmehl, T. Gessler, W. Seeger, T. Kissel, *Journal of Controlled Release* **2005**, *109*, 299.
- [224] S. Nikolic Marija, M. Krack, V. Aleksandrovic, A. Kornowski, S. Forster, H. Weller, *Angewandte Chemie (International ed. in English)* **2006**, *45*, 6577.
- [225] X.-B. Xiong, A. Mahmud, H. Uludag, A. Lavasanifar, *Biomacromolecules* **2007**, *8*, 874.
- [226] M. A. R. Meier, S. N. H. Aerts, B. B. P. Staal, M. Rasa, U. S. Schubert, *Macromolecular Rapid Communications* **2005**, *26*, 1918.
- [227] F. Meng, C. Hiemstra, G. H. M. Engbers, J. Feijen, *Macromolecules* **2003**, *36*, 3004.
- [228] C. Allen, A. Eisenberg, J. Mrcic, D. Maysinger, *Drug Delivery* **2000**, *7*, 139.
- [229] C. Allen, Y. Yu, D. Maysinger, A. Eisenberg, *Bioconjugate Chemistry* **1998**, *9*, 564.

- [230] C.-S. Hwang, I.-H. Cho, *Bulletin of the Korean Chemical Society* **2005**, *26*, 1776.
- [231] H. Ai, C. Flask, B. Weinberg, X. Shuai, M. D. Pagel, D. Farrell, J. Duerk, J. Gao, *Advanced Materials (Weinheim, Germany)* **2005**, *17*, 1949.
- [232] Y. Nagasaki, T. Okada, C. Scholz, M. Iijima, M. Kato, K. Kataoka, *Macromolecules* **1998**, *31*, 1473.
- [233] S. M. Moghimi, A. C. Hunter, J. C. Murray, A. Szewczyk, *Science (Washington, DC, United States)* **2004**, *303*, 626.
- [234] S. Chandrasekaran, A. F. Kluge, J. A. Edwards, *Journal of Organic Chemistry* **1977**, *42*, 3972.
- [235] D. B. Bryan, R. F. Hall, K. G. Holden, W. F. Huffman, J. G. Gleason, *Journal of the American Chemical Society* **1977**, *99*, 2353.
- [236] G. M. Makara, G. R. Marshall, *Tetrahedron Letters* **1997**, *38*, 5069.
- [237] K. A. Stein, P. L. Toogood, *Journal of Organic Chemistry* **1995**, *60*, 8110.
- [238] M. Schultz, P. Hermann, H. Kunz, *Synlett* **1992**, 37.
- [239] B. S. Bal, W. E. Childers, Jr., H. W. Pinnick, *Tetrahedron* **1981**, *37*, 2091.
- [240] J. D. More, N. S. Finney, *Organic Letters* **2002**, *4*, 3001.
- [241] A. P. Thottumkara, M. S. Bowsher, T. K. Vinod, *Organic Letters* **2005**, *7*, 2933.
- [242] M. Hesse, H. Meier, B. Zeeh, *Spektroskopische Methoden in der organischen Chemie Vol. 4. überarbeitete Auflage*, Stuttgart, **1991**.
- [243] T. Nann, *Chemical Communications (Cambridge, United Kingdom)* **2005**, 1735.
- [244] T. Azzam, A. Eisenberg, *Langmuir* **2007**, *23*, 2126.
- [245] X. Shuai, T. Merdan, F. Unger, M. Wittmar, T. Kissel, *Macromolecules* **2003**, *36*, 5751.
- [246] Y. He, J. Li, X. Shuai, Y. Inoue, *Macromolecules* **2001**, *34*, 8166.
- [247] L. Shen, R. Soong, M. Wang, A. Lee, C. Wu, G. D. Scholes, P. M. Macdonald, M. A. Winnik, *Journal of Physical Chemistry B* **2008**, *112*, 1626.
- [248] A. G. Young, N. Al-Salim, D. P. Green, A. J. McQuillan, *Langmuir*, ACS ASAP.
- [249] D. V. Talapin, A. L. Rogach, A. Kornowski, M. Haase, H. Weller, *Nano Letters* **2001**, *1*, 207.
- [250] M. S. Nikolic, C. Olsson, A. Salcher, A. Kornowski, A. Rank, R. Schubert, A. Froemsdorf, H. Weller, S. Foerster, *Angewandte Chemie* **2009**, *48*, 2752.
- [251] G. Schabas, H. Yusuf, M. G. Moffitt, D. Sinton, *Langmuir* **2008**, *24*, 637.
- [252] J. Ge, Y. Hu, M. Biasini, W. P. Beyermann, Y. Yin, *Angewandte Chemie, International Edition* **2007**, *46*, 4342.
- [253] S. Mornet, S. Vasseur, F. Grasset, E. Duguet, *Journal of Materials Chemistry* **2004**, *14*, 2161.
- [254] H. Gu, K. Xu, C. Xu, B. Xu, *Chemical Communications (Cambridge, United Kingdom)* **2006**, 941.
- [255] F. Hu, L. Wei, Z. Zhou, Y. Ran, Z. Li, M. Gao, *Advanced Materials (Weinheim, Germany)* **2006**, *18*, 2553.
- [256] J.-H. Lee, Y.-w. Jun, S.-I. Yeon, J.-S. Shin, J. Cheon, *Angewandte Chemie, International Edition* **2006**, *45*, 8160.
- [257] S. A. Corr, A. O'Byrne, Y. K. Gun'ko, S. Ghosh, D. F. Brougham, S. Mitchell, Y. Volkov, A. Prina-Mello, *Chemical Communications (Cambridge, United Kingdom)* **2006**, 4474.
- [258] J.-H. Park, G. von Maltzahn, E. Ruoslahti, N. Bhatia Sangeeta, J. Sailor Michael, *Angewandte Chemie (International ed. in English)* **2008**, *47*, 7284.
- [259] D. Wang, J. He, N. Rosenzweig, Z. Rosenzweig, *Nano Letters* **2004**, *4*, 409.

- [260] D. K. Yi, S. T. Selvan, S. S. Lee, G. C. Papaefthymiou, D. Kundaliya, J. Y. Ying, *Journal of the American Chemical Society* **2005**, *127*, 4990.
- [261] J. Kim, E. Lee Ji, J. Lee, H. Yu Jung, C. Kim Byoung, K. An, Y. Hwang, C.-H. Shin, J.-G. Park, J. Kim, T. Hyeon, *Journal of the American Chemical Society* **2006**, *128*, 688.
- [262] T. R. Sathe, A. Agrawal, S. Nie, *Analytical Chemistry* **2006**, *78*, 5627.
- [263] B.-S. Kim, T. A. Taton, *Langmuir* **2007**, *23*, 2198.
- [264] E.-Q. Song, G.-P. Wang, H.-Y. Xie, Z.-L. Zhang, J. Hu, J. Peng, D.-C. Wu, Y.-B. Shi, D.-W. Pang, *Clinical Chemistry (Washington, DC, United States)* **2007**, *53*, 2177.
- [265] T. J. Harris, G. von Maltzahn, A. M. Derfus, E. Ruoslahti, S. N. Bhatia, *Angewandte Chemie, International Edition* **2006**, *45*, 3161.
- [266] J. Kim, S. Park, J. E. Lee, S. M. Jin, J. H. Lee, I. S. Lee, I. Yang, J.-S. Kim, S. K. Kim, M.-H. Cho, T. Hyeon, *Angewandte Chemie, International Edition* **2006**, *45*, 7754.
- [267] W. J. M. Mulder, R. Koole, R. J. Brandwijk, G. Storm, P. T. K. Chin, G. J. Strijkers, C. de Donega, K. Nicolay, A. W. Griffioen, *Nano Letters* **2006**, *6*, 1.
- [268] C. Xu, J. Xie, D. Ho, C. Wang, N. Kohler, E. G. Walsh, J. R. Morgan, Y. E. Chin, S. Sun, *Angewandte Chemie, International Edition* **2008**, *47*, 173.
- [269] X. Zhang, M. Brynda, R. D. Britt, E. C. Carroll, D. S. Larsen, A. Y. Louie, S. M. Kauzlarich, *Journal of the American Chemical Society* **2007**, *129*, 10668.
- [270] Y.-M. Huh, E.-S. Lee, J.-H. Lee, Y.-w. Jun, P.-H. Kim, C.-O. Yun, J.-H. Kim, J.-S. Suh, J. Cheon, *Advanced Materials* **2007**, *19*, 3109.
- [271] J. H. Choi, F. T. Nguyen, P. W. Barone, D. A. Heller, A. E. Moll, D. Patel, S. A. Boppart, M. S. Strano, *Nano Letters* **2007**, *7*, 861.
- [272] B. Zebli, A. S. Sussha, G. B. Sukhorukov, A. L. Rogach, W. J. Parak, *Langmuir* **2005**, *21*, 4262.
- [273] G. Beaune, B. Dubertret, O. Clement, C. Vayssettes, V. Cabuil, C. Menager, *Angewandte Chemie, International Edition* **2007**, *46*, 5421.
- [274] F. Dubois, B. Mahler, B. Dubertret, E. Doris, C. Mioskowski, *Journal of the American Chemical Society* **2007**, *129*, 482.
- [275] C. Querner, P. Reiss, J. Bleuse, A. Pron, *Journal of the American Chemical Society* **2004**, *126*, 11574.
- [276] C. Querner, A. Benedetto, R. Demadrille, P. Rannou, P. Reiss, *Chemistry of Materials* **2006**, *18*, 4817.
- [277] J. Aldana, Y. A. Wang, X. Peng, *Journal of the American Chemical Society* **2001**, *123*, 8844.
- [278] J. Allgaier, A. Poppe, L. Willner, D. Richter, *Macromolecules* **1997**, *30*, 1582.
- [279] P. Alexandridis, *Current Opinion in Colloid & Interface Science* **1996**, *1*, 490.
- [280] B. Chu, *Langmuir* **1995**, *11*, 414.
- [281] Z. Tuzar, P. Kratochvil, *Surface and Colloid Science* **1993**, *15*, 1.
- [282] K. Meguro, M. Ueno, K. Esumi, *Surfactant Science Series* **1987**, *23*, 109.
- [283] S. Foerster, *Topics in Current Chemistry* **2003**, *226*, 1.
- [284] S. Foerster, M. Zisenis, E. Wenz, M. Antonietti, *Journal of Chemical Physics* **1996**, *104*, 9956.
- [285] A. Qin, M. Tian, C. Ramireddy, S. E. Webber, P. Munk, Z. Tuzar, *Macromolecules* **1994**, *27*, 120.
- [286] S. Zalipsky, *Bioconjugate Chem. FIELD Full Journal Title:Bioconjugate Chemistry* **1995**, *6*, 150.

- [287] M. S. Thompson, T. P. Vadala, M. L. Vadala, Y. Lin, J. S. Riffle, *Polymer FIELD Full Journal Title:Polymer* **2008**, *49*, 345.
- [288] M. Adinolfi, G. Barone, L. De Napoli, A. Iadonisi, G. Piccialli, *Tetrahedron Letters* **1996**, *37*, 5007.
- [289] D. L. Boger, R. A. Lerner, B. F. Cravatt, *Journal of Organic Chemistry* **1994**, *59*, 5078.
- [290] A. P. Phillips, *Journal of the American Chemical Society* **1953**, *75*, 4725.
- [291] H. Rosemeyer, M. Ahlers, B. Schmidt, F. Seela, *Angewandte Chemie* **1985**, *97*, 500.
- [292] D. B. Dess, J. C. Martin, *Journal of Organic Chemistry* **1983**, *48*, 4155.
- [293] S. D. Meyer, S. L. Schreiber, *Journal of Organic Chemistry* **1994**, *59*, 7549.
- [294] K. E. Pfitzner, J. G. Moffatt, *Journal of the American Chemical Society* **1963**, *85*, 3027.
- [295] B. Waengler, Johannes Gutenberg-university (Mainz, Germany), **2004**.
- [296] R. Huisgen, R. Grashey, H. Knupfer, R. Kunz, M. Seidel, *Chemische Berichte* **1964**, *97*, 1085.
- [297] G. Zemplen, A. Kuntz, *British [Patent Document]* **1923**, *56B*, 1705.
- [298] M. Moore, P. Norris, *Tetrahedron Letters* **1998**, *39*, 7027.
- [299] K. Banert, M. Hagedorn, *Angewandte Chemie* **1989**, *101*, 1710.
- [300] J. Möker, university of Hamburg (research group of Prof. Thiem), **2009**.
- [301] D. Cunningham, R. D. James, *European Journal of Cancer* **2001**, *37*, 826.
- [302] Z.-Y. Tian, G.-J. Du, S.-Q. Xie, J. Zhao, W.-Y. Gao, C.-J. Wang, *Molecules* **2007**, *12*, 2450.
- [303] H. S. Yoo, T. G. Park, *Journal of Controlled Release* **2001**, *70*, 63.
- [304] K. K. Karukstis, E. H. Z. Thompson, J. A. Whiles, R. J. Rosenfeld, *Biophys. Chem. FIELD Full Journal Title:Biophysical Chemistry* **1998**, *73*, 249.
- [305] J. K. Wegrzyn, T. Stephan, R. Lau, R. B. Grubbs, *Journal of Polymer Science, Part A: Polymer Chemistry* **2005**, *43*, 2977.
- [306] H. Huang, E. E. Remsen, T. Kowalewski, K. L. Wooley, *Journal of the American Chemical Society* **1999**, *121*, 3805.
- [307] Y. Kang, T. A. Taton, *Journal of the American Chemical Society* **2003**, *125*, 5650.
- [308] Y. Kang, T. A. Taton, *Angewandte Chemie (International ed. in English)* **2005**, *44*, 409.
- [309] F. E. Bailey, Jr., J. V. Koleske, *Poly(ethylene oxide)*, **1976**.
- [310] K.-J. Liu, J. L. Parsons, *Macromolecules* **1969**, *2*, 529.
- [311] R. Kjellander, E. Florin, *Journal of the Chemical Society, Faraday Transactions 1: Physical Chemistry in Condensed Phases* **1981**, *77*, 2053.
- [312] N. V. Sastry, H. Hoffmann, *Colloids and Surfaces, A: Physicochemical and Engineering Aspects* **2004**, *250*, 247.
- [313] T. De Vringer, J. G. H. Joosten, H. E. Junginger, *Colloid and Polymer Science* **1986**, *264*, 623.
- [314] P. Carstensen, *Makromolekulare Chemie* **1970**, *135*, 219.
- [315] M. A. Golub, C. L. Stephens, *Journal of Polymer Science, Part A-1: Polymer Chemistry* **1968**, *6*, 763.
- [316] S. Saeki, N. Kuwahara, M. Nakata, M. Kaneko, *Polymer* **1976**, *17*, 685.
- [317] B. Jonsson, B. Lindman, K. Holmberg, B. Kronberg, *Surfactants and Polymers in Aqueous Solution*, **1998**.
- [318] A. P. Alivisatos, *Science* **1996**, *271*, 933.

- [319] U. I. Tromsdorf, N. C. Bigall, M. G. Kaul, O. T. Bruns, M. S. Nikolic, B. Mollwitz, R. A. Sperling, R. Reimer, H. Hohenberg, W. J. Parak, S. Foerster, U. Beisiegel, G. Adam, H. Weller, *Nano Letters* **2007**, *7*, 2422.
- [320] J. Xie, C. Xu, Z. Xu, Y. Hou, K. L. Young, S. X. Wang, N. Pourmond, S. Sun, *Chem. Mater. FIELD Full Journal Title: Chemistry of Materials* **2006**, *18*, 5401.
- [321] Y.-M. Huh, Y.-W. Jun, H.-T. Song, S. Kim, J.-S. Choi, J.-H. Lee, S. Yoon, K.-S. Kim, J.-S. Shin, J.-S. Suh, J. Cheon, *Journal of the American Chemical Society* **2005**, *127*, 12387.
- [322] K. Mandal Swapan, N. Lequeux, B. Rotenberg, M. Tramier, J. Fattaccioli, J. Bibette, B. Dubertret, *the ACS journal of surfaces and colloids* **2005**, *21*, 4175.
- [323] N. Gaponik, I. L. Radtchenko, G. B. Sukhorukov, A. L. Rogach, *Langmuir* **2004**, *20*, 1449.
- [324] X. Gao, S. Nie, *Journal of Physical Chemistry B* **2003**, *107*, 11575.
- [325] X. Gao, S. Nie, *Analytical Chemistry* **2004**, *76*, 2406.
- [326] B.-S. Kim, J.-M. Qiu, J.-P. Wang, T. A. Taton, *Nano letters* **2005**, *5*, 1987.
- [327] A. Stoccoa, G. Mountrichasb, S. Pispasb, K. Tauera, R. Sigel, in *7th Liquid Matter Conference, Vol. Abstract 514* (Ed.: U. F. Reinhard Sigel, Fribourg, Swi), Lund, Sweden, **2008**.
- [328] E. A. G. Aniansson, S. N. Wall, M. Almgren, H. Hoffmann, I. Kielmann, W. Ulbricht, R. Zana, J. Lang, C. Tondre, *Journal of Physical Chemistry* **1976**, *80*, 905.
- [329] M. Kahlweit, *Journal of Colloid and Interface Science* **1982**, *90*, 92.
- [330] Y. Rharbi, M. Li, M. A. Winnik, K. G. Hahn, Jr., *Journal of the American Chemical Society* **2000**, *122*, 6242.
- [331] A. Halperin, S. Alexander, *Macromolecules* **1989**, *22*, 2403.
- [332] Y. Wang, C. M. Kausch, M. Chun, R. P. Quirk, W. L. Mattice, *Macromolecules* **1995**, *28*, 904.
- [333] T. Haliloglu, I. Bahar, B. Erman, W. L. Mattice, *Macromolecules* **1996**, *29*, 4764.
- [334] Q. Yang, S. Wang, P. Fan, L. Wang, Y. Di, K. Lin, F.-S. Xiao, *Chemistry of Materials* **2005**, *17*, 5999.
- [335] Y. Zheng, H. T. Davis, *Langmuir* **2000**, *16*, 6453.
- [336] S. Pispas, N. Hadjichristidis, *Langmuir* **2003**, *19*, 48.
- [337] A. M. Derfus, W. C. W. Chan, S. N. Bhatia, *Nano Letters* **2004**, *4*, 11.
- [338] C. Kirchner, T. Liedl, S. Kudera, T. Pellegrino, A. M. Javier, H. E. Gaub, S. Stoezle, N. Fertig, W. J. Parak, *Nano Letters* **2005**, *5*, 331.
- [339] A. Shiohara, A. Hoshino, K.-i. Hanaki, K. Suzuki, K. Yamamoto, *Microbiology and Immunology* **2004**, *48*, 669.
- [340] W. W. Yu, L. Qu, W. Guo, X. Peng, *Chemistry of Materials* **2004**, *16*, 560.
- [341] B. K. Paul, S. P. Moulik, *Current Science* **2001**, *80*, 990.
- [342] I. Csetneki, M. K. Faix, A. Szilagyai, A. L. Kovacs, Z. Nemeth, M. Zrinyi, *Journal of Polymer Science, Part A: Polymer Chemistry* **2004**, *42*, 4802.
- [343] A. Taden, M. Antonietti, A. Heilig, K. Landfester, *Chemistry of Materials* **2004**, *16*, 5081.
- [344] X. Liu, Y. Guan, J. Xing, Z. Ma, H. Liu, *Chinese Journal of Chemical Engineering* **2003**, *11*, 731.
- [345] H. P. Khng, D. Cunliffe, S. Davies, N. A. Turner, E. N. Vulfson, *Biotechnology and Bioengineering* **1998**, *60*, 419.
- [346] J. Park, K. An, Y. Hwang, J.-G. Park, H.-J. Noh, J.-Y. Kim, J.-H. Park, N.-M. Hwang, T. Hyeon, *Nature Materials* **2004**, *3*, 891.

- [347] J. M. Asua, *Progress in Polymer Science* **2002**, 27, 1283.
- [348] X. E. E. Reynhout, L. Hoekstra, J. Meuldijk, A. A. H. Drinkenburg, *Journal of Polymer Science, Part A: Polymer Chemistry* **2003**, 41, 2985.
- [349] A. C. C. Esteves, A. Barros-Timmons, T. Monteiro, T. Trindade, *Journal of Nanoscience and Nanotechnology* **2005**, 5, 766.
- [350] R. H. Ottewill, R. Satgurunathan, F. A. Waite, M. J. Westby, *British Polymer Journal* **1987**, 19, 435.
- [351] P. Gramain, Y. Frere, *Polymer Communications* **1986**, 27, 16.
- [352] A. L. L. Palluel, M. J. Westby, C. W. A. Bromley, S. P. Davies, A. J. Backhouse, *Makromolekulare Chemie, Macromolecular Symposia* **1990**, 35-36, 509.
- [353] B. Leary, C. J. Lyons, *Australian Journal of Chemistry* **1989**, 42, 2055.
- [354] C. W. A. Bromley, *Colloids and Surfaces* **1986**, 17, 1.
- [355] A. H. B. Ilan, I. Noda, L. A. Schechtman, Y. Talmon, *Polymer* **1992**, 33, 2043.
- [356] O. Hevus, A. Kohut, R. Fleychuk, N. Mitina, O. Zaichenko, *Macromolecular Symposia* **2007**, 254, 117.
- [357] E. Aramendia, M. J. Barandiaran, J. C. de la Cal, J. Grade, T. Blease, J. M. Asua, *Journal of Polymer Science, Part A: Polymer Chemistry* **2004**, 42, 4202.
- [358] A. Guyot, C. Graillat, C. Favero, *Comptes Rendus Chimie* **2003**, 6, 1319.
- [359] A. Guyot, K. Tauer, *Advances in Polymer Science* **1994**, 111, 43.
- [360] I. Capek, *Advances in Colloid and Interface Science* **2000**, 88, 295.
- [361] K. Tauer, S. Kosmella, *Polymer International* **1993**, 30, 253.
- [362] A. M. Kohut, O. I. Hevus, S. A. Voronov, *Journal of Applied Polymer Science* **2004**, 93, 310.
- [363] X. J. Xu, H. L. Goh, K. S. Siow, L. M. Gan, *Langmuir* **2001**, 17, 6077.
- [364] K. Takahashi, K. Nagai, *Polymer* **1996**, 37, 1257.
- [365] K. Tauer, *Polymer News* **1995**, 20, 342.
- [366] K. Holmberg, *Progress in Organic Coatings* **1992**, 20, 325.
- [367] H. A. S. Schoonbrood, J. M. Asua, *Macromolecules* **1997**, 30, 6034.
- [368] M. B. Urquiola, E. D. Sudol, V. L. Dimonie, M. S. El-Aasser, *Journal of Polymer Science, Part A: Polymer Chemistry* **1993**, 31, 1403.
- [369] G. F. Meijs, E. Rizzardo, *Journal of Macromolecular Science, Reviews in Macromolecular Chemistry and Physics* **1990**, C30, 305.
- [370] G. E. Scott, E. Senogles, *Journal of Macromolecular Science, Reviews in Macromolecular Chemistry* **1973**, 9, 49.
- [371] C. B. Murray, D. J. Norris, M. G. Bawendi, *Journal of the American Chemical Society* **1993**, 115, 8706.
- [372] S. Levine, *Science* **1956**, 123, 185.
- [373] D. Melville, *Nature* **1975**, 255, 706.
- [374] T. R. Strick, J. F. Allemand, D. Bensimon, A. Bensimon, V. Croquette, *Science (Washington, D. C.)* **1996**, 271, 1835.
- [375] P. S. Doyle, J. Bibette, A. Bancaud, J.-L. Viovy, *Science (Washington, DC, United States)* **2002**, 295, 2237.
- [376] M. Fein, J. Unkeless, F. Y. S. Chuang, M. Sassaroli, R. da Costa, H. Vaananen, J. Eisinger, *Journal of Membrane Biology* **1993**, 135, 83.
- [377] K. Sill, T. Emrick, *Chemistry of Materials* **2004**, 16, 1240.
- [378] F. E. Alemдарoglu, K. Ding, R. Berger, A. Herrmann, *Angewandte Chemie, International Edition* **2006**, 45, 4206.
- [379] Y. H. Yu, B. Xue, Y. Sun, *Bioprocess and Biosystems Engineering* **2001**, 24, 25.

- [380] Y. C. Liu, R. Ledger, E. Stellwagen, *Journal of Biological Chemistry* **1984**, 259, 3796.
- [381] Y. C. Liu, E. Stellwagen, *Journal of Biological Chemistry* **1987**, 262, 583.
- [382] D. Bastos, R. Santos, J. Forcada, R. Hidalgo-Alvarez, F. J. de las Nieves, *Colloids and Surfaces, A: Physicochemical and Engineering Aspects* **1994**, 92, 137.
- [383] R. Clapp Aaron, L. Medintz Igor, J. M. Mauro, R. Fisher Brent, G. Bawendi Mounqi, H. Mattoussi, *Journal of the American Chemical Society* **2004**, 126, 301.
- [384] J. R. Lakowicz, *Principles of Fluorescent Spectroscopy*, **1986**.
- [385] U. I. Tromsdorf, dissertation thesis, university of Hamburg (Hamburg), **2009**.
- [386] P. Gillis, F. Moiny, A. Brooks Rodney, *Magnetic resonance in medicine: official journal of the Society of Magnetic Resonance in Medicine / Society of Magnetic Resonance in Medicine* **2002**, 47, 257.
- [387] S. Forster, T. Plantenberg, *Angewandte Chemie* **2002**, 41, 688.
- [388] M. Antonietti, S. Foerster, *Advanced Materials (Weinheim, Germany)* **2003**, 15, 1323.
- [389] P. L. Soo, A. Eisenberg, *Journal of Polymer Science, Part B: Polymer Physics* **2004**, 42, 923.
- [390] S. Jain, F. S. Bates, *Science (Washington, DC, United States)* **2003**, 300, 460.
- [391] V. Filiz, dissertation thesis, university of Hamburg (Hamburg), **2009**.
- [392] A. G. Skirtach, A. Munoz Javier, O. Kreft, K. Kehler, A. Piera Alberola, H. Moewald, W. J. Parak, G. B. Sukhorukov, *Angewandte Chemie* **2006**, 45, 4612.
- [393] K. Gupta Ajay, S. Wells, *IEEE transactions on nanobioscience* **2004**, 3, 66.
- [394] W. W. Yu, E. Chang, C. M. Sayes, R. Drezek, V. L. Colvin, *Nanotechnology* **2006**, 17, 4483.
- [395] A. G. Tkachenko, H. Xie, Y. Liu, D. Coleman, J. Ryan, W. R. Glomm, M. K. Shipton, S. Franzen, D. L. Feldheim, *Bioconjugate Chemistry* **2004**, 15, 482.
- [396] C. M. Goodman, C. D. McCusker, T. Yilmaz, V. M. Rotello, *Bioconjugate Chemistry* **2004**, 15, 897.
- [397] R. Rothlein, M. Czajkowski, M. M. O'Neill, S. D. Marlin, E. Mainolfi, V. J. Merluzzi, *Journal of Immunology* **1988**, 141, 1665.
- [398] B. I. Ipe, M. Lehnig, C. M. Niemeyer, *Small* **2005**, 1, 706.
- [399] I. Izumi, F.-R. F. Fan, A. J. Bard, *Journal of Physical Chemistry* **1981**, 85, 218.
- [400] A. J. Nozik, *Annual Review of Physical Chemistry* **1978**, 29, 189.
- [401] B. O. Dabbousi, J. Rodriguez-Viejo, F. V. Mikulec, J. R. Heine, H. Mattoussi, R. Ober, K. F. Jensen, M. G. Bawendi, *Journal of Physical Chemistry B* **1997**, 101, 9463.
- [402] R. Xie, U. Kolb, J. Li, T. Basche, A. Mews, *Journal of the American Chemical Society* **2005**, 127, 7480.
- [403] D. V. Talapin, I. Mekis, S. Goetzinger, A. Kornowski, O. Benson, H. Weller, *Journal of Physical Chemistry B* **2004**, 108, 18826.
- [404] S. T. Selvan, T. T. Tan, J. Y. Ying, *Advanced Materials (Weinheim, Germany)* **2005**, 17, 1620.
- [405] O. Seleverstov, O. Zabinnyk, M. Zscharnack, L. Bulavina, M. Nowicki, J.-M. Heinrich, M. Yezhelyev, F. Emmrich, R. O'Regan, A. Bader, *Nano Letters* **2006**, 6, 2826.
- [406] H. C. Fischer, L. Liu, K. S. Pang, W. C. W. Chan, *Advanced Functional Materials* **2006**, 16, 1299.
- [407] T. F. Slater, B. Sawyer, U. Straeuli, *Biochimica et biophysica acta* **1963**, 77, 383.
- [408] M. Piscator, T. Kjellstrom, B. Lind, *Lancet* **1976**, 2, 587.
- [409] K. R. Mahaffey, P. E. Corneliussen, C. F. Jelinek, J. A. Fiorino, *Environmental health perspectives* **1975**, 12, 63.

- [410] H. Spencer, C. R. Asmussen, R. B. Holtzman, L. Kramer, *American Journal of Clinical Nutrition* **1979**, *32*, 1867.
- [411] F. Ushio, M. Doguchi, *Bulletin of Environmental Contamination and Toxicology* **1977**, *17*, 707.
- [412] S. Iwao, *Keio Journal of Medicine* **1977**, *26*, 63.
- [413] D. J. Irvine, A. M. Mayes, S. K. Satija, J. G. Barker, S. J. Sofia-Allgor, L. G. Griffith, *Journal of Biomedical Materials Research* **1998**, *40*, 498.
- [414] W. J. Parak, R. Boudreau, M. Le Gros, D. Gerion, D. Zanchet, C. M. Micheel, S. C. Williams, A. P. Alivisatos, C. Larabell, *Advanced Materials (Weinheim, Germany)* **2002**, *14*, 882.
- [415] J. K. Jaiswal, H. Mattoussi, J. M. Mauro, S. M. Simon, *Nature Biotechnology* **2003**, *21*, 47.
- [416] M. Dahan, T. Laurence, F. Pinaud, D. S. Chemla, A. P. Alivisatos, M. Sauer, S. Weiss, *Optics Letters* **2001**, *26*, 825.
- [417] K.-I. Hanaki, A. Momo, T. Oku, A. Komoto, S. Maenosono, Y. Yamaguchi, K. Yamamoto, *Biochemical and Biophysical Research Communications* **2003**, *302*, 496.
- [418] L. C. Mattheakis, J. M. Dias, Y.-J. Choi, J. Gong, M. P. Bruchez, J. Liu, E. Wang, *Analytical Biochemistry* **2004**, *327*, 200.
- [419] E. C. Sweeney, A. G. Tonevitsky, D. E. Temiakov, I. I. Agapov, S. Saward, R. A. Palmer, *Proteins: Structure, Function, and Genetics* **1997**, *28*, 586.
- [420] E. D. Green, R. M. Brodbeck, J. U. Baenziger, *Journal of Biological Chemistry* **1987**, *262*, 12030.
- [421] R. Hegde, S. K. Podder, *European Journal of Biochemistry* **1998**, *254*, 596.
- [422] K. Yamashita, K. Umetsu, T. Suzuki, Y. Iwaki, T. Endo, A. Kobata, *Journal of Biological Chemistry* **1988**, *263*, 17482.
- [423] B. Abdul-Rahman, E. Ailor, D. Jarvis, M. Betenbaugh, Y. C. Lee, *Carbohydrate Research* **2002**, *337*, 2181.
- [424] F. Medina-Bolivar, R. Wright, V. Funk, D. Sentz, L. Barroso, T. D. Wilkins, W. Petri, C. L. Cramer, *Vaccine* **2003**, *21*, 997.
- [425] S. S. Narayanan, R. Sarkar, S. K. Pal, *Journal of Physical Chemistry C* **2007**, *111*, 11539.
- [426] S. Johansen Julia, V. Jensen Benny, A. Roslind, D. Nielsen, A. Price Paul, *Cancer epidemiology, biomarkers & prevention : a publication of the American Association for Cancer Research, cosponsored by the American Society of Preventive Oncology* **2006**, *15*, 194.
- [427] G. Gopalakrishnan, C. Danelon, P. Izewska, M. Prummer, P.-Y. Bolinger, I. Geissbuhler, D. Demurtas, J. Dubochet, H. Vogel, *Angewandte Chemie, International Edition* **2006**, *45*, 5478.
- [428] B. P. Aryal, K. P. Neupane, M. G. Sandros, D. E. Benson, *Small* **2006**, *2*, 1159.
- [429] Y. Matsumura, H. Maeda, *Cancer Research* **1986**, *46*, 6387.
- [430] R. Duncan, *Nature Reviews Drug Discovery* **2003**, *2*, 347.
- [431] R. K. Jain, *Annual Review of Biomedical Engineering* **1999**, *1*, 241.
- [432] R. K. Jain, *Journal of Controlled Release* **2001**, *74*, 7.
- [433] R. B. Campbell, D. Fukumura, E. B. Brown, L. M. Mazzola, Y. Izumi, R. K. Jain, V. P. Torchilin, L. L. Munn, *Cancer Research* **2002**, *62*, 6831.
- [434] K. C. Weng, C. O. Noble, B. Papahadjopoulos-Sternberg, F. F. Chen, D. C. Drummond, D. B. Kirpotin, D. Wang, Y. K. Hom, B. Hann, J. W. Park, *Nano Letters* **2008**, *8*, 2851.

- [435] T. Jamieson, R. Bakhshi, D. Petrova, R. Pocock, M. Imani, A. M. Seifalian, *Biomaterials* **2007**, *28*, 4717.
- [436] J. Rao, A. Dragulescu-Andrasi, H. Yao, *Current Opinion in Biotechnology* **2007**, *18*, 17.
- [437] S. Pujals, N. G. Bastus, E. Pereiro, C. Lopez-Iglesias, V. F. Puentes, M. J. Kogan, E. Giralt, *ChemBioChem FIELD Full Journal Title: ChemBioChem* **2009**, *10*, 1025.
- [438] K. K. Sandhu, C. M. McIntosh, J. M. Simard, S. W. Smith, V. M. Rotello, *Bioconjugate Chemistry* **2002**, *13*, 3.
- [439] T. M. Allen, P. R. Cullis, *Science* **2004**, *303*, 1818.
- [440] J. Zhang, R. D. K. Misra, *Acta Biomaterialia* **2007**, *3*, 838.
- [441] Z. H. Siddik, *Oncogene* **2003**, *22*, 7265.
- [442] B. Rosenberg, *Cancer treatment reports* **1979**, *63*, 1433.
- [443] L. L. Munchausen, R. O. Rahn, *Cancer Chemotherapy Reports, Part I* **1975**, *59*, 643.
- [444] W. Voigt, A. Dietrich, H.-J. Schmoll, *Pharmazie in unserer Zeit* **2006**, *35*, 134.
- [445] C. X. Zhang, S. J. Lippard, *Current Opinion in Chemical Biology* **2003**, *7*, 481.
- [446] W. Dempke, W. Voigt, A. Grothey, B. T. Hill, H. J. Schmoll, *Anti-cancer drugs* **2000**, *11*, 225.
- [447] B. Stordal, M. Davey, *IUBMB Life* **2007**, *59*, 696.
- [448] P. J. O'Dwyer, J. P. Stevenson, S. W. Johnson, *Drugs* **2000**, *59*, 19.
- [449] P. Freeman Kim, A. Hahn Kevin, F. D. Harris, K. King Glen, *Journal of veterinary internal medicine / American College of Veterinary Internal Medicine* **2003**, *17*, 96.
- [450] S. C. Charney, P. J. Bergman, J. A. McKnight, J. Farrelly, C. A. Novosad, N. F. Leibman, M. A. Camps-Palau, *Veterinary and Comparative Oncology* **2005**, *3*, 171.
- [451] D. M. Mattson, I. M. Ahmad, D. Dayal, A. D. Parsons, N. Aykin-Burns, L. Li, K. P. Orcutt, D. R. Spitz, K. J. Dornfeld, A. L. Simons, *Free Radical Biology & Medicine* **2009**, *46*, 232.
- [452] J. A. Bradford, G. Buller, M. Suter, M. Ignatius, J. M. Beechem, *Cytometry, Part A* **2004**, *61A*, 142.
- [453] B. Dubertret, M. Calame, A. J. Libchaber, *Nature Biotechnology* **2001**, *19*, 365.
- [454] E. Chang, J. S. Miller, J. Sun, W. W. Yu, V. L. Colvin, R. Drezek, J. L. West, *Biochemical and Biophysical Research Communications* **2005**, *334*, 1317.
- [455] B. H. Lee, K.-W. Kwon, M. Shim, *Journal of Materials Chemistry* **2007**, *17*, 1284.
- [456] O. Lehmann, H. Meyssamy, K. Koempe, H. Schnablegger, M. Haase, *Journal of Physical Chemistry B* **2003**, *107*, 7449.
- [457] D. V. Leff, L. Brandt, J. R. Heath, *Langmuir* **1996**, *12*, 4723.
- [458] R. F. Storey, J. W. Sherman, *Macromolecules* **2002**, *35*, 1504.
- [459] W. W. Yu, L. Qu, W. Guo, X. Peng, *Chem. Mater. FIELD Full Journal Title: Chemistry of Materials* **2004**, *16*, 560.
- [460] S. M. Chamow, T. P. Kogan, M. Venuti, T. Gadek, R. J. Harris, D. H. Peers, J. Mordenti, S. Shak, A. Ashkenazi, *Bioconjugate Chemistry* **1994**, *5*, 133.
- [461] A. P. Esteves, L. M. Rodrigues, M. E. Silva, S. Gupta, A. M. F. Oliveira-Campos, O. Machalicky, A. J. Mendonca, *Tetrahedron* **2005**, *61*, 8625.
- [462] S. Deng, U. Gangadharmath, C.-W. T. Chang, *Journal of Organic Chemistry* **2006**, *71*, 5179.
- [463] A. R. Jeanes, C. A. Wilham, G. E. Hilbert, *Journal of the American Chemical Society* **1953**, *75*, 3667.
- [464] E. J. Grayson, S. J. Ward, A. L. Hall, P. M. Rendle, D. P. Gamblin, A. S. Batsanov, B. G. Davis, *Journal of Organic Chemistry* **2005**, *70*, 9740.

- [465] J. D'Onofrio, M. De Champdore, L. De Napoli, D. Montesarchio, G. Di Fabio, *Bioconjugate Chemistry* **2005**, *16*, 1299.
- [466] W. W. Yu, L. Qu, W. Guo, X. Peng, *Chemistry of Materials* **2003**, *15*, 2854.
- [467] M. Kuno, J. K. Lee, B. O. Dabbousi, F. V. Mikulec, M. G. Bawendi, *Journal of Chemical Physics* **1997**, *106*, 9869.
- [468] A. L. Efros, M. Rosen, M. Kuno, M. Nirmal, D. J. Norris, M. Bawendi, *Physical Review B: Condensed Matter* **1996**, *54*, 4843.
- [469] M. Nirmal, D. J. Norris, M. Kuno, M. G. Bawendi, A. L. Efros, M. Rosen, *Physical Review Letters* **1995**, *75*, 3728.
- [470] M. Nirmal, B. O. Dabbousi, M. G. Bawendi, J. J. Macklin, J. K. Trautman, T. D. Harris, L. E. Brus, *Nature (London)* **1996**, *383*, 802.
- [471] M. Kuno, D. P. Fromm, H. F. Hamann, A. Gallagher, D. J. Nesbitt, *Journal of Chemical Physics* **2000**, *112*, 3117.
- [472] R. M. Kraus, P. G. Lagoudakis, J. Mueller, A. L. Rogach, J. M. Lupton, J. Feldmann, D. V. Talapin, H. Weller, *Journal of Physical Chemistry B* **2005**, *109*, 18214.
- [473] V. I. Klimov, D. W. McBranch, C. A. Leatherdale, M. G. Bawendi, *Physical Review B: Condensed Matter and Materials Physics* **1999**, *60*, 13740.
- [474] K. T. Shimizu, R. G. Neuhauser, C. A. Leatherdale, S. A. Empedocles, W. K. Woo, M. G. Bawendi, *Physical Review B: Condensed Matter and Materials Physics* **2001**, *63*, 205316/1.
- [475] T. D. Krauss, L. E. Brus, *Physical Review Letters* **1999**, *83*, 4840.
- [476] A. Issac, C. von Borczyskowski, F. Cichos, *Physical Review B: Condensed Matter and Materials Physics* **2005**, *71*, 161302/1.
- [477] F. Koberling, A. Mews, T. Basche, *Advanced Materials* **2001**, *13*, 672.
- [478] J. Muller, J. M. Lupton, A. L. Rogach, J. Feldmann, D. V. Talapin, H. Weller, *Applied Physics Letters* **2004**, *85*, 381.
- [479] A. Eychmueller, *Journal of Physical Chemistry B* **2000**, *104*, 6514.
- [480] S. A. Empedocles, D. J. Norris, M. G. Bawendi, *Physical Review Letters* **1996**, *77*, 3873.
- [481] S. A. Empedocles, R. Neuhauser, K. Shimizu, M. G. Bawendi, *Advanced Materials* **1999**, *11*, 1243.
- [482] L. P. Balet, S. A. Ivanov, A. Piryatinski, M. Achermann, V. I. Klimov, *Nano Letters* **2004**, *4*, 1485.
- [483] A. Puzder, A. J. Williamson, N. Zaitseva, G. Galli, L. Manna, A. P. Alivisatos, *Nano Letters* **2004**, *4*, 2361.
- [484] J. E. B. Katari, V. L. Colvin, A. P. Alivisatos, *Journal of Physical Chemistry* **1994**, *98*, 4109.
- [485] A. V. Baranov, Y. P. Rakovich, J. F. Donegan, T. S. Perova, R. A. Moore, D. V. Talapin, A. L. Rogach, Y. Masumoto, I. Nabiev, *Physical Review B: Condensed Matter and Materials Physics* **2003**, *68*, 165306/1.
- [486] J. McBride, J. Treadway, L. C. Feldman, S. J. Pennycook, S. J. Rosenthal, *Nano Letters* **2006**, *6*, 1496.
- [487] C. Kittel, *Einführung in die Festkörperphysik*, R. Oldenbourg Verlag, München, **1989**.
- [488] K. J. Klabunde, *Nanoscale Materials in Chemistry*, John Wiley and Sons, Inc., New York, **2001**.
- [489] B. D. Cullity, *Introduction to Magnetic Materials*, Addison-Wesley Publishing Company, **1972**.
- [490] K. J. Kirk, *Contemporary Physics* **2000**, *41*, 61.

-
- [491] N. A. Spaldin, *Magnetic Materials: Fundamentals and Device Applications*, Cambridge University Press, Cambridge, **2003**.
- [492] F. J. Himpsel, J. E. Ortega, G. J. Mankey, R. F. Willis, *Advances in Physics* **1998**, *47*, 511.
- [493] D. L. Leslie-Pelecky, R. D. Rieke, *Chemistry of Materials* **1996**, *8*, 1770.
- [494] G. Schmid, *Nanoparticles - From Theory to Application*, Weinheim, **2004**.
- [495] A. Aharoni, *Introduction to the Theory of Ferromagnetism*, Oxford, **2000**.
- [496] C. B. Murray, S. Sun, H. Doyle, T. Betley, *MRS Bulletin* **2001**, *26*, 985.
- [497] C. P. Bean, J. D. Livingston, *Journal of Applied Physics* **1959**, *30*, 120S.
- [498] S. H. Koenig, K. E. Kellar, *Magnetic Resonance in Medicine* **1995**, *34*, 227.
- [499] K. E. Kellar, D. K. Fujii, W. H. H. Gunther, K. Briley-Saebo, M. Spiller, S. H. Koenig, *Magnetic Resonance Materials in Physics, Biology and Medicine* **1999**, *8*, 207.
- [500] M. P. Morales, S. Veintemillas-Verdaguer, M. I. Montero, C. J. Serna, A. Roig, L. Casas, B. Martinez, F. Sandiumenge, *Chemistry of Materials* **1999**, *11*, 3058.
- [501] Y.-w. Jun, J.-H. Lee, J. Cheon, *Angewandte Chemie* **2008**, *47*, 5122.

9 Appendix

9.1 Optical properties of semiconductor nanoparticles (quantum dots)

A prevalent accepted depiction of the electronic excitation in nano-sized semiconductors is the effective mass approximation^[6]. Hereby instead of the full ensemble of electrons in one crystal the excited electron and the simultaneously created hole are approximated through their effective masses, which comprise the material parameter as well as interactions with the crystal lattice. More precisely, the effective mass is mathematically the curvature, or second derivative, of the energy band with respect to the momentum wave vector, k . Electron and hole compose by reason of their mutual attraction a quasi-particle, a so called exciton^[13, 14], which can adopt hydrogen-like states. Like electrons, excitons can move in solid states, thereby transporting their excitation energy. Recombination of the electron and hole can occur, releasing the energy equivalent to the difference between the valence and conduction band, minus the exciton binding energy.

According to the volume expansion of the electron-hole pair, excitons can be differentiated between Frenkel-excitons, with an average distance of electron and hole in the dimension of a lattice constant, and Wannier-excitons, in which the distance is larger than the lattice constant. Since it is generally the case in semiconductors with covalent bonds between the lattice elements that the exciton possesses an expansion over several lattice constants, a closer examination of Wannier-excitons is warranted.

In the effective mass approximation the electron has the effective mass m_n^* and the hole the effective mass m_p^* . The effective mass comprises the corrections for the movement of the electron and hole respectively. The attraction between them is a coulomb-potential, which admittedly is modified by the lattice polarisation. At this juncture the dielectric constant of the crystal is introduced^[15]. According to this model the exciton energy levels can be found following Schrödinger equation (equation 1), in which the bottom edge of the conduction band has the energy $E = 0$.

$$\left[-\frac{\hbar^2}{2m_n^*} \tilde{N}_n^2 - \frac{\hbar^2}{2m_p^*} \tilde{N}_p^2 - \frac{e^2}{4\pi\epsilon_0\epsilon|\vec{r}_n - \vec{r}_p|} \right] \psi = E\psi, \quad (1)$$

This Schrödinger equation is identical with the equation for a hydrogen atom and can be solved exactly. Therefore relative- and centre-of-mass coordinates are implemented,

$$\vec{r} = \vec{r}_n - \vec{r}_p, \quad \vec{R} = \frac{m_n^* \vec{r}_n + m_p^* \vec{r}_p}{m_n^* + m_p^*},$$

as well as the reduced mass and total mass

$$\frac{1}{\mu} = \frac{1}{m_n^*} + \frac{1}{m_p^*}, \quad M = m_n^* + m_p^*.$$

From this follows equation 2

$$\left[-\frac{\hbar^2}{2\mu} \tilde{N}_r^2 - \frac{\hbar^2}{2M} \tilde{N}_R^2 - \frac{e^2}{4\pi\epsilon_0\epsilon|\vec{r}|} \right] \psi = E\psi. \quad (2)$$

The barycentre \vec{R} of the excitons moves quasi-free and und quantum-mechanical like a planar wave in the crystal, which is specified by the propagation vector \mathbf{K} . Given the kinetic energy of the exciton is $\hbar^2 \mathbf{K}^2 / 2M$ and E_g is the bulk material energy bandgap, the energy states of the Wannier exciton follow a discrete, hydrogen-like spectrum:

$$E_{\text{ex},n}(\mathbf{K}) = E_g - \frac{R_{\text{ex}}}{n^2} + \frac{\hbar^2 \mathbf{K}^2}{2M} = E_g - \frac{\mu e^4}{32\pi^2 \epsilon_0^2 \epsilon^2 \hbar^2} \times \frac{1}{n^2} + \frac{\hbar^2 \mathbf{K}^2}{2M}, \quad n = 1, 2, 3 \dots (3)$$

In the ground state the binding energy of the electron hole pair correlates with the Rydberg energy of the exciton R_{ex} , if the terms $n = 1$ and $\mathbf{K} = 0$ are fulfilled:

$$R_{\text{ex}} = - \frac{\mu e^4}{32\pi^2 \epsilon_0^2 \epsilon^2 \hbar^2} = - \frac{\mu}{m_e} \frac{1}{\epsilon^2} \text{Ry} = - \frac{\mu}{m_e} \frac{1}{\epsilon^2} 13.6 \text{ eV}. \quad (4)$$

Further states of the excited exciton with $n > 1$ are closer to the conduction band and absorption edge respectively. figure 143 illustrates the energy states of the Wannier-exciton according to equation 3.

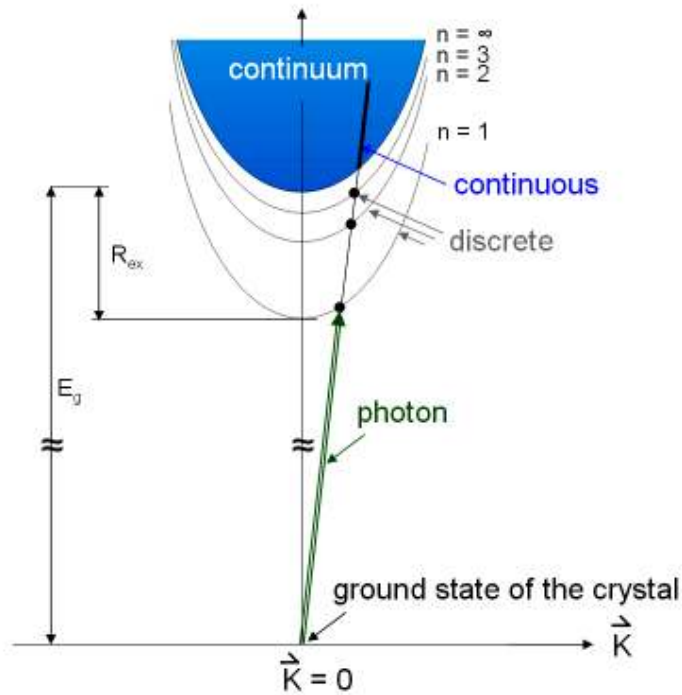


figure 143: energy states of an in a direct process created exciton. The ground state of the crystal is at $\vec{K} = 0$. The energy states show a quadratic dependence of the energy from \vec{K} for each by n characterized state.

Out of this simple model arise two exciton-phenomena: the electron and the hole possess a hydrogen-like bond, which gives reason to spectra with sharp lines, and the barycentre of the exciton can range quasi-free in the crystal, giving it the capacity for energy transportation.

In contrast to the free movement of a Mott-Wannier-exciton in a solid semiconductor, an electron-hole pair in the finite volume of a quantum dot experiences a three dimensional, spatial confinement due to its potential barrier. The nanoparticle is considered as a hypothetical box, wherein both charge carriers are located. The box is one dimensional and features a potential of zero, whereas on its edges the potential rises to infinity.

To approach the spherical shape of a nanoparticle and to describe the electron-hole pair the Hamiltonian operator is expanded in a parabolic effective mass approximation:

$$\hat{H} = -\frac{\hbar^2}{2m_e^*} \tilde{N}_e^2 - \frac{\hbar^2}{2m_h^*} \tilde{N}_h^2 - \frac{e^2}{\epsilon |r_e - r_h|} + V_e^{\text{conf}}(r_e) + V_h^{\text{conf}}(r_h) + V_{\text{Pol}}(r_e, r_h) \quad (5)$$

The first and second term describe the kinetic energy of electron and hole, the third the Coulomb-interaction between electron and hole at a dielectric constant ϵ , the fourth and fifth the finite potential barriers for both charge carriers, and the final term dielectric polarisation effects on the border between the surface of the nanocrystal and host-matrix.

The confinement causes on the one hand quantized energy levels, and on the other hand a revision of the Coulomb-interaction subject to the quantum dot size. There are three cases differentiated for comparing the force of the quantisation with the Coulomb-interaction.

In the limiting case of the weak confinement of an exciton, when the crystal radius R is bigger than the Bohr radius $a_B = 4\pi\epsilon_0\hbar^2\epsilon/\mu e^2$ the Coulomb-interaction between electron and hole dominates over the confinement. In such a case just exciton-like states can appear which are appropriate to expanded semiconductors. Their barycentre movement is constricted upon the influence of the quantum well. Therefore their energy is quantized, whereas the relative movement of electron and hole is barely affected.

The total energy of the exciton can be constituted according to equation 3 from the bandgap E_g , the binding energy, and the quantization energy for the movement.

In the strong confinement regime, the radius of quantum dots is smaller than the Bohr radii of electron and hole. The Coulomb-interaction between electron and hole exerts just a marginal effect in the energies of the spectra. The energy of the luminescence is decisively determined by the quantization energies of the electron and the hole. The total energy of the exciton results then from the bandgap and the separate quantization energies of both charge carriers to:

$$E_{\text{ex}} = E_g + \frac{\hbar^2\pi^2}{2m_e^*a^2} + \frac{\hbar^2\pi^2}{2m_h^*a^2} - 1.78\frac{e^2}{\epsilon a} + V_{\text{Pol}}(r_e, r_h). \quad (6)$$

Hereby is an accessory Coulomb-adjustment introduced, which incorporates the Coulomb-interaction between hole and electron. Since the quantization energy scales with a^2 the radius of quantum dots, in contrast to the Coulomb-interaction which scales with a^1 , the quantization energy will predominate for small radii.

If the Bohr radius of the hole and electron is in the size range of the radius of the nanoparticle, the exciton falls into an intermediate confinement regime. At this juncture it can occur that for instance the Bohr radius of the electron is bigger than the particle radius, while the Bohr radius of the hole is smaller. In this case the hole, whose probability density is highest in the particle centre, moves with an averaged potential of the faster moving electron.

9.1.1 Valence bond degeneracy and spin-orbit coupling

In II-VI semiconductor crystals, e.g. CdSe, the conduction band consists of the 5s-orbital of cadmium. This has angular momentum $L = 0$ and is thereby spatially isotropic and consequently twofold degenerate due to the spin of the electron. The movement of the excited electron can therefore be described with a simple parabolic energy dispersion, for which equation 3 is valid.

The valence band of CdSe, which consists of 4p-orbitals of the selenium, is six-fold degenerate including spin effects. The degeneracy however is nullified by the spin-orbit interaction, which produces a splitting of the valence band at $k = 0$ into a two-fold degenerate split-off band and a four-fold degenerate band. Those are assigned several total angular momentum states $J = L+s, \dots, |L-s|$. Each of these states is, by reason of the spin, two-fold degenerate. Out of the total angular momentum $J = 1/2$ arises the lower situated split-off band with $m_J = \pm 1/2$. In case of $J = 3/2$ the already four-fold degenerate valence band splits into two additional valence bands at $k \neq 0$ with $m_J = \pm 3/2$ and $m_J = \pm 1/2$, which show a different bending and thereby effective mass. Thus they are named heavy (hh) and light hole band (lh). But actually CdSe nanocrystals possess a hexagonal Wurtzite crystal structure. This structure can be included as a slight imperfection in the cubic structure. Such calculation for the valence band results in the disappearance of the degeneracy of the heavy and light hole band for $k = 0$ and an effective division of the band into an A and B band^[6, 467] (vide figure 144).

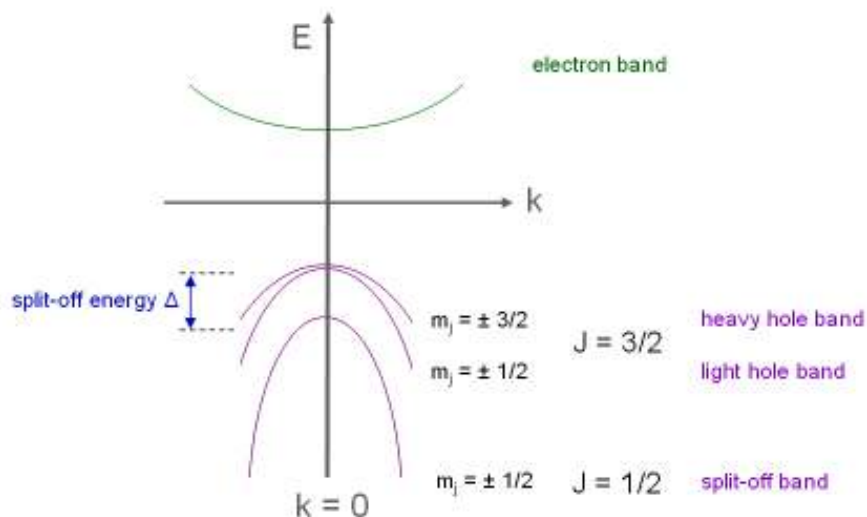


figure 144: dispersion relation of an exciton under abrogation of the valence band degeneracy. The quantum numbers of the hole states and their z-component are denoted.

The confinement maintains due to the minor size of quantum dots to an interference of the different valence bond states, viz. the wave functions are composed of linear combinations of the states of different valence bands with different angular moments. This implies for the energies of the hole states that they are not only dislocated subject to the radius but also contingent on the coupling between the bands.

Luttinger and Kohn introduced a Hamiltonian operator which considers effects of the degeneracy and the influence of the spin-orbit interaction:

$$\hat{H}_{LK} = \left(\gamma_1 + \frac{5}{2} \gamma_2 \right) \frac{\hat{p}^2}{2m} - \frac{\gamma_2}{m^2} (\hat{p} \times \hat{J})^2 - \frac{2\gamma_3}{m} \left(\{p_x p_y\} \{J_x J_y\} + \{p_y p_z\} \{J_y J_z\} + \{p_z p_x\} \{J_z J_x\} \right) \quad (7)$$

with $\{a b\} = (ab + ba)/2$, the free electron mass m , the bandparameters $\gamma_1, \gamma_2, \gamma_3$, the impulse operator of the hole $\hat{p} = (p_x, p_y, p_z)$, and the angular momentum operator $\hat{J} = (J_x, J_y, J_z)$ for $J = 3/2$ valence bond states.

The first term of the Luttinger Hamiltonian operator represents the kinetic energy of the hole with modified mass, the second and third the spin-orbit interaction. Combining this Hamiltonian operator with a spherical potential leads to an interference of the valence bands. The execution of a spherical approximation by Baldereschi and Lipari simplifies the Luttinger Hamiltonian operator:

$$\hat{H}_{Sph} = \frac{\gamma_1}{2m} \hat{p}^2 - \frac{\mu\gamma_1}{18m} (\mathbf{P}^{(2)} \times \mathbf{J}^{(2)}) \quad (8)$$

$\mathbf{P}^{(2)}$ and $\mathbf{J}^{(2)}$ are spherical tensor operators of second order. The coupling parameter μ is defined as:

$$\mu = \frac{6\gamma_3 + 4\gamma_2}{4\gamma_1} \quad (9)$$

The introduction of \hat{H}_{Sph} in the eigenfunction of the exciton, which developed from the effective mass approximation follows:

$$H = E_g + \frac{\hat{p}_e^2}{2m_e^*} + \frac{\gamma_1}{2m} p_h^2 - \frac{\mu\gamma_1}{18m} (\mathbf{P}_h^{(2)} \times \mathbf{J}_h^{(2)}) - \frac{e^2}{\epsilon |r_e - r_h|} + V_{conf}(r) + V_{Pol}(r_e, r_h) \quad (10)$$

The equation is valid for spherical nanocrystals with a cubic lattice structure, in which the band edge near states of excitons ($1S_{3/2}$, $1S_e$) are eightfold degenerate.

9.1.2 Excitonic fine structure

Whereas so far ideal spherical dots with a cubic zinc blende lattice structure were taken as a basis, real crystals can have a more ellipsoidal shape and hexagonal wurtzite lattice structure. The wurtzite structure splits the fourfold degenerate hole state $1S_{3/2}$ by the crystal field of the hexagonal lattice in two-fold degenerate A-states with $j = \pm 3/2$ and twofold degenerate B-states with $j = \pm 1/2$, while a non spherical nanocrystal shape splits these levels by changing the confinement along the short and long axes of the ellipsoid^[468, 469].

The complete equation for the splitting in the wake of the elliptic asymmetry Δ_{sh} and the intrinsic crystal field Δ_{int} is:

$$\Delta = \Delta_{int} + \Delta_{sh}(a, \beta, \mu), \quad (11)$$

where a represents the radius of the quantum dot, β the ratio of the effective masses of the A- and B-bands along to the c-axis, and μ the degree of the elliptic deviation. In addition to this effect, the exchange interaction between electron and hole can also annul the degeneracy. The exchange interaction describes the probability to find an electron and a hole at the same place. The energy distribution of this interaction is dependent upon the spatial constriction of the wave function of electron and hole in the nanocrystal. For the exchange interaction the Hamiltonian operator is:

$$\hat{H}_{exch} = -\frac{2}{3}\epsilon_{exch}a_0^3\delta(\mathbf{r}_e - \mathbf{r}_h)(\hat{\sigma} \times \hat{J}). \quad (12)$$

Hereby $\hat{\sigma}$ is the Pauli-spin operator and \hat{J} the angular momentum operator for the hole with an angular momentum of $3/2$. a_0 is the lattice constant and ϵ_{exch} the exchange constant. The term $(\hat{\sigma} \times \hat{J})$ merges electron-spin states and hole-spin states, which leads to a further division of the eight-fold degenerated state $1S_e, 1S_{3/2}$.

In a hexagonal CdSe bulk material the four-fold degenerate exciton state $1S_{3/2}$ is split into an optically active singlet and an optically passive triplet with an energy difference:

$$\Delta_{exch}^h = \frac{2}{\pi} \left(\frac{a_0}{a_{ex}} \right)^3 \epsilon_{exch} = 0.13 \text{ meV}. \quad (13)$$

In nanocrystals the extent of the exchange interaction is given by:

$$\eta = \chi(\beta) \left(\frac{a_{ex}}{a} \right)^3 \Delta_{exch}^h, \quad (14)$$

where the dimensionless constant $\chi(\beta)$ in CdSe bears the value 0.78.

For CdSe quantum dots the anisotropy and the exchange term can be included within the framework of the perturbation theory. From the eight-fold degenerate band edge near state of the exciton ($1S_{3/2}$, $1S_e$) results five levels, which are characterized by a projection of the total angular momentum $N_m = F_{em} + F_{hm}$ in the direction of the unique crystal axis c , whereas F_{em} (F_{hm}) mark the projection of the electron spin (hole spin). figure 145 illustrates the exciton fine structure. States with $F > 0$ are twofold degenerate. According to the notation after Efros *et al.*^[468] states are distinguished by a superscript U for the upper states and a superscript L for the lower levels. The states with $F = \pm 2$ and 0^L are, according to the electronic dipole approximation, optically passive. The transition from and to the state $F = \pm 2$ ("dark exciton") is by reason of the angular momentum $J = 2$ forbidden. Radiative recombination (under the emission of a photon) from these states is only permitted by absorption or emission of phonons. By virtue of the modest energetic interval to the energetically higher optically active state ("bright" state) with the angular momentum quantum number $F = \pm 1^L$, an excitation is able to recombine over this higher state by absorption of phonons. A Stokes shift is caused by the splitting between ± 2 and $\pm 1^L$ states^[6, 467, 469].

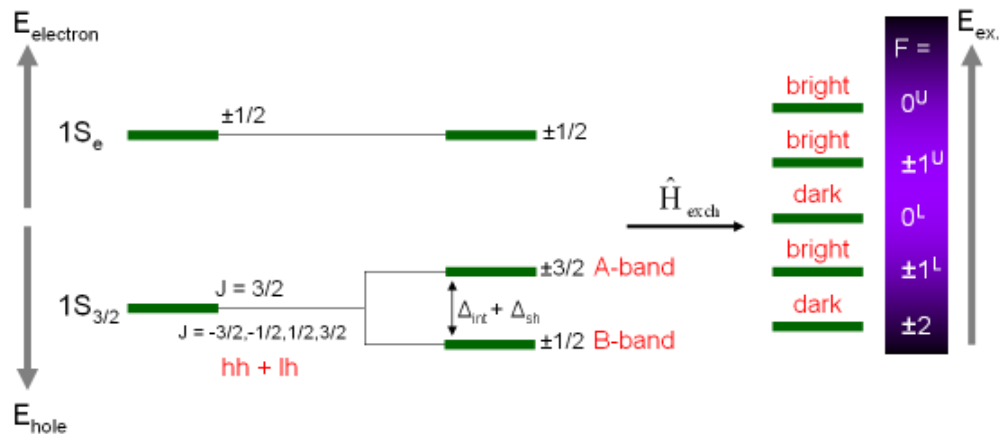


figure 145: The band edge near exciton ($1S_{3/2}$, $1S_e$) splits by reason of the elliptic character of the quantum dot, the intrinsic crystal field, and the extended electron-hole interaction in five transition states.

9.1.3 Blinking behaviour

The phenomenon that the photoluminescence of nanocrystals randomly flickers between emitting ("on") and almost dark ("off") periods under continuous excitation conditions is

commonly referred to as blinking^[6, 470, 471]. Thereby a threshold (intensity-limit) defines the luminescence to be on or off.

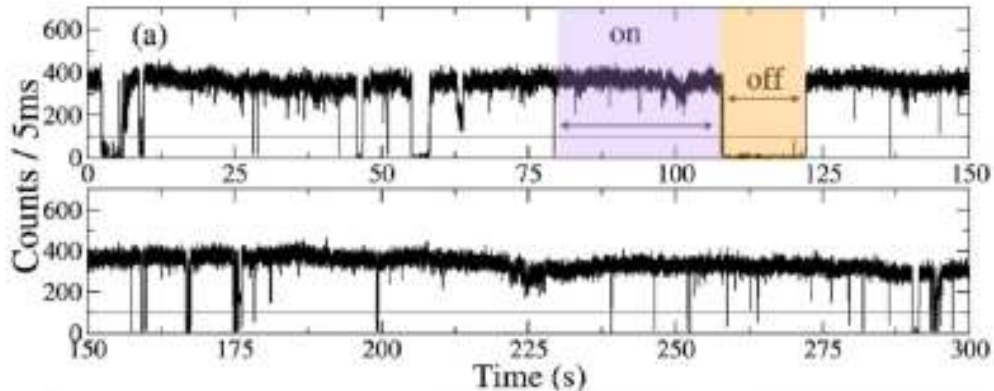


figure 146: Histogram of the time-resolved fluorescence of a single CdSe/ZnS nanocrystals^[6]. The histogram in figure 146 shows a photoluminescence trajectory of a single CdSe/ZnS nanocrystal continuously excited with E 0.6 kW cm⁻² of 488 nm laser light. The light grey line is used to discriminate between on and off events and represents the intensity-limit^[6]. The distribution of times involved in the blinking are distributed according to inverse power-laws of the type:

$$P(t_{\text{on/off}}) = At^{-m_{\text{on/off}}}, \quad (15)$$

where A is a constant and $m_{\text{on/off}}$ are the power-law exponents characterizing the statistics of each type of event. The exponent $-m$ lies in the range of $-3/2$. As a consequence the average on- and off-periods are dependent on the observance time t .

$$\langle t \rangle = \int_{t_{\text{min}}}^{\infty} t P(t) dt \quad (16)$$

9.1.4 Nonradiative processes in quantum dots

The explanation of the blinking event of a nanocrystal is complex. The prevalent model describing the blinking of nanocrystals assumes that a charged nanocrystal cannot emit.

As nanoparticles possess diameters of less than 10 nm, they exhibit a large surface-to-volume ratio. It can be therefore assumed that the surface properties of the crystals have a noticeable influence on the structural and optical attributes of semiconductor nanoparticles. Indeed, in fluorescence measurements of nanocrystals variations are observable depending on different inorganic and organic coatings in regard to quantum yield, spectra, and time depending behaviour. These observations can be associated with trap states, Cd vacant orbitals, on the

surface of the nanoparticles. They create additional energy levels outside of the energy band of the semiconductor, which possess energies located in the bandgap of the semiconductor.

The effect of fluorescence deletion, which is often referred to as quenching, constitutes processes, which diminish the fluorescence intensity of a nanocrystal, where the excitation energy is released by modes other than fluorescent radiation. The dominant radiationless processes of quantum dots are thermal ionization, phonon-supported tunnel processes of the charge carrier into trap states, and Auger effects (Auger-recombination, Auger-ionization). In semiconducting nanostructures with strong quantum confinement, Auger effects are enhanced due to stronger interactions between the charge carriers, while thermal ionisation is hindered with increasing distance between successive energy states. Due to the energy required to get a charge into a trap state thermal ionisation is kinetically disfavored. .

At high excitation energies on account of the high density of excited states a second exciton can be generated (figure 147). In the process of the collision of the two excitons Auger-recombination can occur, which has a higher rate compared to radiative recombination. In this event energy transfer occurs from the first recombining exciton to the second in a single scattering process, normally with the attendance of a phonon^[472].

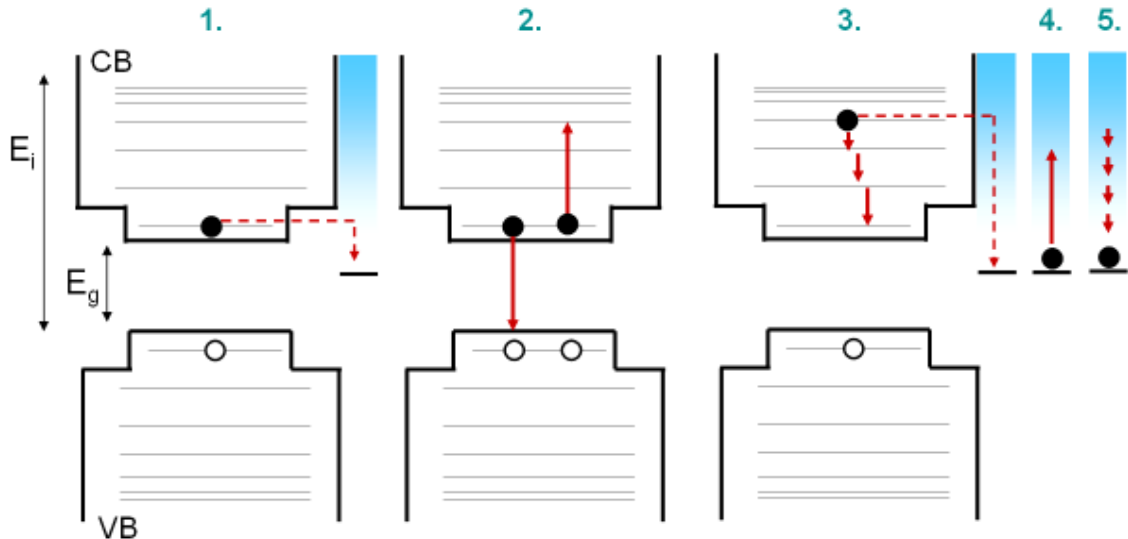


figure 147: non-radiative effects in core/shell-quantum dot with an energy band gap E_g and an ionisation energy E_i . **1.** The tunnel probability of the excited electron is in core/shell particle minimized. **2.** A created secondary exciton can transfer its energy while recombining on the first excited electron. **3.** The tunnel probability to a trap state increases. **4. & 5.** trapped electron can adsorb energy of other excitons and thereby increase the off-time.

The photon-supported tunnel feasibility of the accordingly twofold photoexcited electron in the potential curve of the trap states is increased. Also, concerning the smaller effective mass

compared to the delocalized hole, the electron is more likely to be found at the surface of the nanoparticles, where the traps are located. The trapping rate of such an electron lies in the range of picoseconds^[473], leaving a mobile and delocalized hole within the core.

In a facile and one dimensional model the rate constant k_{tunnel} of the tunnel-process exponential depends on the distance r and the energy barrier ΔE , according to the equation:

$$k_{\text{tunnel}} = k_0 \cdot e^{-\frac{2}{\hbar} \sqrt{2m_e r \Delta E}} \quad (17)$$

While the electron is trapped in the potential well it can absorb the energy of other recombining excitons, elongating the dark state. This quenching event can linger. After excitation the trapped electron can relax to the ground state of the trap potential by the release of vibrational energy. This is also valid for the remaining hole, which can assist the non-radiative recombination of further excitons. The nanocrystal remains dark until the trapped electron recombines or whenever the nanocrystal recovers a charge-neutral state. Recombination can occur after the trapped electron tunnels back into the nanocrystal energy structure. It is also possible that the hole is trapped in the surface region of a nanoparticle. The localisation leads to a quantization of the energy levels and reduces the spatial overlap between the two wave functions of the exciton and the charge carrier, derogating the energy transfer of the exciton to the charge carrier. The charges create a dipole at the surface of the quantum dot, which leads to an alteration of the local electric field. Although subsequently created excitons can recombine radiatively, a STARK-shift of the emission frequency to higher wave numbers is observable. This trap emission is rare compared to the first, very sensitive to the displacement and kind of ligand shell, and decreases with the growing epitaxial shell. Trap emission becomes more probable with decrease of the nanocrystal size, whereby the increase in the band gap is accompanied by a blue shift of the trap emission^[32].

Investigations of the simultaneous increase of the trap emission intensity and decrease in the photoluminescence intensity of CdSe nanocrystals with different ligand shells allude to the resistance of for trap emission accountable surface states to ligand exchange. Kalyuzhny *et al.*^[32] relate such states to trioctylphosphine selenide (TOP=Se), which have a high stability due to the TOP=Se double bond. Aging of CdSe nanocrystals entails the decrease in trap emission, possibly in regard to the oxidation of TOP.

The probability of the occurrence of Auger-process depends on the spatial overlap of the wave functions of the charge carriers and increases in the case of finite and defect barriers.

The statement of the ionisation by tunnel-processes leads to a temperature dependence of the off-periods. The model of the ionisation by tunnel-processes leads to a temperature dependence of the off-periods. With the assumption of a homogeneous spreading of the trap states and the potentiality of the charge to swap between traps the model describes on- and off-periods correctly. If the exchange between traps is faster than charge-neutralisation the model of Shimizu *et al.*^[474] is more appropriate, which applies for adequate overlaps of the wave functions of the charge carriers in the trap states. This depiction entails a correct description of the on-periods with the $P(t_{\text{on/off}}) = At^{-m_{\text{on/off}}}$ coherency. The exponent of the tunnel-probability is similar to the experimentally determined value:

$$p(t) \propto t^{-3/2} \quad (18)$$

According to the observed intermittent charging events on single nanocrystals^[475] the surrounding matrix has an influence on the nanoparticle optical properties. Isaac *et al.*^[476] have observed that an increase in the dielectric constant of the matrix surrounding the nanocrystals leads to a decrease in the value of m_{off} . The matrix in this case was postulated to solvate the ejected charge carrier and, consequently, stabilizes the charge-separated state, which prolongs the off-time events^[471].

The alteration of an argon atmosphere to an oxygen atmosphere decreases the on-periods of a nanoparticle, next to lowering the emission intensities, while leaving the off-periods unchanged^[477]. The creation of additional trap states by the formation of O₂-radicals and charged nanocrystals are cited as a likely reason for this observation.

Müller *et al.*^[478] have found that the presence of molecular oxygen and water increases the value of the off-time exponent for CdSe nanocrystals. The presence of a strongly polar medium such as water leads to a broadening of the O₂ LUMOs, thereby facilitating electron transfer (oxidation) from the nanocrystals to oxygen which leads to a neutralization of the charged, non-emissive particle.

A further factor is the presence of molecules with donor groups, which lengthen the on-periods by dative coordination with unsaturated bonds, which so far have functioned as traps. Similar results can be achieved by epitaxial growth of a nanoparticle-coating with a material, which exhibits a bigger band gap, forming a core-shell nanoparticle and thereby locating the hole in the core^[479].

The theory predicts that in fluorescence spectra discrete emission lines are observable. But the emission of photons of different wavelength according to the size distribution of the nanoparticles, which is reflected in the band gaps, leads to a peak broadening^[480, 481].

9.1.5 Type I/II structures

To diminish the amount of trapped electrons on the surface, nanoparticles are coated with a further semiconducting, inorganic material, which possess a similar crystal structure. Depending on the band gap of the shell material, two different types of structures can result (figure 148).

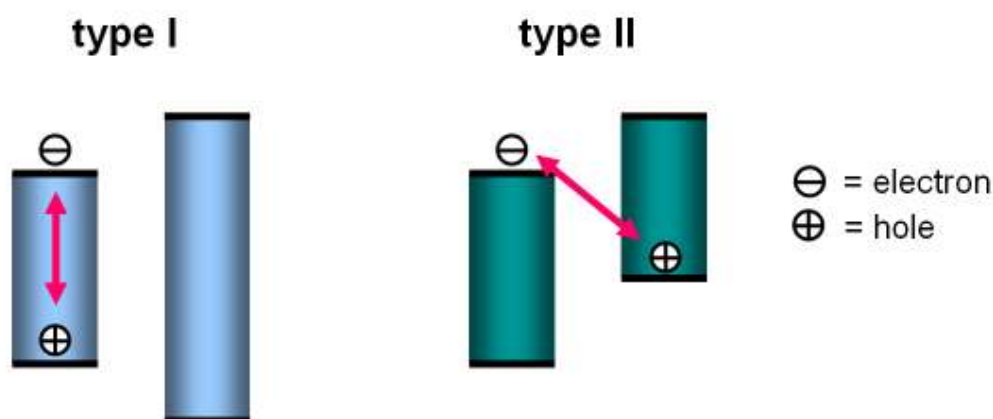


figure 148: illustration of type I and type II structures.

If the semiconducting shell-material has a larger band gap than the core material, the exciton is localized in the core. This type I structure shows higher quantum yields and higher photostability. An example for type I structures are CdSe/ZnS nanoparticles.

In type II structures both materials have approximately equal, but energetically shifted band gaps (figure 7). The positive charge of the exciton will be localized in the material with the highest highest occupied molecular orbital (HOMO) of both materials, while the electron will be localized at the lowest LUMO (lowest unoccupied molecular orbital) of both materials. In consequence the charges will be spatially separated. Accordingly longer life times of electron and hole occur. As a result of indirect transition of the charges in the process of recombination emission energies smaller than the band gap of core- and shell-material can be

observed. Examples of type II structures are CdTe/ZnS and InAs/ZnS nanoparticles, which have an emission in the near infrared (NIR).

Klimov *et al.*^[482] have discovered that wide gap semiconducting nanoparticles (ZnSe), overcoated with a shell of a semiconductor of a narrower gap (CdSe), belong to type-I (both electron and hole wave functions are distributed over the entire nanocrystal) or type-II (electron and hole are spatially separated between the shell and the core), depending on the radius of the core and shell thickness.

9.2 Core/shell- and multishell-nanocrystals with a CdSe-core

The CdSe nanoparticles synthesized in organic solvents feature a tri-n-octylphosphine/tri-n-octylphosphine oxide (TOP/TOPO) passivated shell, which kinetically stabilizes the thermodynamically unstable particles in solution by saturating free valence orbitals. TOPO coordinates through its P=O-group to cadmium atoms, while TOP forms a Se=P double bond to selenium atoms. The facets, curvature, and the inconsistency of the surface of CdSe nanoparticles result in differently coordinated Cd and Se atoms. This is expressed in different binding energies of the TOP/TOPO ligand shell to the nanoparticle surface. Two-fold coordinated Cd atoms are able to transfer more charge into a bond with the ligand^[483].

Katari *et al.*^[484] have estimated by means of X-ray photoelectron spectroscopy that for nanocrystals bigger than 1.5 nm a surface coverage of less than 30% can be achieved with bulky TOPO molecules. Molecules like octylamine show smaller steric requirements and can passivate more efficiently the surface.

The incomplete coverage and vacancies on the surface produces trap states for electrons on the surface. Unsaturated selenium atoms mainly create shallow hole-traps. Deep traps are expected for selenium atoms with two binding sites.

9.2.1 CdSe/CdS- and CdSe/CdS/ZnS-nanocrystals

For biological applications the cytotoxicity of CdSe nanoparticles through the release of Cd²⁺ ions^[337] and formation of free hydroxyl radicals^[398, 399], generated by holes by virtue of the

valence band edge of 1.6 eV^[400], is a handicap. Accordingly, multishell nanocrystals^[401-403] exhibiting higher quantum yields due to inorganic passivation of the nanocrystals surface, ensuring radiative electron and hole recombination^[7, 401], robustness against chemical degradation or photo-oxidation^[7] and the reduction of cytotoxicity^[69, 337, 338, 404-406] have begun to attract particular attention. Among the wide band gap semiconductors used as shell material, ZnS is the best. For the bulk material it has a band gap of 3.8 eV, offers chemical stability and non-toxicity. Two layers of ZnS on top of the CdSe core create a tunnel barrier of 4 eV and confine the wave function of the hole of an exciton inside of the nanoparticle. However, the large mismatch (ca. 12%) between CdSe and ZnS lattice parameters induces an interfacial strain between the core and the shell, which leads to formation of misfit dislocations relaxing the nanoparticle structure^[401, 485, 486] (figure 149). Furthermore, ZnS shells grow preferentially at certain anion rich faces of CdSe nanoparticles, resulting in case of the first few atomic layers of ZnS in an incomplete coverage of the core^[486].

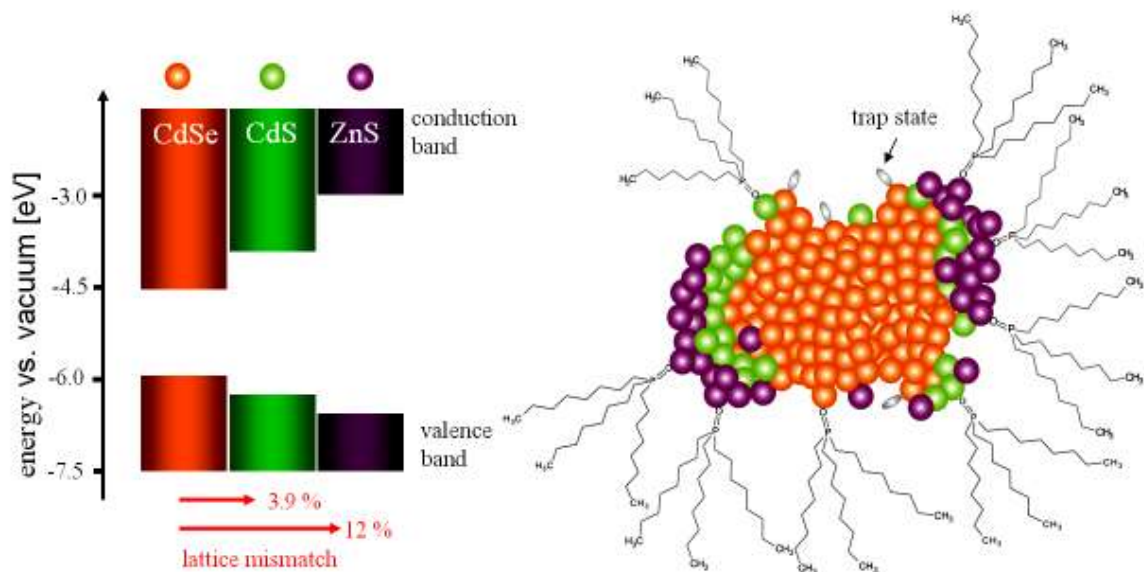


figure 149: energetic position of the band gaps and an illustration of their lattice mismatch.

The integration of CdS as the first shell around the CdSe core mitigates the lattice mismatch between CdSe and ZnS. Notwithstanding that such CdSe/CdS/ZnS^[403] nanoparticles possess a qualitative inorganic passivation layer, their shells are not grown epitaxially due to the residual mismatch of the different crystal lattices. According to this the shells are still inhomogeneous, offering openings and edges, consequently creating traps and irregular tunnel barriers.

9.3 Magnetic nanoparticles (SPIONs)

Next to quantum dots exist nanoparticles with unique magnetic properties, so called superparamagnetic iron oxide nanoparticles (SPIONs). To understand their properties in the following the physical background of magnetism will be explained.

The magnetic moment of a free atom is predicated on^[487]:

1. Each electron exhibits an intrinsic angular moment, the spin s , to which a magnetic moment is assigned.
2. A further magnetic moment is related to the orbital angular momentum l , which arises from the movement of the electron around the atomic nucleus.
3. The variation of the orbital angular momentum, induced by a magnetic field, is the third contribution.

The third effect, consisting with Lenz's law, opposes the field and provides a diamagnetic contribution. In contrast the first two effects yield paramagnetic contributions. Since the moments of the atomic nucleus are by order of magnitudes smaller than the moment of the electron, they can be neglected^[487].

9.3.1 Dia- and paramagnetism

Which of the three above mentioned effects dominates the magnetism of a substance depends on the electron-configuration.

All materials, in which atoms, ions, or molecules possess filled shells, are diamagnetic. They have no magnetic moment, because the single moments of the electrons cancel each other. When circuit currents are generated in the material by an external magnetic field, which in turn induce magnetic moments, they are according to Lenz's law opposite to the external field, resulting in a weakening of the flux lines within the solid state body.

The magnetic susceptibility χ is a dimensionless parameter, which represents a measure for the magnetisation of a material. In the centimetre-gram-second system (cgs system) it is defined as:

$$\chi = \frac{\bar{M}}{\bar{H}} \quad , \quad (19)$$

where \bar{M} constitutes the magnetisation and \bar{H} the magnetic field. These two terms are associated with the magnetic induction \bar{B} as follows:

$$\bar{B} = \bar{H} + 4 \pi \bar{M} \quad (20)$$

Diamagnetic substances hold a susceptibility of $-1 \leq \chi_{\text{dia}} < 0$, but the usual order of magnitude is located in the range of -10^{-5} to -10^{-6} [488]. In case of an ideal diamagnet the magnetic field is been entirely displaced from the inside ($\bar{M} = -\bar{H}$), whereby the diamagnetic susceptibility reaches its maximum value of -1. This effect appears in superconductors and is known as Meissner-effect.

Every substance owns a diamagnetic susceptibility, which however is often overlapped by a para- or ferromagnetic susceptibility.

Paramagnetic substrates possess atoms, ions, or molecules with unpaired electrons, which produce a permanent magnetic moment. Without an external field the magnetic moments due to the thermal energy are statistically distributed, whereby the total moment is zero (figure 150, 1.). Upon applying an external magnetic field, the magnetic moments align parallel to the field direction (figure 150, 2.). This leads to an amplification of the magnetic flux lines in the inside of the paramagnetic substance.

For the paramagnetic susceptibility $\chi_{\text{para}} > 0$, and is typically located in the range of 10^{-3} and 10^{-5} [488].

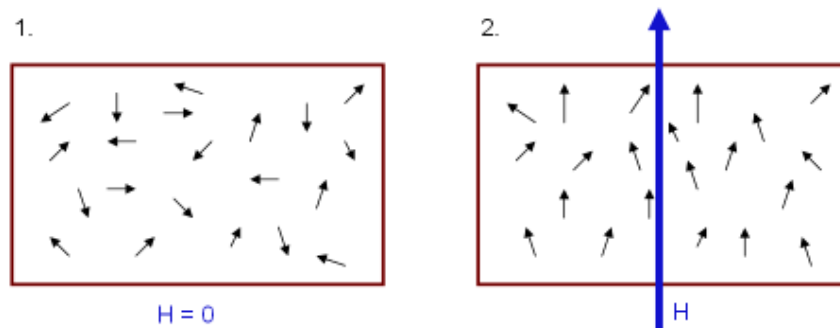


figure 150: paramagnetism: **1.** magnetic moments without an external magnetic field. **2.** adjustment of magnetic moments at a magnetic field.

9.3.2 Ferromagnetism

In contrast to dia- and paramagnetism there are cooperative magnetisms, which depend on the interaction of the magnetic moments of many atoms. Examples include ferromagnetism, ferrimagnetism and antiferromagnetism, which are discussed in the following.

Ferromagnetic behaviour occurs below a critical temperature T_C , which is named Curie-temperature. Here emerges even without an external magnetic field a spontaneous magnetisation, in which the magnetic moments in an internal field, the molecular field, arrange themselves parallel. Above the Curie-temperature the spin order is disrupted by thermal motion and the material behaves paramagnetic.

The ferromagnetic susceptibility is described by the Curie-Weiss-law:

$$\chi = \frac{C}{T - T_C} \quad , \quad (21)$$

wherein C is the Curie-constant.

The interaction of the atoms is quantum mechanically described by the exchange interaction. Considering two electrons, they can be either in the parallel or in the anti-parallel configuration. According to the Pauli principle the electrons must vary at least in one quantum number. Hence the anti-parallel orientation is favoured. So the parallel and anti-parallel spin-configurations have different exchange energies E_{ex} :

$$E_{ex} = -2 J_{ex} \vec{S}_i \vec{S}_j \quad . \quad (22)$$

Here is J_{ex} the exchange integral, \vec{S}_i and \vec{S}_j the adjacent spins.

When the exchange integral is positive, parallel spins have the lowest energetic configuration and ferromagnetism results. Conversely, the anti-parallel orientation is favored in case of a negative exchange integral, wherefore a antiferro- or ferrimagnet is been generated^[488, 489].

To the few elements, which feature a positive exchange integral and are thereby ferromagnetic, belong iron, cobalt, and nickel. The origin of their ferromagnetism can be explained using the energy-band model. Whilst the electrons of atoms have discrete energy states, those in macroscopic solid state bodies are combined into bands with continuous energy levels. In case of 3d-transition metals the 4s-band and the 3d-band overlap because of the intense broadening. In opposition to this are the energy bands, which are located closer to the nucleus, not broadened, and thereby do not overlap. figure 151 shows the overlap of the

3d- and 4s-bands for some transition metals, wherein the density of states of the 3d-band is outlined on the left side and on the right side of the 4s-band.

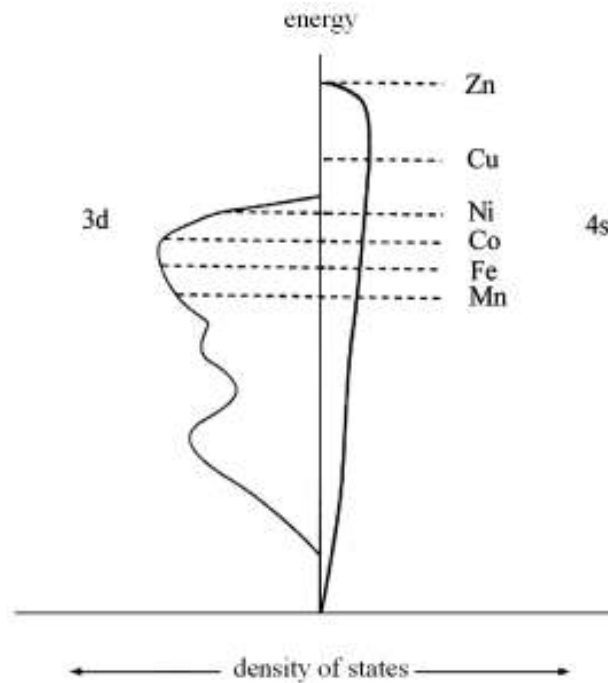


figure 151: schematically depiction of the 3d- and 4s-energy bands of 3d-transition metals^[489].

The density of states specifies the number of energy levels per energy unit. This number varies within a band since the energies of some levels are more closely spaced than others. Since the density of states is very difficult to determine, in the model (figure 151) it has been supposed, that it is the same for all elements. The 3d-band can be filled with maximum of ten electrons and the 4s-band with maximum of two electrons per atom. Depending on the electron configuration of the 3d-band, the bands are differently occupied. The highest occupied energy level at $T = 0$ K is called Fermi-level and is plotted in figure 151 for the elements manganese to zinc. Considering that parallel and anti-parallel spins have different exchange interactions, a splitting of the bands can occur. Table 1 shows the magnetic moments for manganese to nickel ($\mu_B =$ Bohr magneton).

element	Mn	Fe	Co	Ni
(3d+4s)-electrons	7	8	9	10
μ_B per atom	0	2.22	1.72	0.6

table 16: experimental determined values of the magnetic moments of manganese to nickel^[489].

The theoretical value of μ_B per manganese atom is 3.6, although manganese is not a ferromagnet. The reason might be that the exchange interaction of manganese is not strong enough to sustain the great unbalance between the $3d\uparrow$ - (theoretically with five electrons per atom completely filled) and $3d\downarrow$ -band (theoretically with 1.4 electrons per atom $\sim 30\%$ filled). Copper has fully occupied 3d-subbands, so the Fermi-level is located above the 3d-band. Hence the 4s-band experiences no splitting by the exchange interaction, no imbalance of the spins is created, and copper is not ferromagnetic.

9.3.2.1 Domain-formation

The total energy of a ferromagnet consists of the magnetostatic energy, the crystalline anisotropy energy, the exchange energy, and the energy for formation of a domain border. To minimize the total energy of a ferromagnetic material domains are formed, which are specified as Weiss domains. Inside of a domain the spins arrange themselves parallel, but the domains are not aligned parallel to each other.

The main reason for the formation of domains is the magnetostatic energy. A ferromagnetic mono-crystal exhibits just one domain of macroscopic dimension, so its external field will weaken the magnetisation (figure 152 a). In this case the magnetostatic energy is very big. Through formation of domains, the external field can be reduced (figure 152 b) or even absolutely deleted (figure 152 c). This effect is offset by the exchange energy, which increases as more anti-parallel domains are generated^[490].

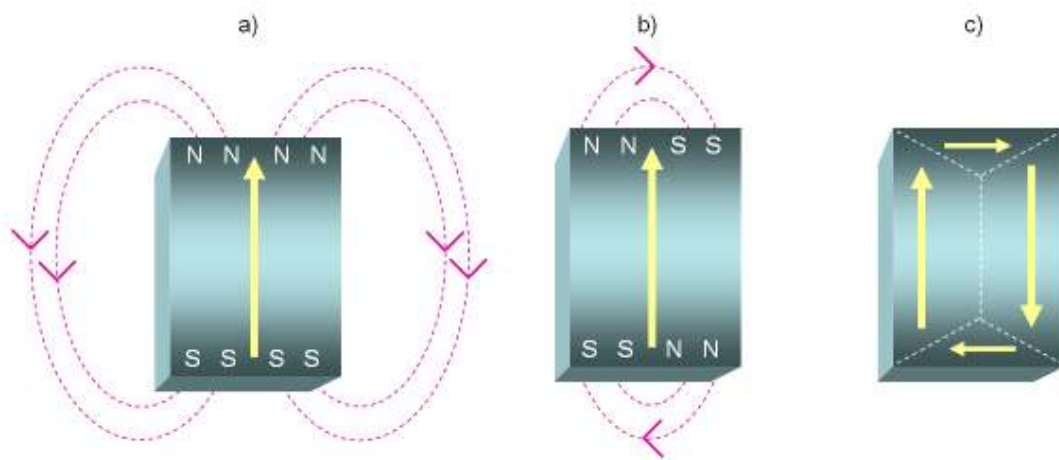


figure 152: minimization of the magnetostatic energy by domain formation^[491].

In order that the exchange energy between anti-parallel spins of contiguous domains does not get too high, domain walls are created. Inside of the so called Bloch wall the magnetisation turns by 180° perpendicular to the linkage axis of the domains as the spins adopt all orientations between the parallel and anti-parallel alignment (figure 153). Via rotation of the spins the Bloch walls can slide, whereby one domain increases at the expense of another domain. In this way the direction of the magnetisation changes. The thicker the domain wall is, the lower is the exchange energy. On the other hand, the anisotropy energy increases as the domain wall gets broader because most spins in the wall are not aligned in the direction of the easy axis. Thence the thickness of the domain wall depends how the total energy is minimized by the several energy contributions. It lies in the size range of $0.1 - 1 \mu\text{m}$ ^[492].

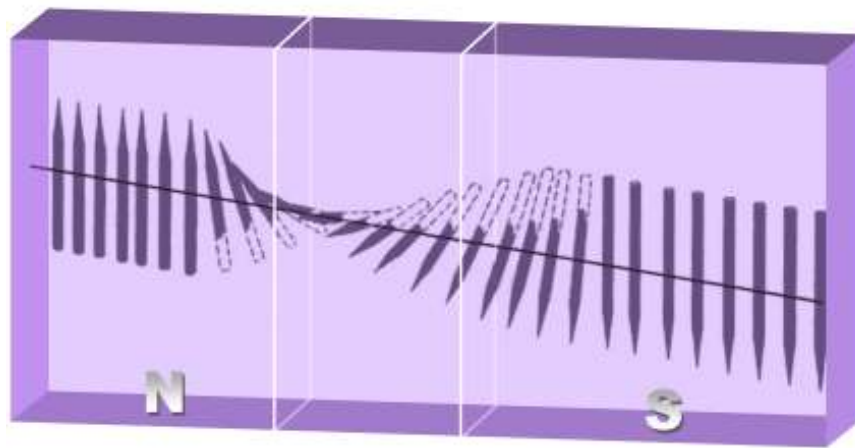


figure 153: Bloch wall^[488].

A magnetic anisotropy appears when the magnetisation in a certain direction is predominant. In case of the magnetocrystalline anisotropy the preferential direction of the magnetisation evolves with the crystal structure. The preferential direction is constituted as easy axis. The easy axis of nickel is consistent with the $[111]$ -axis^[493]. As shown in figure 154 the saturation magnetisation is reached at small fields faster in case of the easy than for the hard axis. The energy difference between the magnetisation of these two axes is called magnetocrystalline anisotropy energy.

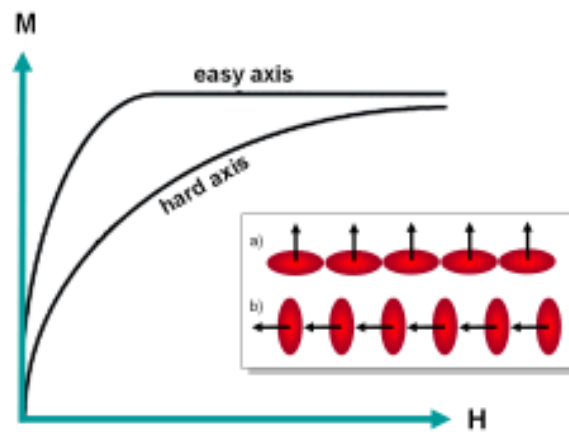


figure 154: Schematic showing the difference in size of field required to achieve the same magnetisation along easy and hard axes^[491]. Orbital overlapping of easy (a) and (b) hard axis^[491].

The magnetocrystalline anisotropy results from the spin-orbit interaction, whereby the atomic orbitals lose their spherical-symmetrical form. By this asymmetry the orbital overlapping for the easy and hard axis differ, with the overlap being larger for the easy axis.

Another magnetic anisotropy is the shape anisotropy. It arises in particles, which are not spherical. In case of an ellipsoidal shape the magnetisation lies preferentially on the longitudinal axis.

9.3.2.2 Magnetisation of a ferromagnet

The resulting magnetic moment is small due to the statistical distribution of the domains. In order for a ferromagnetic substance to reach its saturation magnetisation, a homogeneous magnetic field must be applied.

The magnetisation \vec{M} of a ferromagnet depends nonlinearly on the field intensity \vec{H} ; instead, a hysteresis loop is observed (figure 155). By applying a magnetic field, the magnetic moments orient parallel to the field direction (initial magnetisation curve). At lower field intensities the orientation results from wall-shifts, whereby those domains expand that contain spins parallel to the magnetic field. In this range a phenomenon called Barkhausen effect is observable. Hereby the magnetisation changes not continuously, but in small jumps.

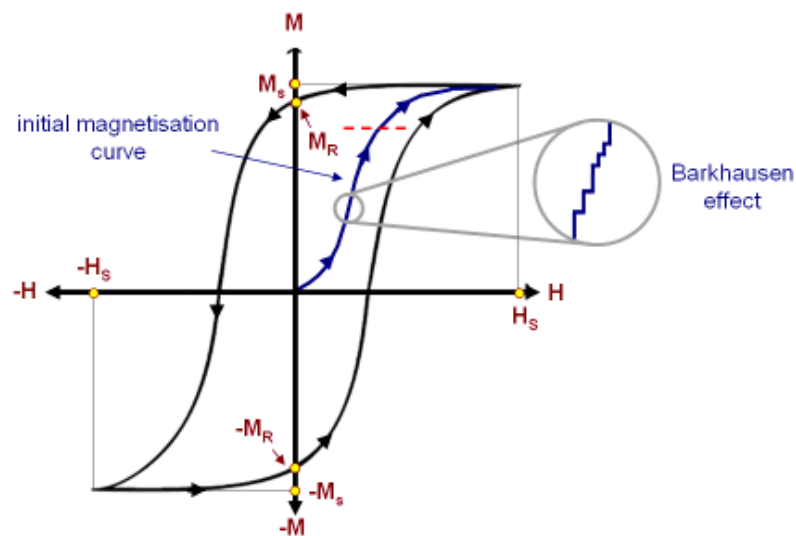


figure 155: Illustration of a hysteresis loop with initial magnetisation curve^[488].

At higher field intensities (above the red dashed line in figure 155) almost all of the magnetic domains are aligned and an additional increase in the magnetizing force will produce very little increase in magnetic flux. The magnetisation increases until the saturation magnetisation M_S is reached. When the field intensity is reduced to zero, a residual magnetisation M_R (remanence) remains. To bring the magnetisation again to zero a coercive field strength $-H_C$ is necessary. Based on coercivity, materials are distinguished between magnetically soft or hard. Magnetically soft materials can already be demagnetised in a small magnetic field and have accordingly a small coercivity ($H_C < 10$ Oe). On the contrary magnetically hard materials have a high coercivity ($H_C < 100$ Oe).

9.3.3 Antiferromagnetism and ferrimagnetism

In contrast to ferromagnetism, the spins in the cases of antiferromagnetism and ferrimagnetism arrange themselves anti-parallel within a domain. The sub-lattices of a ferrimagnet possess different magnitudes, while in antiferromagnets they are of the same size, thus exactly annihilating one another (figure 156).

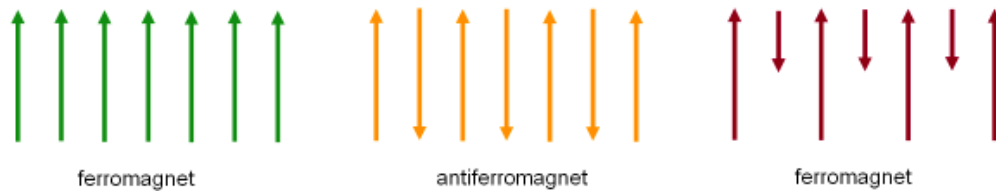


figure 156: cooperative magnetisms: ferro-, ferri-, and antiferromagnetism.

In the case of antiferromagnetism a coupling of anti-parallel spins proceeds as long as the temperature is below the Néel-temperature. A complete alignment of the spins exists at the absolute zero point and the substance is diamagnetic. Above the Néel-temperature the spin-order collapses and the substance shows paramagnetic behavior. It follows in from the spin-order antiferromagnets that in an external field no magnetic polarisation and no macroscopic magnetisation takes place.

Like antiferromagnetism the exchange integral in case of ferrimagnetism has a negative prefix. As the magnetic moments of the sub-lattices do not annihilate each other, a magnetisation exists, which is smaller than the magnetisation of a ferromagnet. The behaviour of a ferrimagnet in a magnetic field is in accordance with that of a ferromagnet. Above the Curie-temperature the spontaneous magnetisation is destroyed by thermal agitation and the material shows paramagnetic behavior.

9.4 Magnetism of nanoparticles

As explained in chapter 9.3.2, ferromagnetic substances are sectioned into domains in which the magnetic moments exhibit the same orientation. These domains are separated in by domain-walls, which hold a characteristic thickness and energy.

When particle size decreases, the existence of domain-walls becomes energetically disfavoured, so that at a critical particle size d_C just one domain per particle exists. Due to the single domain the particle has a high magnetostatic energy but no domain-border-energy. figure 157 illustrates the dependence of the energy from the particle size. Whilst the magnetostatic energy is proportional to d^3 the domain-border-energy is proportional to d^2 . Thus, below the critical particle size d_C , the total energy is minimized by formation of a single domain. Above d_C the formation of multi-domains is energetically favoured.

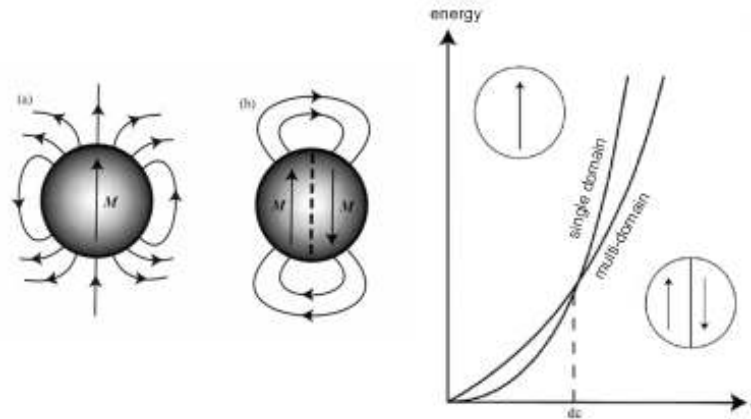


figure 157: formation of single- or multi-domains subject to the energy^[491].

The coercivity H_C also depends strongly on the particle size. As seen in figure 158 the coercivity has its highest value at the particle size d_c . This size represents the transition from particles with multi-domains to particles with a single domain. If the particles are large enough to contain multi-domains, changes in magnetisation occur via movement of the domain-walls. For this reason the coercivity is relatively low. In contrast, the direction of the magnetisation of a particle with a single domain can only change by rotation of the spin. Accordingly, the coercivity of such particles is considerably higher^[489, 493].

For very small particles the coercivity is zero, since in this case the magnetisation shows no definite direction, but rotates due to the thermal fluctuation. Such particles are called superparamagnetic particles.

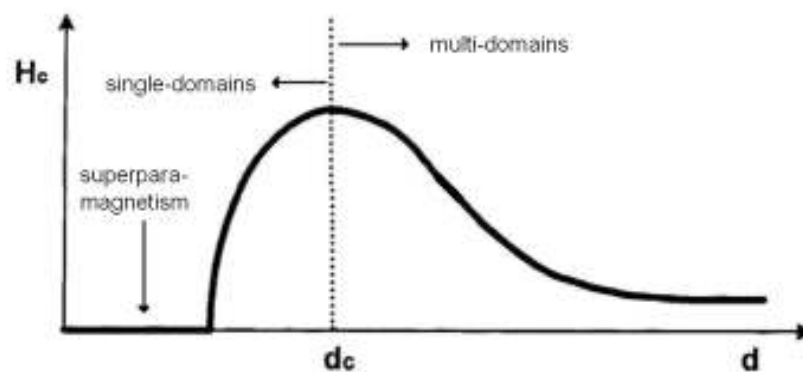


figure 158: dependence of coercivity on particle size^[494].

The reason for the rotation of the magnetisation is the anisotropic energy, which decreases with reducing particle size. Its been stated approximately as^[494, 495]:

$$E = KV \sin^2\theta \quad (23)$$

In this equation E is the anisotropic energy, K the anisotropic constant, V the particle volume, and θ the angle between magnetisation and the easy axis. By decreasing the volume V KV can be tuned in the size range of the thermal energy $k_B T$ ($k_B =$ Boltzmann-constant). This energy is then sufficient for a change of direction of the magnetisation, which fluctuates consequently.

When the magnetisation lie in the direction of the easy axis (at 0 and π , figure 159), the anisotropic energy reaches its minimal value. In contrast the maximum of the anisotropic energy occurs when the magnetisation is oriented perpendicular to the easy axis.

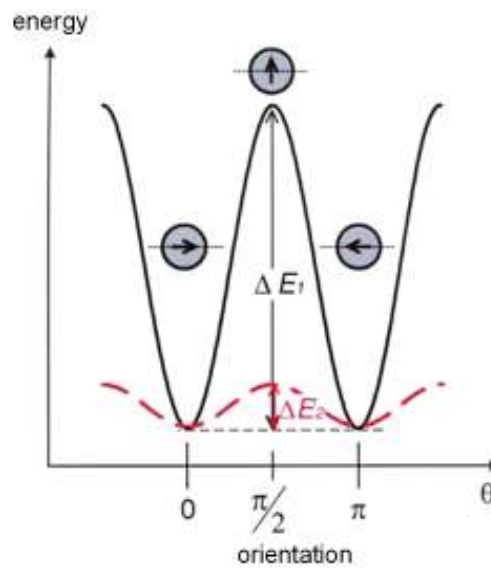


figure 159: energy in dependence of the orientation of the magnetisation^[496].

Hence, thermal fluctuation prevents a stable magnetisation in case of superparamagnetic particles, although fluctuation of the magnetisation can be stopped by intensive cooling. The temperature at which a change over appears from superparamagnetic to ferromagnetic is called blockade-temperature T_B . It depends on the particle volume V and the anisotropic constant K . Approximately it is given as^[497]:

$$T_B = \frac{KV}{25k_B} \quad (24)$$

In the superparamagnetic state the particles behave like paramagnets. Their magnetic moments are rotatable and undirected, but significantly bigger than those of a paramagnet^[495], since it involves the magnetic moment of the whole particle.

When single-domain particles are brought into a magnetic field, the magnetisation is unaffected by domain-barriers. The applied field produces a potential energy $E_{\text{pot}} = -M_S \cdot H$ emerges.

Without a magnetic field the magnetisation is located on the easy axis. By applying a magnetic field perpendicular to the easy axis (with $T < T_B$), the magnetisation rotates in the direction of the applied field until, at the field strength $H = 2 K_V/M_S$, it is parallel to the field direction and thus perpendicular to the easy axis (figure 160 a). In this case the coactivity is zero, so there is no hysteresis (figure 160 c).

By applying a magnetic field that is parallel to the easy axis and anti-parallel to the magnetisation is, the magnetisation is rotated through the hard axis to the easy axis. The inversion of the magnetisation is hindered by an energy barrier in case of a weak magnetic field. However, with increasing field strength the energy barrier decreases, and at $H = 2 K_V/M_S$ the magnetisation can align in the anti-parallel orientation (figure 160 b). At this juncture a high coercivity and a hysteresis is produced (figure 160 d).

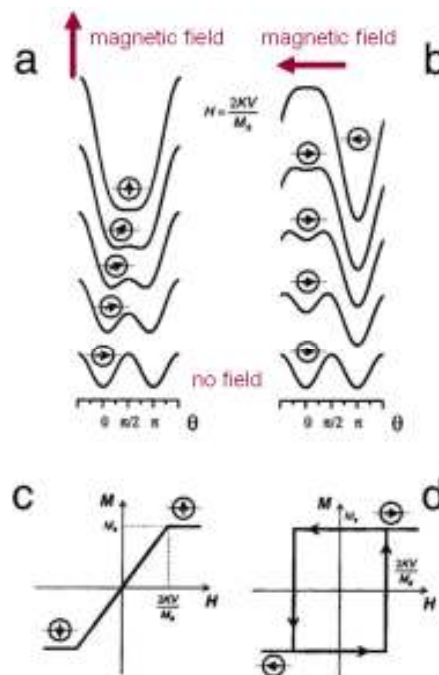


figure 160: dependence of the potential energy from the orientation of the magnetisation in attendance of a magnetic field^[494].

Between those two extreme cases there are further orientations of the magnetic field, which produce a hysteresis loop, and which are intermediate between the named possibilities.

9.4.1 Magnetic resonance imaging

The principle of magnetic resonance imaging (MRI) corresponds to NMR. In an external static magnetic field, B_0 , proton-spins (in general nuclei with an unequal number of protons and neutrons, which exhibit thereby a nonzero angular momentum and magnetization) can populate two possible spin states of different energy. Due to their alignment parallel or antiparallel to the magnetic field. During their alignment, the spins precess under the Larmor frequency, ω_0 (figure 161 a). The rate of this rotation is given by the Larmor equation: $\omega_0 = \gamma B_0$, where ω_0 is called the Larmor frequency and γ is a nuclear constant called the gyromagnetic ratio.

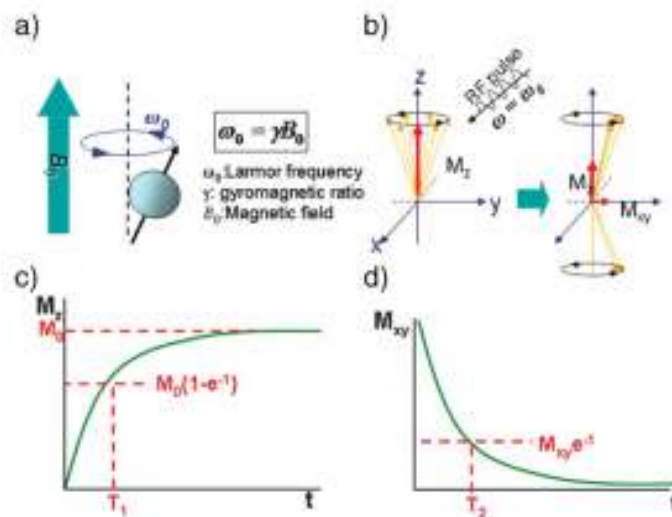


figure 161: Principle of magnetic resonance imaging. a) Spins align parallel or antiparallel to the magnetic field and precess under Larmor frequency (ω_0). b) After induction of RF pulse, magnetization of spins changes. Excited spins take relaxation process of c) T1 relaxation and d) T2 relaxation.

The observed net magnetization vector, M , has two components: longitudinal and transverse magnetization. From a small excess of protons in the lower energy state results a longitudinal magnetization (M_z), which gives a net polarization ($M = M_z + M_{xy}$) parallel to the external field (figure 161 b).

Application of an radio-frequency (RF) pulse (90° pulse), a pulse with energy at the Larmor frequency of the particular nucleus, leads to flipping of the individual magnetic moments from their lower energy spin state (parallel state) to their higher energy spin state (antiparallel state). On that account M_z decreases by the induced net polarization perpendicular to the static, external field in the transverse plane (M_{xy}). The transverse magnetization is due to

coherences forming between the two proton energy states following an RF pulse. Thereon the net magnetization vector, M , rotates with the Larmor frequency (figure 162).

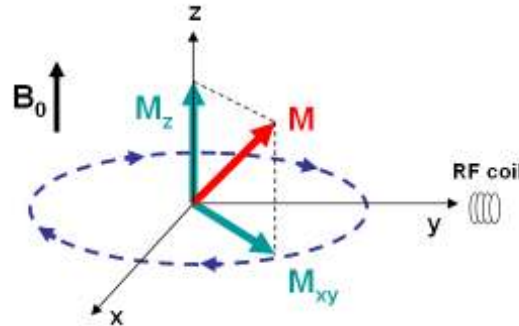


figure 162: The magnetization, M , precesses about the z-axis with the tip angle α , and it is divided into the longitudinal component, M_z and transverse component, M_{xy} . A RF coil is placed in the y-axis direction to collect the MR signal.

The recovery of the decreased longitudinal magnetization (M_z) due to energy transfer is called longitudinal or T_1 relaxation and occurs exponentially with a time constant T_1 (figure 161 c). The loss of phase coherence in the transverse plane (M_{xy}) due to dephasing of the spins is called transverse or T_2 relaxation (figure 161 d).

In the process of relaxation of the magnetization vector the transverse vector component produces an oscillating magnetic field which induces a small current in the receiver coil. This signal is called the free induction decay (FID), whose time constant is approximately consistent with T_2 .

Since there are small differences in the static magnetic field at different spatial locations ("inhomogeneities") the Larmor frequency varies across the body, thus creating destructive interference which shortens the FID ($T_2 \rightarrow T_2^*$). The total relaxation T_2^* is described by:

$$\frac{1}{T_2^*} = \frac{1}{T_2} + \gamma B_s \quad , \quad (25)$$

Where γB_s represents the relaxation by the field inhomogeneities and is called susceptibility effect. Also, when the radio frequency pulse is turned off, the longitudinal magnetization starts to recover exponentially with a time constant T_1 .

The signal intensity in MRI depends on the relaxation rates of the proton spins and can be increased by application of contrast agents. These contain (super)paramagnetic metal ions and can increase the relaxation rates and thereby the relaxivity depending on the concentration.

The relaxivity $r_i = r_i^{IS} + r_i^{OS}$ consists of an inter- (IS) and outer-sphere (OS) part. The smaller the nanoparticle is the smaller will be the interaction with farther proton spins. Thus r_i^{OS} becomes less important and interaction with proton spins of closer water molecules (r_i^{IS}) predominates. Such T_1 -contrast agents have to be in close contact with water, because the energy of the dipole-dipole interaction relies on $E_{dd} \sim 1/r^6$.

Superparamagnetic nanoparticles (SPIONs) create magnetic-field gradients which cause a dephasing of the magnetic moments and an acceleration of the spin-spin relaxation (T_2 shortening). The dipolar outer-sphere interaction between the water proton spins and the magnetic moment of the nanoparticles is the major relaxation mechanism in this process. Therefore spin-spin relaxation is dependent on the magnetic moment of the nanoparticles (μ)^[498, 499], which increases with nanoparticle size. Quantitatively, this dependence is given as:

$$R_2 = \frac{1}{T_2} = \frac{a}{d_{NP}D} \gamma^2 \mu^2 c_{NP} J(\omega, \tau_D) \quad , \quad (26)$$

where R_2 is the relaxation rate, a is a constant, d_{NP} the diameter of the nanoparticle, D the diffusion coefficient, μ the magnetic moment of the nanoparticles, γ the gyromagnetic ration of the water proton, c_{NP} the concentration of the nanoparticles, and $J(\omega, \tau_D)$ the spectral density function.

The equation (26) highlights the strong dependence of the magnetic properties of nanoparticles on their size, shape, and surface property. A dramatic increase in surface area increases preponderant surface-canting effects, and consequently increases the magnetization, as described by the following equation^[500, 501]:

$$m_s = M_s \left[\frac{r-d}{r} \right]^3 \quad , \quad (27)$$

where m_s is the saturation magnetization of the nanoparticle, M_s the saturation magnetization of the bulk material, r the size of the nanoparticle, and d the thickness of the disordered surface layer.

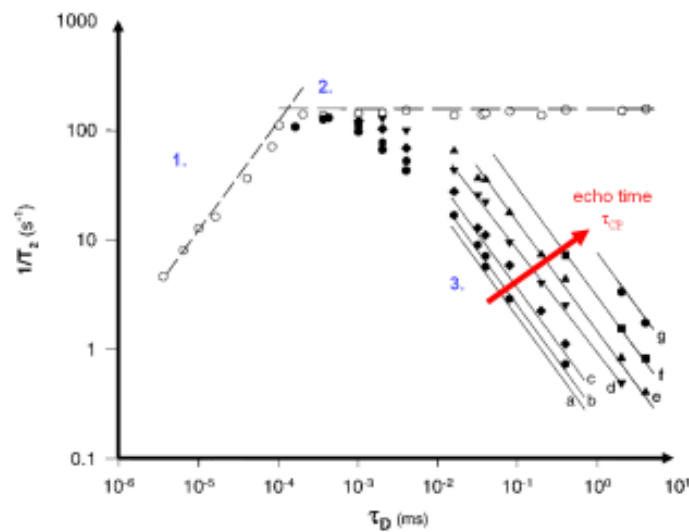


figure 163: depends of relaxation rate on the diffusion time^[386].

The open symbols represent $1/T_2^*$ values, while the filled symbols represent rates obtained, respectively, with $\tau_{CP} = 0.1$ ms (●, and line a), 0.2 ms (●, and line b), 0.5 ms (◆, and line c), 2 ms (▼, and line d), 5 ms (▲, and line e), 10 ms (■, and line f), 20 ms (●, and line g)^[386].

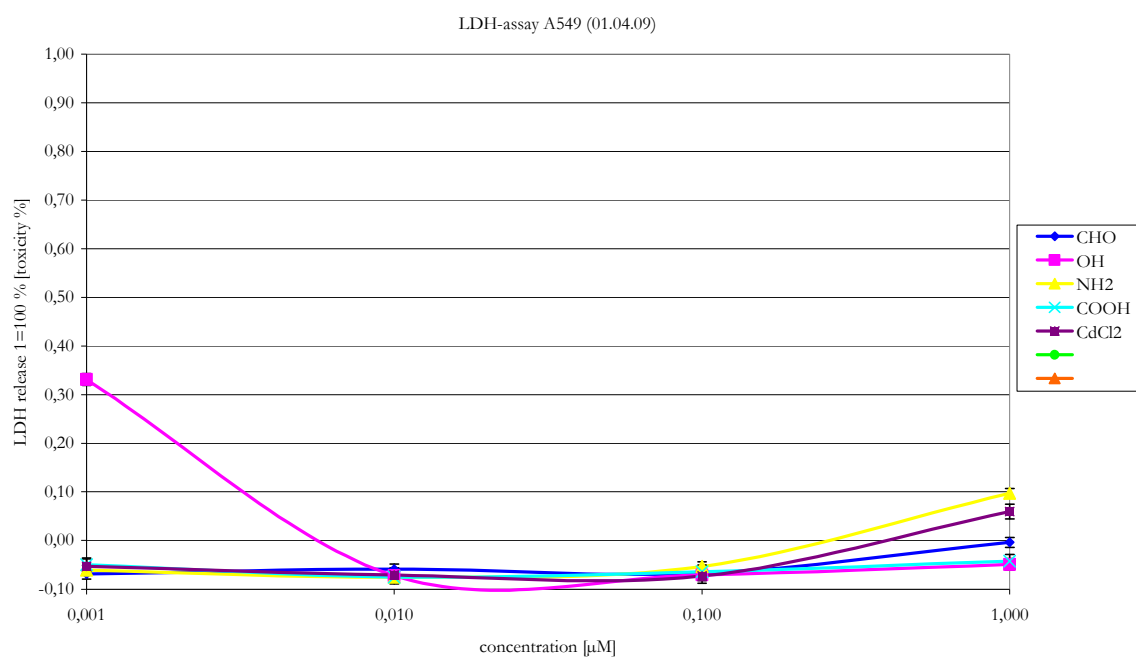
However the spin-spin relaxation rate $R_2 (= 1/T_2)$ does not increase linear and echo time (time between 90° and 180° pulse, τ_{CP}) independent with the diffusion time (τ_D), and thus particle size. Due to dependence of the relaxation rate on particle magnetization and diffusion times ($\tau_D = r^2/D$, where r is the particle radius and D the water diffusion coefficient) a maximum is been reached at a certain size or clustering rate. The simulated rate dependence on the diffusion time for a diffusion coefficient $D = 2.5 \cdot 10^{-5} \text{ cm}^2/\text{s}$ and particle radii ranging from 10^{-3} to $10 \mu\text{m}$ is shown in figure 163^[386]. Seven values of echo-time, ranging from 0.1 ms to 20 ms, are presented. At $\tau_D > 10^{-4}$ ms is a decrease and echo time dependence observable.

Partial refocusing model for strongly magnetized spherical particles^[386] ascribes such observation on a spatial division between an inner region and an outer region. The protons sufficiently close to the particles (inner region) experience gradients so strong that they will be rapidly dephased and are therefore too strong for the refocusing pulses to be efficient. Upon a boundary depending on echo time, magnetization, and volume fraction (outer region) they are efficient.

9.5 Cytotoxicity

The results were obtained with PI-*b*-PEO coated nanoparticles, which were not dialysed. Educts and sideproducts from the nanoparticle syntheses, THF and unbound ligand could have had an influence on the toxicity.

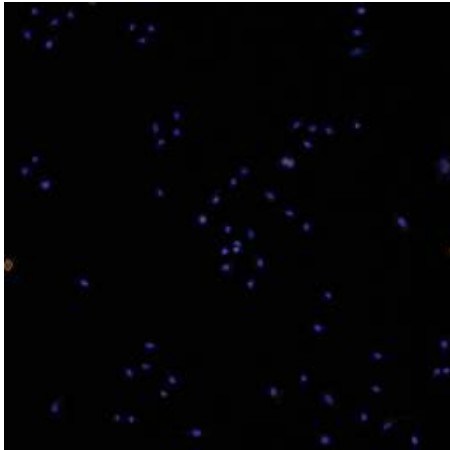
9.5.1 LDH-assay



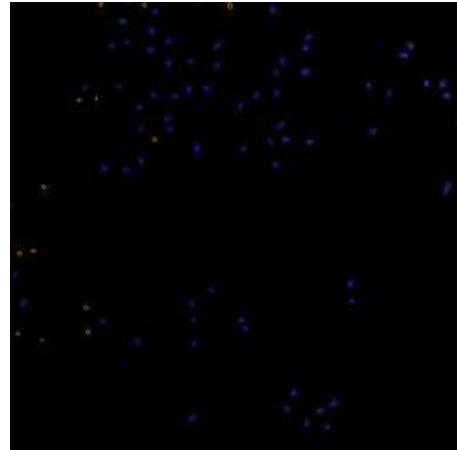
9.5.4 Cellomics pictures (CAN)

9.5.4.1 DEM controls

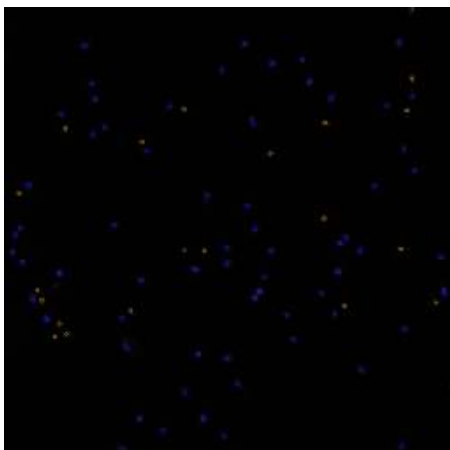
ROS -0137, afterwards stained with Hoechst; 10x objective



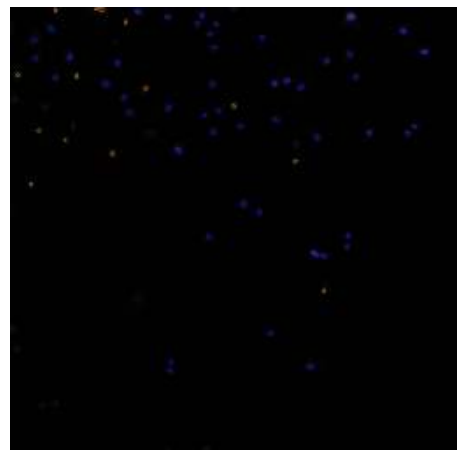
DEM 10 mM Well B3



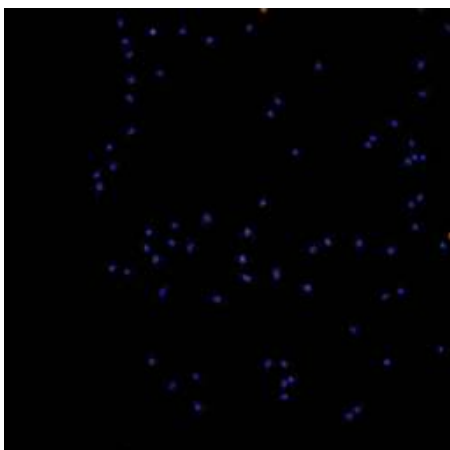
DEM 5 mM Well B4



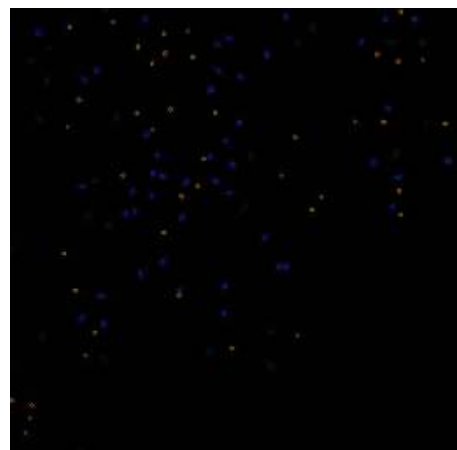
DEM 10 mM Well C3



DEM 5 mM Well C4



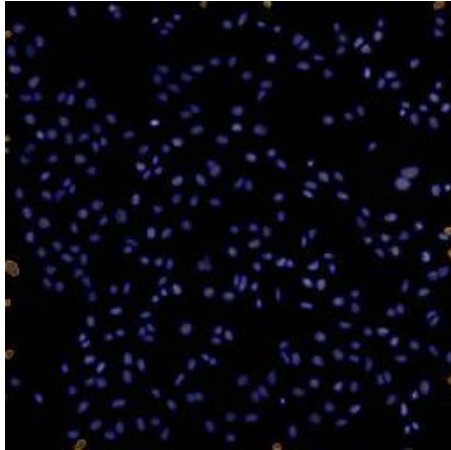
DEM 10 mM Well D3



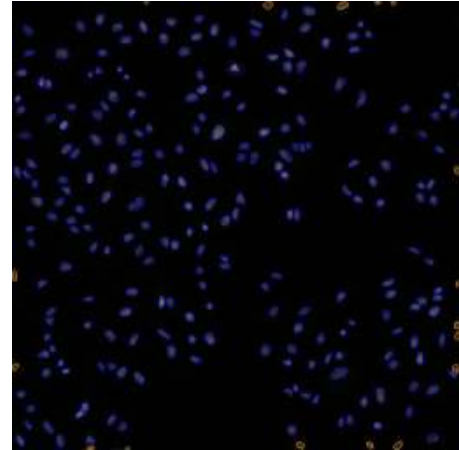
DEM 5 mM Well D4

9.5.4.2 FeCl_3 controls

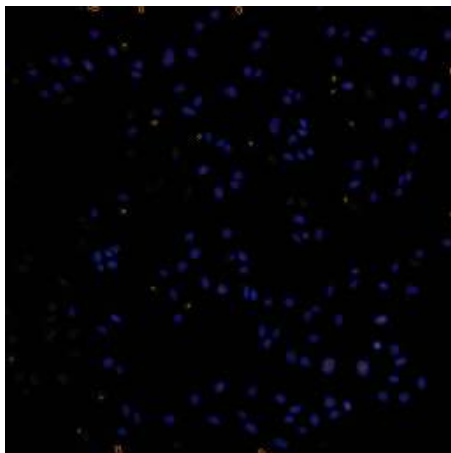
ROS -0137, afterwards stained with Hoechst; 10x objective



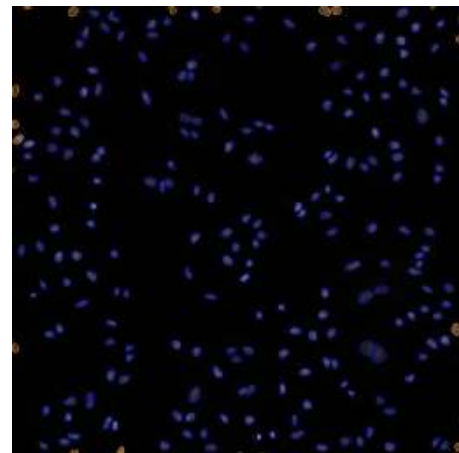
FeCl_3 0.3 mg/ml Well B5



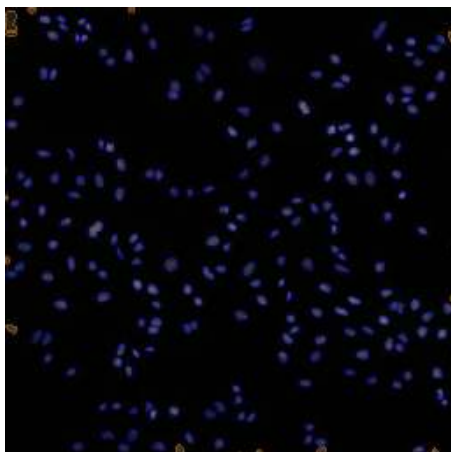
FeCl_3 0.03 mg/mL Well B6



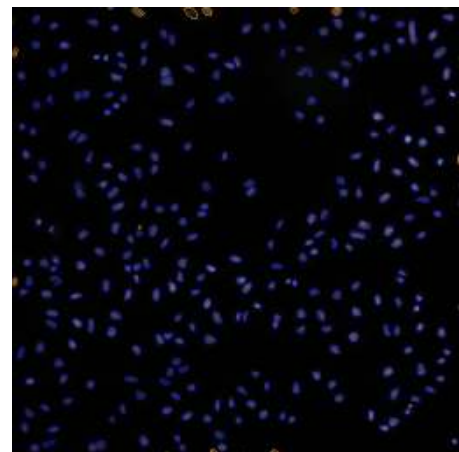
FeCl_3 0.3 mg/mL Well C5



FeCl_3 0.03 mg/mL Well C6

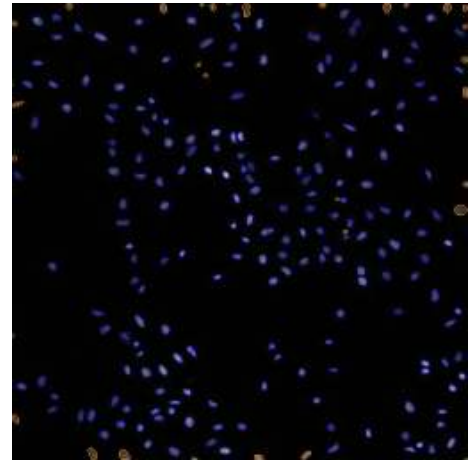
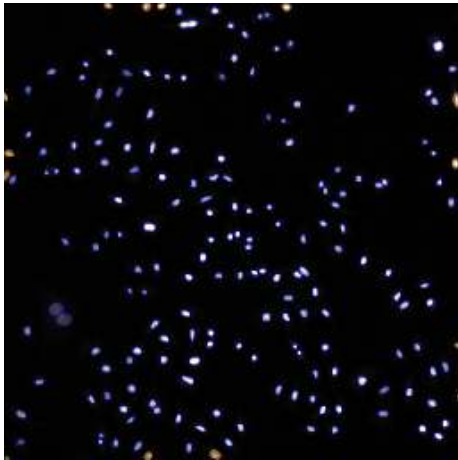
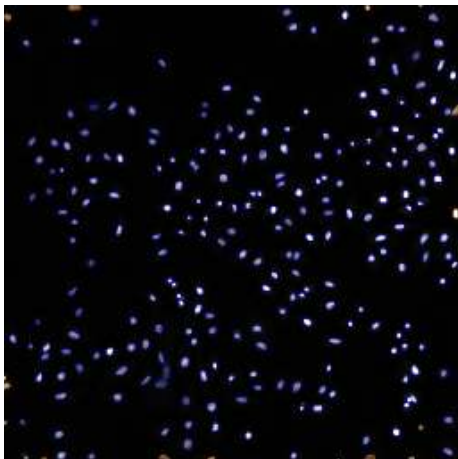
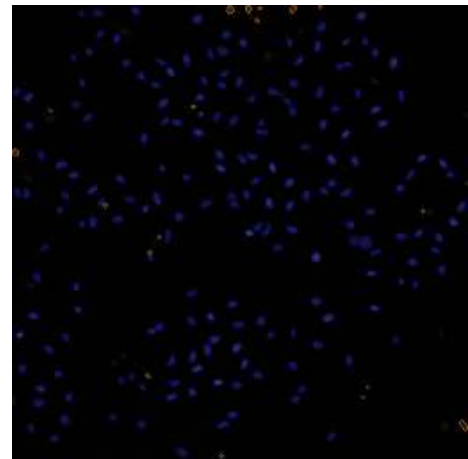
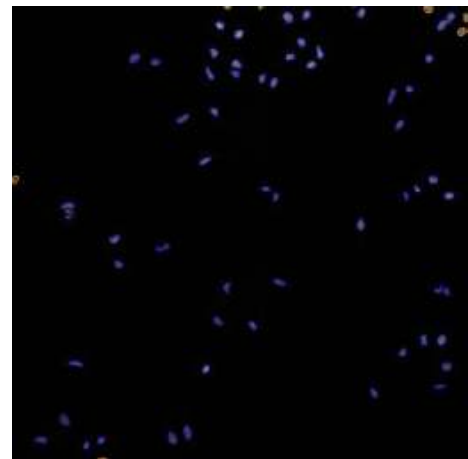
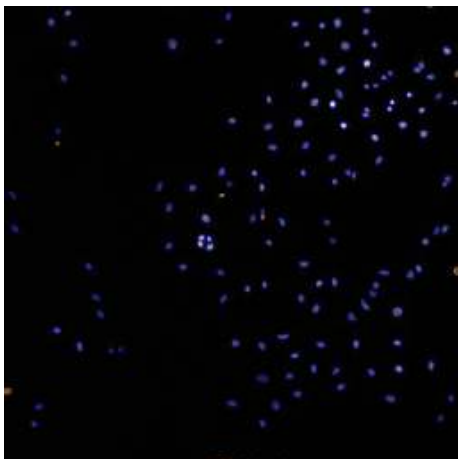


FeCl_3 0.3 mg/mL Well D5



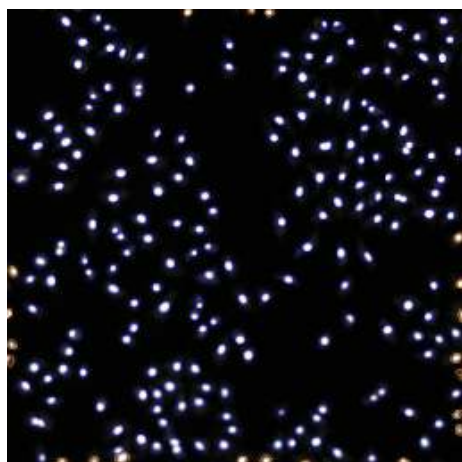
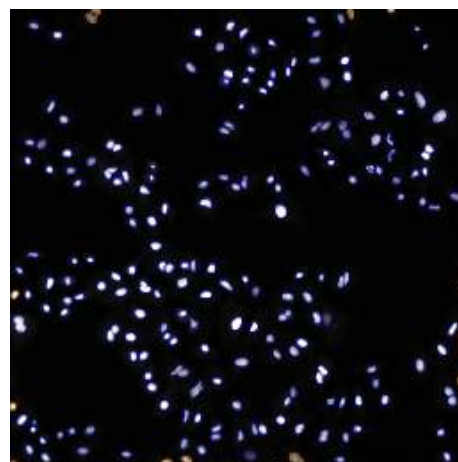
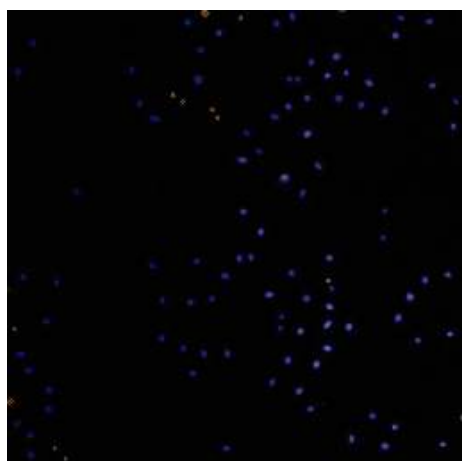
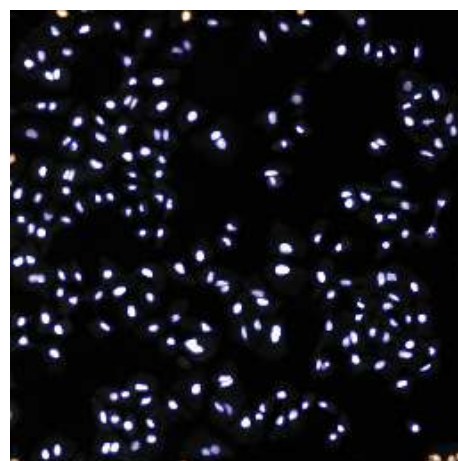
9.5.4.3 PI-*b*-PEO-CHO

ROS -0137, afterwards stained with Hoechst; 10x objective

CHO 0.1 μ M Well B8CHO 1 μ M Well C7CHO 0.1 μ M Well C8CHO 0.1 μ M Well D8

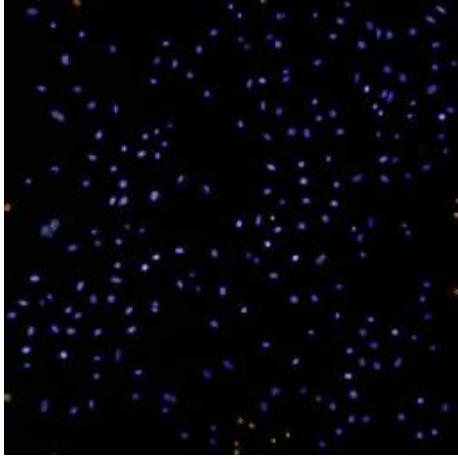
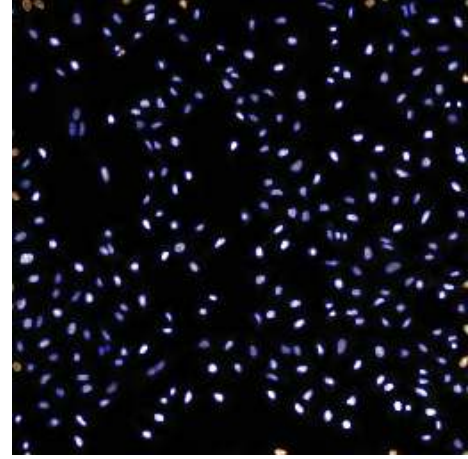
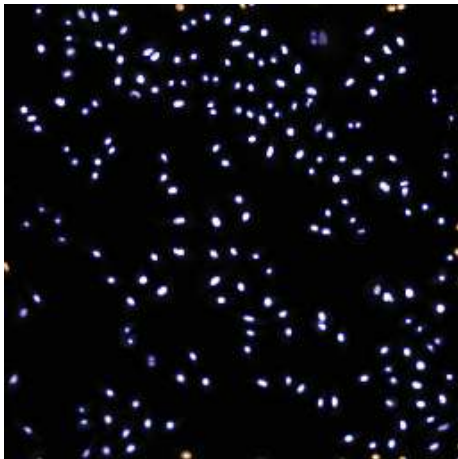
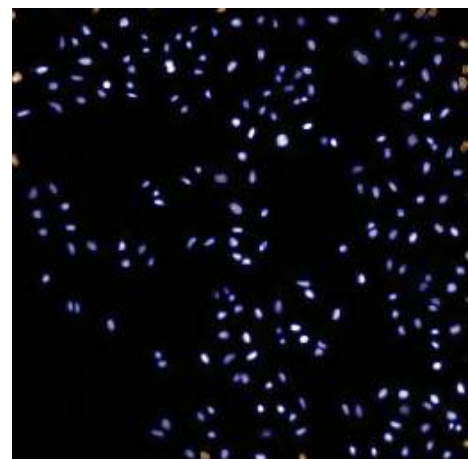
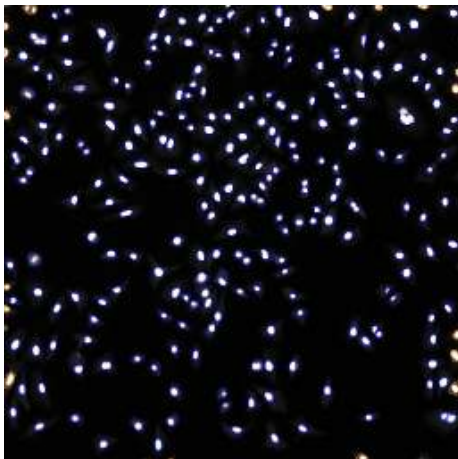
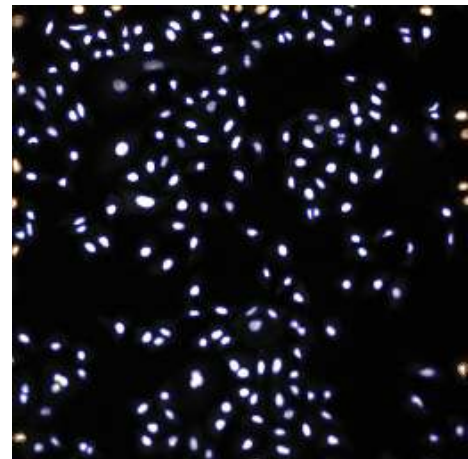
9.5.4.4 PI-*b*-PEO-NH₂

ROS -0137, afterwards stained with Hoechst; 10x objective

NH₂ 1 μM Well B9NH₂ 0.1 μM Well B10NH₂ 1 μM Well C9NH₂ 0.1 μM Well C10NH₂ 1 μM Well D9NH₂ 0.1 μM Well D10

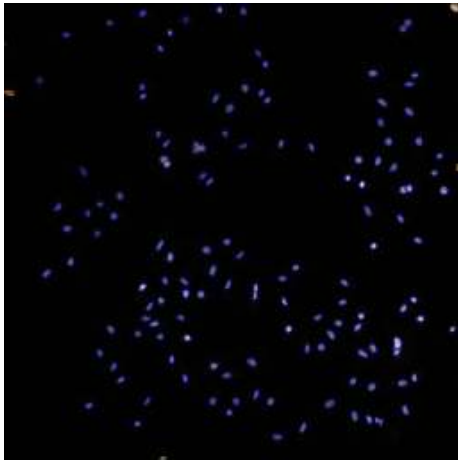
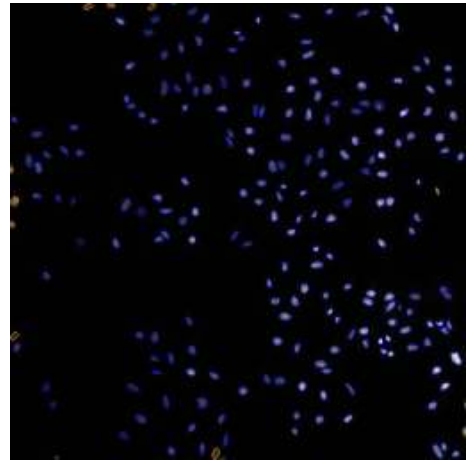
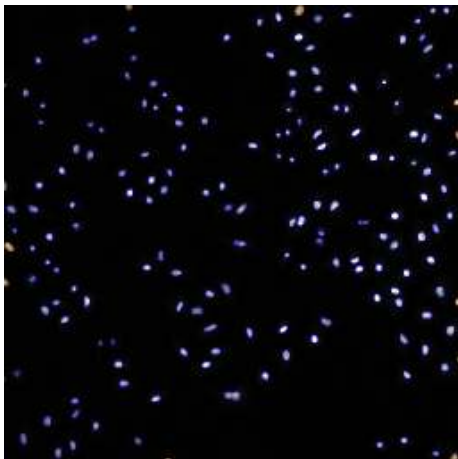
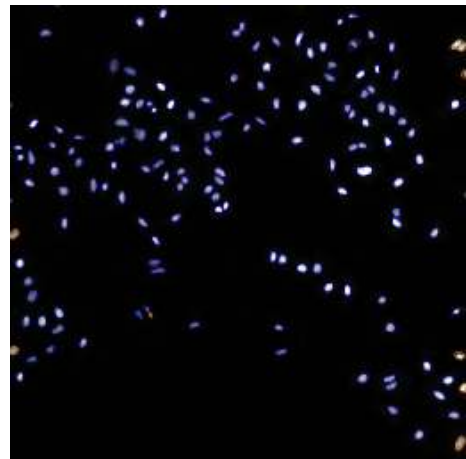
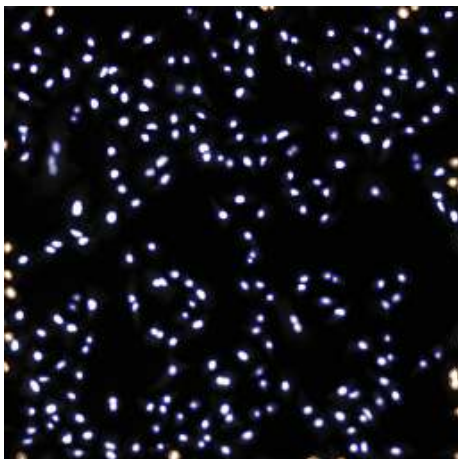
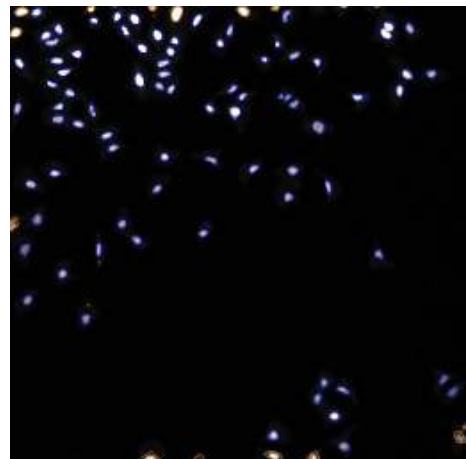
9.5.4.5 PI-*b*-PEO-OH

ROS -0137, afterwards stained with Hoechst; 10x objective

OH 1 μ M Well E2OH 0.1 μ M Well E3OH 1 μ M Well F2OH 0.1 μ M Well F3OH 1 μ M Well G2OH 0.1 μ M Well G3

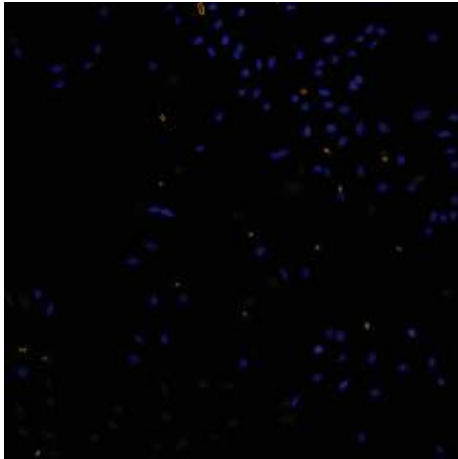
9.5.4.6 PI-*b*-PEO-COOH

ROS -0137, afterwards stained with Hoechst; 10x objective

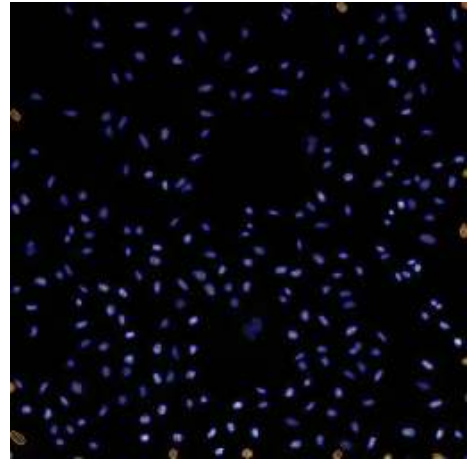
COOH 1 μ M Well E4COOH 0.1 μ M Well E5COOH 1 μ M Well F4COOH 0.1 μ M Well F5COOH 1 μ M Well G4COOH 0.1 μ M Well G5

9.5.4.7 Controll with only cells

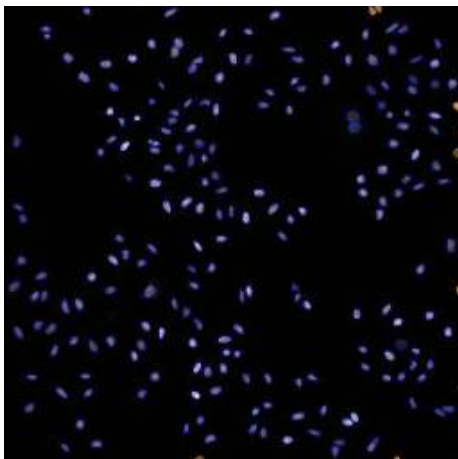
ROS -0137, afterwards stained with Hoechst; 10x objective



controll B2



controll C2

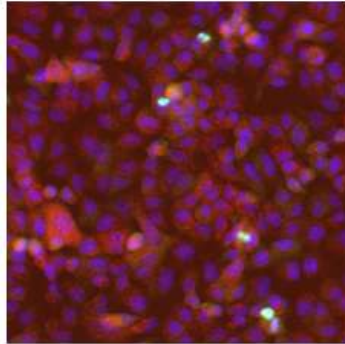


controll D2

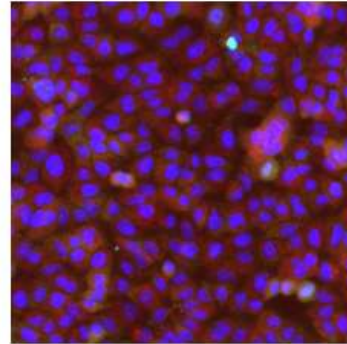
9.5.5 Cellomics pictures (CAN) using cytotoxicity kit 2

A549 cells, after 17 hours of incubation

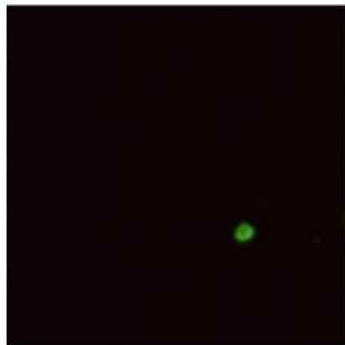
9.5.5.1 Valinomycin



control Well F6



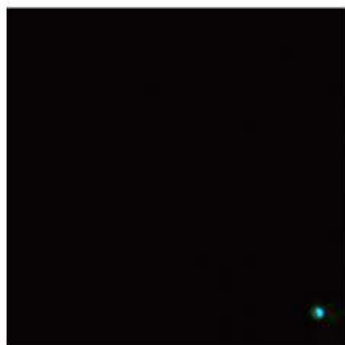
control Well G6



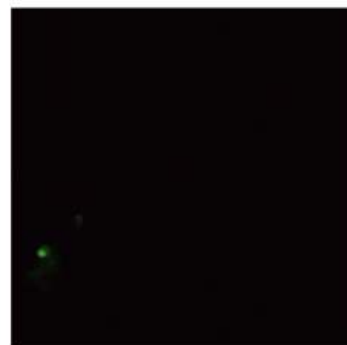
Valinomycin 100 μ M Well B2



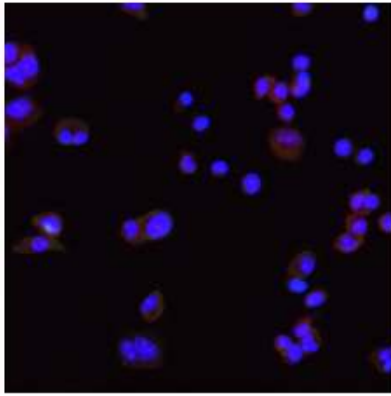
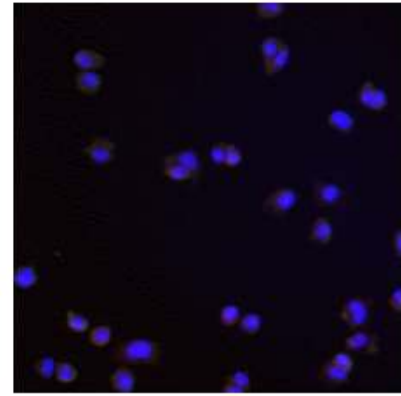
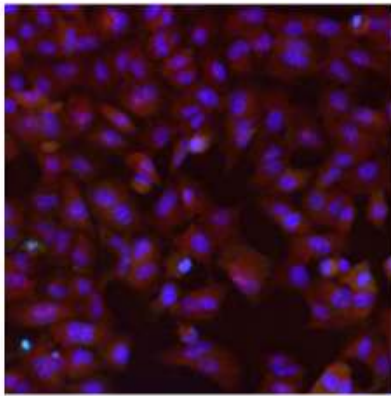
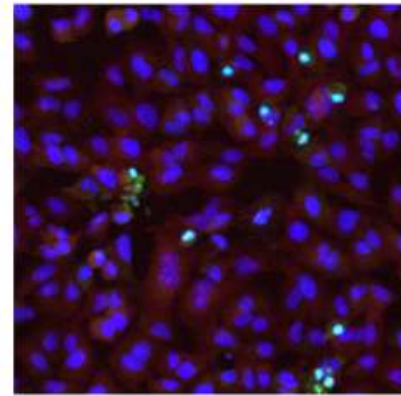
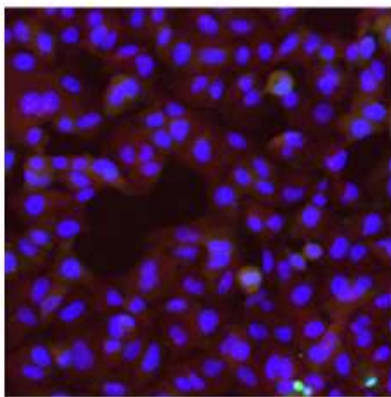
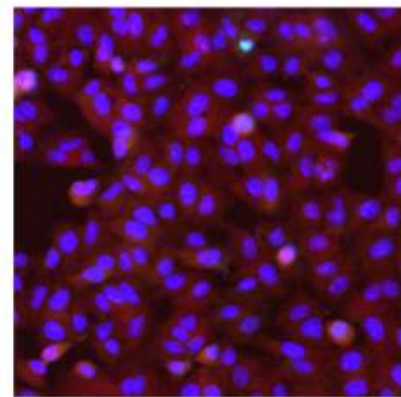
Valinomycin 100 μ M Well C2

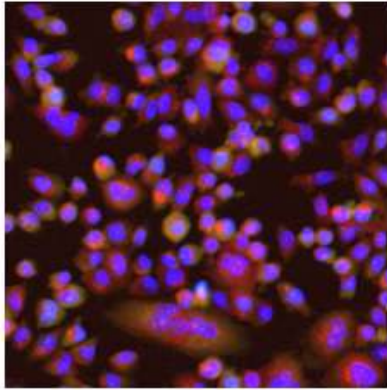


Valinomycin 80 μ M Well B3

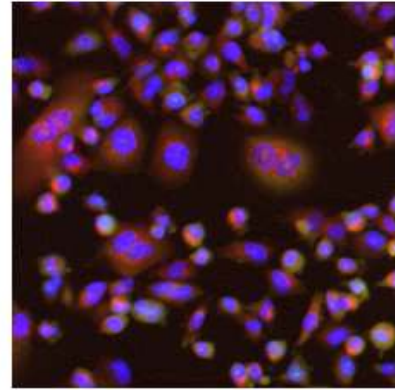


Valinomycin 80 μ M Well C3

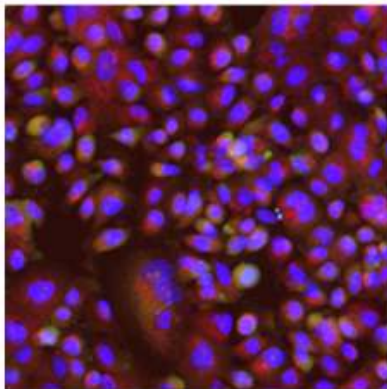
Valinomycin 50 μ M Well B4Valinomycin 50 μ M C4Valinomycin 20 μ M Well B5Valinomycin 20 μ M Well C5Valinomycin 10 μ M Well B6Valinomycin 10 μ M Well C6

9.5.5.2 CdCl_2 & FeCl_3 control

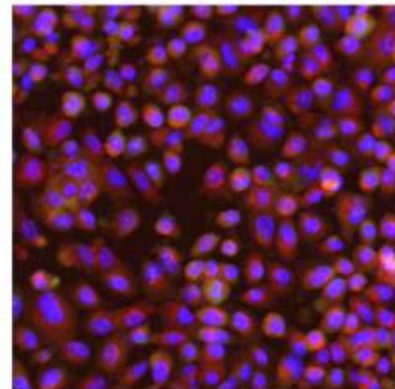
CdCl_2 100 μM Well D2



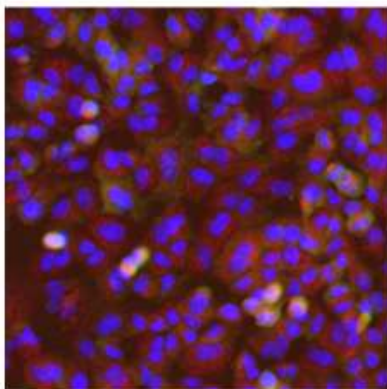
CdCl_2 100 μM Well E2



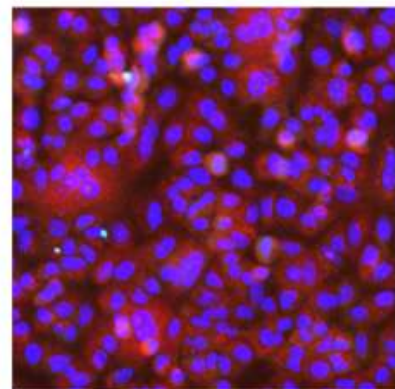
CdCl_2 80 μM Well D3



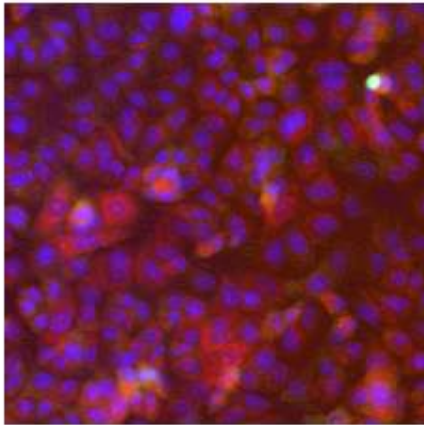
CdCl_2 80 μM Well E3



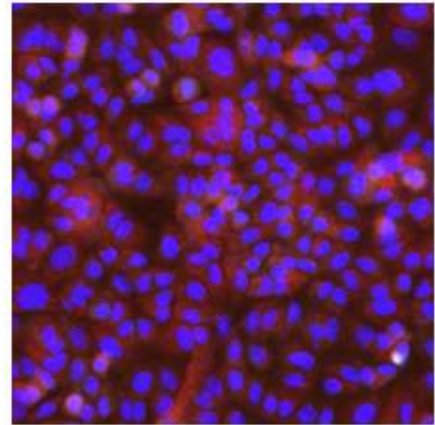
CdCl_2 50 μM Well D4



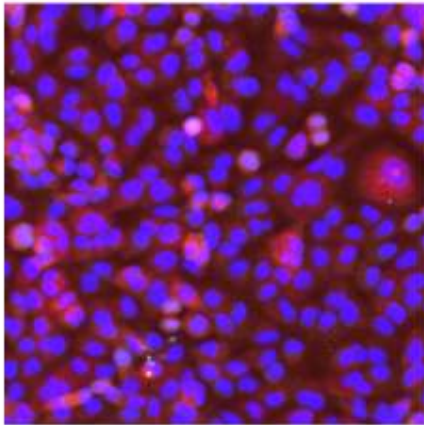
CdCl_2 50 μM Well E4



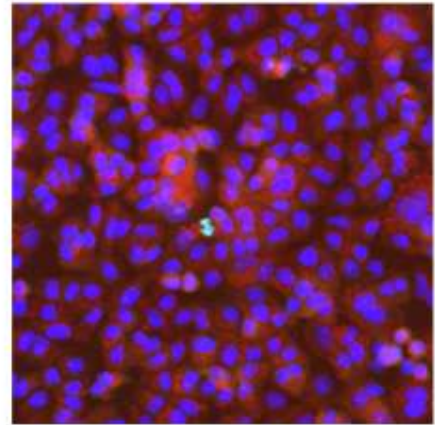
CdCl₂ 20 μM Well D5



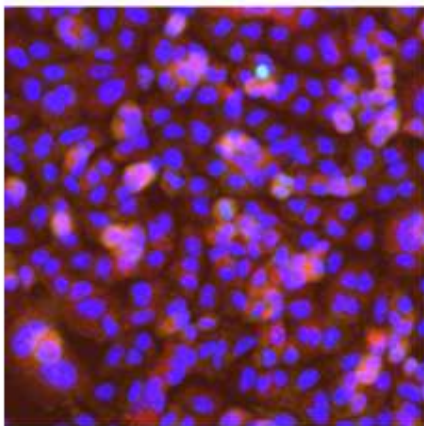
CdCl₂ 20 μM Well E5



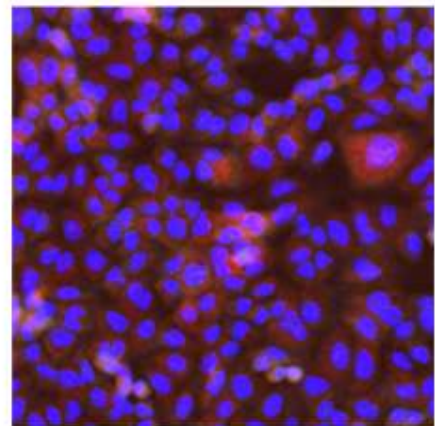
CdCl₂ 10 μM Well D6



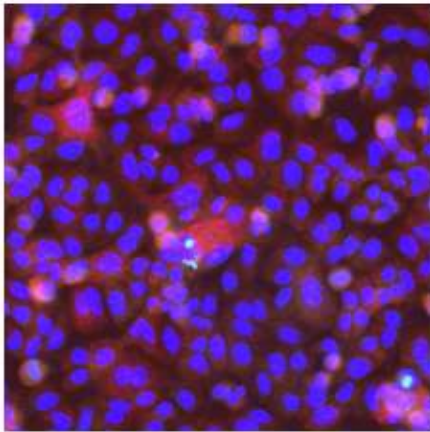
CdCl₂ 10 μM Well E6



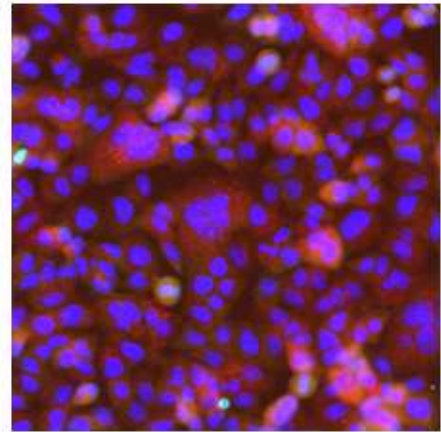
FeCl₃ 100 μM Well F2



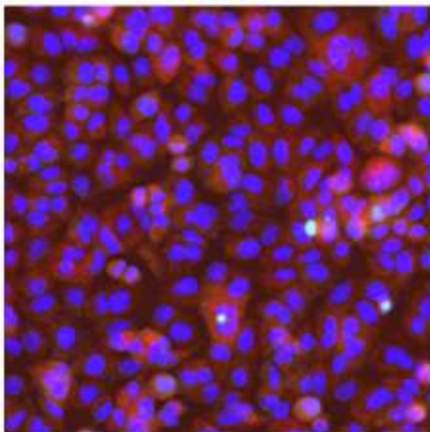
FeCl₃ 100 μM Well G2



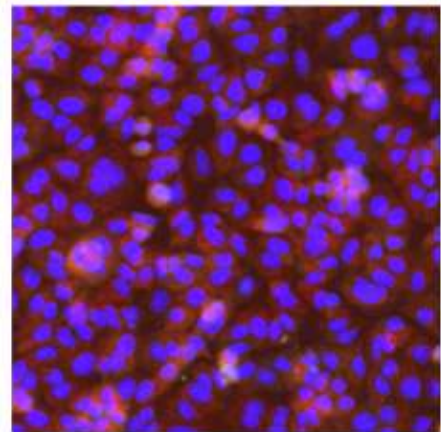
FeCl₃ 80 μM Well F3



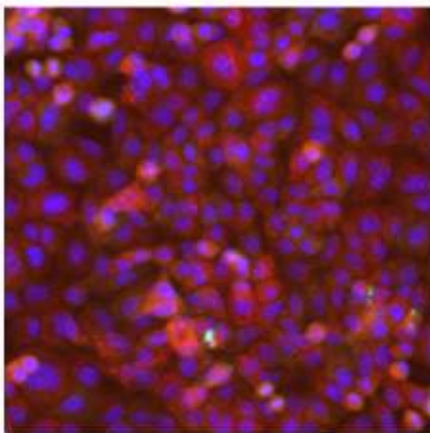
FeCl₃ 80 μM Well G3



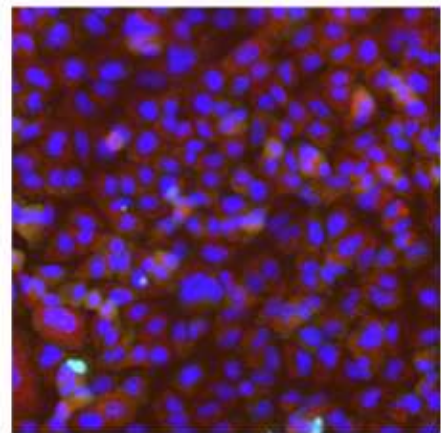
FeCl₃ 50 μM Well F4



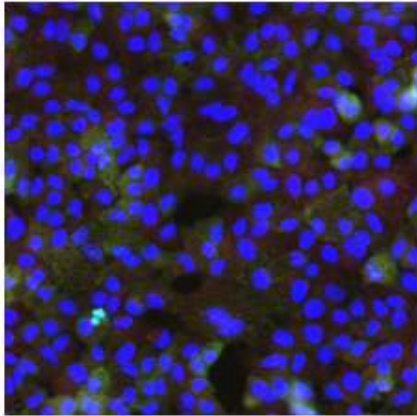
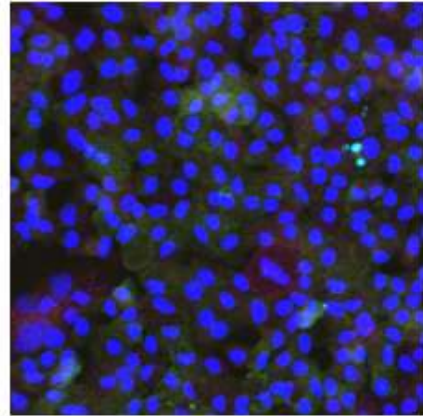
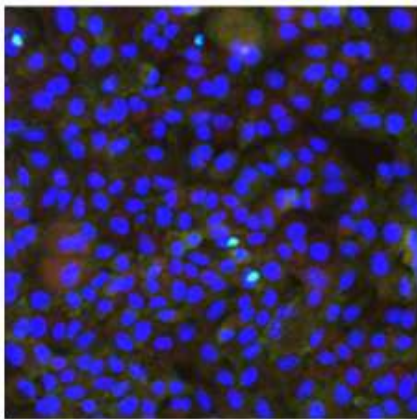
FeCl₃ 50 μM Well G4



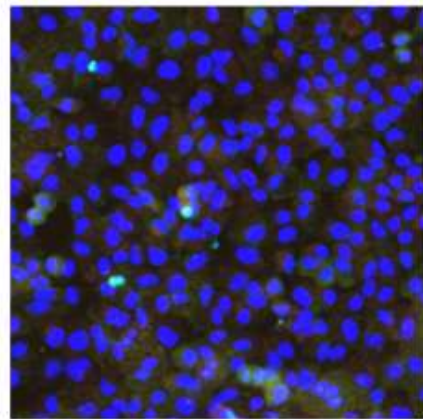
FeCl₃ 20 μM Well F5



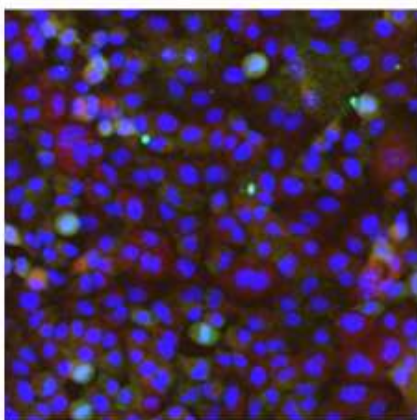
FeCl₃ 20 μM Well G5

9.5.5.3 PI-*b*-PEO-CHOCHO 1 μ M Well B7CHO 1 μ M Well C7

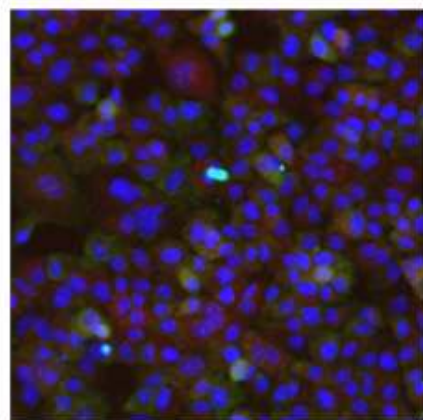
CHO 800 nM Well B8



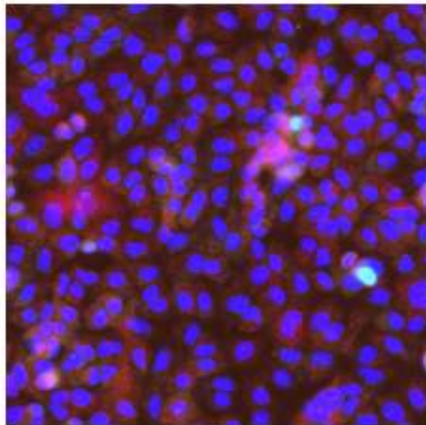
CHO 800 nM Well C8



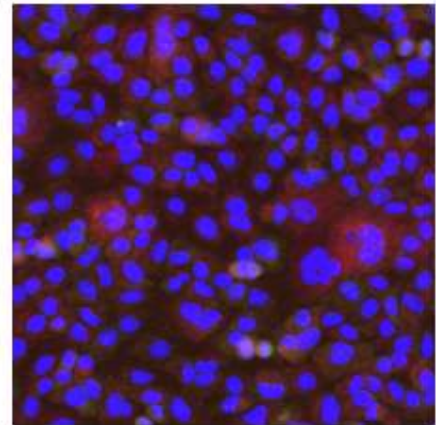
CHO 500 nM Well B9



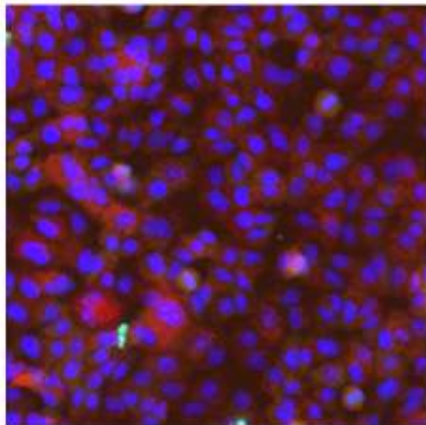
CHO 500 nM Well C9



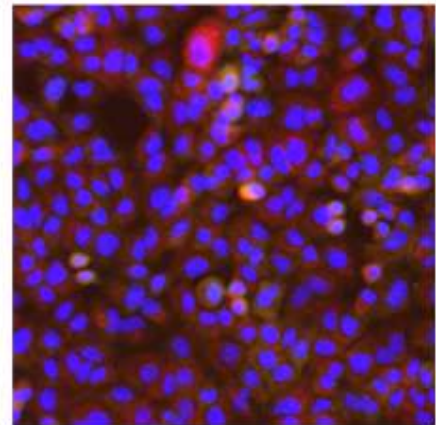
CHO 200nM Well B10



CHO 200nM Well C10

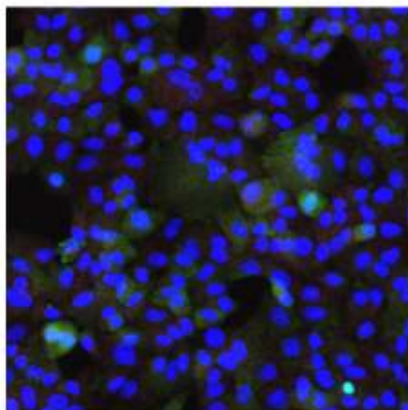


CHO 100nM Well B11

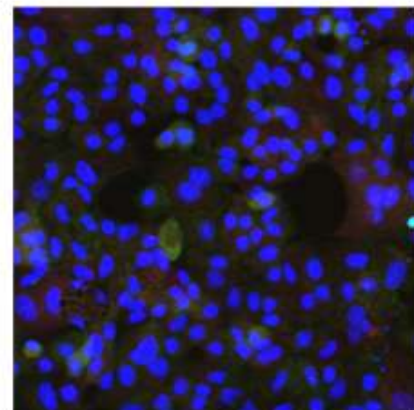


CHO 100nM Well C11

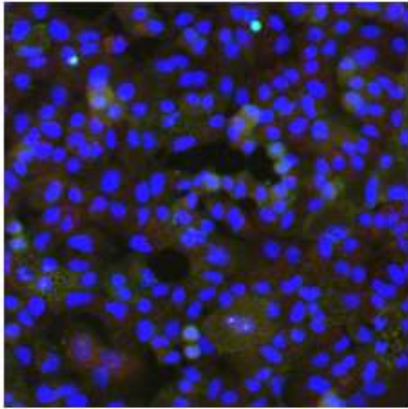
9.5.5.4 PI-*b*-PEO-OH



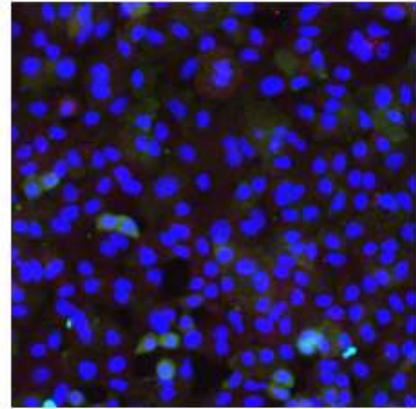
OH 1µM Well D7



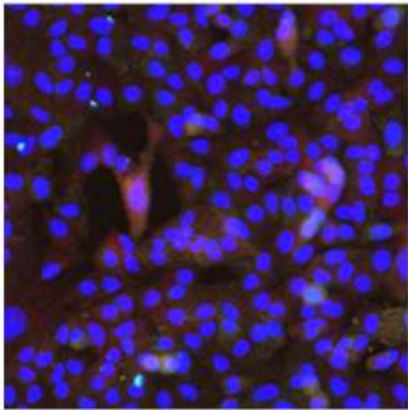
OH 1µM Well E7



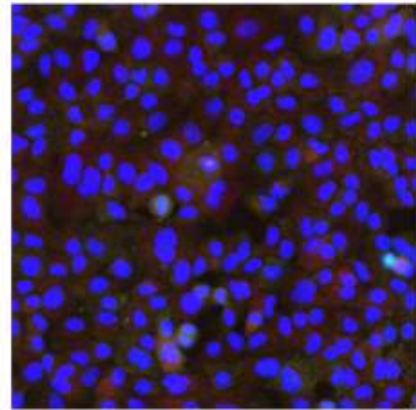
OH 800 nM Well D8



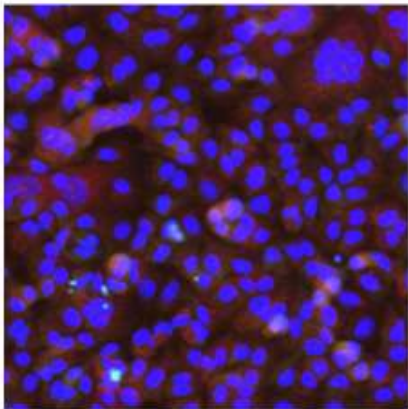
OH 800 nM Well E8



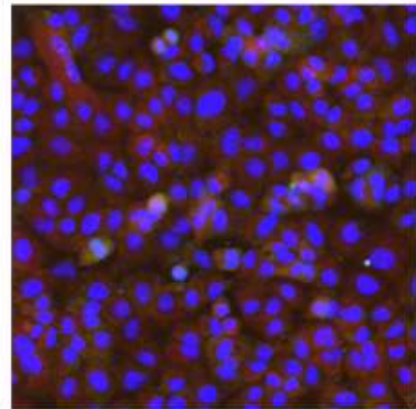
OH 500 nM Well D9



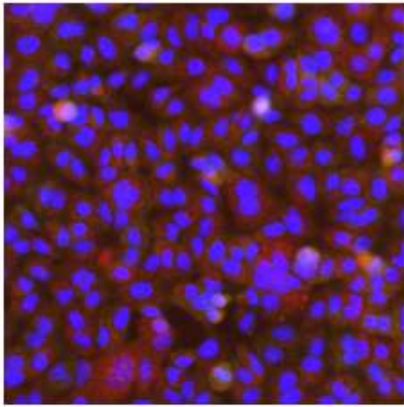
OH 500 nM Well E9



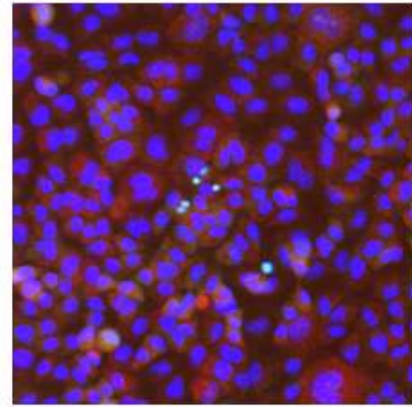
OH 200 nM Well D10



OH 200 nM Well E10

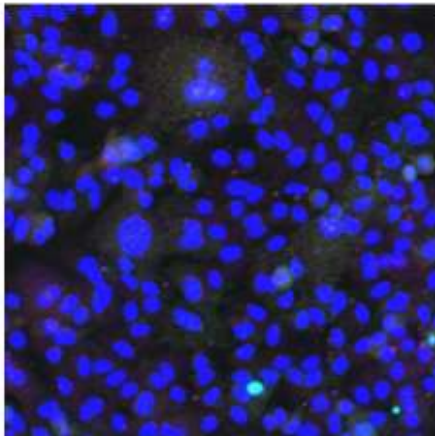


OH 100 nM Well D11

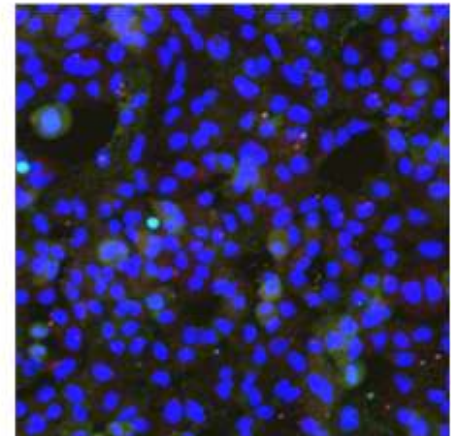


OH 100 nM Well E11

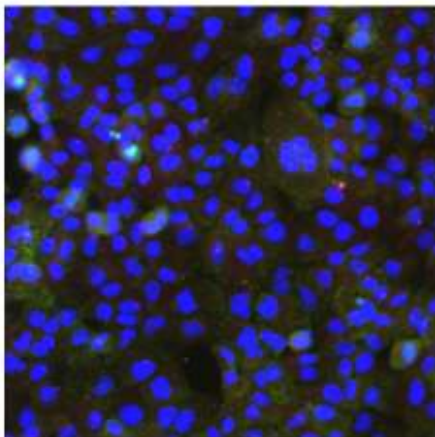
9.5.5.5 PI-*b*-PEO-COOH



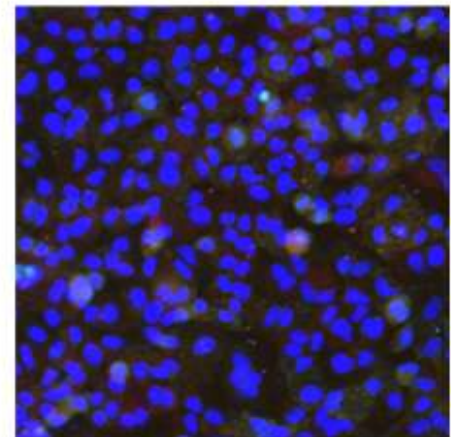
COOH 1 μM Well F7



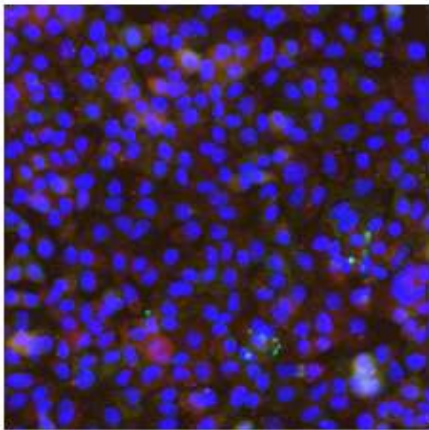
COOH 1 μM Well G7



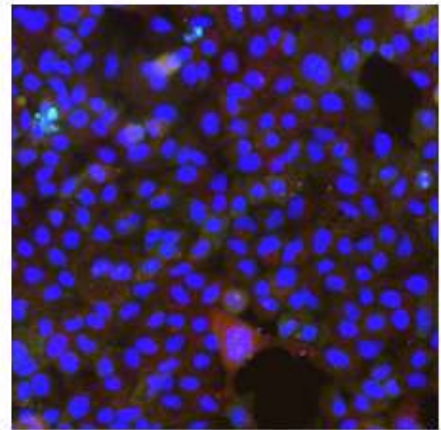
COOH 800 nM Well F8



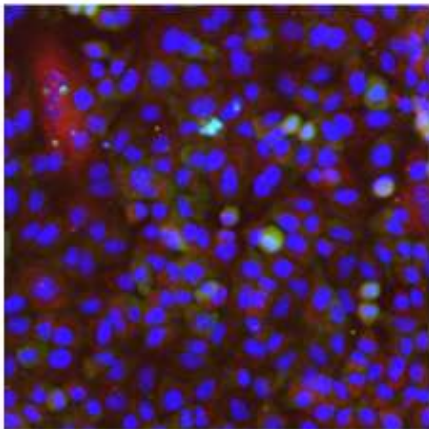
COOH 800 nM Well G8



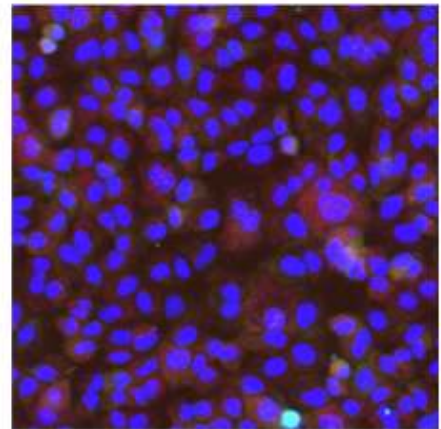
COOH 500 nM Well F9



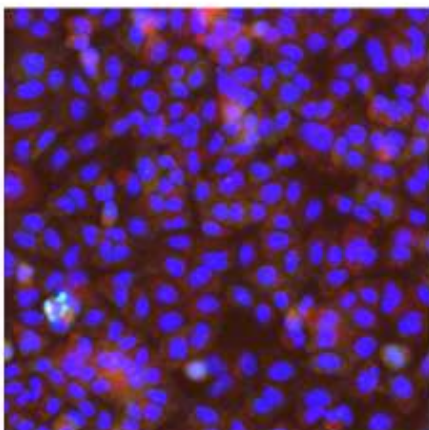
COOH 500 nM Well G9



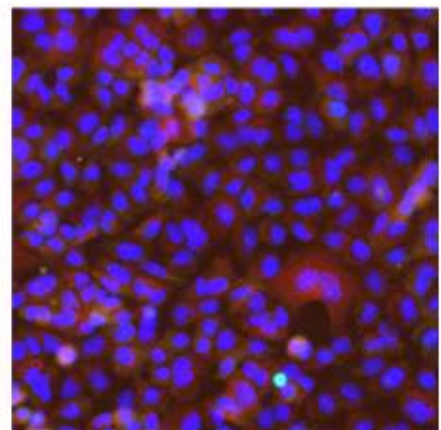
COOH 200 nM Well F10



COOH 200 nM Well G10



COOH 100 nM Well F11



COOH 100 nM Well G11

9.6 Used chemicals and their safety precaution information

Risk (R-) and safety precaution (S-) phrases used in the classification, packaging, labelling and provision of information on dangerous substances.

Substance	Hazard signs	R-phrases	S-phrases
Acetic acid	C	10-35	26-36/36/37/39-45
Acetic anhydride	C	10-20/22-34	26-36/37-45
Aceton	F, Xi	11-36-66-67	9-16-26
Allylamine	F, T, N	11-23/24/25-51/53	9-16-24/25-45-61
Amberlite® IR 120 (H ⁺)	Xi	26-36	36
Azobisisobutyronitrile	E, Xn	2-11-20/22-52/53	39-41-47-61
α -Bromoisobutyryl bromide	C	22-34	26-36/37/39-45
Cadmium acetate	Xn, N	20/21/22-50/53 45-46-60-61-25-26-	53-45-60-61
Cadmium(II)chlorid	T+, N	48/23/25-50/53	26-36/37/39-45
1,1'-Carbonyldiimidazol	C	22-34	36/37
CDCl ₃	Xn	22-38-40-48/20/22	36-37
Chloroform	Xn	22-38-40-48/20/22	26-36 7/8-26-36/37/39-
Copper(I) iodide	Xn, N	22-36/37/38-50/53	43.6-45
Cresyl violet perchlorate	Xi	36/37/38	26-36
Dess-Martin-periodinane	Xn	20/21/22-36/37/38	26-60
1,4 Diaza-bicyclo[2.2.2]octane	F, Xn	11-22-36/37/38-52/53	23-24/25-36/37
Dichlormethan	Xn	40	16-26-36
<i>N,N'</i> -Dicyclohexylcarbodiimid	T	22-24-41-43	53-45
Diethoxymethan	F, Xi	11-36/37/38	9-16-29-33
Diethyl ether	F+, Xn	12-19-22-66	26-28-36/37/39-45
<i>N</i> -(3-Dimethylamino-propyl)- <i>N'</i> -ethylcarbodiimide hydrochloride 4-	Xi	37/38-41	9-16-29-33-36/37-61-62
Dimethylaminopyridine	T+	25-27-36/37/38	26
<i>N,N</i> -Dimethylformamid	T	61-20/21-36	9-16-29-33-61-62
Dimethylsulfoxid	Xi	36/37/38	26-34
Dodecyltrimethylammoniumbromid	Xi	36/37/38	26-39
Epichlorohydrine	T	45-10-23/24/25-34-43	23-26-45

Substance	R-phrases	S-phrases	Hazard signs
1,2-Ethandithiol	T	10-21/22-23-36	26-36/37-45
Ethanol	F	11	26-36/37/39-45
Ethanolamine	C	20/21/22-34	16-23-36
Ethyl acetate	F, Xi	11-36-66-67	23-26-36/37/39-45
Ethylendiamine	C	10-21/22-34-42/43	26-61
Ethylenediaminetetra- acetic acid	Xi	36-52/53 12-23-36/37/38-45-	26-36/37/39-45
Ethylene oxide	F+, T	46	45-53-61
Hexadecylamine	C	34 11-38-48/20-51/53-	22-26-36/37/39-45
<i>n</i> -Hexane	F, Xn, N	62-65-67	22-24/25
Hydrochloric acid > 25 %	Xn, N	34-37	9-16-36-38-45-61
Hydrogen bromide (33%)	C	35-37	(2-)60-61
Hydrogen sulfide	F+, T+, N	12-26-50	26-36
<i>N</i> -Hydroxysuccinimid			24-26-37/39-45
Imidazole	C	22-34	22
Iron(III) chloride	Xn	22-38-41	53-45
Isoprene	F+, T	12-52/53-68	26-27-36/37/39
Lithium aluminium hydride	F, C	14/15-35 11-23/24/25-	7-16-36/37-45
Methanol	F, T	39/23/24/25	28-45-60-61
Oleyl amine	C; Xn	22-34	16-26-36
Pentafluorophenyl trifluoroacetate	Xi	10-36/37/38	16-26-36
<i>n</i> -Pentane	F+, Xn, N	12-51/53-65-66-67 11-38-48/20-51/53-	26-37/39
Petroleum ether 50-70	F, Xn, N	62-65.67	
Phenylacetic acid-4- boronic acid pinacol ester	Not completely proved substance		26-28-36-45-61 16-26-33-36/37/39-
Propargyl alcohol	T, N	10-23/24/25-34-51/53	45
Propargylamine	F, T	11-22-24-34	26-28
Pyridine	F, Xn	11-20/21/22	53-45-60-61
Pyridiniumchlorochromat	O, T, N	49-8-43-50/53	53-45-60-61

Substance	R-phrases	S-phrases	Hazard signs
Pyridiniumdichromate	T	49-43-50/53	26-36/37/39-45
Selenium	T	23/25-33-53	20/21-28-45-61
Silica gel 40			22-24/25-26-61
Sodium azide	T+, N	28-32-50/53	26-36/37
Sodium dodecyl benzene sulfonate	Xn	22-37/38-41	16-26-36
Sodium dodecyl sulfate	F, Xn	11-21/22-36/37/39-45	8-16-26-43-45 7/8-26-36/37/39-43.6-45
Sodium ethoxide	F, C	11-14-34	43.6-45
Sodium hydride-Suspension (60% in Paraffin)	F, C	15-34	26-37/39-45
Sodium hydroxide	C	35	
Sodium sulfate	No dangerous product under the directive 67/548/EWG		26-36/37/39
Succinic anhydrid	Xi	26/37	26-36/37/39-45
Tetrabutylammoniumiodide	Xn	22-36/37/38	16-29-33
<i>n</i> -Tetradecylphosphonic acid	Xn	36/37/38	
Tetrahydrofuran	F, Xi	11-19-36/37	16-25-29-33
Toluene	Xn, F	Nov 20	26-36/37/39-45 3-16-26-29-36/37/39-45
Tosylchloride	C	34	36/37/39-45
Triethylamine	F, C	11-20/21/22-35	26-36/37/39-45
Trioctylphosphan	C	34	26-39
Tri- <i>n</i> -octylphosphine oxide	Xi	38-41	36/37-60
Tri- <i>n</i> -phenyl phosphine	Xn	22-43-53	26-60-61
Zinc acetate	Xn, N	22-36-50/53	22-26-36/37/39-38
Zinc stearate	Xi	37	45-53

9.6.1 Risk phrases (R-Phrases)

- R1: Explosive when dry
- R2: Risk of explosion by shock, friction fire or other sources of ignition
- R3: Extreme risk of explosion by shock friction, fire or other sources of ignition
- R4: Forms very sensitive explosive metallic compounds
- R5: Heating may cause an explosion
- R6: Explosive with or without contact with air
- R7: May cause fire
- R8: Contact with combustible material may cause fire
- R9: Explosive when mixed with combustible material
- R10: Flammable
- R11: Highly flammable
- R12: Extremely flammable
- R13: Extremely flammable liquefied gas
- R14: Reacts violently with water
- R15: Contact with water liberates highly flammable gases
- R16: Explosive when mixed with oxidising substances
- R17: Spontaneously flammable in air
- R18: In use, may form flammable/explosive vapour-air mixture
- R19: May form explosive peroxides
- R20: Harmful by inhalation
- R21: Harmful in contact with skin
- R22: Harmful if swallowed
- R23: Toxic by inhalation
- R24: Toxic in contact with skin
- R25: Toxic if swallowed
- R26: Very toxic by inhalation
- R27: Very toxic in contact with skin
- R28: Very toxic if swallowed
- R29: Contact with water liberates toxic gas
- R30: Can become highly flammable in use

-
- R31: Contact with acids liberates toxic gas
 - R32: Contact with acids liberates very toxic gas
 - R33: Danger of cumulative effects
 - R34: Causes burns
 - R35: Causes severe burns
 - R36: Irritating to eyes
 - R37: Irritating to respiratory system
 - R38: Irritating to skin
 - R39: Danger of very serious irreversible effects
 - R40: Possible risk of irreversible effects
 - R41: Risk of serious damage to eyes
 - R42: May cause sensitisation by inhalation
 - R43: May cause sensitisation by skin contact
 - R44: Risk of explosion if heated under confinement
 - R45: May cause cancer
 - R46: May cause heritable genetic damage
 - R47: May cause birth defects
 - R48: Danger of serious damage to health by prolonged exposure
 - R49: May cause cancer by inhalation
 - R50: Very toxic to aquatic organisms
 - R51: Toxic to aquatic organisms
 - R52: Harmful to aquatic organisms
 - R53: May cause long-term adverse effects in the aquatic environment
 - R54: Toxic to flora
 - R55: Toxic to fauna
 - R56: Toxic to soil organisms
 - R57: Toxic to bees
 - R58: May cause long-term adverse effects in the environment
 - R59: Dangerous to the ozone layer
 - R60: May impair fertility
 - R61: May cause harm to the unborn child
 - R62: Possible risk of impaired fertility

R63: Possible risk of harm to the unborn child

R64: May cause harm to breastfed babies

9.6.2 Combination of risks

R14/15: Reacts violently with water, liberating highly flammable gases

R15/29: Contact with water liberates toxic, highly flammable gas

R20/21: Harmful by inhalation and in contact with skin

R20/21/22: Harmful by inhalation, in contact with skin and if swallowed

R20/22: Harmful by inhalation and if swallowed

R21/22: Harmful in contact with skin and if swallowed

R23/24: Toxic by inhalation and in contact with skin

R23/24/25: Toxic by inhalation, in contact with skin and if swallowed

R23/25: Toxic by inhalation and if swallowed

R24/25: Toxic in contact with skin and if swallowed

R26/27: Very toxic by inhalation and in contact with skin

R26/27/28: Very toxic by inhalation, in contact with skin and if swallowed

R26/28: Very toxic by inhalation and if swallowed

R27/28: Very toxic in contact with skin and if swallowed

R36/37: Irritating to eyes and respiratory system

R36/37/138: Irritating to eyes, respiratory system and skin

R36/38: Irritating to eyes and skin

R37/38: Irritating to respiratory system and skin

R42/43: May cause sensitization by inhalation and skin contact

R48/20: Harmful: danger of serious damage to health by prolonged exposure

R48/20/21: Harmful: danger of serious damage to health by prolonged exposure through inhalation and in contact with the skin

R48/20/21/22: Harmful: danger of serious damage to health by prolonged exposure through inhalation, in contact with skin and if swallowed

R48/20/22: Harmful: danger of serious damage to health by prolonged exposure through inhalation, and if swallowed

- R48/21: Harmful: danger of serious damage to health by prolonged exposure in contact with skin
- R48/21/22: Harmful: danger of serious damage to health by prolonged exposure in contact with skin and if swallowed
- R48/22: Harmful: danger of serious damage to health by prolonged exposure if swallowed
- R48/23: Toxic: danger of serious damage to health by prolonged exposure through inhalation
- R48/23/24: Toxic: danger of serious damage to health by prolonged exposure through inhalation and in contact with skin
- R48/23/24/25: Toxic: danger of serious damage to health by prolonged exposure through inhalation, in contact with skin and if swallowed
- R48/23/25: Toxic: danger of serious damage to health by prolonged exposure through inhalation and if swallowed
- R48/24: Toxic: danger of serious damage to health by prolonged exposure in contact with skin
- R48/24/25: Toxic: danger of serious damage to health by prolonged exposure in contact with skin and if swallowed
- R48/25: Toxic: danger of serious damage to health by prolonged exposure if swallowed
- R50/53: Very toxic to aquatic organisms, may cause long term adverse effects in the aquatic environment
- R51/53: Toxic to aquatic organisms, may cause long term adverse effects in the aquatic environment
- R52/53: Harmful to aquatic organisms, may cause long-term adverse effects in the aquatic environment

9.6.3 Safety precaution phrases (S-Phrases)

- S1: Keep locked up
- S2: Keep out of reach of children
- S3: Keep in a cool place

-
- S4: Keep away from living quarters
 - S5: Keep contents under ... (appropriate liquid to be specified by the manufacturer)
 - S6: Keep under ... (inert gas to be specified by the manufacturer)
 - S7: Keep container tightly closed
 - S8: Keep container dry
 - S9: Keep container in a well ventilated place
 - S12: Do not keep the container sealed
 - S13: Keep away from food, drink and animal feeding stuffs
 - S14: Keep away from ... (incompatible materials to be indicated by the manufacturer)
 - S15: Keep away from heat
 - S16: Keep away from sources of ignition-No Smoking
 - S17: Keep away from combustible material
 - S18: Handle and open container with care
 - S20: When using do not eat or drink
 - S21: When using, do not smoke
 - S22: Do not breathe dust
 - S23: Do not breathe gas/fumes/vapour/spray (appropriate wording to be specified by manufacturer)
 - S24: Avoid contact with skin
 - S25: Avoid contact with eyes
 - S26: In case of contact with eyes, rinse immediately with plenty of water and seek medical advice
 - S27: Take off immediately all contaminated clothing
 - S28: After contact with skin, wash immediately with plenty of ... (to be specified by the manufacturer)
 - S29: Do not empty into drains
 - S30: Never add water to this product
 - S33: Take precautionary measures against static discharges
 - S34: Avoid shock and friction
 - S35: This material and its container must be disposed of in a safe way
 - S36: Wear suitable protective clothing
 - S37: Wear suitable gloves

-
- S38: In case of insufficient ventilation, wear suitable respiratory equipment
- S39: Wear eye/face protection
- S40: To clean the floor and all objects contaminated by this material use (to be specified by the manufacturer)
- S41: In case of fire and/or explosion do not breath fumes
- S42: During fumigation/spraying wear suitable respiratory equipment (appropriate wording to be specified by the manufacturer)
- S43: In case of fire, use ... (indicate in the space the precise type of fire fighting equipment. If water increases the risk, add "never use water")
- S44: If you feel unwell, seek medical advice (show the label where possible)
- S45: In case of accident or if you feel unwell, seek medical advice immediately (show the label where possible)
- S46: If swallowed, seek medical advice immediately and show the container or label
- S47: Keep at temperature not exceeding ... °C (to be specified by the manufacturer)
- S48: Keep wetted with ... (appropriate material to be specified by the manufacturer)
- S49: Keep only in the original container
- S50: Do not mix with ... (to be specified by the manufacturer)
- S51: Use only in well-ventilated areas
- S52: Not recommended for interior use on large surface areas
- S53: Avoid exposure - obtain special instructions before use
- S54: Obtain the consent of pollution control authorities before discharging to waste-water treatment plants
- S55: Treat using the best available techniques before discharge into drains or the aquatic environment
- S56: Do not discharge into drains or the environment, dispose to an authorised waste collection point
- S57: Use appropriate containment to avoid environmental contamination
- S58: To be disposed of as hazardous waste
- S59: Refer to manufacturer/supplier for information on recovery/recycling
- S60: This material and/or its container must be disposed of as hazardous waste
- S61: Avoid release to the environment. Refer to special instructions / safety data sheet
- S62: If swallowed, do not induce vomiting: seek medical advice immediately and show the

container label

9.6.4 Combined safety phrases

- S1/2: Keep locked up and out of reach of children
- S3/9: Keep in a cool, well ventilated place
- S3/7/9: Keep container tightly closed in a cool, well ventilated place
- S3/14: Keep in a cool place away from ... (incompatible materials to be indicated by the manufacturer)
- S3/9/14: Keep in a cool, well-ventilated place away from ... (incompatible materials to be indicated by the manufacturer)
- S3/9/49: Keep only in the original container in a cool, well ventilated place
- S3/9/14/49: Keep only in the original container in a cool, well-ventilated place away from (incompatible materials to be indicated by the manufacturer)
- S3/9/49: Keep only in the original container in a cool, well ventilated place
- S3/14: Keep in a cool place away from ... (incompatible materials to be indicated by the manufacturer)
- S7/8: Keep container tightly closed and dry
- S7/9: Keep container tightly closed and in a well ventilated place
- S7/47: Keep container tightly closed and at a temperature not exceeding...°C (to be specified by manufacturer)
- S20/21: When using do not eat, drink or smoke
- S24/25: Avoid contact with skin and eyes
- S29/56: Do not empty into drains, dispose of this material and its container to hazardous or special waste collection point
- S36/37: Wear suitable protective clothing and gloves
- S36/37/39: Wear suitable protective clothing, gloves and eye/face protection
- S36/39: Wear suitable protective clothing, and eye/face protection
- S37/39: Wear suitable gloves and eye/face protection
- S47/49: Keep only in the original container at temperature not exceeding ...°C (to be specified by the manufacturer)

10 Erklärung

Hiermit erkläre ich an Eides statt, dass ich die vorliegende Arbeit selbständig verfasst und keine anderen als die angegebenen Quellen und Hilfsmittel benutzt habe.

Hiermit erkläre ich, dass ich vorher keine Promotionsversuche unternommen habe.

Elmar Pöselt